Title
Synthesis of Molecules and Materials Containing Boron Cluster Chalcogenides

Author
Mills, Harrison

Publication Date
2021

Peer reviewed|Thesis/dissertation

UNIVERSITY OF CALIFORNIA

Los Angeles

Synthesis of Molecules and Materials Containing Boron Cluster Chalcogenides

A dissertation submitted in partial satisfaction of the

requirements for the degree Doctor of Philosophy

in Chemistry

by

Harrison Anderson Mills

2021

ABSTRACT OF THE DISSERTATION

Synthesis of Molecules and Materials Containing Boron Cluster Chalcogenides

by

Harrison Anderson Mills

Doctor of Philosophy in Chemistry

University of California, Los Angeles, 2021

Professor Alexander Michael Spokoyny, Chair

This dissertation describes the exploration of icosahedral carboranes chalcogenides containing remarkably stable exopolyhedral B-S, B-Se and B-Te bonds. Specifically, we assess their synthesis, reactivity, and ability to act as tunable ligands for metal chalcogenide materials.

Chapter 1 provides a brief overview of carbon-based compounds containing C-S, C-Se, and C-Te bonds and their applications in organic chemistry, chemical biology, organometallic chemistry, and self-assembled materials. The synthesis and characteristic properties of icosahedral boron-rich clusters ($B_{12}H_{12}^{2-}$, $C_2B_{10}H_{12}$) are also discussed in addition to the synthesis and applications of clusters featuring exopolyhedral B-S, B-Se, and B-Te bonds.

Chapter 2 demonstrates the potential for Pd(II)-based precatalysts designed for rapid reduction to the catalytically active Pd(0) species in cross-coupling reactions with carboranes iodinated at the electron-rich boron vertices. Kumada-type cross-coupling between iodocarboranes and Grignard reagents with fast reaction times (< 2h) has been established. Suprisingly, this

method is entirely selective for boron-iodine bonds with no substitution observed and brominated boron vertices.

Chapter 3 explores the synthesis of boron vertex-centered radical precursors featuring exopolyhedral B-[B] ([B]: -$B(OH)_2$, -BF_3K) bonds and the reactivity of said carboranyl radicals. The introduction of exopolyhedral boron-based substituents to the electron-rich boron vertices is made possible by the palldium-catalyzed borylation of iodinated carboranes with a similar catalytic system implemented in chapter 2. The formed B-[B] bond is oxidatively unstable and can be heterolytically cleaved under electrochemical conditions or by inorganic oxidants. The transient carboranyl radical can undergo substitution mechanisms in the presence of several radical traps, affording products with exopolyhedral B-O, B-S, B-Se, B-Te, and B-C bonds.

Chapter 4 is an assessment of the electrophilic and nucleophilic reactivity of *meta*-carboranes containing exopolyhedral B-Se and B-Te bonds at the electron-rich boron vertices. Electrophilic selenyl(II), tellurenyl(II), and tellurenyl(IV) chlorides were prepared by the treatment of the respective biscarboranyl dichalcogenides with thionyl chloride. Despite the electron-rich environment imparted by the carborane, the selenyl(II) and tellurenyl(IV) reagents show good electrophilic reactivity in the presence of carbon-based nucleophiles (e.g. Girgnard reagents, alkene, alkyne, enolate). Futhermore, the isolation of an electron-rich boron-connected carborane tellurol has been reported for the first time, with remarkable air stability. The electron-rich carborane selenols and tellurols have been shown as competent nucleophiles in nucleophilic aromatic substitutions as well.

Chapter 5 highlights the potential for electron-rich carborane chalcogenols as electronically tunable, though sterically invariant, ligands for photoluminescent self-assembled metal chalcogenide materials. By changing between *meta*- and *ortho*-carborane based chalcogenols the

relative carborane dipole to the ligating substituent, in this case a selenolate or thiolate group, can be tuned both in orientation and magnitude. This tuning has then been used to modulate both the crystalline morphology and photophysical properties of copper(I) chalcogenolate microcrystals. In the case of one material, composed of copper(I) and *meta*-carboranyl selenolate, key structural information was obtained by applying microcrystal electron diffraction techniques, a first for this class of materials. The structural characterization revealed that the material was composed of an unprecedented Cu_4Se_4, with steric protection afforded by the *meta*-carboranyl substituents.

The dissertation of Harrison Anderson Mills is approved.

Robin L. Garrell

Miguel A. García-Garibay

Paul S. Weiss

Alexander Michael Spokoyny, Committee Chair

University of California, Los Angeles

2021

To my family and friends,
this would not have been possible without you all

TABLE OF CONTENTS

CHAPTER 4 – ICOSAHEDRAL *META*-CARBORANES CONTAINING EXOPOLYHEDRAL B-SE AND B-TE BONDS

CHAPTER 5 – STERICALLY INVARIANT CARBORANE-BASED LIGANDS FOR THE MORPHOLOGICAL AND ELECTRONIC CONTROL OF METAL ORGANIC CHALCOGENOLATE ASSEMBLIES

LIST OF FIGURES

ACKNOWLEDGMENTS

I first would like to take the time to give my heartfelt thanks to my mentor, Prof. Alexander Spokoyny. Joining your lab back during the summer of 2016, I feel that you took a chance on me, and I appreciate your patience with me as I learned how to be a better scientist and to be critical of my own research, writing, and presentations in order to hold myself to a higher standard than I ever would have on my own. I would also like to take the time to thank the other members of my thesis committee, Prof. Robin Garrell, Prof. Miguel García-Garibay, Prof. Paul Weiss. Your continued guidance of myself throughout my graduate student career has been invaluable to me.

At this point, I would be remiss to not thank current and past members of the Spokoyny group who have helped shaped me into the scientist I am today. While the 8 a.m. Monday group meetings were unbearable at times (particularly the day after daylight savings) I'll always remember the scientific discourse that was almost guaranteed when someone happened to show a slide with some perplexing data. I'm also thankful for all of the group outings that Alex helped facilitate that often ended up being the high points of any given month.

I'm not sure if I would have made it through graduate school were it not for the friendships provided by Nicholas Bernier, Kierstyn Anderson, Mary Waddington, Orlando Martinez, Fadi Alsarhan, QiaoQiao Wang, and Austin Ready. Prior to COVID essentially shutting everything down last year, I was lucky enough to see you all nearly every day of the week for several years and it has definitely taken some adjustment to not always have the ability to discuss science with you all (or have a board game night with).

Coming into graduate school, I didn't really know or appreciate what it meant to be a PhD chemist, and now that I'm leaving UCLA, I go between feeling ready and feeling unready for next step. But I'm most certainly leaving Los Angeles, with a competitive skill set I never expected

myself have. I'm optimistic for my future studies of polychalcogenophenes with the Seferos group at the University of Toronto, despite that Canadian winter I'll need to get used to in January.

Surprisingly, I've found this section of my dissertation to be the most difficult to write. I'm not typically known for emoting to those around me, but the past half a year has felt bittersweet. The company of Jessalyn Smith has made this final stretch of graduate school more bearable in addition to the company of her two dogs, Theo and Teddy, one of which has seemingly been sabotaging my dissertation progress by chewing through my monitor power cords. Lastly, I would like to thank my family. My parents, Russell and Leslie Mills, and younger brother, Edward Mills, have always been supportive of me and trust my judgment when making big decisions.

PREVIOUS PUBLICATION OF THESIS CHAPTERS

Chapter 2. This chapter is a version of Anderson, K. P.[Ψ]; **Mills, H. A.[Ψ]**; Mao, C.; Kirlikovali, K. O.; Axtell, J. C.; Rheingold, A. L.; Spokoyny, A. M.* "Improved Synthesis of Icosahedral Carboranes Containing Exohedral B-C and C-C Bonds" *Tetrahedron* **2019**, *75*, 187-191.

Chapter 3. This chapter is a version of **Mills, H. A.**; Martin, J. L.; Rheingold, A. L.; Spokoyny, A. M.* "Oxidative Generation of Boron-Centered Radicals in Carboranes" *J. Am. Chem. Soc.* **2020**, *142*, 4586-4591.

Chapter 4. This chapter is a version of **Mills, H. A.**; Alsarhan, F.; Ong, T.-C.; Gembicky, M.; Rheingold, A. L.; Spokoyny, A. M.* "Icosahedral Meta-Carboranes Containing Exopolyhedral B-Se and B-Te Bonds" *accepted*.

Chapter 5. This chapter is a version of **Mills, H. A.**; Jones, C. G.; Anderson, K. A.; Ready, A. D.; Djurovich, P. I.; Khan, S. I.; Hohman, J. N.*; Nelson. H. M.*; Spokoyny, A. M.* "Sterically Invariant Carborane-Based Ligands for the Morphological and Electronic Control of Metal Organic Chalcogenolate Assemblies" *to be submitted*.

VITA

Education

UCLA	Chemistry (Inorganic)	M.Sc. (2016-2018)
CSU Chico	Chemistry, Honors	B.S. (2013-2016)

Professional Experience

2020 – 2021 University of California Chemical Symposium (2021)

Chair

Current chair for UCCS 2021, a UC-wide conference with an emphasis on graduate student research attended, on average, by 100 attendees from all UC campuses and partners in industry, publishing, and national labs.

2019 – 2020 University of California Chemical Symposium (2020)

Treasurer and Executive Director of Finance

Treasurer for UCCS 2020 required the collection and distribution of funds for the conference (~$50,000), though the conference was unfortunately canceled due to COVID-19

2016 – 2021 Graduate Student Researcher, Department of Chemistry and Biochemistry, UCLA. Advisor: Alexander M. Spokoyny.

Research Specialization: The synthesis of novel boron clusters for applications in self-assembled materials.

2015 – 2016 Undergraduate Student Researcher, Department of Chemistry and Biochemistry, CSU Chico. Advisor: Sandrine J. Matiasek.

Research Specialization: Evaluating the removal of aqueous heavy metals from urban runoff by natural media.

Selected Awards and Honors

M. Frederick Hawthorne Inorganic Chemistry Dissertation Award (2021)

UCLA Dissertation Year Fellowship, UCLA (2020)

Thomas and Ruth Jacobs Excellence in Research Award, UCLA (2020)

Majeti-Alapati Fellowship, UCLA (2019)

Honors in Chemistry, CSU Chico (2016)

Peer-Reviewed Publications (ψ indicates co-first authorship)

1. **Mills, H. A.**; Jones, C. G.; Anderson, K. A.; Ready, A. D.; Djurovich, P. I.; Khan, S. I.; Hohman, J. N.*; Nelson. H. M.*; Spokoyny, A. M.* "Sterically Invariant Carborane-Based Ligands for the Morphological and Electronic Control of Metal Organic Chalcogenolate Assemblies" *to be submitted*
2. **Mills, H. A.**; Alsarhan, F.; Ong, T.-C.; Gembicky, M.; Rheingold, A. L.; Spokoyny, A. M.* "Icosahedral Meta-Carboranes Containing Exopolyhedral B-Se and B-Te Bonds" *accepted*
3. **Mills, H. A.**; Martin, J. L.; Rheingold, A. L.; Spokoyny, A. M.* "Oxidative Generation of Boron-Centered Radicals in Carboranes" *J. Am. Chem. Soc.* **2020**, *142*, 4586-4591
4. Messina, M. S.*; Graefe, C. T.; Chang, P.; Ebrahim, O. M.; Pathuri, R. S.; Bernier, N. A.; **Mills, H. A.**; Rheingold, A. L.; Frontiera, R. R.*; Maynard, H. D.*; Spokoyny, A. M.* "Carborane RAFT Agents as Tunable and Functional Molecular Probes for Polymer Materials" *Polym. Chem.* **2019**, *10*, 1660-1667
5. Anderson, K. P.$^{\Psi}$; **Mills, H. A.** $^{\Psi}$; Mao, C.; Kirlikovali, K. O.; Axtell, J. C.; Rheingold, A. L.; Spokoyny, A. M.* "Improved Synthesis of Icosahedral Carboranes Containing Exohedral B-C and C-C Bonds" *Tetrahedron* **2019**, *75*, 187-191
6. Serino, A. C.; Anderson, M. E.; Saleh, L. M. A.; Dziedzic, R. M.; **Mills, H.**; Heidenreich, L.; Dunn, B. S.; Spokoyny, A. M.; Weiss, P. S.* "Work Function Control of Germanium through Carborane-Based Carboxylic Acid Ligand Surface Passivation", *ACS Applied Materials and Interfaces* **2017**, *9*, 34592-34596

Public Presentations

1. "Boron-Centered Radical Reactivity in Carborane Clusters" University of Michigan and UCLA Inter-University Chemistry Symposium, online, October 2020 (oral)
2. "A One Electron Chemistry Approach to Boron Cluster Derivatization" UCLA Inorganic Departmental Seminar, UCLA, January 2020 (oral)
3. "Functionalization of Boron Clusters Using Two and One Electron Chemistry" Seaborg Symposium, CNSI, November 2019 (poster)
4. "Harnessing the Reactivity of Boron Vertex-Centered Radicals in Carborane Clusters" Organometallic Chemistry Gordon Research Conference (GRC), Salve Regina, July 2019 (poster)
5. "Harnessing the Reactivity of Boron Vertex-Centered Radicals in Carborane Clusters" Organometallic Chemistry Gordon Research Seminar (GRS), Salve Regina, July 2019 (poster)
6. "Luminescent CuI Nanomaterials Structured by Carborane Selenols" Southern California Inorganic Photophysics (SCIP), Catalina Island, April 2019 (oral)
7. "Harnessing the Reactivity of Boron Vertex-Centered Radicals in Carborane Clusters" University of California Chemical Symposium (UCCS), UCLA Lake Arrowhead Conference Center, March 2019 (oral)
8. "Harnessing the Reactivity of Boron Vertex-Centered Radicals in Carborane Clusters" SoCal Organometallics Meeting, USC, February 2019 (oral)
9. Seaborg Symposium, CNSI, November 2018 (poster)
10. "Evaluating the Removal of Aqueous Metals in Storm Runoff by Natural Media" CSU Chico, May 2016 (oral)
11. EPA 12th Annual People, Prosperity, and the Planet (P3) National Sustainable Design Expo, Washington D. C., April 2016 (poster)
12. This Way to Sustainability Conference XI, CSU Chico, March 2016 (oral)

CHAPTER 1 – INTRODUCTION TO SYNTHESIS OF MOLECULES AND MATERIALS CONTAINING BORON CLUSTERS CHALCOGENIDES

1.1 Introduction and Applications of Chalcogen-Containing Molecules

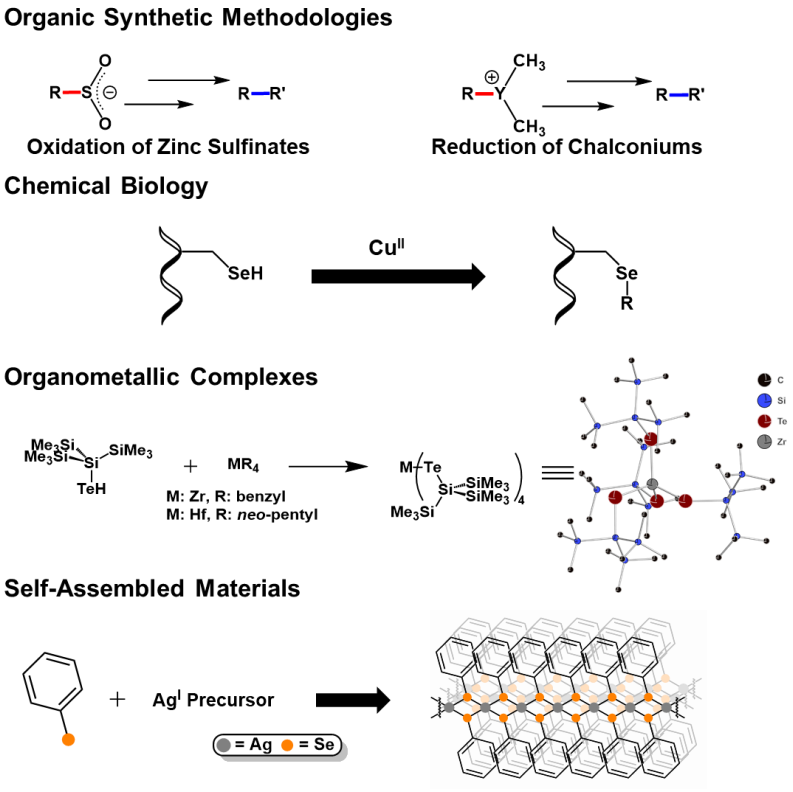

Figure 1.1: Selected examples of chalcogen-containing organic molecules with applications in synthetic methodologies, chemical biology, organometallic complexes, and self-assembled materials.

Carbon based compounds containing carbon-chalcogen (S, Se, Te) bonds have been broadly studied in numerous areas of chemical research (**Figure 1.1**), including organic synthetic methodologies,[1] chemical biology,[2] and ligands for organometallics[3] and materials chemistry.[4] Despite the numerous applications of molecules containing carbon-chalcogen bonds, the molecules most often studied are limited to scaffolds utilizing carbon-sulfur bonds, while examples

of carbon-selenium or -tellurium bonds are significantly rarer. This scarcity can be attributed to two significant factors that generally make the study of molecules containing carbon-selenium and -tellurium bonds challenging. Firstly, carbon-chalcogen bonds are fundamentally weaker than the other bonds that compose the discussed molecular frameworks (e.g. C-C, C-H, C-O), and are prone to heterolytic and homolytic bond cleavage under somewhat mild conditions.[1] In fact, this weakness has been leveraged in the preparation of sulfur-based precursors for carbon-centered radicals (**Figure 1.1**).[1] Secondly, these chalcogen-containing compounds are susceptible to oxidation by atmospheric oxygen or both organic and inorganic oxidants to numerous byproducts.[1d] This potential for oxidation is significantly higher when large, polarizable chalcogens (e.g. Se, Te) are present.

One strategy for mitigating these issues is the introduction of steric bulk proximal to the carbon-selenium or -tellurium bond.[5] In these cases, steric bulk adjacent to the chalcogen (Se, Te) nuclei physically restrict interactions between the chalcogen center and reactive molecules. This strategy has even been used to isolate and characterize free tellurols, which are notoriously unstable in the presence of air and light.[1d]

Even though the above approach is able to limit deleterious side reactions of carbon-based chalcogenides through physical interactions of molecules, the fundamental weakness of carbon-chalcogen bonds persists. Potential scaffolds that are able to combine the benefits of a sterically hindered environment with that of fundamentally stronger covalent bonds to chalcogens are icosahedral boron-rich clusters.

1.2 Introduction to Icosahedral Boron-Rich Clusters

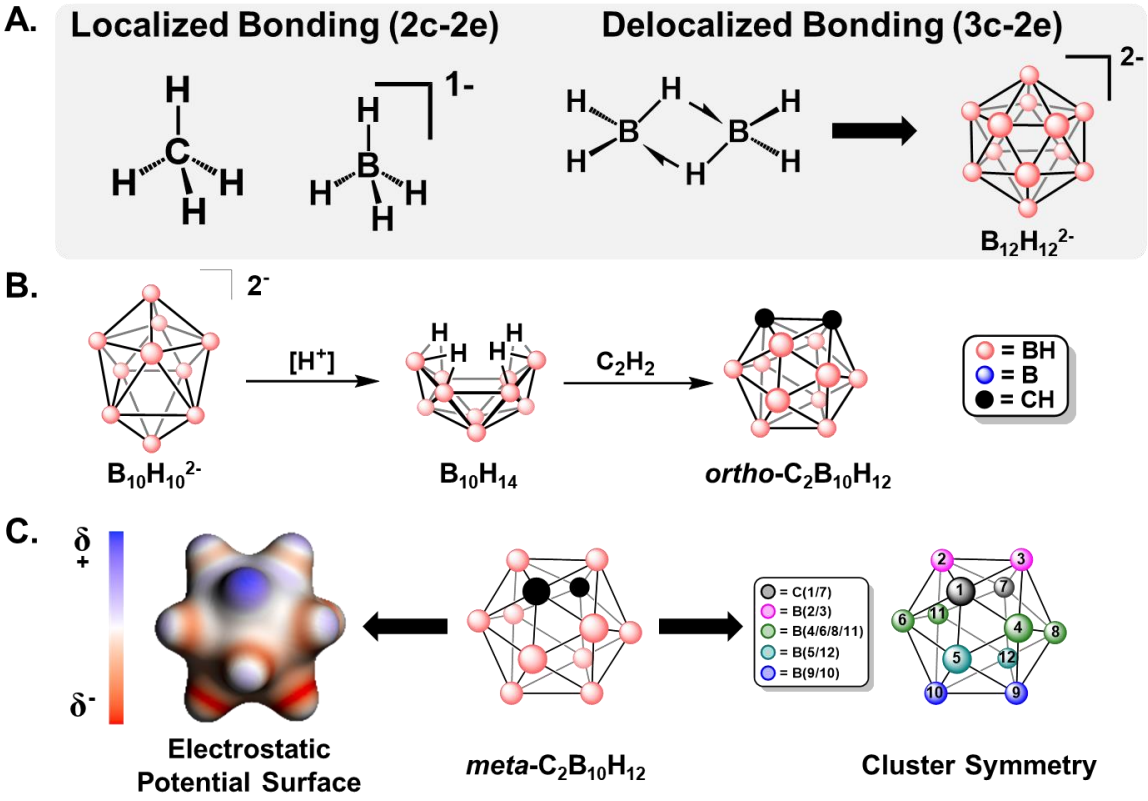

Figure 1.2: A. Comparison of two-center two-electron (2c-2e) bonds and the three-center two electron (3c-2e) bonding interactions found in boron-rich clusters. **B.** Synthesis of *ortho*-$C_2B_{10}H_{12}$ from $B_{10}H_{10}^{2-}$. **C.** Rendering of *meta*-$C_2B_{10}H_{12}$ electrostatic surface potential indicating electron-poor carbon vertices (blue) and electron-rich boron vertices (red). A numbering scheme for *meta*-$C_2B_{10}H_{12}$ is also provided for reference.

Icosahedral boron-rich clusters were first theorized in the mid-1950's,[6] five years prior to their eventual synthesis and discovery by Hawthorne *et al.* in 1960.[7] Since their discovery, the study of icosahedral boron clusters has exploded exponentially due to their unique modes of reactivity and potential applications in material design. Of these clusters, dodecaborate ($B_{12}H_{12}^{2-}$) is known to be remarkably stable both thermally and chemically. For example, dodecaborate clusters can be heated to over 600 °C or treated with strong acid or base with no measurable

decomposition.[8] This unprecedented stability can be correlated to the delocalized bonding arrangements[9] (more specifically, three center-two electron interactions, **Figure 1.2A**) that comprise the three-dimensional framework of the icosahedral cluster and is somewhat reminiscent of the delocalization observed in two-dimensional aromatic systems prevalent in organic chemistry. This is antithetical to the traditional interpretation of organic, aromatic frameworks, that often require a degree of planarity to achieve electron delocalization.

In contrast to $B_{12}H_{12}^{2-}$, some boron clusters can be selectively ruptured to expand the library of accessible clusters. In the case of $B_{10}H_{10}^{2-}$, treatment by strong acid yields decaborane ($B_{10}H_{14}$), which can then undergo cage reconstruction with acetylene (C_2H_2) to form the neutral icosahedral boron cluster, *ortho*-carborane (*o*-$C_2B_{10}H_{12}$, **Figure 1.2B**).[10] *Ortho*-carborane can then be thermally isomerized at elevated temperatures to the *meta*- and *para*- isomer that are distinguished based on the relative positioning of the two carbon vertices.[11] Incorporation of the two carbon vertices into the boron cluster framework significantly impacts the electronic environment (**Figure 1.2C**), and thus reactivity, of individual vertices within the cluster that can be leveraged for selective functionalization of the carborane cluster.[12] Ultimately, there exists three unique regions of carborane clusters (excluding *para*-) with distinct characteristics and reactivity. These regions are described as electron deficient carbon vertices, electron deficient boron vertices adjacent to the carbon vertices, and electron rich boron vertices furthest away from the carbon vertices.[11] The potential for regioselective introduction of exopolyhedral B-Y or C-Y (Y: S, Se, Te) bonds with carboranes ultimately allows for control of the electronic environment experienced by the chalcogen nucleus, in contrast with electronic uniformity of dodecaborate clusters. This control of electronic environment makes carboranes attractive targets for the development of tunable ligand scaffolds.[13]

1.3 Synthesis and Applications of Boron-Rich Clusters Containing Exopolyhedral Boron-Chalcogen Bonds

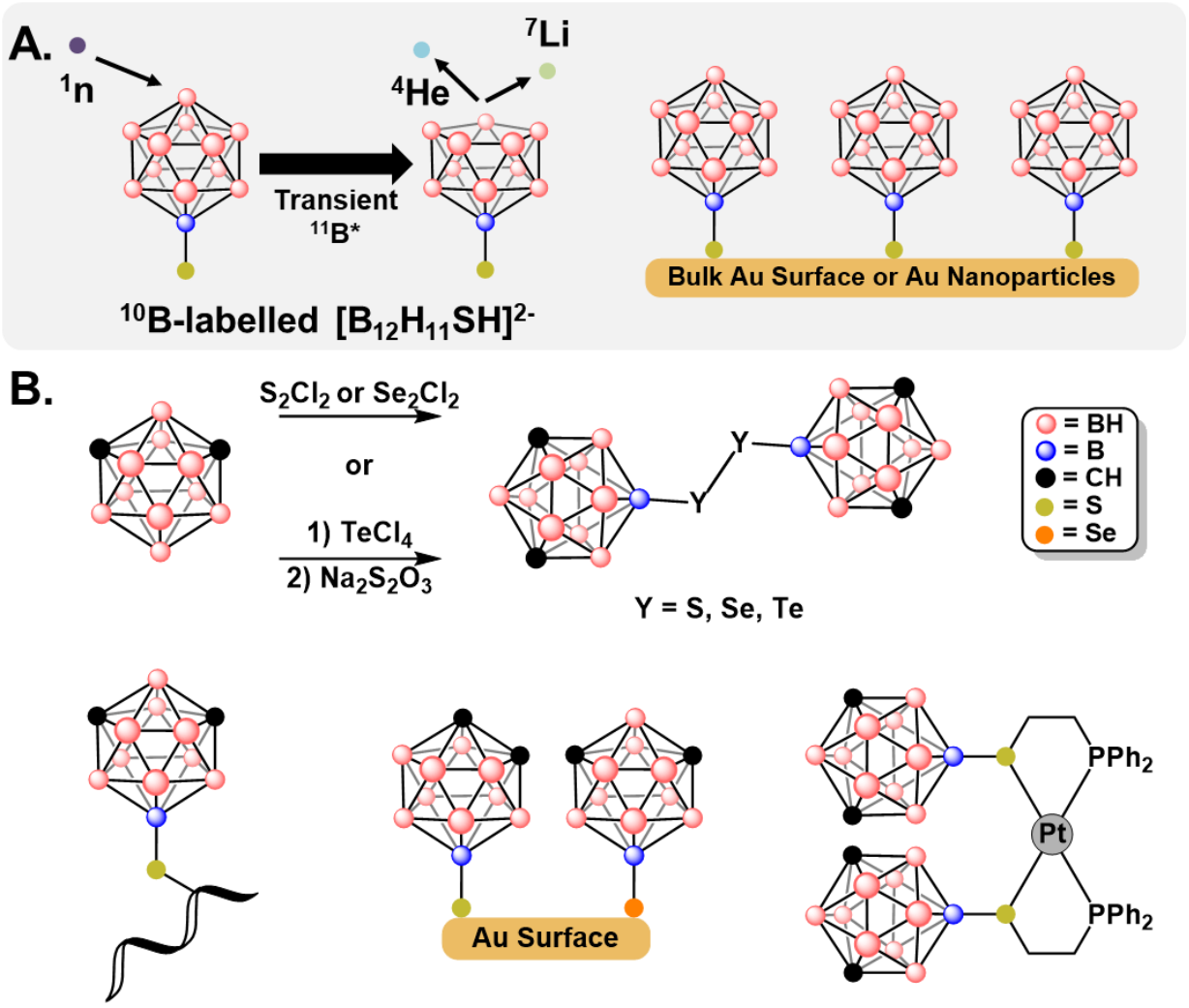

Figure 1.3: A. The synthesis of dodecaborate clusters featuring exopolyhedral B-S or B-Se bonds, including selected examples of BNCT with ^{10}B-labelled $[B_{12}H_{11}SH]^{2-}$ and a self-assembled monolayer of $[B_{12}H_{11}S]^{3-}$ on gold surfaces. **B.** The synthesis of carborane clusters containing B-S, B-Se, or B-Te bonds, including selected examples of a boron-connected carborane thiol bioconjugate, self-assembled monolayers carborane chalcogenolates, and an organometallic complex structured by tunable carborane sulfide ligands.

Boron-rich clusters containing exopolyhedral boron-chalcogen bonds were first synthesized in the mid-1960's.[14] In the case of dodecaborate clusters, molecules featuring an exopolyhedral B-S bond were first prepared in 1964.[14a] Since that time, this class of dodecaborates has been extensively studied as potential drug molecules for boron neutron capture therapy (BNCT, **Figure 1.3A**).[15] In addition to their prevalence as BNCT agents, thiolated dodecaborate clusters are often studied as ligands for surfaces (**Figure 1.3A**).[16] Despite this, only one example of a dodecaborate cluster featuring an exopolyhedral B-Se bond exists,[14b] with no reported examples of B-Te bonds.

In contrast, neutral boron-rich clusters (i.e. carboranes) containing B-S, B-Se, and B-Te bonds were reported during the early 1980's.[14c-e] Unlike with dodecaborates, the synthesis of these chalcogen-substituted clusters is remarkably straightforward (**Figure 1.3B**). Using electrophilic substitution catalyzed by a Lewis-acid ($AlCl_3$) in the presence of electrophilic chalcogen sources (S_2Cl_2, Se_2Cl_2, $TeCl_4$) allows for the facile introduction of chalcogens to the electron rich boron-based vertices (B(9)) of *ortho*- and *meta*-carborane clusters). Despite the electron-rich environment[11, 13, 17] imparted by the carborane, these compounds containing exopolyhedral B-S, B-Se, and B-Te bonds are remarkably stable, even when handled under ambient conditions.[17] This is attributed to the thermodynamic stability of boron-chalcogen bonds combined with the steric bulk of the carborane cluster, which is equivalent to that of a *tert*-butyl or adamantyl group.

Similar to dodecaborate clusters, carboranes featuring B-S have been widely studied, primarily in applications such as chemical biology,[18] and as surface[19] or metal center[20] ligands (**Figure 1.3B**). However, despite their facile synthesis, B-Se containing carboranes have only been studied in one unpublished example,[21] and B-Te containing carboranes have not been further reported since their inception.

1.4 References for Chapter 1

(1) (a) Kaiser, D.; Klose, I.; Oost, R.; Neuhaus, J.; Maulide, N. Bond-forming and -Breaking Reactions at Sulfur(IV): Sulfoxides, Sulfonium Salts, Sulfur Ylides, and Sulfinate Salts. *Chem. Rev.* **2019**, 119, 14, 8701-8780. (b) Petragnani, N.; Stefani, H. *Tellurium in Organic Synthesis* 2nd ed. 2007, Elsevier. (c) Shao, L.; Li, Y.; Lu, J.; Jiang, X. Recent progress in selenium-catalyzed organic reactions. *Org. Chem. Front.* **2019**, 6, 2999-3041. (c) Singh, F. V.; Wirth, T. Selenium and Tellurium Electrophiles in Organic Synthesis. *Phys. Sci. Rev.* **2018** doi: 10.1515/psr-2017-0131. (d) Rappaport, Z. *The Chemistry of Organic Selenium and Tellurium Compounds*; John Wiley & Sons: New York, 2013; Vol. *4* (e) Block, E.; Glass, R. S.; Gruhn, N.; Jin, J.; Lorance, E.; Zakai, U. I.; Zhang, S.-Z. Chemistry of Mixed Sulfur-, Selenium-, or Tellurium- and Silicon, or Tin-Containing Heterocycles. *Phosphorus, Sulfur, and Silicon and the Related Elements* **2008** 183, 4, 856-862. (f) Kumar, S.; Helt, J.-C. P.; Autschbach, J.; Detty, M. R. A New Reaction of Organoselenium Compounds: Alkyl Transfer from Diorganoselenium(IV) Dibromides to Give Alkenoic Acids to Give γ- and δ-Lactones. *Organometallics* **2009**, 28, 12, 3426-3436. (g) Evans, D. H.; Gruhn, N. E.; Jin, J.; Li, B.; Lorance, E.; Okumara, N.; Macías-Ruvalcaba, N. A.; Zakai, U. I.; Zhang, S.-Z.; Block, E.; Glass, R. S. Electrochemical and Chemical Oxidation of Dithia-, Diselena-, Ditellura-, Selenathia-, and Tellurathiamesocycles and the Stability of Oxidized Species. *J. Org. Chem.* **2010**, 74, 6, 1997-2009. (h) Garrett, G. E.; Gibson, G. L.; Straus, R. N.; Seferos, D. S.; Taylor, M. S. Chalcogen Bonding in Solution: Interactions of Benzotelluradiazoles with Anionic and Uncharged Lewis Bases. *J. Am. Chem. Soc.* **2015**, 137, 12, 4126-4133. (i) Zhou, B.; Gabbai, F. P. Lewis Acidic Telluronium Cations: Enhanced Chalcogen-Bond Donor Properties and Application to Transfer Hydrogenation Catalysis. *Organometallics* **2021**, 40, 14, 2371-2354.

(2) (a) Cao, W.; McCallum, N. C.; Ni, Q. Z.; Li, W.; Boyce, H.; Mao, H.; Zhou, X.; Sun, H.; Thompson, M. P.; Battistela, C.; Wasielewski, M. R.; Dhinojwala, A.; Shawkey, M. D.; Burkhart, M. D.; Wang, Z.; Gianneschi, N. C. Selenomelanin: An Abiotic Selenium Analogue of Pheomelanin. *J. Am. Chem. Soc.* **2020**, 142, 29, 12802-12810. (b) Glass, R. B.; Berry, M. J.; Block, E.; Boakye, H. T.; Carlson, B. A.; Gailer, J.; George, G. N.; Gladyshev, V. N.; Hatfield, D. L.; Jacobsen, N. E.; Johnson, S.; Kahakachchi, C.; Kamiński, R.; Manley, S. A.; Mix, H.; Pickering, I. J.; Prenner, E. J.; Saira, K.; Skowrońska, A.; Tyson, J. F.; Uden, P. C; Wu, Q.; Xu, X.-M.; Yamdagni, R.; Zhang, Y. Insights into the Chemical Biology of Selenium. *Phosphorus, Sulfur, and Silicon and the Related Elements* **2008**, 183, 4, 924-930. (c) Block, E.; Booker, S. J.; Flores-Penalba, S.; George, G.; Gundala, G.; Landgraf, B. J.; Liu, J.; Lodge, S. N.; Pushie, M. J.; Rozovsky, S.; Vattekkatte, A.; Yaghi, R.; Zeng, H. Trifluoroselenomethionine – a New Non-Natural Amino Acid. *ChemBioChem* **2016**, 17, 18, 1738-1751. (d) Zhao, Z.; Shimon, D.; Metanis, N. Chemoselective Copper-Mediated Modification of Selenosysteines in Peptides and Proteins. *J. Am. Chem. Soc.* **2021**, 143, 12817-12824. (e) Ferro, C. T. B.; Santos, B. F. D.; da Silva, C. D. G.; Brand, G.; da Silva, B. A. L.; Domingues, N. L. d. C. Review of the Syntheses and Activities of Some Sulfur-Containing Drugs. *Curr. Org. Synth.* **2020**, 17, 3, 192-210.

(3) (a) Lin, T.-P.; Gabbai, F. P. Two-Electron Redox Chemistry at the Dinuclear Core of a TePt Platform: Chlorine Photoreductive Elimination and Isolation of a $Te^{V}Pt^{I}$ Complex. *J. Am. Chem. Soc.* **2012**, 134, 29, 12230-12238. (b) Lin, T.-P.; Gabbai, F. P. Telluronium Ions as σ-Acceptor Ligands. *Angew. Chem. Int. Ed.* **2013**, 52, 14, 3864-3868. (c) Yang, H.; Lin, T.-P.; Gabbai, F. P. Telluroether to Telluroxide Conversion in the Coordination Sphere of a Metal: Oxidation-Induced Umpolung of a Te-Au Bond. *Organometallics* **2014**, 33, 17, 4368-4373. (d) Arnold, J. The Chemistry of Metal Complexes with Selenolate and Tellurolate Ligands. *Progress in*

Inorganic Chemistry 43, **1995**. (e) Christou, V.; Arnold, J. Synthesis of Reactive Homoleptic Tellurolates of Zirconium and Hafnium, and Their Conversion to Terminal Tellurides: A Model for the First Step in a Molecule-to-Solid Transformation. *J. Am. Chem. Soc.* **1992**, 114, 6240-6242.

(4) (a) Kryman, M. W.; Nasca, J. N.; Watson, D. F.; Detty, M. R. Selenorhodamine Dye-Sensitized Solar Cells: Influence of Structure and Surface-Anchoring Mode on Aggregation, Persistence, and Photochemical Performance. *Langmuir* **2016**, 32, 6, 1521-1532. (b) Ye, S.; Jansaz, L.; Zajaczkowski, W.; Manion, J. G.; Mondal, A.; Marszalek, T.; Andrienko, D.; Müllen, K.; Pisula, W.; Seferos, D. S. Self-Organization and Charge Transport Properties of Selenium and Tellurium Analogues of Polythiophene. *Macromol. Rapid Commun.* **2019**, 40, 1, 1800596. (c) Scholes, D. T.; Yee, P. Y.; McKeown, G. R.; Li, S.; Kang, H.; Lindemuth, J. R.; Xia, X.; King, S. C.; Seferos, D. S.; Tolbert, S. H.; Schwartz, B. J. Designing Conjugated Polymers for Molecular Doping: The Roles of Crystallinity, Swelling, and Conductivity in Sequentially-Doped Selenophene-Based Copolymers. *Chem. Mater.* **2019**, 31, 1, 73-82. (d) Manion, J. G.; Panchuk, J. R.; Seferos, D. S. Applying Heteroatom Substitution in Organic Photovoltaics. *Chem. Rec.* **2019**, 19, 6, 1113-1122. (e) Hicks, G. E. J.; Jarrett-Wilkins, C. N.; Panchuk, J. R.; Manion, J. G.; Seferos, D. S. Oxidation promoted self-assembly of π-conjugated polymers. *Chem. Sci.* **2020**, 11, 6383.

(5) (a) Dabbousi, B. O.; Bonasia, P. J.; Arnold, J. $(Me_3Si)_3SiTeH$: Preparation, Characterization, and Synthetic Utility of a Remarkably Stable Tellurol. *J. Am. Chem. Soc.* **1991**, 113, 3186-3188. (b) Bonasia, P. J.; Arnold, J. Lithium Tri(trimethylsilyl)silyltellurolate Bis(tetrahydrofuran) and Tris(trimethylsilyl)silyltellurol. *Inorg. Synth.* **1997**, 31, 162-165.

(6) Longuet-Higgins, H. C.; Roberts, M. De V. The electronic structure of an icosahedron of boron atoms. *Proc. Royal Soc. A* **1955**, 230, 1180, 110-119.

(7) Pitochelli, A. R.; Hawthorne, F. M. The Isolation of the Icosahedral $B_{12}H_{12}^{2-}$. *J. Am. Chem. Soc.* **1960**, 82, 12, 3228-3229.

(8) Sivaev, I. B.; Bregadze, V. I.; Sjöberg, S. Chemistry of *closo*-Dodecaborate Anion $[B_{12}H_{12}]^{2-}$: A Review. *Coll. Of Czech. Chem. Comm.* **2002**, 67, 6, 679-727.

(9) (a) King, R. B. Three-Dimensional Aromaticity in Polyhedral Boranes and Related Molecules. *Chem. Rev.* **2001**, 101, 1119-1152. (b) Parkin, G. Representation of Three-Center-Two-Electron Bonds in Covalent Molecules with Bridging Hydrogen Atoms. *J. Chem. Educ.* **2019**, 96, 11, 2467-2475.

(10) Bondarev, O.; Sevryugina, Y. V.; Jalisatgi, S. S.; Hawthorne, M. F. Acid-Induced Opening of $[$*closo*-$B_{10}H_{10}]^{2-}$ as a New Route to 6-Substituted *nido*-$B_{10}H_{13}$ Decaboranes and Related Carboranes. *Inorg. Chem.* **2012**, 51, 18, 9935-9942.

(11) Grimes, R. N. *Carboranes*, 3rd ed; Elsevier: Oxford, 2016.

(12) (a) Dziedzic, R. M.; Spokoyny A. M. Metal-Catalyzed Cross-Coupling Chemistry with Polyhedral Boranes. *Chem. Commun.* **2019**, 55, 430-442. (b) Quan, Y.; Tang, C.; Xie, Z. Nucleophilic substitutionL a facile strategy for selective B-H functionalization of carboranes. *Dalton Trans.* **2019**, 48, 7494-7498. (c) Quan, Y.; Xie, Z. Controlled functionalization of *o*-carborane *via* transition metal catalyzed B-H activation. *Chem. Soc, Rev,* **2019**, 48, 3660-3673.

(13) (a) Keener, M.; Hunt, C.; Carroll, T. G.; Kampel, V.; Dobrozetsky, R.; Hayton, T. W.; Ménard, G. Redox-switchable carboranes for uranium capture and release. *Nature* **2020**, 577, 652-655. (b) Kim, S.; So, H.; Lee, J. H.; Hwang, H.; Kwon, H.; Park, M. H.; Lee, K. M. Photophysical Properties of Spirobifluorene-Nased *o*-Carboranyl Compounds Altered by Structurally Rotating the Carborane Cages. *Molecules* **2019**, 24, 22, 4135. (c) Böhling, L.; Brockhinke, A.; Kahlert, J.; Weber, L.; Harder, R. A.; Yufit, D. S.; Howard, J. A. K.; MacBride, J. A. H.; Fox, M. A. Substituent Effects on the Fluorescence Properties of *ortho*-Carboranes: Unusual Emission Behaviour in *C*-(2'-Pyridyl)-*ortho*-carboranes. *Eur. J. Inorg. Chem.* **2016**, 3, 403-412. (d) Axtell, J. A.; Kirlikovali, K. O.; Djurovich, P. I.; Jung, D.; Nguyen, V. T.; Munekiyo, B.; Royappa, A. T.; Rheingold, A. L.; Spokoyny, A. M. Blue Phosphorescent Zwitterionic Iridium(III) Complexes Featuring Weakly Coordinating *nido*-Carborane-Base Ligands. *J. Am. Chem. Soc.* **2016**, 138, 48, 15758-15765. (e) Shi, C.; Sun, H.; Jiang, Q.; Zhao, Q.; Wang, J.; Huang, W.; Yan, H. Carborane tuning of photophysical properties of phosphorescent iridium(III) complexes. *Chem. Commun.* **2013**, 49, 4746-4748. (f) Tsang, M. Y.; Viñas, C.; Teixidor, F.; Planas, J. G.; Conde, N.; SanMartin, R.; Herrero, M. T.; Domínguez, E.; Lledós, A.; Vidossich, P.; Choquesillo-Lazarte, D. Synthesis, Structure, and Catalytic Application of *ortho*- and *meta*-Carboranyl Based NBN Pincer-Pd Complexes. *Inorg. Chem.* **2014**, 53, 17, 9284-9295. (g) Spokoyny, A. M.; Lewis, C. D.; Teverovskiy, G.; Buchwald, S. L. Extremely Electron-Rich, Boron-Functionalized, Icosahedral Carborane-Based Phosphinoboranes. *Organometallics* **2012**, 31, 24, 8478-8481.

(14) (a) Knoth, W. H.; Sauer, J. C.; England, D. C.; Hertler, W. R.; Muetterties, E. L. Chemistry of Boranes. XIX. Derivative Chemistry of $B_{10}H_{10}^{-2}$ and $B_{12}H_{12}^{-2}$. *J. Am. Chem. Soc.* **1964**, 86, 19, 3973-3983. (b) Kultyshev, R. G.; Liu, S.; Leung, H. T.; Liu, J.; Shore, S. G. Synthesis of Mono- and Dihalogenated Derivative of $(Me_2S)_2B_{12}H_{10}$ and Palladium-Catalyzed Boron-Carbon Cross-

Coupling Reactions of the Iodides with Grignard Reagents. *Inorg. Chem.* **2003**, 42, 10, 3199-3207. (c) Zakharkin, L. I.; Pisareva, I. V. A New Simple Method for the Production and Some Conversions of B-S Bond-Containing *o*- and *m*-Carboranyl. *Phosphorus and Sulfur* **1984**, 20, 357-370. (d) Zakharkin, L. I.; Pisareva, I. V.; Antonovich, V. A. Synthesis of Di(*o*- and *m*-Carboran-9-yl) Diselenides by Electrophilic-Substitution Reactions of *o*- and *m*-Carboranes with Selenium Chlorides Under the Action of $AlCl_3$, and Reactions of These Products. *Zhurnal Obshchei Khimii* **1986**, 56, 12, 2721-2728. (e) Zakharkin, L. I.; Pisareva, I. V. Electrophilic Telluration of *o*- and *m*-Carboranes with $TeCl_4$ Under the Action of $AlCl_3$. *Izvestiya Akademii Nauk, Seriya Khimicheskaya* **1984**, 2, 472-473.

(15) (a) Asano, R.; Nagami, A.; Fukumoto, Y.; Miura, K.; Yazama, F.; Ito, H.; Sakata, I.; Tai, A. Synthesis and biological evaluation of new BSH-conjugated chlorin derivatives as agetns for both photodynamic therapy and boron neutron capture therapy of cancer. *J. Photochem. Photobiol.* **2014**, 140, 140-149. (b) Tolpin, E. I.; Wellum, G. R.; Dohan Jr.; F. C.; Kornblith, P. L.; Zamenhof, R. G. Boron neutron capture therapy of cerebral gliomas. II. Utilization of the blood-brain barrier and tumor-specific agents for the selective concentration of boron in gliomas. *Oncology* **1975**, 32, 5-6, 223-246. (c) Nakase, I.; Aoki, A.; Sakai, Y.; Hirase, S.; Ishimura, M.; Takatani-Nakase, T.; Hattori, Y.; Kirihata, M. Antibody-Based Receptor Targeting Using and Fc-Binding Peptide-Dodecaborate Conjugate and Macropincytosis Induction for Boron Neutron Capture Therapy. *ACS Omega* **2020**, 5, 36, 22731-22738.

(16) (a) Yeager, L. J.; Saeki, F.; Shelly, K.; Hawthorne, M. F.; Garrell, R. L. A New Class of Self-Assembled Monolayers: *closo*-$B_{12}H_{11}S^{3-}$ on Gold. *J. Am. Chem. Soc.* **1998**, 120, 38, 9961-9962. (b) Assaf, K. I.; Hennig, A.; Peng, S.; Guo, D.-S.; Gabel, D.; Nau, W. M. Hierarchical host-guest

assemblies formed on dodecaborate-coated gold nanoparticles. *Chem. Commun.* **2017**, 53, 4616-4619.

(17) Mills, H. A.; Alsarhan, F.; Ong, T.-C.; Gembicky, M.; Rheingold, A. L.; Spokoyny, A. M. Icosahedral Meta-Carboranes Containing Exopolyhedral B-Se and B-Te Bonds. *ChemRxiv* **2021** doi:10.33774/chemrxiv-2021-01xcb.

(18) Waddington, M. A.; Zheng, A.; Stauber, J. M.; Moully, E. H.; Montgomery, H. E.; Saleh, L. M. A.; Kral, P.; Spokoyny, A. M. An Organometallic Strategy for Cysteine Borylation. *J. Am. Chem. Soc.* **2021**, 143, 8661-8668.

(19) (a) Baše, T.; Bastl, Z.; Šlouf, M.; Klementová, M.; Šubrt, J.; Vetushka, A.; Ledinský, M.; Fejfar, A.; Macháček, J.; Carr, M. J.; Londesborough, M. G. S. Gold Micrometer Crystals Modifed with Carboranethiol Derivatives. *J. Phys. Chem. C* **2008**, 112, 37, 14446-14455. (b) Hohman, J. N.; Zhang, P.; Morin, E. I.; Han, P.; Kim, M.; Kurland, A. R.; McClanahan, P. D.; Balema, V. P.; Weiss, P. S. Self-Assembly of Carboranethiol Isomer on Au{111}: Intermolecular Interactions Determined by Molecular Dipole Orientations. *ACS Nano* **2009**, 3, 3, 527-536. (c) Bould, J.; Macháček, J.; Londesborough, M. G. S.; Macías, R.; Kennedy, J. D.; Bastl, Z.; Rupper, P.; Baše, T. Decaborane Thiols as Building Blocks for Self-Assembled Monolayers on Metal Surfaces. *Inorg. Chem.* **2012**, 51, 3, 1685-1694. (d) Baše, T.; Bastl, Z.; Havránek, V.; Macháček, J.; Langecker, J.; Malina, V. Carboranedithiols: Building Blocks for Self-Assembled Monolayers on Copper Surfaces. *Langmuir* **2012**, 28, 34, 12518-12526. (e) Vetushka, A.; Bernard, L.; Guseva, O.; Bastl, Z.; Plocek, J.; Tomandl, I.; Fejfar, A.; Baše, T.; Schmutz, P. Adsorption of oriented carborane dipole on a silver surface. *Phys. Solid State B* **2015**, 253, 3, 591-600. (f) Thomas, J. C.; Goronzy, D. P.; Serino, A. C.; Auluck, H. S.; Irving, O. R.; Jimenez-Izal, E.; Deirmenjian, J. M.;

Macháček, J.; Sautet, P.; Alexandrova, A. N.; Baše, T.; Weiss, P. S. Acid-Base Control of Valency within Carboranedithiol Self-Assembled Monolayer: Molecules Do the Can-Can. *ACS Nano* **2018**, 12, 3, 2211-2221. (g) Goronzy, D. P.; Staněk, J.; Avery, E.; Guo, H.; Bastl, Z.; Dušek, M.; Gallup, N. M.; Gün, S.; Kučeráková, M.; Levandowski, B. J.; Macháček, J.; Šícha, V.; Thomas, J. C.; Yavuz, A.; Houk, K. N.; Danişman; Mete, E.; Alexandrova, A. N.; Baše, T.; Weiss, P. S. Influence of Terminal Carboxyl Groups on the Structure and Reactivity of Functionalized *m*-Carboranethiolate Self-Assembled Monolayers. *Chem. Mater.* **2020**, 32, 15, 6800-6809. (h) Li, Y.-L.; Wang, Z.-Y.; Ma, X.-H.; Luo, P.; Du, C.-X.; Zang, S.-Q. Distinct photophysical properties in atom-precise silver and copper nanocluster analogues. *Nanoscale* **2019**, 11, 5151-5157. (i) Saini, A.; Saha, A.; Viñas, C.; Teixidor, F. The key to controlling the morphologies of quantum nanocrystals: spherical carborane ligands. *Chem. Commun.* **2019**, 55, 9817-9820. (j) Wang, Q.-Y.; Wang, J.; Wang, S.; Wang, Z.-Y.; Cao, M.; He, C.-L.; Yang, J.-Q.; Zang, S.-Q.; Mak, T. C. W. *o*-Carborane-Based and Atomically Precise Metal Clusters as Hypergolic Materials. *J. Am. Chem. Soc.* **2020**, 142, 28, 12010-12014. (k) Jana, A.; Jash, M.; Poonia, A. K.; Paramasivam, G.; Islam, M. R.; Chakraborty, P.; Antharjanam, S.; Machacek, J.; Ghosh, S.; Adarsh, K. N. V. D.; Base, T.; Pradeep, T. Light-Activated Intercluster Conversion of an Atomically Precise Silver Nanocluster. *ACS Nano* **2021**, 15, 10, 15781-15793. (l) Huang, J.-H.; Si, Y.; Dong, X.-Y.; Liu, L.-Y.; Zang, S.-Q. Mak, T. C. W. Symmetry Breaking of Atomically Precise Fullerene-like Metal Nanoclusters *J. Am. Chem. Soc.* **2021**, 32, 12439-12444.

(20) (a) Jain, L.; Jain, V. K.; Kushwah, N.; Pal, M. K.; Wadawale, A. P.; Bregadez, V. I.; Glazun, S. A. Chalcogenocarboranes: A family of multifaceted sterically demanding ligands. *Coord. Chem. Rev.* **2014**, 258-259, 72-118. (b) Zhang, X.; Tang, X.; Yang, J.; Li, Y.; Yan, H.; Bregadze, V. I. Boron-Substituted *o*-Carboranetrithiol To Construct Trimeric Cobalt Clusters.

Organometallics **2013**, 32, 6, 2014-2018. (c) Oña, O. B.; Alcoba, D. R.; Massaccesi, G. E.; Torre, A.; Lain, L.; Melo, J. I.; Olivia-Enrich, J. M.; Peralta, J. E. Magnetic Properties of Co(II) Complexes with Polyhedral Carborane Ligands. *Inorg. Chem.* **2019**, 58, 4, 2550-2557. (d) Spokoyny, A. M.; Machan, C. W.; Clingerman, D. J.; Rosen, M. S.; Wiester, M. J.; Kenedy, R. D.; Stern, C. L.; Sarjeant, A. A.; Mirkin, C. A. A coordination chemistry dichotomy for icosahedral carborane-based ligands. *Nat. Chem.* **2011**, 3, 590-596.

(21) Goronzy, D. P. (2019) *Intermolecular Interactions and Surface Properties of Self-Assembled Monolayers of Functional Boron Clusters* [Doctoral dissertation, University of California, Los Angeles]. ProQuest Dissertations and Theses database.

CHAPTER 2 – IMPROVED SYNTHESIS OF ICOSAHEDRAL CARBORANES CONTAINING EXOPOLYHEDRAL B-C BONDS

This chapter is a version of Anderson, K. P.; Mills, H. A.; Mao, C.; Kirlikovali, K. O.; Axtell, J. C.; Rheingold, A. L.; Spokoyny, A. M. "Improved Synthesis of Icoashedral Carboranes Containing Exohedral B-C and C-C Bonds", *Tetrahedron* **2019**, *75*, 187-191.

2.1 Abstract

Carboranes are boron-rich molecular clusters possessing electronic characteristics that allow for orthogonal approaches to vertex-selective modifications. We report improved functionalization methods utilizing orthogonal chemistry to achieve efficient substitution at electron-rich B-vertices of carborane. Functionalization of B-vertices with alkyl and (hetero)aryl groups using the corresponding Grignard reagents has been improved through the use of a Pd-based precatalyst featuring an electron-rich biaryl phosphine ligand, resulting in reduced reaction times. The developed method is tolerant towards alkyl-based Grignard reagents containing β-hydrogens, a problematic substrate for older reported methods. Furthermore, the developed cross-coupling methods oxidatively add to exopolyhedral B-I bonds, selectively, with no observable reactivity towards B-Br bonds. The selective substitution of carboranes afforded by this method holds potential for the rational synthesis of heterofunctionalized boron clusters.

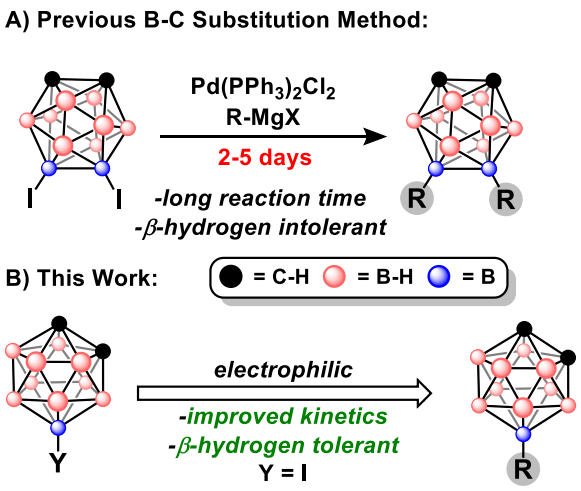

Figure 2.1: A. Previous B-substitution method via Kumada cross-coupling. **B.** Improved B-vertex functionalization procedure.

2.2 Introduction

Since the discovery of neutral carboranes ($C_2B_{10}H_{12}$) more than 50 years ago, these icosahedral clusters have emerged as diverse building blocks for a variety of applications, including organic light emitting diodes,[1] biomedicine,[2] batteries,[3] catalysis[4], self-assembled materials[5] and medicinal drug design.[6] These compounds, which exist as three constitutional isomers (*ortho*, *meta*, and *para*) depending on relative positions of the two C-H vertices on the cage, feature several unique properties, such as three dimensional aromaticity, a large HOMO-LUMO gap, tunable dipole moments as a function of cluster symmetry, and thermal stability.[7a] The diversity of carborane applications, however, requires synthetic methods that can provide access to vertex-selective modification. Selectivity can be achieved, to a certain extent, by utilizing the inherent electronic non-uniformity of the cluster cage whereby certain B–H vertices are rendered more reactive than others towards electrophilic[7a] or organometallic[7b-k] reagents. Furthermore, under basic conditions the acidic protons bound to the carbon vertices can undergo facile deprotonation and subsequent selective functionalization with electrophiles.[8] Nevertheless,

current synthetic methods are still limited in their ability to achieve efficient substitution of carboranes. For example, current C-vertex substitution methods can install (hetero)aryl groups but often require the use of transition metal reagents.[8a-c] Similarly, metal-catalyzed cross-coupling can be used to achieve B-vertex functionalization. However, the substitution of carbon-based nucleophiles is limited by substrate tolerance, long reaction times, and even poor reproducibility (**Figure 2.1A**).[9a-d] To improve on these procedures, we report a fast, high yielding B-vertex substitution method for B-substituted carboranes (**Figure 2.1B**). Importantly, this method can be utilized in the presence of both B-I and B-Br bonds without any substitution observed at the brominated boron vertex.

The boron vertices of carboranes have been especially difficult to substitute relative to traditional organic molecules. This is largely due to their hindered steric environment, variable electronic character, and strong non-hydridic B-H bonds.[7a] Friedel-Crafts halogenation, however, has been a vital tool for harnessing electrophilic reactivity at the electron-rich boron vertices of carboranes. The resulting B-halogenated carborane electrophiles provide access to B-C, B-O, or B-N substitution through metal-catalyzed cross-coupling. Zakharkin *et al*. was the first to report a Pd-mediated cross-coupling process with $Pd(PPh_3)_2Cl_2$ between 9-I-*ortho*-carborane (**9-I-oCB**) or 9-I-*meta*-carborane (**9-I-mCB**) and several organomagnesium reagents, claiming to produce B-substituted clusters in a manner reminiscent to classical Kumada cross-coupling chemistry used for aryl halides.[9a,b] Subsequently, Li *et al*. reported a similar protocol for transformations between 9,12-I_2-*ortho*-carborane (**9,12-I_2-oCB**) and alkylmagnesium reagents.[9c] In both cases, authors claimed yields from 60-99% for coupling reactions that required 24-30 h for completion. Notably, a later report by Zheng *et al*. called the obtained yields and reaction times by the original authors into question, claiming that: "In our hands, the product yields of these reactions are not as high as

been reported, and in most cases we have studied the yields are extremely low."[9d] Additionally, Zheng *et al*. determined that reproducible cross-coupling could be obtained in 20-75% yield only after the introduction of a catalytic amount of CuI. While the method by Zheng *et al*. has improved the overall cross-coupling chemistry, several limitations, including long reaction times (2-5 days) and limited tolerance for Grignard reagents containing β-hydrogens, persisted. We hypothesize that these drawbacks can be further mitigated by replacing the $Pd(PPh_3)_2Cl_2$ precatalyst with a system containing a biaryl phosphine ligand as was observed previously for B-O, B-N, and B-CN metal-catalyzed cross-coupling chemistry.[9e-g]

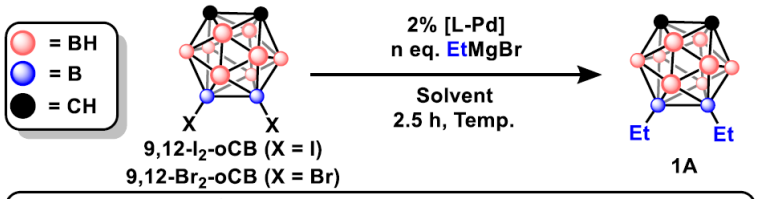

Entry #	X	L	n	Solvent	T	% Conv. (% Yield)
1 [a]	I	XPhos	5	THF	75	2
2	I	XPhos	4.2	1,4-dioxane	65	30
3	I	XPhos	4.2	1,4-dioxane	75	89 [b] (77)
4	I	SPhos	4.2	1,4-dioxane	75	90 [b] (66)
5	Br	XPhos	4.2	1,4-dioxane	75	0

Figure 2.2: Optimization table for Kumada cross-coupling with **9,12-I_2-oCB** or **9,12-Br_2-oCB** and EtMgBr. % Conv. Indicates the % of **9,12-Et_2-oCB** present in the crude reaction mixture as determined by GC-MS. [a]Included 2 mol% CuI additive. [b]Reaction mixture contained 5-10% dehalogenated product by GC-MS.

2.3 Results and Discussion

We initially targeted the coupling of **9,12-I_2-oCB** with EtMgBr in the presence of XPhos-Pd-G3[10] precatalyst under the reaction conditions reported by Zheng *et al*. to probe the tolerance of β-hydrogens presented by the Grignard nucleophile. Even with the inclusion of catalytic CuI, which has been reported[9d] to improve the yield of this reaction when using $Pd(PPh_3)_2Cl_2$ as a precatalyst, very low conversion was observed (<5%) to the desired 9,12-diethyl-*ortho*-carborane (**1A**) after 2.5 h (**Figure 2.2**, Entry 1, see Appendix A for experimental details). A solvent (Entries 1-2) and temperature (Entries 2-3) screen revealed 1,4-dioxane as a promising solvent when employed at 75 °C with XPhos-Pd-G3. Notably, comparable yields were obtained with SPhos-Pd-G3 (Entry 4) under otherwise identical conditions. Furthermore, these conditions are selective for B-I bonds, with no desired product observed when using B-Br electrophiles (Entry 5). Under these optimized conditions, the issue of β-hydride elimination suggested in the previously reported system does not appear to be problematic.

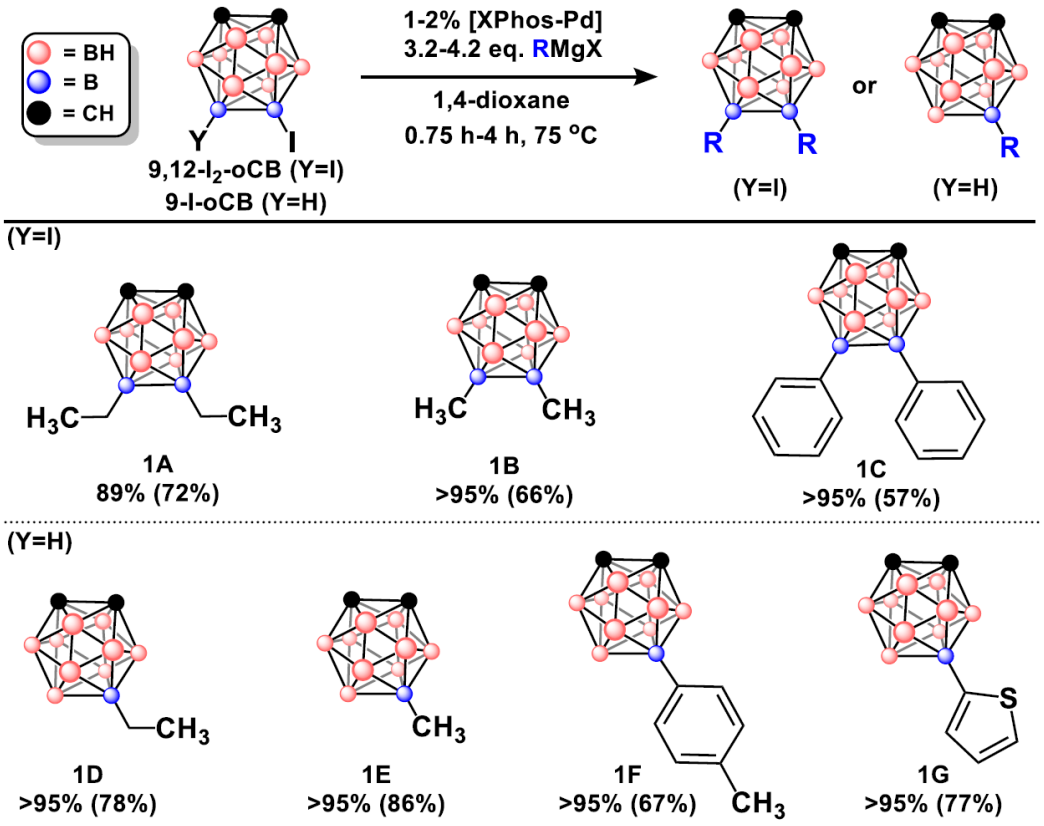

Figure 2.3: Reaction scheme for mono- and disubstitution of *ortho*-carborane. *Ortho*-carborane coupling products with GC-MS conversion and percent isolated yields in parentheses. See Table A2 in Appendix A for exact reaction conditions.

With optimized conditions established, we assessed the scope of this method with *ortho*-carboranyl electrophiles (**Figure 2.3**). Starting with **9,12-I$_2$-oCB**, we observed nearly full conversions (>90%) to the disubstituted products in the presence of alkyl or arylmagnesium reagents. These compounds were purified *via* silica gel column chromatography providing products **1A**, **1B**, and **1C** in 57-72% isolated yields. While these conditions allow for the isolation of disubstituted products (**1A-C**), we note that approximately 5-10% of the partially dehalogenated products (**1D-E**) are present in the reaction mixture of **1A-B**. Interestingly, no observable dehalogenation is encountered when **9-I-oCB** is used as a substrate and >95% conversions to the

monosubstituted products **1D**, **1E**, and **1F** are observed within 2 hours. Notably, a heterocycle compatible with magnesium reagents afforded >95% conversion to **1G**, although slightly longer reaction time was needed (4 h).

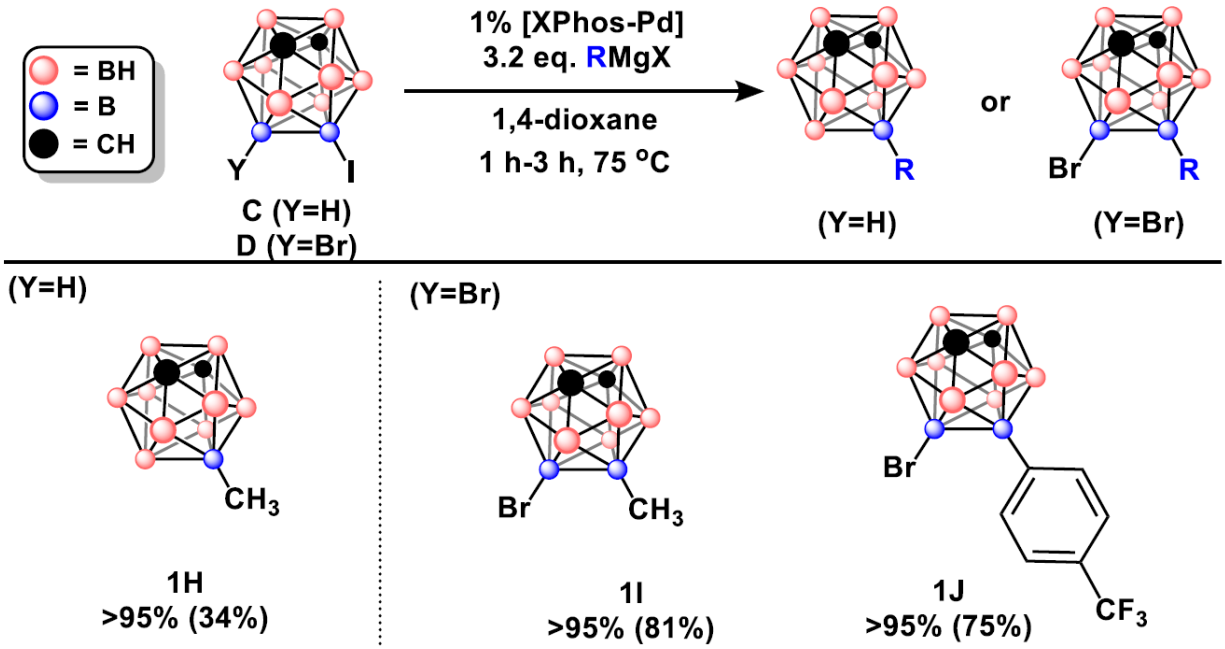

Figure 2.4: Reaction scheme for monocoupling of *meta*-carborane in the presence of B-Br bonds. *Meta*-carborane coupling products with GC-MS conversion and percent isolated yields in parentheses. See Table A2 in Appendix A for exact reaction conditions.

To expand the utility of this method, we tested our conditions with **9-I-mCB** and **9-Br-10-I-mCB** to determine the tolerance of *meta*-carboranyl electrophiles and B-Br bonds (**Figure 2.4**). Slightly longer reaction times were required to reach >95% conversion for products **1H**, **1I**, and **1J**. Despite >95% conversion observed for **1H**, the low isolated yield (34%) likely resulted from the high volatility of the compound, as evidenced by observed sublimation *in vacuo* at room temperature when removing solvent. For products **1I** and **1J**, no substitution and/or reduction at the brominated vertex was observed, lending further evidence to the selectivity of this method for

B-I bonds over B-Br bonds. This stands in contrast to the previously developed B-N and B-O cross-coupling methods using Pd-based catalysts with biaryl ligands that showed preferential functionalization of B-Br bonds over B-I congeners.[9f]

2.4 Conclusions

We have developed an improved B-vertex functionalization method that can effectively afford previously inaccessible carborane derivatives. Specifically, by employing biaryl phosphine ligands, we have introduced an improved B-vertex substitution method that increases the rate of Pd-catalyzed Kumada cross-coupling conditions. These improved methods represent a robust addition of transformations now available to the practitioners in boron cluster chemistry.

2.5 References for Chapter 2

(1) (a) Axtell, J. C.; Kirlikovali, K. O.; Djurovich, P. I.; Jung, D.; Nguyen, V. T.; Munekiyo, B.; Royappa, A. T.; Rheingold, A. L.; Spokoyny, A. M. *J. Am. Chem. Soc.* **2016,** *138* (48), 15758; (b) Prokhorov, A. M.; Hofbeck, T.; Czerwieniec, R.; Suleymanova, A. F.; Kozhevnikov, D. N.; Yersin, H. *J. Am. Chem. Soc.* **2014,** *136* (27), 9637.

(2) (a) Paxton, R. J.; Beatty, B. G.; Hawthorne, M. F.; Varadarajan, A.; Williams, L. E.; Curtis, F. L.; Knobler, C. B.; Beatty, J. D.; Shively, J. E. *Pro. Natl. Acad. Sci.* **1991,** *88* (8), 3387; (b) Hawthorne, M. F.; Maderna, A. *Chem. Rev.* **1999,** *99* (12), 3421; (c) Neirynck, P.; Schimer, J.; Jonkheijm, P.; Milroy, L. G.; Cigler, P.; Brunsveld, L. *J. Mater. Chem. B* **2015,** *3* (4), 539.

(3) McArthur, S. G.; Geng, L.; Guo, J.; Lavallo, V. *Inorg. Chem. Front.* **2015,** *2* (12), 1101.

(4) Selg, C.; Neumann, W.; Lönnecke, P.; Hey-Hawkins, E.; Zeitler, K. *Chem. Eur. J.* **2017,** *23* (13), 7932.

(5) (a) Farha, O. K.; Spokoyny, A. M.; Mulfort, K. L.; Hawthorne, M. F.; Mirkin, C. A.; Hupp, J. T. *J. Am. Chem. Soc.* **2007,** *129* (42), 12680; (b) Serino, A. C.; Anderson, M. E.; Saleh, L. M. A.; Dziedzic, R. M.; Mills, H.; Heindreich, L. K.; Spokoyny, A. M.; Weiss, P. S. *ACS Appl. Mater. Interfaces* **2017**, 9, 40, 34592; (c) Kim, J.; Rim, Y. S.; Liu, Y.; Serino, A. C.; Thomas, J. C.; Chen, H.; Yang, Y.; Weiss, P. S. *Nano Lett.* **2014**, *14* (5), 2946; (d) Spokoyny, A.M.; Farha, O.K.; Mulfort, K.L.; Hupp, J.T.; Mirkin, C.A. *Inorg. Chim. Acta.* **2010**, *364* (1), 266.

(6) (a) Issa, F.; Kassiou, M.; Rendina, L. M. *Chem. Rev.* **2011,** *111* (9), 5701; (b) Leśnikowski, Z.J. *J. Med. Chem.* **2016**, *59* (17), 7738; (c) Adamska, A.; Rumijowska,-Galewicz, A.; Ruszczynska, A.; Studzińska, M.; Jabłońska, A.; Paradowska, E.; Bulska, E.; Munier-Lehman, H.; Dziadek, J.; Leśnikowski, Z.J.; Olejniczak, A.B. *Eur. J. Med. Chem.* **2016**, *121* (4), 71.

(7) For a general overview of carboranes: (a) R. N. Grimes, Carboranes, 3rd edn, Elsevier, Oxford, 2016. For examples of B–H activation: (b) Cheng, R.; Li, B.; Wu, J.; Zhang, J.; Qiu, Z.; Tang, W.; You, S.; Tang, Y.; Xie, Z. *J. Am. Chem. Soc.***2018**, 140, 13, 4508-4511; (c) Quan, Y.; Qiu, Z.; Xie, Z. *Chem. Eur. J.* **2018**, *24*, 2795-2805; (d) Cheng, R.; Qiu, Z.; Xie, Z. *Nat. Comm.* **2017**, 8, 14827. (e) Guo, S.; Cui, P.; Gao, Y.; Jin, G. *Dalton Trans.* **2018**, 47, 13641-13646; (f) Eleazer, B. J.; Peryshkov, D. V. *Inorg. Chem.* **2018**, *3*, 79-109; (g) Eleazer, B. J.; Smith, M. D.; Popov, A. A.; Peryshkov, D. V. *Chem. Sci.* **2018**, *9*, 2601-2608. (h) Tang, C.; Zhang, J.; Xie, Z. *Angew. Chem.* **2017**, *129*, 8768-8772. (i) Lyu, H.; Quan, Y.; Xie, Z. *Chem. Sci.* **2018**, 9, 6390-6394. (j) Mirabelli, M.; Sneddon, L. *J. Am. Chem. Soc.* **1998**, 110, 449-453. (k) Estrada, J.; Lee, S.; McArthur, S.; El-Hellani, A.; Tham. F.; Lavallo, V. *J. Organomet. Chem.* **2015**, 798, 214-217.

(8) For a general overview of C-vertex substitution: (a) Lu, J.-Y.; Wan, H.; Zhang, J.; Wang, Z.; Li, Y.; Du, Y.; Li, C.; Liu, Z.-T.; Liu, Z.-W.; Lu, J. *Chem. Eur. J.* **2016,** *22* (49), 17542; (b) Coult, R.; Fox, M. A.; Gill, W. R.; Herbertson, P. L.; MacBride, J. A. H.; Wade, K. *J. Organomet. Chem.*

1993, *462* (1), 19; (c) Tang, C.; Xie, Z. *Angew. Chem. Int. Ed.* **2015**, *54* (26), 7662; (d) Chan, A.L.; Estrada, J.; Kefalidis, C.E.; Lavallo, V. *Organometallics* **2016**, *35* (19), 3257; (e) Cabrera-González, J.; Viñas, C.; Haukka, M.; Bhattacharyya, S.; Gierschner, J.; Núñez, R. *Chem. Eur. J.* **2016**, *22* (38), 13588; (f) Powley, S.L.; Schaefer, L.; Man, W.Y.; Ellis, D.; Rosair, G.M.; Welch, A.J. *Dalton Trans.* **2016**, *45*, 3635.

(9) (a) Zakharkin, L. I., Kovredov, A.I., Ol'Shevskaya, V.A., Shaugumbekova, Zh. S., *Izv. Akad. Nauk SSSR, Ser. Khim.* **1980**, *7*. (b) Zakharkin, L. I.; Kovredov, A. I.; Ol'shevskaya, V. A.; Shaugumbekova, Z. S. *J. Organomet. Chem.* **1982**, *226* (3), 217 (c) Li, J.; Logan, C. F.; Jones, M. *Inorg. Chem.* **1991**, *30* (25), 4866; (d) Zheng, Z.; Jiang, W.; Zinn, A. A.; Knobler, C. B.; Hawthorne, M. F. *Inorg. Chem.* **1995**, *34* (8), 2095; (e) Sevryugina, Y.; Julius, R. L.; Hawthorne, M. F. *Inorg. Chem.* **2010,** *49* (22), 10627; (f) Dziedzic, R. M.; Saleh, L. M. A.; Axtell, J. C.; Martin, J. L.; Stevens, S. L.; Royappa, A. T.; Rheingold, A. L.; Spokoyny, A. M. *J. Am. Chem. Soc.* **2016**, *138* (29), 9081; (g) Dziedzic, R. M.; Martin, J. L.; Axtell, J. C.; Saleh, L. M. A.; Ong, T.-C.; Yang, Y.-F.; Messina, M. S.; Rheingold, A. L.; Houk, K. N.; Spokoyny, A. M. *J. Am. Chem. Soc.* **2017**, *139* (23), 7729.

(10) For article on the synthesis of 3rd generation Pd-precatalysts: (a) Bruno, N. C.; Tudge, M. T.; Buchwald, S. L. *Chem. Sci.* **2013**, *4* (3), 916; For general literature on biaryl phosphine based precatalysts: (b) Biscoe, M. R.; Fors, B. P.; Buchwald, S. L. *J. Am. Chem. Soc.* **2008**, *130* (21), 6686; (c) Düfert, M. A.; Billingsley, K. L.; Buchwald, S. L. *J. Am. Chem. Soc.* **2013**, *135* (34), 12877.

(11) Ohta, K.; Goto, T.; Endo, Y. *Tetrahedron Lett.* **2005**, *46* (3), 483.

(12) (a) Henly, T.J.; Knobler, C.B.; Hawthorne, M.F. *Organometallics* **1992**, *11*, 2313; (b) Islam, M.J.; Smith, M.D.; Peryshkov, D.V. *J. Organomet. Chem.* **2018,** *867*, 208.

(13) Kirlikovali, K. O.; Axtell, J. C.; Anderson, K.; Djurovich, P. I.; Rheingold, A. L.; Spokoyny, A. M. *Organometallics* **2018**, *37* (18), 3122.

(14) (a) Getman, T.D. *Inorg. Chem.* **1998**, 37, 3422-3423; (b) Fox, M.A.; MacBride, J.A.H.; Wade, K. *Polyhedron* **1996**, *16* (14), 2499; (c) Yoo, J.; Hwang, J.-W.; Do, Y. *Inorg. Chem.* 2001, *40* (3), 568.

(15) Bae, H. J.; Kim, H.; Lee, K. M.; Kim, T.; Lee, Y. S.; Do, Y.; Lee, M. H. *Dalton Trans.* **2014**, *43* (13), 4978.

2.6 Appendix A

2.6.1 General Considerations

Meta-$C_2B_{10}H_{12}$ (Katchem), *ortho*-$C_2B_{10}H_{12}$ (Boron Specialties), were sublimed prior to use. XPhos (Sigma-Aldrich) and SPhos (Ark Pharm) were used as received. XPhos-Pd-G3 and SPhos-Pd-G3 were prepared according to literature procedures.[1] Iodomethane (Sigma-Aldrich), Bromoethane (Sigma-Aldrich), Iodobenzene (Sigma-Aldrich), 2-Bromothiophene (Oakwood), and 4-Bromobenzotrifluoride (Oakwood) were stored over molecular sieves in ambient conditions and used as is. Grignard reagents were prepared by the dropwise addition of alkyl or aryl halides to an excess of Magnesium chips (Sigma-Aldrich) in anhydrous ether and left to stir overnight at room temperature (MeMgI and EtMgBr were instead stirred at reflux overnight) and filtered before use. The concentration of the Grignard reagents was determined by titration of iodine (~63.5 mg in 5 mL of anhydrous THF) with a 0.20 mL aliquot until the equivalence point was observed. Deuterated solvents were purchased from Cambridge Isotope Laboratories and used as received. Glass-backed Silica Gel 60 GLA TLC plates were purchased from Fisher Scientific. Silica used for flash column chromatography was SiliaFlash® G60 60-200 μm (70-230 mesh) purchased from Silicycle.

All experiments were performed air and moisture free under an atmosphere of nitrogen using standard Schlenk techniques. Anhydrous dioxane (Sigma-Aldrich) was used as received. THF and diethyl ether used for reactions were purified and dried using a Grubbs column. All post-Schlenk work-up and characterization was performed under ambient conditions. The “ambient conditions” for this manuscript refer to room temperature (20 - 25°C) and uncontrolled laboratory

air. Thin layer chromatography (TLC) samples for carborane-containing compounds were stained with 1 wt. % $PdCl_2$ in 6M HCl and developed with heat.

2.6.2 Instrumentation

^{1}H, $^{13}C\{^{1}H\}$, ^{11}B, $^{11}B\{^{1}H\}$, and ^{19}F NMR spectra were recorded on either a Bruker DRX500, Bruker AV500 or Bruker AVIII 400 spectrometer in ambient conditions unless stated otherwise. MestreNova v6.0.2-5475 software was used to process the FID data and visualize the spectra. ^{1}H and ^{13}C NMR spectra were referenced to residual solvent resonances in deuterated solvents ($CDCl_3$: ^{1}H, 7.26 ppm; ^{13}C, 77.16 ppm. Acetone-d_6: ^{1}H, 2.05 ppm; ^{13}C, 29.84 ppm. Note: due to high humidity H_2O resonances are often present). ^{11}B and $^{11}B\{^{1}H\}$ NMR spectra were referenced externally to $Et_2O{\cdot}BF_3$ (δ = 0 ppm). ^{19}F NMR spectra were referenced externally to fluorobenzene (δ = -113.15 ppm). Gas Chromatography Mass Spectrometry (GC-MS) measurements were carried out using an Agilent Model 7693 Autosampler, 7890B Gas Chromatograph, and 7250 Q-TOF Mass Selective Detector in the Electron Ionization mode. Sample injection was carried out on an Agilent HP5-MS column with dimensions 30 m x 250 μm x 0.25 μm. Ultra High Purity Grade He (Airgas) was used as carrier gas. Data collection and analysis were performed using Mass Hunter Acquisition and Qualitative Analysis software (Agilent).

2.6.3 Experimental

2.6.3.1 Precursor Synthesis

9-I-1,2-dicarba-*closo*-dodecaborane (**9-I-oCB**)[2], 9-I-1,7-dicarba-*closo*-dodecaborane (**9-I-mCB**)[2], 9,12-I_2-1,2-dicarba-*closo*-doedecaborane (**9,12-I_2-oCB**)[3], 9,12-Br_2-1,2-dicarba-*closo*-dodecaborane (**9,12-Br2-oCB**)[2], and 9-Br, 10-I-1,7-dicarba-*closo*-dodecaborane (**9-Br-10-I-**

mCB)[2] were synthesized according to or adapted from previously reported procedures. All characterization data are consistent with those previous reports.

2.6.3.2 Optimization of Kumada-type Cross-Coupling with Iodo-Carboranes

9,12-I_2-oCB (40 mg, 0.1 mmol), catalyst (2%), and phosphine ligand (2%) were added to an oven-dried reaction tube with a PTFE septum cap. The reaction tube was evacuated and backfilled with N_2 three times before transferring into an N_2-filled glovebox. Under an inert atmosphere, anhydrous solvent (0.6 mL) was added before the dropwise addition of ethylmagnesium bromide in ether (~2 M, 4.2-5 eq.). The reaction mixture was heated and the reaction progress was monitored by GC-MS after 2.5 hours.

Table A1 Kumada coupling optimizations

Entry #	Substrate	Ligand	Grig. Eq.	Additive	Solvent	Temp.	% Et_2-oCB by GC-MS
1	I_2-oCB	XPhos	5 eq.	CuI	THF	75 ºC	2
2	I_2-oCB	XPhos	4.2 eq	-----	Dioxane	65 ºC	30
3	I_2-oCB	XPhos	4.2 eq	-----	Dioxane	75 ºC	89
4	I_2-oCB	SPhos	4.2 eq	-----	Dioxane	75 ºC	90
5	Br_2-oCB	XPhos	4.2 eq	-----	Dioxane	75 ºC	0

Note: Although most entries and products utilize XPhos-Pd-G3 and XPhos ligand catalytic system, Entry 4 as well as products **1A**^{I} and **1D**^{I} provide evidence to suggest that SPhos-Pd-G3 and SPhos ligand would be competent in these transformations. When using EtMgBr, only slight variations in isolated yields were observed and reaction times remained consistent between using XPhos or SPhos.

2.6.3.3 Procedure for Kumada Cross-Coupling with 9,12-I_2-oCB

9,12-I_2-oCB (0.5-1 mmol), L-Pd-G3 (2 mol%), and L (2 mol%) were added to an oven-dried Schlenk flask and evacuated/backfilled with N_2 three times before leaving under an inert atmosphere. Using a syringe, anhydrous dioxane (6 mL) was added to dissolve all solids. Next the Grignard reagent (~2 M, 2.1-4.2 mmol, 4.2 eq.) was added dropwise to this stirring solution at room temperature. The reaction mixture was then stirred at 75 ºC until the reaction was determined to be complete by GC-MS. The reaction mixture was then diluted with Et_2O (~20 mL) and the excess Grignard was quenched by the addition of H_2O. The solution was transferred to a separatory funnel and the aqueous layer was extracted with Et_2O (3 x 20 mL). During the extraction, brine (~5 mL) was added to improve separation between organic and aqueous layers. The organic fractions were combined and dried with $MgSO_4$, then filtered into a round-bottomed flask. The solvent was removed under reduced pressure to yield the crude product as a colored oil or solid. The crude product was dry loaded onto silica and purified using silica gel column chromatography to yield the desired product (see product details for exact purification conditions).

2.6.3.4 General procedure for Kumada Cross-Coupling with 9-I-oCB, 9-I-mCB, or 9-Br-10-I-mCB

Mono-iodinated carborane (**9-I-oCB**, **9-I-mCB**, or **9-Br-10-I-mCB**; 0.5-1 mmol), L-Pd-G3 (1-1.5 mol%), and L (1-1.5 mol%) were added to an oven-dried Schlenk flask and evacuated/backfilled with N_2 three times before leaving under an inert atmosphere. Using a syringe, anhydrous dioxane (6 mL) was added to dissolve all solids before the dropwise addition of the chosen Grignard reagent (~2 M, 3.2 mmol, 3.2 eq.) to the stirring solution at room temperature. The reaction mixture was then left to stir at 75 ºC until the reaction was confirmed complete by GC-MS. Once the reaction was complete, the solution was diluted with Et_2O (~20

mL) and the excess Grignard was quenched by the addition of H_2O. The solution was transferred to a separatory funnel and the aqueous layer was extracted with Et_2O (3 x 20 mL). During the extraction, brine (~5 mL) was added to improve separation between organic and aqueous layers. The organic fractions were combined and dried with $MgSO_4$, the filtered into a round-bottomed flask. The solvent was removed under reduced pressure to yield the crude product as a colored oil or solid. The crude product was dry loaded onto silica and purified using silica gel flash column chromatography to yield the desired product (see product details for exact purification conditions).

Table A2. Masses and reaction times for the synthesis of products **1A**-**1J**.

Product	Iodocarborane	L-Pd-G3	L	Time
1A	9,12-I_2-oCB	XPhos-Pd-G3	XPhos	2.5 h
	(394 mg, 1.0 mmol)	(16.8 mg, 0.02 mmol)	(9.4 mg, 0.02 mmol)	
1A^I	9,12-I_2-oCB	SPhos-Pd-G3	SPhos	2.5 h
	(197 mg, 0.5 mmol)	(7.8 mg, 0.01 mmol)	(4.1 mg, 0.01 mmol)	
1B	9,12-I_2-oCB	XPhos-Pd-G3	XPhos	1.5 h
	(394 mg, 1.0 mmol)	(16.8 mg, 0.02 mmol)	(9.4 mg, 0.02 mmol)	
1C	9,12-I_2-oCB	XPhos-Pd-G3	XPhos	3.0 h
	(394 mg, 1.0 mmol)	(16.8 mg, 0.02 mmol)	(9.4 mg, 0.02 mmol)	
1D	9-I-oCB	XPhos-Pd-G3	XPhos	2.0 h
	(270 mg, 1.0 mmol)	(12.6 mg, 0.01 mmol)	(7.1 mg, 0.01 mmol)	
1D^I	9-I-oCB	SPhos-Pd-G3	SPhos	2.0 h
	(135 mg, 0.5 mmol)	(5.9 mg, 0.005 mmol)	(3.2 mg, 0.005 mmol)	
1E	9-I-oCB	XPhos-Pd-G3	XPhos	0.75 h
	(270 mg, 1.0 mmol)	(8.4 mg, 0.01 mmol)	(4.7 mg, 0.01 mmol)	
1F	9-I-oCB	XPhos-Pd-G3	XPhos	2.0 h

	(270 mg, 1.0 mmol)	(8.4 mg, 0.01 mmol)	(4.7 mg, 0.01 mmol)	
1G	9-I-oCB	XPhos-Pd-G3	XPhos	4.0 h
	(270 mg, 1.0 mmol)	(8.4 mg, 0.01 mmol)	(4.7 mg, 0.01 mmol)	
1H	9-I-mCB	XPhos-Pd-G3	XPhos	1.0 h
	(270 mg, 1.0 mmol)	(8.4 mg, 0.01 mmol)	(4.7 mg, 0.01 mmol)	
1I	9-Br-10-I-mCB	XPhos-Pd-G3	XPhos	1.0 h
	(350 mg, 1.0 mmol)	(8.4 mg, 0.01 mmol)	(4.7 mg, 0.01 mmol)	
1J	9-Br-10-I-mCB	XPhos-Pd-G3	XPhos	3.0 h
	(350 mg, 1.0 mmol)	(8.4 mg, 0.01 mmol)	(4.7 mg, 0.01 mmol)	

2.6.3.5 Reaction, Product and Purification Details

9,12-(CH_2CH_3)$_2$-1,2-dicarba-*closo*-dodecaborane (1A)

Reaction time: 2.5 h

Purification: Hexanes ($\mathbf{R_f}$: 0.31) , 154 mg (77%), clear liquid

^{1}H NMR (400 MHz, $CDCl_3$): δ 3.38 (s, 2H, $C_{carborane}$-H), 2.97 – 1.28 (m, 8H, $B_{carborane}$-*H*), 0.87 (m, br, 6H, Et-CH_3), 0.69 (s, br, 4H, Et-CH_2-B). **^{11}B NMR (128 MHz, $CDCl_3$):** δ 9.14 (s, 2B), -8.97 (d, 2B, $^1J_{BH}$ = 148 Hz), -14.86 (d, 4B, $^1J_{BH}$ = 166 Hz), -16.84 (d, 2B, $^1J_{BH}$ = 200 Hz). **^{13}C NMR (126 MHz, $CDCl_3$):** δ 47.52, 13.38, 8.94 (br). **GC-MS** *m/z*: 200.2560 (calc. 200.2568)

9,12-(CH_3)$_2$-1,2-dicarba-*closo*-dodecaborane (1B)

Reaction time: 1.5 h

Purification: Hexanes ($\mathbf{R_f}$: 0.45), 114 mg (66%), white solid

^{1}H NMR (400 MHz, $CDCl_3$): δ 3.34 (s, 2H, $C_{carborane}$-H), 2.96 – 1.24 (m, 8H, $B_{carborane}$-*H*), 0.20 (s, br, 6H, B-CH_3). **^{11}B NMR (128 MHz, $CDCl_3$):** δ 7.13 (s, 2B), -7.66 (d, 2B, $^{1}J_{BH}$ = 148 Hz), -14.14 (d, 4B, $^{1}J_{BH}$ = 148 Hz), -16.64 (d, 2B, $^{1}J_{BH}$ = 181 Hz). **^{13}C NMR (126 MHz, $CDCl_3$):** δ 47.38. **GC-MS** *m/z*: 172.2252 (calc. 172.2255)

9,12-(C_6H_5)-1,2-dicarba-*closo*-dodecaborane (1C)

Reaction time: 3 h

Purification: 3:7 DCM:Hexanes + 1% TFA (**R_f**: 0.35), 170 mg (57%), white solid

^{1}H NMR (400 MHz, $(CD_3)_2CO$): δ 7.17 (m, 4H), 7.04 (m, 6H), 4.64 (s, 2H, $C_{carborane}$-H), 3.32 – 1.42 (m, 8H, $B_{carborane}$-*H*). **^{11}B NMR (128 MHz, $(CD_3)_2CO$):** δ 7.02 (s, 2B), -9.93 (d, 2B, $^{1}J_{BH}$ = 152 Hz), -14.16 (d, 4B, $^{1}J_{BH}$ = 166 Hz), -16.42 (d, 2B, $^{1}J_{BH}$ = 180 Hz). **^{13}C NMR (126 MHz, $CDCl_3$):** δ 132.75, 127.01, 126.76, 50.88. **GC-MS** *m/z*: 296.2563 (calc. 296.2568)

9-CH_2CH_3-1,2-dicarba-*closo*-dodecaborane (1D)

Reaction time: 2 h

Purification: 2:8 DCM:Hexanes (**R_f**: 0.57), 126 mg (73%), clear liquid

^{1}H NMR (400 MHz, $CDCl_3$): δ 3.48 (s, 1H, $C_{carborane}$-H), 3.41 (s, 1H, $C_{carborane}$-H), 3.02 – 1.34 (m, 9H, $B_{carborane}$-*H*), 0.86 (s, br, 3H, Et-CH_3), 0.72 (s, br, 2H, Et-CH_2-B). **^{11}B NMR (128 MHz, $CDCl_3$):** δ 9.39 (s, 1B), -2.42 (d, 1B, $^{1}J_{BH}$ = 163 Hz), -9.24 (d, 2B, $^{1}J_{BH}$ = 148 Hz), -14.10 – -15.82 (m, 6B). **^{13}C NMR (126 MHz, $CDCl_3$):** δ 53.11, 47.80, 13.45, 10.00 (q, br, $^{1}J_{CB}$ = 60.00 Hz). **GC-MS** *m/z*: 172.2241 (calc. 172.2252)

9-CH_3-1,2-dicarba-*closo*-dodecaborane (1E)

Reaction time: 45 min

Purification: 2:8 DCM:Hexanes (**R_f**: 0.50), 134 mg (86%), white solid

^{1}H NMR (400 MHz, $CDCl_3$): δ 3.49 (s, 1H, $C_{carborane}$-H), 3.37 (s, 1H, $C_{carborane}$-H), 3.00 – 1.34 (m, 9H, $B_{carborane}$-*H*), 0.24 (s, br, 3H, B-CH_3). **^{11}B NMR (128 MHz, $CDCl_3$):** δ 7.25 (s, 1B), -1.78 (d, 1B, $^1J_{BH}$ = 148 Hz), -8.57 (d, 2B, $^1J_{BH}$ = 148 Hz), -13.59 (d, 2B, $^1J_{BH}$ = 148 Hz), -14.59 (d, 2B, $^1J_{BH}$ = 132 Hz), -15.72 (d, 2B, $^1J_{BH}$ = 181 Hz). **^{13}C NMR (126 MHz, $CDCl_3$):** δ 53.45, 47.21, B-CH_3 not observed. **GC-MS** *m/z*: 158.2094 (calc. 158.2099)

9-(4-CH_3-C_6H_4)-1,2-dicarba-*closo*-dodecaborane (1F)

Reaction time: 2 h

Purification: 1:9 DCM:Hexanes (**R_f**: 0.25), 157 mg (67%), white solid

^{1}H NMR (400 MHz, $CDCl_3$): δ 7.28 (d, 2H, $^1J_{HH}$ = 7.72 Hz), 7.06 (d, 2H, $^1J_{HH}$ = 7.35 Hz), 3.58 (s, 1H, $C_{carborane}$-H), 3.48 (s, 1H, $C_{carborane}$-H), 3.25 – 1.60 (m, 9H, $B_{carborane}$-*H*), 2.30 (s, 3H). **^{11}B NMR (128 MHz, $CDCl_3$):** δ 7.50 (s, 1B), -2.41 (d, 1B, $^1J_{BH}$ = 163 Hz), -8.95 (d, 2B, $^1J_{BH}$ = 150 Hz), -14.08 – -15.68 (m, 6B). **^{13}C NMR (126 MHz, $CDCl_3$):** δ 136.91, 132.37, 128.27, 53.09, 48.64, 21.20. **GC-MS** *m/z*: 234.2406 (calc. 234.2412)

9-(2-C_4H_3S)-1,2-dicarba-*closo*-dodecaborane (1G)

Reaction time: 4 h

Purification: 2:8 DCM:Hexanes (**R_f**: 0.34), 183 mg (77%, average of two independent runs), white solid

^{1}H NMR (400 MHz, $CDCl_3$): δ 7.32 (dd, 1H, $^{1}J_{HH}$ = 4.61 Hz, $^{2}J_{HH}$ = 0.80 Hz), 7.01 (m, 2H), 3.60 (s, 1H, $C_{carborane}$-H), 3.49 (s, 1H, $C_{carborane}$-H), 3.20 – 1.50 (m, 9H, $B_{carborane}$-*H*). **^{11}B NMR (128 MHz, $CDCl_3$):** δ 4.49 (s, 1B), -2.22 (d, 1B, $^{1}J_{BH}$ = 149 Hz), -8.82 (d, 2B, $^{1}J_{BH}$ = 155 Hz), -13.97 – -15.75 (m, 6B). **^{13}C NMR (126 MHz, $CDCl_3$):** δ 130.75, 127.91, 127.80, 53.00, 48.87. **GC-MS** *m/z*: 226.1815 (calc. 226.1819)

9-CH_3-1,7-dicarba-*closo*-dodecaborane (1H)

Reaction time: 1 h

Purification: Hexanes (**R_f**: 0.71), 54 mg (34%), white solid

^{1}H NMR (400 MHz, $CDCl_3$): δ 3.33 – 1.57 (m, 9H, $B_{carborane}$-*H*), 2.86 (s, 2H, $C_{carborane}$-H), 0.36 (s, 3H). **^{11}B NMR (128 MHz, $CDCl_3$):** δ -0.69 (s, 1B), -6.35 (d, 2B, $^{1}J_{BH}$ = 160 Hz), -9.72 (d, 1B, $^{1}J_{BH}$ = 148 Hz), -13.10 (d, 2B, $^{1}J_{BH}$ = 160 Hz), -14.32 (d, 2B, $^{1}J_{BH}$ = 160 Hz), -17.98 (d, 1B, $^{1}J_{BH}$ = 184 Hz), -21.23 (d, 1B, $^{1}J_{BH}$ = 180 Hz). **^{13}C NMR (126 MHz, $CDCl_3$):** δ 54.34, B-CH_3 not observed. **GC-MS** *m/z*: 158.2092 (calc. 158.2099)

9-Br-10-(CH_3)-1,7-dicarba-*closo*-dodecaborane (1I)

Reaction time: 1 h

Purification: 1:9 DCM:Hexanes (**R_f**: 0.52), 192 mg (81%), white solid

^{1}H NMR (400 MHz, $CDCl_3$): δ 3.49 – 1.70 (m, 8H, $B_{carborane}$-*H*), 2.91 (s, 2H, $C_{carborane}$-H), 0.46 (s, 3H). **^{11}B NMR (128 MHz, $CDCl_3$):** δ -1.05 (s, 1B), -5.89 (d, 2B), -5.89 (s, 1B), -13.84 (d, 4B, $^{1}J_{BH}$ = 158 Hz), -21.80 (d, 2B, $^{1}J_{BH}$ = 182 Hz). **^{13}C NMR (126 MHz, $CDCl_3$):** δ 52.61, B-CH_3 not observed. **GC-MS** *m/z*: 237.1175 (calc. 237.1167)

9-Br-10-(4-CF_3-C_6H_4)-1,7-dicarba-*closo*-dodecaborane (1J)

Reaction time: 3 h

Purification: 1:9 DCM:Hexanes (**R_f** : 0.38), 272 mg (75%), light yellow solid

^{1}H NMR (400 MHz, $CDCl_3$): δ 7.66 (d, br, 2H, $^1J_{HH}$ = 7.77 Hz), 7.57 (d, br, 2H, $^1J_{HH}$ = 7.94 Hz), 3.71 – 1.64 (m, 8H, $B_{carborane}$-*H*), 3.07 (s, 2H, $C_{carborane}$-H). **^{11}B NMR (128 MHz, $CDCl_3$):** δ -1.18 (s, 1B), -6.03 (s, 1B), -6.44 (d, 2B), -13.15 (d, 2B), -13.90 (d, 2B), -20.31 (d, 1B), -21.27 (d, 1B). **^{13}C NMR (126 MHz, $CDCl_3$):** δ 133.64, 124.36, 52.16. **^{19}F NMR (376 MHz, $CDCl_3$):** δ -62.59 (s, 3F). **GC-MS** *m/z*: 367.1208 (calc. 367.1198)

2.6.4 NMR Spectroscopy and Mass Spectrometry of Isolated Compounds

2.6.4.1 Characterization of 1A

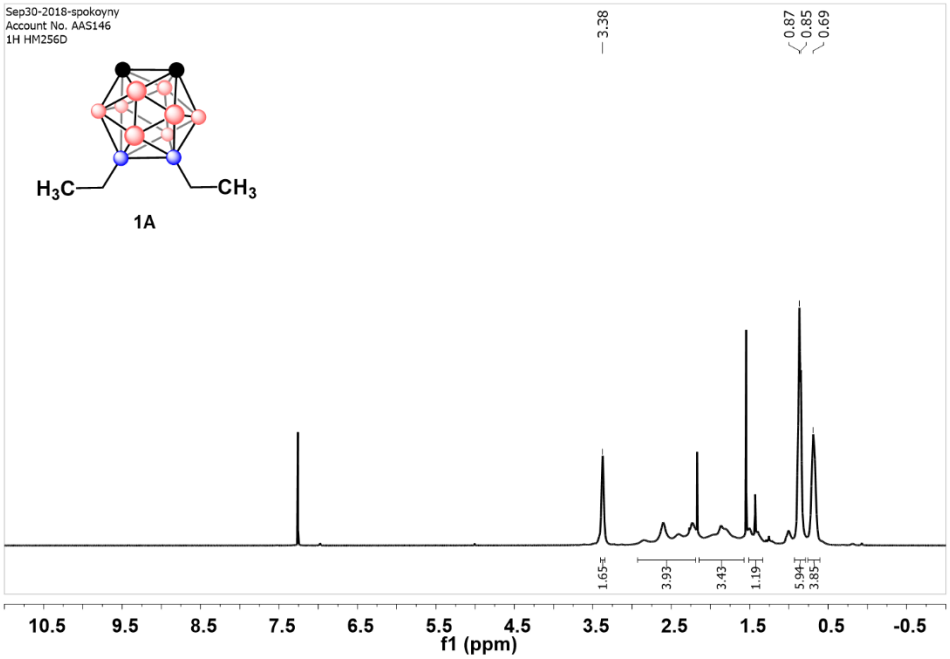

Figure A1.1 ^{1}H NMR of **1A**

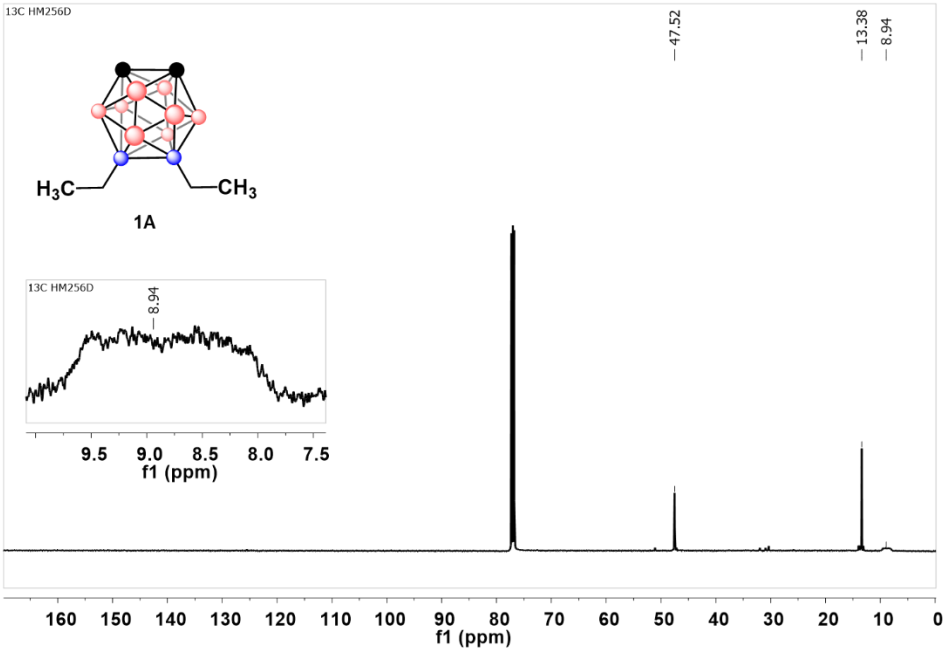

Figure A1.2 ^{13}C NMR of **1A**

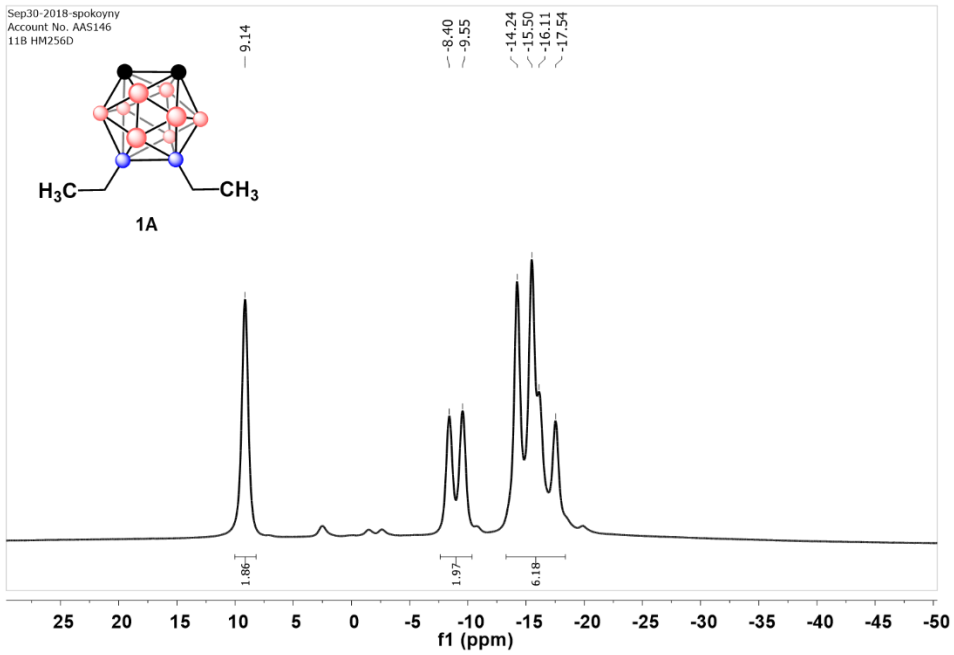

Figure A1.3 ^{11}B NMR of **1A**

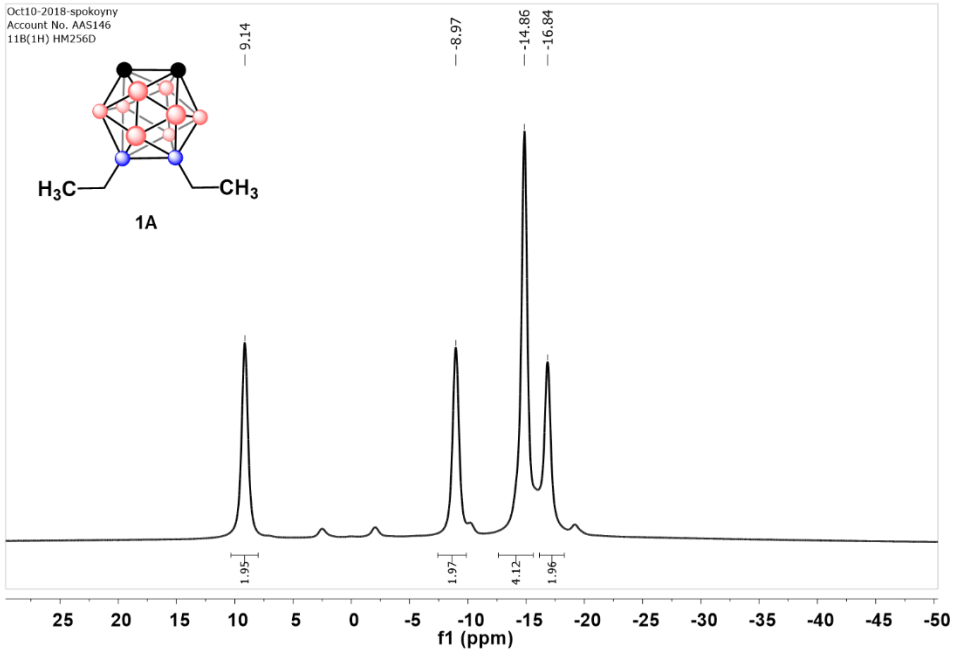

Figure A1.4 ^{11}B{^{1}H} NMR of **1A**

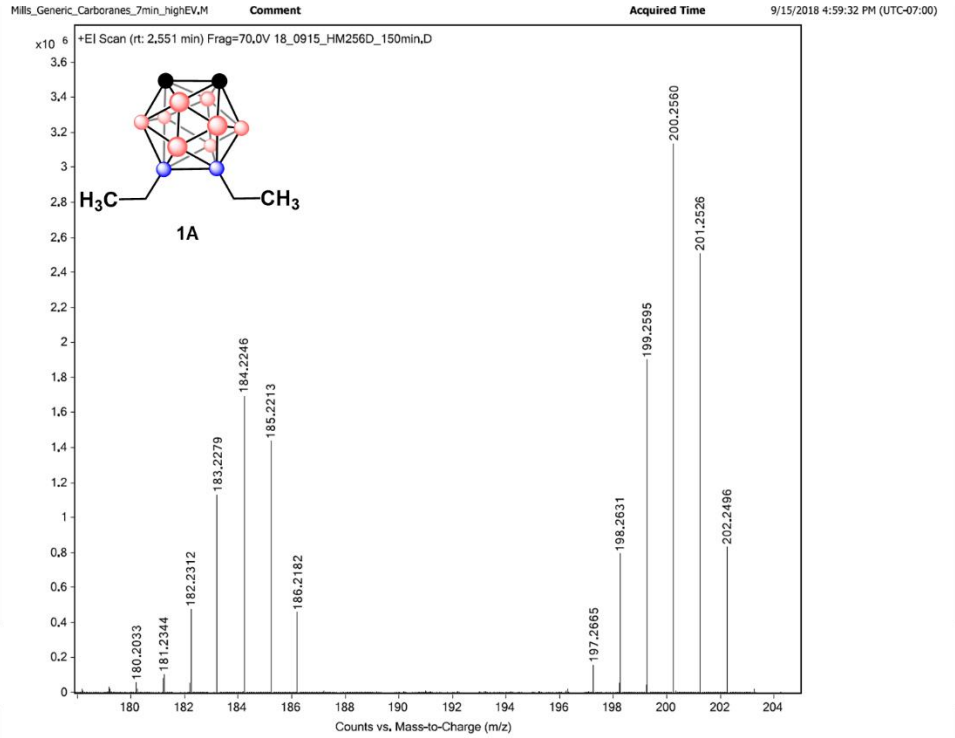

Figure A1.5 GC-MS of **1A**

2.6.4.2 Characterization of 1B

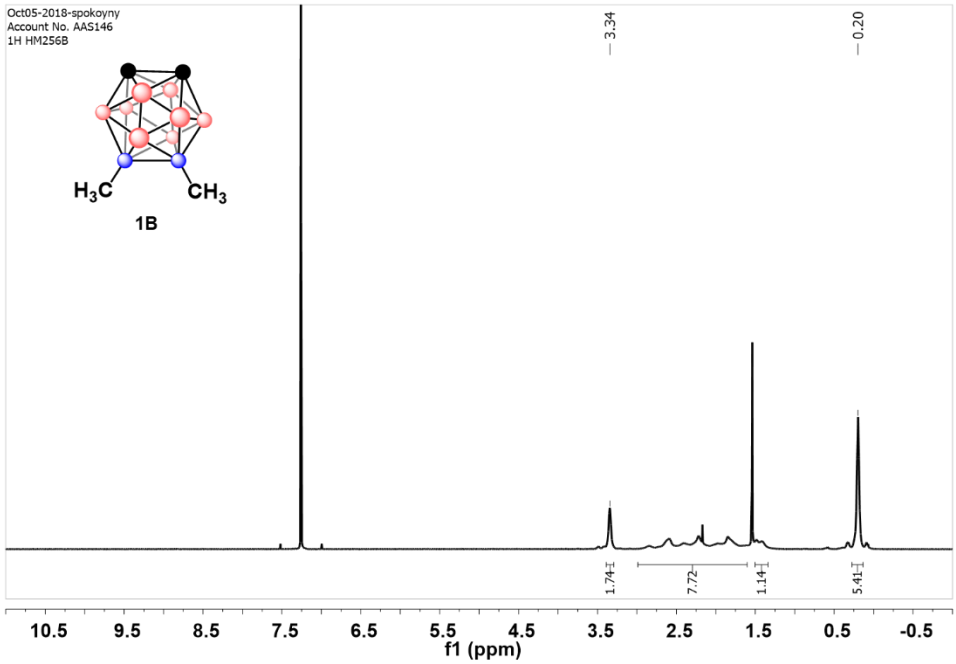

Figure A2.1 ^{1}H NMR of **1B**

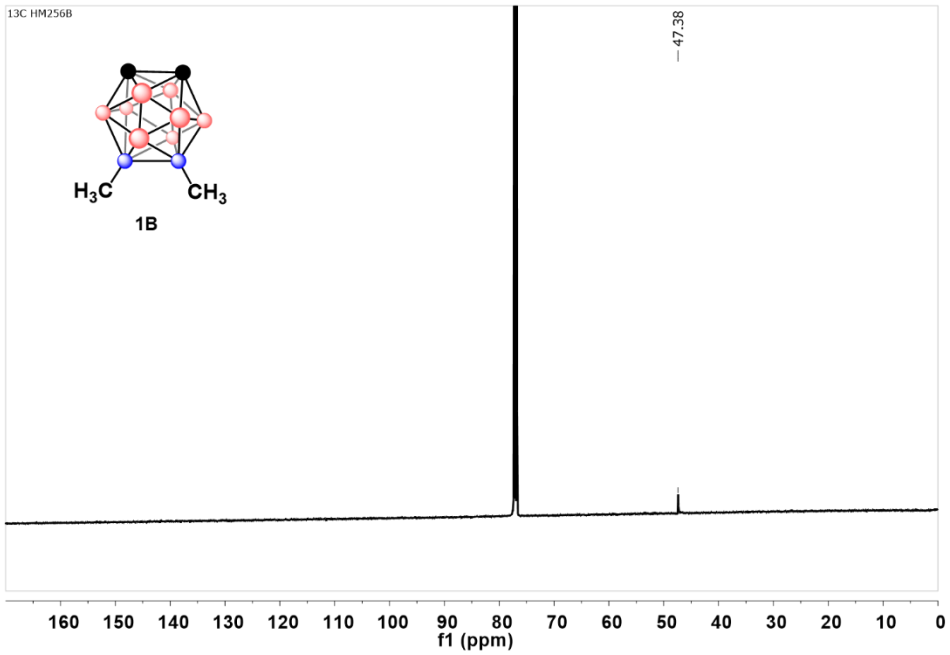

Figure A2.2 ^{13}C NMR of **1B**

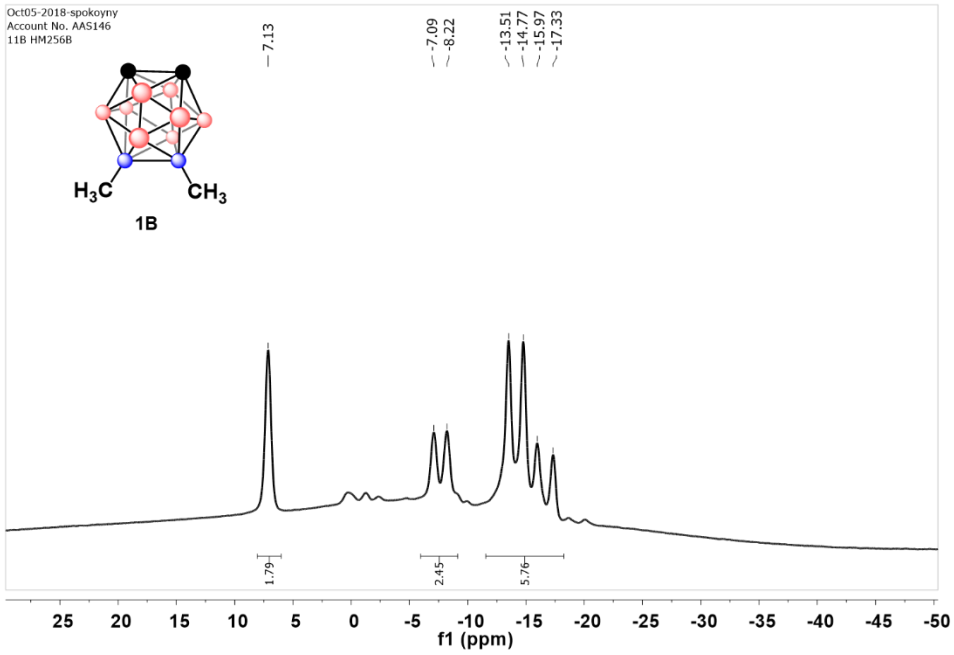

Figure A2.3 ^{11}B NMR of **1B**

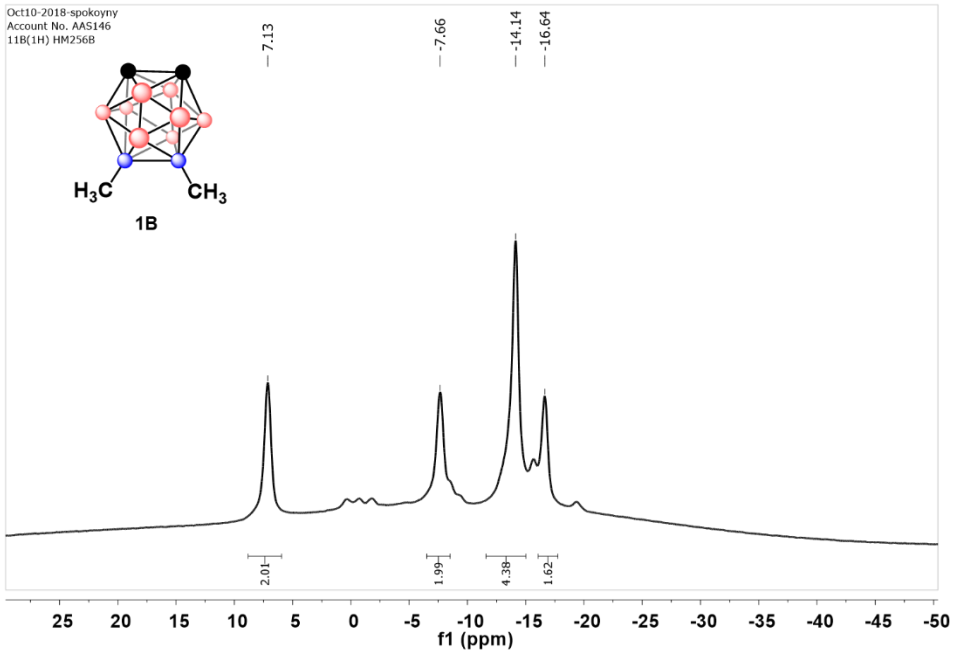

Figure A2.4 $^{11}B\{^{1}H\}$ NMR of **1B**

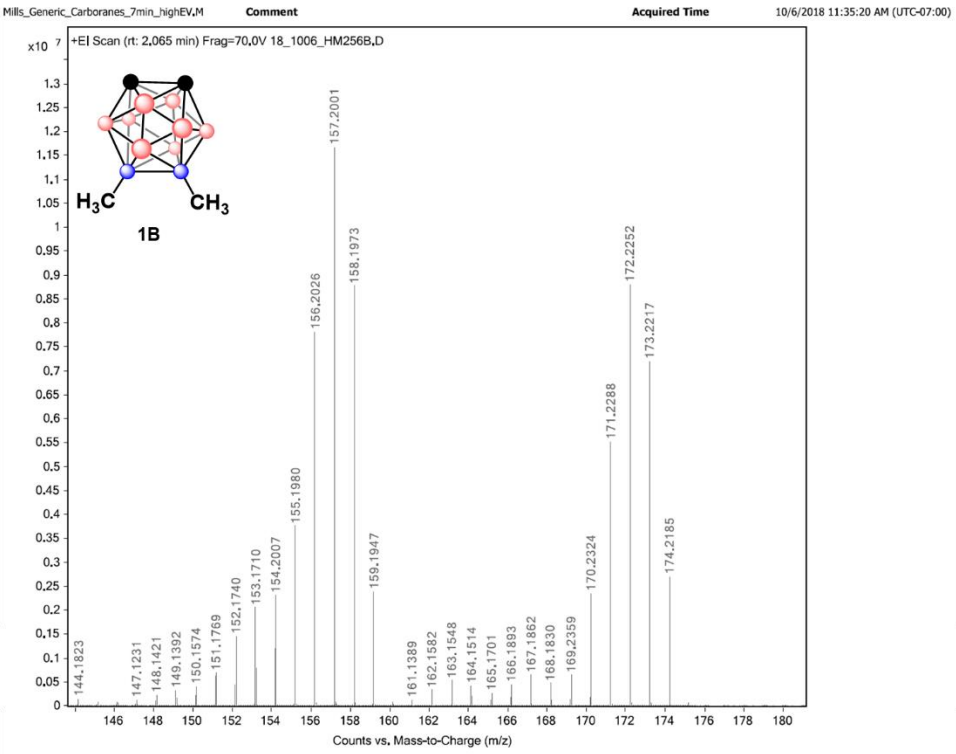

Figure A2.5 GC-MS of **1B**

2.6.4.3 Characterization of 1C

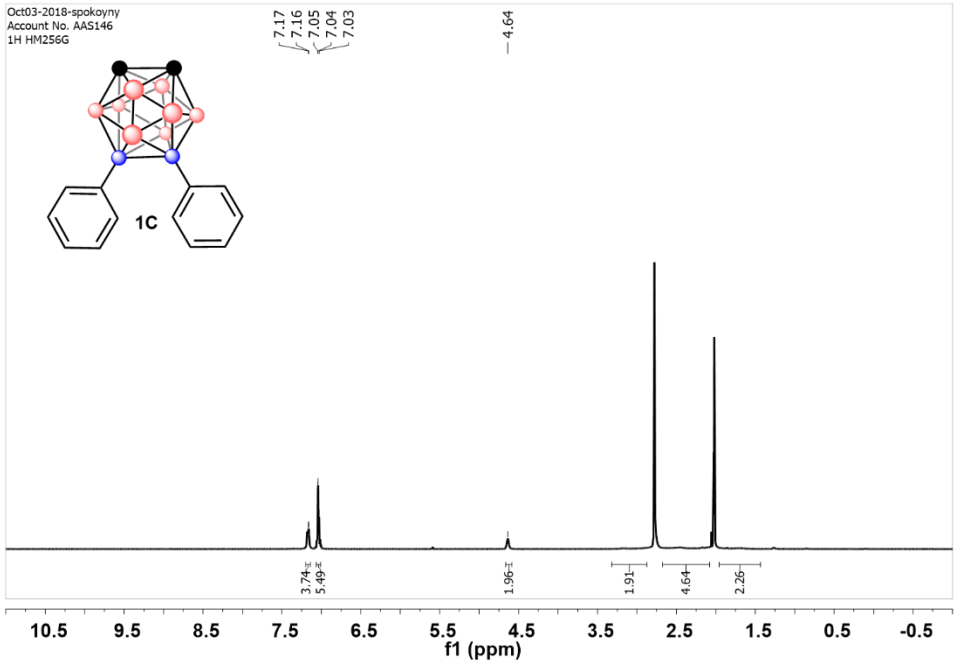

Figure A3.1 ^{1}H NMR of **1C**

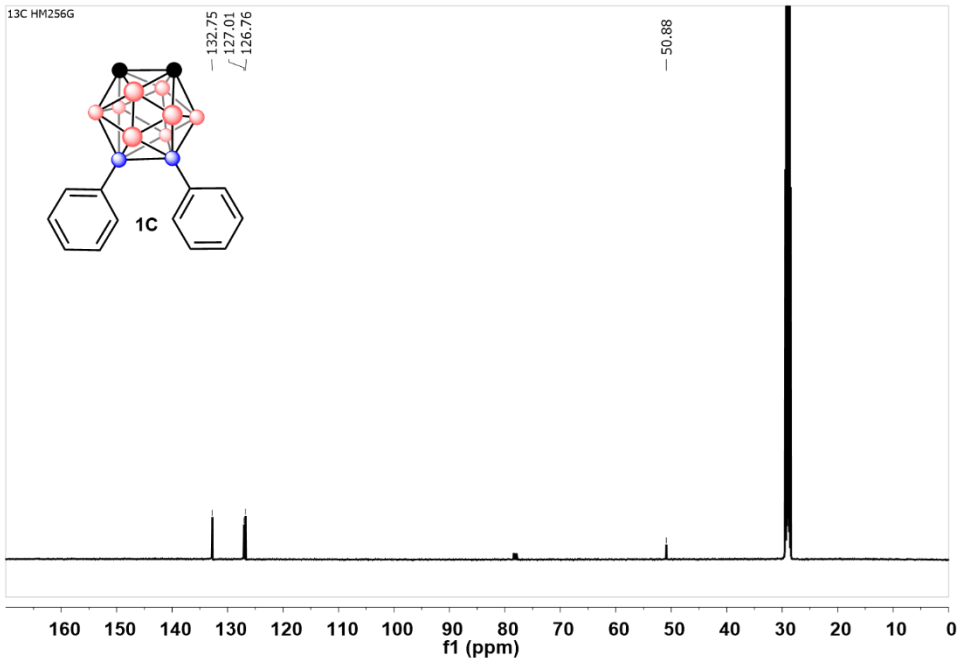

Figure A3.2 ^{13}C NMR of **1C**

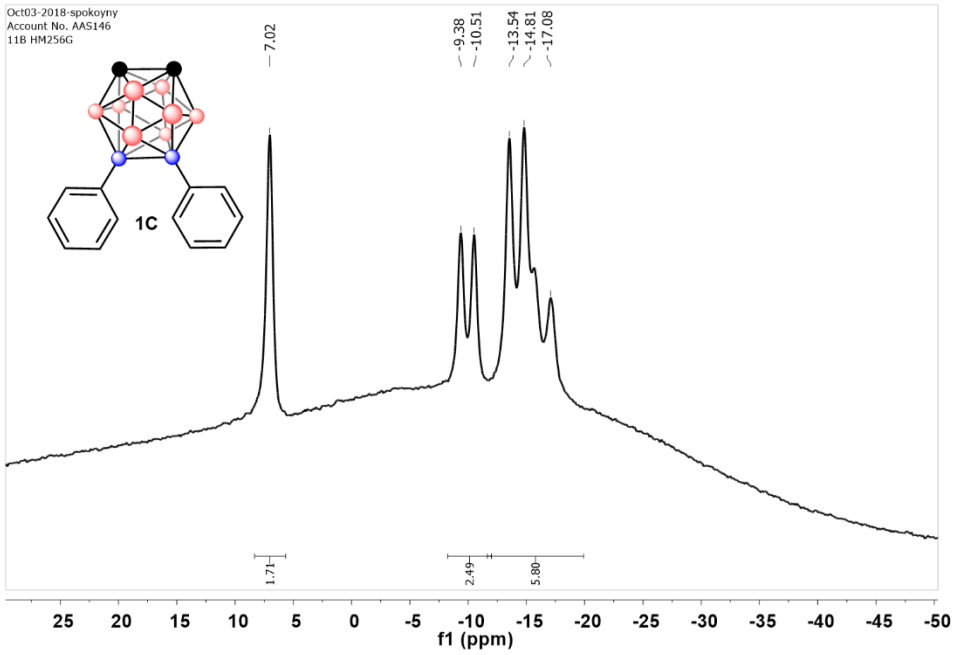

Figure A3.3 ^{11}B NMR of **1C**

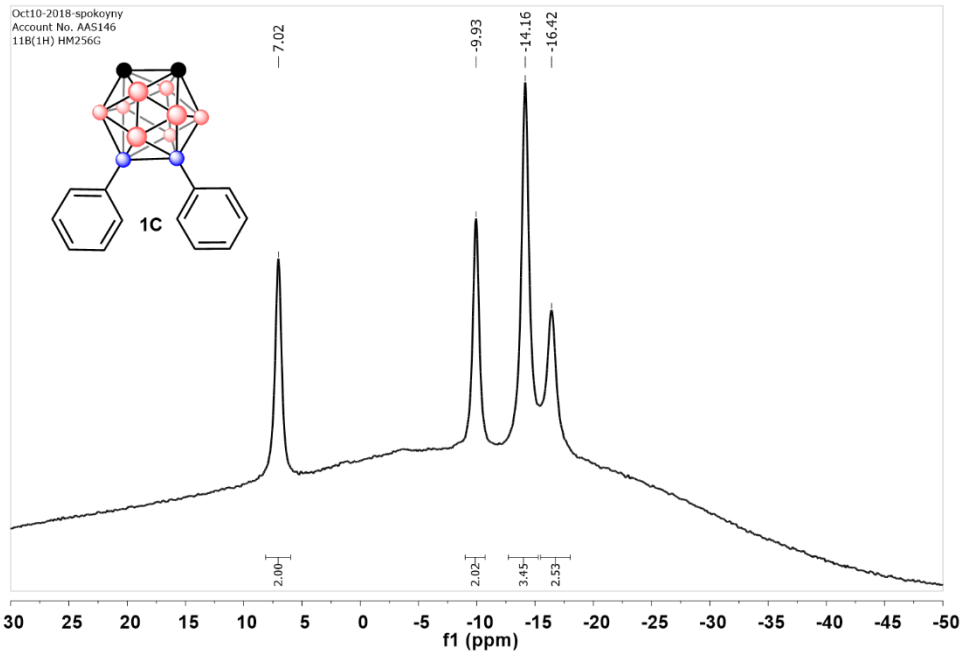

Figure A3.4 ^{11}B{^{1}H} NMR of **1C**

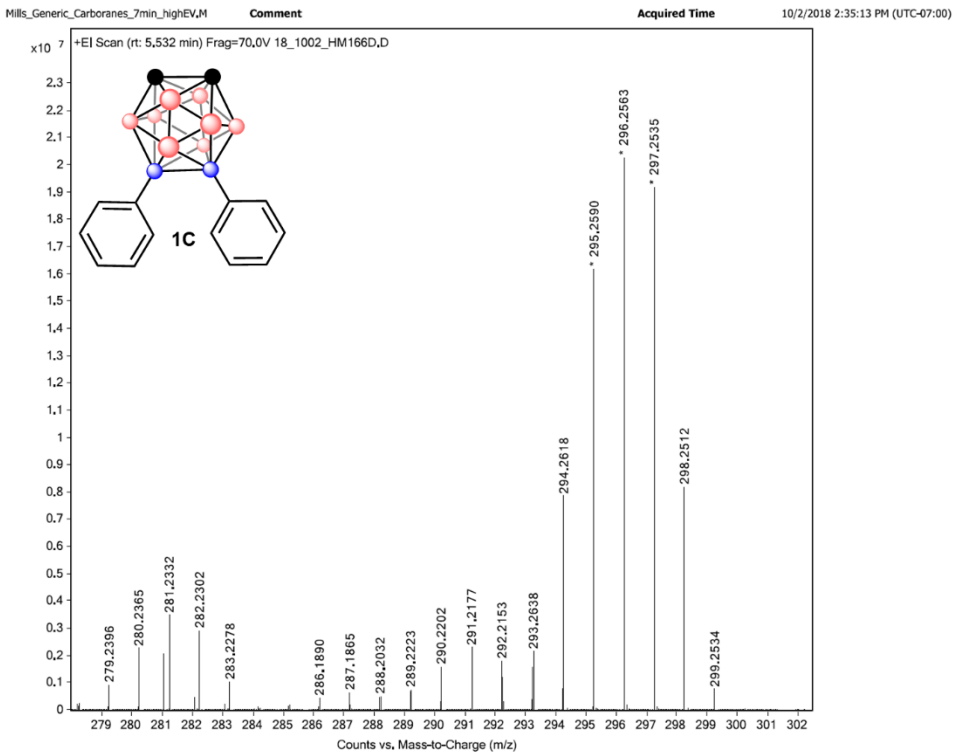

Figure A3.5 GC-MS of **1C**

2.6.4.4 Characterization of 1D

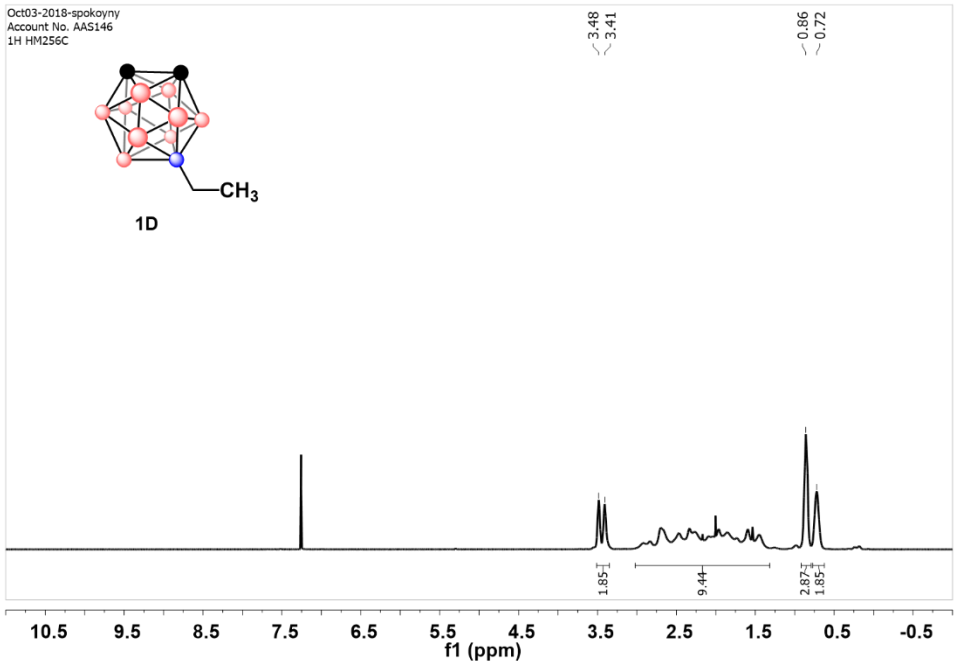

Figure A4.1 ^{1}H NMR of **1D**

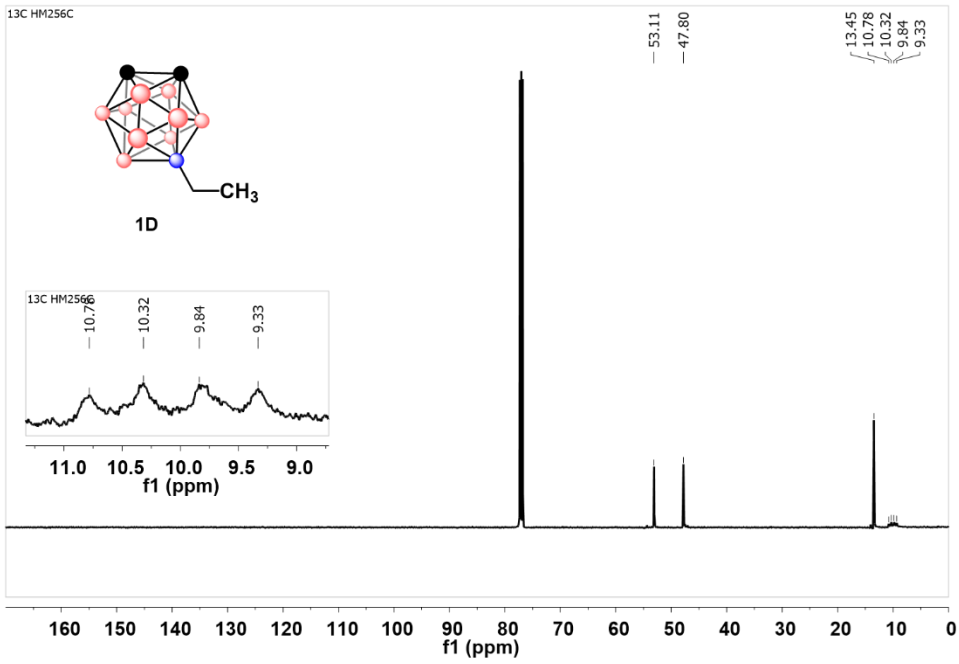

Figure A4.2 ^{13}C NMR of **1D**

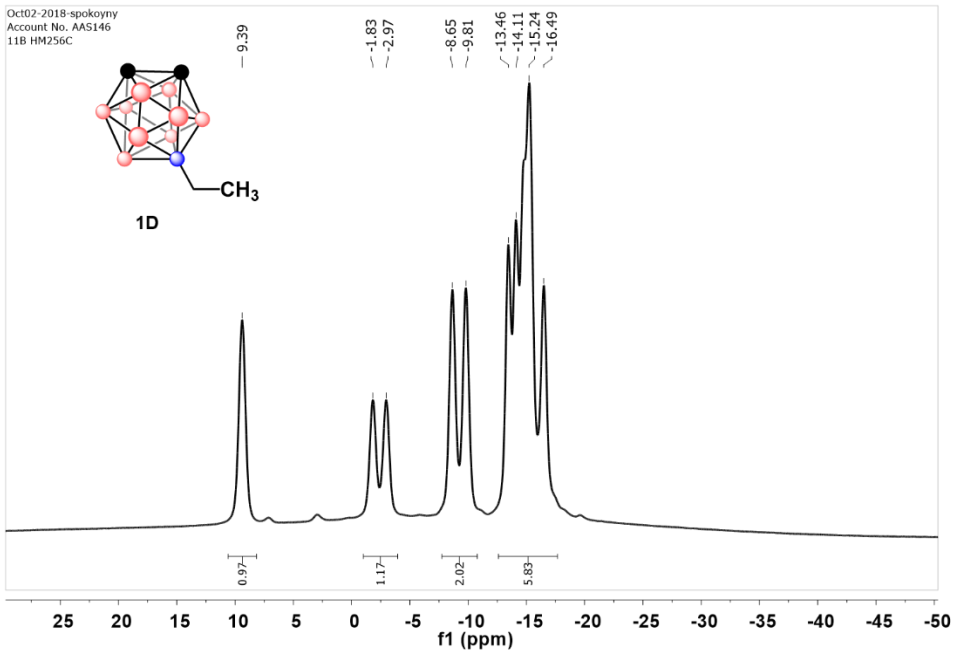

Figure A4.3 ^{11}B NMR of **1D**

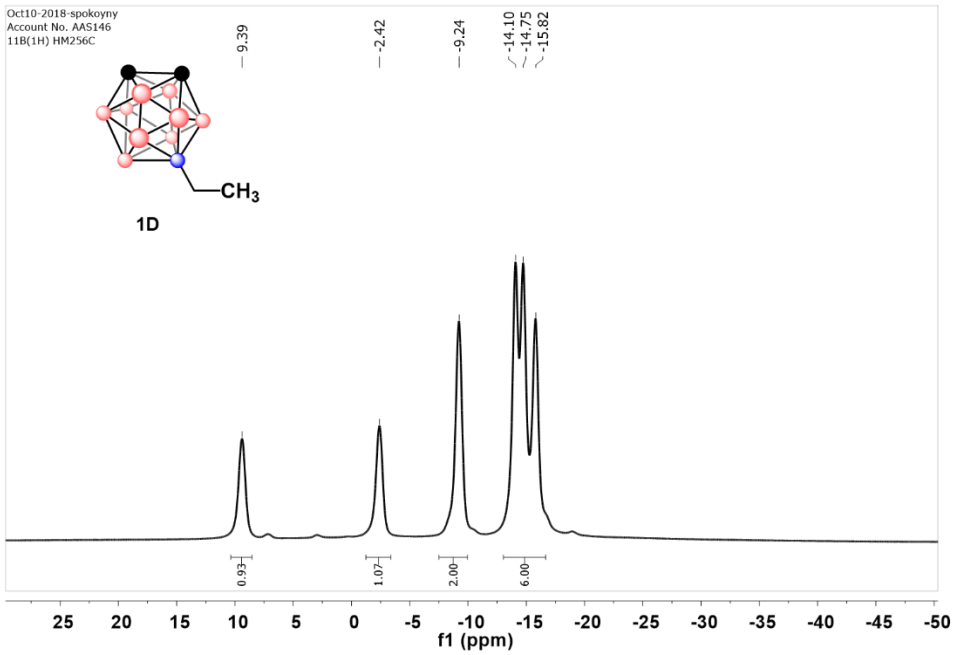

Figure A4.4 $^{11}B\{^{1}H\}$ NMR of **1D**

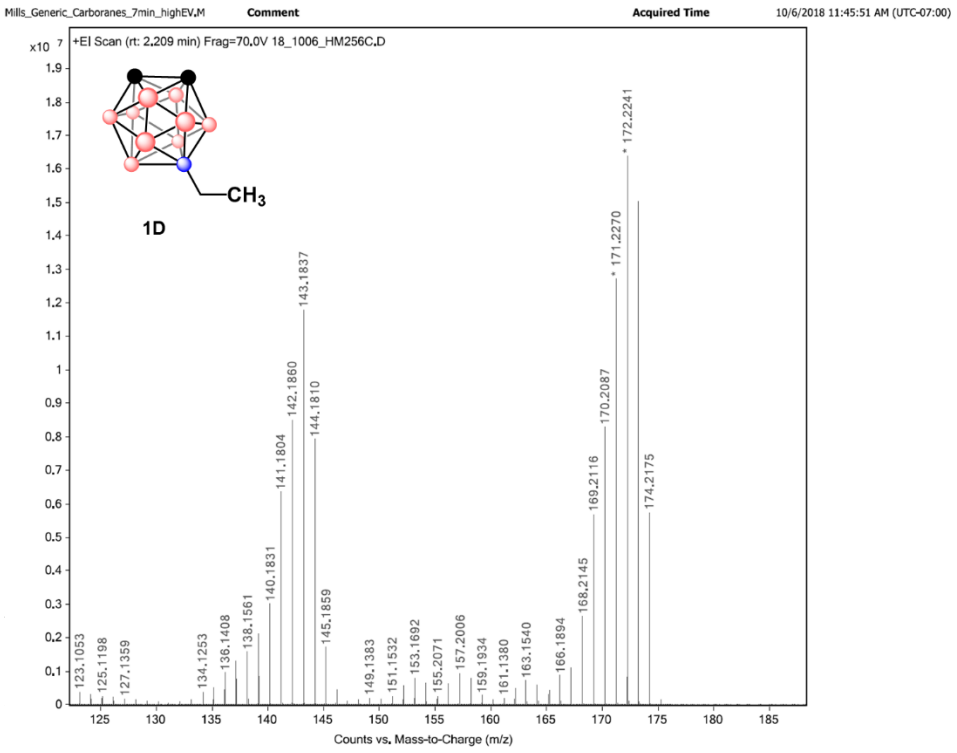

Figure A4.5 GC-MS of **1D**

2.6.4.5 Characterization of 1E

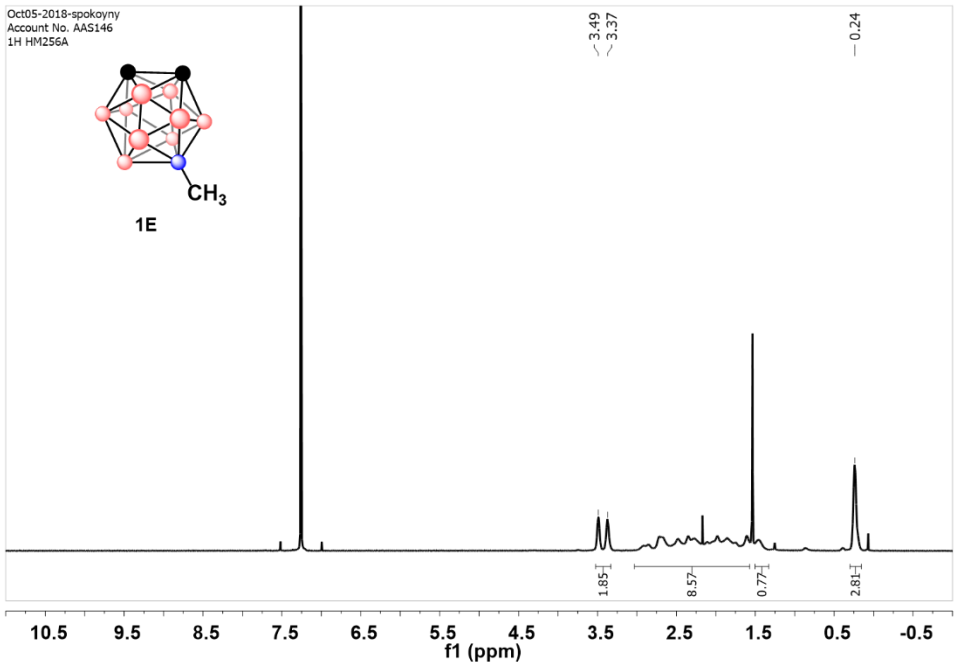

Figure A5.1 ^{1}H NMR of **1E**

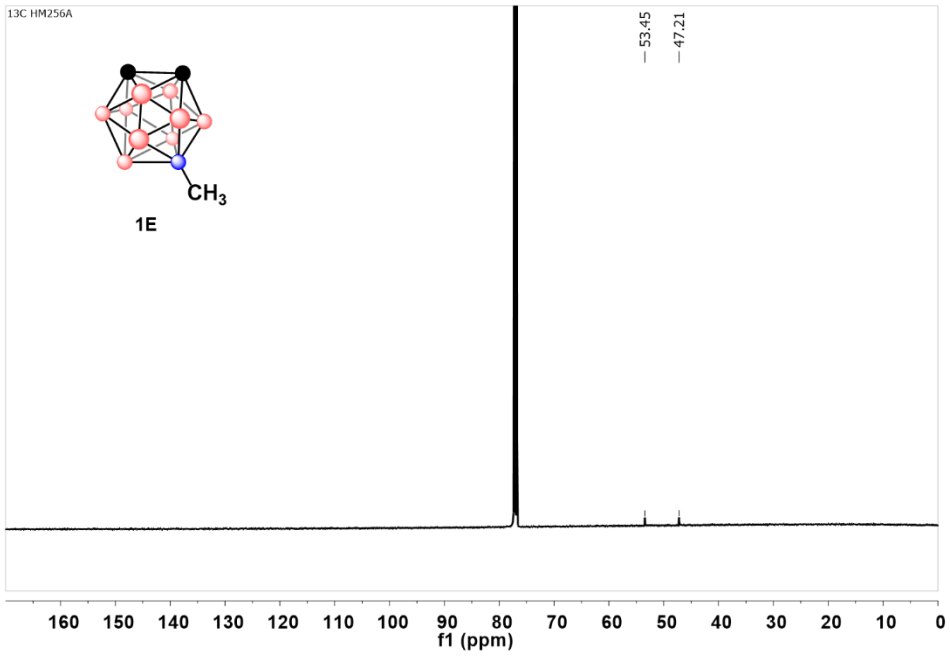

Figure A5.2 ^{13}C NMR of **1E**

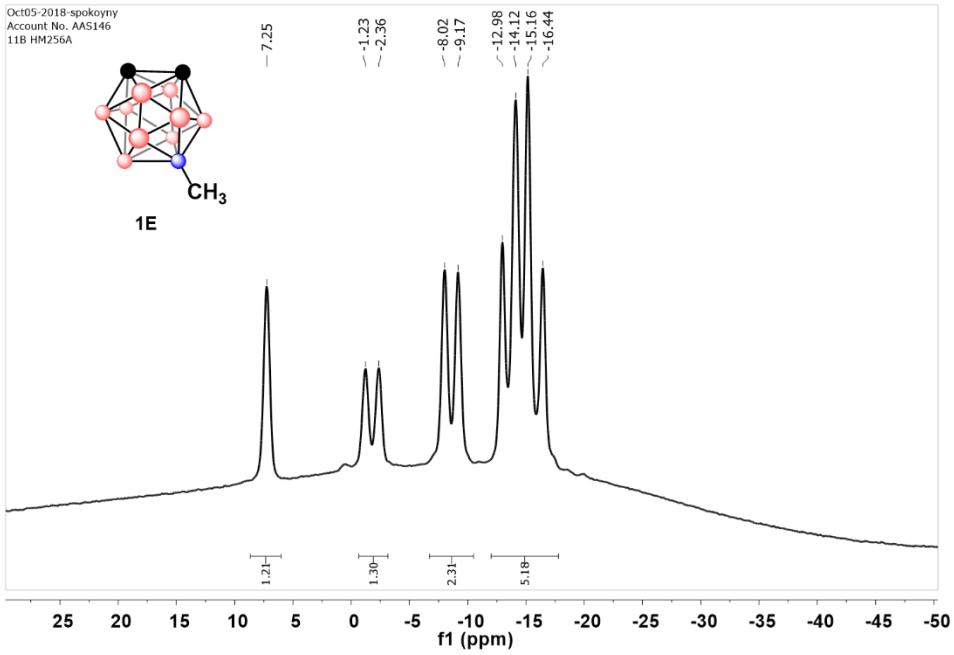

Figure A5.3 ^{11}B NMR of **1E**

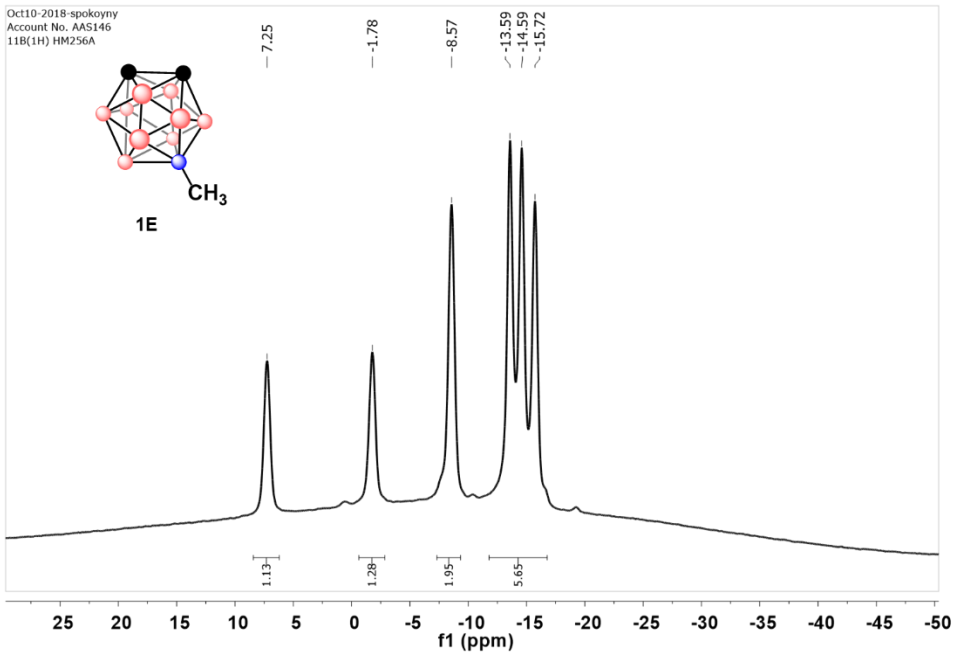

Figure A5.4 ^{11}B{^{1}H} NMR of **1E**

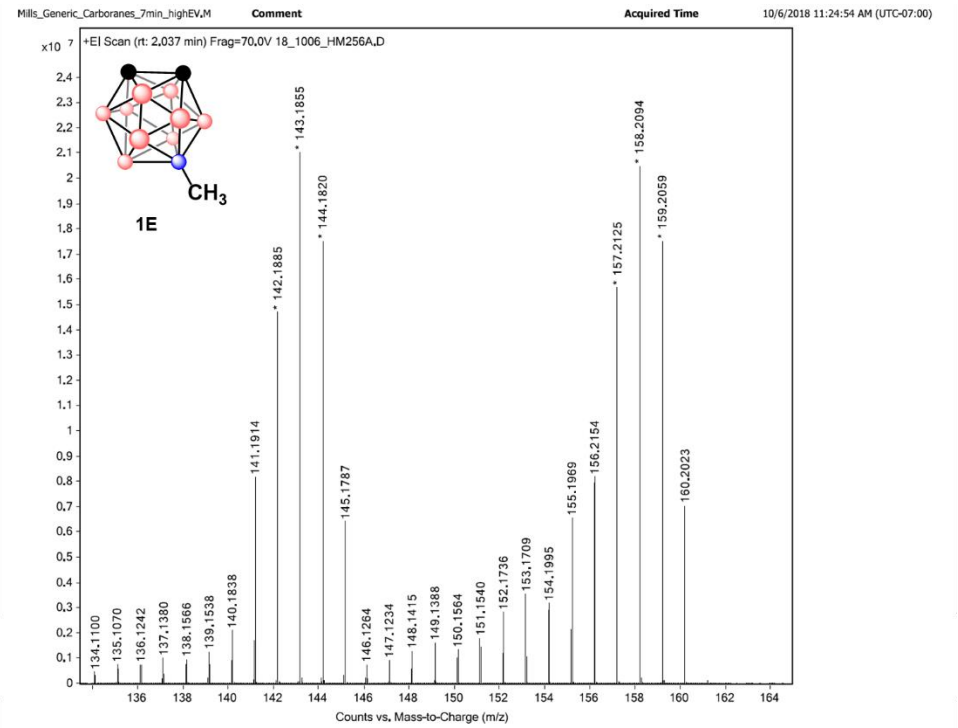

Figure A5.5 GC-MS of **1E**

2.6.4.6 Characterization of 1F

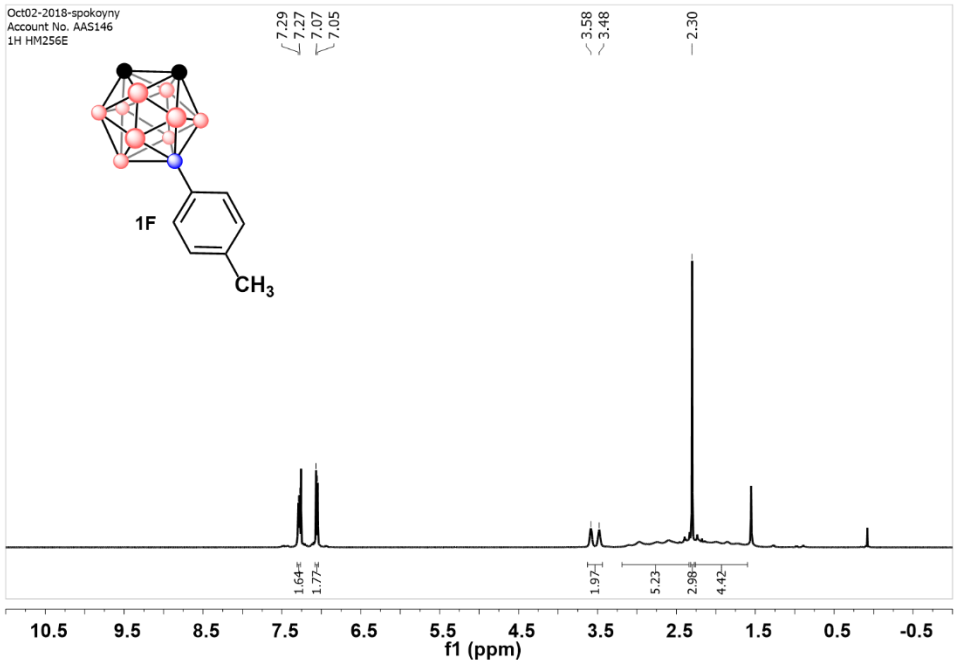

Figure A6.1 ^{1}H NMR of **1F**

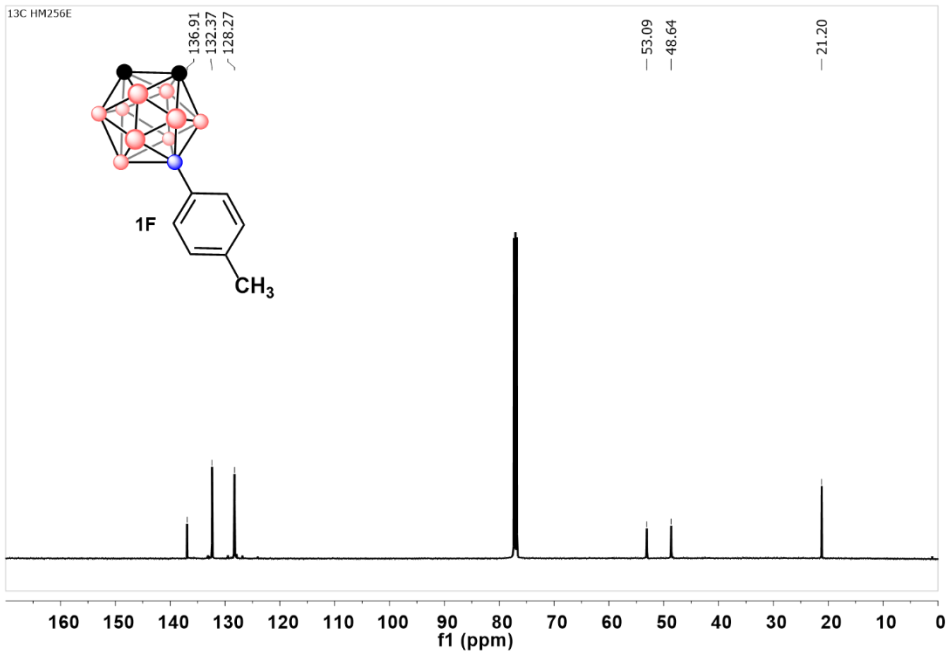

Figure A6.2 ^{13}C NMR of **1F**

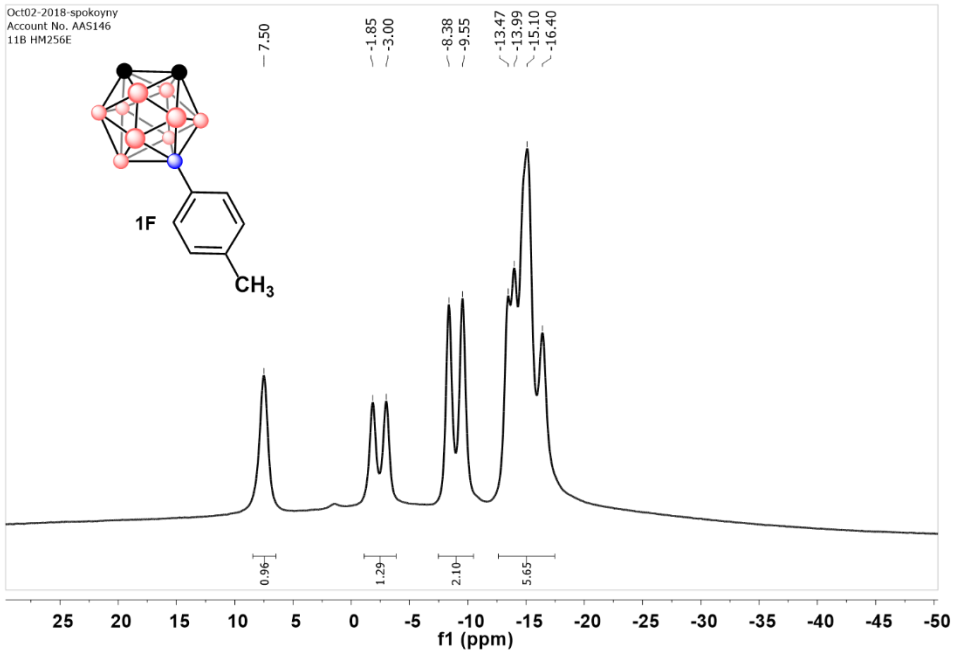

Figure A6.3 ^{11}B NMR of **1F**

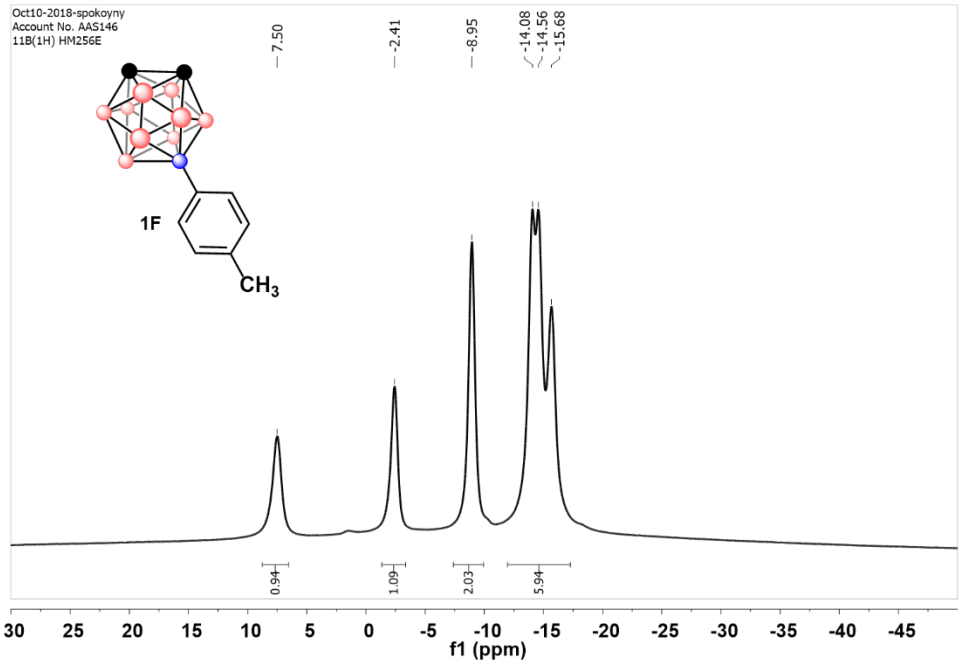

Figure A6.4 $^{11}B\{^{1}H\}$ NMR of **1F**

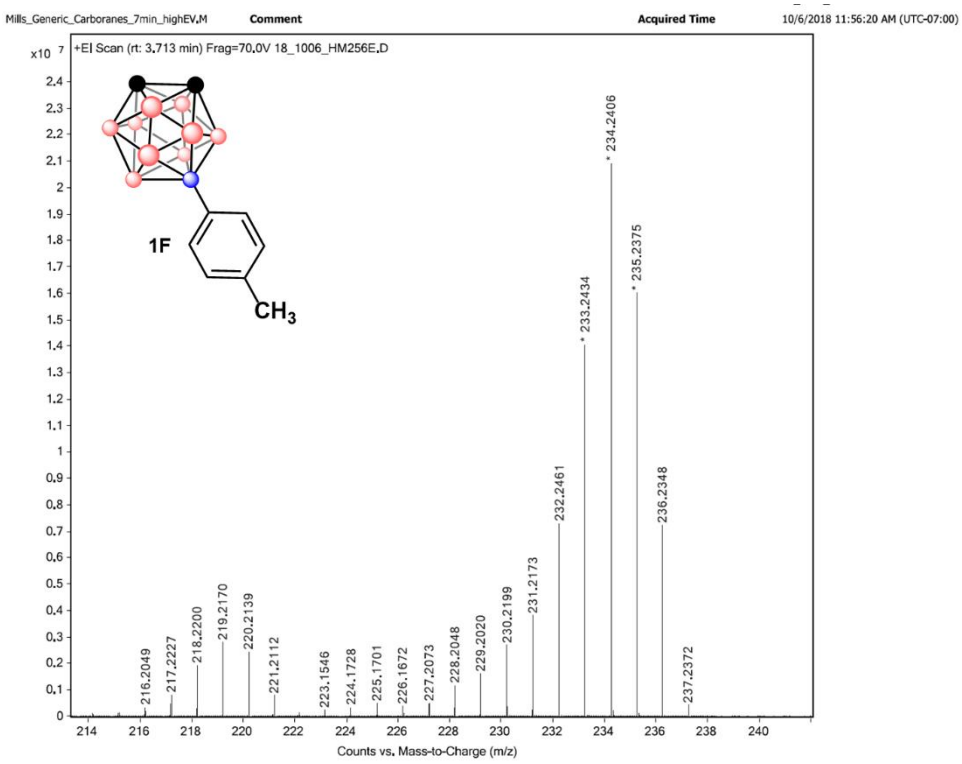

Figure A6.5 GC-MS of **1F**

2.6.4.7 Characterization of 1G

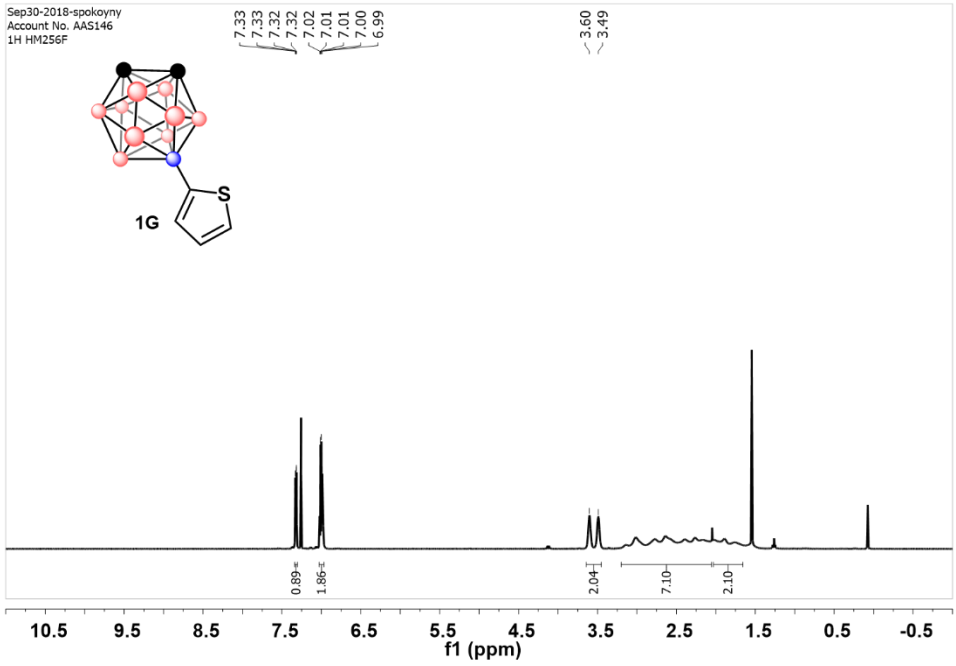

Figure A7.1 ^{1}H NMR of **1G**

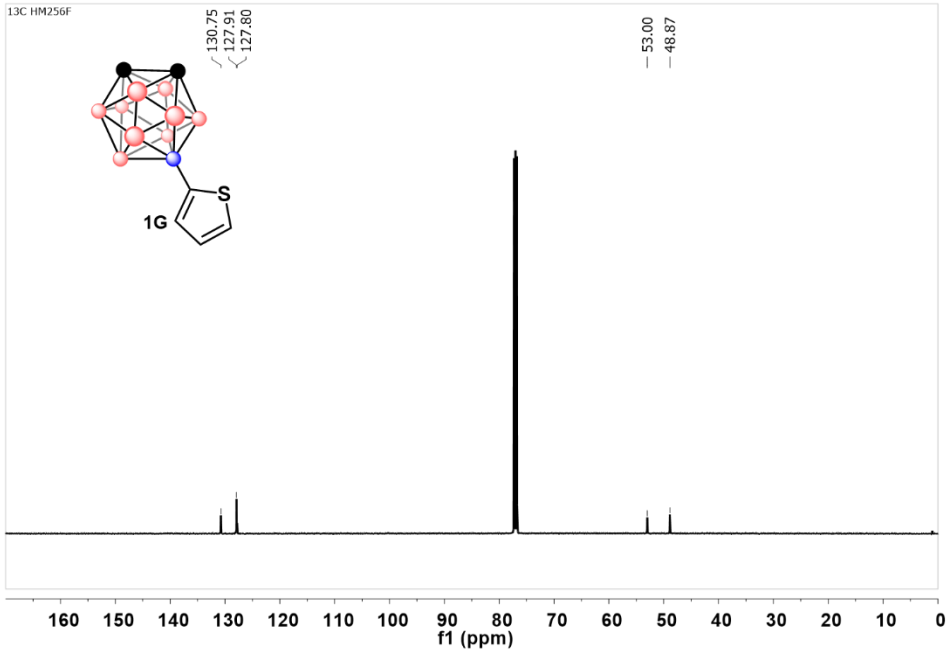

Figure A7.2 ^{13}C NMR of **1G**

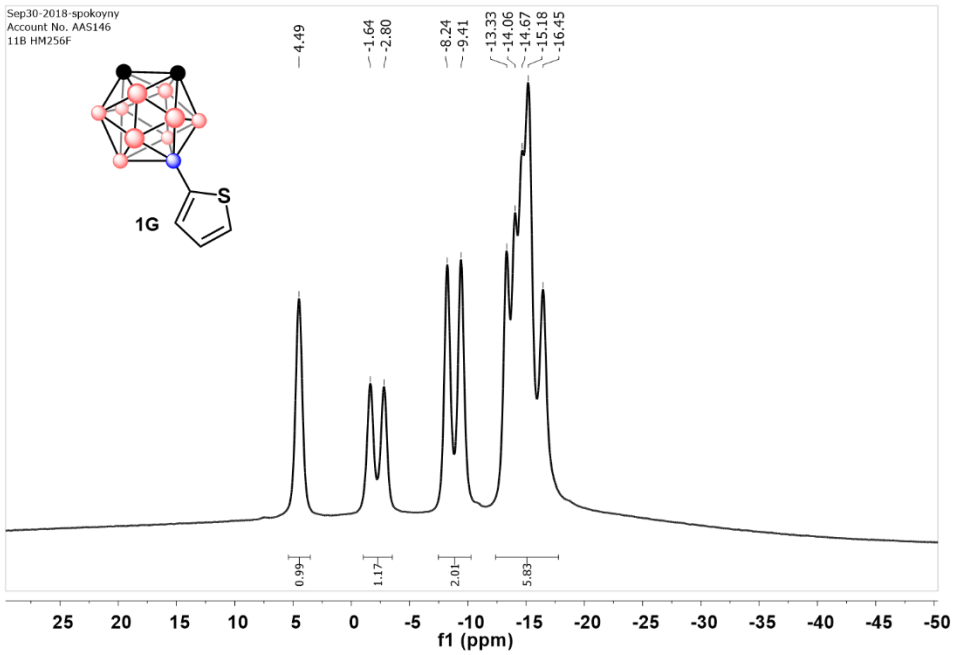

Figure A7.3 ^{11}B NMR of **1G**

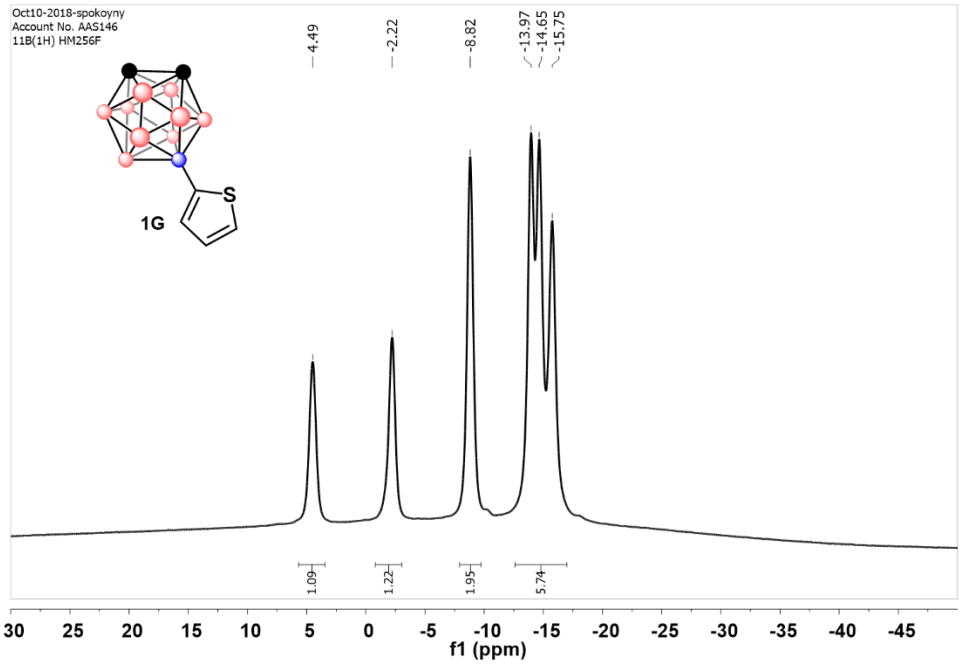

Figure A7.4 ^{11}B{^{1}H} NMR of **1G**

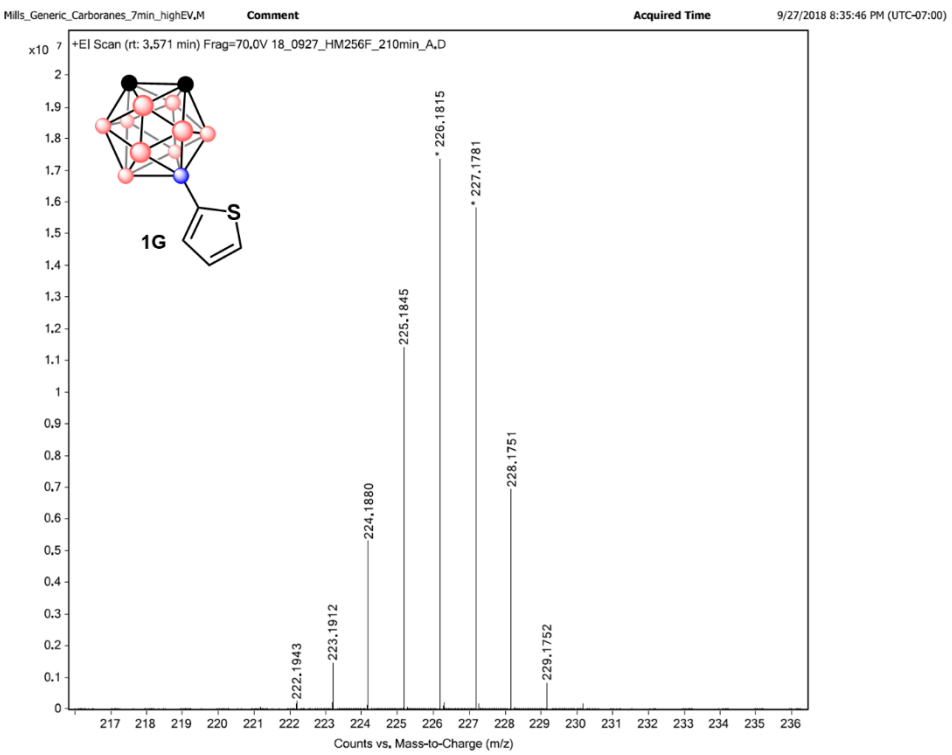

Figure A7.5 GC-MS of **1G**

2.6.4.8 Characterization of 1H

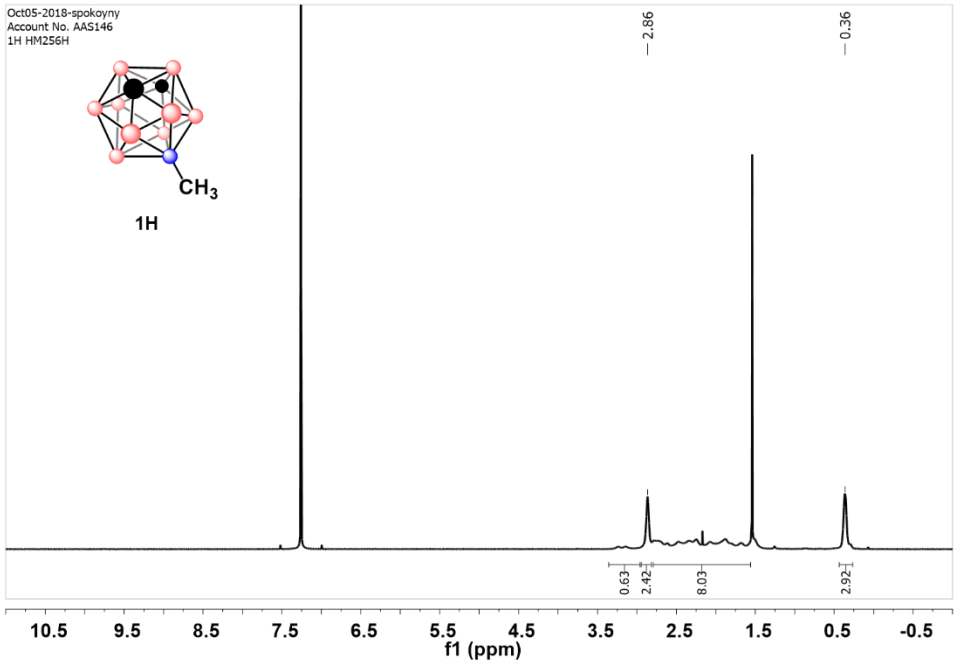

Figure A8.1 ^{1}H NMR of **1H**

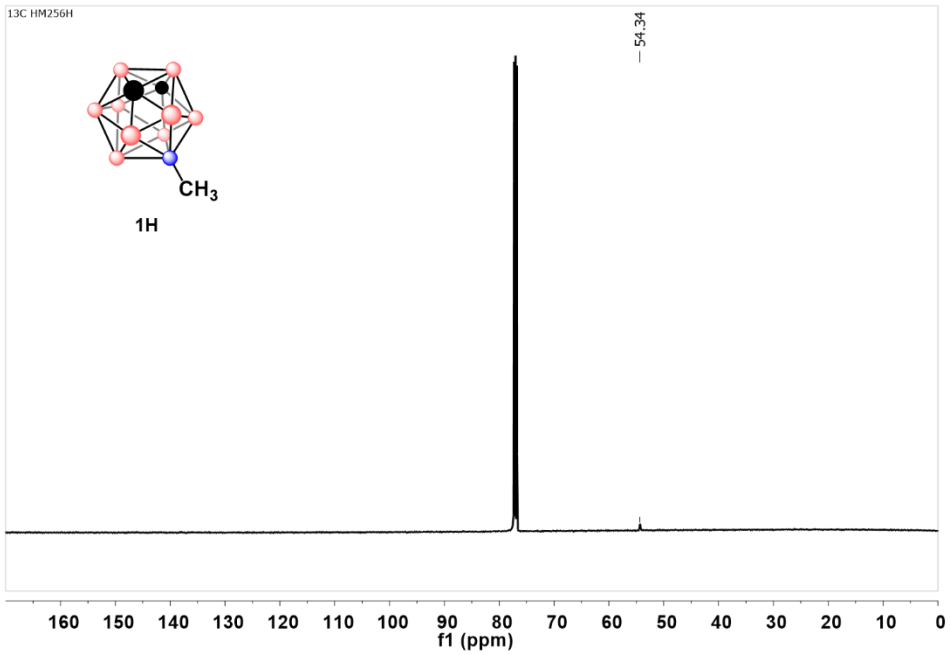

Figure A8.2 ^{13}C NMR of **1H**

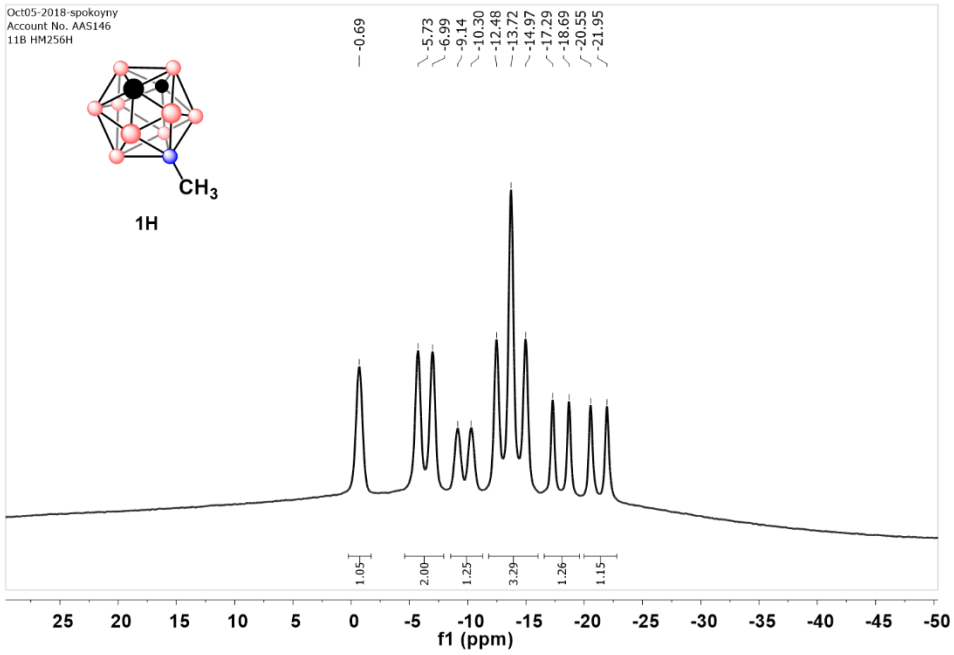

Figure A8.3 ^{11}B NMR of **1H**

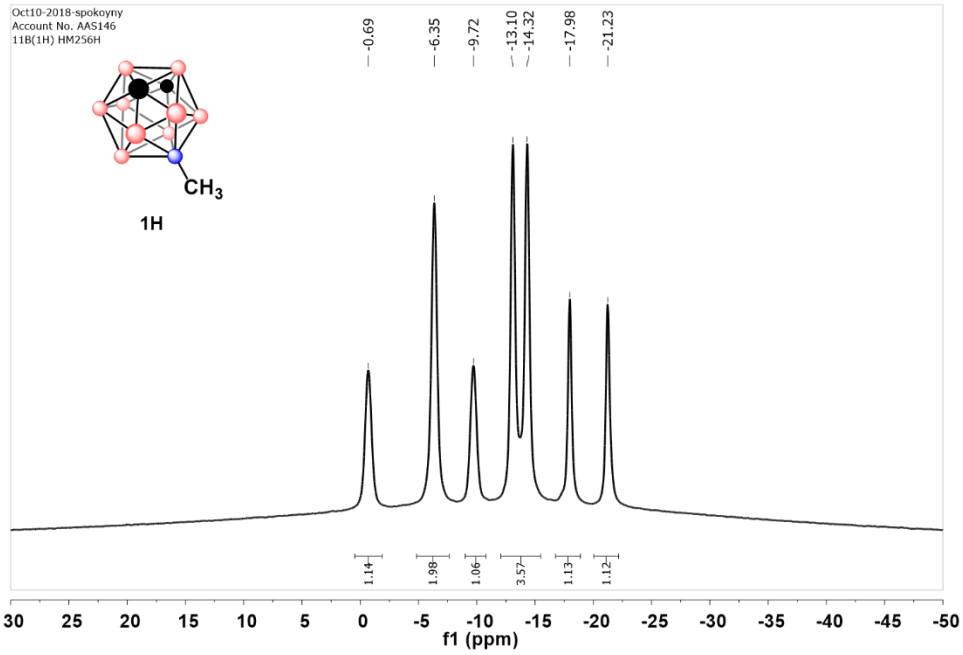

Figure A8.4 $^{11}B\{^{1}H\}$ NMR of **1H**

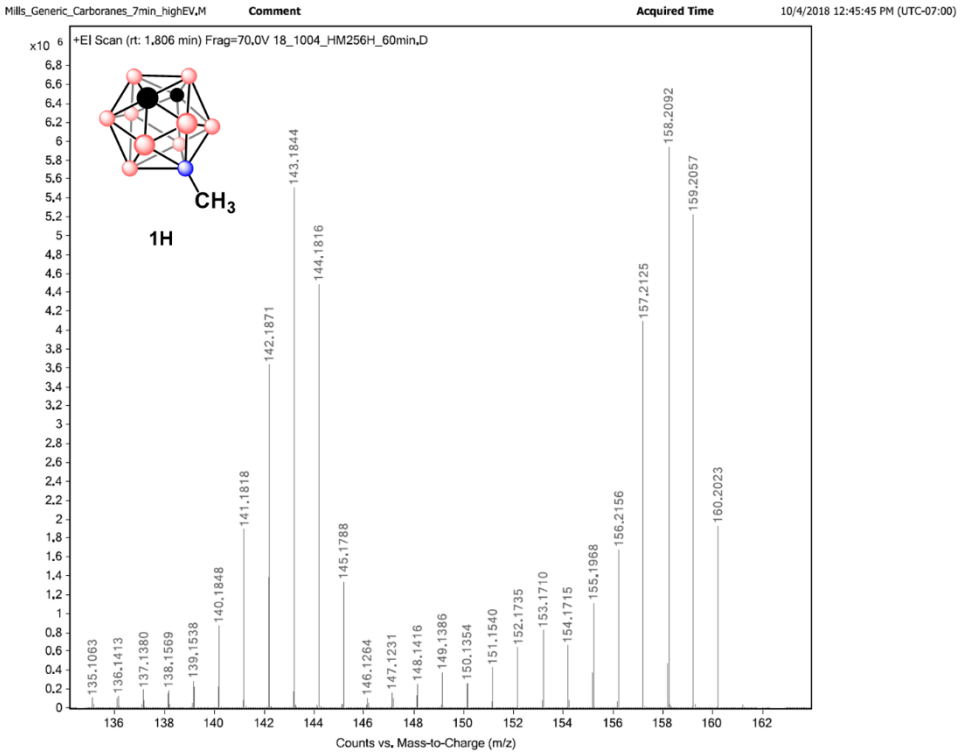

Figure A8.5 GC-MS of **1H**

2.6.4.9 Characterization of 1I

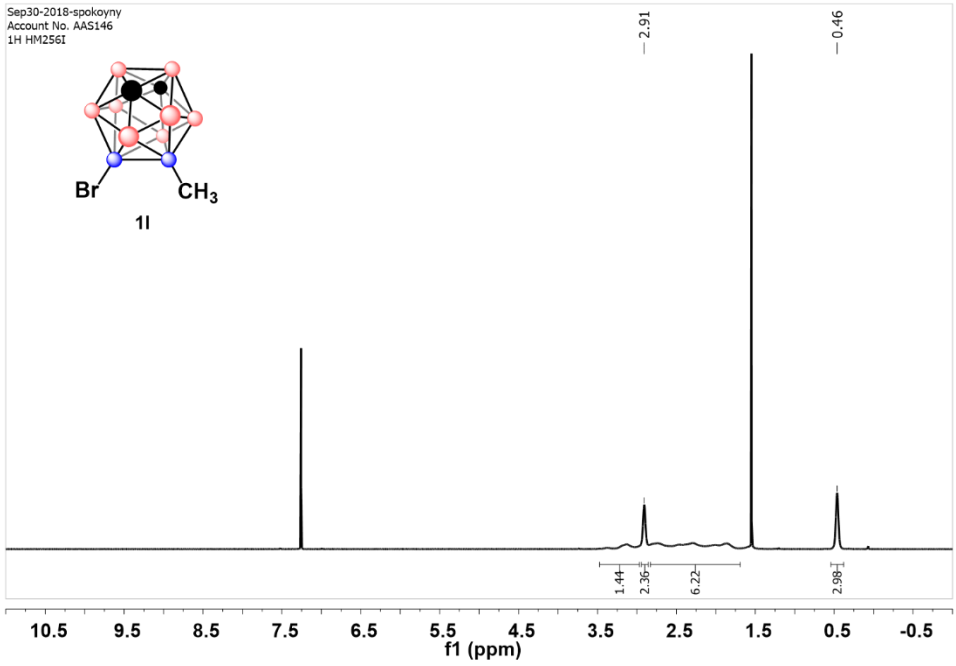

Figure A9.1 ^{1}H NMR of **1I**

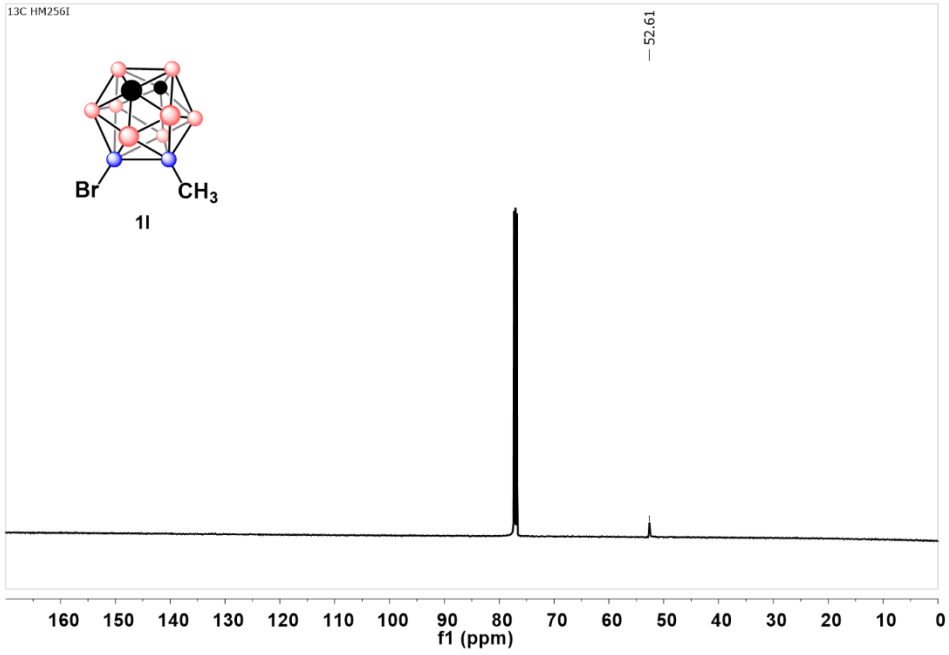

Figure A9.2 ^{13}C NMR of **1I**

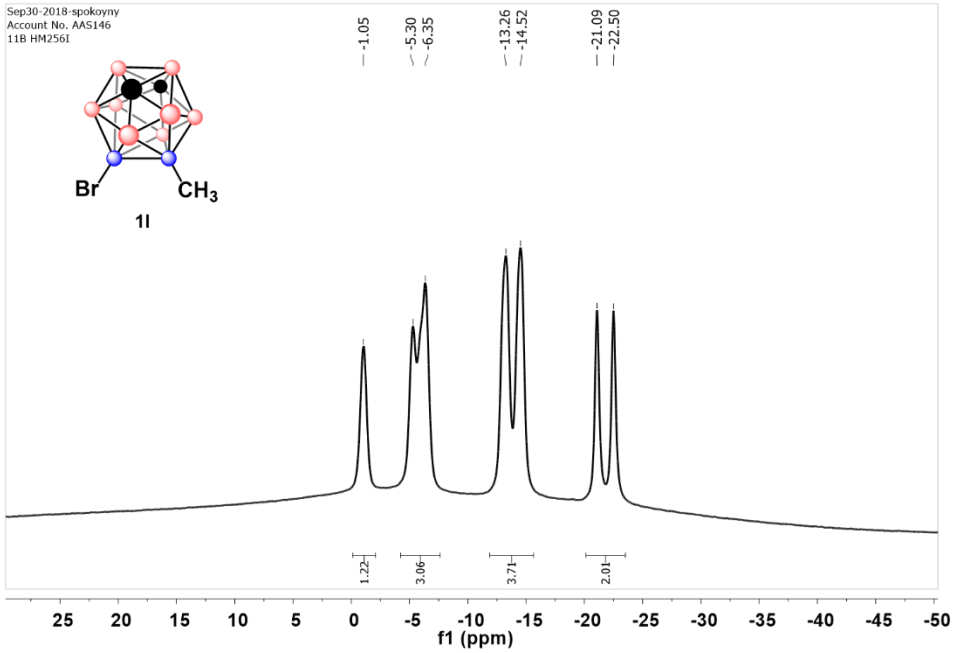

Figure A9.3 ^{11}B NMR of **1I**

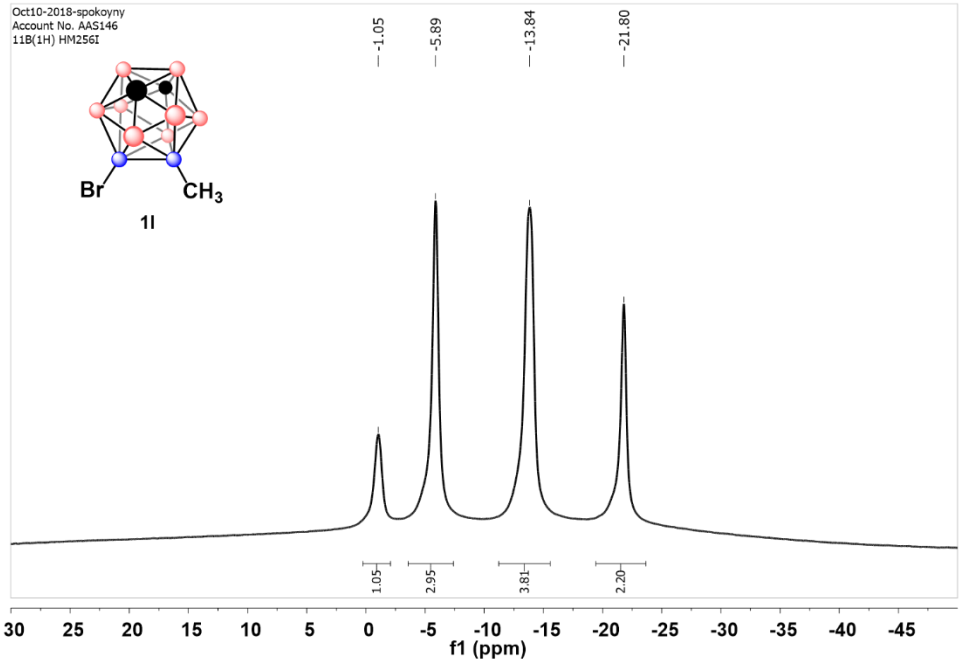

Figure A9.4 ^{11}B{^{1}H} NMR of **1I**

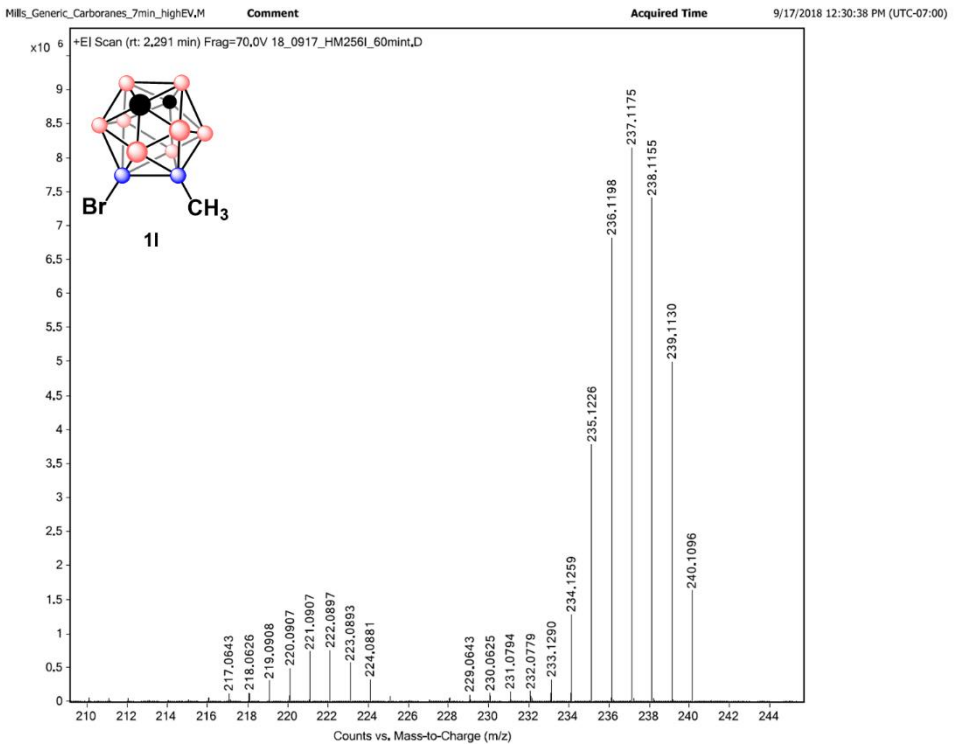

Figure A9.5 GC-MS of **1I**

2.6.4.10 Characterization of 1J

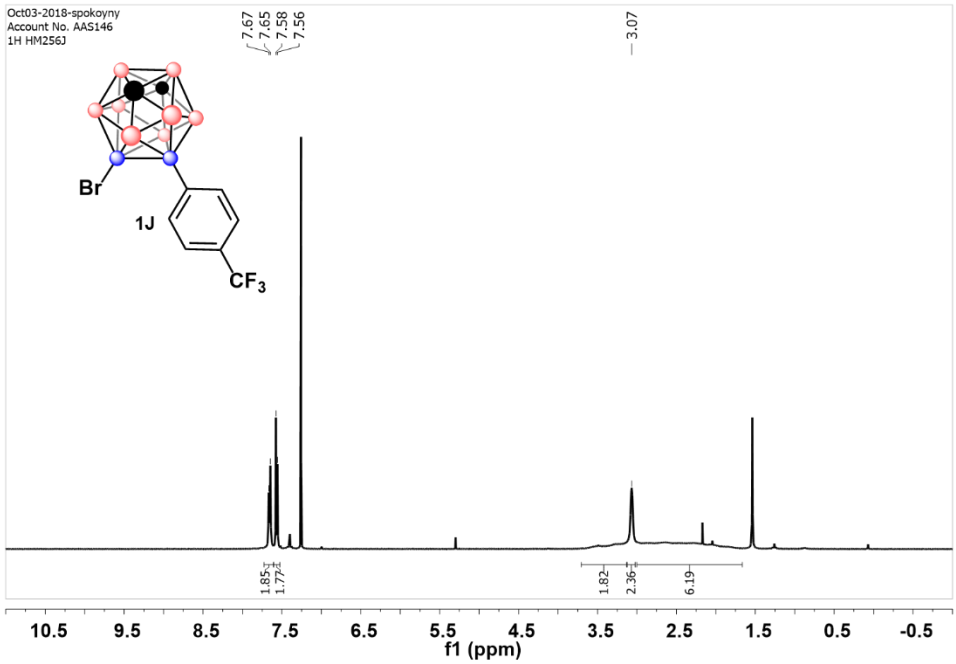

Figure A10.1 ^{1}H NMR of **1J**

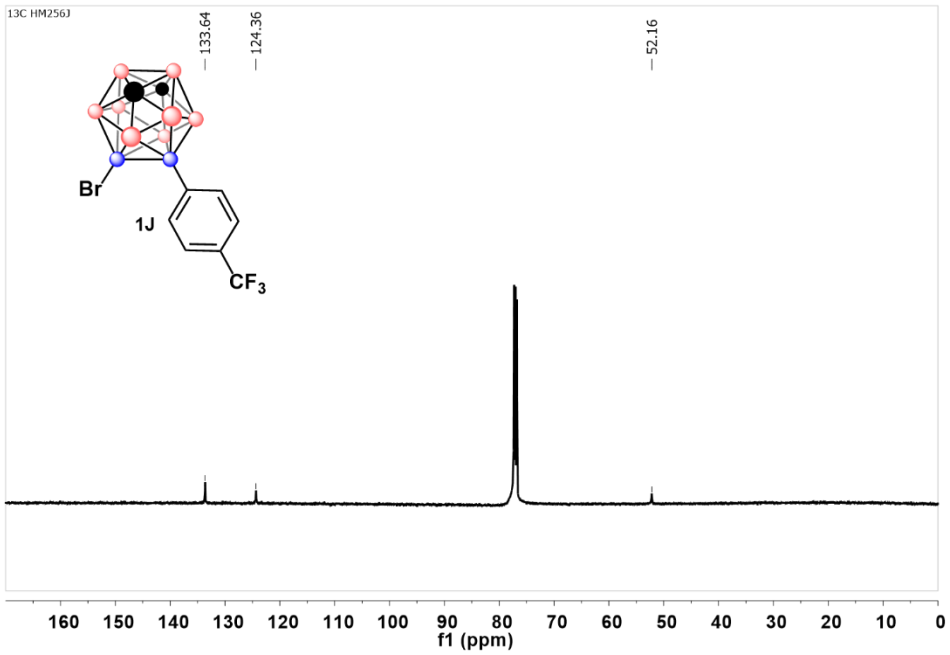

Figure A10.2 ^{13}C NMR of **1J**

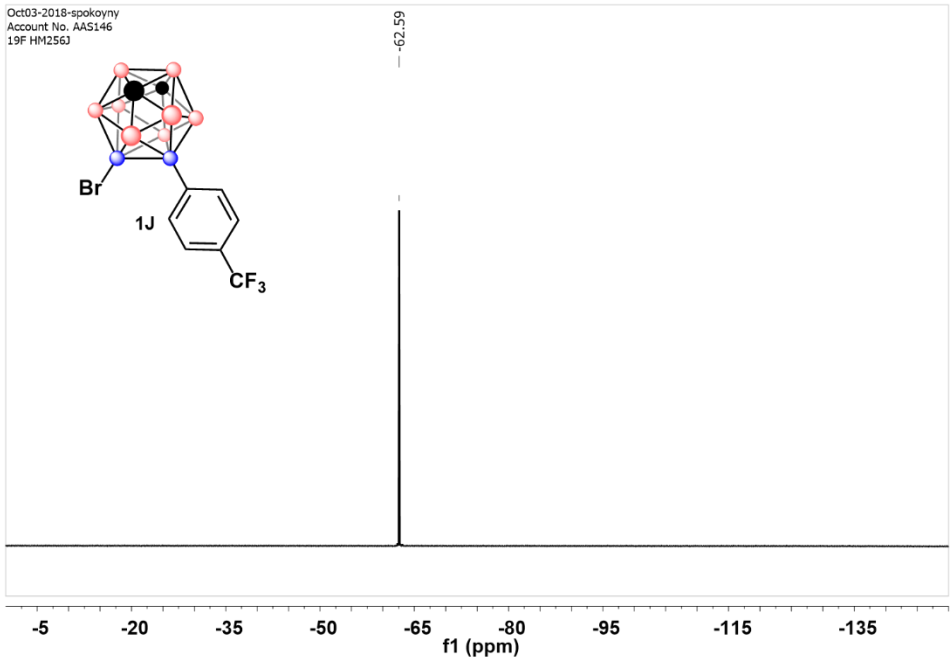

Figure A10.3 ^{19}F NMR of **1J**

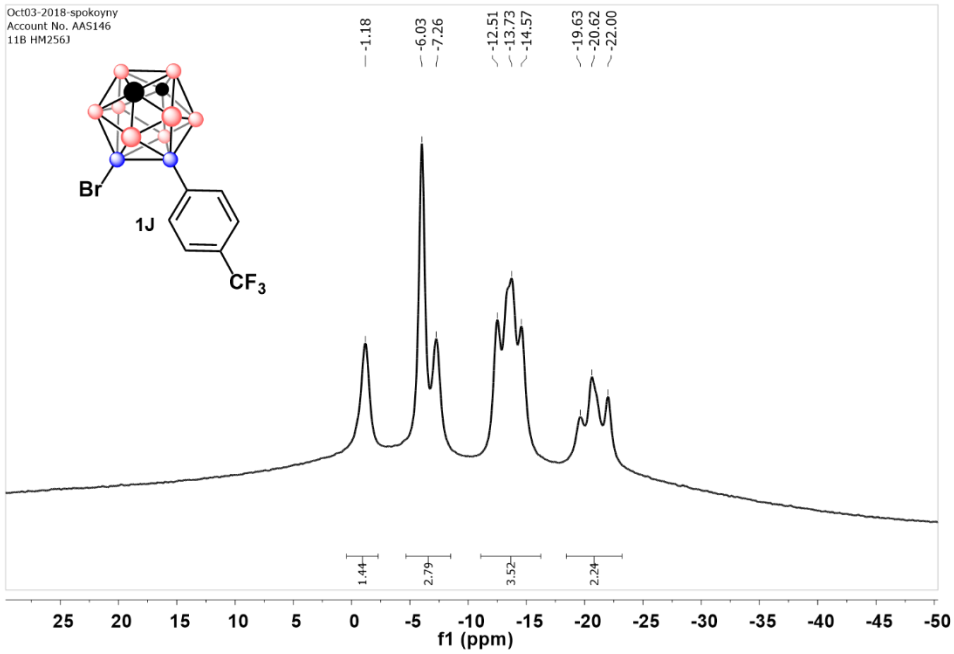

Figure A10.4 ^{11}B NMR of **1J**

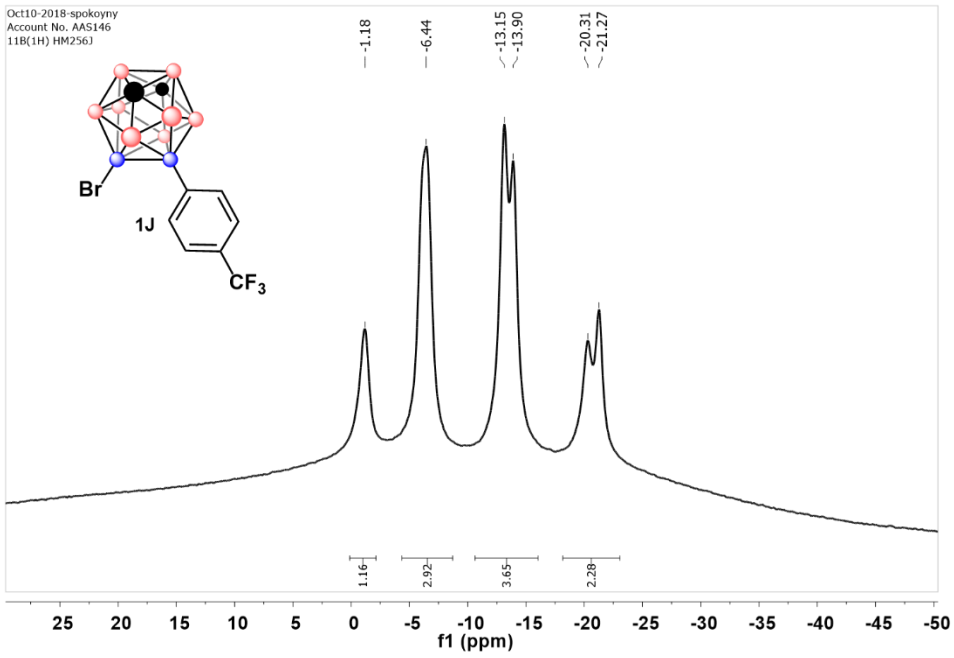

Figure A10.5 ^{11}B{^{1}H} NMR of **1J**

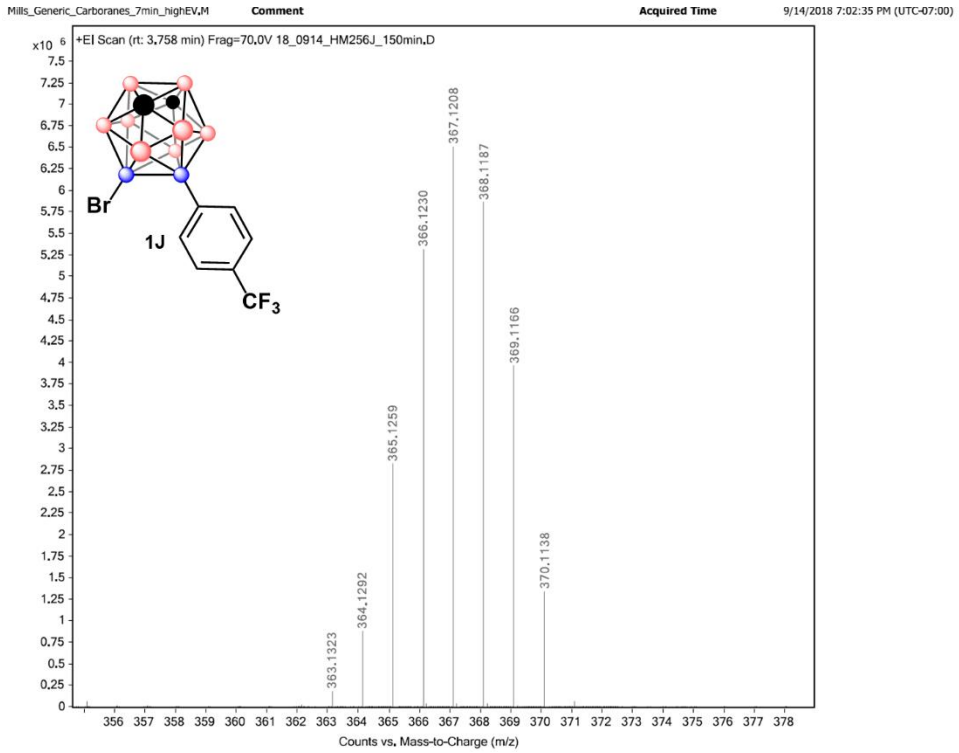

Figure A10.5 GC-MS of **1J**

2.6.5 References for Appendix A

1. Bruno, N. C.; Tudge, M. T.; Buchwald, S. L. *Chem. Sci.* **2013**, 4, 916-920.

2. Dziedzic, R. M.; Saleh, L. M. A.; Axtell, J. C.; Martin, J. L.; Stevens, S. L.; Royappa, A. T.; Rheingold, A. L.; Spokoyny, A. M. *J. Am. Chem. Soc.* **2016**, *138*, 9081-9084.

3. Kirlikovali, K. O.; Axtell, J. C., Gonzalez, A.; Phung, A. C.; Khan, S. I.; Spokoyny, A. M. *Chem. Sci.* **2016**, *7*, 5132-5138.

CHAPTER 3 – OXIDATIVE GENERATION OF BORON-CENTERED RADICALS IN CARBORANES

This chapter is a version of Mills, H. A.; Martin, J. L.; Rheingold, A. L.; Spokoyny, A. M. "Oxidative Generation of Boron-Centered Radicals in Carboranes", *J. Am. Chem. Soc.* **2020**, *142*, 4586-4591.

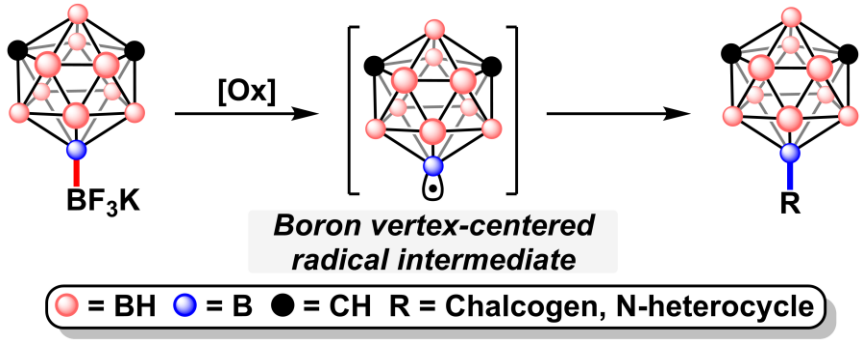

Figure 3.1: Graphical abstract for Chapter 3.

3.1 Abstract

We report the first indirect observation and use of boron vertex-centered carboranyl radicals generated by the oxidation of modified carboranyl precursors. These radical intermediates are formed by the direct oxidation of a B-B bond between a boron cluster cage and an exopolyhedral boron-based substituent (*e.g.*, -BF_3K, -$B(OH)_2$). The *in situ* generated radical species are shown to be competent substrates in reactions with oxygen-based radicals, dichalcogenides, and N-heterocycles, yielding the corresponding substituted carboranes containing B-O, B-S, B-Se, B-Te, and B-C bonds. Remarkably, this chemistry tolerates various electronic environments, providing access to facile substitution chemistry at both electron-rich and electron-poor B-H vertices in carboranes.

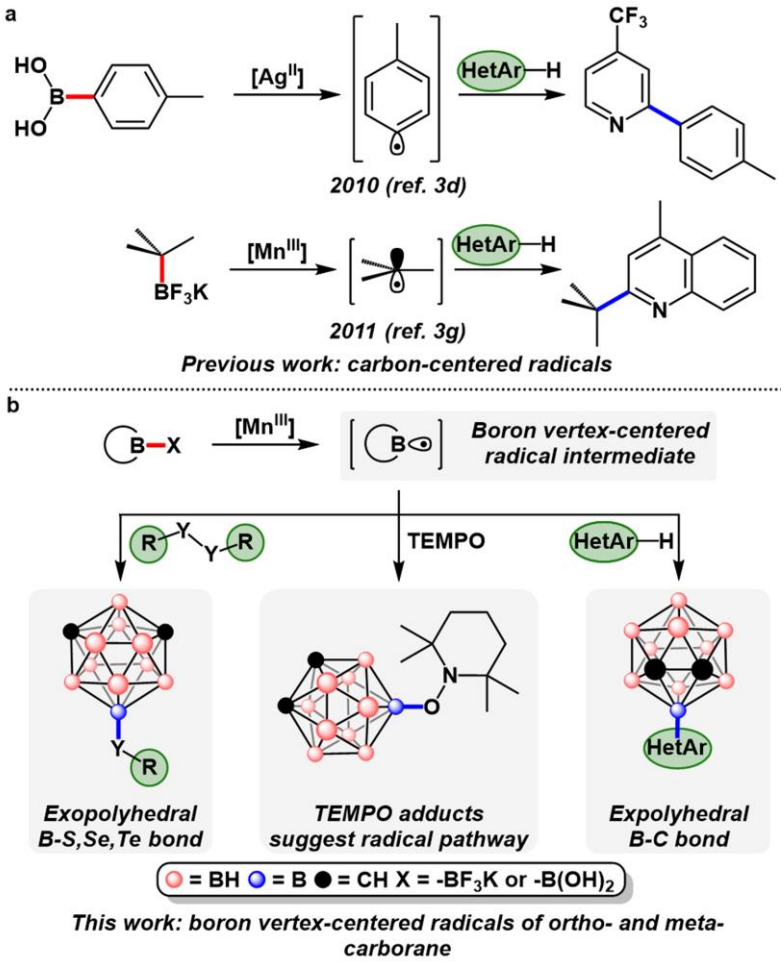

Figure 3.2: A. Literature examples of carbon-centered radicals generated by the oxidation of C-B bonds. **B.** This work, oxidation of carboranes containing exopolyhedral B-[B] bonds.

3.2 Introduction

Carbon-centered radicals are ubiquitous in chemistry and have garnered significant interest due to their utility in building complex organic molecules.[1,2] Particularly, methods utilizing carbon-centered radical intermediates have made use of stable radical precursors containing cleavable C-X bonds (X: -COOH,[3a] $(-SO_2)_2Zn$,[3b,c] $-B(OH)_2$,[3d-f] and $-BF_3K$[3f-i]) that undergo homolytic C-X bond scission in the presence of oxidants. These radical intermediates have

subsequently been used to substitute various substrates including N-heterocycles,[3a-d,f,g,i] extended aromatic systems,[3e] and oxygen-based radical traps (**Figure 3.2A**).[3h]

Icosahedral carboranes ($C_2B_{10}H_{12}$)[4] are molecular clusters that exist as three distinct isomers (*ortho*-, *meta*-, *para*-), featuring steric profiles similar to that of adamantane.[5] Due to the inherent asymmetry of the electronic structures, various vertices in these species feature orthogonal reactivity. For example, C-H vertices (pK_a: 22−27)[4a] exhibit nucleophilic reactivity after deprotonation with a base. Conversely, B-H vertices in these molecules have been amenable to electrophilic substitution on the electron-rich boron vertices furthest away from the carbon sites.[4] Most recently, new methods have enabled metal-catalyzed cross-coupling,[6a] metal-catalyzed B-H activation,[6b,c] and nucleophilic substitution[6d] strategies at most B-H vertices in carboranes. While the majority of the above methods rely on two-electron transformations, one-electron chemistry has remained underexplored with these clusters.[7]

Recently, an example showcasing the possibility of efficiently generating boron vertex-centered radicals in carboranes was accomplished by Xie and co-workers.[7d] In their elegant report, Xie *et al.* utilized the reduction of *ortho*-carboranyl diazonium salts to generate boron vertex-centered radical intermediates. Subsequently, the generated radical intermediates exhibited reactivity toward five-membered heterocycles and simple arenes. We hypothesized that, complementary to the reductive approach for generating boron vertex-centered radicals, one could develop oxidative chemistry, akin to chemistry developed with borylated aryl and alkyl-based species (*vide supra*, **Figure 3.2B**).

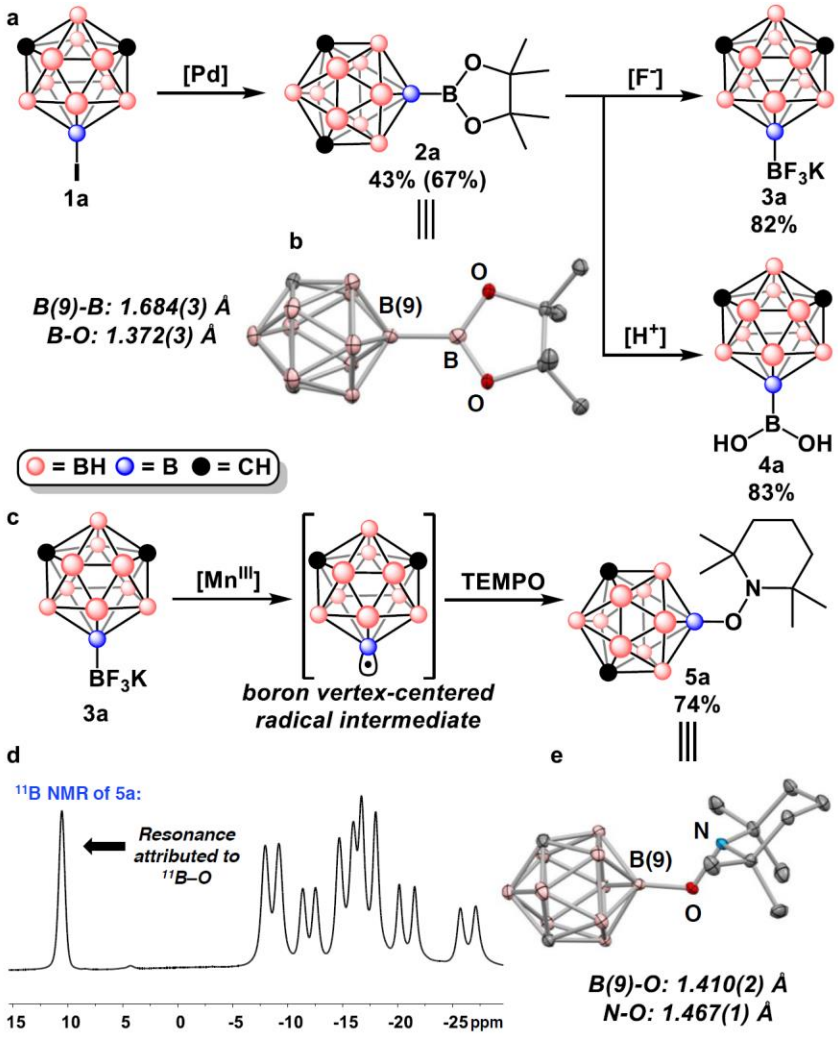

Figure 3.3: A. Synthesis of substituted carboranes containing exopolyhedral boron-based substituents (see Appendix B for experimental details). **B.** Single-crystal X-ray structure of **2A**. **C.** Oxidation of **3A** in the presence of TEMPO. **D.** ^{11}B NMR spectrum of **5A**. **E.** Single-crystal X-ray structure of **5A**. Thermal ellipsoids are drawn at 50% probability; hydrogens are omitted for clarity.

3.3 Results and Discussion

In order to test our hypothesis, we set out to prepare potassium 9-meta-carboranyltrifluoroborate (**3A**, **Figure 3.3A**). Importantly, **3A** would provide a similar steric and

electronic environment to alkyl trifluoroborates, which have been widely studied as radical precursors.[3g-i] To prepare **3A**, we first developed borylation conditions to transform 9-iodo-metacarboranyl (**1A**, **Figure 3.3A**) into the corresponding 9-metacarboranyl boronic ester (**2A**, **Figure 3.3A**, Appendix B, sec. 3.6.4) while monitoring the progress of the reaction by HRGC-MS. After isolation of **2A**, ^{11}B NMR spectroscopy of **2A** revealed two diagnostic resonances corresponding to a substituted ^{11}B site of the boron cage and a ^{11}B of the boronic ester in a 1:1 ratio. The crystallographically derived structure of **2A** (Appendix B, sec. 3.6.12) was found to be consistent with its proposed structural formulation (**Figure 3.3B**), featuring an exopolyhedral B(9)-Bpin bond. The measured B(9)-Bpin bond length (1.684(3) Å) for **2A** is consistent with that of the previously studied electron-poor, 3-*ortho*-carboranyl boronic ester obtained *via* direct B-H borylation (1.680(6) Å).[8] Notably, similar to alkyl and aryl boronic esters,[9] **2A** undergoes deprotection in the presence of fluoride or acid, yielding the corresponding trifluoroborate salt (**3A**) and boronic acid (**4A**) derivatives in 82% and 83% yields, respectively (**Figure 3.3A**, Appendix B, sec. 3.6.5) Additionally, it was possible to prepare the analogous 9-*ortho*-carboranyl boronic ester and acid, **2B** and **4B**, though the fluoride-sensitivity[10] of *ortho*-carborane prevented the synthesis of the 9-*ortho*-carboranyltrifluoroborate derivative (see Appendix B for full experimental details).

With a library of carborane-based reagents (**3A** and **4A**-**B**) in hand, we commenced our studies to probe the propensity of these B-borylated carboranes to undergo oxidative B-[B] ([B]: -BF_3K or -$B(OH)_2$) bond cleavage. We first performed the oxidation of **3A** in acetic acid with manganese(III) acetate dihydrate ($Mn(OAc)_3 \cdot 2H_2O$) in the presence of (2,2,6,6-tetramethylpiperidin-1-yl)oxyl (TEMPO, **Figure 3.3C**, Appendix B, sec. 3.6.6 and 3.6.9) with the intent of trapping any radical intermediates formed in situ. During the course of the reaction, we

observed the exclusive formation of a boron cluster-containing species corresponding to a TEMPO adduct of meta-carborane (**5A**) by HRGC-MS that could be isolated *via* silica gel column chromatography in 74% yield. ^{11}B NMR spectroscopy of purified 5a revealed a ^{11}B resonance within a chemical shift range indicative of an exopolyhedral ^{11}B-O bond (**Figure 3.3D**), which was subsequently confirmed by single-crystal X-ray crystallography (**Figure 3.3E**).

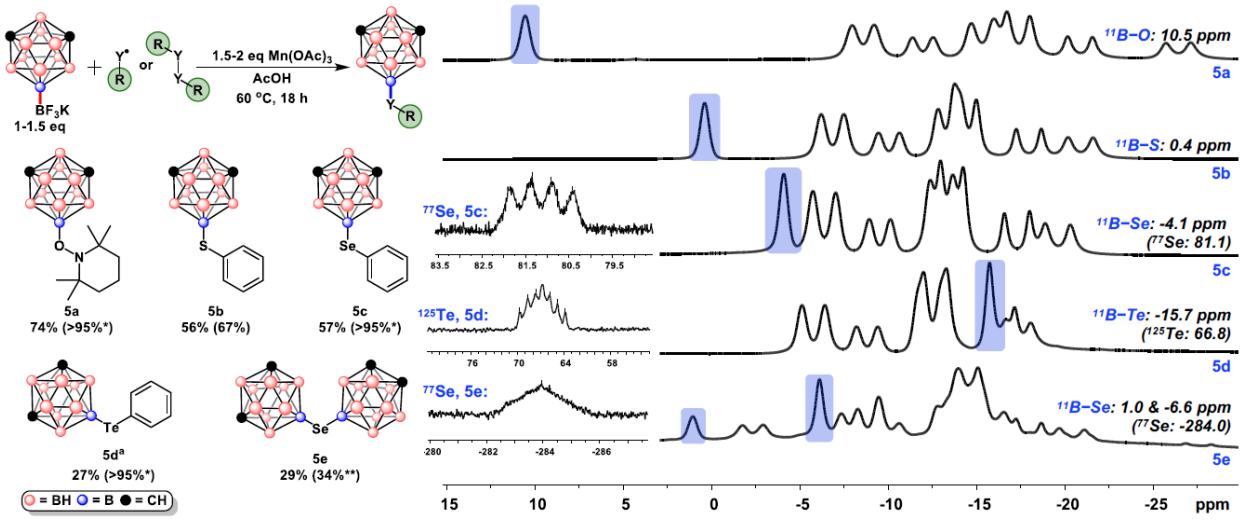

Figure 3.4: Oxidation of **3A** and reaction with TEMPO and dichalcogenides. ^{11}B NMR (and heteronuclear NMR, where relevant) spectra of compounds **5A-E**. Resonances highlighted in blue are attributed to the exopolyhedral ^{11}B-Y bond. Isolated yields are given as percentages and conversion by HRGC-MS in parentheses. *No starting material was observed by HRGC-MS. **Conversion was determined by ^{11}B NMR spectroscopy. [a]Reaction was performed under an atmosphere of argon.

Isolation of **5A** suggested the intermediacy of the boron vertex-centered radical, which could be trapped by other reagents besides TEMPO. To explore this generality, we evaluated a series of dichalcogenides as trapping agents under similar oxidizing conditions (**Figure 3.4**, Appendix B, sec. 3.6.10). First, we performed the oxidation of **3A** in the presence of diphenyl

disulfide. This reaction generated a product mixture containing a species corresponding to **5B** by HRGC-MS. Compound **5B** was isolated from the product mixture as an air-stable solid *via* silica gel column chromatography in 56% yield, and its identity was confirmed by ^{1}H, ^{13}C, and ^{11}B NMR spectroscopy. The ^{11}B NMR spectrum of **5B** featured a diagnostic ^{11}B resonance consistent with the formation of an exopolyhedral ^{11}B-S bond and is in agreement to the proposed structural formulation (**Figure 3.4**).

Similarly, oxidation of **3A** in the presence of diphenyl diselenide and subsequent purification produced **5C** in 57% isolated yield. Consistent with the presence of an exopolyhedral B-Se bonding interaction in **5C**, one can observe a ^{77}Se-^{11}B quartet resonance in the ^{77}Se NMR of **5C** (**Figure 3.4**). When the oxidation of **3A** is performed under inert atmosphere in the presence of diphenyl ditelluride, a species containing an exopolyhedral B-Te bond (**5D**) is formed, as suggested by HR-GCMS. This species could be isolated *via* a similar purification protocol (*vide supra*), albeit in a lower isolated yield (27%), likely due to the poor oxidative stability of telluroether compounds.[11] NMR spectroscopy experiments of **5D**, including ^{11}B and ^{125}Te NMR spectra, are fully consistent with its proposed structural formulation. Finally, utilizing this approach, we were able to demonstrate the formation of a selenoether species (**5E**) containing two boron-connected substitutions, and the first example of a mixed-isomer dicarboranyl selenide (see Appendix B for full experimental details). Interestingly, given the dramatic electron donating capabilities of the B(9) position of *ortho*- and *meta*-carboranes, **5E** exhibits the most downfield ^{77}Se NMR chemical shift (**Figure 3.4**, $\delta = -284.0$ ppm) for any known selenoether-type compound reported to date.[11] Overall, formation of products **5B-E** further reinforces our hypothesis of the intermediacy of the boron vertex-centered radicals during the course of **3A** oxidation.

Carbon-centered radical intermediates have been known to undergo C-H activation processes with N-heterocycles, thereby allowing the formation of C-C bonds. We therefore hypothesized that the oxidatively generated boron vertex-centered radical intermediate could undergo a similar C-H activation mechanism, forming the desired exopolyhedral B-C bond (Appendix B, sec. 3.6.10). To investigate the potential for the carboranyl radical intermediate to participate in C-H activation mechanisms with N-heterocycles, we chose 4-methylquinoline[3g] as a model substrate. 4-Methylquinoline was treated with an excess of $Mn(OAc)_3 \cdot 2H_2O$ (3 equiv.) and **3A** (1.5 equiv.) in acetic acid (1 mL). Monitoring of this reaction by HRGC-MS suggested partial conversion (17%) of 4-methylquinoline to a carborane-containing heterocyclic product. Increasing the stoichiometric ratio of $Mn(OAc)_3 \cdot 2H_2O$ and **3A**, however, resulted in a substantial increase of the product formation (up to 32% conversion, Appendix B, sec. 3.6.7). When this reaction is performed on a larger scale (0.25 mmol), the product mixture can be subjected to purification *via* silica gel column chromatography to produce **5F** in 30% isolated yield as suggested by diagnostic ^{1}H, ^{13}C, and ^{11}B NMR spectroscopy. Notably, the efficiency of the carboranyl radical-heterocycle coupling is limited in this case and is consistent with the sterically hindered nature of carboranes. Similar reactions utilizing sterically hindered carbon-based substrates (*e.g.*, *tert*-butyl radical synthons) usually exhibit conversions up to 58%.[3g] Previous mechanistic studies into the C-H activation of N-heterocycles by carbon-centered radicals highlighted the innate reactivity of certain positions in pyridines that could, in theory, be extended to other heterocyclic systems.[3c] To confirm the paralleled reactivity between boron vertex- and carbon-centered radicals further, we employed benzothiazole as a model five-membered heterocycle with innate reactivity toward carbon-centered radicals at C(2). When the oxidation of **3A** is performed in a 1:1 mixture of acetic acid/water with benzothiazole as a trapping reagent, formation of a carborane-containing

heterocyclic product was possible as indicated by HRGC-MS. Compound **5G** was isolated from the product mixture *via* a similar purification protocol (*vide supra*) and obtained in 41% yield. ^{1}H, ^{13}C, and ^{11}B NMR spectroscopy of **5G** suggested likely C-H activation by the carboranyl radical at C(2) of benzothiazole, and single-crystals of **5G** suitable for X-ray crystallography were subsequently grown from an acetone/ pentane mixture.

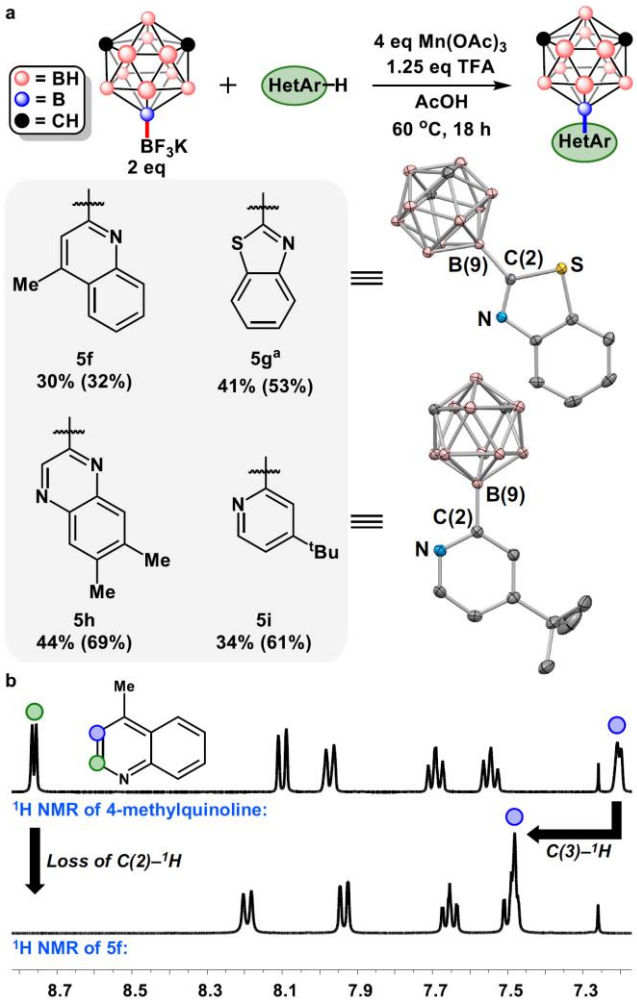

Figure 3.5: A. Oxidation of **3A** and reaction with N-heterocycles. **B.** ^{1}H NMR experiemnts of 4-methylquinoline and **5F**. [a]Reaction was performed in 1:1 AcOH/H_2O. Isolated yields are given as

percentages and conversion by HRGC-MS in parentheses. Thermal ellipsoids are drawn at 50% probability; hydrogens are omitted for clarity.

The crystallographically derived structure of **5G** (**Figure 3.5A**) is in agreement with the proposed structural formulation and definitively indicates substitution at C(2) position of the heterocycle leading to the formation of an exopolyhedral B(9)-C(2) bond. Furthermore, reactivity toward pyridines and quinoxalines was tested to further confirm that the regioselective substitution of the carboranyl radical onto the N-heterocycle is consistent with proposed radical-promoted C-H functionalization mechanisms.[3c] Under identical oxidation conditions and following similar isolation procedures used in the synthesis of **5F**, the radical-heterocycle coupling works comparably well with pyridines and quinoxalines, affording **5H** and **5I** in 44% and 34% isolated yields, respectively. Single crystal X-ray crystallography of **5I** (**Figure 3.5A**) confirms the anticipated regioselectivity of the C-H functionalization. Importantly, formation of products **5F-I** are indicative of the paralleled reactivity between oxidatively generated boron vertex- and carbon-centered radicals when participating in analogous C-H functionalization mechanisms (**Figure 3.5B**). Interestingly, when highly activated N-heterocycles are used (*e.g.*, 4-trifluoromethylpyridine), disubstitution is observed in significant quantities (Appendix B, sec. 3.6.9).

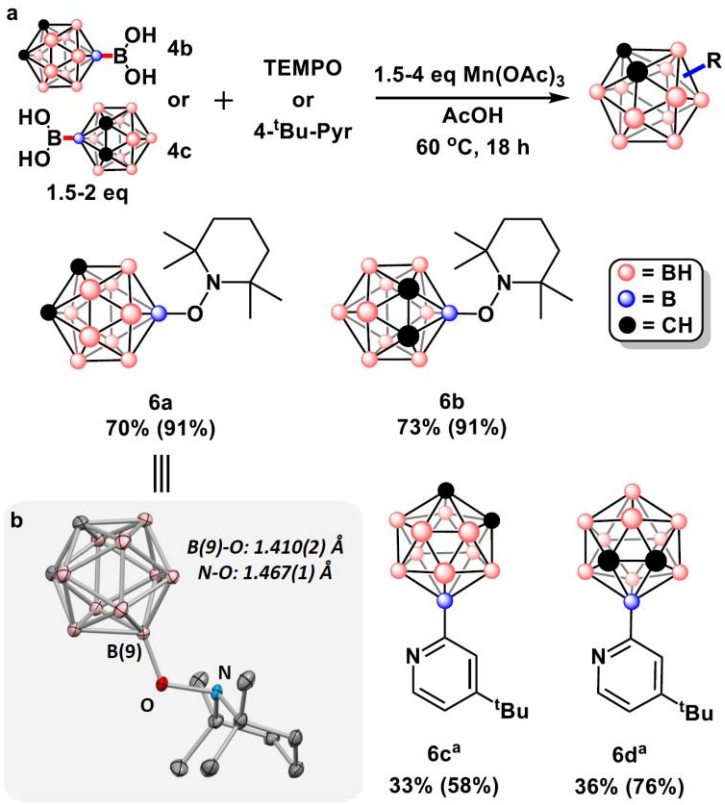

Figure 3.6: A. Oxidation of **4B-C**. **B.** Single-crystal X-ray structure of **6A**. [a]Reaction also included 1.25 equiv. of TFA. Isolated yields are given as percentages and conversion by HRGC-MS in parentheses. Thermal ellipsoids are drawn at 50% probability; hydrogens are omitted for clarity.

In order to determine the accessibility of other carboranyl radical intermediates, we probed the susceptibility of **4B** and 3-*ortho*-carboranyl boronic acid (**4C**) to undergo homolytic B-B(OH)$_2$ bond scission in the presence of Mn(OAc)$_3$·2H$_2$O (**Figure 3.6A**, Appendix B, sec. 3.6.11). Initially, **4B** was treated with identical oxidation conditions used in the preparation of **5A** (**Figure 3.6A**), and the formation of **6A** was monitored by HRGC-MS. After 18 h, **6A** was isolated from the reaction mixture *via* silica gel column chromatography in a similar yield to that of **5A** (70%). Analogous to **5A**, ^{11}B NMR spectroscopy of **6A** revealed a diagnostic ^{11}B resonance typical of the formation of an exopolyhedral ^{11}B-O bond and can be crystallographically characterized.

Likewise, when using **4C** as a radical precursor, it was possible to synthesize and isolate **6B** in 73% yield following the same procedure (*vide supra*). Carboranyl radical intermediates from the oxidation of **4B** and **4C** formed in the presence of 4-^{t}Bu-pyridine also participate in the anticipated C-H functionalization pathway. As a result, products **6C** and **6D** were prepared and isolated in comparable yields to **5I** (33% and 36%, respectively). Surprisingly, compounds **6C** and **6D** are the first known examples of substituted *ortho*-carboranes containing pyridyl groups at any boron vertex of the cluster. The synthesis of compounds **6A-D** suggests that the reactivity of the carboranyl radical intermediates is independent of any perceivable difference in the electronic nature of the exopolyhedral boron-based substituent.

3.4 Conclusion

In conclusion, we report the first example of boron vertex-centered carboranyl radicals generated *via* oxidative exopolyhedral B-[B] bond scission. Once generated, the carboranyl radical intermediates have been observed to participate in substitution chemistry similar to that of carbon-centered radicals, as manifested by both the chemoselectivity for chalcogen-based radical traps (TEMPO, dichalcogenides) and the regioselectivity of heterocycle substitution. The use of reactive, boron-centered carboranyl radical intermediates has afforded new avenues to forge exopolyhedral B-X bonds with boron-rich clusters. Additionally, this new method for carboranyl radical generation expands upon the existing repertoire of reactive boron cluster species[12] and main group-centered radicals.[13]

3.5 References for Chapter 3

(1) (a) Yan, M.; Lo, J. C.; Edwards, J. T.; Baran, P. S. Radicals: Reactive Intermediates with Translational Potential. *J. Am. Chem. Soc.* **2016**, 138 (39), 12692−12714. (b) Plesniak, M. P.;

Huang, H.-M.; Procter, D. J. Radical Cascade Reactions Triggered by Single Electron Transfer. *Nature Reviews Chemistry* **2017**, 1, 0077. (c) Lear, J. M.; Buquoi, J. Q.; Gu, X.; Pan, K.; Mustafa, D. N.; Nagib, D. A. Multi-Component Heteroarene Couplings *via* Polarity-Reversed Radical Cascades. *Chem. Commun.* **2019**, 55, 8820−8823.

(2) Romero, K. J.; Galliher, M. S.; Pratt, D. A.; Stephenson, C. R. J. Radicals in Natural Product Synthesis. *Chem. Soc. Rev.* **2018**, 47, 7851−7866.

(3) (a) Minisci, F.; Fontana, F.; Vismara, E. Substitutions by Nucleophilic Free Radicals: A New General Reaction of Heteroaromatic Bases. *J. Heterocycle. Chem.* **1990**, 27 (1), 79−96. (b) Fujiwara, Y.; Dixon, J. A.; O'Hara, F.; Funder, E. D.; Dixon, D. D.; Rodriguez, R. A.; Baxter, R. D.; Herle, B.; Sach, N.; Collins, R. M.; Ishihara, Y.;́ Baran, P. S. Practical and Innate Carbon-Hydrogen Functionalization of Heterocycles. *Nature* **2012**, 492, 95−99. (c) O'Hara, F.; Blackmond, D. G.; Baran, P. S. Radical-Based Regioselective C-H Functionalization of Electron-Deficient Heteroarenes: Scope, Tunability, and Predictability. *J. Am. Chem. Soc.* **2013**, 135 (32), 12122− 12134. (d) Seiple, I. B.; Su, S.; Rodriguez, R. A.; Gianatassio, R.; Fujiwara, Y.; Sobel, A. L.; Baran, P. S. Direct C-H Arylation of Electron-Deficient Heterocycles with Arylboronic Acids. *J. Am. Chem. Soc.* **2010**, 132, 13194−13196. (e) Castro, S.; Fernández, J. J.; Fañanás, F. J.; Vicente, R.; Rodríguez, F. Manganese-Mediated C-H Alkylation of Unbiased Arenes Using Alkylboronic Acids. *Chem. Eur. J.* **2016**, 22, 9068−9071. (f) Duan, K.; Yan, X.; Liu, Y.; Li, Z. Recent Progress in the Radical Chemistry of Alkylborates and Alkylboronates. *Adv. Synth. Catal.* **2018**, 360, 2781−2795. (g) Molander, G. A.; Colombel, V.; Braz, V. A. Direct Alkylation of Heteroaryls Using Potassium Akyl- and Alkoxymethyltrifluoroborates. *Org. Lett.* **2011**, 13 (7), 1852−1855. (h) Sorin, G.; Mallorquin, R. M.; Contie, Y.; Baralle, A.; Malacria, M.; Goddard, J.-

P.; Fensterbank, L. Oxidation of Alkyl Trifluoroborates: An Opportunity for Tin-Free Radical Chemistry. *Angew. Chem., Int. Ed.* **2010**, 49, 8721−8723. (i) Matsui, J. K.; Primer, D. N.; Molander, G. A. Metal-free C-H alkylation of Heteroarenes with Alkyltrifluoroborates: a General Protocol for 1°, 2°, and 3° Alkylation. *Chem. Sci.* **2017**, 8, 3512−3522.

(4) (a) For a general review of carboranes, see: Grimes, R. N. Carboranes, 3rd ed.; Elsevier: Oxford, 2016. (b) Olid, D.; Nuñez, R.; Viñas, C.; Teixidor, F. Methods to produce B-C, B-P, B-N and B-S bonds in boron clusters. *Chem. Soc. Rev.* **2013**, 42, 3318−3336.

(5) (a) Hohman, J. N.; Zhang, P.; Morin, E. I.; Han, P.; Kim, M.; Kurland, A. R.; McClanahan, P. D.; Balema, V. P.; Weiss, P. S. Self-Assembly of Carboranethiol Isomers on Au{111}: Intermolecular Interactions Determined by Molecular Dipole Orientations. *ACS Nano* **2009**, 3 (3), 527−536. (b) Yan, H.; Hohman, J. N.; Li, F. H.; Jia, C.; Solis-Ibarra, D.; Wu, B.; Dahl, J. E. P.; Carlson, R. M. K.; Tkachenko, B. A.; Fokin, A. A.; Schreiner, P. R.; Vailionis, A.; Kim, T. R.; Devereaux, T. P.; Shen, Z.-X.; Melosh, N. A. Hybrid Metal-Organic Chalcogenide Nanowires with Electrically Conductive Inorganic Core through Diamondoid-Directed Assembly. *Nat. Mater.* **2017**, 16, 349. (c) Dziedzic, R. M.; Axtell, J. C.; Rheingold, A. L.; Spokoyny, A. M. Off-Cycle Processes in Pd-Catalyzed Cross-Coupling of Carboranes. *Org. Process Res. Dev.* **2019**, 23 (8), 1638− 1645.

(6) (a) For a general review of palladium-catalyzed substitutions of carboranes: Dziedzic, R. M.; Spokoyny, A. S. Metal-catalyzed cross-coupling with chemistry with polyhedral boranes. *Chem. Commun.* **2019**, 55, 430−442. (b) For a general review of transition metalcatalyzed B−H activation of carborane: Quan, Y.; Xie, Z. Controlled Functionalization of o-carborane via Transition Metal Catalyzed B-H Activation. *Chem. Soc. Rev.* **2019**, 48, 3660−3673. (c) Lin, F.; Yu, J.- L.; Shen, Y.;

Zhang, S.-Q.; Spingler, B.; Liu, J.; Hong, X.; Duttwyler, S. Palladium-Catalyzed Selective Five-fold Cascade Arylation of the 12- Vertex Monocarborane Anion by B-H Activation. *J. Am. Chem. Soc.* **2018**, 140 (42), 13798−13807. (d) For a general review of direct B−H nucleophilic substitution of carboranes: Quan, Y.; Tang, C.; Xie, Z. Nucleophilic Substitution: a Facile Strategy for Selective B-H Functionalization of Carboranes. *Dalton Trans.* **2019**, 48, 7494− 7498. (e) For a general review on mechanistic aspects of B−H functionalization in carboranes: Eleazer, B. J.; Peryshkov, D. V. Coordination Chemistry of Carborane Clusters: Metal-Boron Bonds in Carborane, Carboranyl and Carboryne Complexes. Comments *Inorg. Chem.* **2018**, 38, 79−109.

(7) (a) Tumanskii, B. L.; Valetskii, P. M.; Kabachii, Y. A.; Bubnov, N. N.; Solodovnikov, S. P.; Korshak, V. V.; Prokof'ev, A. I.; Kabachnik, M. I. ESR Spectra of Adduct of Boron-Centered o-, m-, p-carboranyl-12 Radicals with 4-methyl-s,4,6-tri-tert-butyl-2,5-cyclohexadien-1-one. *Bull. Acad. Sci. USSR, Div. Chem. Sci.* **1984**, 33, 2210. (b) Tumansky, B. L.; Lebedev, V. N.; Bubnov, N. N.; Solodovnikov, S. P.; Gervits, L. L.; Balagurova, E. V.; Zakharkin, L. I. ESR Study of Carborane Containing Organofluorine Radicals. *Russ. Chem. Bull.* **1993**, 42, 1259. (c) Lyakhovetsky, Y. I.; Shilova, E. A.; Bashilov, V. V.; Sokolov, V. I.; Nekrasov, Y. S.; Tumanskii, B. L. Homolytic Reactive Mass Spectrometry of Fullerenes: Interaction of C60 and C70 with Organo- and Organoelement Mercurials in the Electron Impact Ion Source of a Mass Spectrometer; EPR, CIDEP, and MS Studies of several Analogous Reactions of C60 Performed in Solution. *J. Phys. Chem. A* **2009**, 113 (49), 13700−13710. (d) Zhao, D.; Xie, Z. Visible Light-Promoted Photocatalytic B-C Coupling via a Boron-Centered Carboranyl Radical: Facile Synthesis of B(3)-Arylated o-Carboranes. *Angew. Chem., Int. Ed.* **2016**, 55, 3166−3170.

(8) Cheng, R.; Qiu, Z.; Xie, Z. Iridium-Catalysed Regioselective Borylation of Carboranes via Direct B-H Activation. *Nat. Commun.* **2017**, 8, 14827.

(9) (a) Chen, I.-H.; Yin, L.; Itano, W.; Kanai, M.; Shibasaki, M. Catalytic Asymmetric Synthesis of Chiral Tertiary Organoboronic Esters through Conjugate Boration of β-Substituted Cyclic Enones. *J. Am. Chem. Soc.* **2009**, 131 (33), 11664−11665. (b) Lennox, A. J. J.; Lloyd-Jones, G. C. Preparation of Organotrifluoroborate Salts: Precipitation-Driven Equilibrium under Non-Etching Conditions. *Angew. Chem., Int. Ed.* **2012**, 51, 9385−9388.

(10) (a) Fox, M. A.; Wade, K. Cage-Fluorination During Deboronation of meta-caboranes. *Polyhedron* **1997**, 16 (14), 2517− 2525. (b) Getman, T. D. Investigation of Potassium Fluoride Supported on Alumina in the Deboronation of o-Carborane. *Inorg. Chem.* **1998**, 37 (13), 3422−3423. (c) Yoo, J.; Hwang, J.-W.; Do, Y. Facile and Mild Deboronation of o-Carboranes Using Cesium Fluoride. *Inorg. Chem.* **2001**, 40 (3), 568−570.

(11) Rappoport, Z. *The Chemistry of Organic Selenium and Tellurium Compounds*; John Wiley & Sons: New York, 2013; Vol. 4, Pt. 1.

(12) (a) Wright, J. H.; Kefalidis, C. E.; Tham, F. S.; Maron, L.; Lavallo, V. Click-Like Reactions with Inert HCB11Cl11− Anion Lead to Carborane-Fused Heterocycles with Unusual Aromatic Character. *Inorg. Chem.* **2013**, 52 (10), 6223−6229. (b) Zhao, D.; Xie, Z. [3-N_2-o-$C_2B_{10}H_{11}$][BF_4]: a Useful Synthon for Multiple Cage Boron Functionalizations of o-carborane. *Chem. Sci.* **2016**, 7, 5635. (c) Saleh, L. M. A.; Dziedzic, R. M.; Khan, S. I.; Spokoyny, A. M. Forging Unsupported Metal-Boryl Bonds with Icosahedral Carboranes. *Chem. Eur. J.* **2016**, 22, 8466−8470. (d) Mu, X.; Axtell, J. C.; Bernier, N. A.; Kirlikovali, K. O.; Jung, D.; Umanzor, A.; Qian, K.; Chen, X.; Bay, K. L.; Kirollos, M.; Rheingold, A. L.; Houk, K. N.; Spokoyny, A. M. Sterically Unprotected

Nucleophilic Boron Cluster Reagents. *Chem.* **2019**, 5, 2461−2469. (e) Saxena, A. K.; Maguire, J. A.; Hosmane, N. S. Recent Advances in the Chemistry of Heterocarborane Complexes Incorporating s- and p-Block Elements. *Chem. Rev.* **1997**, 97, 2421−2462.

(13) (a) Power, P. P. Persistent and Stable Radicals of the Heavier Main Group Elements and Related Species. *Chem. Rev.* **2003**, 103 (3), 789−810. (b) Martin, C. D.; Soleilhavoup, M.; Bertrand, G. Carbene-stabilized main group radicals and radical ions. *Chem. Sci.* **2013**, 4, 3020. (c) Le, C.; Chen, T. Q.; Liang, T.; Zhang, P.; MacMillan, D. W. C. A Radical Approach to the Copper Oxidative Addition Problem: Trifluoromethylation of Bromoarenes. *Science* **2018**, 360, 1010−1014. (d) Buquoi, J. Q.; Lear, J. M.; Gu, X.; Nagib, D. A. Heteroarene Phosphinylalkylation via a Catalytic, Polarity-Reversing Radical Cascade. *ACS Catal.* **2019**, 9, 5330−5335. (e) Moret, M.-E.; Zhang, L.; Peters, J. C. A Polar Copper-Boron One-Electron σ-Bond. *J. Am. Chem. Soc.* **2013**, 135 (10), 3792−3795. (f) Hoefelmeyer, J. D.; Gabbai, F. P. An Intermolecular Boron-Boron One-Electron σ-Bond. *J. Am. Chem. Soc.* **2000**, 122 (37), 9054−9055. (g) Tsai, H.-C.; Lin, Y.-F.; Liu, W.-C.; Lee, G.-S.; Peng, S.-M.; Chiu, C.-W. N-Heterocyclic Silylene Coordinated Dialkyl Borenium Equivalent. *Organometallics* **2017**, 36 (20), 3879−3882. (h) Liu, L. L.; Stephan, D. W. Radicals derived from Lewis acid/base pairs. *Chem. Soc. Rev.* **2019**, 48, 3454. (i) Yang, W.; Krantz, K. E.; Freeman, L. A.; Dickie, D. A.; Molino, A.; Frenking, G.; Pan, S.; Wilson, D. J. D.; Gilliard, R. J., Jr. Persistent Borafluorene Radicals. *Angew. Chem., Int. Ed.* **2020**, 59, 10, 3850-3854.

3.6 Appendix B

3.6.1 General Considerations

Meta-$C_2B_{10}H_{12}$ (Katchem), *ortho*-$C_2B_{10}H_{12}$ (Boron Specialties), and bis(pinacolato)diboron (Oakwood) were sublimed prior to use. Dry dichloromethane was obtained from a Grubbs column with an activated alumina and copper catalyst. N,N-dimethylformamide (Sigma-Aldrich) was vacuum distilled over CaH_2 and stored in a Teflon valve-sealed flask **without** molecular sieves. The duration of stirring with CaH_2 is noted to be quite critical. DMF used for the synthesis of 9-Bpin-oCB (**2B**) was stirred with CaH_2 overnight while DMF used for 9-Bpin-mCB (**2A**) was stirred with CaH_2 for 4-6 hours. DPPF (Oakwood) was recrystallized for 24 h from benzene layered with pentane prior to use. Palladium precatalysts were prepared according to reference 1. Cs_2CO_3 (Fisher) was used as received and stored in an N_2-filled glovebox. Acetic acid was dried by distilling 50 mL from 1 g CrO_3 with 2 mL of acetic anhydride and stored under argon. $(9\text{-Se-oCB})_2$ used in the synthesis of **5E** was prepared by making the corresponding selenol (reference 2) and oxidizing it in refluxing methanol exposed to air for three days. Benzothiazole and 4-methylquinoline were vacuum distilled prior to use. All solvents used for cross-couplings and oxidations were deoxygenated by sparging with argon gas before use. All other chemicals were used as received.

Plastic-backed Baker-flex Silica Gel IB2-F TLC plates were used for thin layer chromatography. Silica used for flash column chromatography was SiliaFlash® G60 60- 200 μm (70-230 mesh) purchased from Silicycle. TLC samples for carborane-containing compounds were stained with 1 wt. % $PdCl_2$ in 6M HCl and developed with heat.

3.6.2 Instrumentation

^{1}H, $^{13}C\{^{1}H\}$, ^{11}B, $^{11}B\{^{1}H\}$, ^{19}F, $^{19}F\{^{1}H\}$, ^{77}Se, and ^{125}Te NMR spectra were recorded on either a Bruker DRX500 or Bruker AVIII 400 spectrometer in ambient conditions unless stated otherwise. MestReNova v6.0.2-5475 software was used to process the FID data and visualize the spectra. ^{1}H and $^{13}C\{^{1}H\}$ NMR spectra were referenced to residual solvent resonances in deuterated solvents ($CDCl_3$: ^{1}H, 7.26 ppm; ^{13}C, 77.16 ppm, Note: due to high humidity H_2O resonances are often present) and are reported relative to tetramethylsilane (δ = 0 ppm). ^{11}B and $^{11}B\{^{1}H\}$ NMR spectra were referenced externally to $Et_2O{\cdot}BF_3$ (δ = 0 ppm). ^{19}F and $^{19}F\{^{1}H\}$ NMR spectra were referenced externally to fluorobenzene (δ = - 113.15 ppm). ^{77}Se NMR spectra were referenced externally to diphenyldiselenide (δ = 463.15 ppm). ^{125}Te NMR spectra were referenced externally to diphenylditelluride in tetrahydrofuran at room temperature (δ = 408 ppm)

High Resolution Gas Chromatography Mass Spectrometry (HRGC-MS) measurements were carried out using an Agilent Model 7693 Autosampler, 7890B Gas Chromatograph, and 7250 Q-TOF Mass Selective Detector in the Electron Ionization mode. Samples injection was carried out on an Agilent HP5-MS column with dimensions 30 m x 250 μm x 0.25 μm. Ultra High Purity Grade He (Airgas) was used as a carrier gas. Data collection and analysis were performed using Mass Hunter Acquisition and Qualitative Analysis software (Agilent).

DART-MS spectra were collected on a Thermo Exactive Plus MSD (Thermo Scientific) equipped with an ID-CUBE ion source and a Vapur Interface (IonSense). Both the source and MSD were controlled by Excalibur v. 3.0. The analyte was spotted onto OpenSpot sampling cards (IonSense). Ionization was accomplished using He plasma with no additional ionization agents. Mass calibration was carried out using Pierce LTQ Velos ESI (+) and (-) Ion calibration solutions (Thermo Fisher Scientific).

Elemental analysis of compounds 2a and 5f was performed by Atlantic Microlab.

3.6.3 Precursor Synthesis

9-I-1,7-dicarba-*closo*-dodecaborane (1A)

Meta-$C_2B_{10}H_{12}$ (1.44 g, 10 mmol) was added to an oven-dried Schlenk flask capped with a rubber septum and evacuated/backfilled with N_2 three times. I_2 (2.54 g, 10 mmol) was added under a positive N_2 flow before the addition of dry CH_2Cl_2 (50 mL) *via* cannula. $AlCl_3$ (0.199 g, 15 mol%) was added to the stirring solution under a positive N_2 flow before the rubber septum was replaced with a greased ground-glass stopper. The reaction mixture was then left to stir overnight at room temperature. Upon completion of the reaction, determined by GC-MS, the reaction was slowly quenched by the addition of distilled H_2O (20 mL), yielding a cloudy suspension. The opaque organic layer was separated from the aqueous layer and the aqueous layer was extracted with CH_2Cl_2 (2 x 10 mL). The organic portions were combined and dried with $MgSO_4$ resulting in a clear, colorless solution. The solution was then filtered through a pad of Celite on a fritted funnel and the CH_2Cl_2 was removed under reduced pressure to yield a white solid that was further purified by sublimation at 100 °C to produce the title compound as a white solid. Yields and spectra are in agreement to previously reported syntheses (reference 3)

9-I-1,2-dicarba-*closo*-dodecaborane (1B)

Prepared in an analogous method to **1A**, where instead *ortho*-$C_2B_{10}H_{12}$ was used. Yields and spectra are in agreement to previously reported syntheses (reference 3)

3.6.4 Optimization of Borylation Protocol

Optimizations were originally performed using **1B** and subsequently transferred to **1A** for final optimizations. Optimization was used to identify a suitable catalyst (ML), base (B), solvent (S), and temperature (T) required to achieve optimal conversion to **2A**. Catalyst, B_2Pin_2, and **1A** were added to an oven-dried reaction tube and sealed with a PTFE septum cap. The reaction tube was evacuated and backfilled with N_2 three times before transferring into an N_2-filled glovebox. Under an inert atmosphere, dry base and solvent were added and the reaction tube was brought out and placed in a preheated oil bath when heating was necessary. Reaction progress was monitored by using a syringe to take an aliquot to be analyzed with HRGC-MS. Note: Later optimizations included the addition of deoxygenated H_2O prior to heating. **1A** was used in later optimizations to avoid deboronation present when using **1B**.

Table B1. Base screen w/ DMF for solvent and [dppf-Pd-G3] as catalyst

Entry #	**Experimental Conditions**					**% conversion by HRGC-MS**	
	ML	**B**	**S**	**T**	**Time**	**2B**	**1B**
1	[dppf-Pd-G3], 5 mol%	CsF, 1 eq	DMF	25 °C	3h	11	89
2	[dppf-Pd-G3], 5 mol%	Cs_2CO_3, 1 eq	DMF	25 °C	3h	37.5	62.5
3	[dppf-Pd-G3], 5 mol%	K^{t}BuO, 1 eq	DMF	25 °C	3h	32	68
4	[dppf-Pd-G3], 5 mol%	KF, 1 eq	DMF	25 °C	3h	<1	>99
5	[dppf-Pd-G3], 5 mol%	KOAc, 1 eq	DMF	25 °C	3h	0	100
6	[dppf-Pd-G3], 5 mol%	K_3PO_4, 1 eq	DMF	25 °C	3h	5	95

7	[dppf-Pd-G3], 5 mol%	K_2CO_3, 1 eq	DMF	25 ºC	3h	2	98
8	[dppf-Pd-G3], 5 mol%	KH_2PO_4, 1 eq	DMF	25 ºC	3h	0	100
9	[dppf-Pd-G3], 5 mol%	NaOMe, 1 eq	DMF	25 ºC	3h	13.5	86.5
10	[dppf-Pd-G3], 5 mol%	LiOAc, 1 eq	DMF	25 ºC	3h	0	100

Table B2. Solvent screen w/ Cs_2CO_3 for base and [dppf-Pd-G3] as catalyst

Entry #	**Experimental Conditions**					**% conversion by HRGC-MS**	
	ML	**B**	**S**	**T**	**Time**	**2B**	**1B**
1	[dppf-Pd-G3], 5 mol%	Cs_2CO_3, 1 eq	DMF	25 ºC	6h	55	45
2	[dppf-Pd-G3], 5 mol%	Cs_2CO_3, 1 eq	THF	25 ºC	6h	0	100
3	[dppf-Pd-G3], 5 mol%	Cs_2CO_3, 1 eq	Dioxane	25 ºC	6h	0	100
4	[dppf-Pd-G3], 5 mol%	Cs_2CO_3, 1 eq	Toluene	25 ºC	6h	0	100
5	[dppf-Pd-G3], 5 mol%	Cs_2CO_3, 1 eq	DMAc	25 ºC	6h	10	90
6	[dppf-Pd-G3], 5 mol%	Cs_2CO_3, 1 eq	DME	25 ºC	6h	15	85

Table B3. Catalyst Loading Screen

Entry #	**Experimental Conditions**					**% conversion by HRGC-MS**	
	ML	**B**	**S**	**T**	**Time**	**2B**	**1B**

1	[dppf-Pd-G3], 2.5 mol%	Cs_2CO_3, 1 eq	DMF	25 °C	6h	53	47
2	[dppf-Pd-G3], 5 mol%	Cs_2CO_3, 1 eq	DMF	25 °C	6h	61	39
3	[dppf-Pd-G3], 7.5 mol%	Cs_2CO_3, 1 eq	DMF	25 °C	6h	50	50
4	[dppf-Pd-G3], 10 mol%	Cs_2CO_3, 1 eq	DMF	25 °C	6h	38	62

Table B4. Condition Screen for **1A** as substrate

Entry #	**Experimental Conditions**					**% conversion by HRGC-MS**		
	ML	**B**	**S**	**T**	**Time**	**2A**	**1A**	**mCB**
1	[dppf-Pd-G3], 5 mol%	Cs_2CO_3, 1 eq	DMF	25 °C	20 h	51	48	<1
2	[dppf-Pd-G3], 5 mol%	Cs_2CO_3, 1 eq	DMF	50 °C	6 h	56	38	7
3	[dppf-Pd-G3], 5 mol%	Cs_2CO_3, 1 eq Et_3N, 0.25 eq	DMF	50 °C	6 h	53	42	5
4	[dppf-Pd-G3], 5 mol%	Cs_2CO_3, 1.5 eq	DMF	50 °C	6 h	68	26	7
5	[dppf-Pd-G3], 5 mol%	Cs_2CO_3, 2 eq	DMF	50 °C	6 h	72	22	6

Table B5. Effect of H_2O on cross coupling

Entry #	**Experimental Conditions**				**% conversion by HRGC-MS**		
	ML	**B**	**S**	**Time**	**2A**	**1A**	**mCB**

1	[dppf-Pd-G3], 5 mol%	Cs_2CO_3(from glovebox), 2.5 eq	DMF	8 h	68	19	13
2	[dppf-Pd-G3], 5 mol%	Cs_2CO_3(from dessicator), 2.5 eq	DMF	8 h	72	17	11
3	[dppf-Pd-G3], 5 mol%	Cs_2CO_3(gb), 2.5 eq	DMF, 5%(v/v) H_2O	2 h	67	23	10
4	[dppf-Pd-G3], 5 mol%	Cs_2CO_3(gb), 2.5 eq	DMF, 20%(v/v) H_2O	2 h	58	37	5

Representative HRGC-MS of Crude Reaction Mixture for 2A

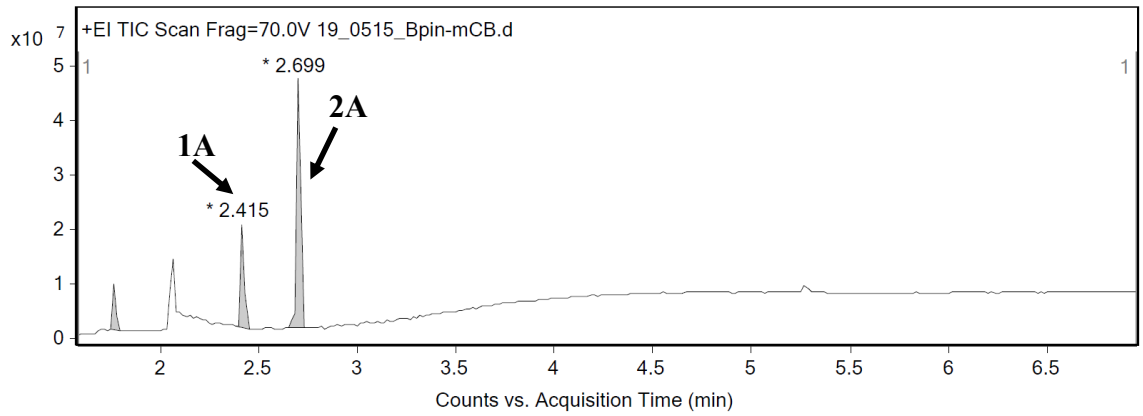

9-B(OCMe$_2$CMe$_2$O)-1,7-dicarba-*closo*-dodecaborane (2A, 5 mmol scale)

9-I-mCB (1.35 g, 5 mmol), B_2pin_2 (2.0 g, 7.5 mmol, 1.5 eq), and dppf-Pd-G3 precatalyst (231 mg, 5 mol%) were added to an oven-dried Schlenk flask and capped with a rubber septum. The flask was evacuated and backfilled with N_2 three times and transferred into an N_2-filled glovebox where Cs_2CO_3 (4.13 g, 12.5 mmol, 2.5 eq) and DMF (18.75 mL) were added. The flask was then transferred outside of the glovebox, where deoxygenated H_2O (5% v/v, 0.94 mL) was added and the reaction was allowed to stir for 2 h at 50 °C. After 2 h, the reaction was quenched by the

addition of distilled H_2O (200 mL) to yield a cloudy/tan solution. Upon addition of hexanes (7 x 20 mL) for extraction, a dark red emulsion formed and the hexanes layer was carefully decanted, making sure to keep the emulsion in the separatory funnel for subsequent extractions. The combined organic layers were washed with H_2O (2 x 50 mL) and dried with $MgSO_4$ before filtering through a pad of Celite on a fritted funnel to yield a clear, lightly colored solution. The solvent was then removed under reduced pressure to yield an off-white/orange crude solid. The crude product was subjected to purification by column chromatography with 1:1 DCM:Hexanes with 1% TFA as eluent to yield a white solid that was further purified via sequential sublimation (50 ºC, 0.1 torr to remove residual TFA for 1 hour, then 75 ºC, 0.1 torr to sublime the desired product).

Yield: 580 mg (43%), white solid

^{1}H NMR (400 MHz, C_6D_6): δ 3.5-1.4 (m, 9H, $B_{carborane}$-H), 2.01 (s, 2H, $C_{carborane}$-H), 1.06 (s, 12H)

$^{13}C\{^1H\}$ NMR (100 MHz, C_6D_6): δ 82.61, 56.75, 24.76

^{11}B NMR (128 MHz): δ 35.26 (s, 1B), -5.74 (d, 2B, $^1J_{BH}$ = 163 Hz), -8.88 (d, 1B, $^1J_{BH}$ = 154 Hz), -10.73 (s, 1B), -12.28 (d, 4B, $^1J_{BH}$ = 166 Hz), -15.53 (d, 1B), -16.19 (d, 1B)

HRGC-MS *m/z*: 270.2765 (calc. 270.1800)

Elemental Analysis Calculated for $C_8B_{11}H_{23}O_2$: C, 35.27; H, 8.52; found: C, 35.57; H, 8.77

9-B(OCMe$_2$CMe$_2$O)-1,2-dicarba-*closo*-dodecaborane (2B, 1 mmol scale)

B_2pin_2 (400 mg, 1.5 mmol, 1.5 eq) and $CsOH \cdot H_2O$ (252 mg, 1.5 mmol, 1.5 eq) were added to an oven-dried reaction tube equipped with a PTFE septum cap and evacuated and backfilled with N_2 three times. Then, DMF (1.88 mL) was added and the resulting solution was allowed to stir at

room temperature for five minutes before the addition of **1B** (270 mg, 1 mmol) and dppf-Pd-G3 precatalyst (45 mg, 5 mol%) under positive N_2 pressure. The reaction was allowed to stir at room temperature for 6 h. After 6 h, the reaction was quenched by the addition of distilled H_2O (20 mL) to yield a cloudy/tan solution. The quenched reaction mixture was subsequently extracted with hexanes (5 x 10 mL) and the combined organic layers were washed with H_2O (2 x 25 mL) and dried with $MgSO_4$ before filtering through a pad of Celite on a fritted funnel to yield a clear, lightly colored solution. The solvent was then removed under reduced pressure to yield an off-white/orange crude solid. The crude product was subjected to purification by column chromatography with 1:1 DCM:Hexanes with 1% TFA as eluent to yield a white solid that was further purified via sequential sublimation (50 ºC, 0.1 torr to remove residual TFA for 1 hour, then 85 ºC, 0.1 torr to sublime the desired product).

Yield: 114 mg (42%), white solid

^{1}H NMR (400 MHz, C_6D_6): δ 3.7-1.4 (m, 9H, $B_{carborane}$-H), 2.09 (s, 1H, $C_{carborane}$-H), 2.03 (s, 1H, $C_{carborane}$-H), 1.03 (s, 12H)

$^{13}C\{^1H\}$ NMR (100 MHz, C_6D_6): δ 82.40, 57.00, 55.79, 24.74

^{11}B NMR (128 MHz): δ 34.53 (s, 1B), -1.68 (d, 1B, $^1J_{BH}$ = 145 Hz), -2.82 (s, 1B), -8.44 (d, 2B, $^1J_{BH}$ = 148 Hz), -13.31 (d, 4B, $^1J_{BH}$ = 172 Hz), -14.64 (d, 2B, $^1J_{BH}$ = 175 Hz)

HRGC-MS *m/z*: 270.2796 (calc. 270.1800)

3.6.5 Reactions with 2A, 2B, and 3-Bpin-oCB

Synthesis of 9-BF_3K-1,7-dicarba-*closo*-dodecaborane (3A)

Synthetic procedures adapted from reference 4. 9-Bpin-mCB (675mg, 2.5 mmol) was added to a round-bottomed flask equipped with a stir bar and suspended in a methanol and acetonitrile mixture (1:1, 25.0 mL). While stirring the dissolved boronic ester, a solution of potassium fluoride in H_2O (1.19 g in 6.25 mL) was added dropwise over 5 minutes while heating at 45 °C. Once addition was complete, the reaction was stirred for an additional 25 minutes at 45 °C. Subsequently, a solution of L-(+)-tartaric acid in a minimal amount of THF (1.58 g in ~10 mL, sonication and heat may be required to fully dissolve the acid) was added dropwise over 10 minutes to the stirring mixture at 45 °C as a white precipitate formed. The reaction was stirred for an additional 20 min at 45 °C before the slow addition of two acetonitrile portions (2 x 15 mL) over a 10 min period before removing from heat. The precipitate was filtered off and washed with acetonitrile. The filtrate was then concentrated under reduced pressure to yield a white, crystalline powder. Remaining **2A** and pinacol were removed by heating with a heat gun under high vacuum until pinacol no longer condensed inside the flask, yielding **3A** as a fine, white powder.

Yield: 510 mg (82%), white solid

^{1}H NMR (500 MHz, CD_3CN): δ 3.10 (s, 2H, $C_{carborane}$-H), 2.8-1.3 (m, 9H, $B_{carborane}$-H)

$^{13}C\{^{1}H\}$ NMR (100 MHz, CD_3CN): δ 57.15

^{11}B NMR (160 MHz): δ 4.74 (s, 1B), -2.49 (s, 1B), -5.54 (d, 2B, $^{1}J_{BH}$ = 161 Hz), -8.96 (d, 1B, $^{1}J_{BH}$ = 146 Hz), -11.79 (d, 2B, $^{1}J_{BH}$ = 158 Hz), -12.34 (d, 2B, $^{1}J_{BH}$ = 158 Hz), -15.52 (d, 1B, $^{1}J_{BH}$ = 174 Hz), -16.64 (d, 1B, $^{1}J_{BH}$ = 170 Hz)

^{19}F NMR (376 MHz): δ -127.07 (s, br)

DART-MS *m/z*: 211.1916 (calc. 211.1903)

Synthesis of 9-B(OH)$_2$-1,7-dicarba-*closo*-dodecaborane (4A)

Synthetic procedures adapted from reference 5. 9-Bpin-mCB (135 mg, 0.5 mmol) was added to a screw-top reaction tube equipped with a stir bar and dissolved in EtOH (1.7 mL) and conc. HCl (3.4 mL). The resulting solution was stirred at room temperature for 10 minutes before refluxing the solution (~80 °C) for 8 h. After 8 h, the reaction mixture was allowed to cool to room temperature and was extracted with Et_2O (3 x 10 mL). The organic layers were combined and the solvent was subsequently removed under reduced pressure to yield a light grey oil that solidifies into an off-white solid.

Yield: 79 mg (83%), off-white solid

^{1}H NMR (400 MHz, DMSO-*d*$_6$): δ 7.27 (s, 2H), 3.85 (s, 2H, $C_{carborane}$-H), 3.1-1.3 (m, 9H, $B_{carborane}$-H)

^{13}C{^{1}H} NMR (100 MHz, DMSO-*d*$_6$): δ 58.33

^{11}B NMR (128 MHz): δ 33.88 (s, 1B), -11.11 (m, 10B)

DART-MS *m/z*: 187.1943 (calc. 187.1934)

Synthesis of 9-B(OH)2-1,2-dicarba-closo-dodecaborane (4B)

Prepared in an analogous method to **4A**, where instead **2B** was used.

Yield: 50 mg (53%), off-white solid

^{1}H NMR (400 MHz, DMSO-d$_6$): δ 6.98 (s, 2H), 4.73 (s, 2H, $C_{carborane}$-H), 2.9-1.2 (m, 9H, $B_{carborane}$-H)

$^{13}C\{^{1}H\}$ NMR (100 MHz, DMSO-d_6): δ 58.91, 58.38

^{11}B NMR (128 MHz): δ 34.35 (s, 1B), -1.64 (m, 2B), -7.84 (d, 2B, $^{1}J_{BH}$ = 150 Hz), -12.29 (m, 6B)

DART-MS *m/z*: 187.1938 (calc. 187.1934)

Synthesis of 3-B(OH)$_2$-1,2-dicarba-*closo*-dodecaborane (4C)

Prepared in an analogous method to **4A**, where instead 3-Bpin-oCB (prepared according to reference 6) was used.

Yield: 78 mg (83%), off-white solid

^{1}H NMR (400 MHz, DMSO-*d_6*): δ 5.00 (s, br, 2H), 4.57 (s, 2H, $C_{carborane}$-H), 2.8-1.2 (m, 9H, $B_{carborane}$-H)

$^{13}C\{^{1}H\}$ NMR (100 MHz, DMSO-*d_6*): δ 58.17

^{11}B NMR (128 MHz): δ 32.16 (s, 1B), -2.78 (d, 2B, $^{1}J_{BH}$ = 135 Hz), -12.07 (m, 8B)

DART-MS *m/z*: 187.1937 (calc. 187.1934)

3.6.6 Cyclic Voltammetry of 3A

Cyclic voltammetry measurements of **3A** (2 mM) were performed with a Gamry Instruments Interface 1010E potentiostat using a glassy carbon working electrode, platinum wire counter electrode and Ag/Ag+ pseudo-reference electrode wire. Measurements were conducted at a scan rate of 100 mV/s with [TBA][PF_6] (0.15 M) supporting electrolyte under an inert atmosphere of N_2 in dry acetonitrile, and referenced vs. Fc/Fc^{+}.

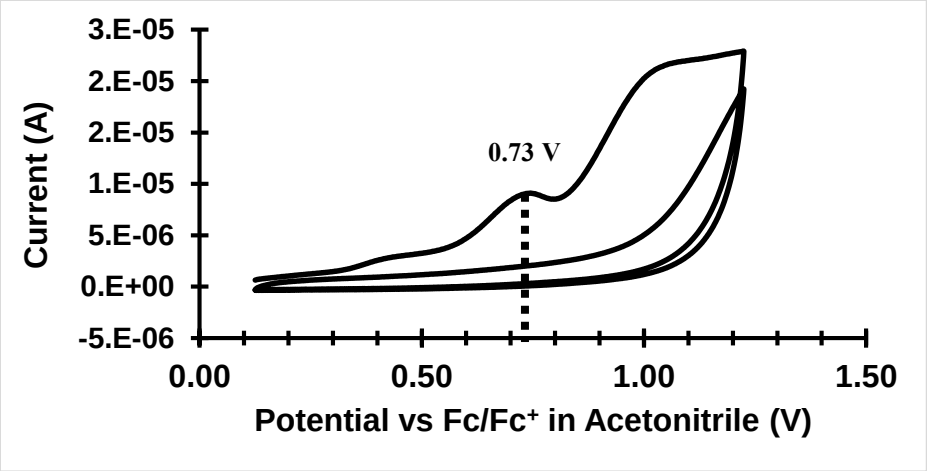

3.6.7 Optimization of Oxidation Protocols with N-Heterocycles

Optimizations were used to identify a suitable excess of trifluoroborate salt (**3A)** and manganese(III) acetate dihydrate ($Mn(OAc)_3 \cdot 2H_2O$), solvent type and amount (**S**) required to achieve optimal conversion to (4-methylquinoline)-mCB. Manganese(III) acetate used in Entry 6 was dried under high vacuum for 4 h at 150 ^oC. **3A** was added to reaction tube and dissolved in solvent. Once dissolved, 4-methylquinoline (0.05 mmol, 1 eq) and TFA (1 eq) were added to the solution. After stirring the reaction mixture for two minutes at room temperature, $Mn(OAc)_3 \cdot 2H_2O$ was added before the reaction tube was sealed with a PTFE septum cap. The reaction tube was then placed in a preheated oil bath at 60 ^oC and stirred for 18 h before removing from heat. All volatiles were removed by high vacuum before resuspending the crude reaction mixture in ~1 mL of ethyl acetate and washing with ~1 mL of aqueous sat. $NaHCO_3$. An aliquot was taken from the organic layer and analyzed by HRGC-MS.

Table B6. Optimization of oxidation conditions for carboranyl radical-heterocycle coupling

Entry #	**Experimental Conditions**			**% conversion by HRGC-MS**
	3A	**$Mn(OAc)_3 \cdot 2H_2O$**	**Solvent**	**5F**

1	1.5 eq	3 eq	AcOH, 1 mL	17
2	2 eq	4 eq	AcOH, 1 mL	28
3	2 eq	4 eq	AcOH, 0.5 mL	32
4	2 eq	4 eq	1:1 AcOH:H_2O, 0.5 mL	10
5	2 eq	4 eq	AcOH, 0.25 mL	32
6	2 eq	4 eq	AcOH, 0.4 mL	35

HRGC-MS for Entry 1

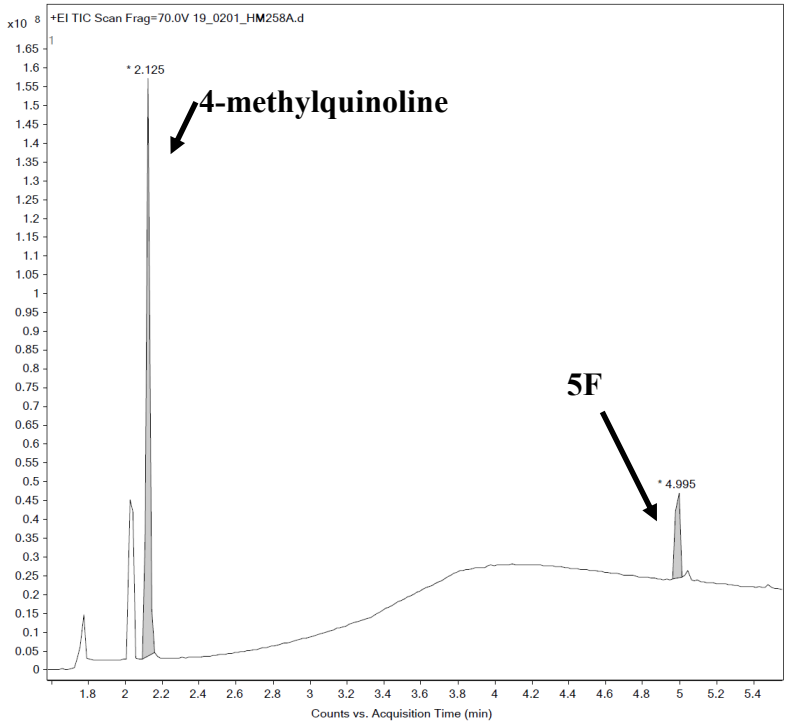

HRGC-MS for Entry 3

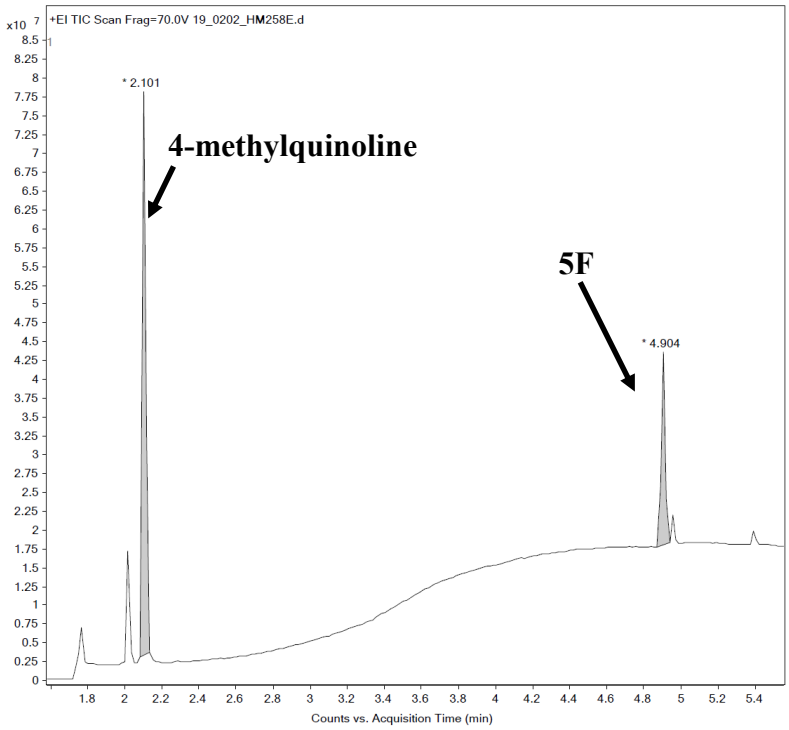

3.6.8 Inhibition by 9,10-Dihydroanthracene

Radical inhibition experiments were used to confirm the need for a radical intermediate in the oxidation of **3A** and subsequent trapping by 4-methylquinoline. Three trials were prepared where **3A** (25 mg, 0.1 mmol, 2 eq) and 4-methylquinoline (6.6 µL, 0.05 mmol, 1 eq) were added to a reaction tube and dissolved in distilled acetic acid (0.4 mL). Subsequently, trifluoroacetic acid (5 µL, 1.25 eq), 9,10-dihydroanthracene, and manganese(III) acetate dihydrate (54 mg, 0.2 mmol, 4 eq) were added to the stirring solution. The reaction was sealed with a PTFE cap and the reaction mixture was stirred for 18 h at 60 °C. After 18 h the reaction was then allowed to cool to room temperature and the solvent was removed under reduced pressure. The crude residue was re-suspended in EtOAc (1 mL) and washed with an aqueous solution of sat. $NaHCO_3$ (1 mL). An aliquot of the organic layer was subsequently taken for analysis by HRGC-MS.

Table B7. Inhibition by 9,10-Dihydroanthracene

Entry #	Experimental Conditions	% inhibition of 5F by HRGC-MS
	9,10-dihydroanthracene	
1	-----	0%
2	0.5 eq	68%
3	2 eq	71%

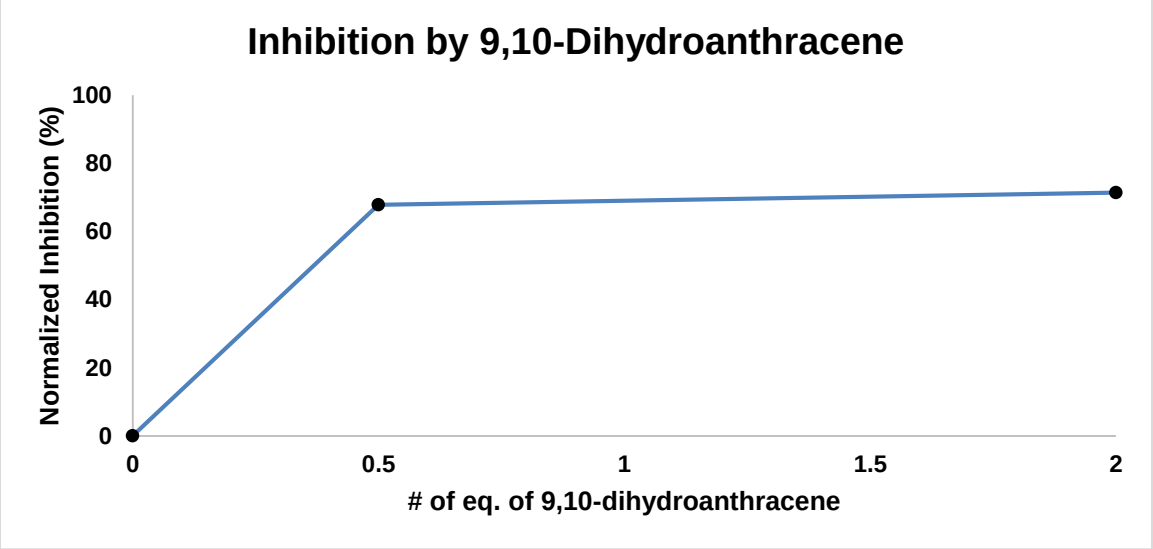

3.6.9 NMR and GC-MS Experiments for Reactions with Electron-Poor and Sterically Blocked N-Heterocycles

NMR and GC-MS experiments were used to further validate the anticipated regioselectivity of N-heterocycle substitution when using electron-poor N-heterocycles (4-triflouoromethylpyridine) or when some positions on the N-heterocycle are sterically blocked (3,5-dimethylpyridine, 2,4,6-trimethylpyridine). These reactions were prepared where **3A** (25 mg, 0.1 mmol, 2 eq) and substrate (0.05 mmol, 1 eq) of interest were added to a reaction tube and dissolved in distilled acetic acid (0.4 mL) and TFA (5 µL, 1.25 eq) was added. Once all of the solids had dissolved, manganese(III) acetate dihydrate (54 mg, 0.2 mmol, 4 eq) was added to the stirring solution. The reactions were

then sealed with a PTFE cap and the reaction mixture was stirred for 18 h at 60 °C. After 18 h the reaction was then allowed to cool to room temperature and EtOAc (1 mL) was added, followed by the addition of an aqueous solution of sat. $NaHCO_3$ (~4 mL) to neutralize the mixture. The organic layer was removed, and the aqueous layer was further extracted with EtOAc (2 x 2 mL). An aliquot of the combined organic layers was subsequently taken for analysis by HRGC-MS. The remaining EtOAc was removed under reduced pressure and the crude residue was redissolved in dichloromethane-d_6 for analysis by NMR spectroscopy.

Reaction with 4-trifuoromethylpyridine

HRGC-MS of Crude Reaction Mixture

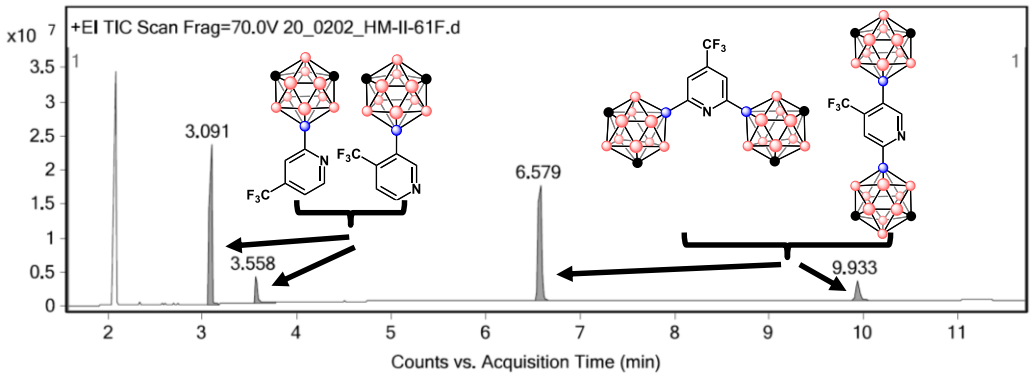

^{1}H NMR (^{19}F NMR inlay) of Crude Reaction Mixture (10-6.5 ppm)

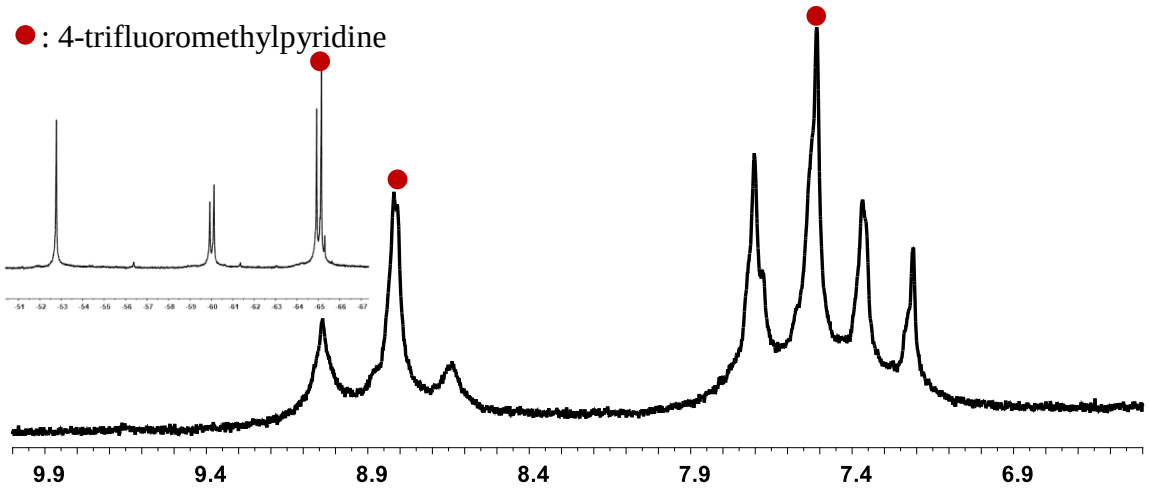

Reaction with 3,5-dimethylpyridine

HRGC-MS of Crude Reaction Mixture

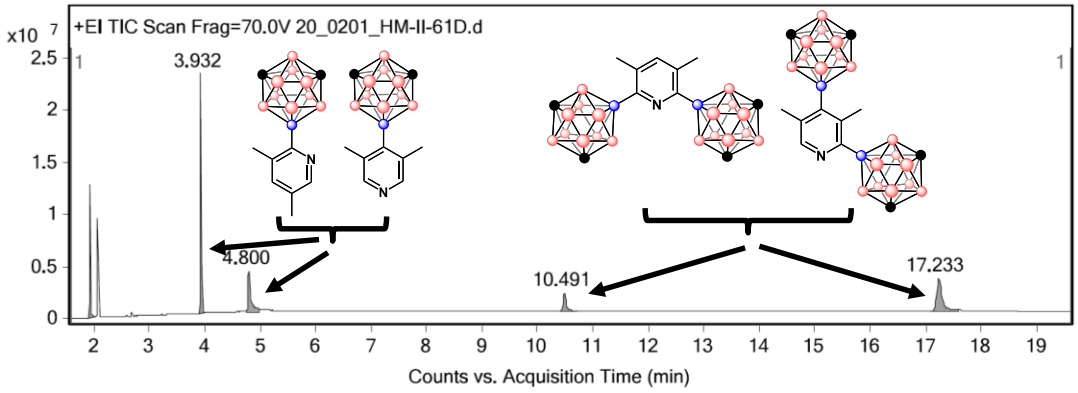

^{1}H NMR of Crude Reaction Mixture (10-6.5 ppm)

●: 3,5-dimethylpyridine

●: impurity present in 3,5-dimethylpyridine

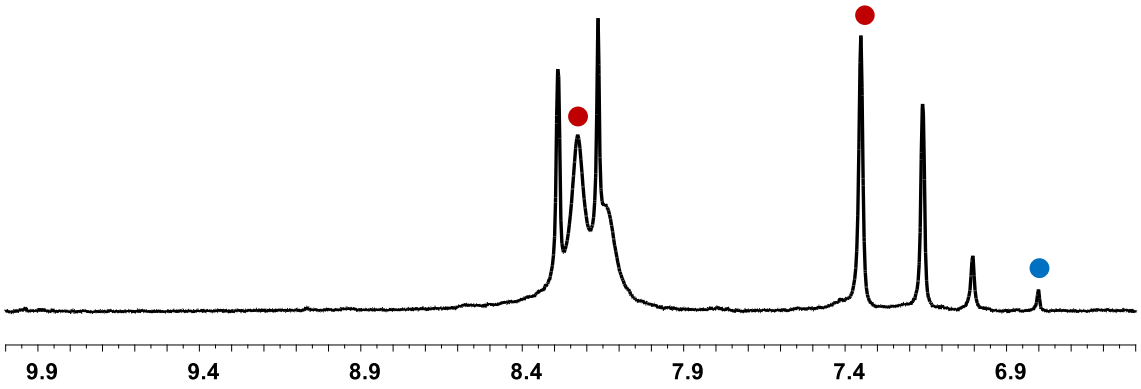

Reaction with 2,4,6-trimethylpyridine

HRGC-MS of Crude Reaction Mixture

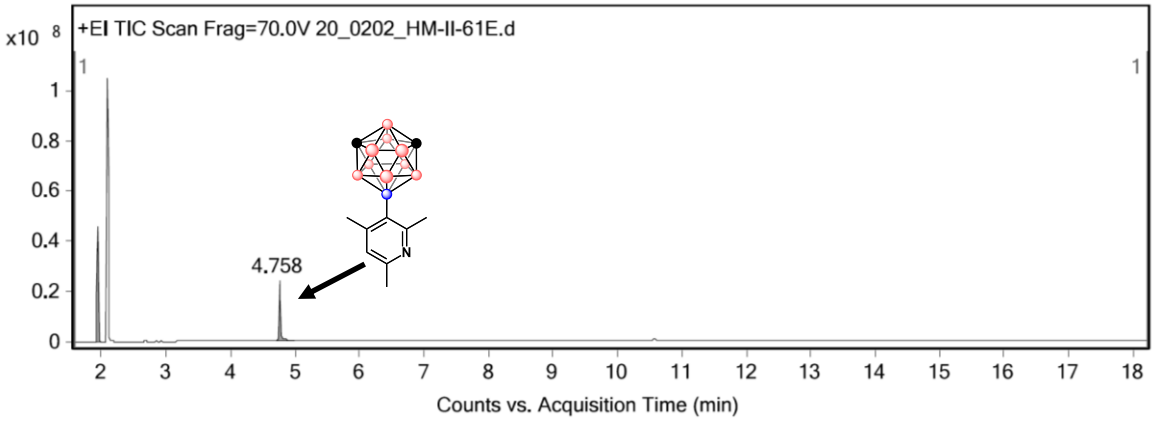

^{1}H NMR of Crude Reaction Mixture (10-6.5 ppm)

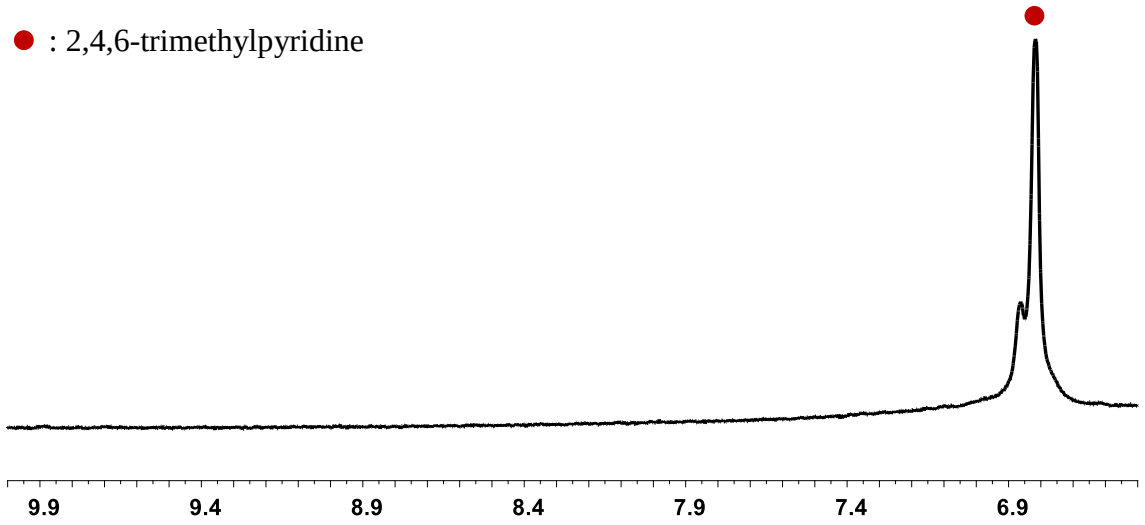

3.6.10 General Procedures for the Oxidation of 3A

General Procedure A

3A (125 mg, 0.5 mmol, 2 eq) and the substrate (0.25 mmol, 1 eq) of interest were added to a reaction tube and dissolved in distilled acetic acid (2 mL). Subsequently, manganese(III) acetate dihydrate (270 mg, 1 mmol, 4 eq) was added to the stirring solution. The reaction tube was sealed with a PTFE cap and the reaction mixture was stirred for 18 h at 60 °C. After 18 h the reaction was then allowed to cool to room temperature and the solvent was removed under reduced pressure. The crude residue was re-suspended in EtOAc (2 mL) and washed with an aqueous solution of sat. $NaHCO_3$ (2 mL). The organic layer was separated from aqueous layer before subsequent extractions with EtOAc (3 x 2 mL). The combined organic layers were dried under reduced pressure to yield the crude product that was further purified by column chromatography. All compounds subjected to purification by column chromatography were dry loaded with silica onto the column.

General Procedure B

3A (125 mg, 0.5 mmol, 2 eq) and the substrate (0.25 mmol, 1 eq) of interest were added to a reaction and dissolved in distilled acetic acid (2 mL). Subsequently, trifluoroacetic acid (25 μL, 1.25 eq) and manganese(III) acetate dihydrate (270 mg, 1 mmol, 4 eq) were added to the stirring solution. The reaction tube was sealed with a PTFE cap and the reaction mixture was stirred for 18 h at 60 °C. The reaction was then allowed to cool to room temperature and the solvent was removed under reduced pressure. The crude residue was re-suspended in EtOAc (2 mL) and washed with an aqueous solution of sat. $NaHCO_3$ (2 mL). The organic layer was separated from aqueous layer before subsequent extractions with EtOAc (3 x 2 mL). The combined organic layers were dried under reduced pressure to yield the crude product that was further purified by column chromatography. All compounds subjected to purification by column chromatography were dry loaded with silica onto the column.

9-*O*-(2,2,6,6-tetramethylpiperidin-1-yl)oxyl-1,7-dicarba-*closo*-dodecaborane (5A)

Procedure A, though **3A** (93.75 mg, 0.375 mmol, 1.5 eq) and manganese(III) acetate dihydrate (101.25 mg, 0.375 mmol, 1.5 eq) was used instead

Isolation: Flash column chromatography, 1:9 Ethyl Acetate:Hexanes

Yield: 55 mg (74%), light orange solid

^{1}H NMR (400 MHz, $CDCl_3$): δ 3.30-1.25 (m, 9H, $B_{carborane}$-H), 2.65 (s, 2H, $C_{carborane}$-H), 1.45 (s, 6H), 1.19 (m, 12H)

^{13}C{^{1}H} NMR (100 MHz, $CDCl_3$): δ 60.79, 48.85, 40.20, 35.00, 19.93, 17.14

^{11}B NMR (128 MHz): δ 10.54 (s, 1B), -8.58 (d, 2B, $^{1}J_{BH}$ = 157 Hz), -11.96 (d, 1B, $^{1}J_{BH}$ = 146 Hz), -15.32 (d, 2B, $^{1}J_{BH}$ = 169 Hz), -17.37 (d, 2B, $^{1}J_{BH}$ = 169 Hz), -20.86 (d, 1B, $^{1}J_{BH}$ = 185 Hz), -26.41 (d, 1B, $^{1}J_{BH}$ = 182 Hz)

HRGC-MS *m/z***:** 299.3244 (calc. 299.3252)

9-*S*-phenylsulfide-1,7-dicarba-*closo*-dodecaborane (5B)

Procedure A

Isolation: Flash column chromatography, 1:99 Ethyl Acetate:Hexanes

Yield: 70 mg (56%), white solid

^{1}H NMR (400 MHz, $CDCl_3$): δ 7.52 (m, 2H), 7.26 (m, 3H), 3.40-1.40 (m, 9H, $B_{carborane}$-H), 2.91 (s, 2H, $C_{carborane}$-H)

^{13}C{^{1}H} NMR (100 MHz, $CDCl_3$): δ 135.06, 128.73, 127.13, 54.05

^{11}B NMR (128 MHz): δ 0.38 (s, 1B), -6.86 (d, 2B, $^{1}J_{BH}$ = 164 Hz), -10.05 (d, 1B, $^{1}J_{BH}$ = 154 Hz), -13.48 (d, 2B, $^{1}J_{BH}$ = 152 Hz), -14.34 (d, 2B, $^{1}J_{BH}$ = 154 Hz), -17.96 (d, 1B, $^{1}J_{BH}$ = 180 Hz), -20.89 (d, 1B, $^{1}J_{BH}$ = 185 Hz)

HRGC-MS *m/z***:** 252.1957 (calc. 252.1976)

9-*Se*-phenylselenide-1,7-dicarba-*closo*-dodecaborane (5C)

Procedure A

Isolation: Flash column chromatography, Hexanes to 1:99 Ethyl Acetate:Hexanes gradient

Yield: 85 mg (57%), white solid

^{1}H NMR (400 MHz, $CDCl_3$): δ 7.63 (d, 2H, $^{1}J_{HH}$ =6.78 Hz), 7.24 (m, 3H), 3.50-1.50 (m, 9H, $B_{carborane}$-H), 2.95 (s, 2H, $C_{carborane}$-H)

^{13}C{^{1}H} NMR (100 MHz, $CDCl_3$): δ 136.37, 129.00, 128.76, 127.20, 55.17

^{11}B NMR (128 MHz): δ -4.09 (s, 1B), -6.39 (d, 2B, $^{1}J_{BH}$ = 170 Hz), -9.53 (d, 1B, $^{1}J_{BH}$ = 154 Hz), -13.02 (d, 2B, $^{1}J_{BH}$ = 159 Hz), -13.60 (d, 2B, $^{1}J_{BH}$ = 170 Hz), -17.28 (d, 1B, $^{1}J_{BH}$ = 180 Hz), -19.60 (d, 1B, $^{1}J_{BH}$ = 185 Hz)

^{77}Se NMR (95 MHz): δ 81.13 (q, $^{1}J_{SeB}$ = 45 Hz)

HRGC-MS *m/z***:** 300.1881 (calc. 300.1420)

9-*Te*-phenyltelluride-1,7-dicarba-*closo*-dodecaborane (5D)

Procedure A, though the reaction was performed under an inert atmosphere of argon.

Isolation: Flash column chromatography, Hexanes to 1:99 Ethyl Acetate:Hexanes gradient

Yield: 46 mg (27%), off-white solid

^{1}H NMR (400 MHz, $CDCl_3$): δ 7.82 (d, 2H, $^{1}J_{HH}$ = 7.78 Hz), 7.29 (t, 1H, $^{1}J_{HH}$ = 7.29 Hz), 7.14 (t, 1H, $^{1}J_{HH}$ = 8.10 Hz), 3.60-1.60 (m, 9H, $B_{carborane}$-H), 3.01 (s, 2H, $C_{carborane}$-H)

^{13}C{^{1}H} NMR (100 MHz, $CDCl_3$): δ 140.81, 128.80, 127.46, 108.71, 57.00

^{11}B NMR (128 MHz): δ -5.78 (d, 2B, $^{1}J_{BH}$ = 175 Hz), -8.81 (d, 1B, $^{1}J_{BH}$ = 157 Hz), -12.64 (m, 4B), -15.70 (s, 1B), -17.00 (m, 2B)

^{125}Te NMR (158 MHz): δ 66.76 (sept.)

HRGC-MS *m/z***:** 349.1301 (calc. 349.1263)

9-*Se*-(9-seleno-1,2-dicarba-*closo*-dodecaborane)-1,7-dicarba-*closo*-dodecaborane (5E)

Procedure A

Isolation: Flash column chromatography, Hexanes to 3:7 Ethyl Acetate:Hexanes gradient

Yield: 53 mg, (29%), pale yellow solid

^{1}H NMR (400 MHz, CD_2Cl_2): δ 3.66 (s, 1H, $C_{ortho\text{-}carborane}$-H), 3.61 (s, 1H, $C_{ortho\text{-}carborane}$-H), 3.40-1.60 (m, 18H, $B_{carborane}$-H), 3.01 (s, 2H, $C_{meta\text{-}carborane}$-H)

^{13}C{^{1}H} NMR (100 MHz, CD_2Cl_2): δ 55.06, 54.09, 49.34

^{11}B NMR (128 MHz): δ 1.04 (s, 1B), -2.36 (d, 2B), -6.60 (s, 1B), -6.62 (d, 2B), -8.90 (d, 2B), -10.05 (d, 1B), -14.45 (m, 9H), -17.98 (d, 1B), -20.41 (d, 1B)

^{77}Se NMR (95 MHz): δ -283.96 (m, br)

HRGC-MS *m/z***:** 366.2893 (calc. 366.2893)

9-(2)-4-methylquinoline-1,7-dicarba-*closo*-dodecaborane (5F)

Procedure B

Isolation: Flash column chromatography, 1:9 Ethyl Acetate:Hexanes

Yield: 22 mg (30%), white solid

^{1}H NMR (400 MHz, $CDCl_3$): δ 8.19 (d, 1H, $^{1}J_{HH}$ = 8.05 Hz), 7.94 (d, 1H, $^{1}J_{HH}$ = 8.62 Hz), 7.65 (t, 1H, $^{1}J_{HH}$ = 8.05 Hz), 3.60-1.80 (m, 9H, $B_{carborane}$-H), 3.07 (s, 2H, $C_{carborane}$-H), 2.67 (s, 3H)

^{13}C{^{1}H} NMR (100 MHz, $CDCl_3$): δ 148.36, 141.49, 130.53, 128.55, 127.10, 126.23, 125.75, 123.49, 54.45, 18.63

^{11}B NMR (128 MHz): δ -0.67 (s, 1B), -6.45 (d, 2B, $^{1}J_{BH}$ = 176 Hz), -9.71 (d, 1B, $^{1}J_{BH}$ = 159 Hz), -12.91 (d, 2B, $^{1}J_{BH}$ = 131 Hz), -13.82 (d, 2B, $^{1}J_{BH}$ = 154 Hz), -17.40 (d, 1B, $^{1}J_{BH}$ = 186 Hz), -19.27 (d, 1B, $^{1}J_{BH}$ = 235 Hz)

HRGC-MS *m/z***:** 285.2964 (calc. 285.2521)

Elemental Analysis Calculated for $C_{12}B_{10}H_{19}N$: C, 50.15; H, 6.67; found: C, 50.18; H, 6.85

9-(2)-benzothiazole-1,7-dicarba-*closo*-dodecaborane (5G)

Procedure B, though the reaction was performed in 1:1 distilled acetic acid:H_2O

Isolation: Flash column chromatography, Hexanes to 2:8 Acetone:Hexanes gradient

Yield: 28 mg (40 %), pale yellow solid

^{1}H NMR (400 MHz, $CDCl_3$): δ 8.15 (dq, 1H, $^{1}J_{HH}$ = 8.27 Hz, $^{2}J_{HH}$ = 0.88 Hz), 7.88 (dq, 1H, $^{1}J_{HH}$ = 7.97, $^{2}J_{HH}$ = 0.63 Hz), 7.44 (m, 1H), 7.34 (m, 1H), 3.5-1.5 (m, 9H, $B_{carborane}$-H), 3.10 (s, 2H, $C_{carborane}$-H)

^{13}C{^{1}H} NMR (100 MHz, $CDCl_3$): δ 155.86, 152.03, 136.74, 125.69, 124.77, 123.19, 121.27, 54.73

^{11}B NMR (128 MHz): δ -3.95 (s, 1B), -6.38 (d, 2B, $^{1}J_{BH}$ = 162 Hz), -9.64 (d, 1B, $^{1}J_{BH}$ = 154 Hz), -12.95 (d, 2B, $^{1}J_{BH}$ = 154 Hz), -13.66 (d, 2B, $^{1}J_{BH}$ = 161 Hz), -17.32 (d, 1B, $^{1}J_{BH}$ = 183 Hz), -18.55 (d, 1B, $^{1}J_{BH}$ = 163 Hz)

HRGC-MS *m/z***:** 277.1914 (calc. 277.1928)

9-(2)-7,8-dimethylquinoxaline-1,7-dicarba-*closo*-dodecaborane (5H)

Procedure B

Isolation: Flash column chromatography, 15:85 Ethyl Acetate:Hexanes. Residual 9-HO-mCB was removed by sublimation at 85 ºC and 0.1 torr

Yield: 33 mg (44%), pale yellow solid

^{1}H NMR (400 MHz, $CDCl_3$): δ 8.87 (s, 1H), 7.91 (s, 1H), 7.78 (s, 1H), 3.60-1.60 (m, 9H, $B_{carborane}$-H), 3.11 (s, 2H, $C_{carborane}$-H), 2.47 (s, 6H)

^{13}C{^{1}H} NMR (100 MHz, $CDCl_3$): δ 139.85, 139.82, 128.95, 128.11, 54.77, 20.33, 20.22

^{11}B NMR (128 MHz): δ -1.87 (s, 1B), -6.38 (d, 2B, $^{1}J_{BH}$ = 164 Hz), -9.66 (d, 1B, $^{1}J_{BH}$ = 159 Hz), -12.90 (d, 2B, $^{1}J_{BH}$ = 159 Hz), -13.58 (d, 2B, $^{1}J_{BH}$ = 148 Hz), -17.23 (d, 1B, $^{1}J_{BH}$ = 185 Hz), -18.76 (d, 1B, $^{1}J_{BH}$ = 176 Hz)

HRGC-MS *m/z***:** 300.3110 (calc. 300.2630)

9-(2)-4-tert-butylpyridine-1,7-dicarba-*closo*-dodecaborane (5I)

Procedure B

Isolation: Flash column chromatography, Hexanes to 3:7 Ethyl Acetate:Hexanes gradient

Yield: 24 mg (34%), white solid

^{1}H NMR (400 MHz, $CDCl_3$): δ 8.59 (dd, 1H, $^{1}J_{HH}$ = 5.51 Hz, $^{2}J_{HH}$ = 0.51 Hz), 7.53 (d, 1H, $^{1}J_{HH}$ = 1.58 Hz), 7.16 (dd, 1H, $^{1}J_{HH}$ = 5.46 Hz, $^{2}J_{HH}$ = 2.17 Hz), 3.6-1.5 (m, 9H, $B_{carborane}$-H), 3.04 (s, 2H, $C_{carborane}$-H), 1.30 (s, 9H)

^{13}C{^{1}H} NMR (100 MHz, $CDCl_3$): δ 158.46, 149.08, 125.14, 119.22, 54.40, 34.61, 30.53

^{11}B NMR (128 MHz): δ -0.93 (s, 1B), -6.55 (d, 2B, $^{1}J_{BH}$ = 161 Hz), -9.79 (d, 1B, $^{1}J_{BH}$ = 154 Hz), -13.04 (d, 2B, $^{1}J_{BH}$ = 145 Hz), -13.90 (d, 2B, $^{1}J_{BH}$ = 147 Hz), -17.47 (d, 1B, $^{1}J_{BH}$ = 183 Hz), -19.36 (d, 1B, $^{1}J_{BH}$ = 170 Hz)

HRGC-MS *m/z***:** 277.2807 (calc. 277.2834)

3.6.11 General Procedures for Oxidation Reactions with 4B and 4C

The synthesis of compounds **6A**-**D** followed identical procedures used in the synthesis of compounds **5A** or **5I**, depending on substrate, where the addition of **3A** was replaced with either **4B** or **4C**.

9-*O*-(2,2,6,6-tetramethylpiperidin-1-yl)oxyl -1,2-dicarba-*closo*-dodecaborane (6A)

Isolation: Flash column chromatography, Hexanes to 1:9 Ethyl Acetate:Hexanes gradient

Yield: 21 mg (70%), light yellow solid

^{1}H NMR (400 MHz, $CDCl_3$): δ 3.28 (s, 2H, $C_{carborane}$-H), 3.1-1.1 (m, 9H, $B_{carborane}$-H), 1.44 (s, 6H), 1.13 (s, br, 12H)

^{13}C{^{1}H} NMR (100 MHz, $CDCl_3$): δ 60.54, 48.24, 40.19, 38.39, 34.94, 19.98, 17.11

^{11}B NMR (128 MHz): δ 16.21 (s, 1B), -4.52 (d, 1B, $^{1}J_{BH}$ = 144 Hz), -10.54 (d, 2B, $^{1}J_{BH}$ = 144 Hz), -17.20 (m, 6B)

HRGC-MS *m/z***:** 299.3131 (calc. 299.3244)

3-*O*-(2,2,6,6-tetramethylpiperidin-1-yl)oxyl-1,2-dicarba-*closo*-dodecaborane (6B)

Isolation: Flash column chromatography, Hexanes to 1:9 Ethyl Acetate:Hexanes gradient

Yield: 22 mg (73%), light yellow solid

^{1}H NMR (400 MHz, $CDCl_3$): δ 3.70 (s, 2H, $C_{carborane}$-H), 3.0-1.0 (m, 9H, $B_{carborane}$-H), 1.52 (s, 6H), 1.21 (s, br, 12H)

^{13}C{^{1}H} NMR (100 MHz, $CDCl_3$): δ 61.39, 55.84, 40.12, 34.79, 20.06, 16.88

^{11}B NMR (128 MHz): δ 1.32 (s, 1B), -5.67 (d, 1B, $^{1}J_{BH}$ = 154 Hz), -11.30 (d, 2B, $^{1}J_{BH}$ = 145 Hz), -15.43 (m, 5B), -19.25 (d, 1B, $^{1}J_{BH}$ = 154 Hz)

HRGC-MS *m/z***:** 299.3131 (calc. 299.3244)

9-(2)-4-tert-butylpyridine-1,2-dicarba-*closo*-dodecaborane (6C)

Isolation: Flash column chromatography, Hexanes to 3:7 Ethyl Acetate:Hexanes gradient

Yield: 9 mg (33%), white solid

^{1}H NMR (400 MHz, $CDCl_3$): δ 8.55 (d, 1H, $^{1}J_{HH}$ = 5.33 Hz), 7.39 (d, 1H, $^{1}J_{HH}$ = 1.53 Hz), 7.11 (dd, 1H, $^{1}J_{HH}$ = 5.27 Hz, $^{2}J_{HH}$ = 1.76 Hz), 3.70 (s, 1H, $C_{carborane}$-H), 3.60 (s, 1H, $C_{carborane}$-H), 3.1-1.5 (m, 9H, $B_{carborane}$-H)), 1.28 (s, 9H)

$^{13}C\{^{1}H\}$ NMR (100 MHz, $CDCl_3$): δ 158.27, 149.91, 124.43, 118.92, 53.38, 50.01, 34.59, 30.53

^{11}B NMR (128 MHz): δ 6.32 (s, 1B), -2.34 (d, 1B, $^{1}J_{BH}$ = 142 Hz), -8.78 (d, 2B, $^{1}J_{BH}$ = 150 Hz), -14.40 (m, 6B)

HRGC-MS *m/z***:** 277.2813 (calc. 277.2834)

3-(2)-4-tert-butylpyridine-1,2-dicarba-*closo*-dodecaborane (6D)

Isolation: Flash column chromatography, Hexanes to 3:7 Ethyl Acetate:Hexanes gradient

Yield: 10 mg (36%), white solid

^{1}H NMR (400 MHz, $CDCl_3$): δ 8.44 (dd, 1H, $^{1}J_{HH}$ = 5.30 Hz, $^{2}J_{HH}$ = 0.66 Hz), 7.85 (d, 1H, $^{1}J_{HH}$ = 1.32 Hz), 7.28 (dd, 1H, $^{1}J_{HH}$ = 5.36 Hz, $^{2}J_{HH}$ = 2.04 Hz), 4.08 (s, 2H, $C_{carborane}$-H, 3.3-1.4 (m, 9H, $B_{carborane}$-H)), 1.35 (s, 9H)

$^{13}C\{^{1}H\}$ NMR (100 MHz, $CDCl_3$): δ 159.39, 149.19, 126.50, 121.01, 57.28, 34.78, 30.52

^{11}B NMR (128 MHz): δ -2.90 (d, 2B, $^{1}J_{BH}$ = 145 Hz), -7.11 (s, 1B), -12.79 (m, 7B)

HRGC-MS *m/z***:** 277.2807 (calc. 277.2834)

3.6.12 X-ray Crystallography Details

Table B8. Crystal data and structure refinement for **2A**.

CCDC number	1967645	
Empirical formula	$C_8H_{23}B_{11}O_2$	
Formula weight	270.17	
Temperature	100.0 K	
Wavelength	0.71073 Å	
Crystal system	Monoclinic	
Space group	*P 21/n*	
Unit cell dimensions	a = 13.2848(13) Å	α= 90°.
	b = 17.384(2) Å	β= 91.954(5)°.
	c = 14.224(3) Å	γ = 90°.
Volume	3283.0(8) $Å^3$	
Z	8	
Density (calculated)	1.093 Mg/m^3	
Absorption coefficient	0.059 mm^{-1}	
F(000)	1136	

Crystal size	0.32 x 0.28 x 0.25 mm^3
Theta range for data collection	1.851 to 25.380°.
Index ranges	-16<=*h*<=11, -20<=*k*<=20, -17<=*l*<=17
Reflections collected	20454
Independent reflections	5982 [*R*(int) = 0.0471]
Completeness to theta = 25.242°	99.5 %
Absorption correction	Semi-empirical from equivalents
Max. and min. transmission	0.7452 and 0.6989
Refinement method	Full-matrix least-squares on F^2
Data / restraints / parameters	5982 / 0 / 387
Goodness-of-fit on F^2	1.015
Final R indices [$I>2\sigma(I)$]	$R1$ = 0.0509, w$R2$ = 0.1152
R indices (all data)	$R1$ = 0.0832, w$R2$ = 0.1307
Extinction coefficient	n/a
Largest diff. peak and hole	0.287 and -0.274 e.$Å^{-3}$

Table B9. Crystal data and structure refinement for **5A**.

CCDC number	1967643	
Empirical formula	$C_{11}H_{29}B_{10}NO$	
Formula weight	299.45	
Temperature	100.0 K	
Wavelength	0.71073 Å	
Crystal system	Orthorhombic	
Space group	*Pbca*	
Unit cell dimensions	a = 16.1941(6) Å	α= 90°.
	b = 13.2477(4) Å	β= 90°.
	c = 16.5076(4) Å	γ = 90°.
Volume	3541.45(19) $Å^3$	
Z	8	
Density (calculated)	1.123 Mg/m^3	
Absorption coefficient	0.059 mm^{-1}	
F(000)	1280	
Crystal size	0.32 x 0.31 x 0.28 mm^3	

Theta range for data collection	2.338 to 28.281°.
Index ranges	-17<=*h*<=21, -17<=*k*<=17, -21<=*l*<=21
Reflections collected	26580
Independent reflections	4392 [*R*(int) = 0.0559]
Completeness to theta = 25.242°	100.0 %
Absorption correction	Semi-empirical from equivalents
Max. and min. transmission	0.7457 and 0.6931
Refinement method	Full-matrix least-squares on F^2
Data / restraints / parameters	4392 / 0 / 212
Goodness-of-fit on F^2	1.051
Final *R* indices [$I>2\sigma(I)$]	*R*1 = 0.0482, w*R*2 = 0.1177
R indices (all data)	*R*1 = 0.0635, w*R*2 = 0.1274
Extinction coefficient	n/a
Largest diff. peak and hole	0.323 and -0.288 e.Å^{-3}

Table B10. Crystal data and structure refinement for **5G**.

CCDC number	1667644	
Empirical formula	$C_9H_{15}B_{10}NS$	
Formula weight	277.38	
Temperature	100.0 K	
Wavelength	0.71073 Å	
Crystal system	Monoclinic	
Space group	*P 21/n*	
Unit cell dimensions	a = 16.4854(6) Å	α= 90°.
	b = 9.7782(4) Å	β= 113.470(2)°.
	c = 19.2767(7) Å	γ = 90°.
Volume	2850.28(19) $Å^3$	
Z	8	
Density (calculated)	1.293 Mg/m^3	
Absorption coefficient	0.205 mm^{-1}	
F(000)	1136	
Crystal size	0.33 x 0.32 x 0.3 mm^3	

Theta range for data collection	1.380 to 28.355°.
Index ranges	-20<=*h*<=22, -13<=*k*<=13, -25<=*l*<=25
Reflections collected	25121
Independent reflections	7084 [*R*(int) = 0.0724]
Completeness to theta = 25.242°	100.0 %
Absorption correction	Semi-empirical from equivalents
Max. and min. transmission	0.7457 and 0.6496
Refinement method	Full-matrix least-squares on F^2
Data / restraints / parameters	7084 / 0 / 379
Goodness-of-fit on F^2	1.028
Final *R* indices [I>2σ(I)]	*R*1 = 0.0446, w*R*2 = 0.1159
R indices (all data)	*R*1 = 0.0563, w*R*2 = 0.1256
Extinction coefficient	n/a
Largest diff. peak and hole	0.368 and -0.359 e.Å^{-3}

Table B11. Crystal data and structure refinement for **5I**.

CCDC number	1967642	
Empirical formula	$C_{11}H_{23}B_{10}N$	
Formula weight	277.40	
Temperature	100.0 K	
Wavelength	1.54178 Å	
Crystal system	Monoclinic	
Space group	*P 21/c*	
Unit cell dimensions	a = 11.0668(2) Å	α= 90°.
	b = 11.6755(2) Å	β= 91.0920(10)°.
	c = 13.1623(2) Å	γ = 90°.
Volume	1700.40(5) Å^3	
Z	4	
Density (calculated)	1.084 Mg/m^3	
Absorption coefficient	0.374 mm^{-1}	
F(000)	584	
Crystal size	0.29 x 0.28 x 0.26 mm^3	

Theta range for data collection	3.995 to 68.277°.
Index ranges	-13<=*h*<=13, -14<=*k*<=13, -15<=*l*<=15
Reflections collected	21437
Independent reflections	3115 [*R*(int) = 0.0247]
Completeness to theta = 67.679°	100.0 %
Absorption correction	Semi-empirical from equivalents
Max. and min. transmission	0.7531 and 0.6585
Refinement method	Full-matrix least-squares on F^2
Data / restraints / parameters	3115 / 0 / 202
Goodness-of-fit on F^2	1.099
Final *R* indices [$I>2\sigma(I)$]	*R*1 = 0.0456, w*R*2 = 0.1213
R indices (all data)	*R*1 = 0.0480, w*R*2 = 0.1237
Extinction coefficient	n/a
Largest diff. peak and hole	0.314 and -0.287 e.$Å^{-3}$

Table B12. Crystal data and structure refinement for **6A**.

CCDC number	1967641	
Empirical formula	$C_{11}H_{29}B_{10}NO$	
Formula weight	299.45	
Temperature	100.0 K	
Wavelength	1.54178 Å	
Crystal system	Orthorhombic	
Space group	*Pbca*	
Unit cell dimensions	a = 13.1543(5) Å	α= 90°.
	b = 16.2210(5) Å	β= 90°.
	c = 16.6984(5) Å	γ = 90°.
Volume	3563.0(2) $Å^3$	
Z	8	
Density (calculated)	1.116 Mg/m^3	
Absorption coefficient	0.427 mm^{-1}	
F(000)	1280	
Crystal size	0.31 x 0.29 x 0.27 mm^3	

Theta range for data collection	5.075 to 68.154°.
Index ranges	-15<=*h*<=15, -18<=*k*<=19, -20<=*l*<=19
Reflections collected	14603
Independent reflections	3224 [*R*(int) = 0.0284]
Completeness to theta = 67.679°	99.3 %
Absorption correction	Semi-empirical from equivalents
Max. and min. transmission	0.7531 and 0.6802
Refinement method	Full-matrix least-squares on F^2
Data / restraints / parameters	3224 / 0 / 212
Goodness-of-fit on F^2	1.024
Final R indices [$I>2\sigma(I)$]	$R1$ = 0.0475, w$R2$ = 0.1303
R indices (all data)	$R1$ = 0.0522, w$R2$ = 0.1360
Extinction coefficient	n/a
Largest diff. peak and hole	0.309 and -0.359 e.Å^{-3}

3.6.13 NMR Spectroscopy and Mass Spectrometry of Isolated Compounds

3.6.13.1 Characterization of 2A

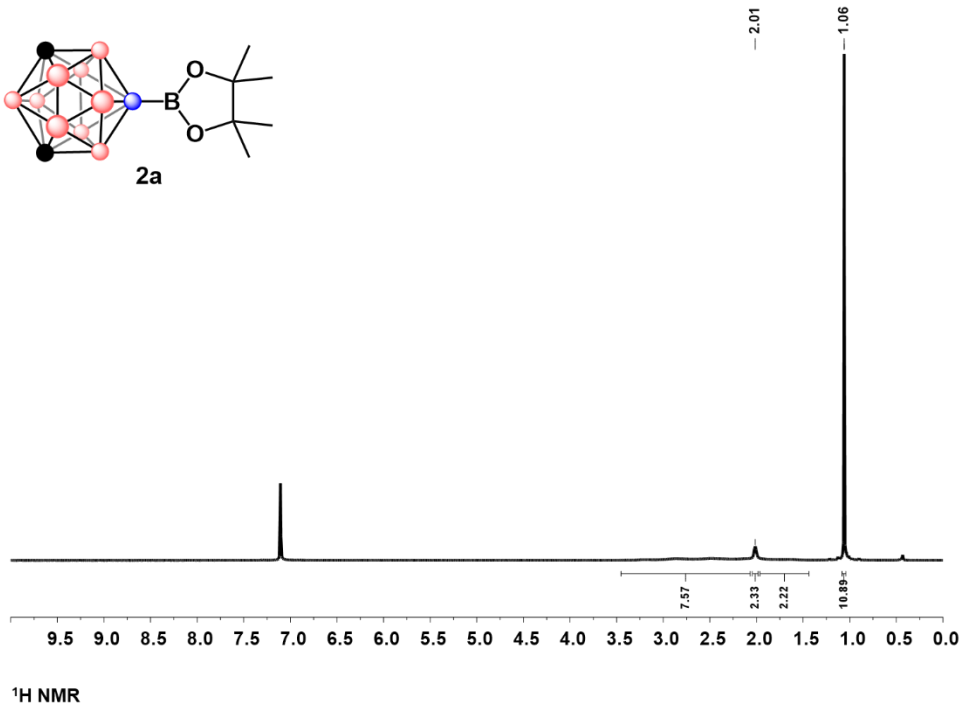

Figure B1.1 ^{1}H NMR of **2A**

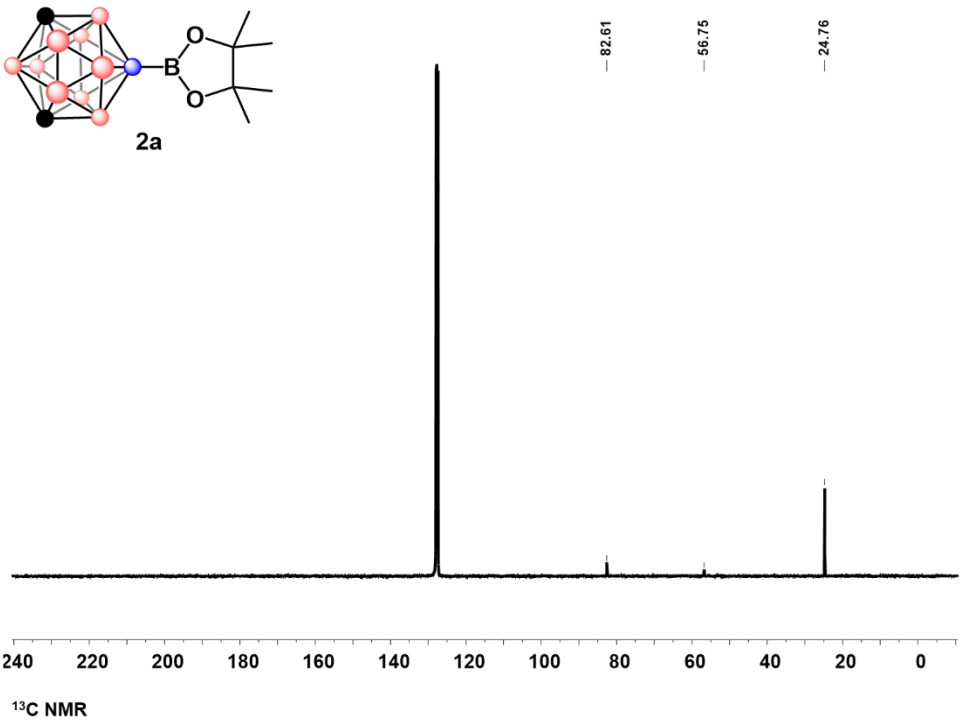

Figure B1.2 ^{13}C NMR of **2A**

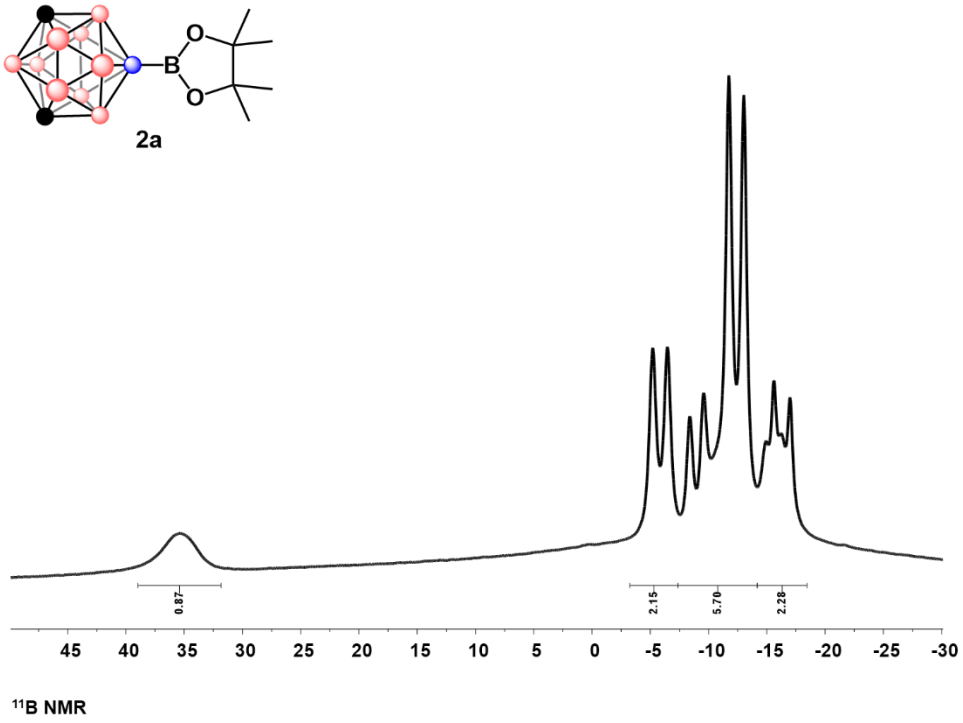

Figure B1.3 ^{11}B NMR of **2A**

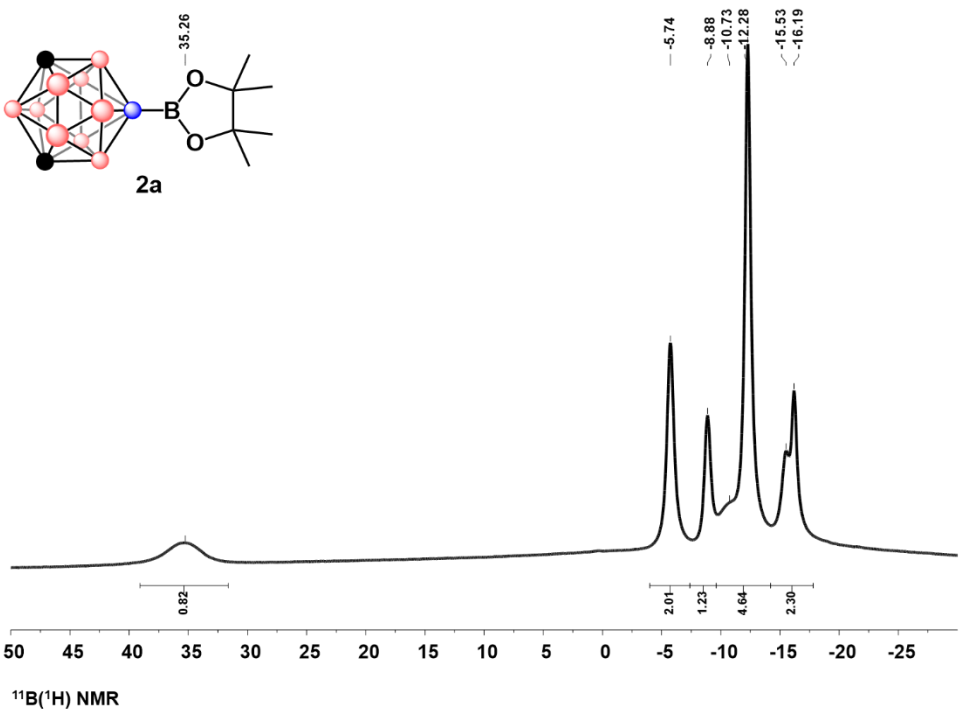

Figure B1.4 $^{11}B\{^{1}H\}$ NMR of **2A**

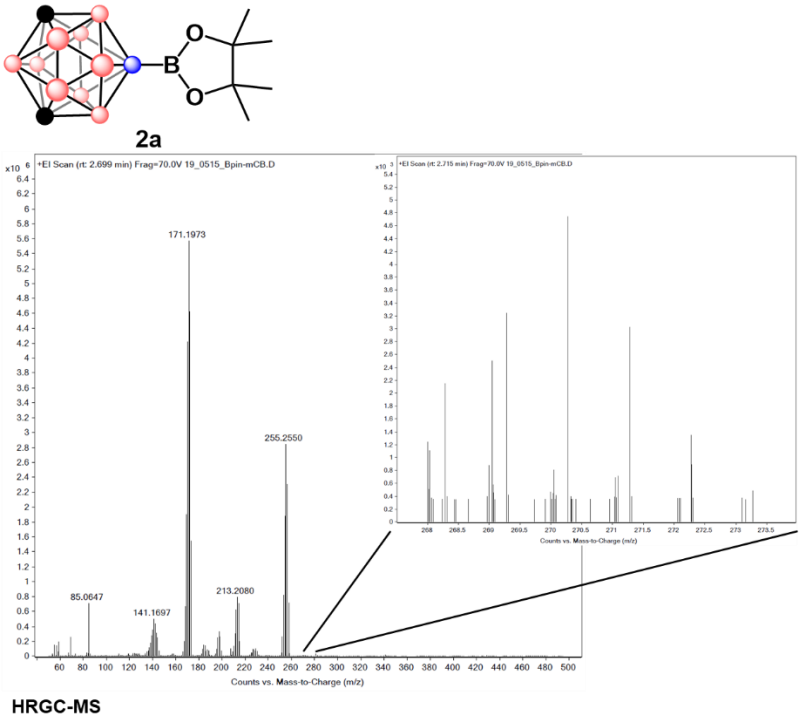

Figure B1.5 GC-MS of **2A**

3.6.13.2 Characterization of 2B

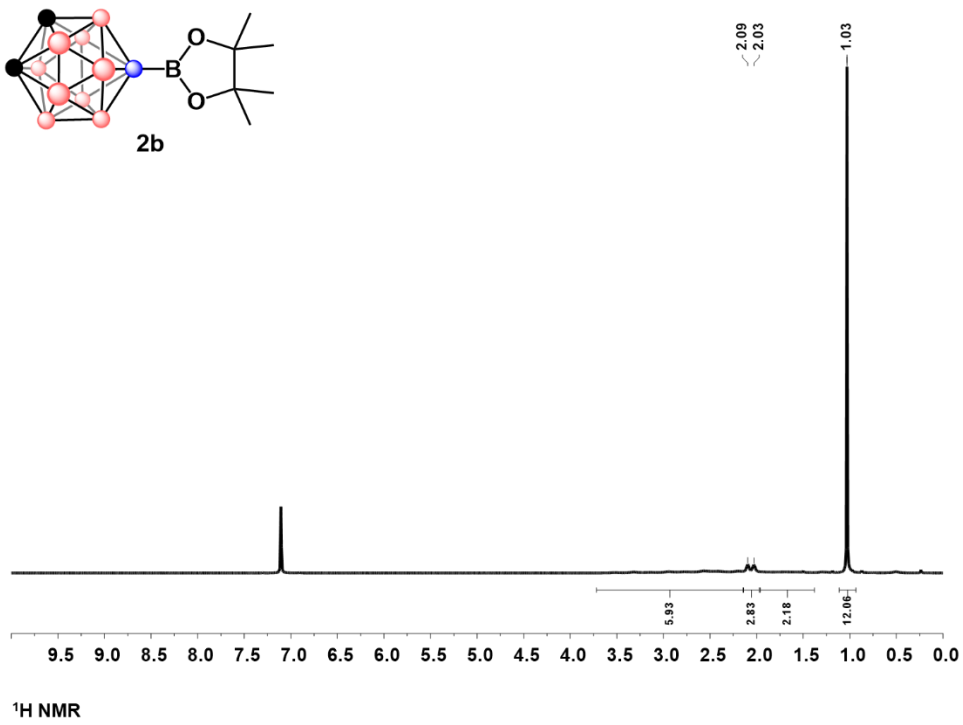

Figure B2.1 ^{1}H NMR of **2B**

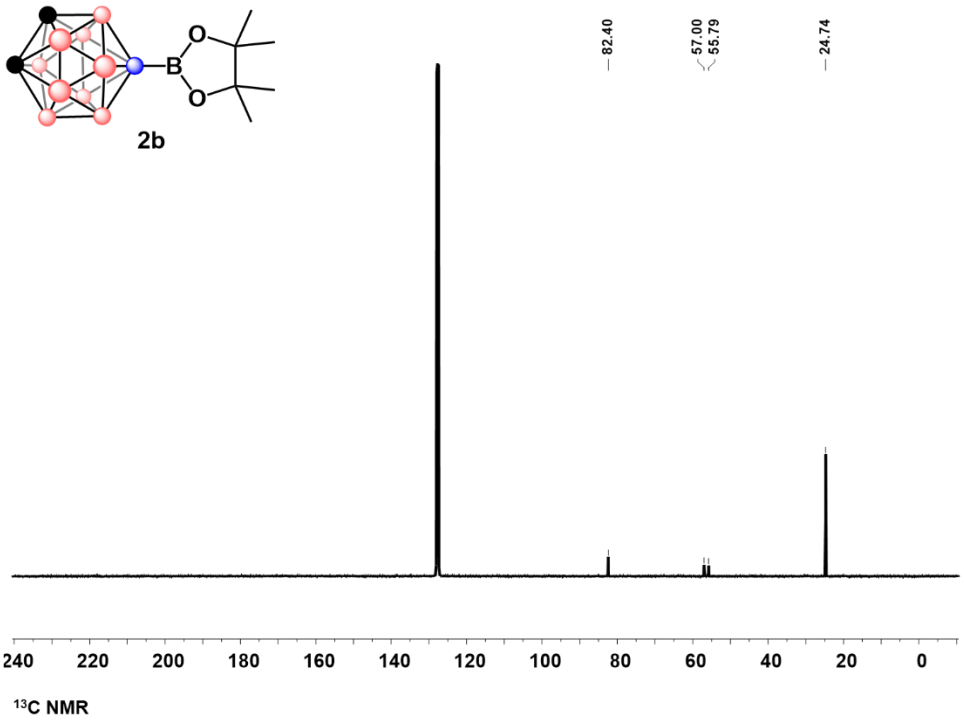

Figure B2.2 ^{13}C NMR of **2B**

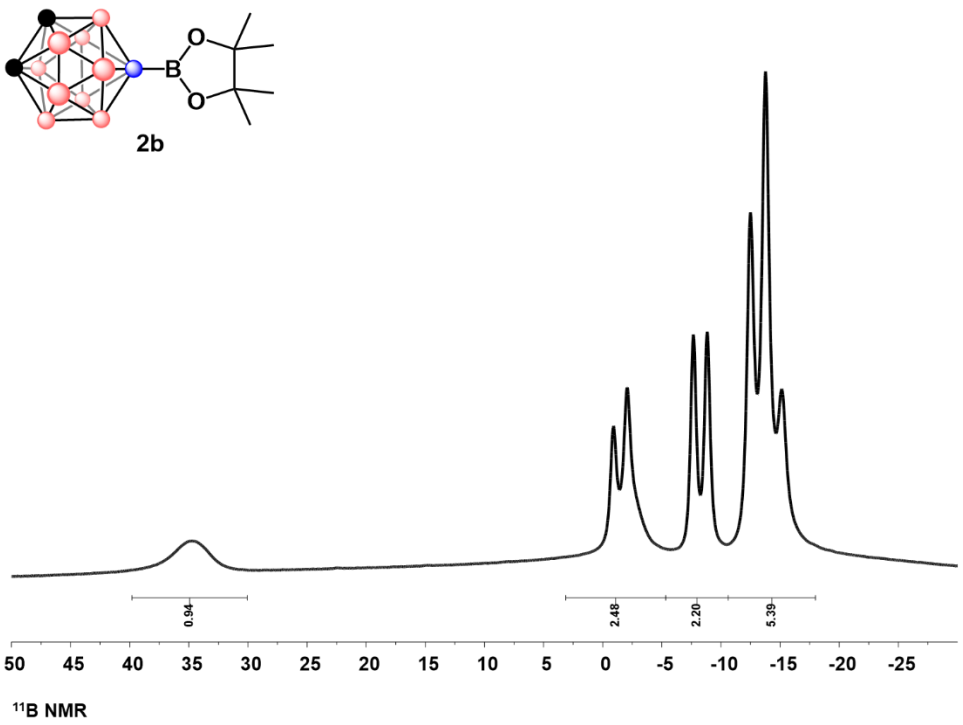

Figure B2.3 ^{11}B NMR of **2B**

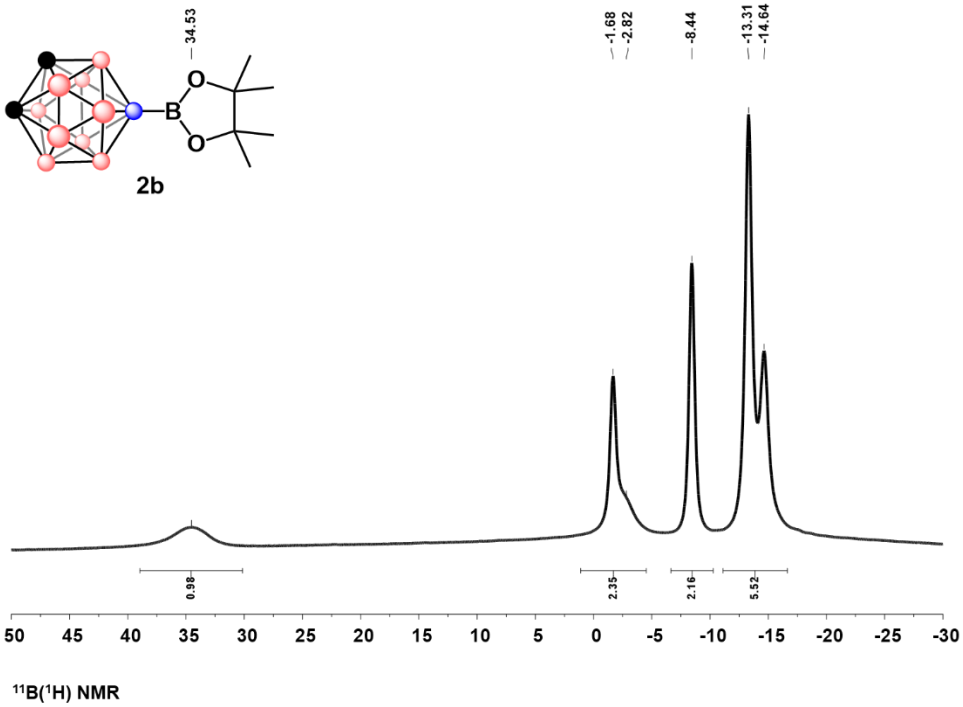

Figure B2.4 $^{11}B\{^{1}H\}$ NMR of **2B**

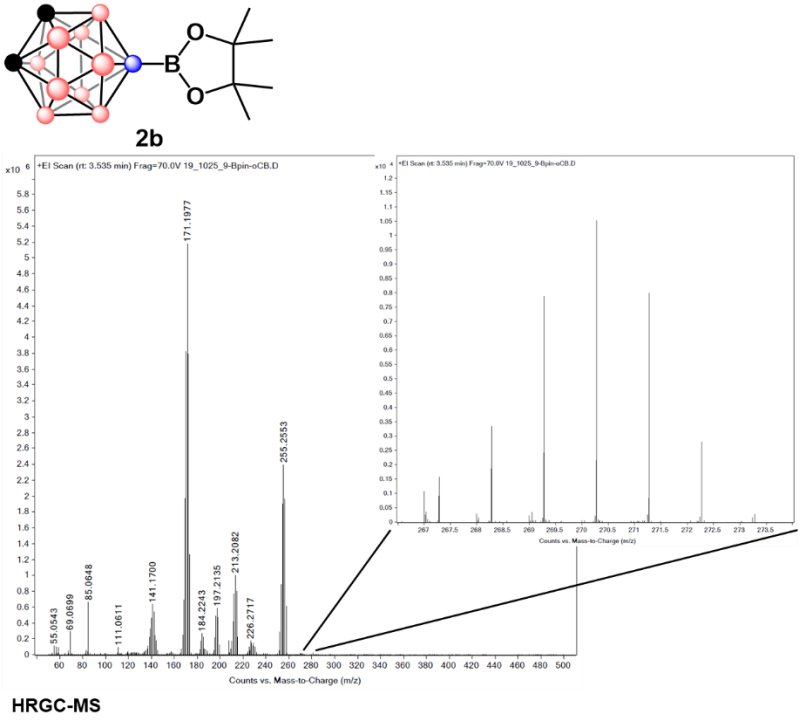

Figure B2.5 GC-MS of **2B**

3.6.13.3 Characterization of 3A

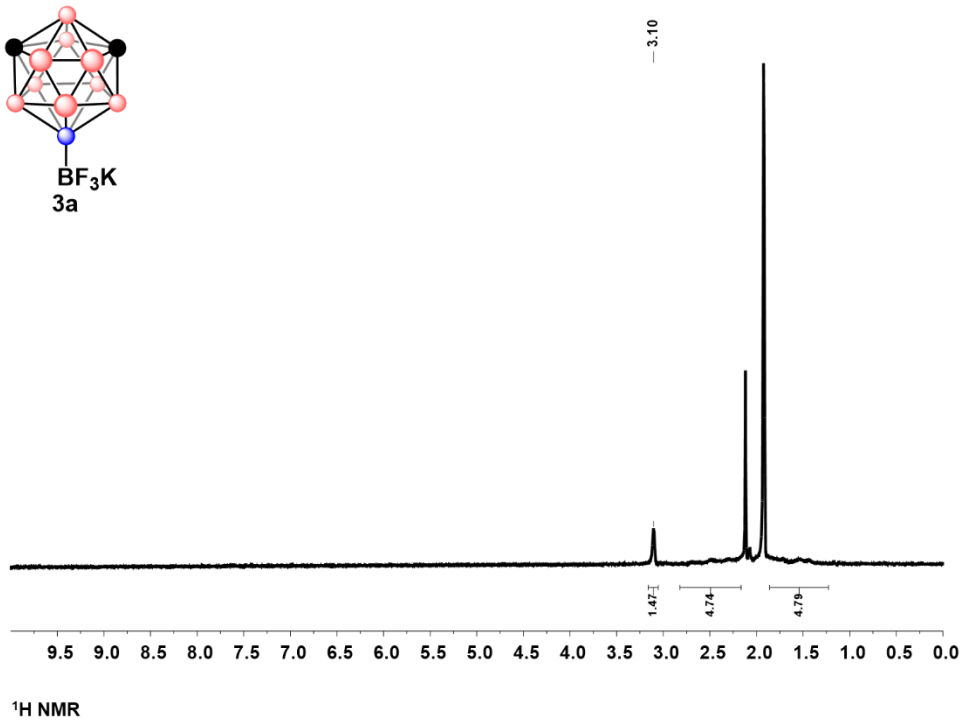

Figure B3.1 ^{1}H NMR of **3A**

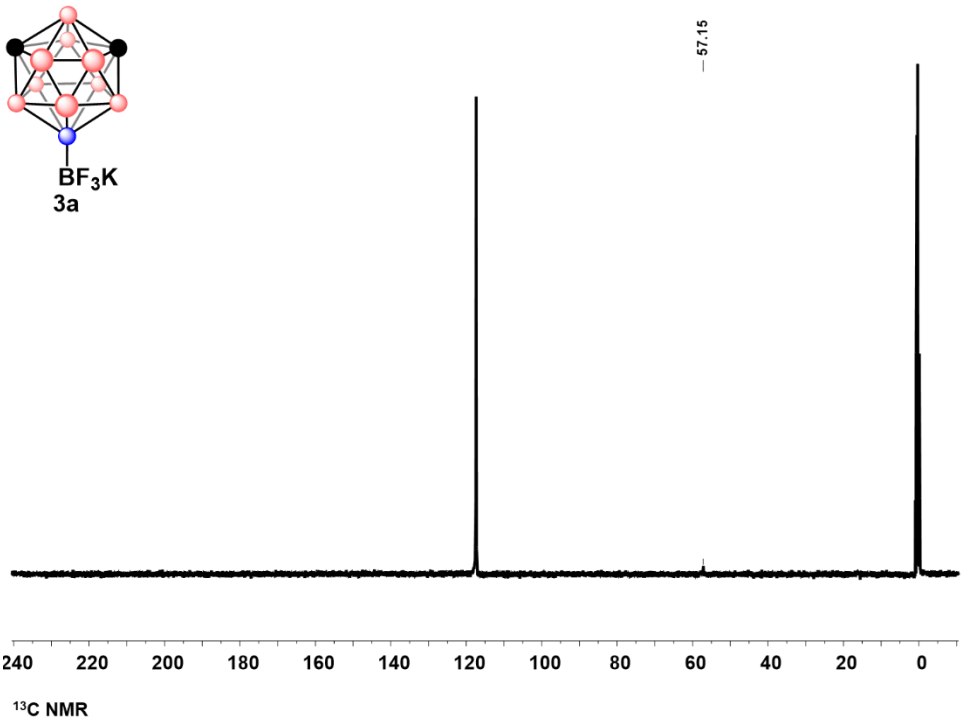

Figure B3.2 ^{13}C NMR of **3A**

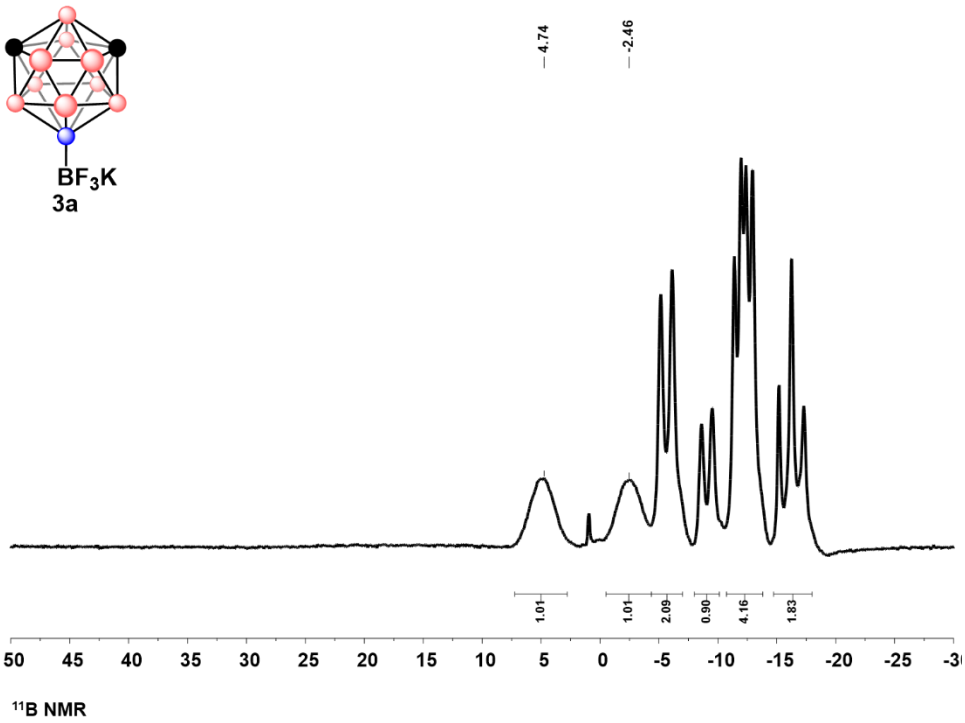

Figure B3.3 ^{11}B NMR of **3A**

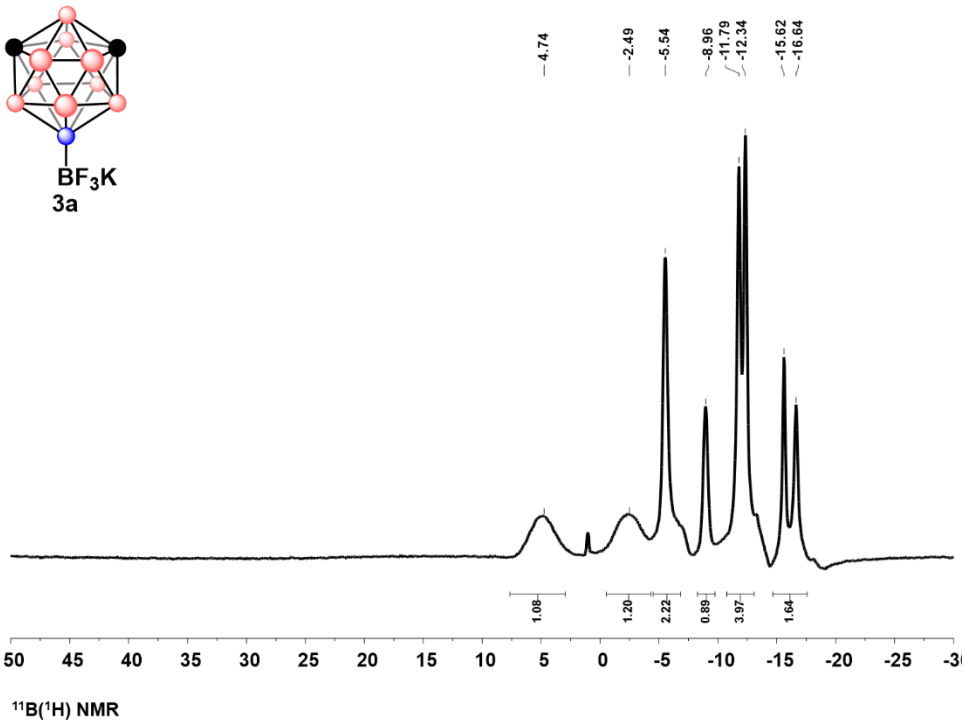

Figure B3.4 ^{11}B{^{1}H} NMR of **3A**

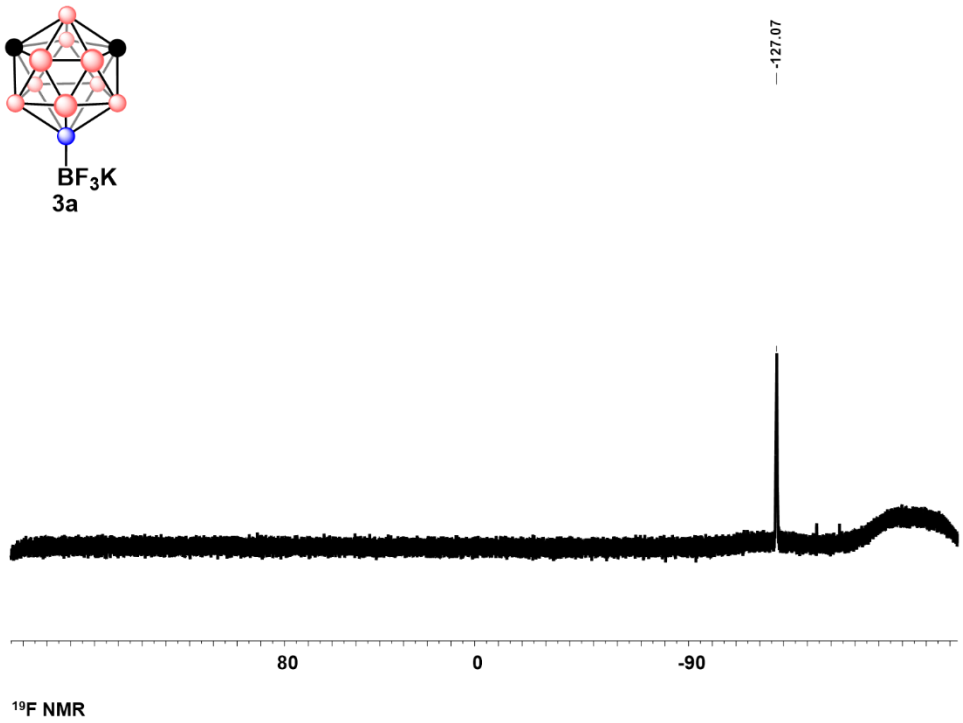

Figure B3.5 ^{19}F NMR of **3A**

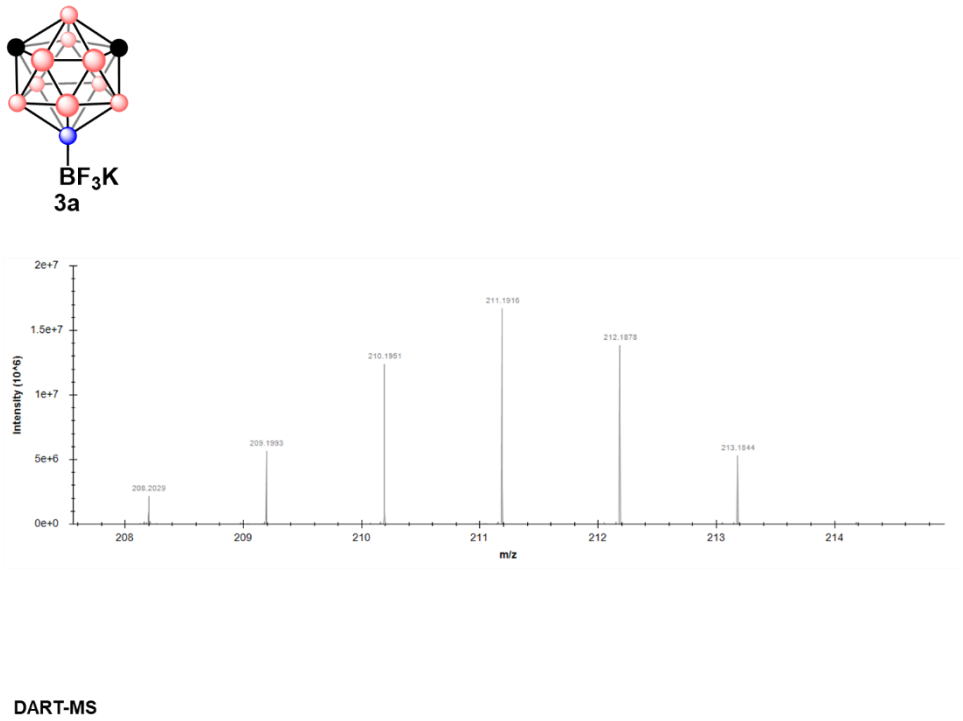

Figure B3.6 DART-MS of **3A**

3.6.13.4 Characterization of 4A

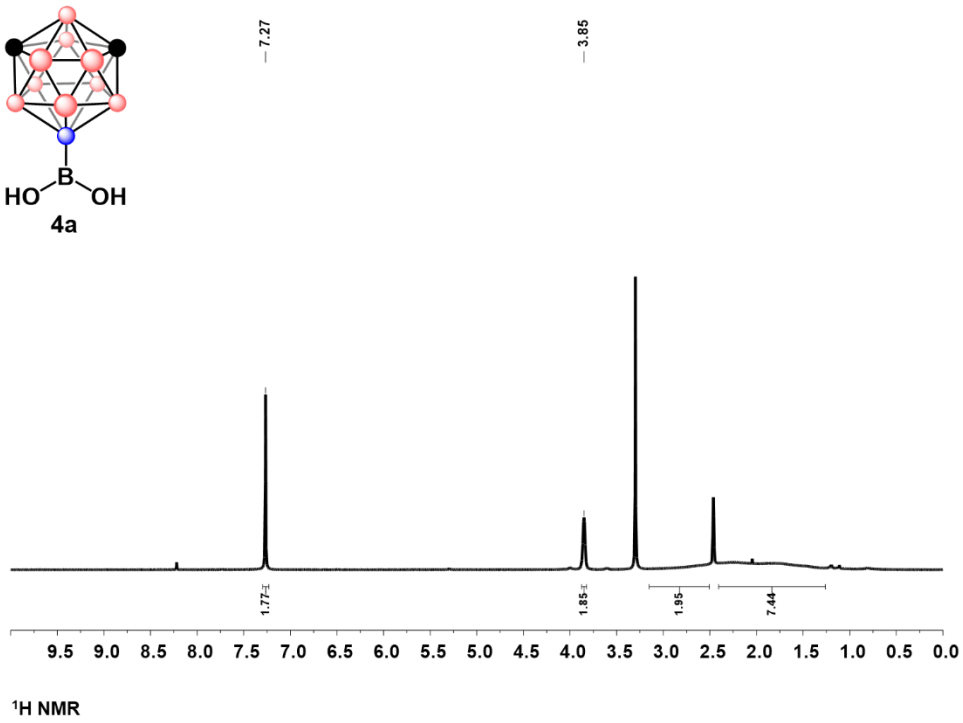

Figure B4.1 ^{1}H NMR of **4A**

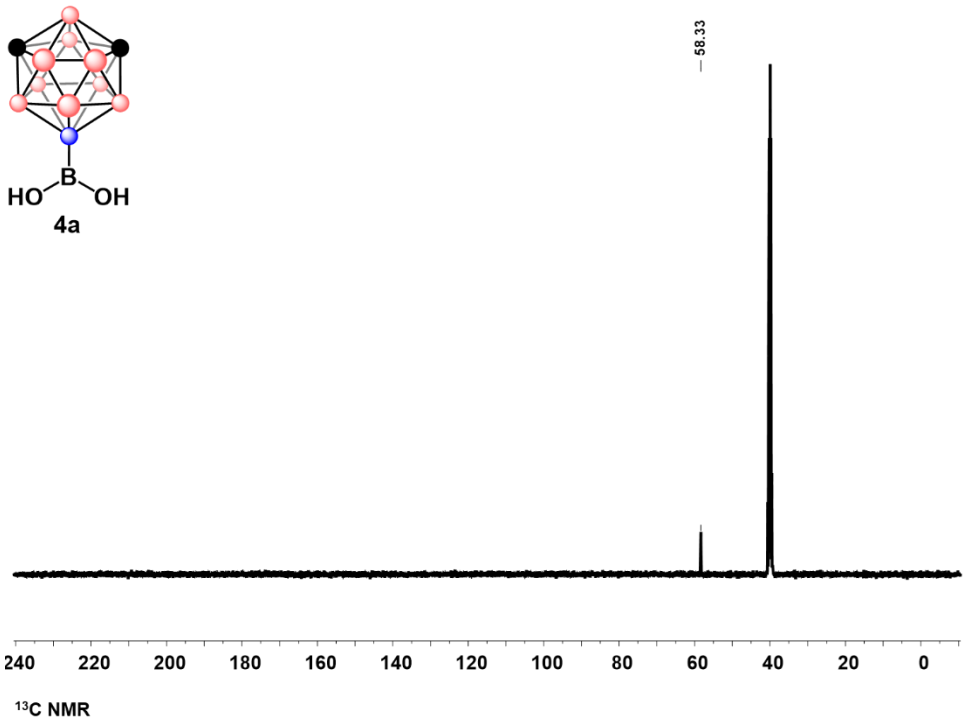

Figure B4.2 ^{13}C NMR of **4A**

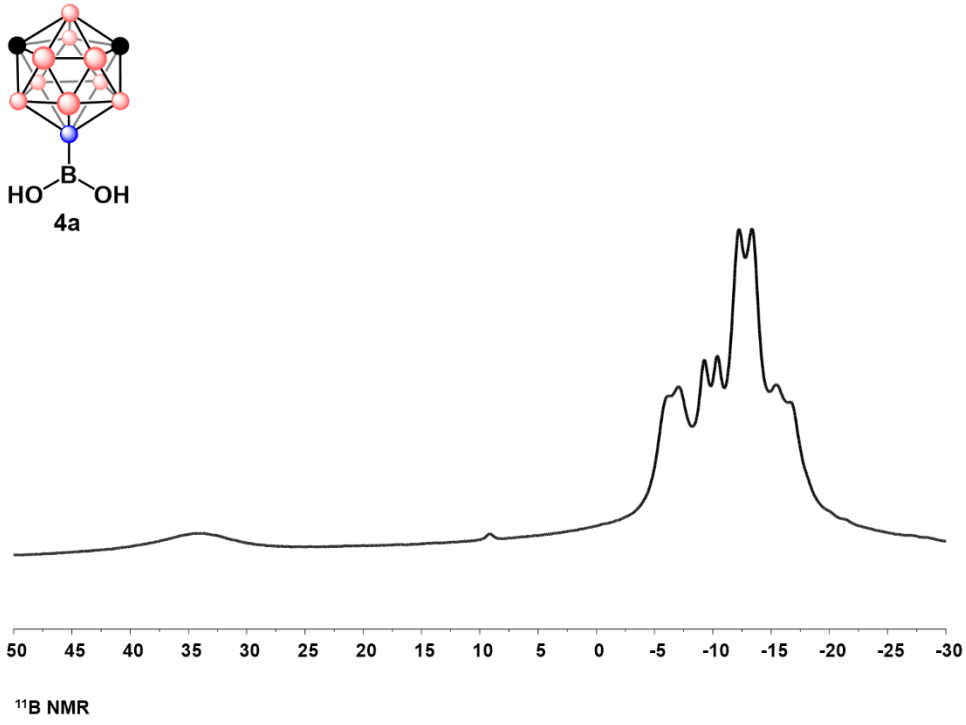

Figure B4.3 ^{11}B NMR of **4A**

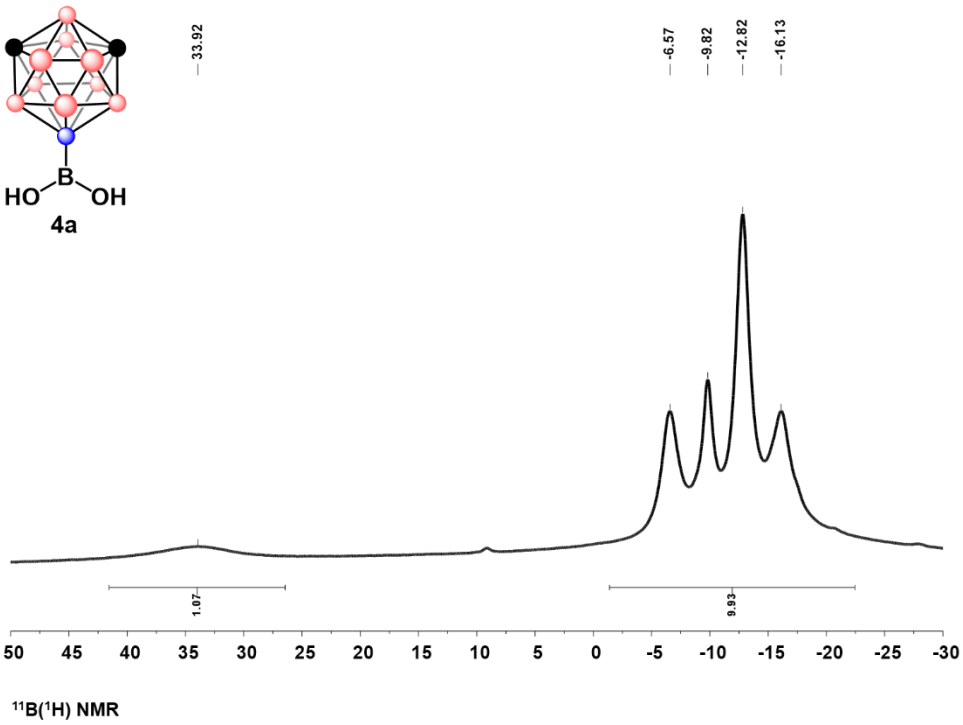

Figure B4.4 $^{11}B\{^{1}H\}$ NMR of **4A**

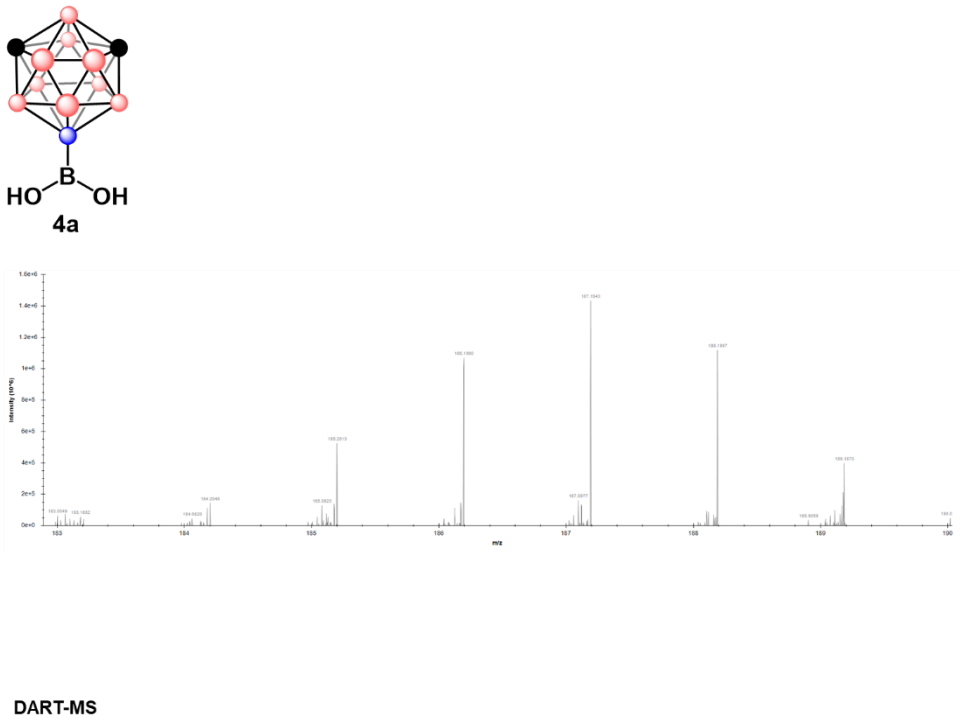

Figure B4.5 DART-MS of **4A**

3.6.13.5 Characterization of 4B

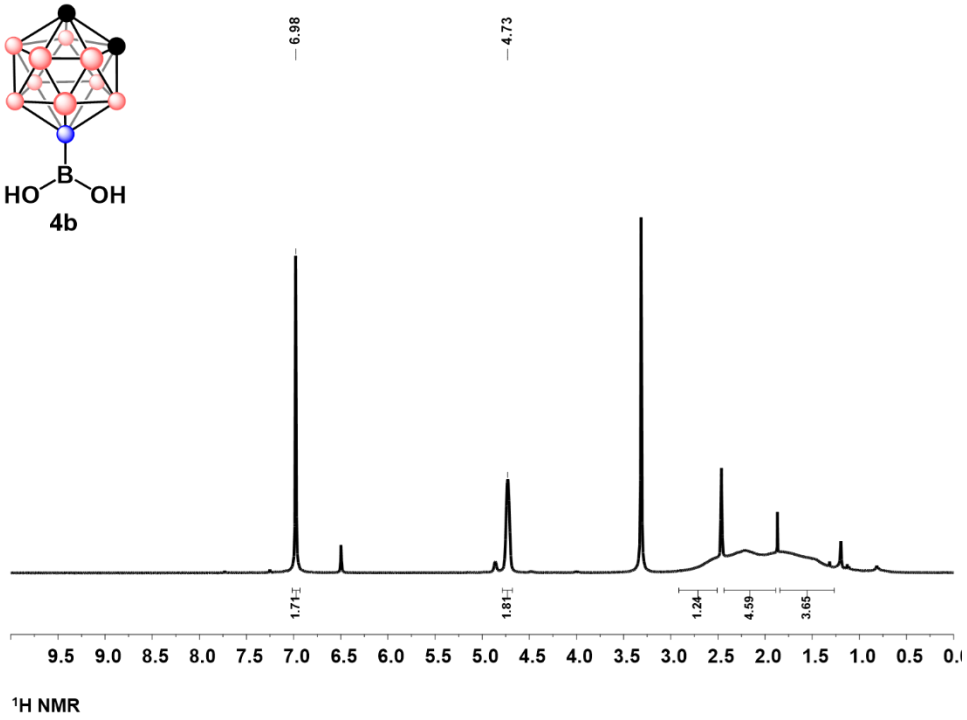

Figure B5.1 ^{1}H NMR of **4B**

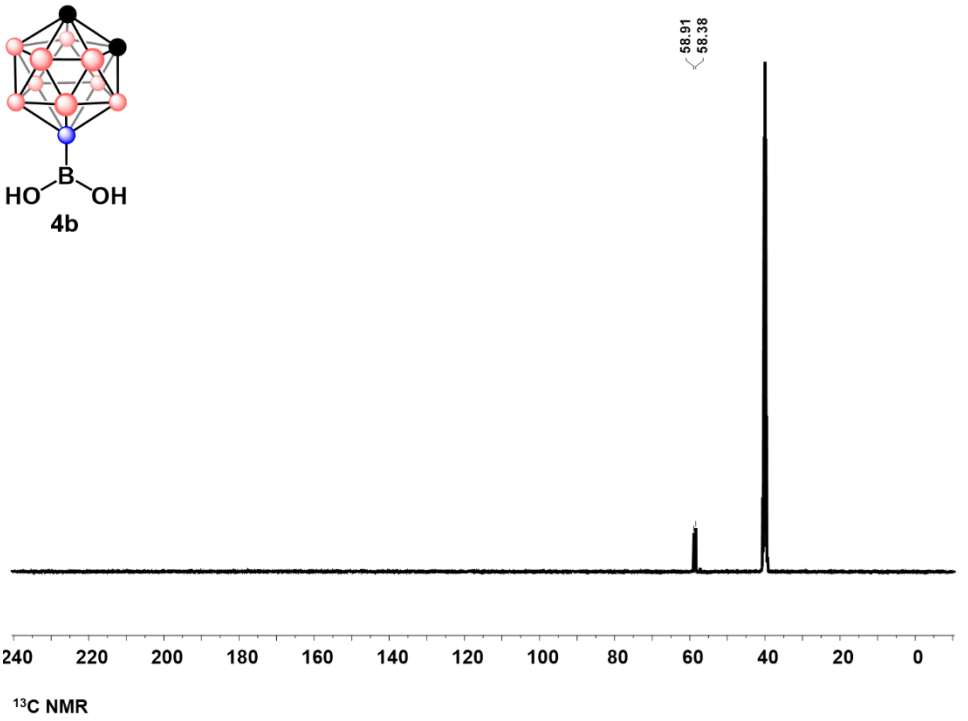

Figure B5.2 ^{13}C NMR of **4B**

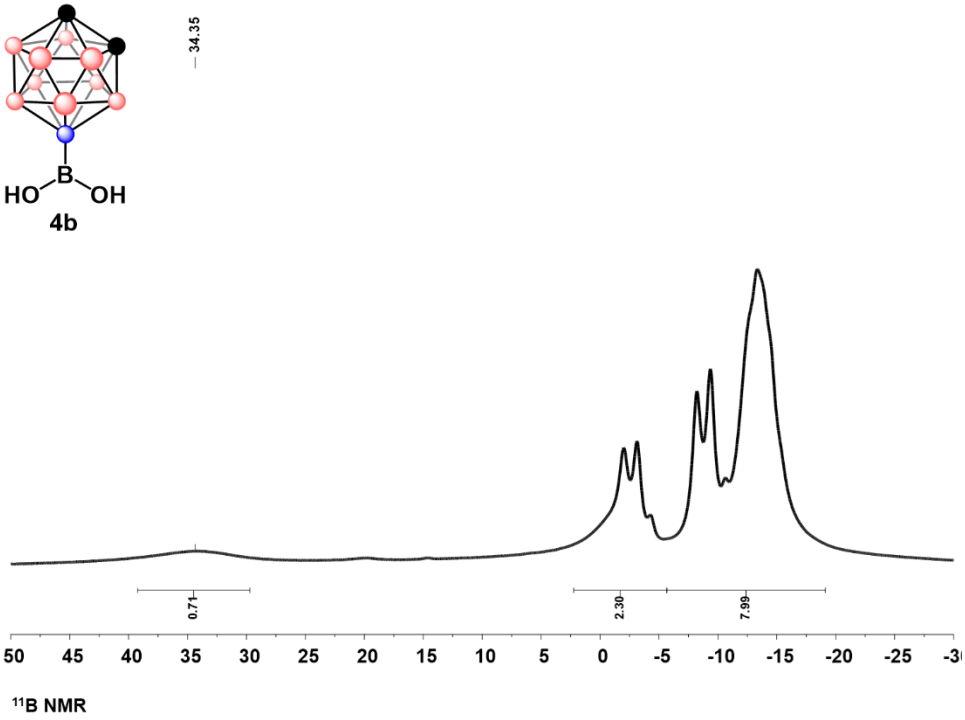

Figure B5.3 ^{11}B NMR of **4B**

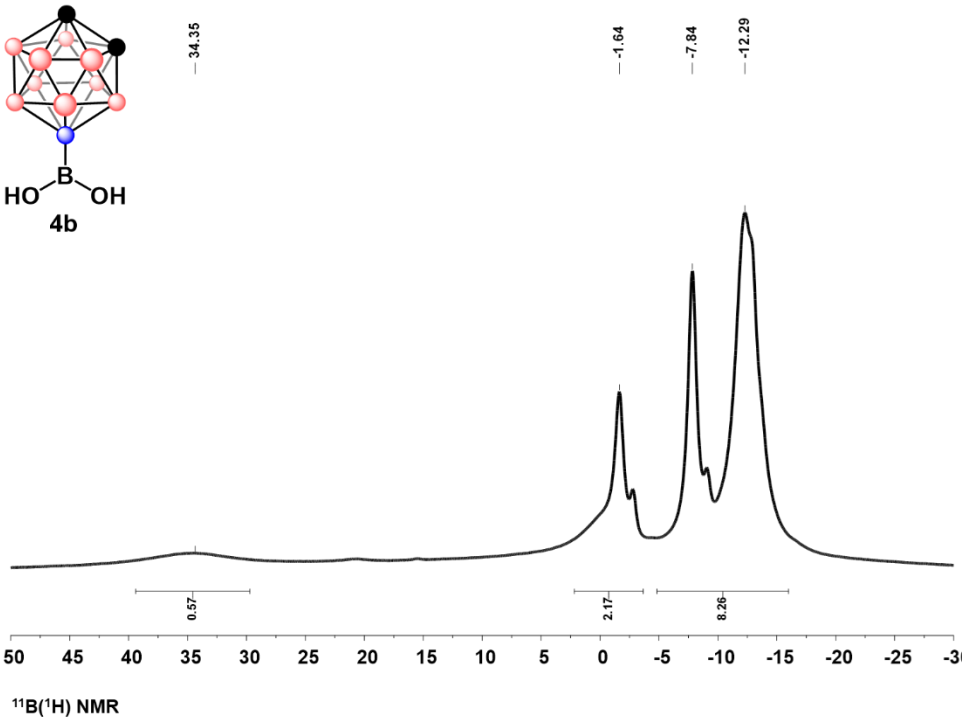

Figure B5.4 $^{11}B\{^{1}H\}$ NMR of **4B**

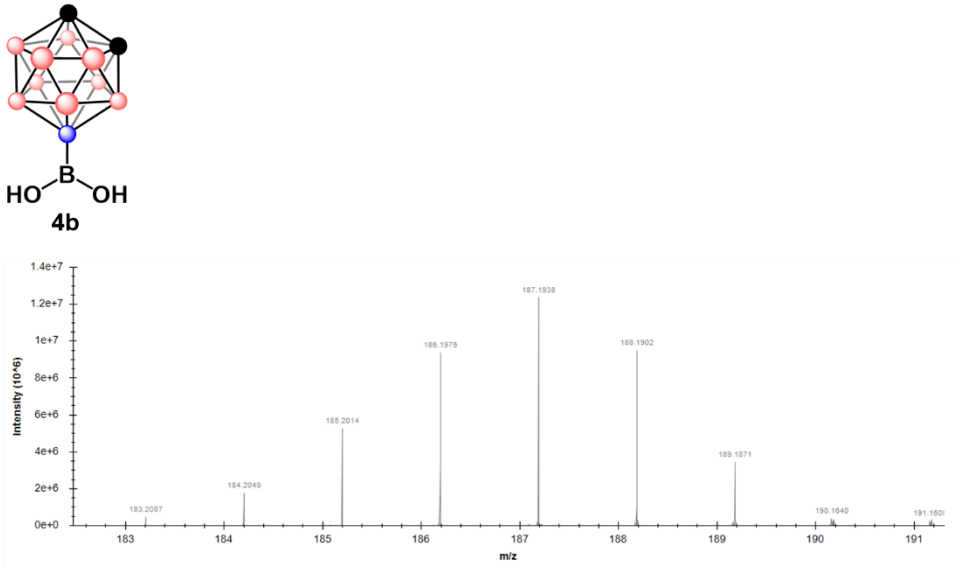

Figure B5.5 DART-MS of **4B**

3.6.13.6 Characterization of 4C

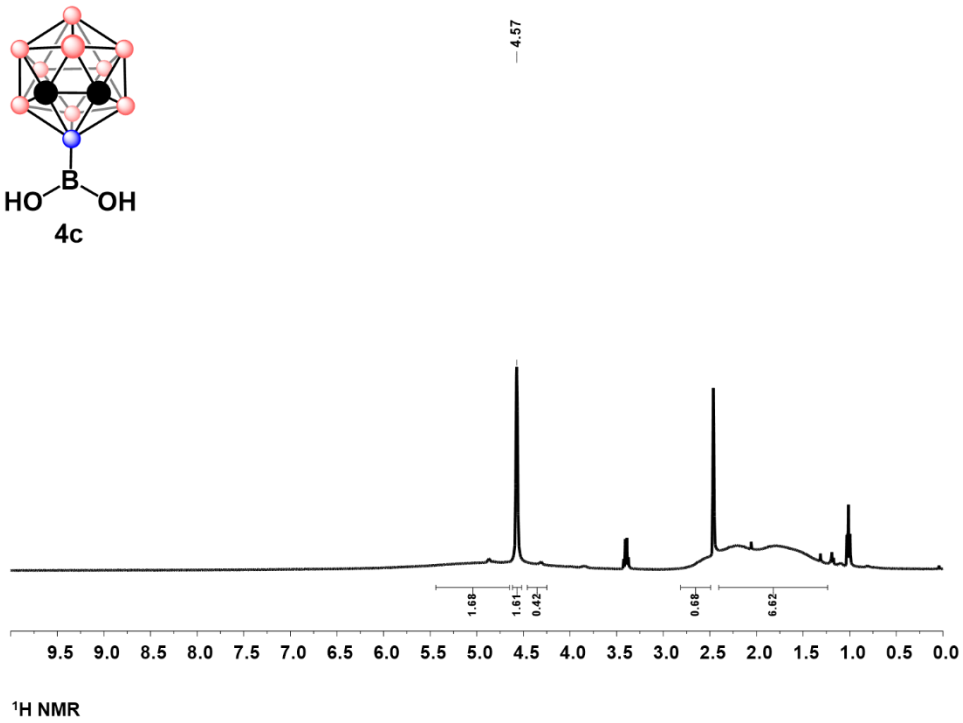

Figure B6.1 ^{1}H NMR of **4C**

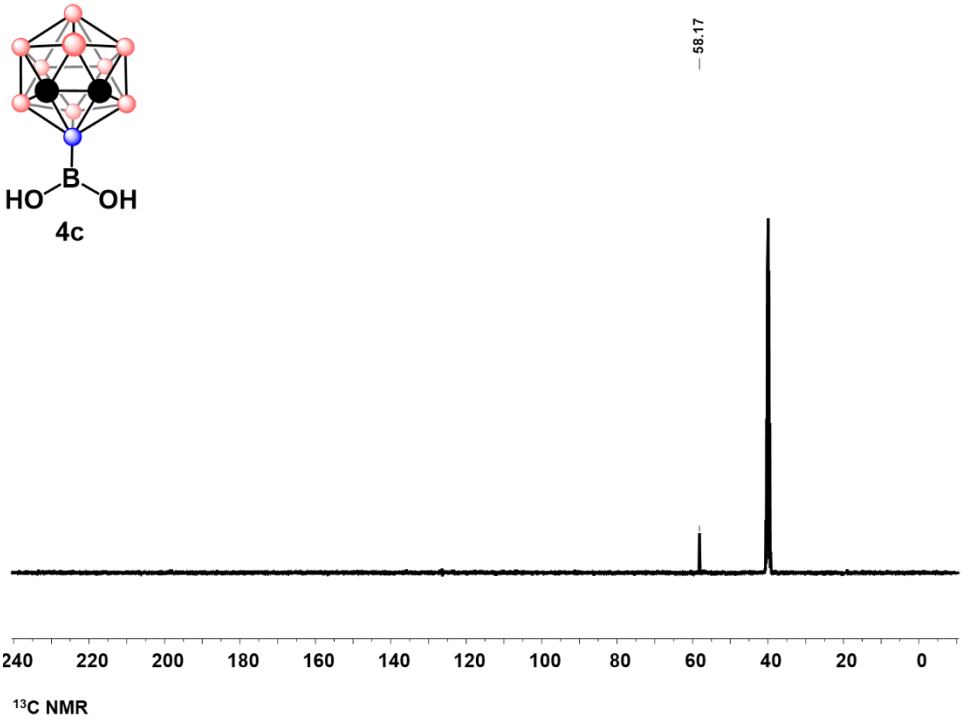

Figure B6.2 ^{13}C NMR of **4C**

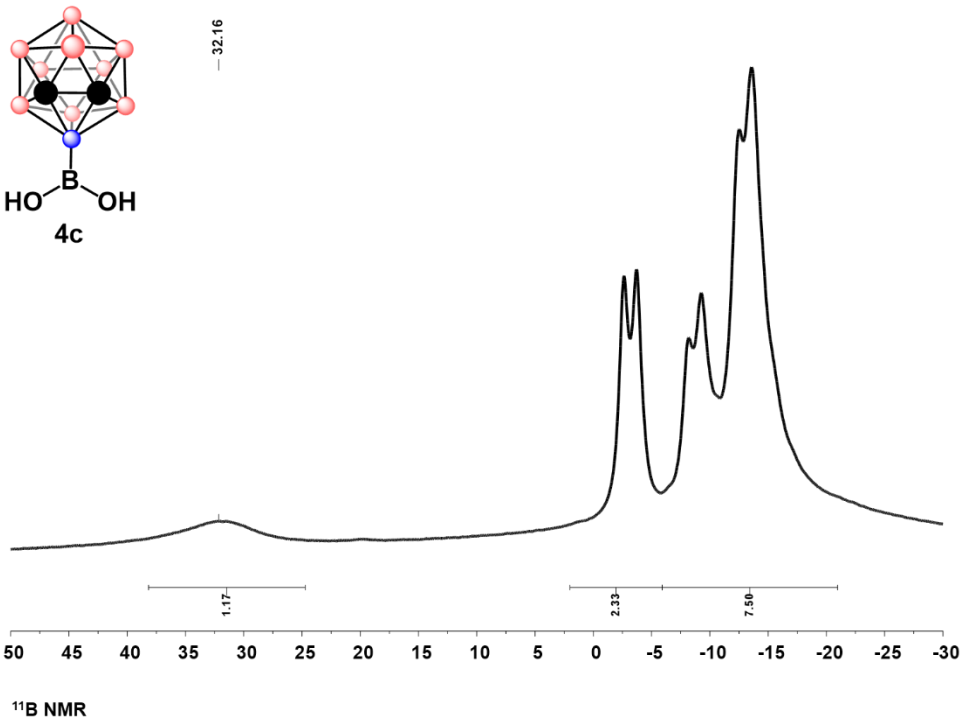

Figure B6.3 ^{11}B NMR of **4C**

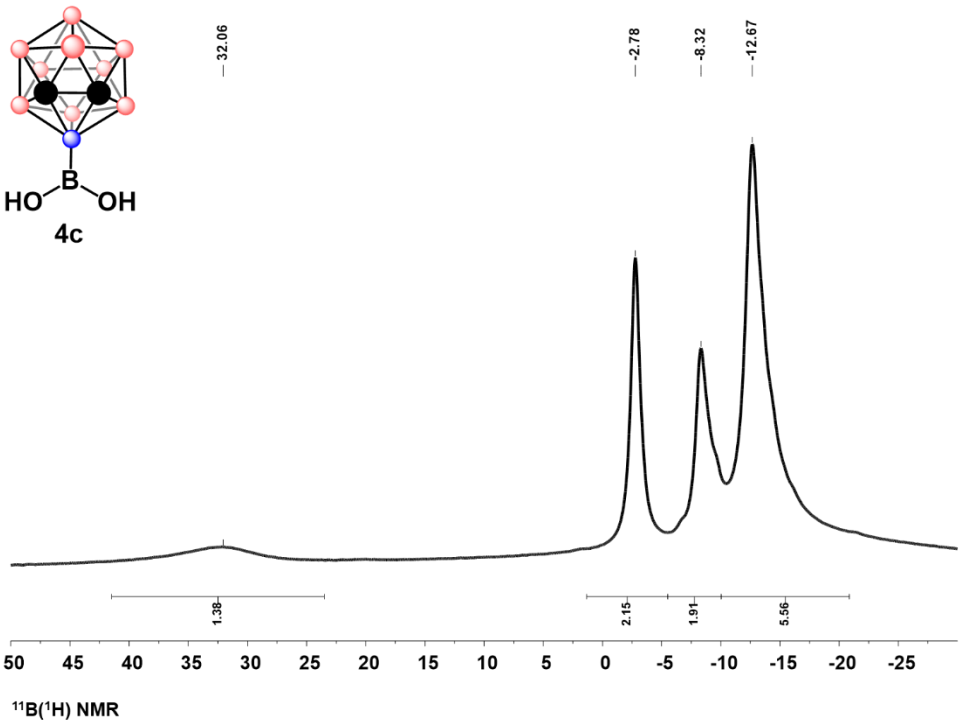

Figure B6.4 ^{11}B{^{1}H} NMR of **4C**

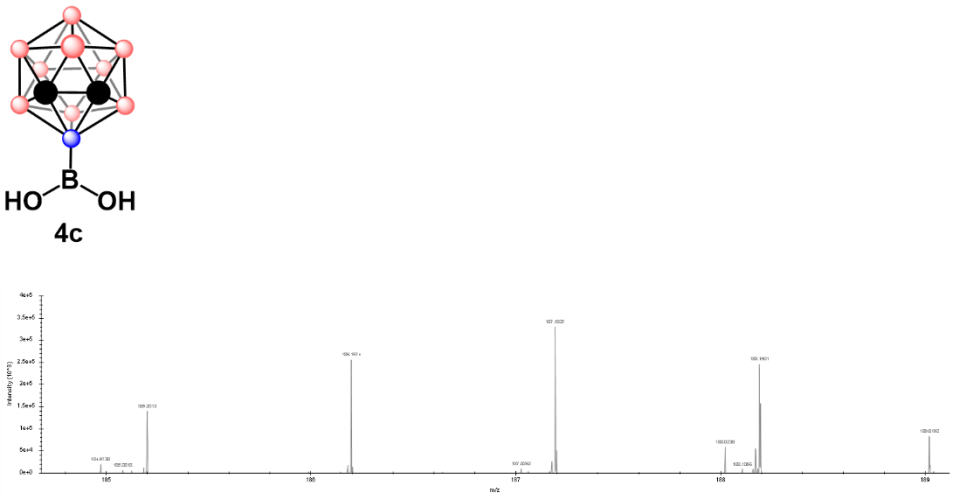

Figure B6.5 DART-MS of **4C**

3.6.13.7 Characterization of 5A

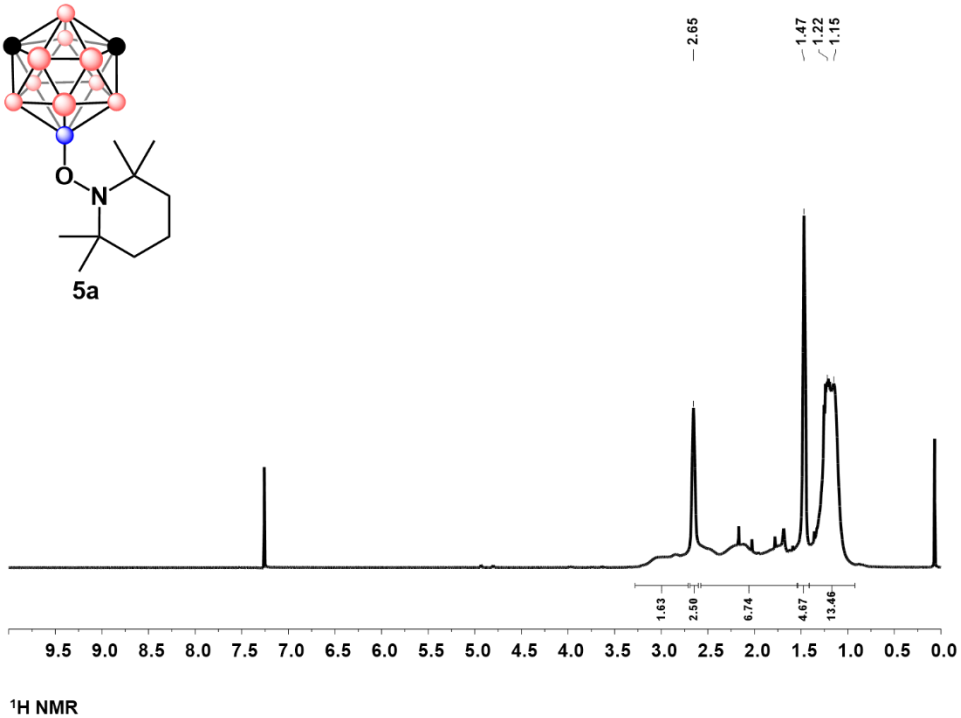

Figure B7.1 ^{1}H NMR of **5A**

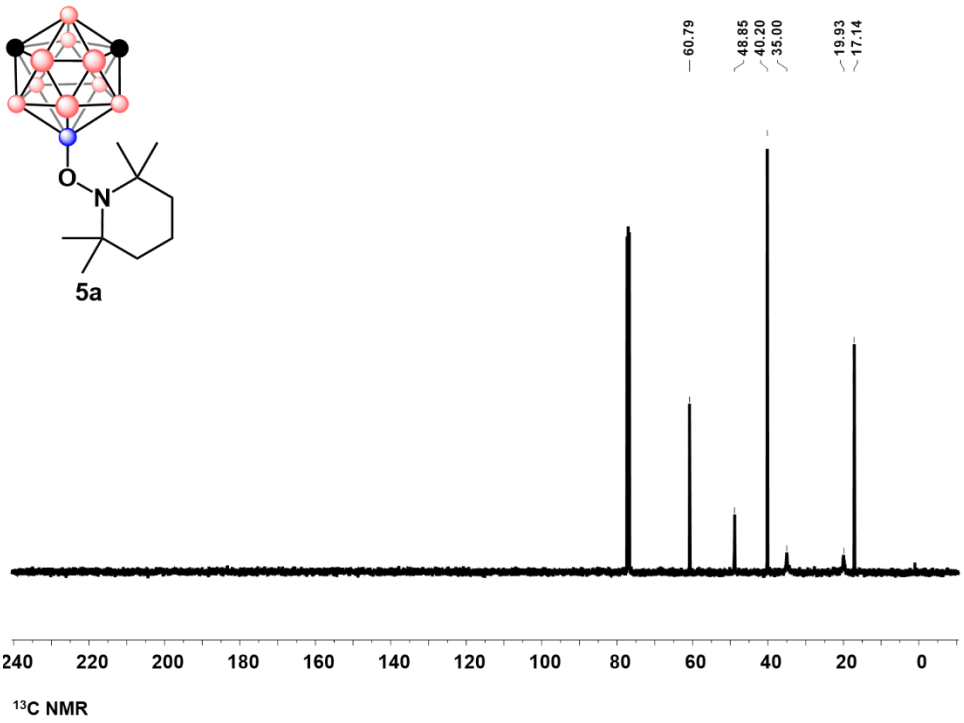

Figure B7.2 ^{13}C NMR of **5A**

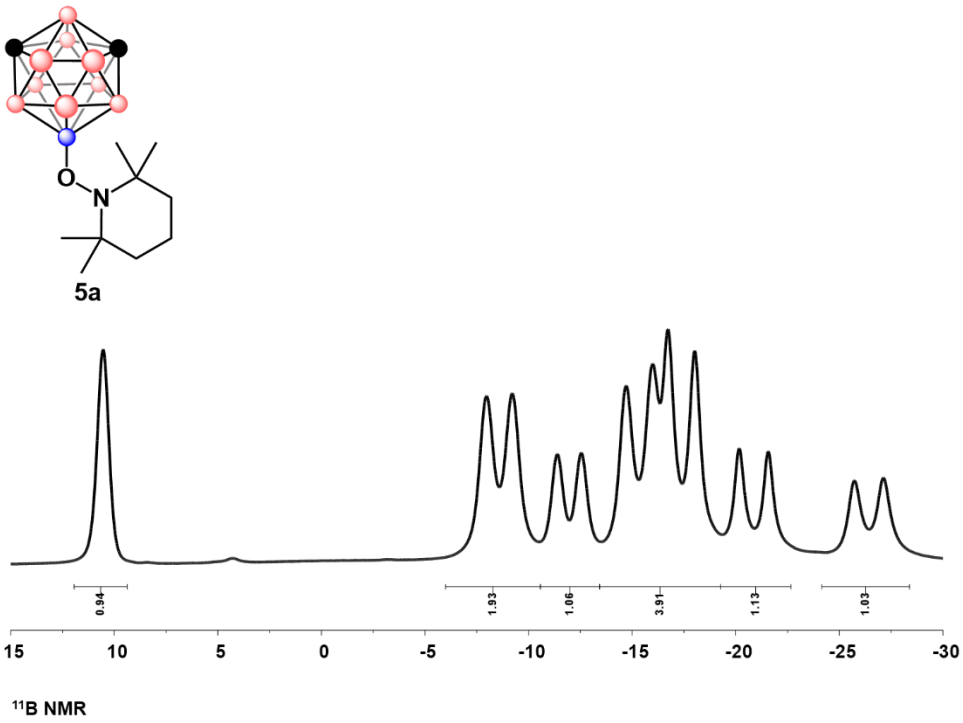

Figure B7.3 ^{11}B NMR of **5A**

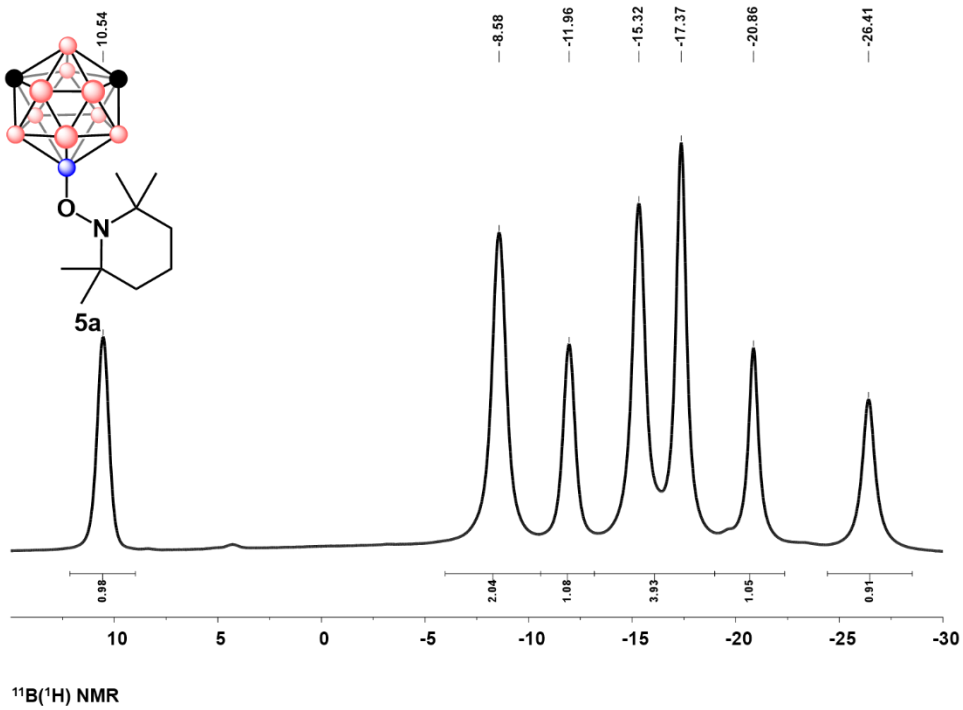

Figure B7.4 ^{11}B{^{1}H} NMR of **5A**

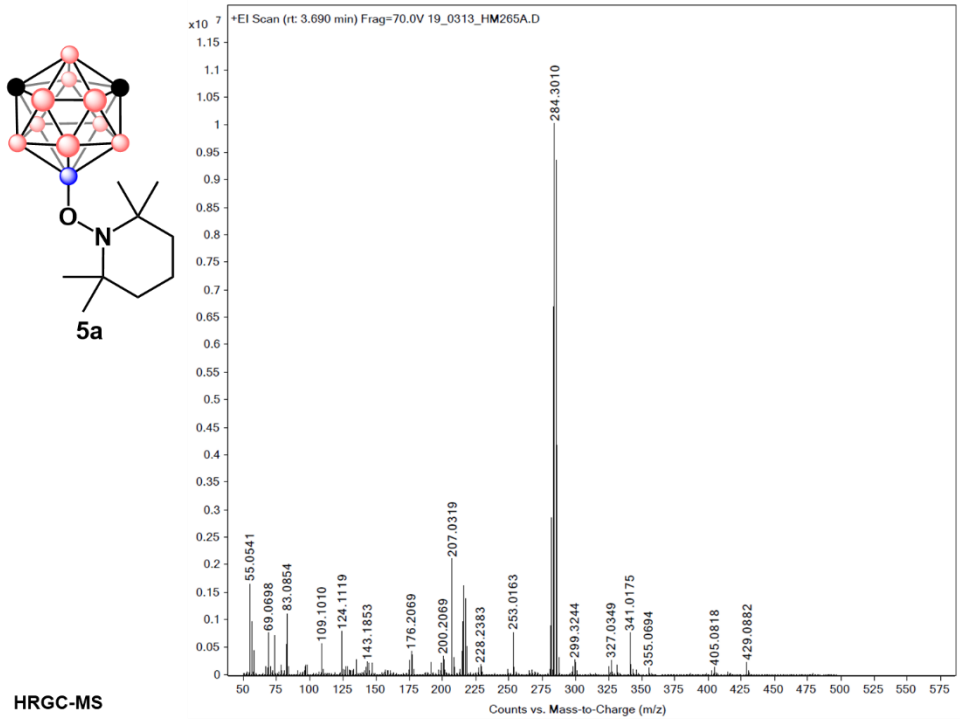

Figure B7.5 HRGC-MS of **5A**

3.6.13.8 Characterization of 5B

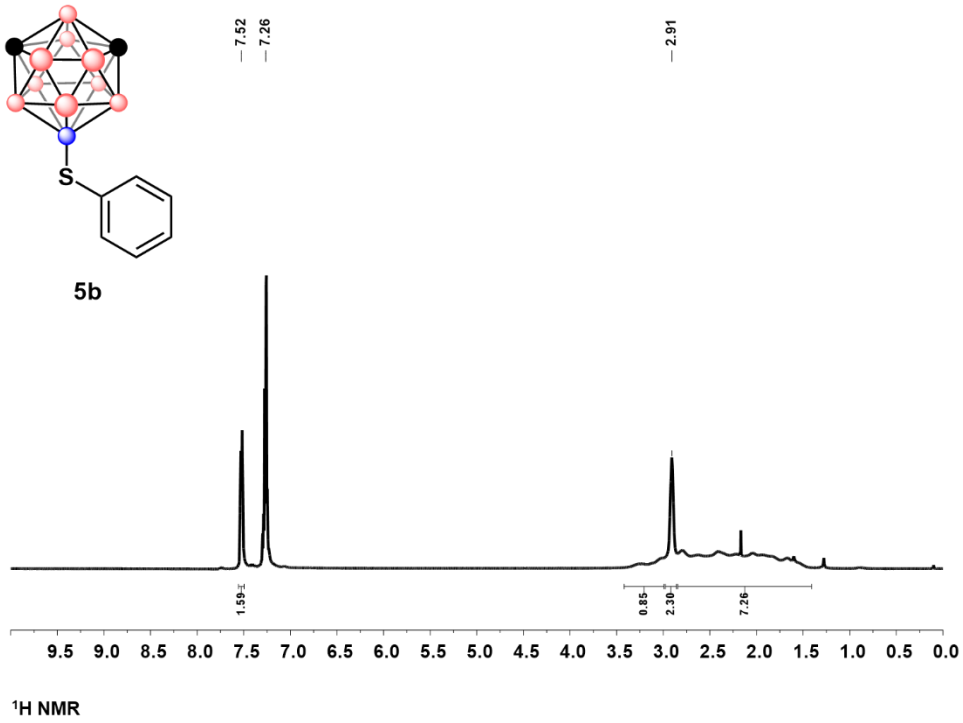

Figure B8.1 ^{1}H NMR of **5B**

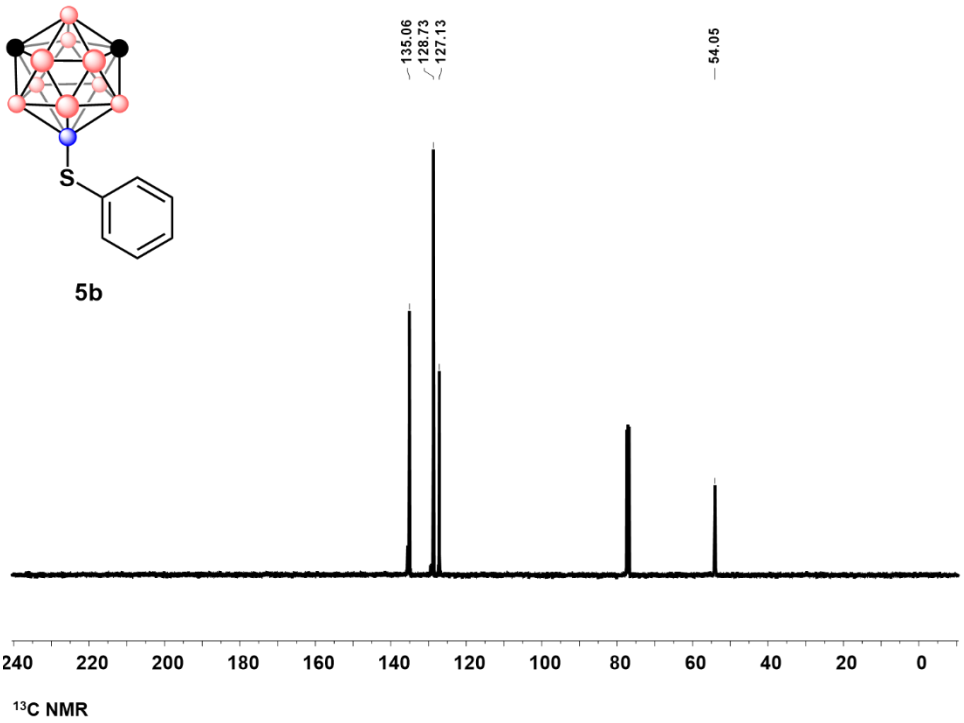

Figure B8.2 ^{13}C NMR of **5B**

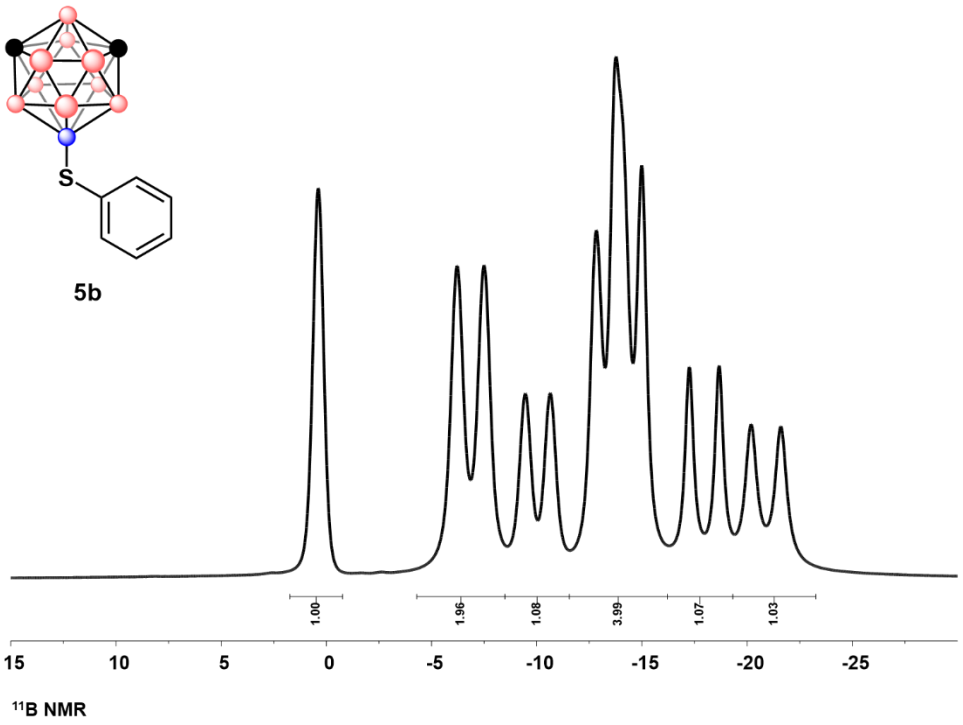

Figure B8.3 ^{11}B NMR of **5B**

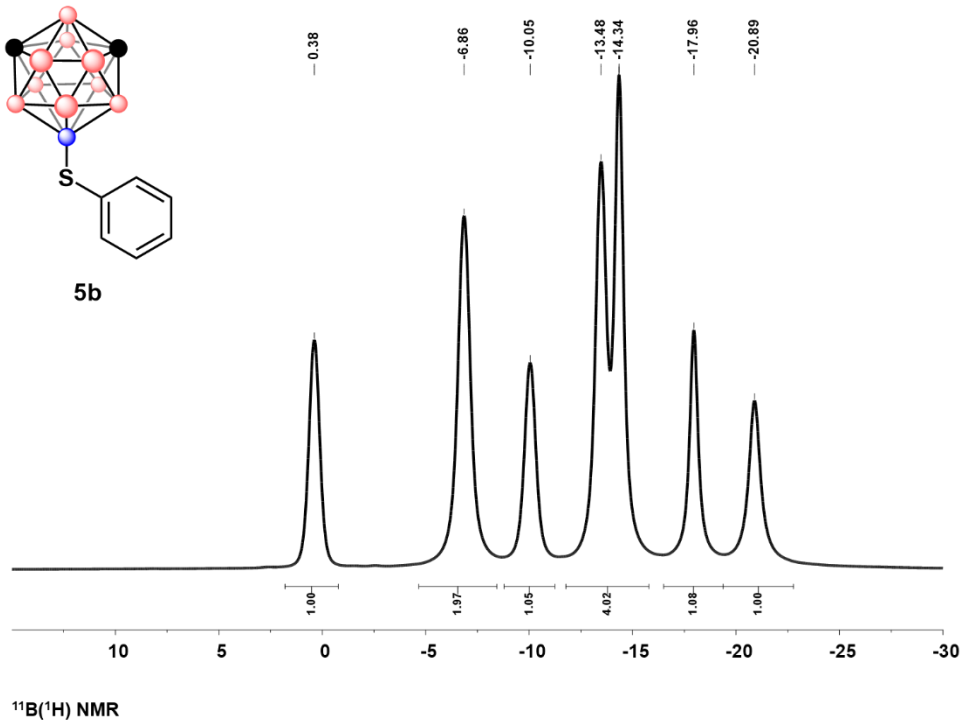

Figure B8.4 $^{11}B\{^{1}H\}$ NMR of **5B**

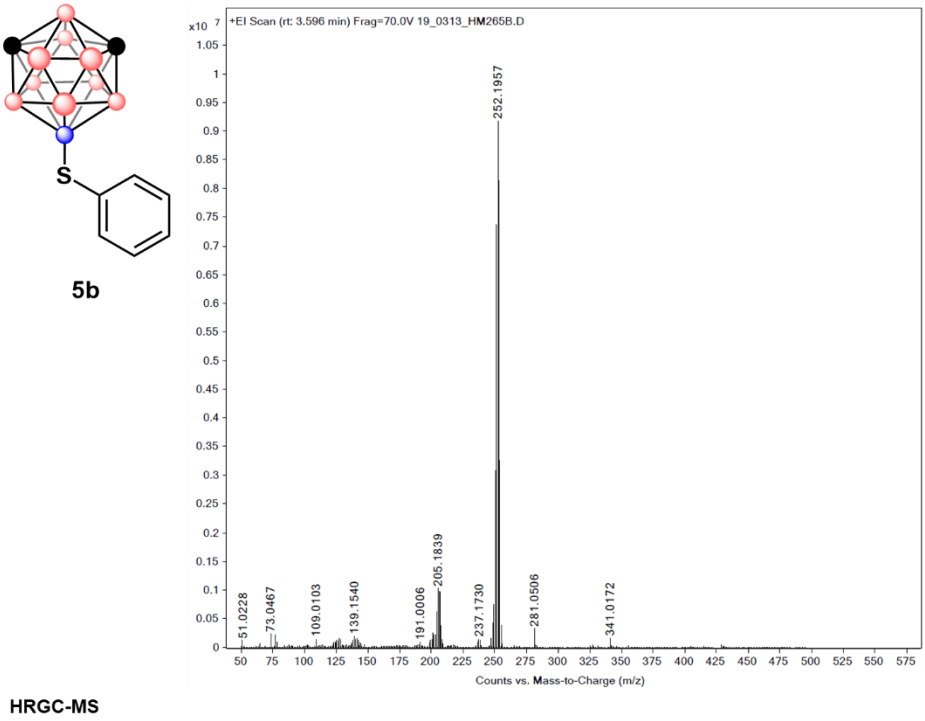

Figure B8.5 HRGC-MS of **5B**

3.6.13.9 Characterization of 5C

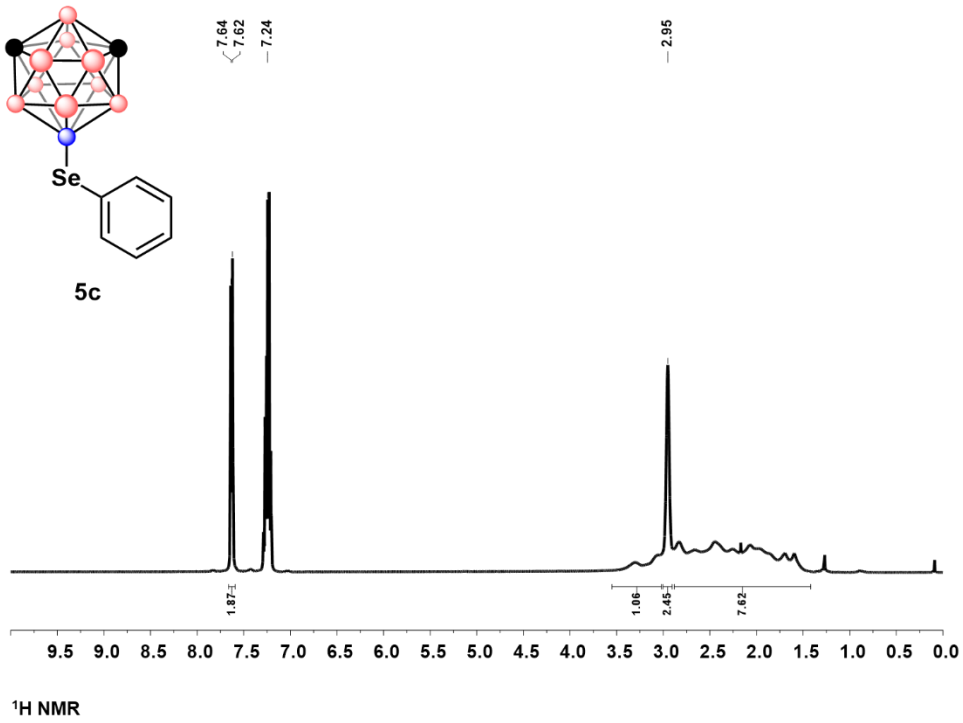

Figure B9.1 ^{1}H NMR of **5C**

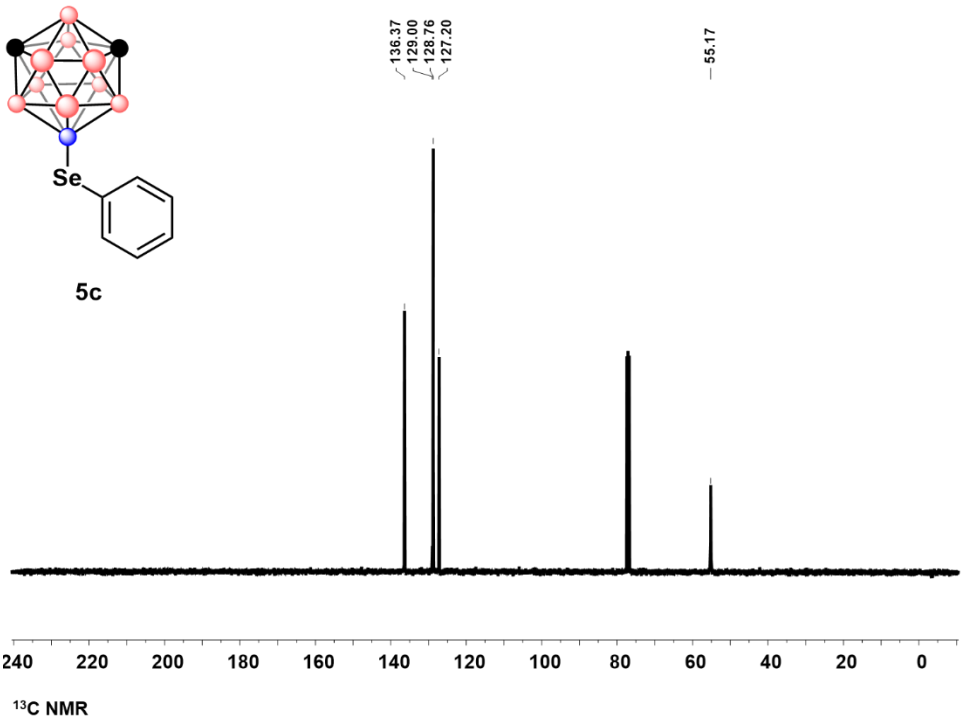

Figure B9.2 ^{13}C NMR of **5C**

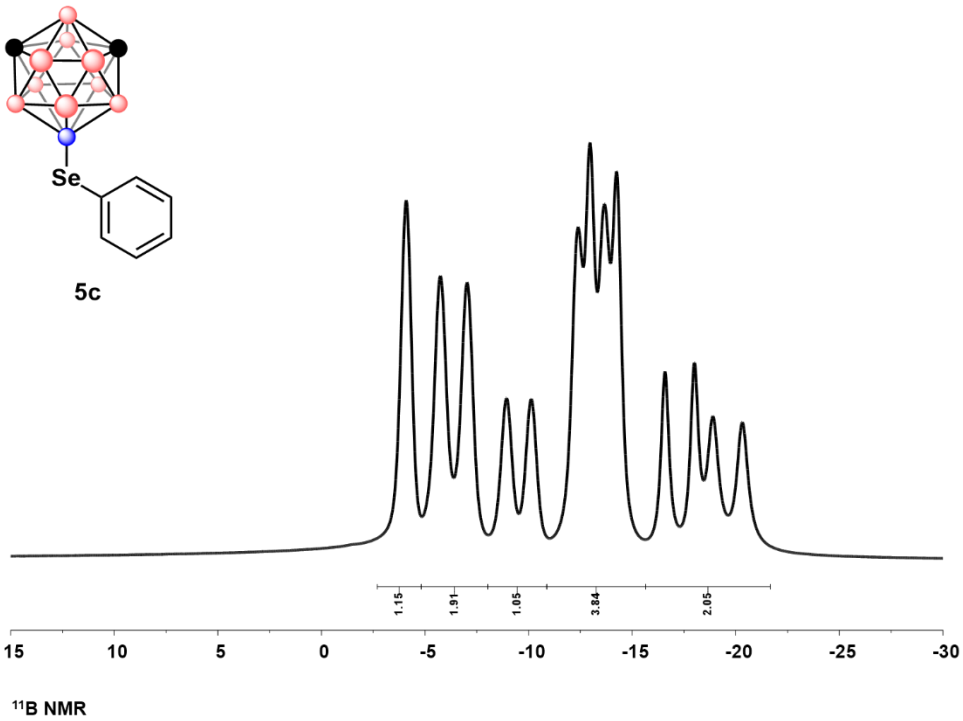

Figure B9.3 ^{11}B NMR of **5C**

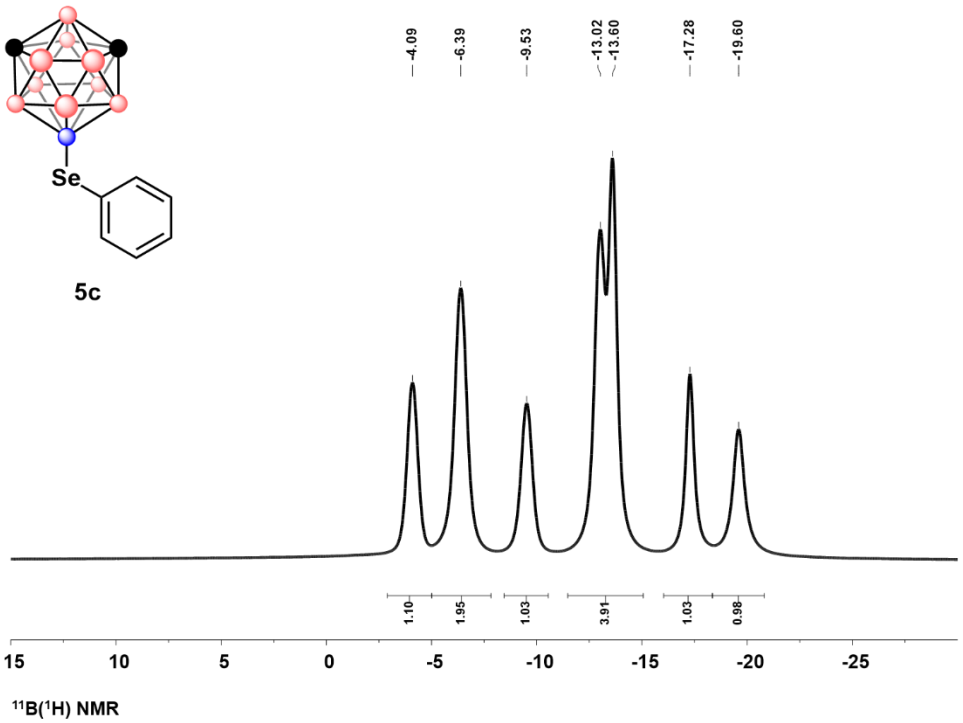

Figure B9.4 $^{11}B\{^{1}H\}$ NMR of **5C**

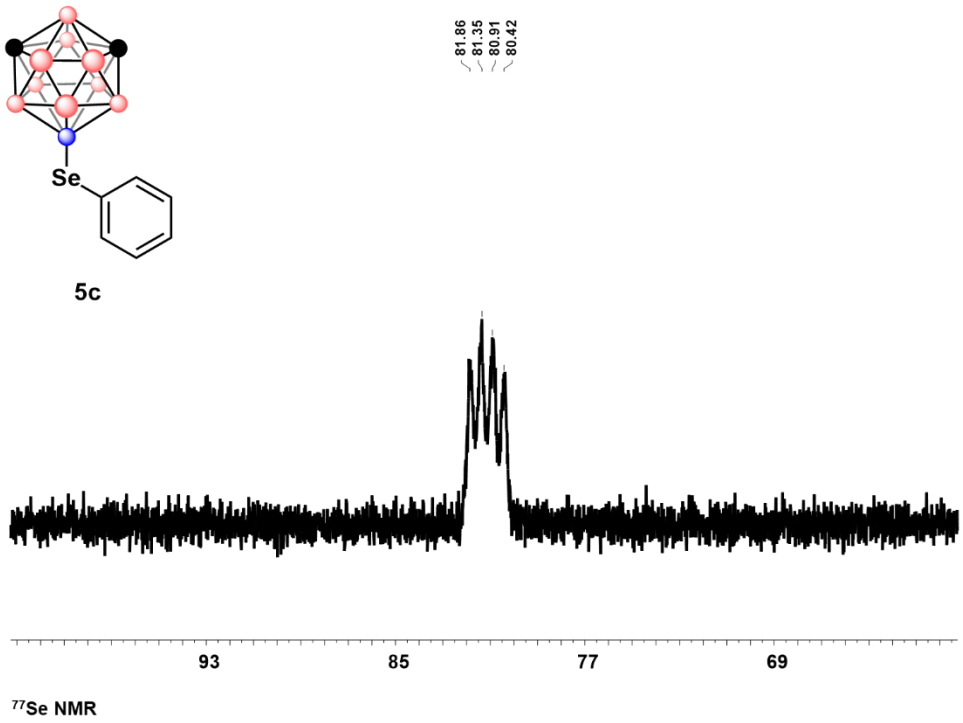

Figure B9.5 ^{77}Se NMR of **5C**

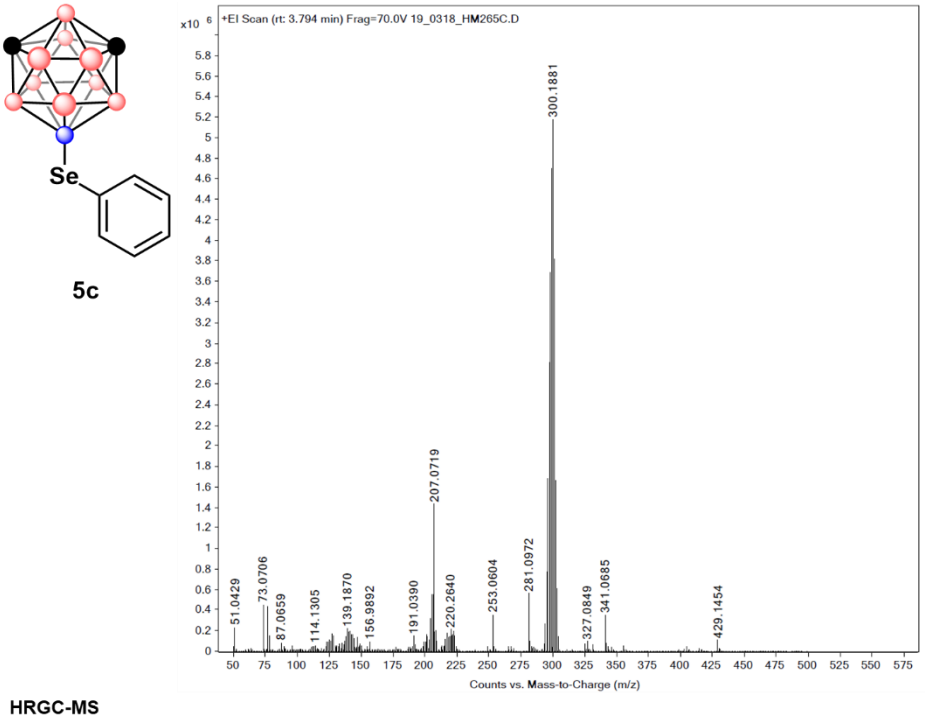

Figure B9.6 HRGC-MS of **5C**

3.6.13.10 Characterization of 5D

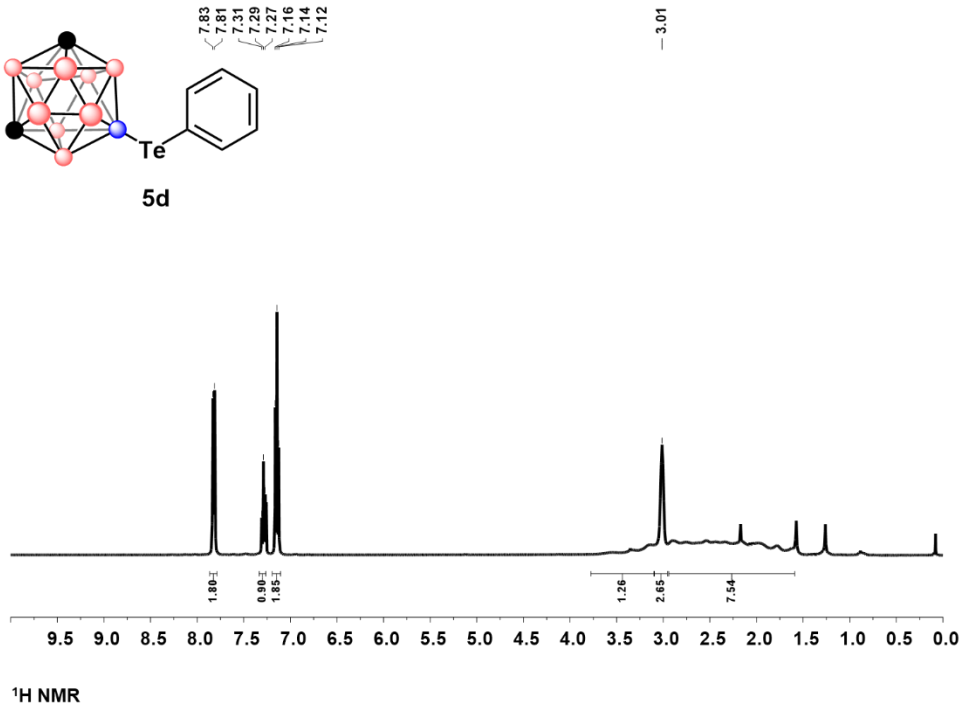

Figure B10.1 ^{1}H NMR of **5D**

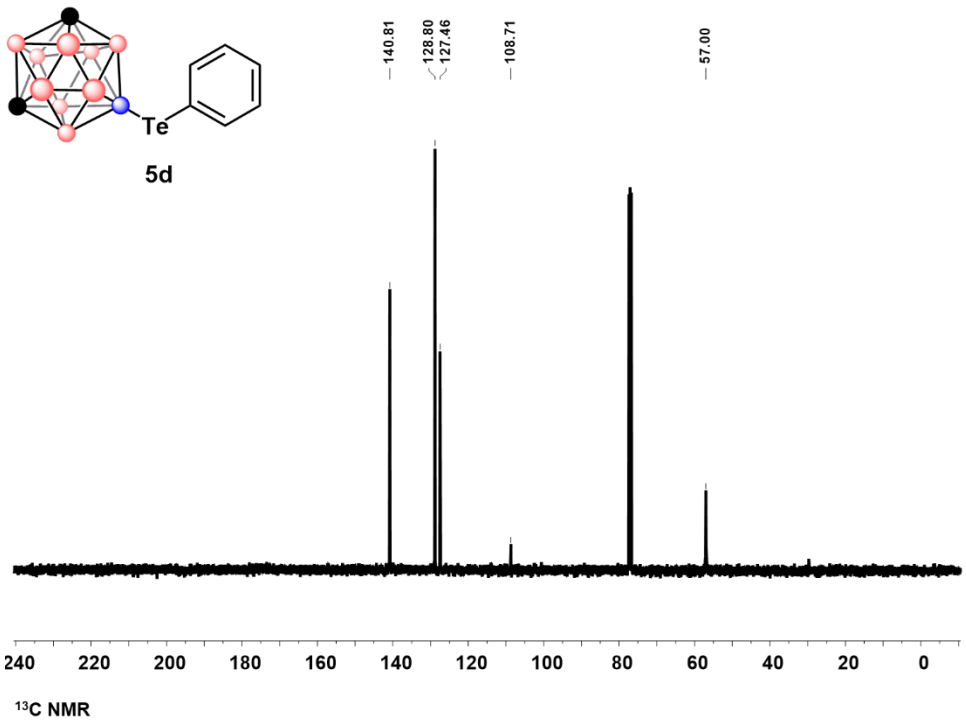

Figure B10.2 ^{13}C NMR of **5D**

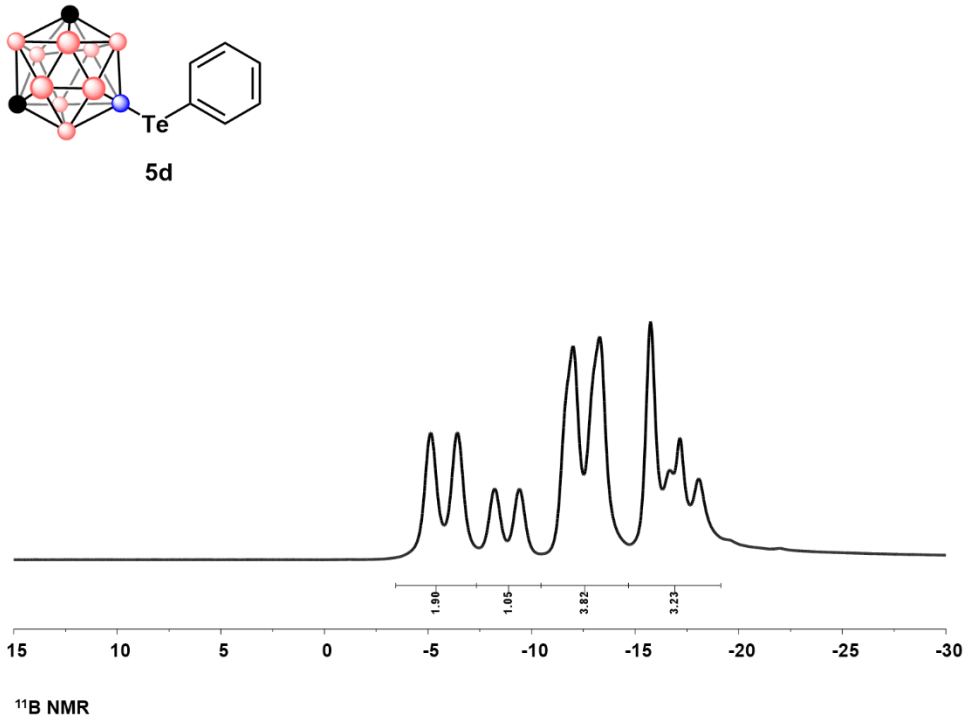

Figure B10.3 ^{11}B NMR of **5D**

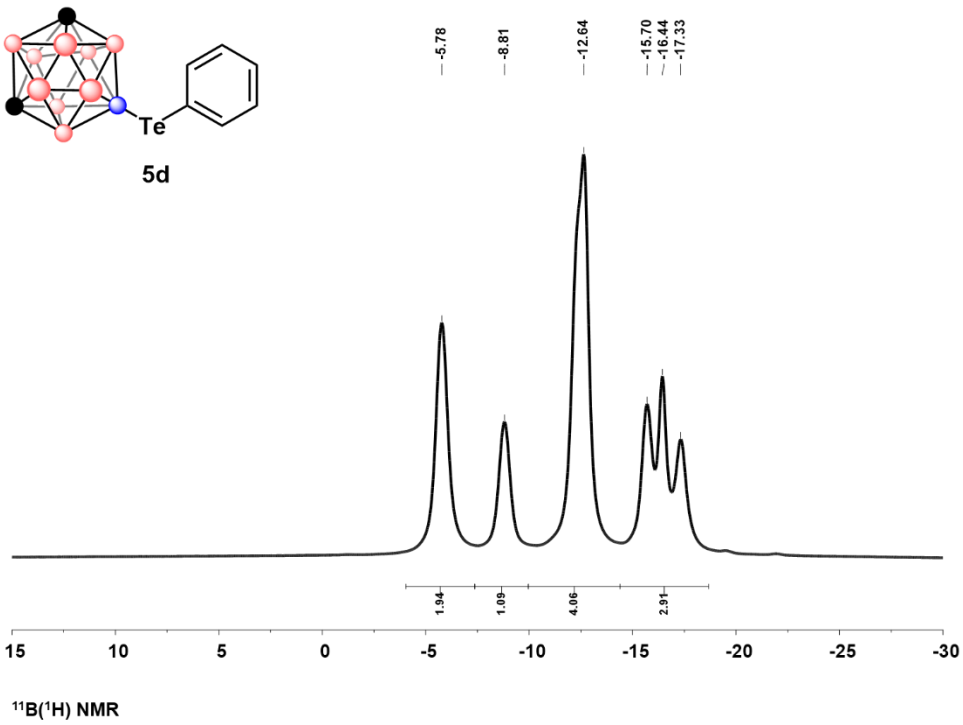

Figure B10.4 $^{11}B\{^{1}H\}$ NMR of **5D**

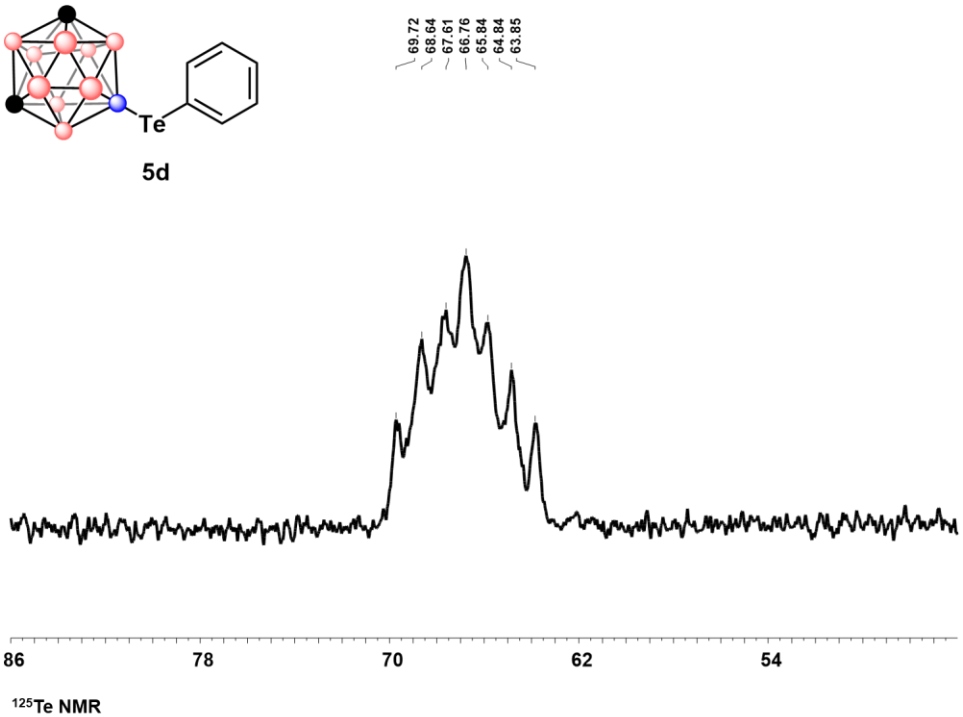

Figure B10.5 ^{125}Te NMR of **5D**

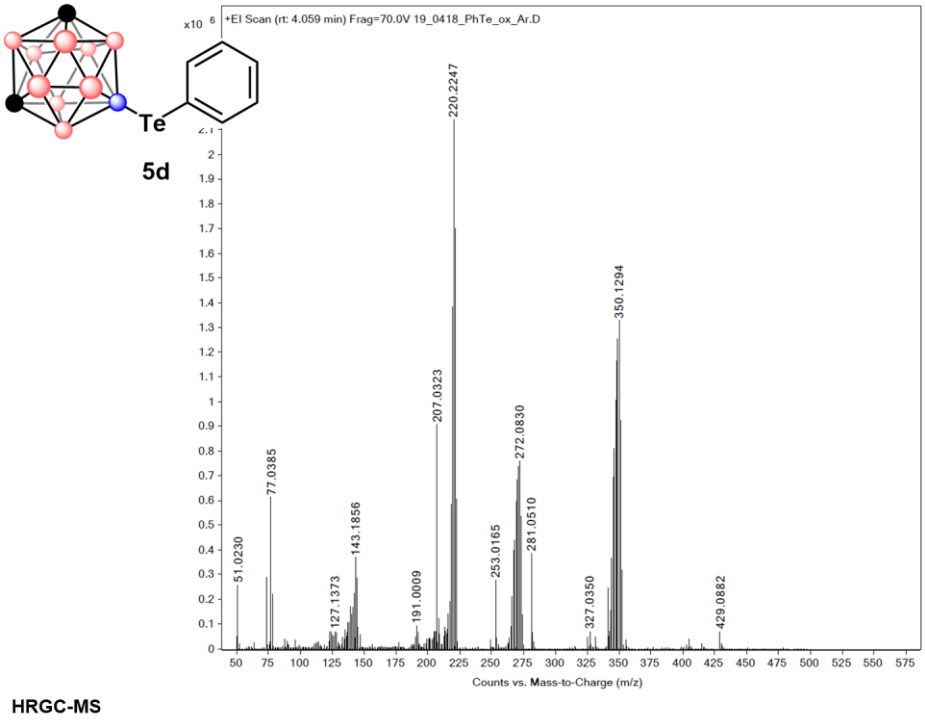

Figure B10.6 HRGC-MS of **5D**

3.6.13.11 Characterization of 5E

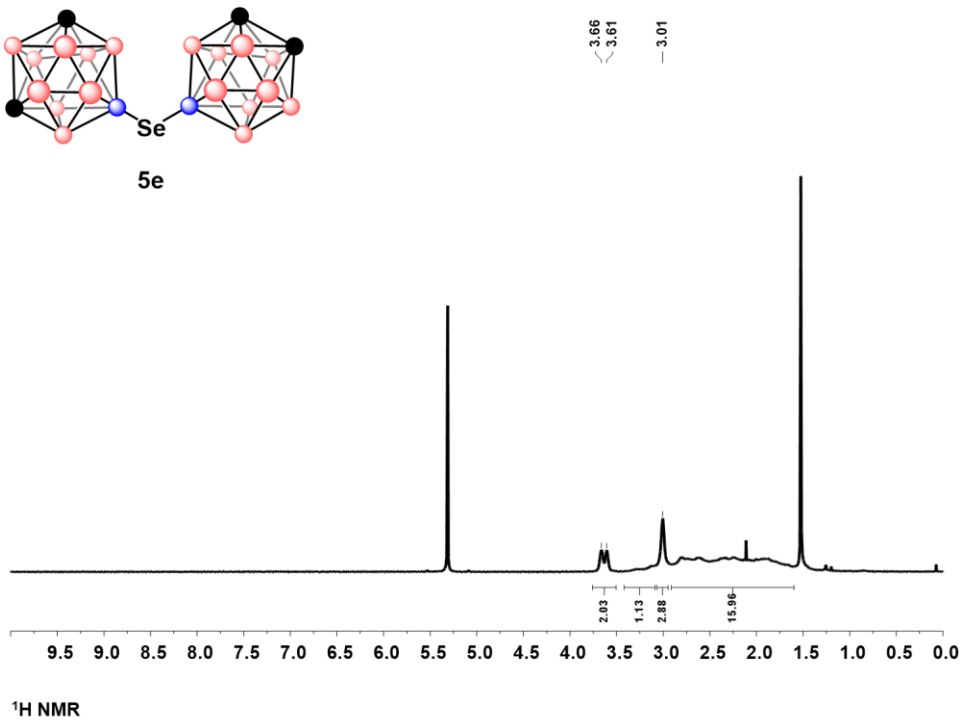

Figure B11.1 ^{1}H NMR of **5E**

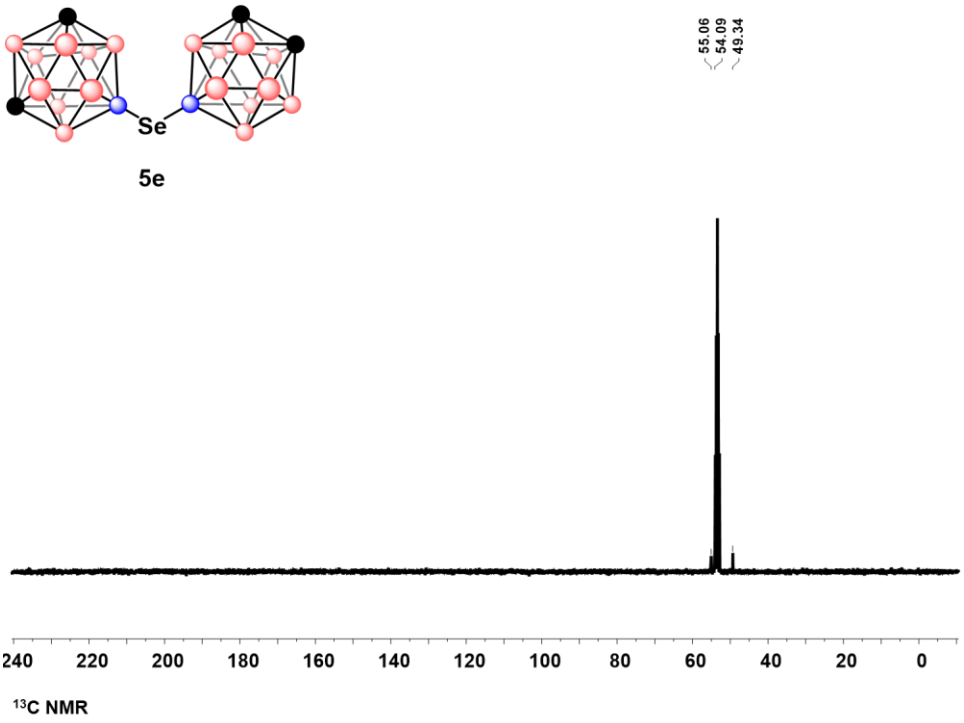

Figure B11.2 ^{13}C NMR of **5E**

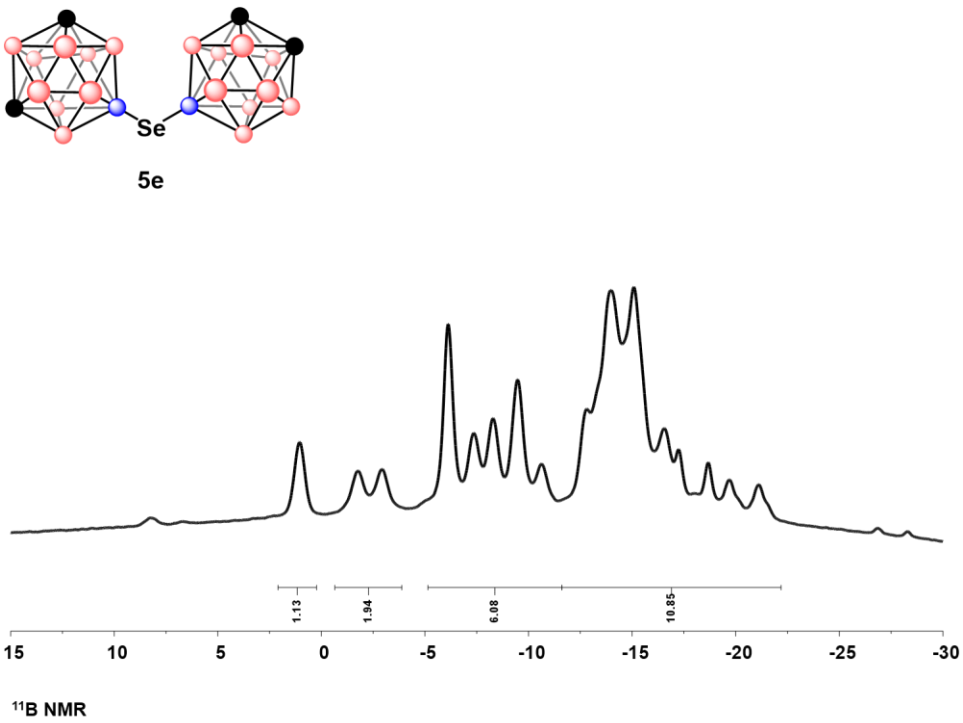

Figure B11.3 ^{11}B NMR of **5E**

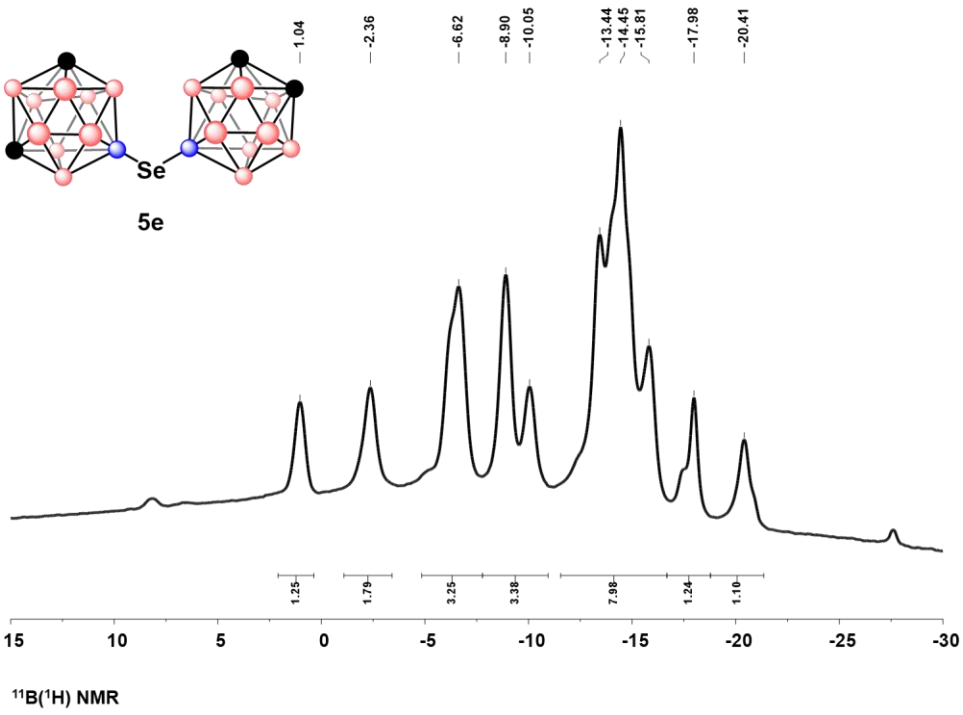

Figure B11.4 ^{11}B{^{1}H} NMR of **5E**

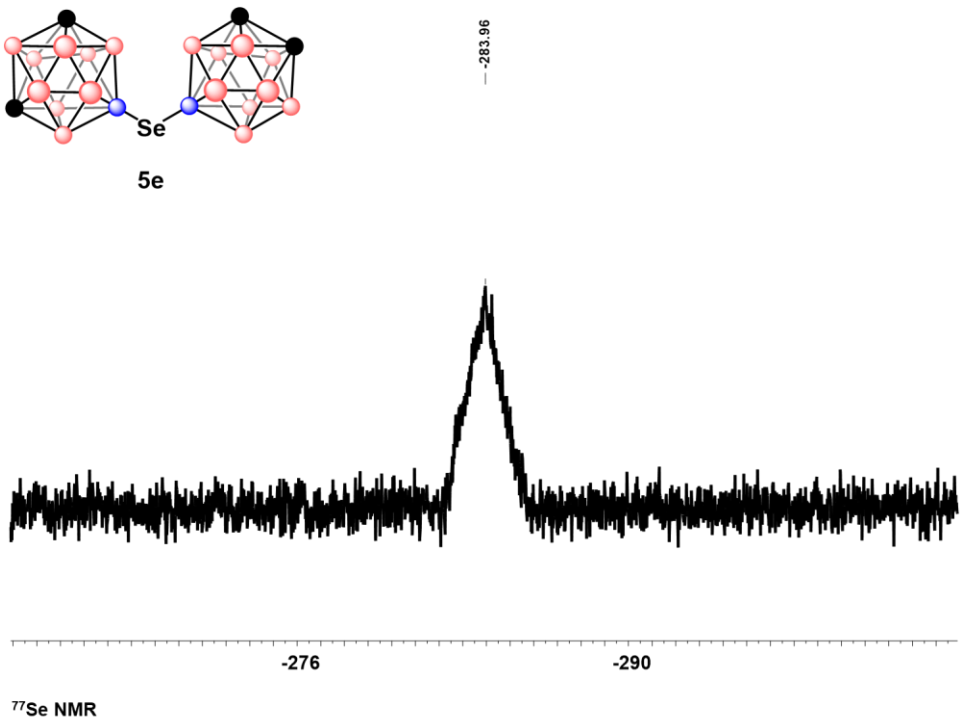

Figure B11.5 ^{77}Se NMR of **5E**

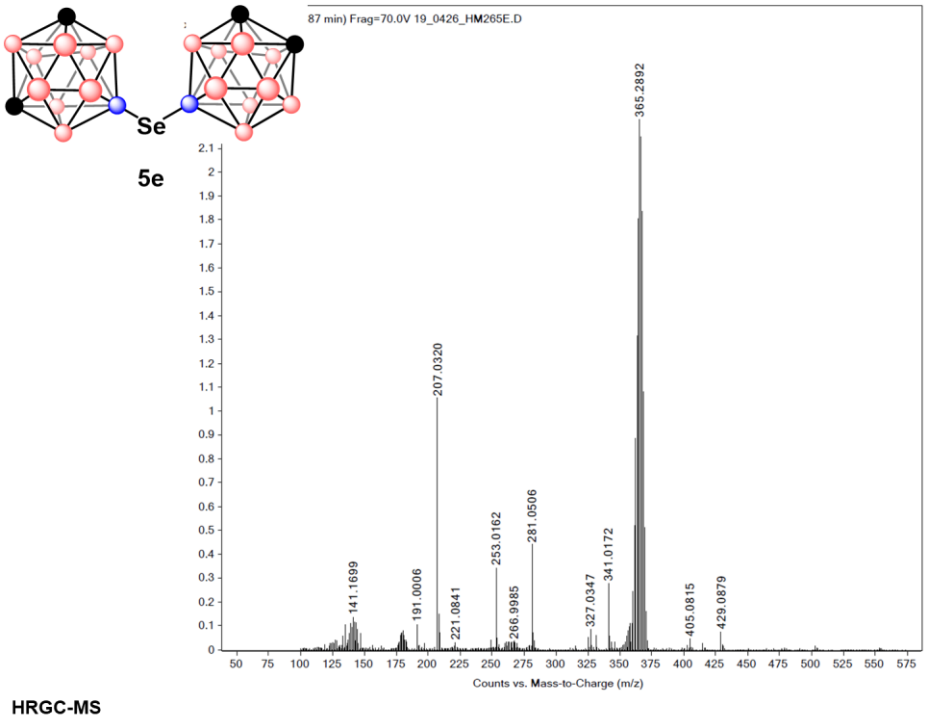

Figure B11.6 HRGC-MS of **5E**

3.6.13.12 Characterization of 5F

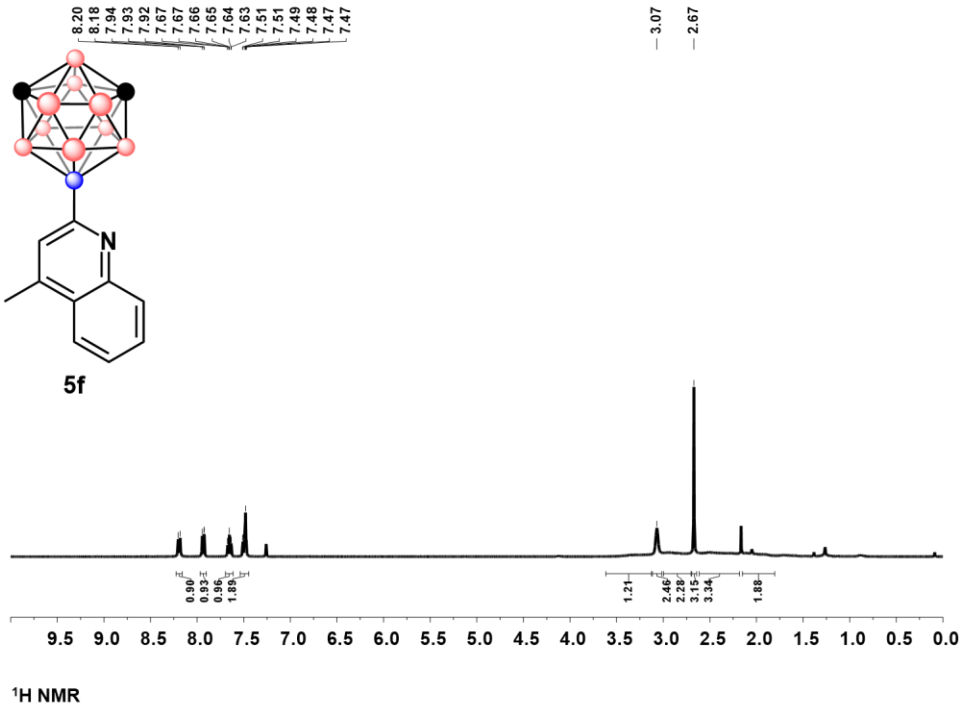

Figure B12.1 ^{1}H NMR of **5F**

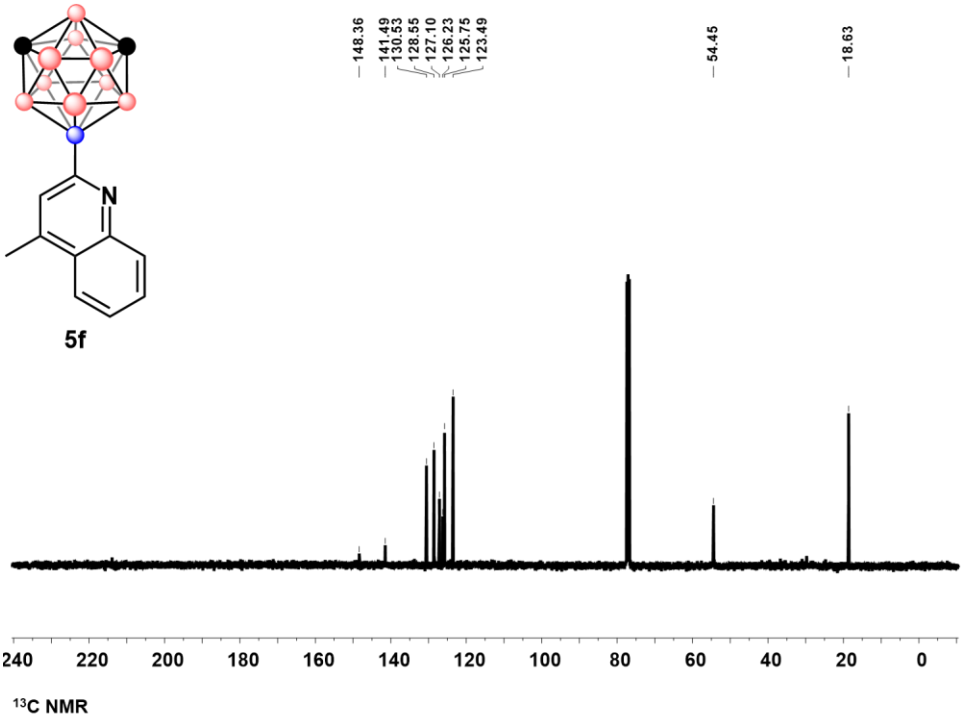

Figure B12.2 ^{13}C NMR of **5F**

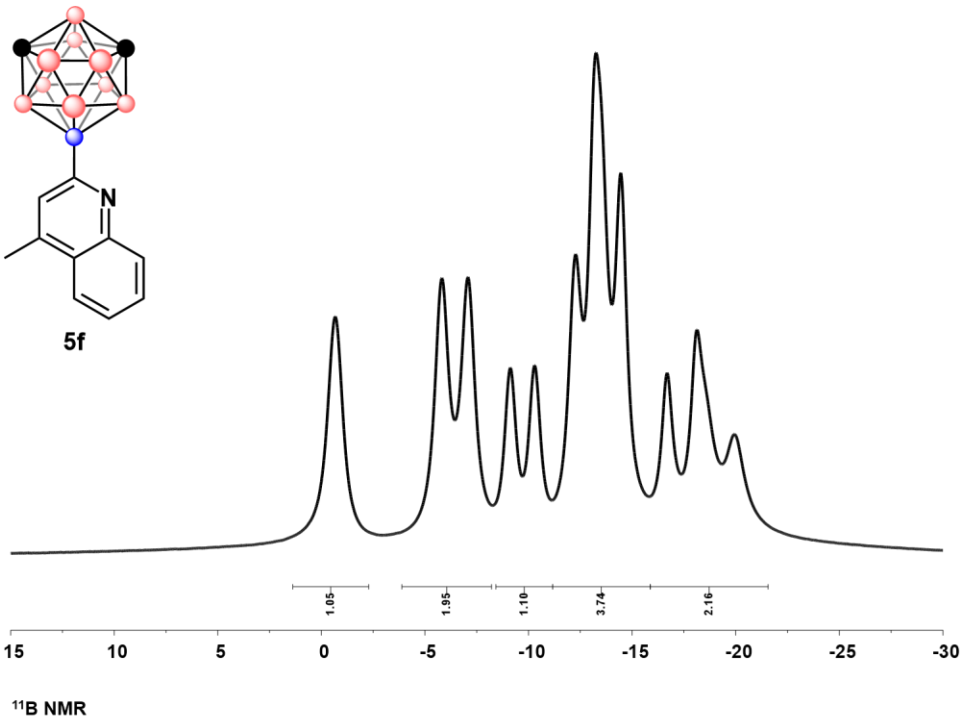

Figure B12.3 ^{11}B NMR of **5F**

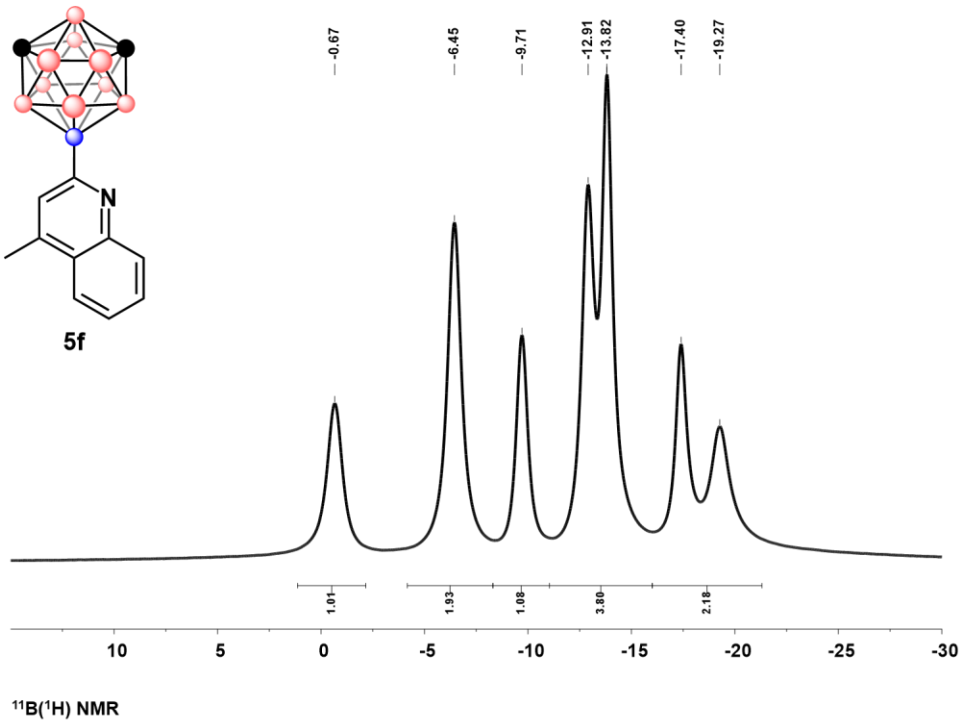

Figure B12.4 $^{11}B\{^{1}H\}$ NMR of **5F**

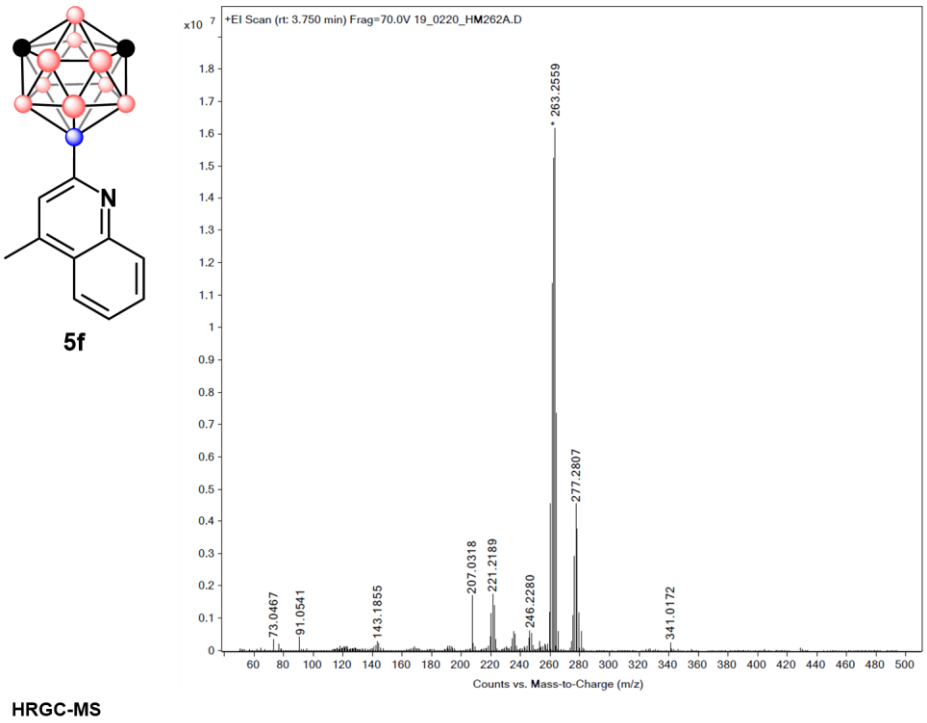

Figure B12.5 HRGC-MS of **5F**

3.6.13.13 Characterization of 5G

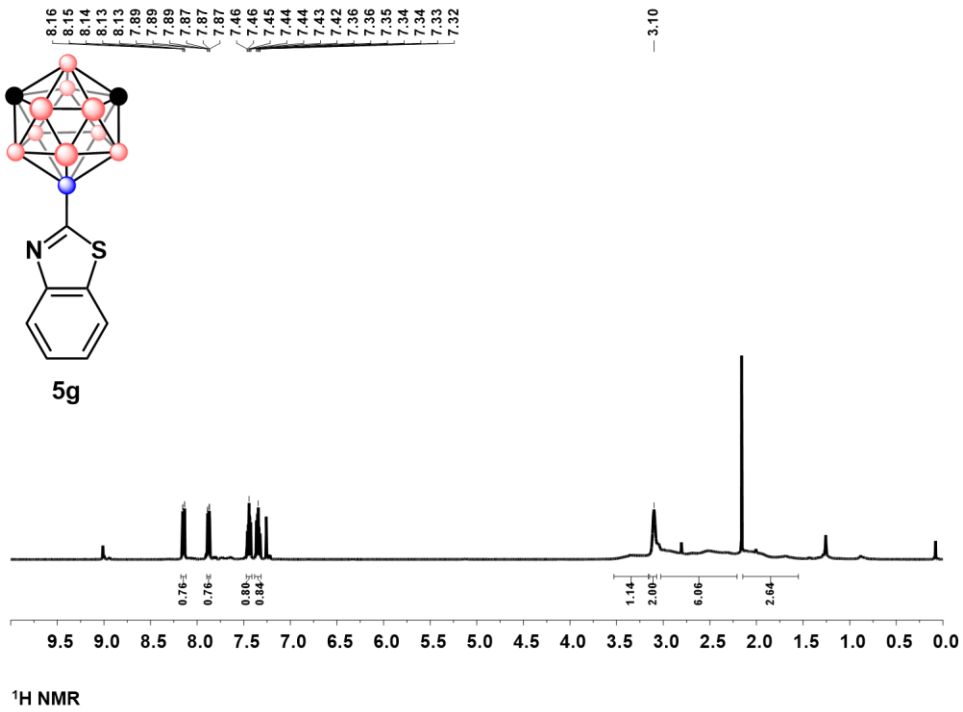

Figure B13.1 ^{1}H NMR of **5G**

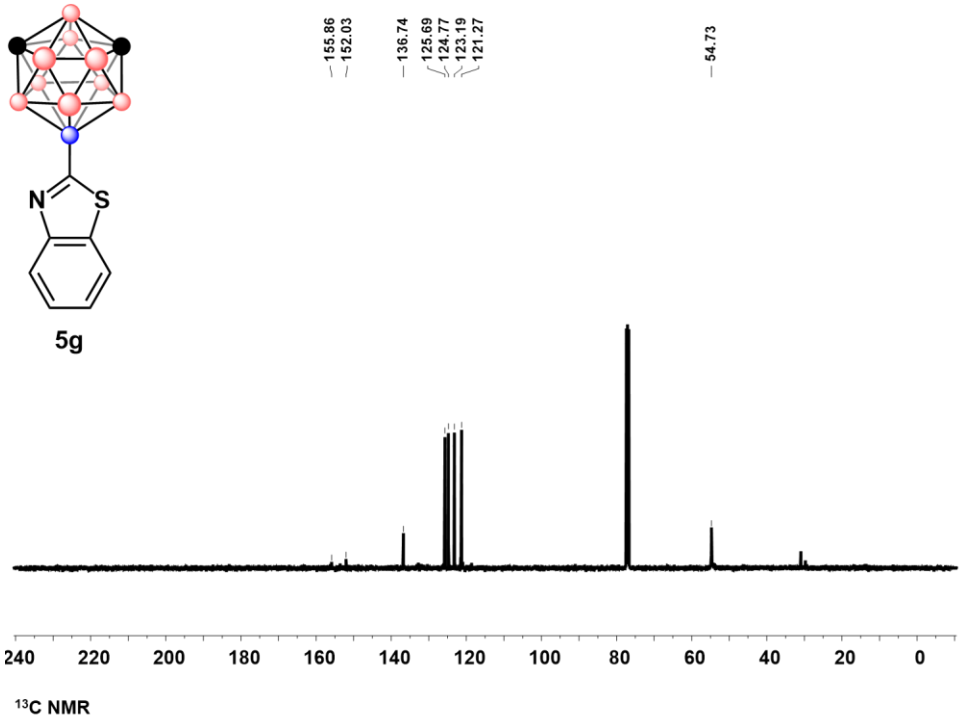

Figure B13.2 ^{13}C NMR of **5G**

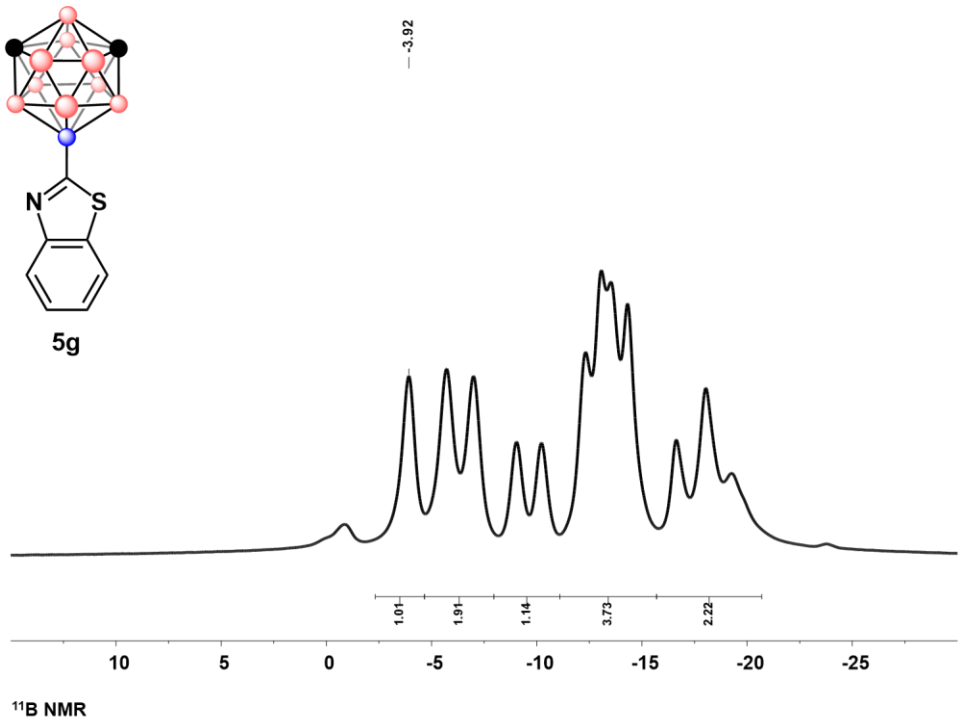

Figure B13.3 ^{11}B NMR of **5G**

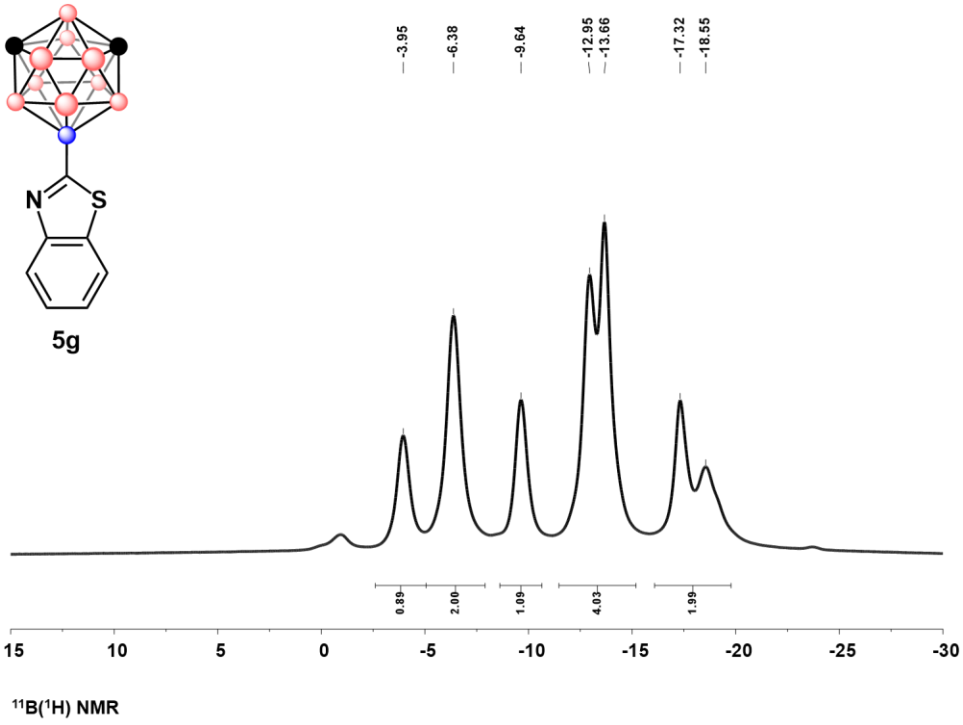

Figure B13.4 ^{11}B{^{1}H} NMR of **5G**

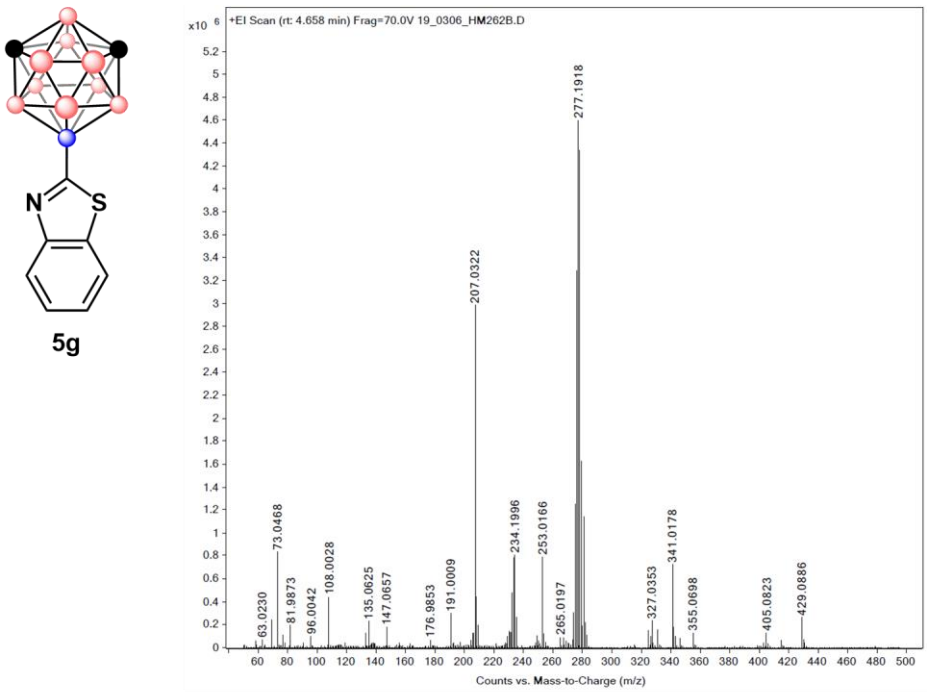

Figure B13.5 HRGC-MS of **5G**

3.6.13.14 Characterization of 5H

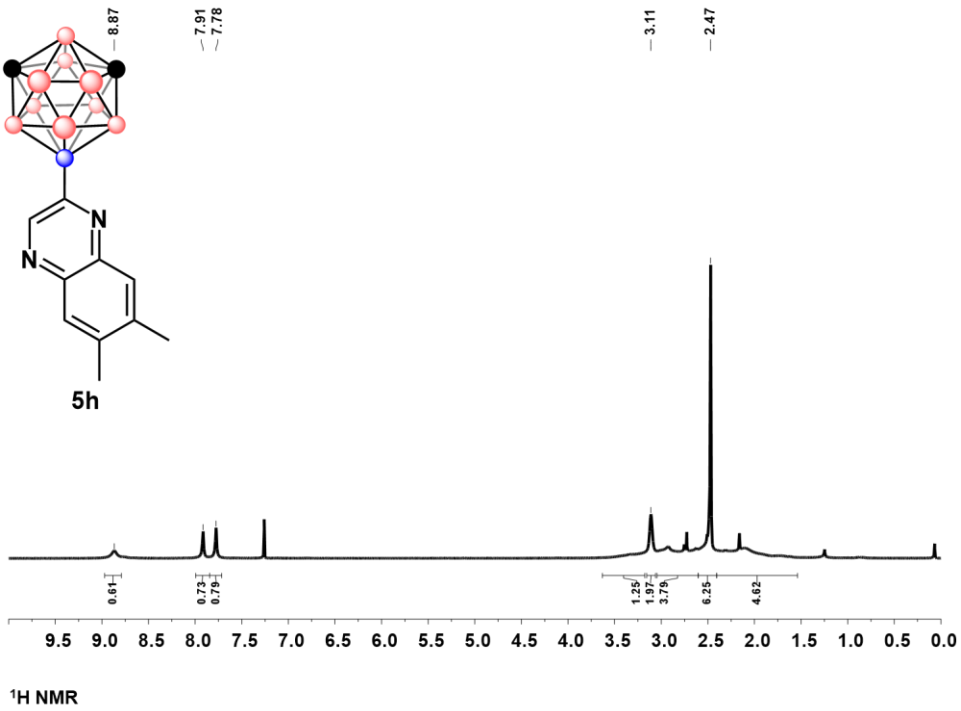

Figure B14.1 ^{1}H NMR of **5H**

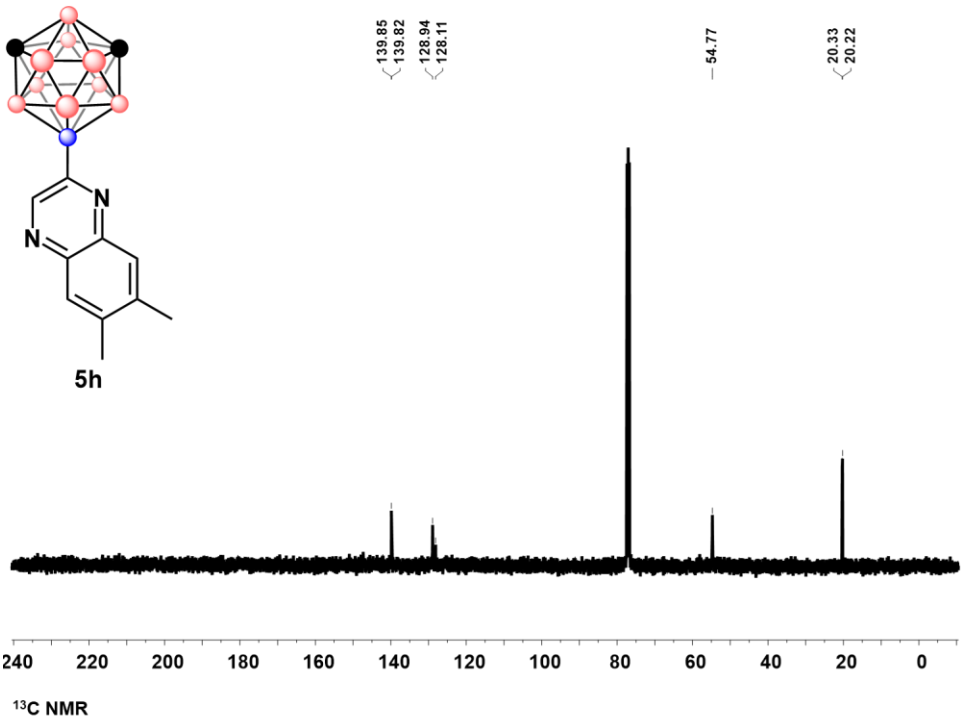

Figure B14.2 ^{13}C NMR of **5H**

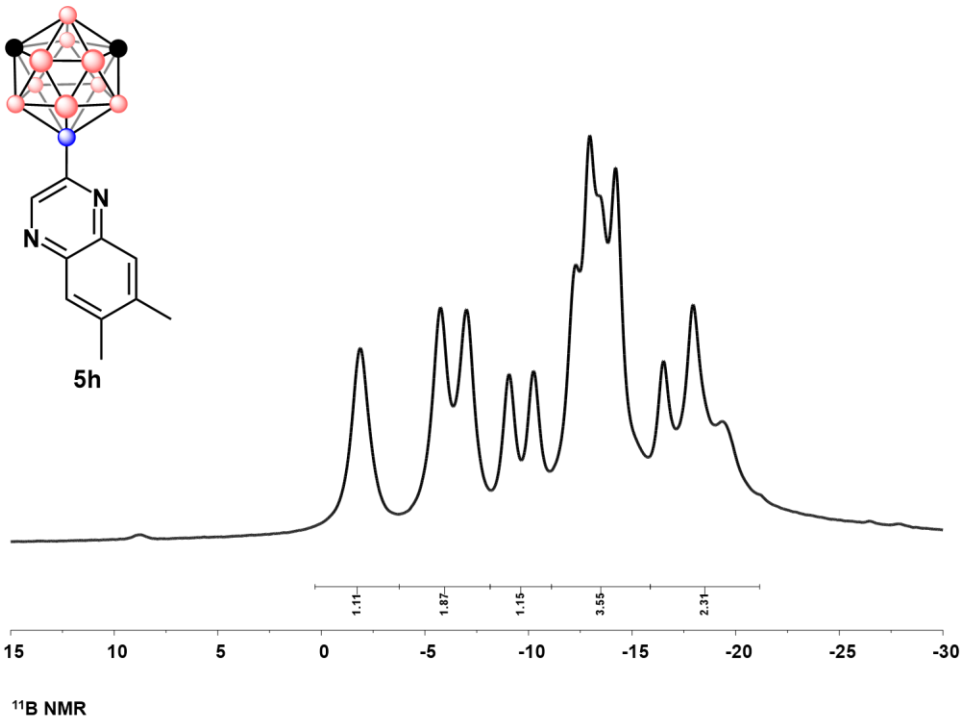

Figure B14.3 ^{11}B NMR of **5H**

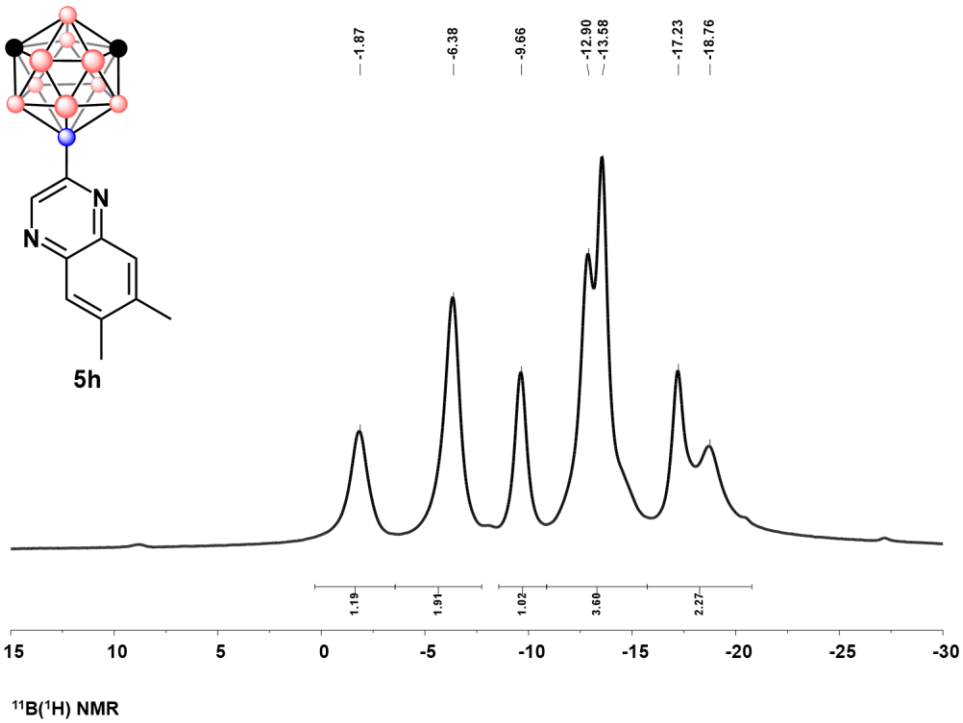

Figure B14.4 ^{11}B{^{1}H} NMR of **5H**

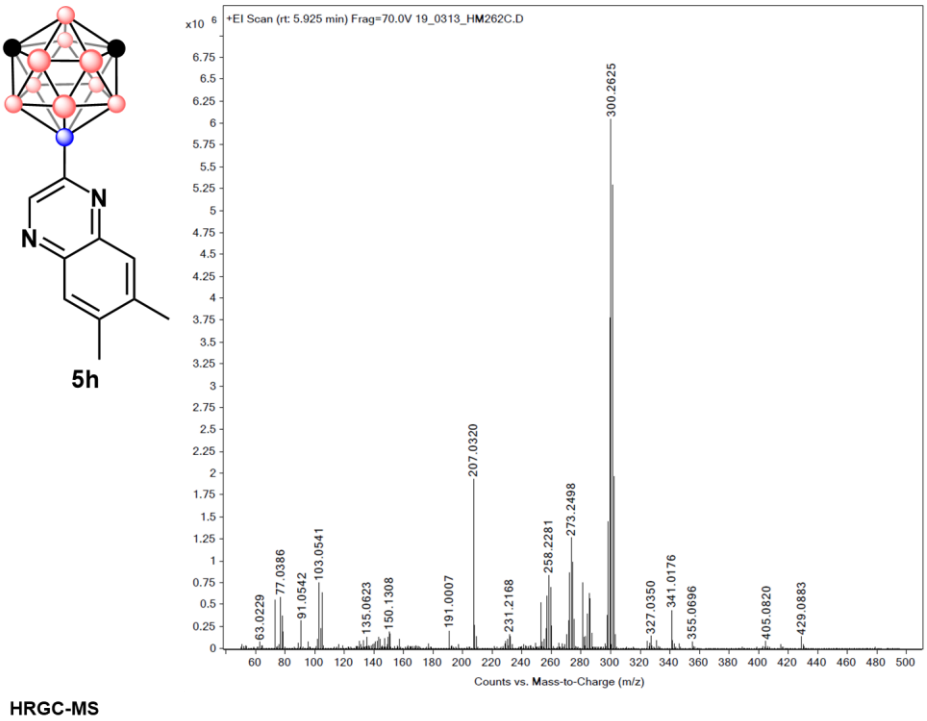

Figure B14.5 HRGC-MS of **5H**

3.6.13.15 Characterization of 5I

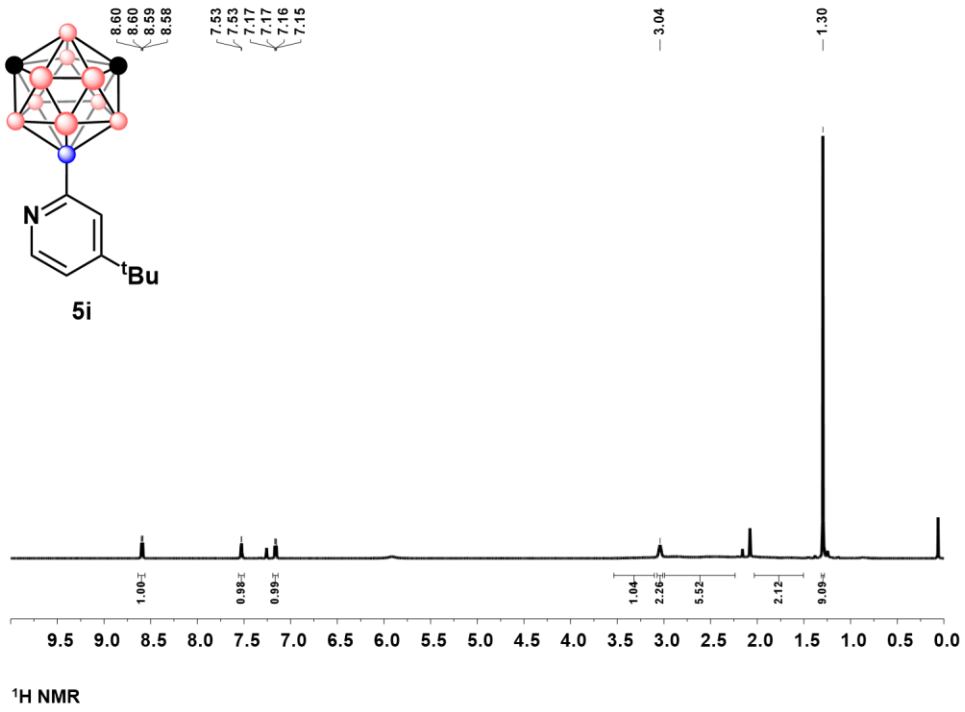

Figure B15.1 ^{1}H NMR of **5I**

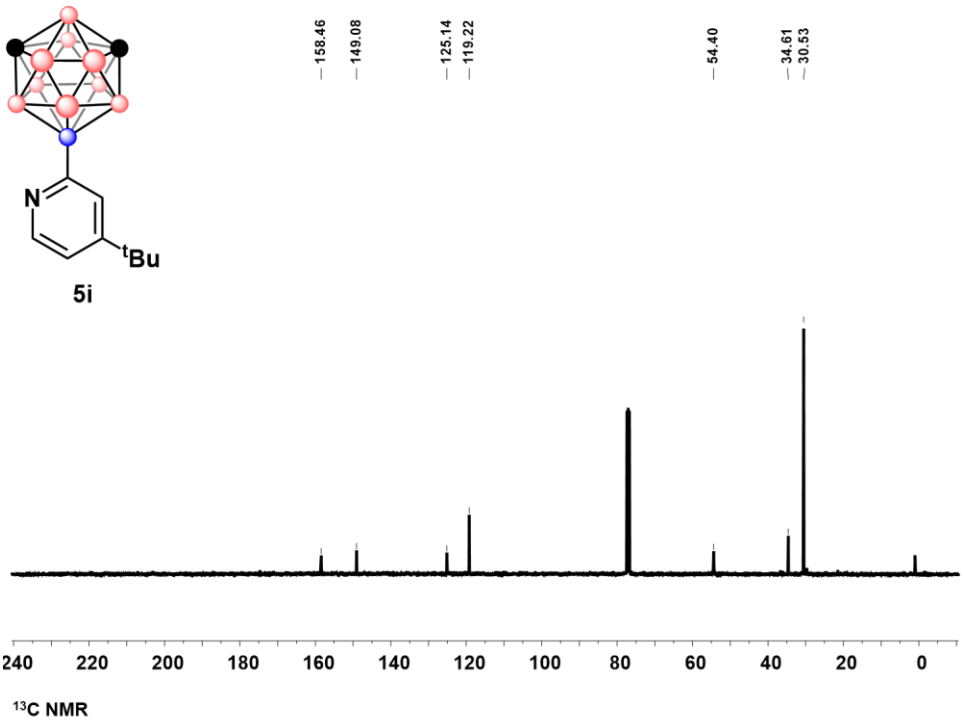

Figure B15.2 ^{13}C NMR of **5I**

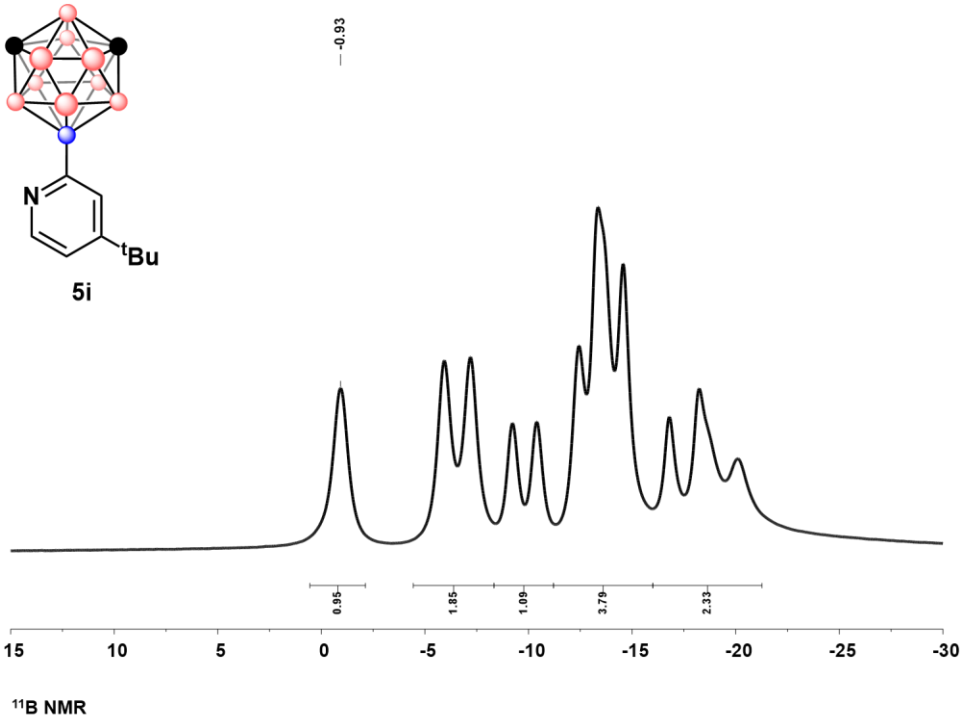

Figure B15.3 ^{11}B NMR of **5I**

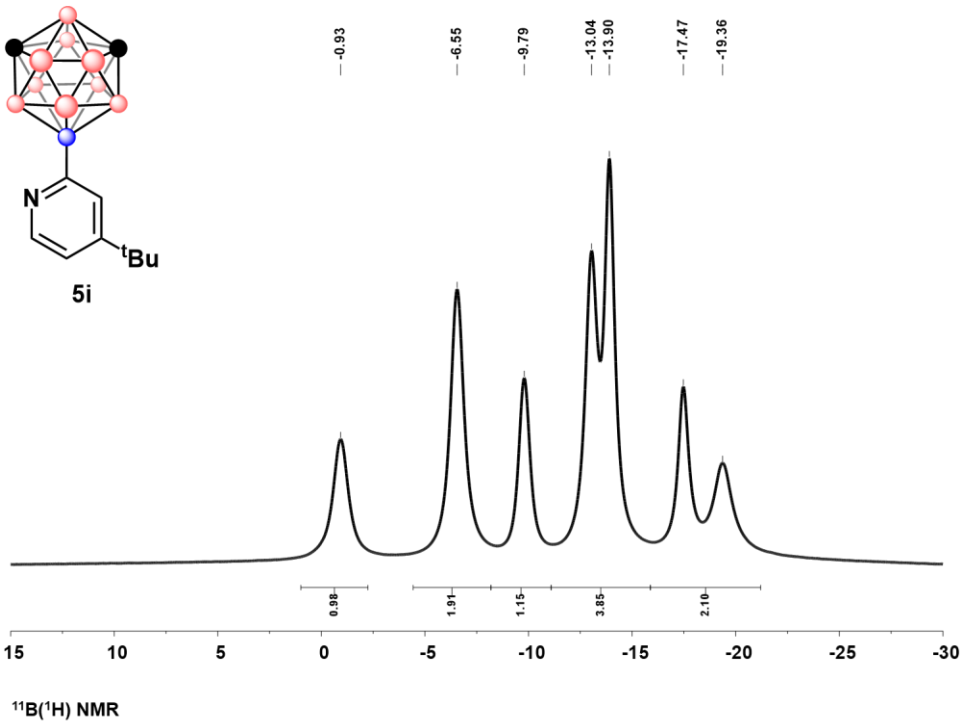

Figure B15.4 $^{11}B\{^{1}H\}$ NMR of **5I**

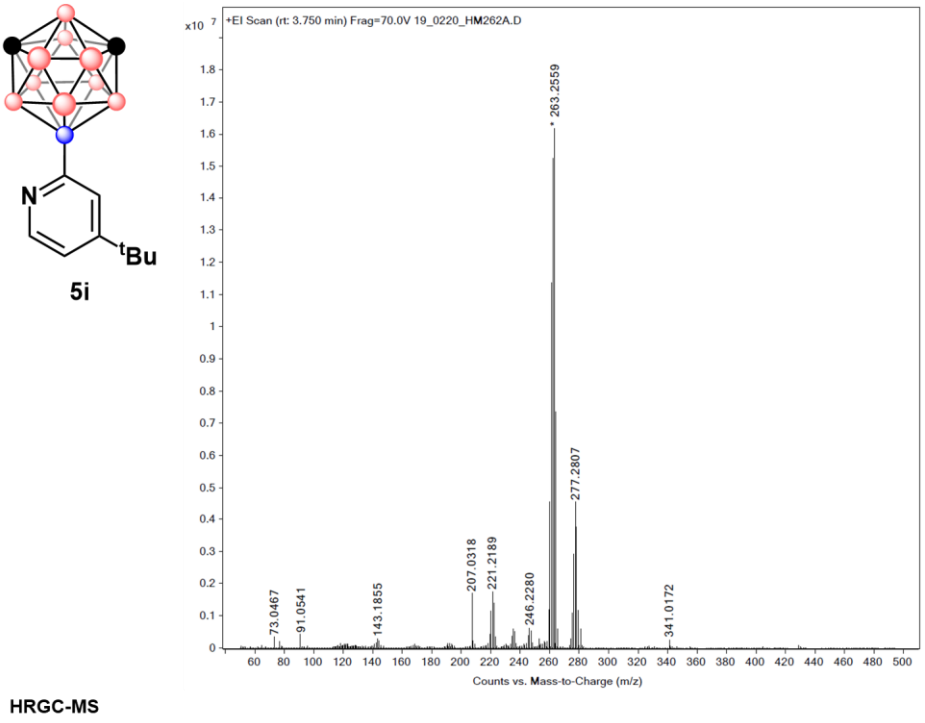

Figure B15.5 HRGC-MS of **5I**

3.6.13.16 Characterization of 6A

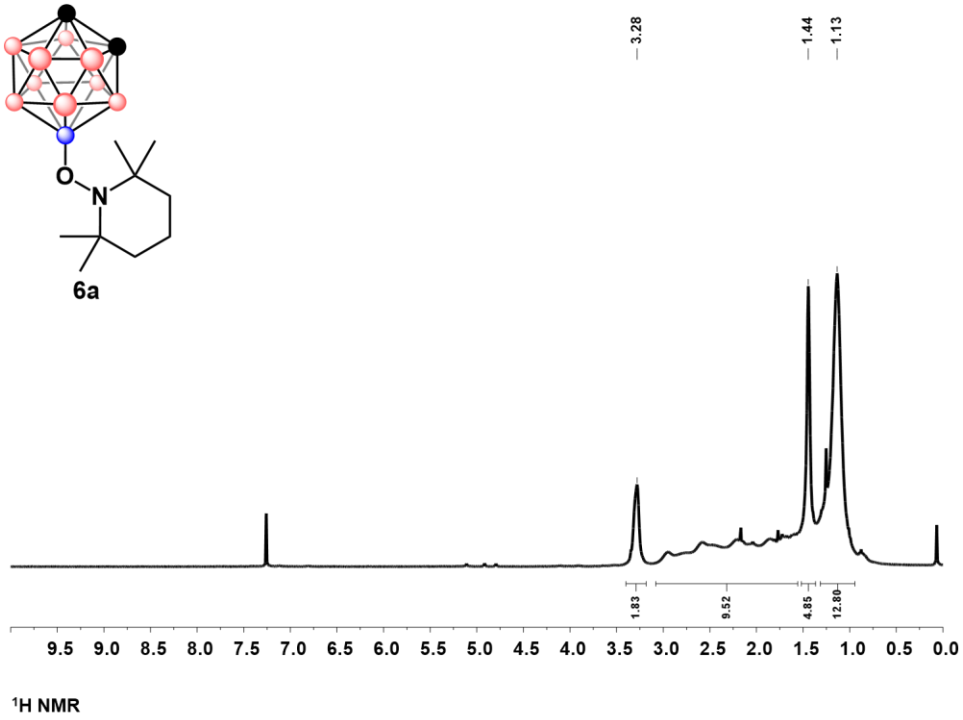

Figure B16.1 ^{1}H NMR of **6A**

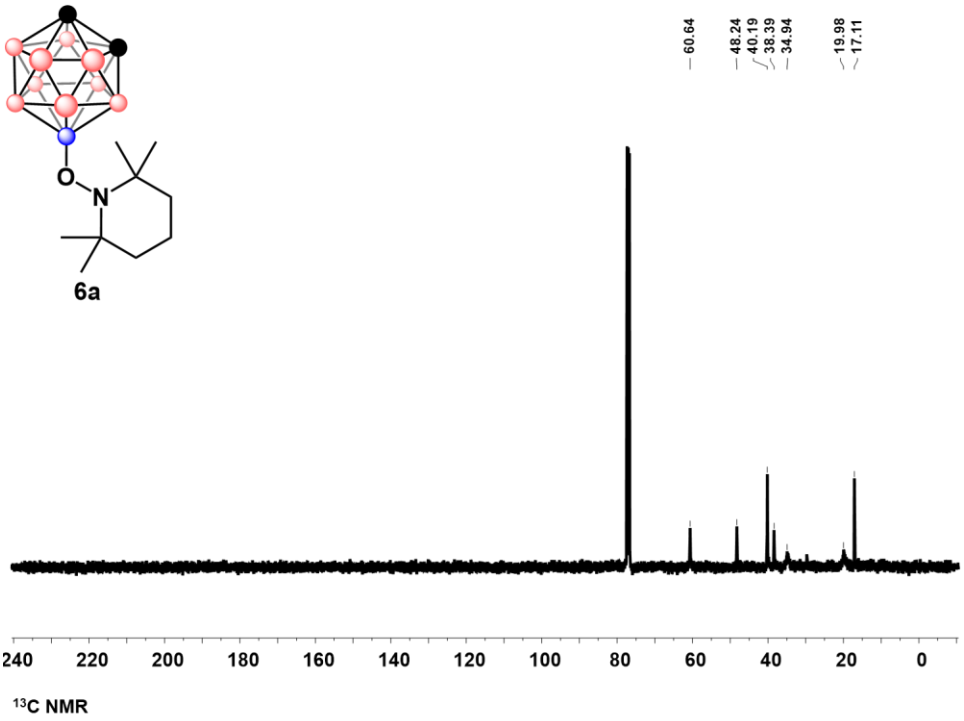

Figure B16.2 ^{13}C NMR of **6A**

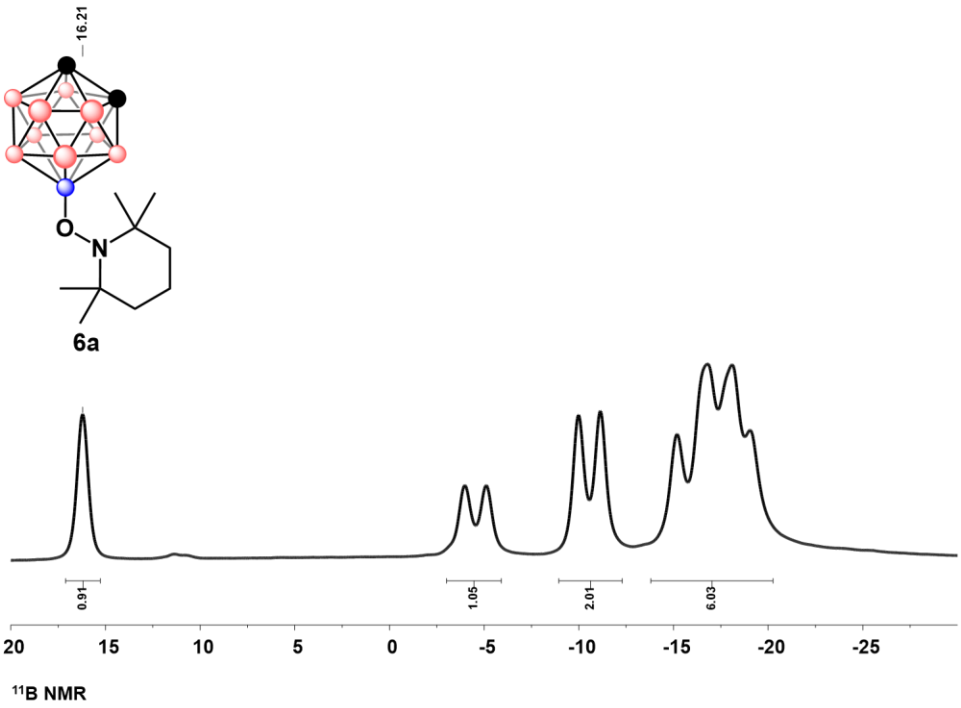

Figure B16.3 ^{11}B NMR of **6A**

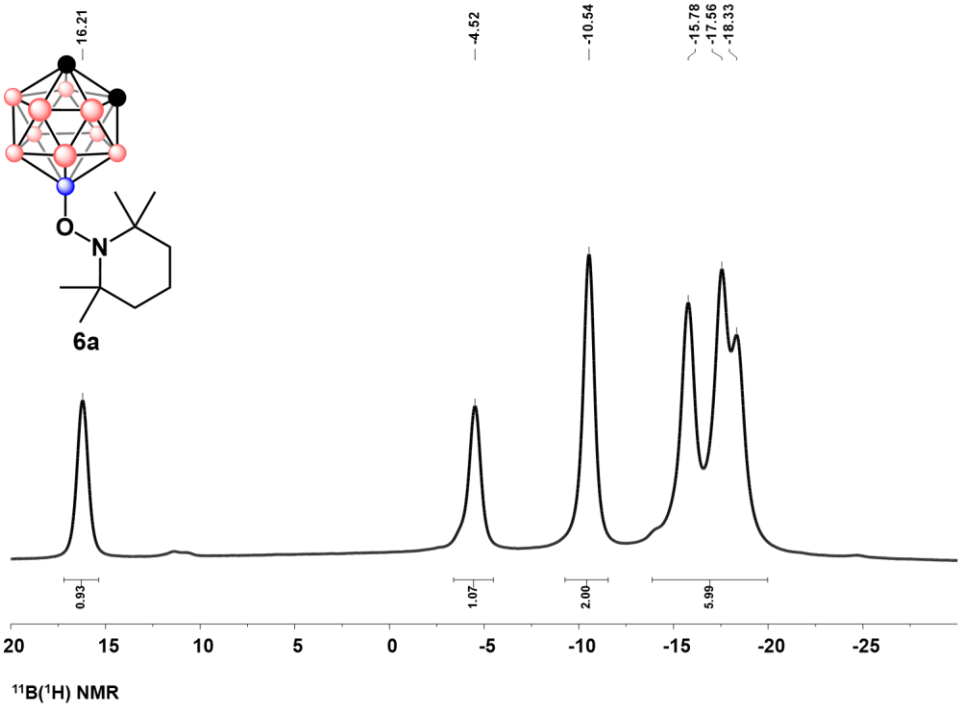

Figure B16.4 $^{11}B\{^{1}H\}$ NMR of **6A**

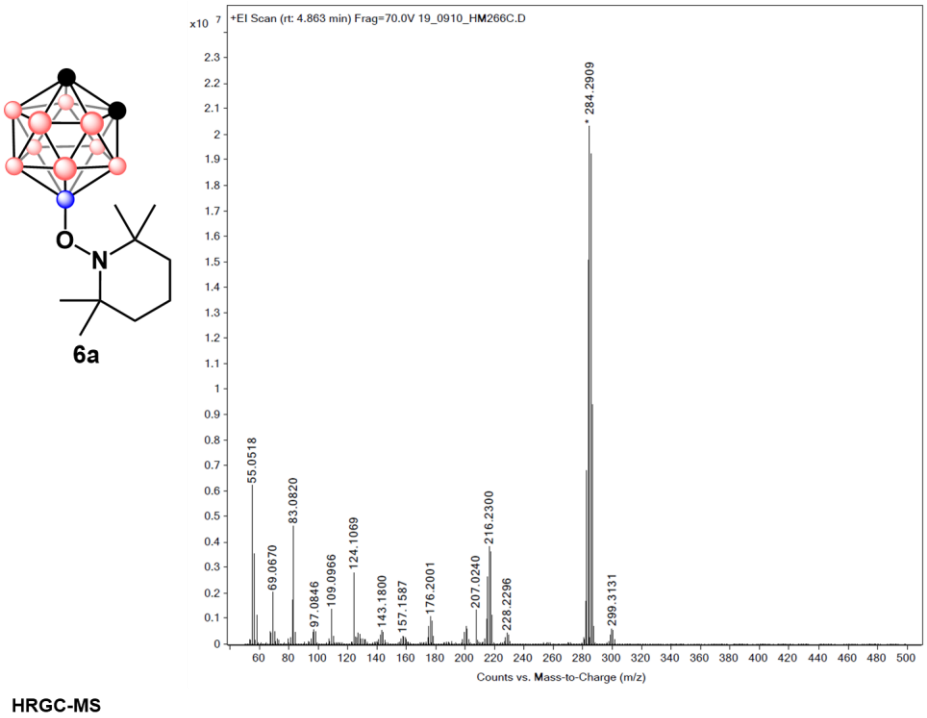

Figure B16.5 HRGC-MS of **6A**

3.6.13.17 Characterization of 6B

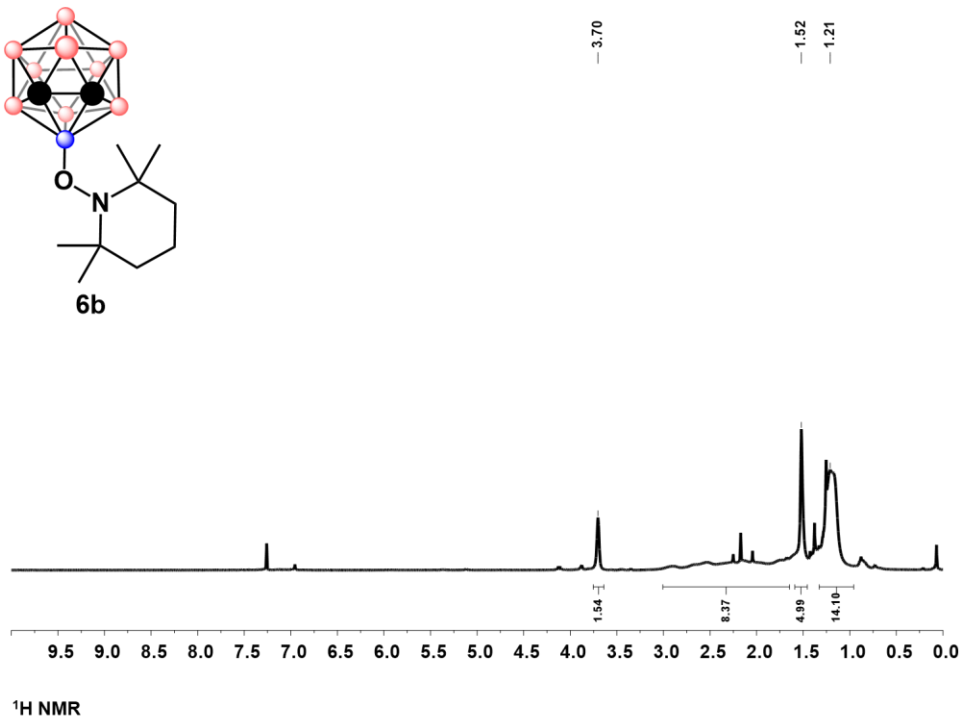

Figure B17.1 ^{1}H NMR of **6B**

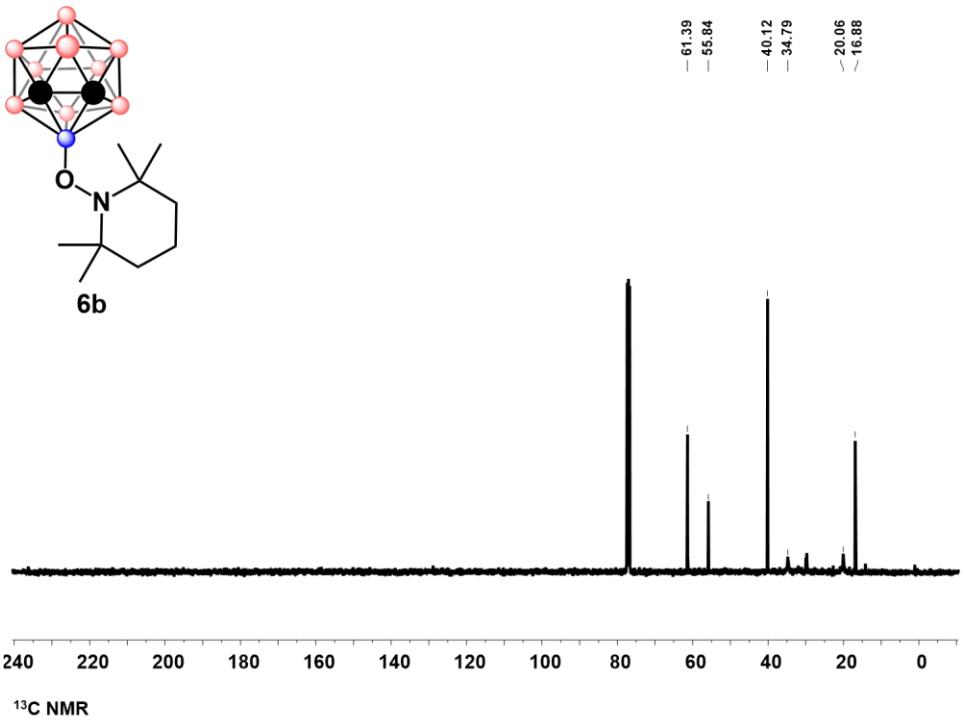

Figure B17.2 ^{13}C NMR of **6B**

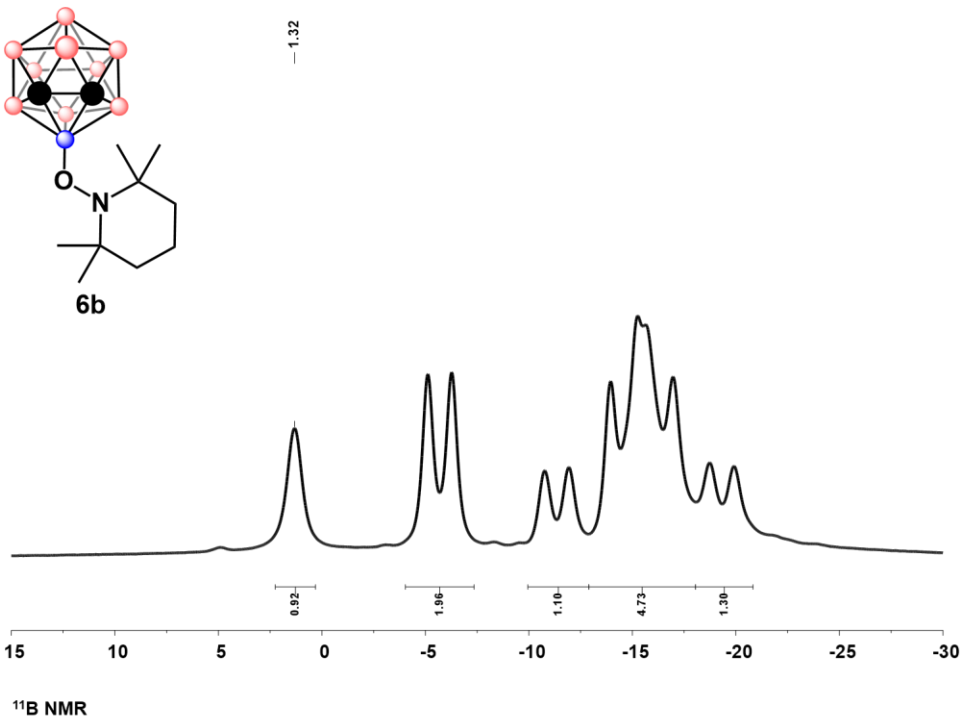

Figure B17.3 ^{11}B NMR of **6B**

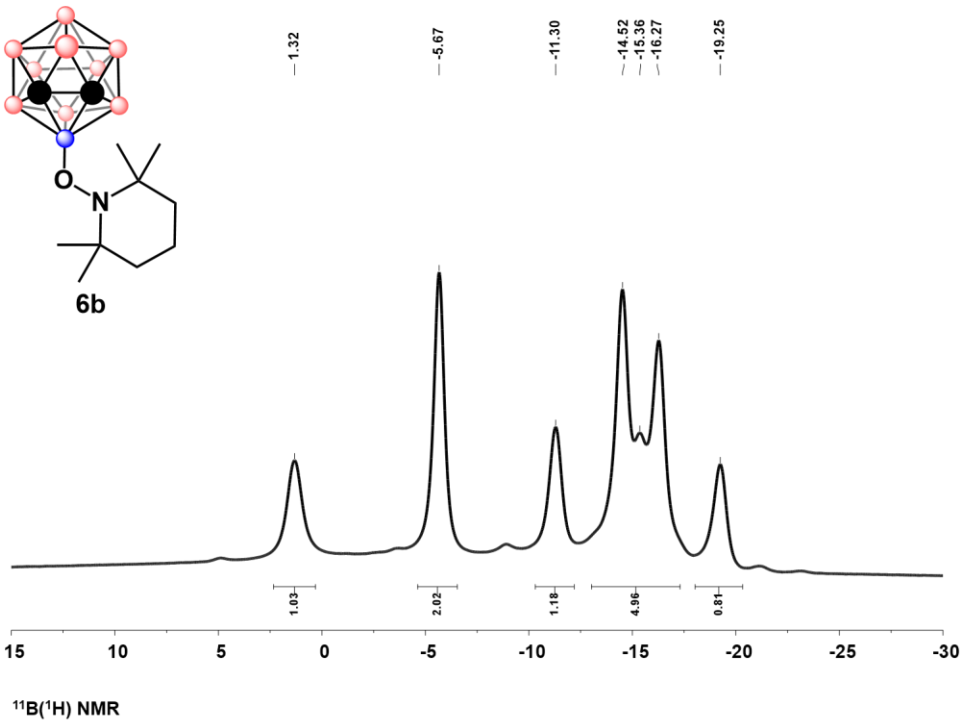

Figure B17.4 ^{11}B{^{1}H} NMR of **6B**

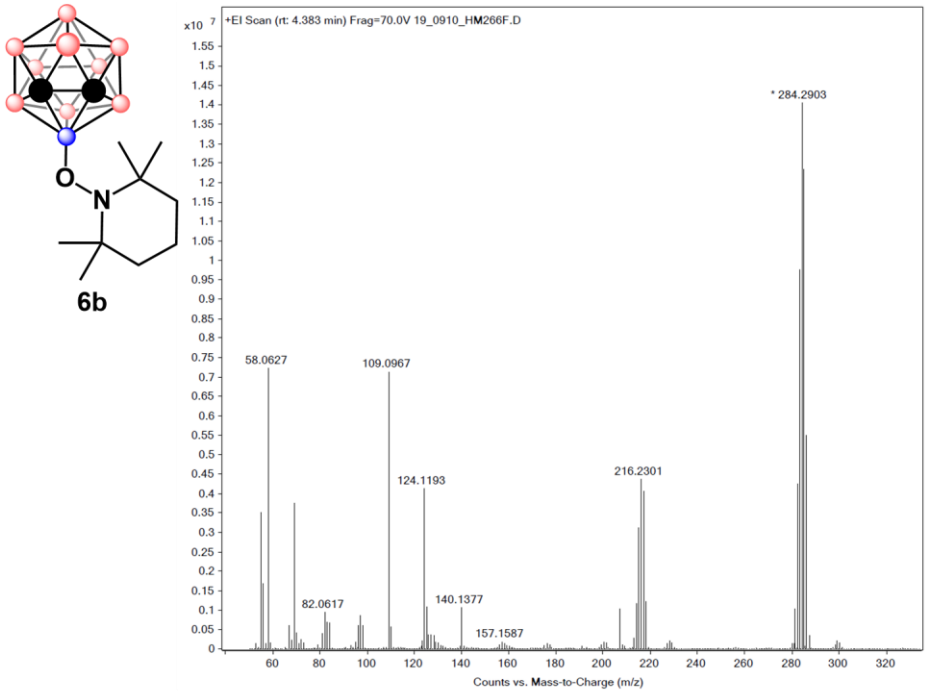

Figure B17.5 HRGC-MS of **6B**

3.6.13.18 Characterization of 6C

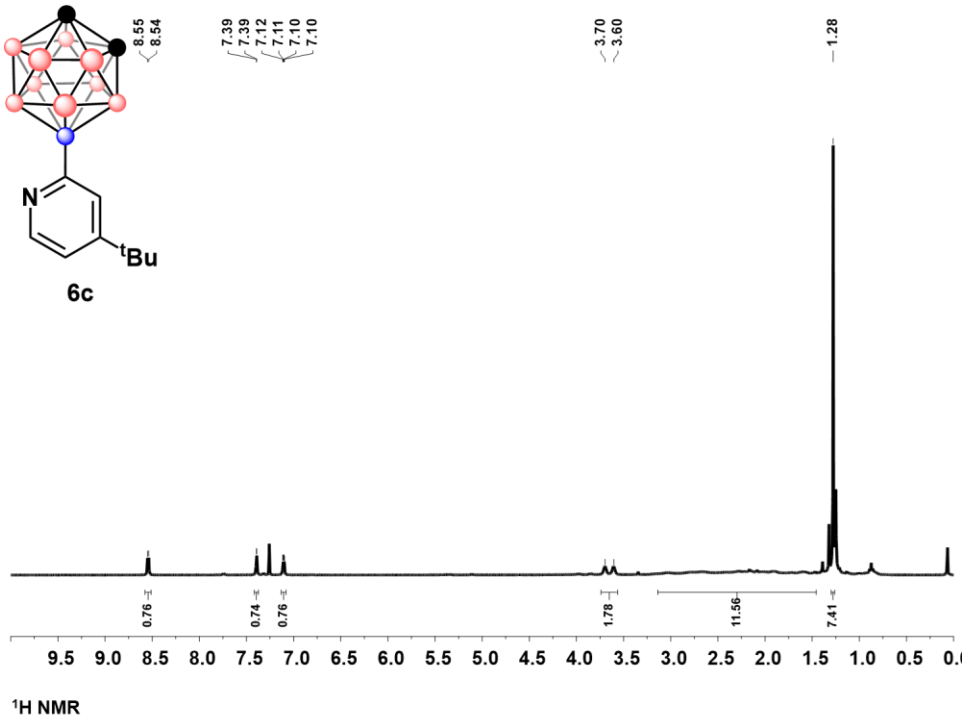

Figure B18.1 ^{1}H NMR of **6C**

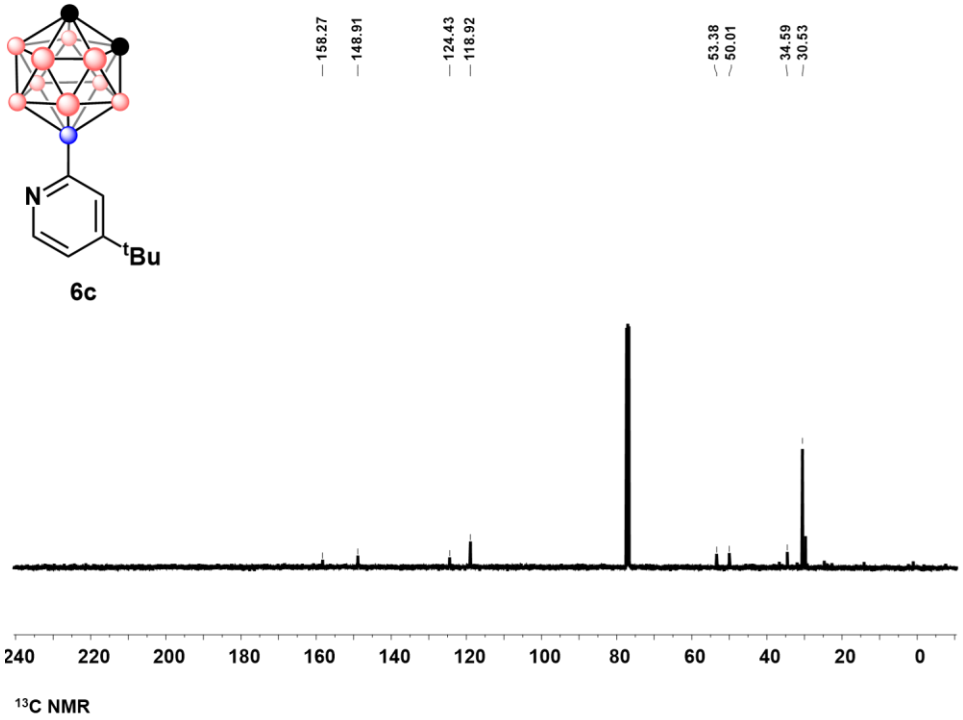

Figure B18.2 ^{13}C NMR of **6C**

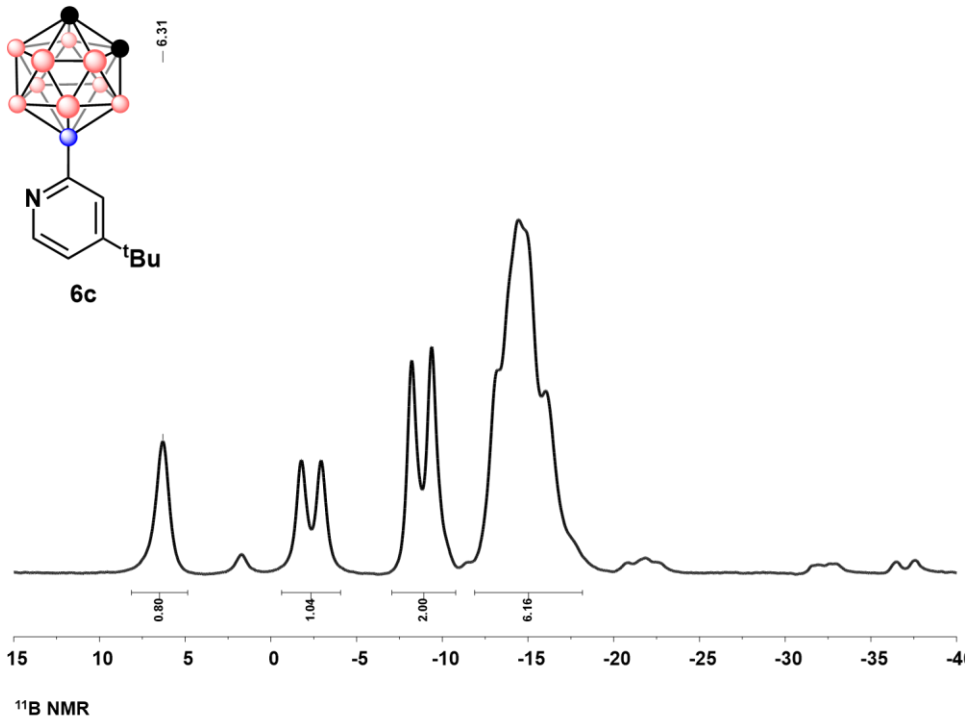

Figure B18.3 ^{11}B NMR of **6C**

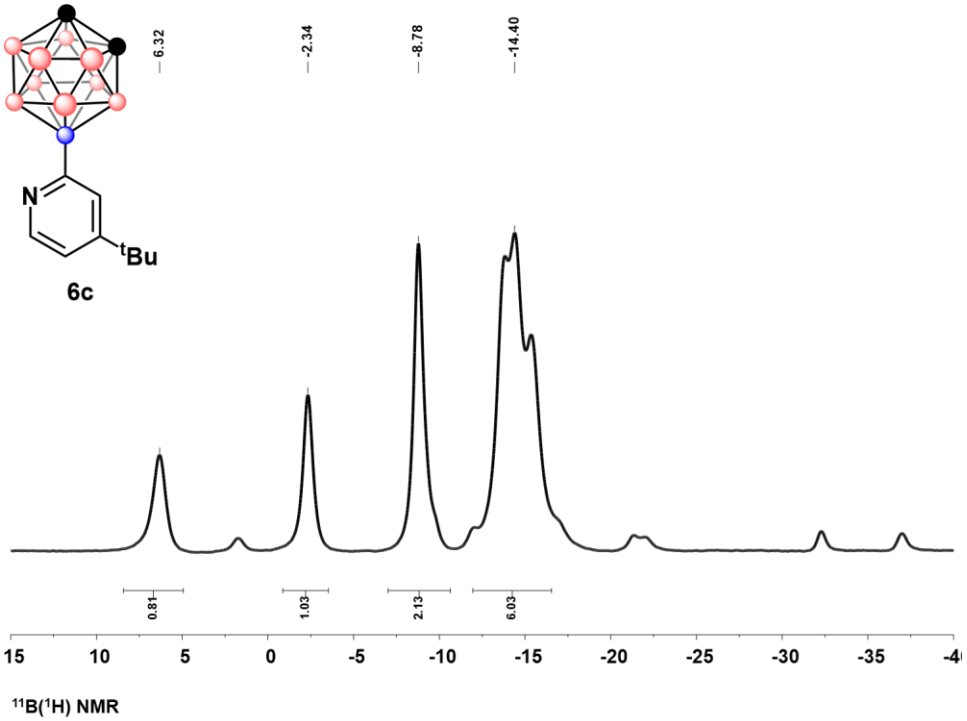

Figure B18.4 ^{11}B{^{1}H} NMR of **6C**

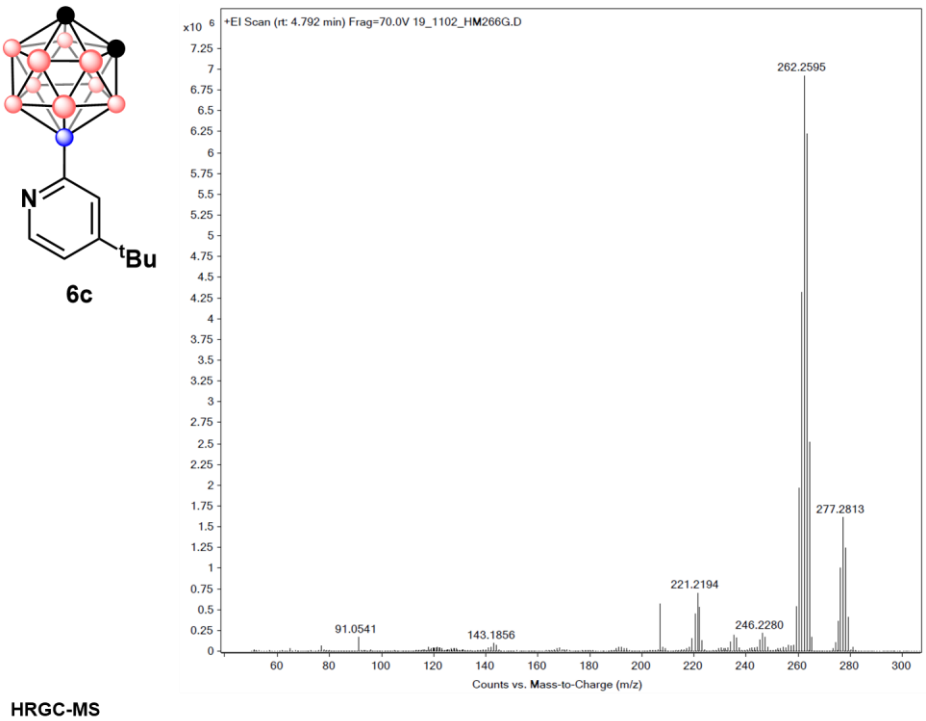

Figure B18.5 HRGC-MS of **6C**

3.6.13.19 Characterization of 6D

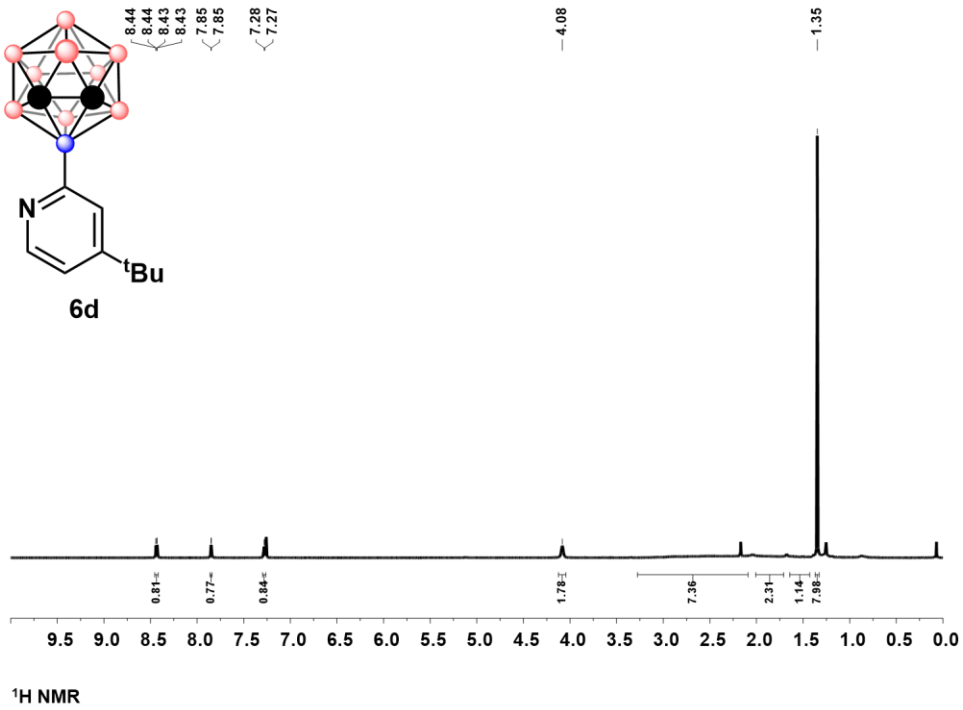

Figure B19.1 ^{1}H NMR of **6D**

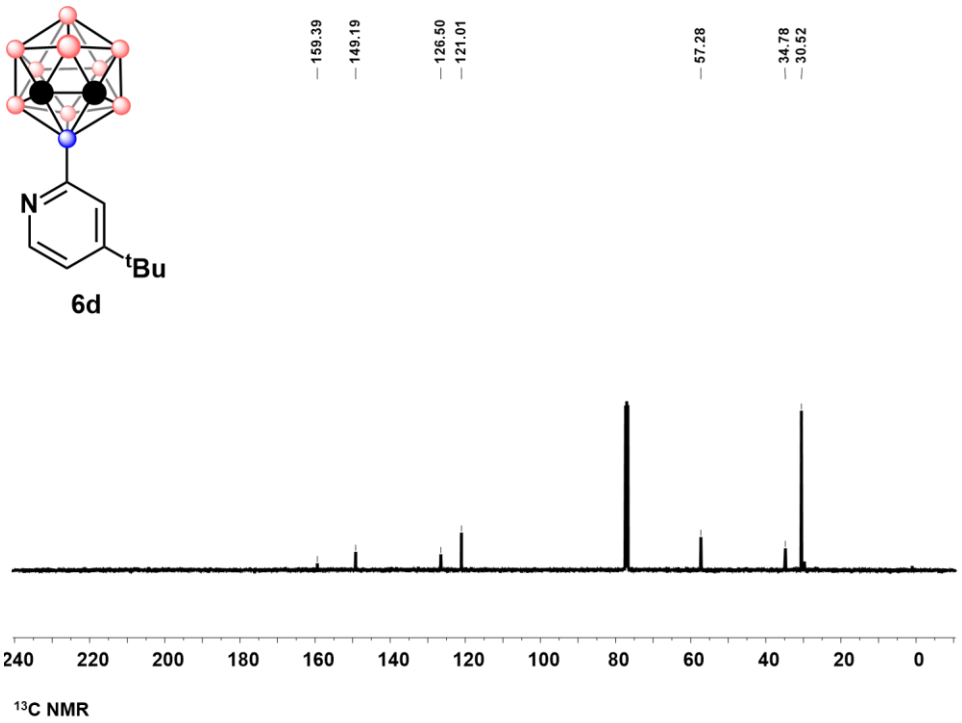

Figure B19.2 ^{13}C NMR of **6D**

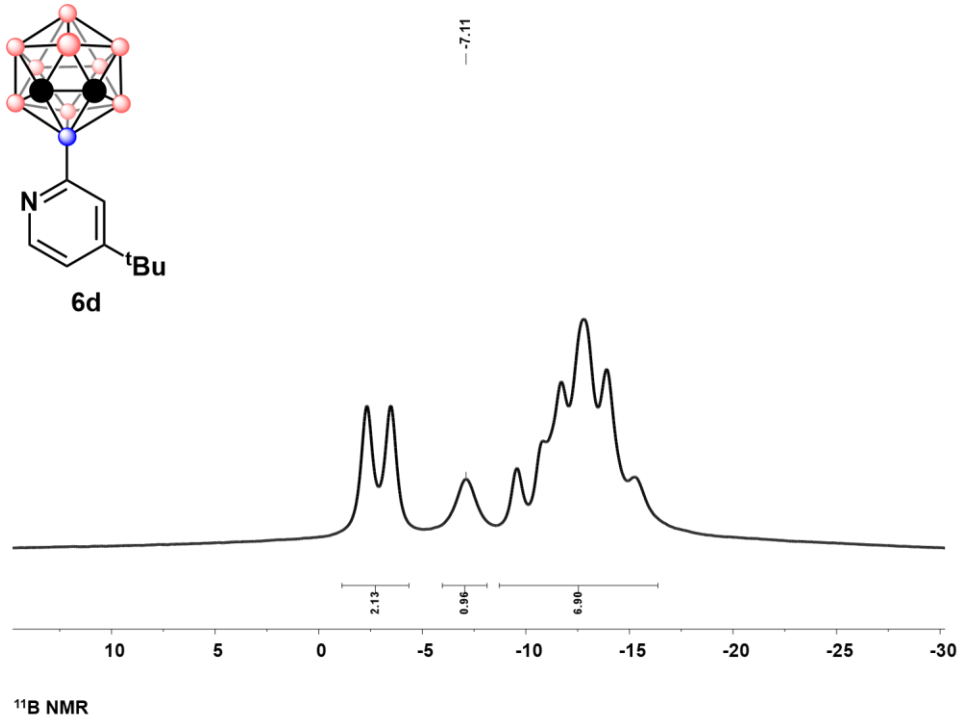

Figure B19.3 ^{11}B NMR of **6D**

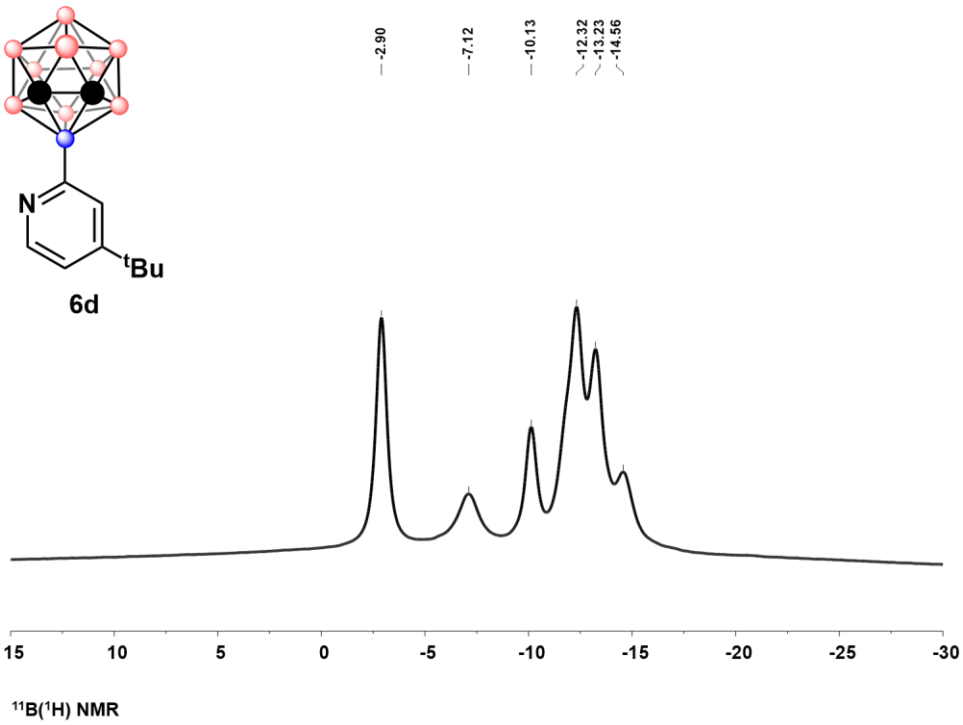

Figure B19.4 $^{11}B\{^{1}H\}$ NMR of **6D**

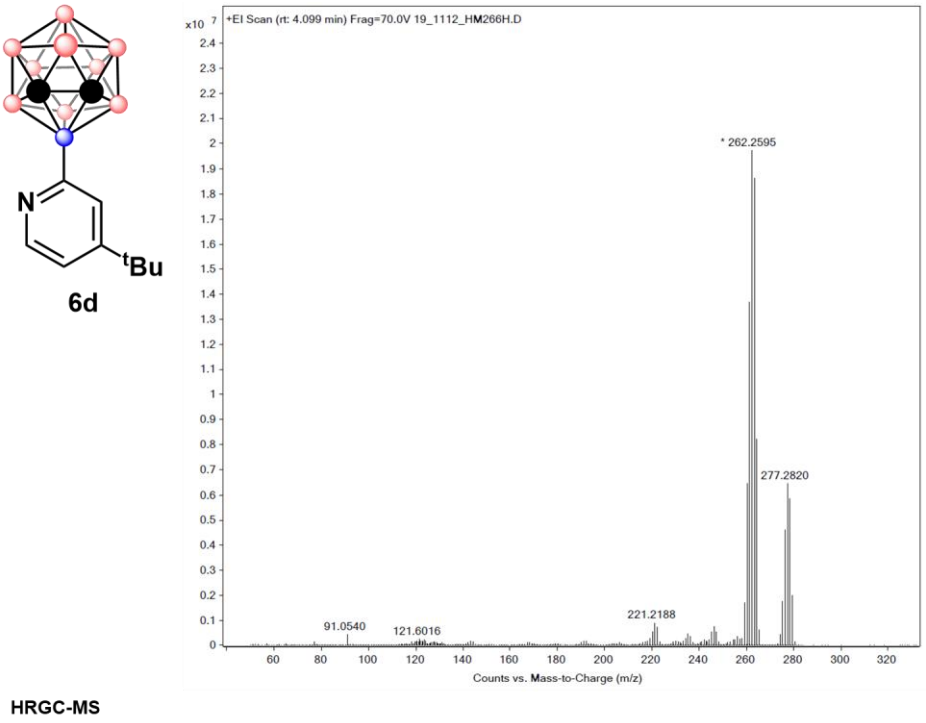

Figure B19.5 HRGC-MS of **6D**

3.6.14 References for Appendix B

1. Bruno, N. C.; Tudge, M. T.; Buchwald, S. L. Design and preparation of new palladium precatalysts for C-C and C-N cross-coupling reactions. *Chem. Sci.* **2013** 4, 916-920
2. Spokoyny, A. M.; Machan, C. W.; Clingerman, D. J.; Rosen, M. S.; Weister, M. J.; Kennedy, R. D.; Stern, C. L.; Sarjeant, A. A.; Mirkin, C. A. A coordination chemistry dichotomy for icosahedral carborane-based ligands. *Nature Chemistry* **2011**, 3, 590-596.
3. Anderson, K. P.; Mills, H. A.; Mao, C.; Kirlikovali, K. O.; Actell, J. C.; Rhenigold, A. L.; Spokoyny, A. M. Improved Synthesis of Icosahedral Carboranes Containing Exohedral B-C and C-C bonds. *Tetrahedron* **2019**, 75, 187-191.
4. Lennox, A. J. J.; Lloyd-Jones, G. C. Preparation of Organotrifluoroborate Salts: Precipitation-Driven Equilibrium under Non-Etching Conditions. *Angew. Chem. Int. Ed.* **2012**, 51, 9385-9388.
5. Chen, I-H.; Yin, L.; Itano, W.; Kanai, M.; Shibasaki, M. Catalytic Asymmetric Synthesis of Chiral Tertiary Organoboronic Esters through Conjugate Boration of β-Substituted Cyclic Enones. *J. Am. Chem. Soc.* **2009**, 131, 33, 11664-11665.
6. Cheng, R.; Qiu, Z.; Xie, Z. Iridium-catalysed regioselective borylation of carboranes via direct B-H activation. *Nature Communications* **2017**, 8, 14827.
7. O'Hara, F.; Blackmond, D. G.; Baran, P. S. Radical-Based Regioselective C-H Functionalization of Electron-Deficient Heteroarenes: Scope, Tunability, and Predictability. *J. Am. Chem. Soc.* **2013**, 135, 32, 12122-12134.

CHAPTER 4 – ICOSAHEDRAL *META*-CARBORANES CONTAINING EXOPOLYHEDRAL B-SE AND B-TE BONDS

This chapter is a version of Mills, H. A.; Alsarhan, F. A.; Ong, T.-C.; Gembicky, M.; Rheingold, A. L.; Spokoyny, A. M. "Icosahedral *Meta*-Carboranes Containing Exopolyhedral B-Se and B-Te Bonds" *accepted*

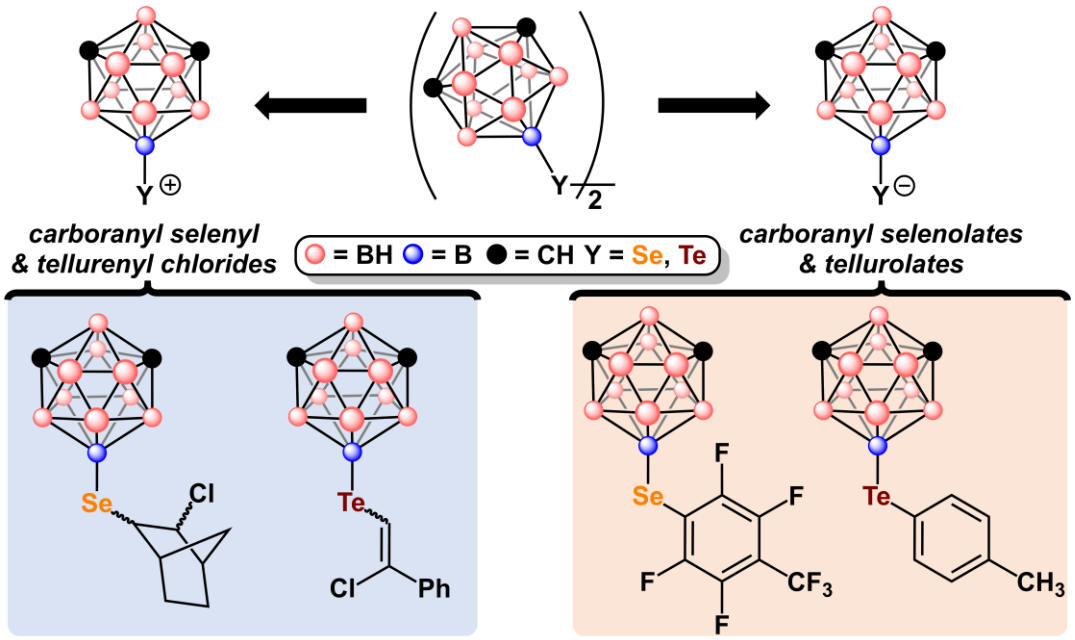

Figure 4.1: Graphical abstract for Chapter 4.

4.1 Abstract

Chalcogen-containing carboranes have been known for several decades and possess stable exopolyhedral B(9)-Se and B(9)-Te σ bonds despite the electron-donating ability of the B(9) vertex. While these molecules are known, little has been done to thoroughly evaluate their electrophilic and nucleophilic behavior. Herein, we report an assessment of the electrophilic reactivity of *meta*-carboranyl selenyl (II), tellurenyl (II), and tellurenyl (IV) chlorides and establish their reactivity pattern with Grignard reagents, alkenes, alkynes, enolates, and electron-rich arenes. These electrophilic reactions afford unique electron-rich B-Y-C (Y = Se, Te) bonding motifs not

commonly found before. Furthermore, we show that *meta*-carboranyl selenolate, and even *meta*-carboranyl tellurolate, can be competent nucleophiles and participate in nucleophilic aromatic substitution reactions. Arene substitution chemistry is shown to be further extended to electron-rich species *via* palladium mediated cross-coupling chemistry.

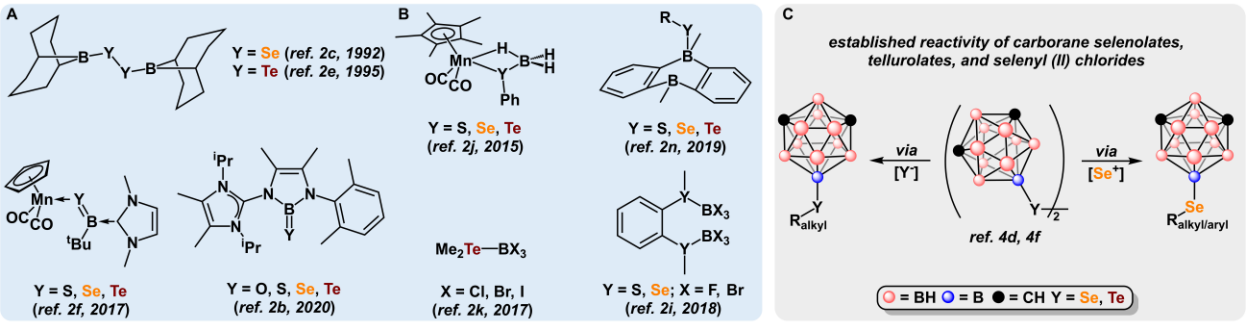

Figure 4.2: **A.** Literature examples of tricoordinate boron centers containing a boron-chalcogen single bond or double bond. **B.** Literature examples of tetracoordinate boron centers containing boron-chalcogen single bonds. **C.** Extent of previous studies regarding the reactivity of B-Se and B-Te containing carboranes. Nucleophilic reactivity has been shown between carboranyl chalcogenolates (Y = Se, Te) and electrophilic reactivity has been shown with carboranyl selenyl (II) chlorides, though not with tellurenyl (II) or (IV) chlorides.

4.2 Introduction

Organoselenium and organotellurium compounds containing carbon-selenium and -tellurium bonds have been widely studied for the past decades and have recently found a variety of uses in nearly all aspects of chemical research, including: organic synthesis,[1a-f] organometallics,[1g-i] self-assembled and applied materials,[1j-n] photochemistry,[1o-s] and chemical biology.[1t-w] In contrast to organochalcogen compounds, the reactivity of boronochalcogens containing boron-selenium and -tellurium bonds is significantly less established. Of currently known molecules containing boron-selenium or -tellurium bonds, a large portion consist of

tricoordinate mononuclear boron centers (**Figure 4.2A**).[2a-i] Boron sites in these molecules contain a lowest unoccupied molecular orbital (LUMO) capable of accepting some electron density from the bound Se or Te atom, resulting in a shortening of the boron chalcogen bond. Additionally, several examples containing tetracoordinate boron centers[2i-r] exist as well (**Figure 4.2B**). In these cases, tricoordinate BR_3 (R: C, F, Cl, Br, I, H) are typically stabilized by coordination of chalcogen-based ligands where lone pair electrons on the chalcogen are shared with the vacant boron-centered *p*-orbital. Lesser known molecular platforms that can support boron-selenium and -tellurium bonding interactions, are boron-rich clusters.[3] Among these, icosahedral carboranes ($C_2B_{10}H_{12}$) in particular have afforded a unique and stable scaffold for the study of compounds containing boron chalcogen bonds.[4] Similar in size to adamantane, this cluster type exists in three isomeric forms (*ortho*-, *meta*-, *para*-).[5] In all cases, electrons responsible for the cluster bonding are delocalized in three dimensions. Given the presence of the carbon vertices and the above delocalization, the resulting asymmetry in the *ortho*- and *meta*- isomers causes boron vertices most distal from the carbon sites to exhibit strong electron-donating character through induction, similar in magnitude to tertiary alkyl groups.[6] Furthermore, electron delocalization in the cluster results in an inaccessible LUMO, affording B-Y single bond character.

Carboranes functionalized with exopolyhedral chalcogens (Se, Te) at these electron-rich boron-vertices were first reported in the early 1980's,[4d-f] but surprisingly little has been established in terms of understanding the reactivity of these compounds. In previous reports, Zakharkin and coworkers have shown examples of nucleophilic reactivity between caborane-based selenolates or tellurolates with alkyl halides, as well as examples of electrophilic reactivity between carborane-based selenyl (II) reagents and Grignard reagents with no reported electrophilic reactivity of the tellurenyl (II) or tellurenyl (IV) congeners (**Figure 4.2C**).[4d-f] Notably, the reported compounds

have only been characterized by melting point and elemental analysis with no rigorously reported NMR spectroscopy or structural studies. In this work, we report a reactivity map for B(9) functionalized *meta*-carborane, appended with selenium- and tellurium-based functional groups (**Figure 4.3**). Specifically, we show that B(9)-bound *meta*-carboranyl selenyl (II), tellurenyl (II), and tellurenyl (IV) chlorides participate in electrophilic substitution reactions reminiscent to the established reactivity of analogous carbon-based electrophilic chalcogen reagents.[1a] Furthermore, we show the ability of B(9)-bound *meta*-carboranyl selenolates and tellurolates to participate in nucleophilic aromatic substitution reactions as well as the ability of the corresponding tellurol congener to undergo palladium mediated cross-coupling with an aromatic electrophile. For all compounds, we provide full heteronuclear NMR characterization (^{1}H, ^{13}C, ^{11}B, ^{19}F, ^{77}Se, and/or ^{125}Te) in addition to single-crystal X-ray structural characterization for key intermediates studied in this work (**Figure 4.3**). Our findings reveal that the electrophilic and nucleophilic reactivity of selenium- and tellurium-containing *meta*-carboranes is largely analogous to carbon-based reagents.

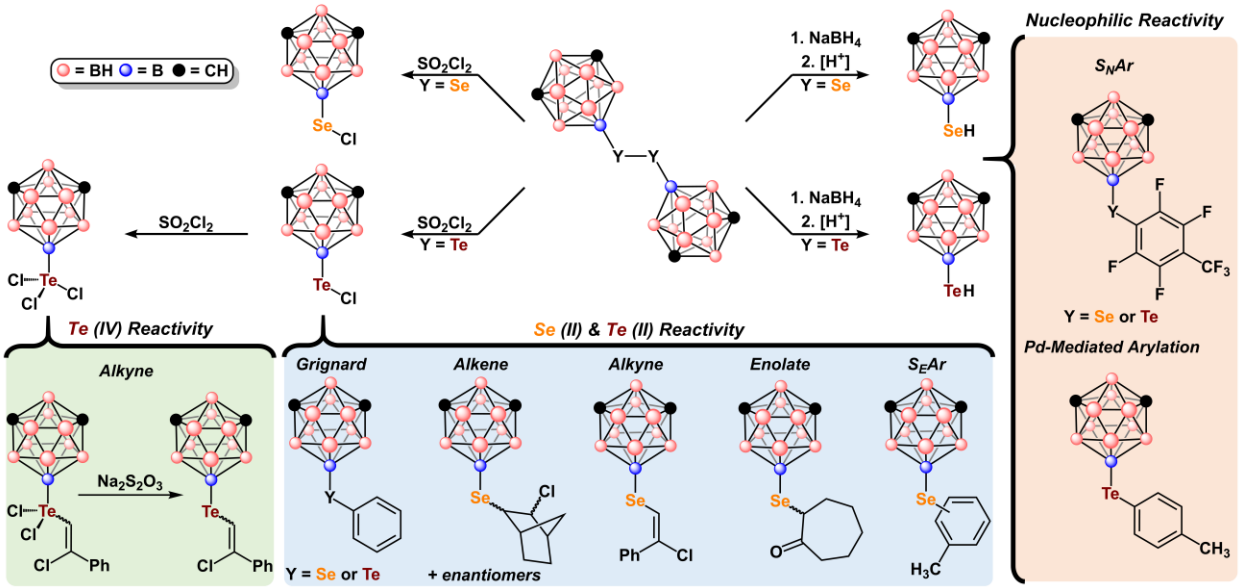

Figure 4.3: This work, overview of compounds synthesized by the electrophilic and nucleophilic reactions of selenium and tellurium-containing *meta*-carboranes.

4.3 Results and Discussion

To ascertain the electrophilic reactivity of these compounds, we first sought to prepare the 9,9'-*meta*-carboranyl diselenide (**1A)** and ditelluride (**1B)** using modified procedures from previous reports (**Figure 4.4**, see Appendix C, sec. 4.6.3).[4d-f,6b] Analytically pure dichalcogenides **1A** and **1B** were isolated *via* silica gel column chromatography as air stable red-orange and dark red solids, respectively (Appendix C, sec. 4.6.3). The isolated dichalcogenides were characterized by heteronuclear NMR spectroscopy (^{1}H, ^{13}C, ^{11}B, ^{77}Se, and/or ^{125}Te), revealing diagnostic resonances consistent with the proposed structural formulations.[4d-f,6b] Single crystals suitable for X-ray crystallography of both dichalcogenides were subsequently grown from layered solutions of dichloromethane and hexanes. The crystallographically derived structures of **1A** and **1B** further corroborate the presence of exopolyhedral B-Y bonds (1.995 Å (Y=Se, **1A**) and 2.215 Å (Y=Te, **1B**) in length respectively) located at the B(9) position of *meta*-carborane (**Figure 4.4A**). The measured Y-Y dichalcogenide bond lengths and torsional angles, 2.338 Å/96.900^{o} (Y=Se, **1A**) and 2.716 Å/95.694 (Y=Te, **1B**) are similar in length to other crystallographically characterized dichalcogenides in addition to torsional angles greater that 90^{o} being consistent with more sterically hindered dichalcogenides.[7]

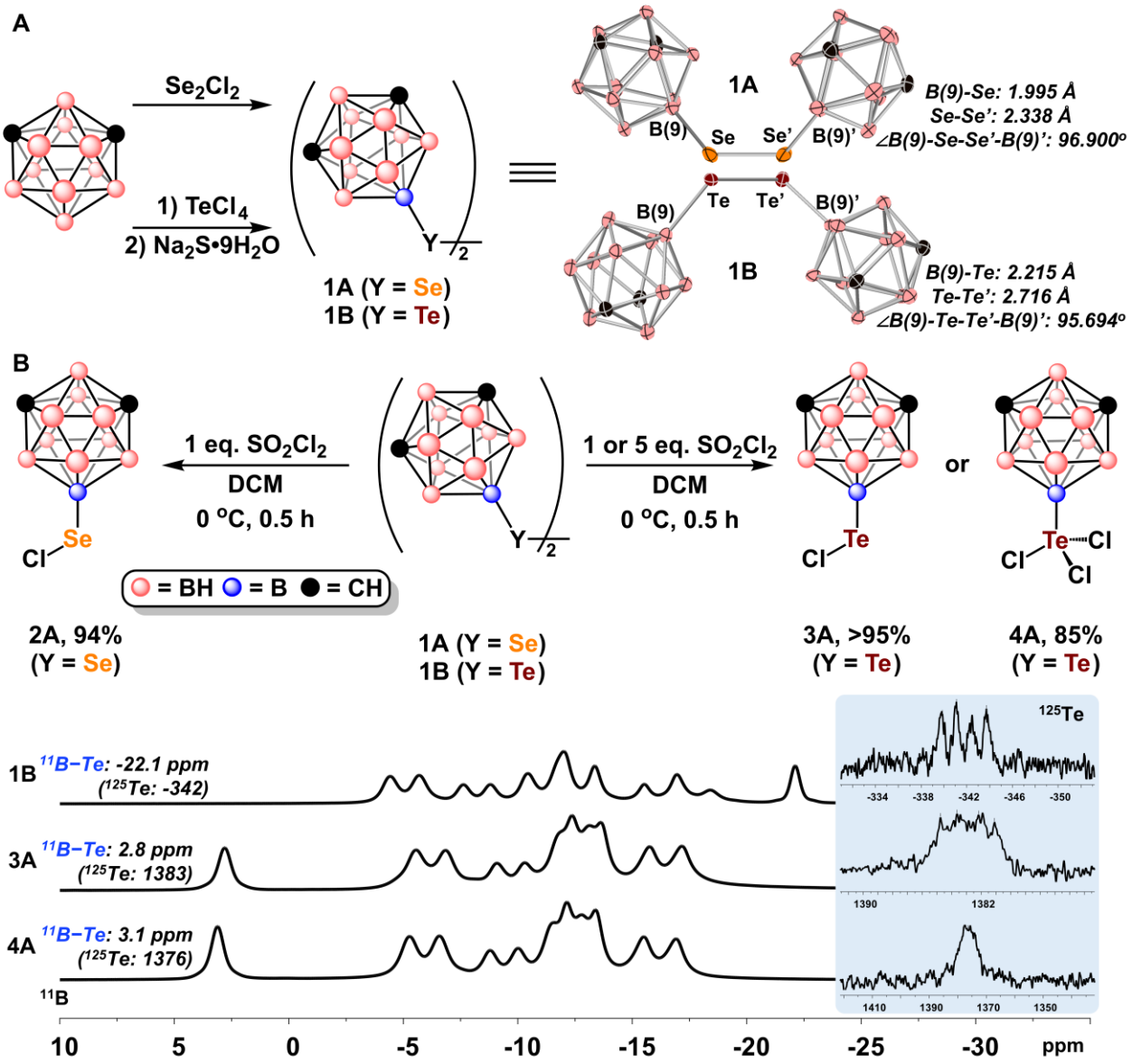

Figure 4.4: **A.** Synthesis of dichalcogenides **1A** and **1B** including their respective crystallographically derived structures. Thermal ellipsoids are drawn at 50% probability, hydrogens are omitted for clarity. **B.** Synthesis of electrophilic selenyl (II), tellurenyl (II), and tellurenyl (IV) reagents **2A**, **3A**, and **4A** from carboranyl dichalcogenides. Comparison of ^{11}B and ^{125}Te NMR for compounds **1B**, **3A**, and **4A**.

1A was then subjected to chlorination by treatment with SO_2Cl_2 in anhydrous dichloromethane at 0 ºC. After stirring the mixture for 30 minutes all volatiles were removed, and NMR spectroscopy revealed full consumption of **1A** as determined by diagnostic downfield shifts in both the ^{11}B and ^{77}Se resonances attributed to the exopolyhedral boron-selenium bond. The observed downfield shifts in signal resonances are consistent with an increase in the oxidation state of the bound selenium and confirms the formation of **2A** (**Figure 4.4B**, Appendix C, sec. 4.6.4). By applying similar chlorination procedures to **1B** with varying equivalencies of SO_2Cl_2, isolation of tellurenyl (II) chloride (**3A)** and tellurenyl (IV) trichloride (**4A)** was accomplished (**Figure 4.4B**, Appendix C, sec. 4.6.3). Like with **2A**, NMR spectroscopy (^{11}B, ^{125}Te) of **3A** and **4A** revealed significant downfield shifts in the ^{11}B and ^{125}Te resonances attributed to the corresponding boron and tellurium nuclei within the exopolyhedral boron-tellurium bond (see **Figure 4.4B** for a comparison of ^{11}B and ^{125}Te NMR spectra for compounds **1B**, **3A**, and **4A**) and are consistent with an increase in oxidation state at tellurium. While the majority of carbon-based selenyl and tellurenyl chlorides are sensitive to moisture, resulting in selenininc or tellurenic acids,[1a] compounds **2A**, **3A**, and **4A** exhibit improved stability and do not show any signs of decomposition when exposed to an atmosphere of laboratory air on a time scale of several months.

The anticipated electrophilicity of **2A** prompted us to explore its reactivity with several common nucleophiles. Thus, **2A** was treated with an excess of phenylmagnesium bromide in anhydrous diethyl ether at room temperature. After stirring for 16 hours, analysis of the reaction mixture by GC-MS indicated quantitative formation of phenyl selenide (**2B**). The resulting product was then isolated in 91% yield after purification *via* silica gel column chromatography and characterized by heteronuclear NMR spectroscopy (**Figure 4.5**, Appendix C, sec. 4.6.5.1). Characterization of **2B** is in agreement with previously reported data of *meta*-carboranyl phenyl

selenide obtained *via* an independent chemical route,[8] and confirms the electrophilic behavior of **2A**. Considering the successful outcome of the reaction between **2A** and a model Grignard reagent, we wanted to assess whether less reactive carbon-based nucleophiles would still undergo transformations with **2A**. Previously, researchers have established the reactivity of selenyl chlorides with unsaturated hydrocarbons and enolates.[1a] As such, norbornene, phenylacetylene, and cycloheptanone were chosen as model compounds potentially susceptible to electrophilic substitution by **2A**.

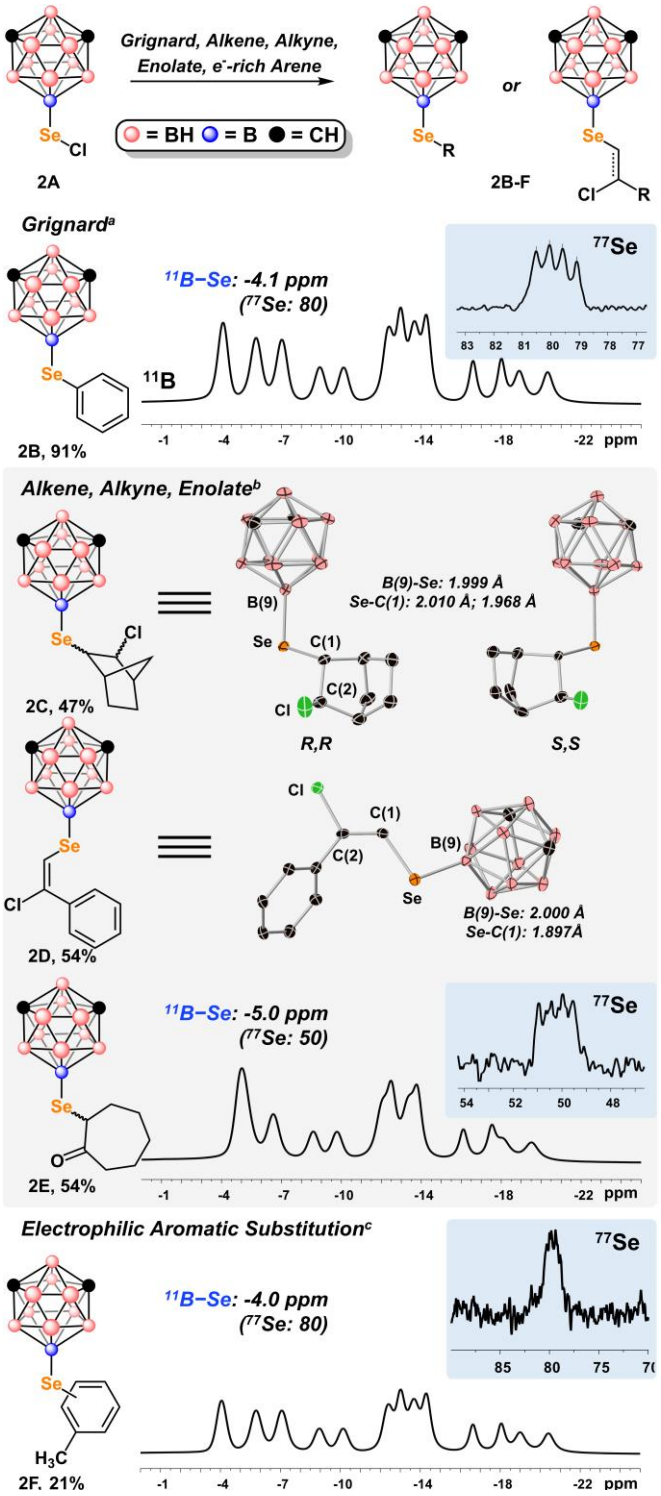

Figure 4.5: Reactions of **2A** with common carbon-based nucleophiles. [a]Reaction was performed in anhydrous diethyl ether under an inert atmosphere at r.t.. [b]Reaction was performed in anhydrous

dichloromethane at r.t.. [c]Reaction was performed in anhydrous toluene with 2 eq. of $AlCl_3$ at 50 ^oC. See SI for full experimental details. Thermal ellipsoids are drawn at 50% probability, hydrogens are omitted for clarity.

A solution of **2A** in anhydrous dichloromethane was treated with norbornene and the progress of the reaction was monitored by GC-MS. After stirring the mixture overnight, GC-MS indicated the presence of two isomers (**2C** and **2C',** *m/z*: 352.10, Appendix C, sec. 4.6.5.2 and 4.6.5.5) approximately in a 1:2 ratio consistent with the anticipated reaction between the electrophilic RSe-Cl fragment in **2A** and the C=C in norbornene, forming a distribution of *endo* and *exo* isomers. Separation of the two isomers *via* silica gel column chromatography proved difficult and thus the products were isolated as a mixture in 47% yield and characterized by heteronuclear NMR spectroscopy. While ^{13}C, ^{11}B, and ^{77}Se NMR spectroscopic data of the isomeric mixture provided little insight on the relationship between **2C** and **2C'**, they confirmed the formation of the anticipated selenium-carbon bond as indicated by the upfield shift in the resonances associated with the exopolyhedral boron-selenium bond. 600 MHz and 400 MHz ^1H NMR spectroscopy was used in an attempt to resolve proton resonances in the alkyl region that would correlate to protons bound to the selenium-bound and chlorine-bound carbons of the norbornene (Appendix C, sec. 4.6.5.4). While there was still difficulty resolving ^1H resonances for individual isomers, the presence of more than just two isomers was evident due to there being multiple unique resonances that integrated together as a single proton, in contrast to the isomer distribution observed by GC-MS. To further understand the substitutional isomers present in the purified product, single crystals suitable for X-ray crystallography were grown from a solution of the isomer mixture in dichloromethane layered with hexanes. The crystallographically derived structure indicated the co-crystallization of enantiomeric **2C'**, revealing the (*R*,*R*) and (*S*,*S*) *exo*-

products (**Figure 4.5**), further confirming the formation of the desired selenium-carbon bond. The measured B(9)-Se and Se-C(1) bond lengths, 1.999 Å and 2.010(*R*,*R*)/1.968(*S*,*S*) Å respectively, are typical of other crystallographically measured boron-selenium and selenium-carbon bonds.[9] Furthermore, when compared more closely to crystallographically studied compounds, the exopolyhedral B-Se bond present in **2C** is notably longer than tri-coordinate boron-selenium bonds (average: 1.940 Å)[9] that would expectedly have partial double-bond character due to the unoccupied *p*-orbital of tri-coordinate boron centers. The length of the exopolyhedral B-Se bond in **2C** more closely parallels reported tetra-coordinate boron-selenium bonds (average: 2.093 Å)[9] with a higher degree of single bond character. All characterization of **2C** and **2C'** suggests the formation of both possible diastereomeric products (*endo* and *exo*), resulting from the addition of **2A** across the double bond within norbornene in addition to their corresponding enantiomers (*R*,*R* and *S*,*S*), producing four isomers in total. When subjecting **2A** to similar reaction conditions in the presence of phenylacetylene or cycloheptanone, compounds **2D** and **2E** (Appendix C, sec. 4.6.5.3), were both coincidentally isolated in 54% yield (**Figure 4.5**). ^{1}H NMR spectroscopy of purified **2D** revealed the exclusive formation of a single isomer due to presence of only one olefinic ^{1}H resonance. Single crystals of **2D** suitable for X-ray crystallography were then grown from a cold (0 ^{o}C) solution of dichloromethane layered with hexanes. The crystallographically derived structure revealed the formation of the *E*-1-SeR-2-Cl-2-Ph isomer (**Figure 4.5**), having resulted from Markovnikov, *anti*-addition of **2A** across the carbon-carbon triple bond in phenylacetylene. The formation of the thermodynamically-favored Markovnikov products from the addition of RSeCl reagents across unsaturated hydrocarbons is expected for this type of process.[1a] In contrast to products **2C** and **2D**, **2E** does not incorporate the chloride of the electrophilic reagent, but still

forms the expected selenium-carbon bond as indicated by ^{11}B and ^{77}Se NMR spectroscopy (**Figure 4.5**).

Beyond reactions of **2A** with alkenes, alkynes, and enolates, we also explored its ability to participate in electrophilic aromatic substitution (S_EAr) with toluene. **2A** was treated with an excess of anhydrous toluene and aluminum chloride to catalyze the transformation at 50 ºC, with the reaction progress monitored by GC-MS. After stirring the mixture overnight, GC-MS indicated the formation of three isomers consistent (**Figure 4.5**) with S_EAr occurring between toluene and **2A**. The crude products were then purified *via* silica gel column chromatography, affording a mixture of aryl selenide isomers (**2F**) in 21% isolated yield. In addition to ^{11}B and ^{77}Se NMR spectroscopy revealing the formation of the desired aryl selenide, ^{1}H NMR spectroscopy also indicates the *para* tolyl isomer as the major component in the isomeric mixture (Appendix C, sec. 4.6.5.3), consistent for S_EAr mechanisms with toluene. Resolving all three isomers by ^{1}H NMR spectroscopy proved to be quite difficult not only due to the low abundance of the *ortho*- and *meta*-isomers, but also the prevalence of ^{1}H resonances attributed to the carborane B-H vertices in the alkyl region. In order to deconvolute the ^{1}H NMR and obtain a more accurate ratio of isomer, the S_EAr between **2A** and toluene was repeated with perdeuterated toluene (Appendix C, sec. 4.6.5.7). ^{2}H NMR spectroscopy of the isolated product clearly revealed the distribution (*para*:*ortho*/*meta*) of isomers to be 89:11, in agreement with the distribution determined by GC-MS.

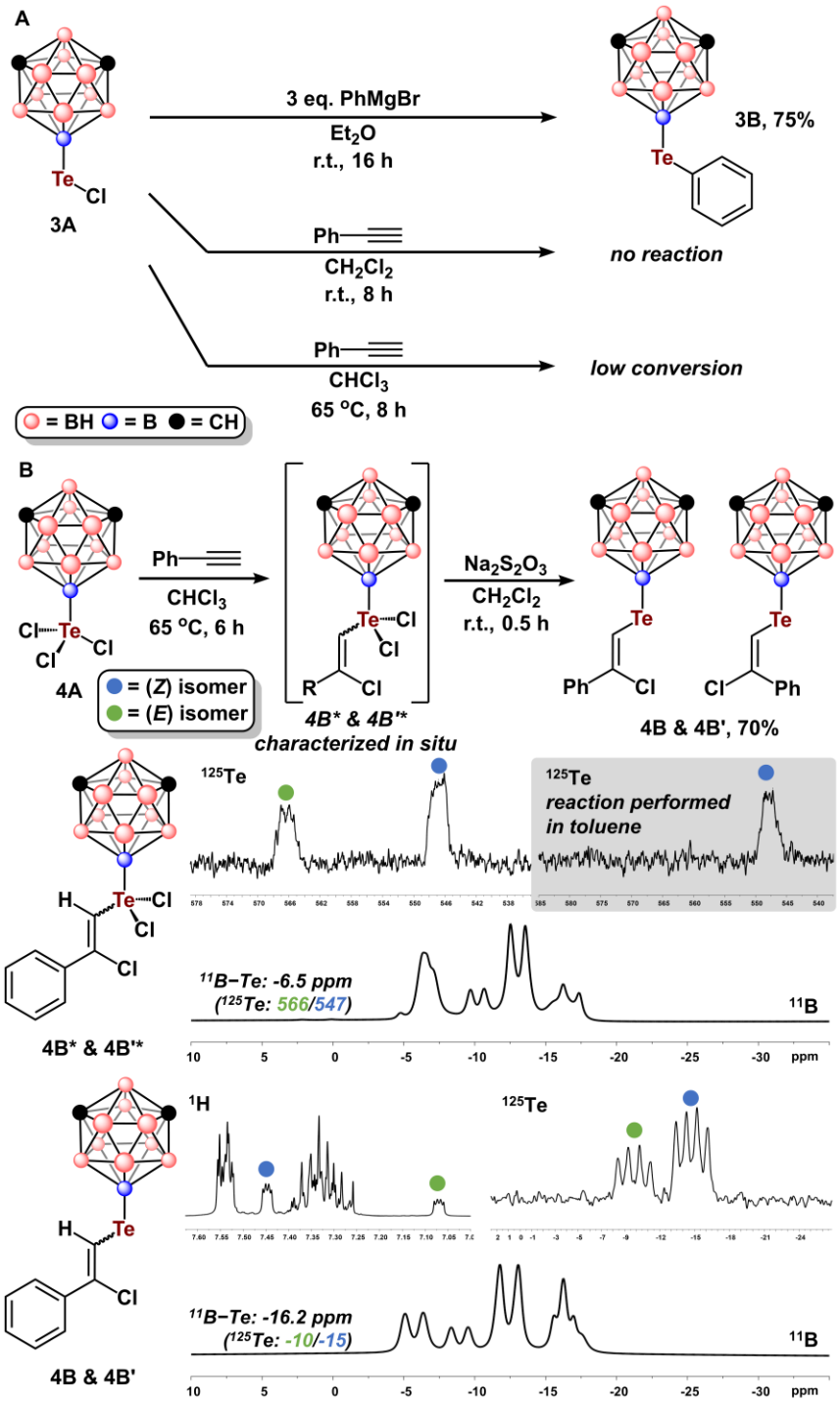

Figure 4.6: **A.** Reaction of **3A** with phenylmagnesium bromide in anhydrous Et_2O and phenylacetylene in various solvents. **B.** Reaction of **4A** with phenylacetylene, including *in situ* ^{11}B and ^{125}Te NMR characterization of reaction intermediates, **4B*** and **4B*'**.

With the electrophilicity of **2A** established, we chose next to explore that of **3A**. First, the reaction of **3A** with phenylmagnesium bromide was assessed to confirm the electrophilic character of **3A**. After addition of the Grignard reagent to form the desired phenyl telluride (**3B)**, the product was isolated *via* silica gel column chromatography in 75% yield (Appendix C, sec. 4.6.6.1). Importantly, the NMR characterization of **3B** agrees with previously reported characterization by our group of *meta*-carboranyl phenyltelluride obtained *via* an independent chemical route (**Figure 4.6A**).[8] We then attempted the reaction of **3A** with phenylacetylene to determine its ability to react with unsaturated hydrocarbons. **3A** was suspended in anhydrous dichloromethane before the addition of phenylacetylene. After stirring the suspension at room temperature for 16 hours, ^{11}B NMR spectroscopy of the reaction mixture revealed only the presence of **3A** and **1B** as a decomposition product (**Figure 4.6A**, Appendix C, sec. 4.6.6.2). In an attempt to improve conversion to the desired telluride, the reaction was attempted in chloroform at reflux temperature. However, after stirring the reaction mixture for 8 hours, conversion to the desired telluride was lower than anticipated (Appendix C, sec. 4.6.6.3) and contained significant quantities of starting material (**3A**) and **1B** as indicated by ^{11}B NMR spectroscopy. We attribute this general decrease in reactivity to a combination of both the inherently lower electronegativity of tellurium and the electron donating ability of *meta*-carborane at the B(9) position,[6] resulting in the diminished electrophilicity of **3A**.

To test our hypothesis, we attempted the reaction between **4A** and phenylacetylene in refluxing chloroform. In contrast to the selectivity of organic selenyl (II) chlorides and **2A** to form products with unsaturated hydrocarbons resulting from Markovnikov *anti*-addition, the preferred substitution mechanisms of organic tellurenyl (IV) trichlorides are much more difficult to predict, due to the possible formation of four-centered intermediates (Markovnikov, *syn* in nonpolar

solvents), three-centered intermediates (Markovnikov, *anti*), or radical-based intermediates.[1a,10] Notably, the reactions of tellurenyl (IV) trichlorides with phenylacetylene have typically afforded Markovnikov *syn*-addition products, consistent with the *in situ* formation of a four-centered intermediate, and selectivity for *syn* over *anti*-addition predicated on the polarity of solvent used for the reaction medium.

To assess the reactivity of **4A**, it was first suspended in chloroform followed by the addition of phenylacetylene. After stirring the white suspension for 6 hours at reflux (65 ^{o}C), a clear, yellow solution remained (Appendix C, sec. 4.6.7.1). *In situ* ^{11}B NMR spectroscopy of the reaction mixture revealed full consumption of **4A** and a diagnostic upfield shift in the resonance attributed to the exopolyhedral boron-tellurium bond (**Figure 4.6B**). This change in resonance chemical shift is consistent with the presence of the key dichlorotelluride intermediate (**4B***), and suggests the formation of the desired tellurium-carbon bond. However, in contrast to the formation of the selenium-containing congener (**2D**), *in situ* ^{125}Te NMR spectroscopy revealed the presence of two tellurium-containing isomers with similar chemical shifts approximately in a 2:1 ratio, attributed to **4B*** and **4B*'** *Z*/*E* isomers. To further understand the reaction mechanism being employed by **4A** in the reaction with phenylacetylene, a series of control reactions were performed to rule out the possible intermediates previously shown to be accessible with tellurenyl (IV) trichlorides *vide supra* (Appendix C, sec. 4.6.7.2 and 4.6.7.3)[1a,10] and probed *via in situ* ^{125}Te NMR spectroscopy. When the reaction was performed in the presence of a radical inhibitor, no significant change in the distribution of **4B*** and **4B*'** was observed, likely ruling out the possibility of a radical-mediated substitution mechanism. However, when the reaction was performed in toluene, a relatively non-polar solvent, **4B*** was formed exclusively with no measurable amount of **4B*'** by ^{125}Te NMR. This selectivity, as influenced by solvent polarity, is reminiscent to the behavior of

four-centered tellurenyl (IV) trichloride intermediates, resulting in selective Markovnikov *syn* addition (**4B***) of **4A** to phenylacetylene when conducting the reaction in toluene and a mixture of four-centered and three-centered tellurenyl (IV) trichloride intermediates forming *syn* (**4B***) and *anti*-addition (**4B*'**) products when in chloroform. The isomeric mixture of **4B*** and **4B*'** was then reduced to the desired telluride (**4B** and **4B'**) by treatment with an aqueous solution of sodium thiosulfate and the progress of the reduction was monitored by TLC. Once the reduction was complete, **4B** and **4B'** were isolated from the crude reaction mixture *via* silica gel column chromatography as a mixture of Z/E isomers in 70% yield and characterized by heteronuclear NMR spectroscopy to confirm the formation of the desired tellurium-carbon bond. ^{1}H and ^{125}Te NMR spectroscopy revealed the isolation of two distinct isomers, **4B** and **4B'** in approximately a 2:1 ratio (**Figure 4.6B**, Appendix C, sec. 4.6.7.1). Two broad quartet resonances in the ^{1}H aromatic region (7.45 and 7.07 ppm) are attributed to the olefinic ^{1}H's and are used to determine the isomer distribution. Furthermore, ^{125}Te NMR spectroscopy revealed two ^{125}Te resonances at -10 and -15 ppm, with approximate relative intensities of 1:2, respectively, and agrees with the distribution observed by ^{1}H NMR (**Figure 4.6B**, Appendix C, sec. 4.6.7.1). This additional isomer is likely attributed to the formation of *E*-1-TeR-2-Ph-2-Cl (R: *meta*-carboranyl) as the minor product that was enabled by the increased polarity of the reaction solvent. This minor product is produced from a portion of **4A** reacting with phenylacetylene through a three-centered intermediate, similar to the substitution mechanism employed by **2A**.

In summary, the assessment of electrophilic behavior for *meta*-carboranyl selenyl (II), tellurenyl (II), and tellurenyl (IV) chlorides reveal that their reactivity is reminiscent to carbon-based reagents. **2A** reacts with Grignard reagents, alkenes, alkynes, enolates, and electron-rich aromatics to form products that would generally be expected for organic selenyl chlorides. Despite,

the electron-donating ability of the B(9) position to which the selenyl (II) chloride in **2A** is appended to, no deleterious effects to the overall electrophilic reactivity of **2A** are observed. In contrast, the electrophilic reactivity of the tellurenyl (II) chloride **3A** is significantly dampened, only showing good reactivity with Grignard reagents. To enhance the electrophilic reactivity, the tellurenyl (IV) chloride **4A** was studied. An increase in oxidation state at tellurium significantly enhanced the electrophilic reactivity causing it to react more readily with terminal alkynes. The regioselective and stereoselective behavior of **4A** when reacting with terminal alkynes in various solvents closely parallels the behavior of organic tellurenyl (IV) chlorides, forming either the *syn* or *anti*-addition products as a function of solvent polarity.

With the electrophilicity of **2A**, **3A**, and **4A** established, we proceeded to expand the nucleophilic substitution chemistry available with selenium and tellurium-containing *meta*-carboranes. The ability of *meta*-carborane-based selenolates and tellurolates to participate in S_N2 substitution mechanisms with alkyl halides is well established.[4d,f] However, their ability to participate in S_NAr substitution mechanisms is not known. To further understand the nucleophilic behavior of boron-bound selenium and tellurium-containing carboranes, we prepared the 9-*meta*-carboranyl selenol (**5A**) and tellurol (**6A**). We envisioned that these compounds, upon deprotonation, would act as precursors to the corresponding nucleophilic chalcogenolates. Selenol (**5A**), was synthesized according to previously reported methods and its spectroscopic characterization is in agreement to the proposed formulation (Appendix C, sec. 4.6.8.1).[4d,6b] While the boron-bound tellurol (**6A**) has not been reported previously, we were able to successfully synthesize **6A** using modified reduction procedures (Appendix C, sec. 4.6.9.1). **6A** is isolated in 67% yield as a colorless, odorless, air sensitive solid that nevertheless can be handled in air for short periods of time (~10 minutes) without significant decomposition. In contrast to all other

known carborane chalcogenols, **6A** is light sensitive and reverts to the ditelluride (**1B**) when exposed to ambient light, even when stored in a nitrogen-filled glovebox. The ^{1}H and ^{125}Te resonances measured by NMR spectroscopy, -7.15 ppm and -596.5 ppm respectively, are indicative of the exceedingly electron-rich environment experienced by the tellurol from the B(9) *meta*-carboranyl susbstituent and are consistent with other reported sterically hindered electron-rich tellurols.[11] This is the first reported synthesis of an isolable carboranyl tellurol, and is a rare example of an isolable tellurol.

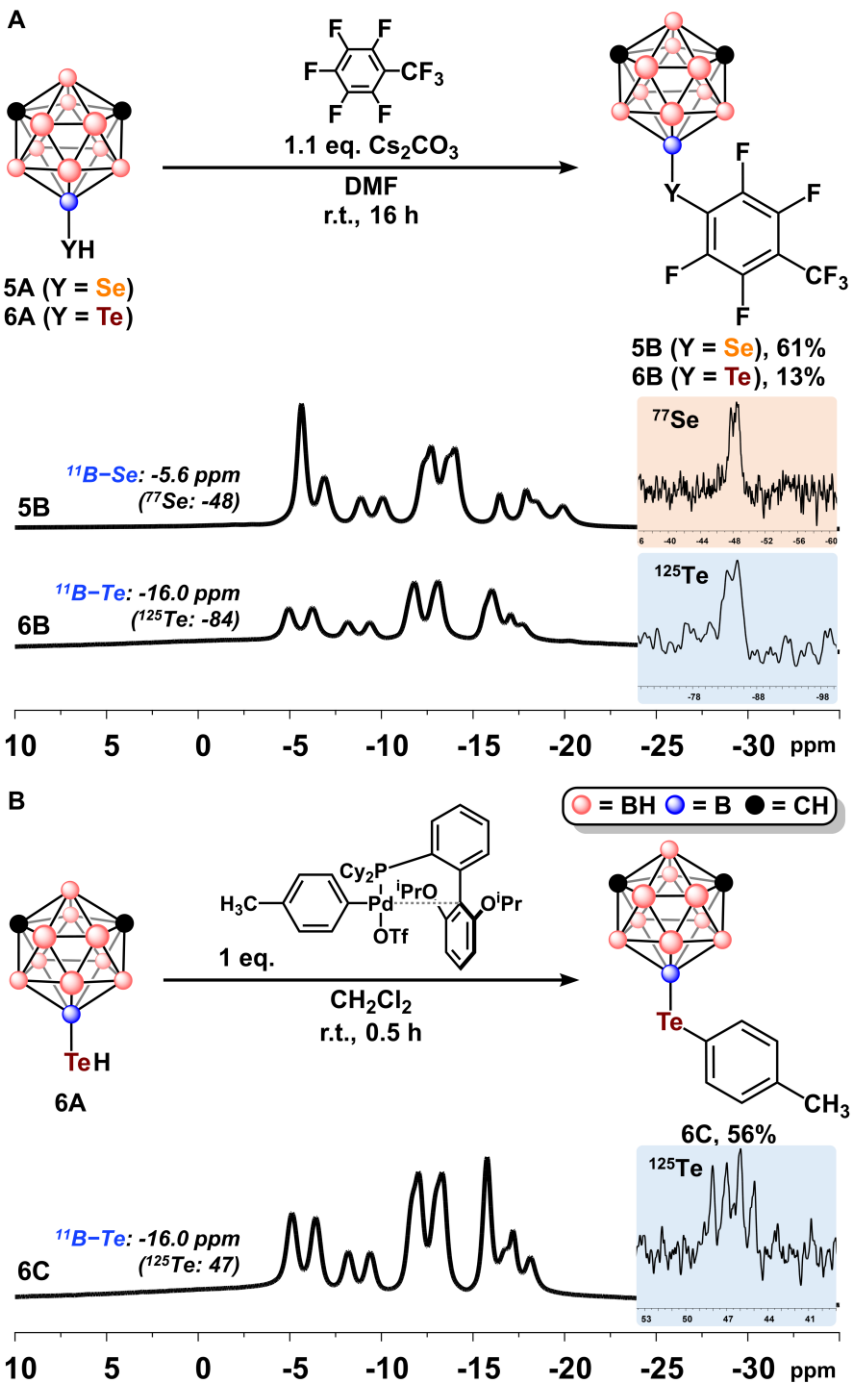

Figure 4.7: **A.** S_NAr of **5A** and **6A** with perfluorotoluene. ^{77}Se and ^{125}Te NMR of **5B** and **6B**. **B.** Reaction of **6A** with palladium oxidative addition complex.

S_NAr with the *meta*-carboranyl chalcogenolates was first attempted with **5A** by deprotonating the selenol with Cs_2CO_3 in dimethylformamide (Appendix C, sec. 4.6.8.2). Perfluorotoluene was then introduced to the mixture as the electrophilic substrate to initiate S_NAr with the *in situ* generated selenolate. After stirring the mixture overnight, GC-MS indicated full conversion to a single isomer with an *m/z* (223.20) consistent with the formation of the desired aryl selenide (**5B**). The compound was subsequently purified from the crude reaction mixture *via* silica gel column chromatography in 61% isolated yield and characterized by NMR spectroscopy. ^{19}F NMR revealed a diagnostic resonance pattern consistent with mono-substituted perfluorotoluene in the *para*- position and is in agreement with the proposed structure formulation. Furthermore, ^{77}Se NMR showed a downfield shift in the resonance attributed to the exopolyhedral boron-selenium bond found in **5B**, and is consistent with the formation of an aryl selenide (**Figure 4.7A**). S_NAr was then attempted with the tellurol (**6A**) using similar conditions, though taking additional precautions to limit exposure to light and oxygen (Appendix C, sec. 4.6.9.2). Following similar isolation procedures to **5B**, the desired aryl telluride (**6B**) was isolated in small yield (13%), sufficient for full characterization by NMR spectroscopy. Due to the general instability of the *in situ* generated tellurolate under the reaction conditions, ditelluride (**1B**) was a major byproduct formed during the reaction between **6A** and perfluorotoluene (Appendix C, sec. 4.6.9.4).

To study the reactivity of **6A** further with more electron-rich aryl-based electrophiles, we attempted arylation with a stochiometric palladium-based oxidative addition complex. These oxidative addition complexes are typically used stoichiometrically for the arylation of sensitive substrates due to their high degree of selectivity for chalcogenols and ease of preparation.[12] A solution of **6A** in dichloromethane was prepared in a dark, nitrogen filled glovebox without the addition of base to avoid incompatibilities of the tellurolate with the oxidative addition complex

(Appendix C, sec. 4.6.9.3). Subsequently, [4-tolyl-PdRuPhos][OTf] (**Figure 4.7B**) was added and the reaction progress was monitored by GC-MS. After 30 minutes, GC-MS indicated the formation of a compound with an *m/z* of 363.20, suggesting the formation of the desired tolyl telluride (**6C**). **6C** was isolated from the crude reaction mixture *via* silica gel column chromatography in 56% yield and characterized by NMR spectroscopy. ^{125}Te NMR revealed a resonance with a chemical shift of 46.5 ppm, similar to that of **3A** (**Figure 4.6, 4.7B**). Overall, these studies indicate that B(9) *meta*-carboranyl selenolate and tellurolate can be competent nucleophiles and are able to participate in S_NAr and Pd-mediated arylation processes, leading to the formation of selenoether and telluroether moieties with B-Y-C connectivity.

4.4 Conclusion

In conclusion, B(9)-connected *meta*-carboranyl selenyl and tellurenyl reagents have been shown to participate in electrophilic substitution reactions with unsaturated hydrocarbons, including alkenes, alkynes, enolates, and aromatic substrates; reminiscent to other electrophilic organochalcogen compounds. We further show the first examples of nucleophilic aromatic substitution with carborane selenolates and tellurolates as well as the first use of palladium-based oxidative addition complexes for the arylation of a free tellurol. All formed products contained the unique B-Se-C or B-Te-C bonding motifs and are stable in air despite the exceedingly electron-rich environment experienced by either the selenium or tellurium nucleus as suggested by the ^{77}Se and ^{125}Te NMR spectroscopic experiments. The reactivity map developed in this work serves as an expansion of available modification reactions for carboranes and other polyhedral boron clusters containing C- or B-connected exopolyhedral heteroatom substituents,[13] as well as

benchmarks similarities and differences in terms of reactivity and stability with the fundamental chemistry of electron-rich chalcogen-containing molecules.[1a,10,11,14]

4.5 References for Chapter 4

(1) (a) Rappaport, Z. *The Chemistry of Organic Selenium and Tellurium Compounds*; John Wiley & Sons: New York, 2013; Vol. *4* (b) Block, E.; Glass, R. S.; Gruhn, N.; Jin, J.; Lorance, E.; Zakai, U. I.; Zhang, S.-Z. Chemistry of Mixed Sulfur-, Selenium-, or Tellurium- and Silicon, or Tin-Containing Heterocycles. *Phosphorus, Sulfur, and Silicon and the Related Elements* **2008** 183, 4, 856-862. (c) Kumar, S.; Helt, J.-C. P.; Autschbach, J.; Detty, M. R. A New Reaction of Organoselenium Compounds: Alkyl Transfer from Diorganoselenium(IV) Dibromides to Give Alkenoic Acids to Give γ- and δ-Lactones. *Organometallics* **2009**, 28, 12, 3426-3436. (d) Evans, D. H.; Gruhn, N. E.; Jin, J.; Li, B.; Lorance, E.; Okumara, N.; Macías-Ruvalcaba, N. A.; Zakai, U. I.; Zhang, S.-Z.; Block, E.; Glass, R. S. Electrochemical and Chemical Oxidation of Dithia-, Diselena-, Ditellura-, Selenathia-, and Tellurathiamesocycles and the Stability of Oxidized Species. *J. Org. Chem.* **2010**, 74, 6, 1997-2009. (e) Garrett, G. E.; Gibson, G. L.; Straus, R. N.; Seferos, D. S.; Taylor, M. S. Chalcogen Bonding in Solution: Interactions of Benzotelluradiazoles with Anionic and Uncharged Lewis Bases. *J. Am. Chem. Soc.* **2015**, 137, 12, 4126-4133. (f) Zhou, B.; Gabbai, F. P. Lewis Acidic Telluronium Cations: Enhanced Chalcogen-Bond Donor Properties and Application to Transfer Hydrogenation Catalysis. *Organometallics* **2021** DOI: 10.1021/cas.organomet.1c00279. (g) Lin, T.-P.; Gabbai, F. P. Two-Electron Redox Chemistry at the Dinuclear Core of a TePt Platform: Chlorine Photoreductive Elimination and Isolation of a $Te^{V}Pt^{I}$ Complex. *J. Am. Chem. Soc.* **2012**, 134, 29, 12230-12238. (h) Lin, T.-P.; Gabbai, F. P. Telluronium Ions as σ-Acceptor Ligands. *Angew. Chem. Int. Ed.* **2013**, 52, 14, 3864-3868. (i) Yang, H.; Lin, T.-P.; Gabbai, F. P. Telluroether to Telluroxide Conversion in the Coordination

Sphere of a Metal: Oxidation-Induced Umpolung of a Te-Au Bond. *Organometallics* **2014**, 33, 17, 4368-4373. (j) Kryman, M. W.; Nasca, J. N.; Watson, D. F.; Detty, M. R. Selenorhodamine Dye-Sensitized Solar Cells: Influence of Structure and Surface-Anchoring Mode on Aggregation, Persistence, and Photochemical Performance. *Langmuir* **2016**, 32, 6, 1521-1532. (k) Ye, S.; Jansaz, L.; Zajaczkowski, W.; Manion, J. G.; Mondal, A.; Marszalek, T.; Andrienko, D.; Müllen, K.; Pisula, W.; Seferos, D. S. Self-Organization and Charge Transport Properties of Selenium and Tellurium Analogues of Polythiophene. *Macromol. Rapid Commun.* **2019**, 40, 1, 1800596. (l) Scholes, D. T.; Yee, P. Y.; McKeown, G. R.; Li, S.; Kang, H.; Lindemuth, J. R.; Xia, X.; King, S. C.; Seferos, D. S.; Tolbert, S. H.; Schwartz, B. J. Designing Conjugated Polymers for Molecular Doping: The Roles of Crystallinity, Swelling, and Conductivity in Sequentially-Doped Selenophene-Based Copolymers. *Chem. Mater.* **2019**, 31, 1, 73-82. (m) Manion, J. G.; Panchuk, J. R.; Seferos, D. S. Applying Heteroatom Substitution in Organic Photovoltaics. *Chem. Rec.* **2019**, 19, 6, 1113-1122. (n) Hicks, G. E. J.; Jarrett-Wilkins, C. N.; Panchuk, J. R.; Manion, J. G.; Seferos, D. S. Oxidation promoted self-assembly of π-conjugated polymers. *Chem. Sci.* **2020**, 11, 6383. (o) Kryman, M. W.; Schamerhorn, G. A.; Yung, K.; Sathyamoorthy, B.; Sukumaran, D. K.; Ohulchanskyy, T. Y.; Benedeict, J. B.; Detty, M. R. Organotellurium Fluorescence Probes for Redox Reactions: 9-Aryl-3,6-diaminotelluroxanthylium Dyes and Their Telluroxides. *Organometallics* **2013**, 32, 15, 4321-4333. (p) Stockett, M. H.; Kjær, C.; Linder, M. K.; Detty, M. R.; Nielsen, S. B. Luminescence spectroscopy of chalcogen substituted rhodamine cation *in vacuo*. *Photochem. Photobiol. Sci.* **2017**, 16, 779-784. (q) Carrera, E. I.; Seferos, D. S. Ring Opening of π-delocalized 2,5-Diphenyltelurophene by Chemical or Self-Sensitized Aerobic Photooxidation. *Organometallics* **2017**, 36, 14, 2612-2621. (r) Lutkus, L. V.; Rettig, I. D.; Davies, K. S.; Hill, J. E.; Lohman, J. E.; Eskew, M. W.; Detty, M. R.; McCormick, T. M. Photocatalytic Aerobic Thiol

Oxidation with a Self-Sensitized Tellurorhodamine Chromophore. *Organometallics* **2017**, 36, 14, 2588-2596. (s) Drummond, B. H.; Hoover, G. C.; Gillet, A. J.; Aizawa, N.; Myers, W. K.; McAllister, B. T.; Jones, S. T. E.; Pu, Y.-J.; Credgington, D.; Seferos, D. S. Selenium Susbtitution Enhances Reverse Intersystem Crossing in a Delayed Fluorescence Emitter. *J. Phys. Chem. C* **2020**, 124, 6364-6370. (t) Cao, W.; McCallum, N. C.; Ni, Q. Z.; Li, W.; Boyce, H.; Mao, H.; Zhou, X.; Sun, H.; Thompson, M. P.; Battistela, C.; Wasielewski, M. R.; Dhinojwala, A.; Shawkey, M. D.; Burkhart, M. D.; Wang, Z.; Gianneschi, N. C. Selenomelanin: An Abiotic Selenium Analogue of Pheomelanin. *J. Am. Chem. Soc.* **2020**, 142, 29, 12802-12810. (u) Glass, R. B.; Berry, M. J.; Block, E.; Boakye, H. T.; Carlson, B. A.; Gailer, J.; George, G. N.; Gladyshev, V. N.; Hatfield, D. L.; Jacobsen, N. E.; Johnson, S.; Kahakachchi, C.; Kamiński, R.; Manley, S. A.; Mix, H.; Pickering, I. J.; Prenner, E. J.; Saira, K.; Skowrońska, A.; Tyson, J. F.; Uden, P. C; Wu, Q.; Xu, X.-M.; Yamdagni, R.; Zhang, Y. Insights into the Chemical Biology of Selenium. *Phosphorus, Sulfur, and Silicon and the Related Elements* **2008**, 183, 4, 924-930. (v) Block, E.; Booker, S. J.; Flores-Penalba, S.; George, G.; Gundala, G.; Landgraf, B. J.; Liu, J.; Lodge, S. N.; Pushie, M. J.; Rozovsky, S.; Vattekkatte, A.; Yaghi, R.; Zeng, H. Trifluoroselenomethionine – a New Non-Natural Amino Acid. *ChemBioChem* **2016**, 17, 18, 1738-1751. (w) Zhao, Z.; Shimon, D.; Metanis, N. Chemoselective Copper-Mediated Modification of Selenosysteines in Peptides and Proteins. *J. Am. Chem. Soc.* **2021**, 143, 12817-12824.

(2) (a) Wentz, K. E.; Molino, A.; Weisflog, S. L.; Kaur, A.; Dickie, D. A.; Wilson, D. D.; Gilliard, R. J. Stabilization of the Elusive 9-Carbene-9-Borafluorene Monoanion. *Angew. Chem. Int. Ed.* **2021**, 60, 23, 13065-13072. (b) Clive, D. L. J.; Menchen, S. M. Conversion of Aldehydes and Ketones into Selenoacetals: Use of Tris(phenylseleno)borane and Tris(methylseleno)borane. *J. Org. Chem.* **1979**, 44, 24, 4279-4285. (c) Dolati, H.; Denker, L.; Trzaskowski, B.; Frank, R.

Superseeding β-Diketiminato Ligands: An Amido Imidazoline-2-Imine Ligand Stabilizes the Exhaustive Series of B=X Boranes (X=O, S, Se, Te). *Angew. Chem. Int. Ed.* **2020**, 60, 9, 4633-4639. (d) Köster, R.; Seidel, G.; Yalpani, M.; Siebert, W.; Gangus, B. 1,5-Cyclooctanediboryl Selenides. *Inorganic Synthesis* **1992**, 29, 70-77. (e) Männig, D.; Narula, C. K.; Nöth, H.; Wietelmann, U. Beiträge zur Chemie des Bors, 159. [2 + 2]-Cycloadditionen von (*tert*-Butylimino)(2,2,6,6-tetramethylpiperdino)boran mit Kohlenstoffdichalkogeniden. *Chem. Ber.* **1985**, 118, 9, 3748-3758. (f) Yalpani, M.; Köster, R.; Boese, R. Nitrogen Base – Dialkyl-1,2,4,3,5-triselenadiborolanes. *Chem. Ber.* **1990**, 123, 4, 707-712. (g) Köuster, R.; Seidel, G.; Schüuβler, W.; Wrackmeyer, B. Die ersten Organobor-Tellur-Verbindungen. *Chem. Ber.* **1995**, 128, 1, 87-89. (h) Liu, S.; Légaré, M.-A.; Auerhammer, D.; Hofmann, A.; Braunschweig, H. The First Boron-Tellurium Double Bond: Direct Insertion of Heavy Chalcogens into a Mn=B Double Bond. *Angew. Chem. Int. Ed.* **2017**, 56, 49, 15760-15763. (i) Liu, S.; Légaré, M.-A.; Hofmann, A.; Rempel, A.; Hagspiel, S.; Braunschweig, H. Synthesis of unsymmetrical B_2E_2 and B_2E_3 heterocycles by borylene insertion into boradichalcogeniranes. *Chem. Sci.* **2019**, 10, 4662-4666. (j) Liu, S.; Légaré, M.-A.; Hofmann, A.; Braunschweig, H. A Boradiselenirane and a Boraditellurirane: Isolable Heavy Analogs of Dioxiranes and Dithiiranes. *J. Am. Chem. Soc.* **2018**, 140, 36, 11223-11226. (k) Joseph, B.; Gomosta, S.; Prakash, T.; Phukan, A. K.; Ghosh, S. Chalcogen Stabalized bis-Hydridoborate Complexes of Cobalt: Analogues of Tetracyclo[4.3.0.$0^{2,4}$.$0^{3,5}$]nonane. *Chem. Eur. J.* **2020**, 26, 70, 16824-16832. (l) Ramalalshmi, R.; Saha, K.; Roy, D. K.; Varghese, B.; Phukan, A. K.; Ghosh, S. New Routes to a Series of σ-Borane/Borate Complexes of Molybdenum and Ruthenium. *Chem. Eur. J.* **2015**, 21, 48, 17191-17195. (m) Okio, C. K. Y. A.; Levason, W.; Monzittu, F. M.; Reid, G. Complexes of BX_3 with EMe_2 (X = F, Cl, Br, I; E = Se or Te): Synthesis, multinuclear NMR spectroscopic and structural studies. *J. Organomet. Chem.* **2017**, 848, 232-238.

(n) Okio, C. K. Y. A.; Levason, W.; Monzittu, F. M.; Reid, G. Systematics of boron halide complexes with dichalcogenoether ligands – Synthesis, structures, and reaction chemistry. *J. Organomet. Chem.* **2018**, 854, 140-149. (o) Tokoro, Y.; Nagai, A. Kokado, K. Chujo, Y. Synthesis of Organoboron Quinoline-8-thiolate and Quinoline-8-selenolate Complexes and Their Incorporation into the π-Conjugated Polymer Main-Chain. *Macromolecules* **2009**, 42, 8, 2988-2993. (p) Grotthuss, E.; Nawa, F.; Bolte, M.; Lerner, H.-W.; Wagner, M. Chalcogen-chalcogen-bond activation by an ambiphilic, doubly reduced organoborane. *Tetrahedron* **2019**, 75, 1, 26-30. (q) Braunschweig, H.; Constantinidis, P.; Dellermann, T.; Ewing, W. C.; Fischer, I.; Hess, M.; Knight, F. R.; Rempel, A.; Schneider, C.; Ullrich, S.; Vargas, A.; Woollins, J. D. Highly Strained Heterocycles Constructed from Boron-Boron Multiple Bonds and Heavy Chalcogens. *Angew. Chem. Int. Ed.* **2016**, 55, 18, 5606-5609. (r) Geetharani, K.; Bose, S. K.; Basak, D.; Suresh, V. M.; Ghosh, S. A new entry into ferraborane chemistry: Synthesis and characterization of heteroferraborane complexes. *Inorganica Chim. Acta* **2011**, 372, 42-46.

(3) (a) Chakrahari, K. K. V.; Thakur, A.; Mondal, B.; Dhayal R. S.; Ramkumar, V.; Ghosh, S. A close-packed boron-rich 11-vertex molybdaborane with novel geometry. *J. Organomet. Chem.* **2012**, 710, 75-79. (b) Mondal, B.; Bhattacharyya, M.; Varghese, B.; Ghosh, S. Hypo-electronic triple-decker sandwich complexes: synthesis and structural characterization of $[(Cp^*Mo)_2\{\mu\text{-}\eta^6\text{:}\eta^6\text{-}B_4H_4E\text{-}Ru(CO)_3\}]$ (E = S, Se, Te or $Ru(CO)_3$ and $Cp^* = \eta^5\text{-}C_5Me_5$). *Dalton Trans.* **2016**, 45, 10999-11007. (c) Roy, D. K.; Bose, S. K.; Geetharani, K.; Chakrahari, K. K. V.; Mobin, S. M.; Ghosh, S. Synthesis and Structural Characterization of New Divanada- and Diniobaboranes Containing Chalcogen Atoms. *Chem. Eur. J.* **2012**, 18, 32, 9983-9991. (d) Chakrahari, K. K.; Thakur, A.; Mondal, B.; Ramkumar, V.; Ghosh, S. Hypoelectronic Dimetallaheteroboranes of Group 6 Transition Metals Containing Heavier Chalcogen Elements. *Inorg. Chem.* **2013**, 52, 14,

7923-7932. (e) Kultyshev, R. G.; Liu, S.; Leung, H. T.; Liu, J.; Shore, S. G. Synthesis of Mono- and Dihalogenated Derivatives of $(Me_2S)_2B_{12}H_{10}$ and Palladium-Catalyzed Boron-Carbon Cross-Coupling Reactions of the Iodides with Grignard Reagents. *Inorg. Chem.* **2003**, 42, 10, 3199-3207. (f) Paetzold, P.; Englert, U.; Hansen, H.-P.; Meyer, F.; Leuschner, E. 11-Vertex *arachno*-Clusters with an NB_{10}, SNB_9, and $SeNB_9$ Skeleton. *Z. Anorg. Allg. Chem.* **2001**, 627, 3, 498-506. (g) di Biani, F. F.; Laschi, F.; Zanello, P.; Ferguson, G.; Trotter, J.; O'Riordan, G. M.; Spalding, T. R. Synthesis, structure, spectroscopic and electrochemical study of the paramagnetic compound [2-(η^7-C_7H_7)-7,11-F_2-2,1-*closo*-$MoTeB_{10}H_8$]. *J. Chem. Soc., Dalton Trans.* **2001**, 1520-1523. (h) Ferguson, G.; Gallagher, J. F.; Kenedy, J. D.; Kelleher, A.-M.; Spalding, T. R. Pentahapto-bonded gold heteroborane clusters [3-(R_3P)-*closo*-2,1-$AuTeB_{10}H_{10}]^-$ and [3-(R_3P)-*closo*-3,1,2-$AuAs_2B_9H_9]^-$. *Dalton Trans.* **2006**, 2133-2139. (i) Faridoon, McGarth, M.; Spalding, T. R.; Fontaine, X. L. R.; Kennedy, J. D.; Thorton-Pett, M. Metallaheteroborane Chemistry. Part 6. Synthesis of *closo*-[2-(η-ligand)-1,2-$TeMB_{10}H_{10}$] Complexes with M(η-ligand) = Rh(η^5-C_5Me_5) (1), Ru(η^6-*p*-$MeC_6H_4Pr^i$) (2), Ru(η^6-C_6Me_6) (3), and of *nido*-[6-(η^6-C_6Me_6)-8-(OEt)-6-RuB_9H_{12}] (4), their Characterisation by Nuclear Magnetic Resonance Spectroscopy and, for (1) and (3), by X-Ray Crystallography. *J. Chem. Soc., Dalton Trans.* **1990**, 1819-1829.

(4) (a) Zakharkin, L. I.; Pisareva, I. V. A New Simple Method for the Production and Some Conversions of B-S Bond-Containing *o*- and *m*-Carboranyl. *Phosphorus and Sulfur* **1984**, 20, 357-370. (b) Chen, M.; Zhao, D.; Xu, J.; Li, C.; Lu, C.; Yan, H. Electrooxidative B-H Functionalization of *nido*-Carboranes. *Angew. Chem. Int. Ed.* **2021**, 60, 14, 7838-7844. (c) Chen, Y.; Quan, Y.; Xie, Z. 8-Aminoquinoline as a bidentate traceless directing group for Cu-catalyzed selective B(4,5)-H disulfenylation of *o*-carboranes. *Chem. Comm.* **2020**, 56, 12997-13000. (d) Zakharkin, L. I.; Pisareva, I. V.; Antonovich, V. A. Synthesis of Di(*o*- and *m*-Carboran-9-yl) Diselenides by

Electrophilic-Substitution Reactions of *o*- and *m*-Carboranes with Selenium Chlorides Under the Action of $AlCl_3$, and Reactions of These Products. *Zhurnal Obshchei Khimii* **1986**, 56, 12, 2721-2728. (e) Zakharkin, L. I.; Pisareva, I. V. Electrophilic Telluration of *o*- and *m*-Carboranes with $TeCl_4$ Under the Action of $AlCl_3$. *Izvestiya Akademii Nauk, Seriya Khimicheskaya* **1984**, 2, 472-473. (f) Zakharkin, L. I.; Pisareva, I. V. Synthesis and Some Conversions of Derivatives of *o*- and *m*-Carborane Containing a B-Te σ Bond. *Izvestiya Akademii Nauk SSSR* **1987**, 4, 877-880. (g) Olid, D.; Núñez, R.; Viñas, C.; Teixidor, F. Methods to produce B-C, B-P, B-N and B-S bonds in boron clusters. *Chem. Soc. Rev.* **2013**, 42, 3318– 3336

(5) For a general review of carboranes, see: Grimes, R. N. *Carboranes*, 3rd ed; Elsevier: Oxford, 2016.

(6) (a) Hohman, J. N.; Zhang, P. P.; Morin, E. I.; Han, P.; Kim, M. H.; Kurland, A. R.; McClanahan, P. D.; Balema, V. P.; Weiss, P.S. Self-Assembly of Carboranethiol Isomers on Au[111]: Intermolecular Interactions Determined by Molecular Dipole Orientations. *ACS Nano* **2009**, 3, 527. (b) Spokoyny, A. M.; Machan, C. W.; Clingerman, D. J.; Rosen, M. S.; Wiester, M. J.; Kenedy, R. D.; Stern, C. L.; Sarjeant, A. A.; Mirkin, C. A. A coordination chemistry dichotomy for icosahedral carborane-based ligands. *Nat. Chem.* **2011**, 3, 590-596. (c) Serino, A. C.; Anderson, M. E.; Saleh, L. M. A.; Dziedzic, R. M.; Mills, H.; Heidenreich, L. K.; Spokoyny, A. M.; Weiss, P.S. Work Function Control of Germanium through Carborane-Carboxylic Acid Surface Passivation. *ACS Appl. Mater. Interfaces* **2017**, 9, 34592-34596.

(7) Search was performed using Mogul 1.8.4, provided by the CCDC. Ph-Se-Se-Ph was drawn in the search window and analysis of all fragments was conducted.

(8) Mills, H. A.; Martin, J. L.; Rheingold, A. L.; Spokoyny, A. M. Oxidative Generation of Boron-Centered Radicals in Carboranes. *J Am. Chem. Soc.* **2020**, 142, 10, 4586-4591.

(9) Search was performed using Mogul 1.8.4 and/or ConQuest 2.0.4, provided by the CCDC. Structures containing B-Se, Se-C, and B-Se-C were analyzed.

(10) (a) Comasseto, J. V.; Stefani, H. A.; Chieffi, A.; Zukerman-Schpector, J. Addition of Organotellurium Trihalides to Acetylenes. *Organometallics* **1991**, 10, 845-846. (b) Zukerman-Schpector, J.; Castellano, E. E.; Oliva, G.; Comasseto, J. V.; Stefani, H. A. Structure of dichloro[(Z)-2-chloro-2-*p*-tolylvinyl](*p*-methoxyphenyl)tellurium(VI) *Acta Cryst.* **1991**, C47, 960-962. (c) Zukerman-Schpector, J.; Comasseto, J. V.; Stefani, H. A. Dichloro[(Z)-2-chloro-2-phenylvinyl](4-methoxyphenyl)tellurium(IV). *Acta Cryst.* **1995**, C51, 861-863. (d) Zukerman-Schpector, J.; Camillo, R. L.; Comasseto, J. V.; Santos, R. A.; Caracelli, J. Trichloro[(Z)-2-chloro-1,2-diphenylvinyl]-tellurium(IV). *Acta Cryst.* **1999**, C55, 1577-1579. (e) Huang, X.; Wang, Y.-P. Stereoselective Synthesis of (Z)- or (E)-β-Bromovinyl Tellurides and Their Application in the Synthesis of Trisubstituted Alkenes. *Tet. Lett.* **1996**, 37, 41, 7417-7420. (f) Chauhan, A. K. S.; Bharti, S. N.; Srivastava, R. C.; Butcher, R. J.; Duthie, A. Stereospecific chlorotelluration of terminal acetylenes. *J. Organomet. Chem.* **2012**, 708-709, 75-81.

(11) (a) Dabbousi, B. O.; Bonasia, P. J.; Arnold, J. $(Me_3Si)_3SiTeH$: Preparation, Characterization, and Synthetic Utility of a Remarkably Stable Tellurol. *J. Am. Chem. Soc.* **1991**, 113, 3186-3188. (b) Bonasia, P. J.; Arnold, J. Lithium Tri(trimethylsilyl)silyltellurolate Bis(tetrahydrofuran) and Tris(trimethylsilyl)silyltellurol. *Inorg. Synth.* **1997**, 31, 162-165.

(12) (a) Vinogradova, E. V.; Zhang, C.; Spokoyny, A. M.; Pentelute, B. L.; Buchwald, S. L. Organometallic palladium reagents for cysteine bioconjugation. *Nature* **2015**, 526, 687-691. (b) Uehling, M. R.; King, R. P.; Krska, S. W.; Cernak, T.; Buchwald, S. L. Pharmaceutical diversification via palladium oxidative addition complexes. *Science* **2019**, 363, 6425, 405-408.

(13) (a) Batsanov, A. S.; Fox, M. A.; Hibbert, T. G.; Howard, J. A. K.; Kivekäs, R.; Laromaine, A.; Sillanpää, R.; Viñas, C.; Wade, K. Sulfur, tin and gold derivatives of 1-(2'-pyridyl)-*ortho*-carborane, 1-R-2-X-1,2-$C_2B_{10}H_{10}$ (R = 2'-pyridyl, X = SH, $SnMe_3$ or $AuPPh_3$. *Dalton Trans.* **2004**, 3822-3828. (b) Laromaine, A.; Teixidor, F.; Kivekäs, R.; Sillanpää, R.; Arca, M.; Lippolis, V.; Crespo§, F.; Viñas, C. Synthesis, reactivity and structural studies of selenide bridged carboranyl compounds. *Dalton Trans.* **2006**, 5240-5247. (c) Popescu, A. R.; Teixidor, F.; Viñas, C. Metal promoted charge and hapticities of phosphines: The uniqueness of carboranylphosphines. *Coord. Chem. Rev.* **2014**, 269, 54-84. (d) Wong, Y. O.; Smith, M. D.; Peryshkov, D. V. Reversible water activation driven by contraction and expansion of a 12-vertex-*closo*-12-vertex-*nido* biscaborane cluster. *Chem. Commun.* **2016**, 52, 12710-12713. (e) Kleinsasser, J. F.; Reinhart, E. D.; Estrada, J.; Jordan, R. F.; Lavallo, V. Ethylene Oligomerization and Polymerization by Palladium(II) Methyl Complexes Supported by Phosphines Bearing a Perchlorinated 10-Vertex *closo*-Carborane Anion Substituent. *Organometallics* **2018**, 37, 24, 4773-4783. (f) Ali, O. M. Lasseter, J. C.; Żurawiński, R.; Pietrzak, Pecyna, J.; Wojciechowski, J.; Friedli, A. C.; Pociecha, D.; Kaszyński, P. Thermal and Photophysical Properties of Highly Quadrupolar Liquid-Crystalline Derivatives of the [*closo*-$B_{12}H_{12}$]$^{2-}$ Anion. *Chem. Eur. J.* **2019**, 25, 10, 2616-2630. (g) Yruegas, S.; Axtell, J. C.; Kirlikovalli, K. O.; Spokoyny, A. M.; Martin, C. D. Synthesis of 9-borafluorene analogues featuring a three-dimensional 1,1'-bis(*o*-carborane) backbone. *Chem. Commun.* **2019**, 55, 2892-2895. (h) Lyu, H.; Zhang, J.; Yang, J.; Quan, Y.; Xie, Z. Catalytic Regioselective Cage B(8)-H

Arylation of *o*-Carboranes via "Cage-Walking" Strategy. *J. Am. Chem. Soc.* **2019**, 141, 10, 4219-4224. (i) Eleazer, B. J.; Smith, M. D.; Peryshkov, D. V. Reaction of a ruthenium B-carboranyl hydride complex and $BH_3(SMe_2)$: Selective formation of a pincer-supported metallaborane $LRu(B_3H_8)$. *Tetrahedron* **2019**, 75, 11, 1471-1474. (j) Quan, Y.; Tang, C.; Xie, Z. Nucleophilic substitution: a facile strategy for selective B-H functionalization of carboranes. *Dalton Trans.* **2019**, 48, 7494-7498. (k) Jiang, T.; Zhang, K.; Shen, Y.; Hamadaoui, M.; Dontha, R.; Liu, J.; Spingler, B.; Duttwyler, S. The 12-ethynylmonocarba-*closo*-dodecaborate anion as a versatileligand for Cu(I) alkyne and heterobimetallic Cu(I)/M(II) (M = Pd, Pt) alkynide complexes. *Dalton Trans.* **2019**, 48, 17192-17199. (l) Fanfrlik, J.; Hnyk, D.; Hobza, P. Chalcogen Bonding due to the Exo-Substitution of Icosahedral Dicarbaborane. *Molecules* **2019**, 24, 14, 2657. (m) Londesborough, M. G. S.; Macías, R.; Kennedy, J. D.; Clegg, W.; Bould, J. Macropolyhedral Nickelaboranes from the Metal-Assisted Fusion of KB_9H_{14}. *Inorg. Chem.* **2019**, 58, 19, 13258-13267. (n) Fisher, S. P.; McArthur, S. G.; Tej, V.; Lee, S. E.; Chan, A. L.; Banda, I.; Gregory, A.; Berkley, K.; Tsay, C.; Rheingold, A. L.; Guisado-Barrios, G.; Lavallo, V. Strongly Coordinating Ligands Form Weakly Coordinating Yet Functional Organometallic Anions. *J. Am. Chem. Soc.* **2020**, 142, 1, 251-256. (o) Keener, M.; Hunt, C.; Carroll, T. G.; Kampel, V.; Dobrovetsky, R.; Hayton, T. W.; Ménard, G. Redox-switchable carboranes for uranium capture and release. *Nature* **2020**, 577, 652-655. (p) Kamin, A. A.; Juhasz, M. A. Exhaustive Cyanation of the Dodecaborate Dianion: Synthesis, Characterization, and X-ray Crystal Structure of $[B_{12}(CN)_{12}]^{2-}$. *Inorg. Chem.* **2020**, 59, 1, 189-192. (q) Zheng, F.; Yui, T. H.; Zhang, J.; Xie, Z. Synthesis and X-ray characterization of 15- and 16-vertex *closo*-carboranes. *Nature Commun.* **2020**, 11, 5943. (r) Chan, A. P. Y.; Parkinson, J. A.; Rosair, G. M.; Welch, A. J. Bis(phosphine)hydridorhodacarborane erivatives of 1,1'-Bis(*ortho*-carborane) and Their Catalysis of Alkene Isomerization and the

Hydrosilylation of Acetophenone. *Inorg. Chem.* **2020**, 59, 3, 2011-2023. (s) Couto, M.; Alamón, C.; Nievas, S.; Perona, M.; Dagrosa, M. A.; Teixidor, F.; Cabral, P.; Viñas, C.; Cerecetto, H. Bimodal Therapeutic Agents Against Glioblastoma, One of the Most Lethal Forms of Cancer. *Chem. Eur. J.* **2020**, 26, 63, 14335-14340. (t) Zhu, T.-C.; Xing, Y.-Y.; Sun, Y.; Duttwyler, S.; Hong, X. Directed B-H functionalization of the *closo*-dodecaborate cluster *via* concerted iodination-deprotonation: reaction mechanism and origins of regioselectivity. *Org. Chem. Front.* **2020**, 7, 3648-3655. (u) Kravchenko, E. A.; Gippius, A. A.; Kuznetsov, N. T. Noncovalent Interactions in Compounds Based on Perchlorinated Boron Cluster as Monitored by ^{35}Cl NQR (Review). *Russ. J. Inorg. Chem.* **2020**, 65, 546-566. (v) Mu, X.; Hopp, M.; Dziedzic, R. M.; Waddington, M. A.; Rheingold, A. L.; Sletten, E. M.; Axtell, J. C.; Spokoyny, A. M. Expanding the Scope of Palladium-Catalyzed B-N Cross-Coupling Chemistry in Carboranes. *Organometallics* **2020**, 39, 23, 4380-4386. (w) Rončević, I.; Bastien, G.; Cvačka, J.; Kaleta, J.; Michl, J. $CB_{11}H_{10}^-$ and Related Carborenes. *Inorg. Chem.* **2020**, 59, 17, 12453-12460. (x) Hoppenz, P.; Els-Heindl, S.; Kellert, M.; Kuhnert, R.; Saretz, S.; Lerchen, H.-G.; Köbberling, J.; Riedl, B.; Hey-Hawkins, E.; Beck-Sickinger, A. G. A Selective Carborane-Functionalized Gastrin-Releasing Peptide Receptor Agonist as Boron Delivery Agent for Boron Neutron Capture Therapy. *J. Org. Chem.* **2020**, 85, 3, 1446-1457. (y) Kataki-Anastasakou, A.; Axtell, J. C.; Hernandez, S.; Dziedzic, R. M.; Balaich, G. J.; Rheingold, A. L.; Spokoyny, A. M.; Sletten, E. M. Carborane Guests for Cucurbit[7]uril Facilitate Strong Binding and On-Demand Removal. *J. Am. Chem. Soc.* **2020**, 142, 49, 20513-20518. (z) Guo, S.-T.; Cui, P.-F.; Yuan, R.-Z.; Jin, G.-X. Transition metal-mediated B(4)-H hydroxylation/halogenation of *o*-carboranes bearing a 2-pyridylsulfenyl ligand. *Chem. Commun.* **2021**, 57, 2412-2415. (aa) Lee, S. H.; Lee, J. H.; Mun, M. S.; Yi, S.; Yoo, E.; Hwang, H.; Lee, K. M. Influence of Electronic Environment on the Radiative Efficiency of 9-

Phenyl-9*H*-carbazole-Based *ortho*-Carboranyl Luminophores. *Molecules* **2021**, 26, 6, 1763. (bb) Soldevilla-Sanmartín, J.; Ruiz, E.; Choquesillo-Lazarte, D.; Light, M. E.; Viñas, C.; Teixidor, F.; Núñez, R.; Pons, J.; Planas, J. G. Tuning the architectures and luminescence properties of Cu(I) compounds of phenyl and carboranyl pyrazoles: the impact of 2D *versus* 3D aromatic moieties in the ligand backbone. *J. Mater. Chem. C* **2021**, 9, 7643-7657. (cc) Xiong, Y.; Chen, D.; Yao, S.; Zhu, J.; Ruzicka, A.; Driess, M. New Types of Ge_2 and Ge_4 Assemblies Stabalized by a Carbanionic Dicarborandiyl-Silylene Ligand. *J. Am. Chem. Soc.* **2021**, 143, 16, 6229-6237. (dd) Zhang, C.; Wang, J.; Su, W.; Lin, Z.; Ye, Q. Synthesis, Characterization, and Density Functional Theory Studies of Three-Dimensional Inorganic Analogues of 9,10-Diboraanthracene-A New Class of Lewis Superacids. *J. Am. Chem. Soc.* **2021**, 143, 23, 8552-8558. (ee) Murphy, N.; McCarthy, E.; Dwyer, R.; Farrás, P. Boron clusters as breast cancer therapeutics. *J. Inorg. Biochem.* **2021**, 218, 111412. (ff) Vrána, J.; Holub, J.; Samsonov, M. A.; Růžičková, Z.; Cvačka, J.; McKee, M. L.; Fanfrlík, J.; Hnyk, D.; Růžička, A. Access to cationic polyhedral carboranes via dynamic cage surgery with *N*-heterocyclic carbenes. *Nat. Commun.* **2021**, 12, 4971. (gg) Waddington, M. A.; Zheng, X.; Stauber, J. M.; Moully, E. H.; Montgomery, H. R.; Saleh, L. M. A.; Král, P.; Spokoyny, A. M. An Organometallic Strategy for Cysteine Borylation. *J. Am. Chem. Soc.* **2021**, 143, 23, 8661-8668. (hh) Jaiswal, K.; Malik, N.; Tumanskii, B.; Ménard, G.; Dobrovetsky, R. Carborane Stablized "19-Electron" Molybdenum Metalloradical. *J. Am. Chem. Soc.* **2021**, 143, 26, 9842-9848. (ii) Gange, G. B.; Humphries, A. L.; Royzman, D. E.; Smith, M. D.; Peryshkov, D. V. Metal-Free Bond Activation by Carboranyl Diphosphines. *J. Am. Chem. Soc.* **2021**, 143, 29, 10842-10846. (jj) Al-Joumhawy, M.; Marei, T.; Shmalko, A.; Cendoya, P.; La Borde, J.; Gabel, D. B-N Bond Formation through Palladium-Catalyzed, Microwave-Assisted

Cross-Coupling of Nitrogen Compounds with Iodo-dodecaborate. *Chem. Commun.* **2021**, 57, 10007-10010.

(14) (a) Giselbrecht, K.; Bildstein, B.; Sladky, F. Tris(trimethylsilyl)methanetellurenyl halides $(Me_3Si)_3CTeX$ (X = Cl, Br, I): synthesis of stable slkanetellurenyl halides. *Chem. Ber.* **1989**, 122, 7, 1255-1256. (b) Ostrowski, M.; Wagner, I.; du Mont, W. W.; Jones, P. G.; Jeske, J. Tris(trimethylsilyl)methaneselenyl halides and chalcogenides. *Z. Anorg. Allg. Chem.* **1993**, 619, 10, 1693-1698. (c) Potapov, V. A.; Amosova, S. V.; Petrov, B. V.; Starkova, A. A.; Malyushenko, R. N. Electrophilic addition of organic selenyl chlorides and bromides to acetylene. *Sulfur Lett.* **1998**, 21, 3, 109-114. (d) Barrientos-Astigarraga, R. E.; Castelani, P.; Sumida, C. Y.; Zukerman-Schpector, J.; Comasseto, J. V. A general method of synthesis of functionalized Z-vinylic tellurides starting from β-dicarboynl compounds. *Tetrahedron* **2002**, 58, 6, 1051-1059. (e) Marino, J. P.; Nguyen, H. N. Electrotelluration: A New Approach to Tri- and Tetrasubstituted Alkenes. *J. Org. Chem.* **2002**, 67, 18, 6291-6296. (f) Klapötke, T. M.; Krumm, B.; Polborn, K. Isolation of a Stable Covalent Selenium Azide $RSeN_3$. *J. Am. Chem. Soc.* **2004**, 126, 3, 710-711. (g) Klapötke, T. M.; Krumm, B.; Nöth, H.; Gálvez-Ruiz, J. C.; Polborn, K.; Schwab, I.; Suter, M. Kinetic and Donor Stabilization of Organotellurenyl Iodides and Azides. *Ionrg. Chem.* **2005**, 44, 15, 5254-5265. (h) Senol, E.; Scattolin, T.; Schoenebeck, F. Selenolation of Aryl Iodides and Bromides Enabled by a Bench-Stable Pd^{I} Dimer. *Chem. Eur. J.* **2019**, 25, 40, 9419-9422.

4.6 Appendix C

4.6.1 General Considerations

Meta-$C_2B_{10}H_{12}$ (Katchem or Alfa Aesar) was used as is. Dry dichloromethane was obtained from a Grubbs column with activated alumina and copper catalyst. For the synthesis of **1B**, dichloromethane was further dried by stirring over CaH_2 for 24 h before distilling the solvent into the reaction flask. Se_2Cl_2 used in the synthesis of **1A** was prepared according to the procedure found in reference 1 and subsequently stored in a PTFE-capped vial at -15 ^oC. $TeCl_4$ used in the synthesis of **1B** was prepared according the procedure found in reference 2 and stored in a N_2-filled glovebox at -30 ^oC. [4-tolyl-PdRuPhos][OTf] used in the synthesis of **6C** was prepared following procedures found in reference 3. All other reagents were purchased from commercial vendors and used as is. Unless otherwise stated, all reactions and manipulations were performed under ambient atmosphere of laboratory air exposed to ambient light.

Plastic-backed Baker-flex Silica Gel IB2-F TLC plates were used for thin layer chromatography. Silica used for flash column chromatography was SiliaFlash® G60 60-200 μm (70-230 mesh) purchased from Silicycle. TLC samples for carborane-containing compounds were stained with 1 wt. % $PdCl_2$ in 6M HCl and developed with heat using a Master Appliance VT-750C Varitemp Heat Gun at full heat for 30-60 seconds (until spots develop).

4.6.2 Instrumentation

^1H, $^{13}C\{^1H\}$, ^{11}B, $^{11}B\{^1H\}$, ^{19}F, ^{77}Se, and ^{125}Te NMR spectra were recorded on either a Bruker AVII 600, Bruker DRX500, or Bruker AVII 400 spectrometers in ambient conditions at room temperature. MestReNova v6.0.2-5475 software was used to process the FID data and visualize the spectra. ^1H and $^{13}C\{^1H\}$ NMR spectra were referenced to residual solvent resonances in

deuterated solvents (note: due to high humidity H_2O resonances are often present) and are reported relatice to tetramethylsilane (δ = 0 ppm). ^{11}B and $^{11}B\{^1H\}$ NMR spectra were referenced externally to $Et_2O{\cdot}BF_3$ (δ = 0 ppm). ^{19}F NMR spectra were referenced externally to fluorobenzene (δ = -113.15 ppm). ^{77}Se NMR spectra were referenced externally to diphenyldiselenide (δ = 463.15 ppm). ^{125}Te NMR spectra were referenced externally to diphenylditelluride in tetrahydrofuran at room temperature (δ = 408 ppm). Exponential apodization (5-30 MHz) was applied through MestReNova to ^{77}Se and ^{125}Te NMR spectra for most compounds reported in order to enhance the signal to noise ratio.

GCMS measurements were carried out using an Agilent Model 7683 Autosampler, 6890 Gas Chromatograph, and 5975 Inert Mass Selective Detector in the Electron Impact (EI) mode. EI energy was set to 70 eV. Data collection was controlled using MSD Enhanced Chemstation software (Agilent). Separation was carried out on an Agilent HP5-MS column with dimensions 30m x 250 um x 0.25 um. Ultra High Purity Grade He (Airgas) was used as carrier gas with the flow set to 0.8 ml/min in constant flow mode.

UV-Vis absorption measurements were taken using an Ocean Optics Flame Miniature Spectrometer detector and Ocean Optics DH-2000 UV-Vis-NIR source. All samples were dissolved in THF and measurements were taken in a 1 cm quartz cuvette.

Elemental analysis of compounds **1A** and **1B** was performed by Atlantic Microlabs.

4.6.3 Precursor Synthesis

Synthesis of 1A

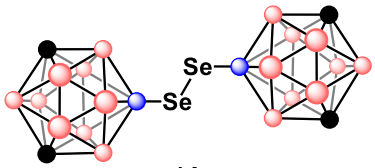

1A

Synthetic procedures adapted from reference 4. *Meta*-$C_2B_{10}H_{12}$ (1.44 g, 10 mmol) and $AlCl_3$ (1.33 g, 10 mmol, 1 eq) were added to an oven-dried Schlenk flask equipped with a stir bar and rubber septum and evacuated/backfilled with N_2 three times. Anhydrous CH_2Cl_2 (25 ml), collected from a Grubb's column, was added to the Schlenk flask *via* cannula and the solids were allowed to dissolved. Subsequently, Se_2Cl_2 (0.42 mL, 5 mmol, 0.5 eq) was added dropwise to the stirring suspension *via* syringe, forming a dark red solution that was allowed to stir overnight at room temperature. Upon completion of the reaction, determined by TLC, the reaction was carefully quenched by the addition of distilled H_2O (15 mL), yielding a dark yellow, cloudy suspension. The yellow organic later was separated from the aqueous layer and the aqueous layer was extracted with CH_2Cl_2 (3 x 15 mL). The organic layers were combined and dried with Na_2SO_4, resulting in a clear yellow/orange solution. The solution was then decanted from the Na_2SO_4 and silica gel was added before the CH_2Cl_2 was removed under reduced pressure in order to dry load the crude product onto the silica gel. The crude product was subsequently purified *via* silica gel column chromatography using a Hexanes to 30% CH_2Cl_2:Hexanes gradient column. The product containing fractions were then collected and the solvent was removed under reduced pressure, affording **1A** as a yellow-orange solid.

Yield: 1.3 g (56%), yellow-orange solid

^{1}H NMR (400 MHz, THF-d_8): δ 3.57 (s, 4H, $C_{carborane}$-H), 3.3-1.3 (m, 18H, $B_{carborane}$-H)

^{13}C{^{1}H} NMR (100 MHz, THF-d_8): δ 55.82

^{11}B NMR (128 MHz): δ -4.82 (s, 1B), -6.07 (d, 2B, $^{1}J_{BH}$ = 190 Hz), -9.47 (d, 1B, $^{1}J_{BH}$ = 155 Hz), -12.48 (d, 2B, $^{1}J_{BH}$ = 161 Hz), -13.71 (d, 2B, $^{1}J_{BH}$ = 158 Hz), -17.14 (d, 1B, $^{1}J_{BH}$ = 184 Hz), -19.68 (d, 1B, $^{1}J_{BH}$ = 183 Hz)

^{77}Se NMR (95 MHz): δ -67.5 (q, $^{1}J_{SeB}$ = 63 Hz)

GC-MS *m/z***:** 445.20 (calc. 445.20)

UV-Vis (nm): 355

Elemental Analysis Calculated for $(C_2B_{10}H_{11}Se)_2$: C, 10.81; H, 4.99; found: C, 10.96; H, 4.86 (average of two duplicate runs, from two different batches of **1A**)

Synthesis of 1B

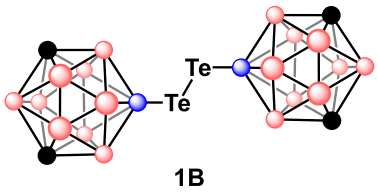

1B

Synthetic procedures adapted from reference 5. CH_2Cl_2 used in this reaction needs to be dried thoroughly before use in order to achieve good and reproducible yields. Anhydrous CH_2Cl_2 (50 mL), collected from a Grubb's column, was added to an oven-dried two-neck round bottomed flask equipped with a stir bar. CaH_2 (~1g) was added to the CH_2Cl_2 and stirred overnight at room temperature under N_2. The following day, $TeCl_4$ (2.70 g, 10 mmol, 1 eq) was added to an oven-dried Schlenk flask, equipped with a stir bar and rubber septum, in an N_2-filled glovebox and then transferred out. Subsequently, under a positive flow of N_2, CH_2Cl_2 was distilled away from the CaH_2 and collected in the $TeCl_4$-containing Schlenk flask. While stirring, the suspension of $TeCl_4$ in CH_2Cl_2 was then cooled to 0 ^{o}C using an ice bath before the addition of *Meta*-$C_2B_{10}H_{12}$ (1.44 g, 10 mmol) and $AlCl_3$ (2.66 g, 20 mmol, 2 eq). The resulting suspension was then stirred at 0 ^{o}C for an additional 30 minutes before transferring the flask to a stirring oil bath set to 45 ^{o}C. The reaction

progress was then monitored by TLC and the reaction was stopped once no more *meta*-$C_2B_{10}H_{12}$ was consumed (approx. 24 hours). After stopping the reaction, CH_2Cl_2 was removed from the Schlenk flask under reduced pressure, leaving behind a viscous, dark purple oil. Once all CH_2Cl_2 was removed, the crude material was redissolved in absolute EtOH (75 mL), sonication will likely be required. To the resulting, dark brown, suspension, an excess of $Na_2S{\cdot}9H_2O$ (4.3 g) was added and the resulting suspension was left to stir overnight at room temperature, covered in aluminum foil to limit light exposure. After stirring overnight, the reaction mixture was then suspended in distilled H_2O (750 mL) before the addition of Et_2O (50 mL). The deep red organic layer was separated from the aqueous layer and the aqueous layer was extracted further with Et_2O (3 x 50 mL). The organic layers were combined and dried with Na_2SO_4, resulting in a clear, dark red solution. The solution was then decanted from the Na_2SO_4, and the organic solvents were removed under reduced pressure, leaving a dark red powder. The crude product was then dissolved in CH_2Cl_2 and silica gel was added. CH_2Cl_2 was then removed under reduced pressure in order to dry load the crude product onto the silica gel. The crude product was subsequently purified *via* silica gel column chromatography using a Hexanes to 30% CH_2Cl_2:Hexanes gradient column. The product containing fractions were then collected and the solvent was removed under reduced pressure, affording **1B** as a dark red solid.

Yield: 4.1 g (76%), dark red solid (color can vary between hues of red or brown from batch to batch)

^{1}H NMR (400 MHz, THF-*d*$_8$): δ 3.61 (s, 4H, $C_{carborane}$-H), 3.5-1.5 (m, 18H, $B_{carborane}$-H)

^{13}C{^{1}H} NMR (100 MHz, THF-*d*$_8$): δ 57.83

^{11}B NMR (128 MHz): δ -5.05 (d, 2B, $^{1}J_{BH}$ = 161 Hz), -8.21 (d, 1B, $^{1}J_{BH}$ = 152 Hz), -11.08 (d, 2B, $^{1}J_{BH}$ = 203 Hz), -12.72 (d, 2B, $^{1}J_{BH}$ = 174 Hz), -16.23 (d, 1B, $^{1}J_{BH}$ = 181 Hz), -17.72 (d, 1B, $^{1}J_{BH}$ = 186 Hz), -22.12 (s, 1B)

^{125}Te NMR (158 MHz): δ -341.8 (q, $^{1}J_{TeB}$ = 207 Hz)

GC-MS *m/z***:** 542.20 (calc. 542.18)

UV-Vis (nm): 295, 417

Elemental Analysis Calculated for $(C_2B_{10}H_{11}Te)_2$: C, 8.87; H, 4.09; found: C, 9.34; H, 4.16 (average of two duplicate runs)

4.6.4 Synthesis of Electrophilic Reagents (2A, 3A, 4A)

Synthesis of 2A

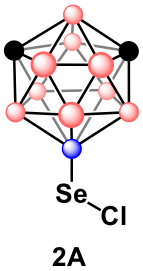

2A

Synthetic procedures adapted from reference 4. **1A** (223 mg, 0.5 mmol; 1 eq) was added to an oven dried Schlenk flask equipped with a stir bar and rubber septum. The reaction tube was evacuated and backfilled with N_2 three times before adding 5 mL of anhydrous CH_2Cl_2 *via* syringe. The resulting suspension was allowed to stir and the reaction tube was immersed in an ice bath to cool the solution to 0 ˚C. Subsequently, SO_2Cl_2 (81 µL, 0.5 mmol, 1 eq) was added to the stirring solution of **1A** by micropipette, and the reaction was left to stir for 30 minutes at 0 ˚C. After 30 minutes, the solvent was removed from the reaction flask *via* the high-vacuum line on the Schlenk line and dried to completion. The remaining burnt orange solid was collected from the Schlenk flask and used as is.

Yield: 241 mg (94%), burnt orange solid

^{1}H NMR (400 MHz, $CDCl_3$): δ 3.75 (s, 2H, $C_{carborane}$-H), 3.5-1.5 (m, 9H, $B_{carborane}$-H)

$^{13}C\{^{1}H\}$ NMR (100 MHz, $CDCl_3$): δ 56.32

^{11}B NMR (128 MHz): δ -3.74 (s, 1B), -6.34 (d, 2B, $^{1}J_{BH}$ = 171 Hz), -9.97 (d, 1B, $^{1}J_{BH}$ = 155 Hz), -12.85 (d, 2B, $^{1}J_{BH}$ = 165 Hz), -13.34 (d, 2B, $^{1}J_{BH}$ = 165 Hz), -16.73 (d, 1B, $^{1}J_{BH}$ = 184 Hz), -18.20 (d, 1B, $^{1}J_{BH}$ = 188 Hz)

^{77}Se NMR (95 MHz): δ 808.4 (m)

Synthesis of 3A

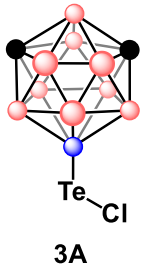

3A

Synthetic procedures adapted from reference 5. Prepared in an analogous method to **2A**, where **1B** was used instead of **1A**.

Yield: 300 mg (quantitative), burgundy solid

^{1}H NMR (400 MHz, THF-d_8): δ 3.86 (s, 2H, $C_{carborane}$-H), 3.5-1.5 (m, 9H, $B_{carborane}$-H)

$^{13}C\{^{1}H\}$ NMR (100 MHz, THF-d_8): δ 57.12

^{11}B NMR (128 MHz): δ 2.80 (s, 1B), -6.20 (d, 2B, $^{1}J_{BH}$ = 161 Hz), -9.68 (d, 1B, $^{1}J_{BH}$ = 161 Hz), -12.57 (d, 2B, $^{1}J_{BH}$ = 161 Hz), -13.00 (d, 2B, $^{1}J_{BH}$ = 165 Hz), -16.48 (d, 2B, $^{1}J_{BH}$ = 184 Hz)

^{125}Te NMR (158 MHz): δ 1382.9 (m)

Synthesis of 4A

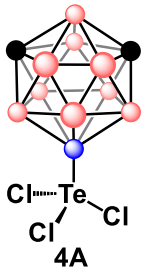

4A

Synthetic procedures modified from reference 5. **1B** (163 mg, 0.3 mmol; 1 eq) was added to an oven dried reaction tube equipped with a stir bar and PTFE cap. The reaction tube was evacuated and backfilled with N_2 three times before adding 5 mL of anhydrous CH_2Cl_2 *via* syringe. The resulting suspension was allowed to stir and the reaction tube was immersed in an ice bath to cool the solution to 0 ˚C. Subsequently, SO_2Cl_2 (121 µL, 1.5 mmol, 5 eq) was added by micropipette to the stirring solution of **1B**, and the reaction was left to stir for 30 minutes at 0 ˚C. After 30 minutes, the now cloudy white reaction mixture was centrifuged and the supernatant was carefully decanted. The remaining white solid was washed with hexanes (3 x 5 mL) and dried *in vacuo* to yield a free-flowing white powder.

Yield: 192 mg (85%), white solid

^{1}H NMR (400 MHz, THF-*d*$_8$): δ 3.88 (s, 2H, $C_{carborane}$-H), 3.7-1.4 (m, 9H, $B_{carborane}$-H)

^{13}C{^{1}H} NMR (100 MHz, THF-*d*$_8$): δ 57.09

^{11}B NMR (128 MHz): δ 3.13 (s, 1B), -5.96 (d, 2B, $^{1}J_{BH}$ = 168 Hz), -9.43 (d, 1B, $^{1}J_{BH}$ = 153 Hz), -12.25 (d, 2B, $^{1}J_{BH}$ = 153 Hz), -12.79 (d, 2B, $^{1}J_{BH}$ = 158 Hz), -16.25 (d, 2B, $^{1}J_{BH}$ = 178 Hz)

^{125}Te NMR (158 MHz): δ 1376 (m)

4.6.5 Reactions of Selenyl (II) Chloride (2A)

4.6.5.1 Synthesis and Characterization of 2B

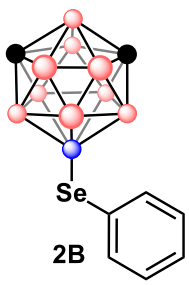

2B

2A (39 mg, 0.15 mmol, 1 eq) was added to an oven dried reaction tube equipped with a stir bar and PTFE cap. The reaction tube was evacuated and backfilled with N_2 three times before adding ~1 mL of anhydrous Et_2O *via* cannula transfer to the tube. The resulting solution was allowed to stir for 5 minutes to ensure all solids

had dissolved. Subsequently, a solution of phenylmagnesium bromide (0.15 mL, 3M, 0.45 mmol, 3 eq) was added dropwise to the stirring solution of **2A** (caution: heat is evolved during the addition of the Grignard reagent). Once the addition of the Grignard reagent was complete, the reaction was left to stir for 16 h at room temperature. After 16 h, the reaction was quenched by the careful addition of H_2O (5 mL). The quenched reaction mixture was then extracted with Et_2O (2 x 5 mL) and the combined organic layers were dried with Na_2SO_4 before passing the solution through a silica plug and eluting with Et_2O. The solvent was then removed under reduced pressure to yield a white solid.

Yield: 41 mg (91%), white solid

^{1}H NMR (400 MHz, $CDCl_3$): δ 7.63 (d, 2H, $^{1}J_{HH}$ = 6.7 Hz), 7.25 (m, 3H), 3.4-1.5 (m, 9H, $B_{carborane}$-H), 2.95 (s, 2H, $C_{carborane}$-H)

^{13}C{^{1}H} NMR (100 MHz, $CDCl_3$): δ 136.38, 128.97, 128.75, 127.20, 55.16

^{11}B NMR (128 MHz): δ -4.09 (s, 1B), -6.39 (d, 2B, $^{1}J_{BH}$ = 165 Hz), -9.52 (d, 1B, $^{1}J_{BH}$ = 152 Hz), -13.02 (d, 2B, $^{1}J_{BH}$ = 165 Hz), -13.59 (d, 2B, $^{1}J_{BH}$ = 169 Hz), -17.28 (d, 1B, $^{1}J_{BH}$ = 183 Hz), -19.60 (d, 1B, $^{1}J_{BH}$ = 183 Hz)

^{77}Se NMR (95 MHz): δ 79.8 (q, $^{1}J_{SeB}$ = 45 Hz)

GC-MS ***m/z*****:** 299.20 (calc. 299.15)

4.6.5.2 General Procedure and Characterization for Compounds 2C-2E

2A (39 mg, 0.15 mmol, 1 eq) was added to a reaction tube equipped with a stir bar and PTFE cap before the addition of anhydrous CH_2Cl_2 *via* syringe. The resulting mixture was then stirred for several minutes, forming a clear orange solution. Substrate (0.15 mmol, 1 eq) was then added to

the stirring solution at room temperature, and left to stir overnight. Over time, the reaction solution was observed to become clear and colorless/pale yellow, indicating the consumption of the starting material, **2A**. After stirring the reaction overnight at room temperature, the crude reaction mixture was subsequently dry loaded onto silica and then purified *via* silica gel column chromatography. See individual entries for specific isolation procedures.

Characterization of 2C

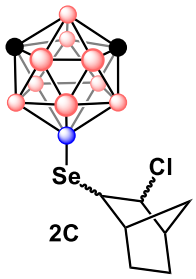

Isolation: Hexanes to 20% CH_2Cl_2:Hexanes gradient

Yield: 25 mg (47%), white solid

^{1}H NMR (400 MHz, $CDCl_3$): δ 4.08 (m, 1H), 3.4-1.5 (m, 9H, $B_{carborane}$-H), 3.02 (s, 2H, $C_{carborane}$-H), 2.75 (s, 1H), 2.37 (m, 2H), 1.96 (m, 1H), 1.80 (d, 1H, $^{1}J_{HH}$ = 10.8 Hz), 1.67 (m, 1H), 1.41 (m, 3H)

^{13}C{^{1}H} NMR (100 MHz, $CDCl_3$): δ 70.23, 55.32, 51.43, 46.51, 44.39, 35.94, 29.56, 21.43

^{11}B NMR (128 MHz): δ -5.08 (s, 1B), -6.38 (d, 2B, $^{1}J_{BH}$ = 183 Hz), -9.57 (d, 1B, $^{1}J_{BH}$ = 152 Hz), -13.04 (d, 2B, $^{1}J_{BH}$ = 161 Hz), -13.56 (d, 2B, $^{1}J_{BH}$ = 165 Hz), -17.30 (d, 1B, $^{1}J_{BH}$ = 183 Hz), -19.47 (d, 1B, $^{1}J_{BH}$ = 184 Hz)

^{77}Se NMR (95 MHz): δ 57.2 (m)

GC-MS ***m/z*****:** 352.20 (calc. 352.15)

Characterization of 2D

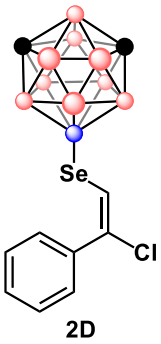

2D

Isolation: Hexanes to 15% CH_2Cl_2:Hexanes gradient

Yield: 29 mg (54%), white solid

^{1}H NMR (400 MHz, $CDCl_3$): δ 7.61 (dd, 2H, $^{1}J_{HH}$ = 8.5 Hz, 1.4Hz), 7.35 (m, 3H), 6.84 (m, b, 1H), 3.5-1.6 (m, 9H, $B_{carborane}$-H), 3.06 (s, 2H, $C_{carborane}$-H)

^{13}C{^{1}H} NMR (100 MHz, $CDCl_3$): δ 137.47, 128.70, 128.65, 128.10, 126.81, 117.47, 55.49

^{11}B NMR (128 MHz): δ -5.44 (s, 1B), -6.49 (d, 2B, $^{1}J_{BH}$ = 206 Hz), -9.79 (d, 1B, $^{1}J_{BH}$ = 149 Hz), -13.47 (d, 4B, $^{1}J_{BH}$ = 168 Hz), -17.27 (d, 1B, $^{1}J_{BH}$ = 184 Hz), -19.20 (d, 1B, $^{1}J_{BH}$ = 196 Hz)

^{77}Se NMR (95 MHz): δ 58.2 (q, $^{1}J_{SeB}$ = 37 Hz)

GC-MS *m/z***:** 360.20 (calc. 360.12)

Characterization of 2E

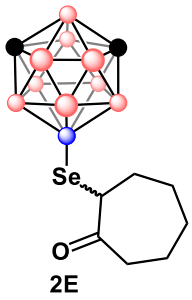

2E

Isolation: Hexanes to CH_2Cl_2 gradient

Yield: 27 mg (54%), white solid

^{1}H NMR (400 MHz, $CDCl_3$): δ 3.58 (m, 1H), 3.4-1.1 (m, 9H, $B_{carborane}$-H), 3.01 (s, 2H, $C_{carborane}$-H), 2.80 (m, 1H), 2.38 (m, 1H), 2.27 (m, 1H), 1.90 (m, 2H), 1.68 (m, 2H), 1.47 (m, 2H), 1.27 (m, 1H)

^{13}C{^{1}H} NMR (100 MHz, $CDCl_3$): δ 210.17, 55.30, 47.88, 39.75, 33.19, 30.13, 27.84, 25.61

^{11}B NMR (128 MHz): δ -4.90 (s, 1B), -5.93 (d, 2B, $^{1}J_{BH}$ = 202 Hz), -9.19 (d, 1B, $^{1}J_{BH}$ = 153 Hz), -13.14 (d, 4B, $^{1}J_{BH}$ = 165 Hz), -16.84 (d, 1B, $^{1}J_{BH}$ = 186 Hz), -18.86 (d, 1B, $^{1}J_{BH}$ = 193 Hz)

^{77}Se NMR (95 MHz): δ 50.2 (q, $^{1}J_{SeB}$ = 44 Hz)

GC-MS *m/z***:** 334.20 (calc. 334.18)

4.6.5.3 Synthesis and Characterization of 2F

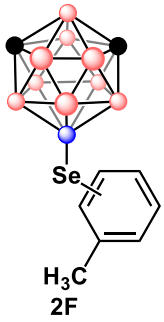

2A (117 mg, 0.45 mmol, 1 eq) and $AlCl_3$ (120 mg, 0.90 mmol, 2 eq) were added to a reaction tube equipped with a stir bar and PTFE cap before the addition of anhydrous toluene (1.5 mL, excess) *via* syringe. The resulting dark red mixture was then stirred for several minutes at room temperature, before immersing the reaction tube in a preheated oil bath set to 50 ^{o}C. The reaction was then left to stir for 16 h. After 16 h, the reaction tube was removed from the oil bath and allowed to cool to room temperature. Once cooled, distilled H_2O (10 mL) was carefully added to quench the remaining $AlCl_3$. The resulting biphasic mixture was then extracted with CH_2Cl_2 (3 x 5 mL) and the collected organic layers were dried over Na_2SO_4. The product-containing solution was decanted away, and the solvent was removed under reduced pressure, leaving the crude product as a red oil. The crude product was then purified *via* silica gel column chromatography with a Hexanes to 10% CH_2Cl_2:Hexanes gradient. The product-containing fractions were collected and volatiles were removed under reduced pressure, affording the product as a yellow-orange oil in 21% isolated yield.

Yield: 30 mg (21%), pale yellow solid

^{1}H NMR (400 MHz, $CDCl_3$): δ 7.73-6.87 (m, 4H), 3.4-1.6 (m, 9H, $B_{carborane}$-H), 2.94 (s, 2H, $C_{carborane}$-H), 2.31 (s, 3H)

^{13}C{^{1}H} NMR (100 MHz, $CDCl_3$): δ 138.32-125.28, 55.11, 23.94-21.17

^{11}B NMR (128 MHz): δ -4.06 (s, 1B), -6.43 (d, 2B, $^{1}J_{BH}$ = 161 Hz), -9.54 (d, 1B, $^{1}J_{BH}$ = 152 Hz), -13.05 (d, 2B, $^{1}J_{BH}$ = 161 Hz), -13.65 (d, 2B, $^{1}J_{BH}$ = 161 Hz), -17.33 (d, 1B, $^{1}J_{BH}$ = 180 Hz), -19.69 (d, 1B, $^{1}J_{BH}$ = 183 Hz)

^{77}Se NMR (95 MHz): δ 79.4 (m)

GC-MS *m/z***:** 314.20 (calc. 314.16)

4.6.5.4 Comparison of High and Low-Field (400-600 MHz) ^{1}H NMR Spectroscopy of 2C

High-Field ^{1}H NMR spectroscopy was used in attempt to resolve ^{1}H resonances in the alkyl region that could be correlated to the four expected norbornyl selenide isomers present in the purified reaction mixture. However, even using the higher field spectrometer, the ^{1}H resonances are not sufficiently resolved to assign. See stacked spectra below, including inset. Top spectrum was obtained on a 400 MHz NMR spectrometer, while the bottom spectrum was obtained on a 600 MHz NMR spectrometer. NMR samples were obtained from two separate batches of **2C** with slight variances in purity.

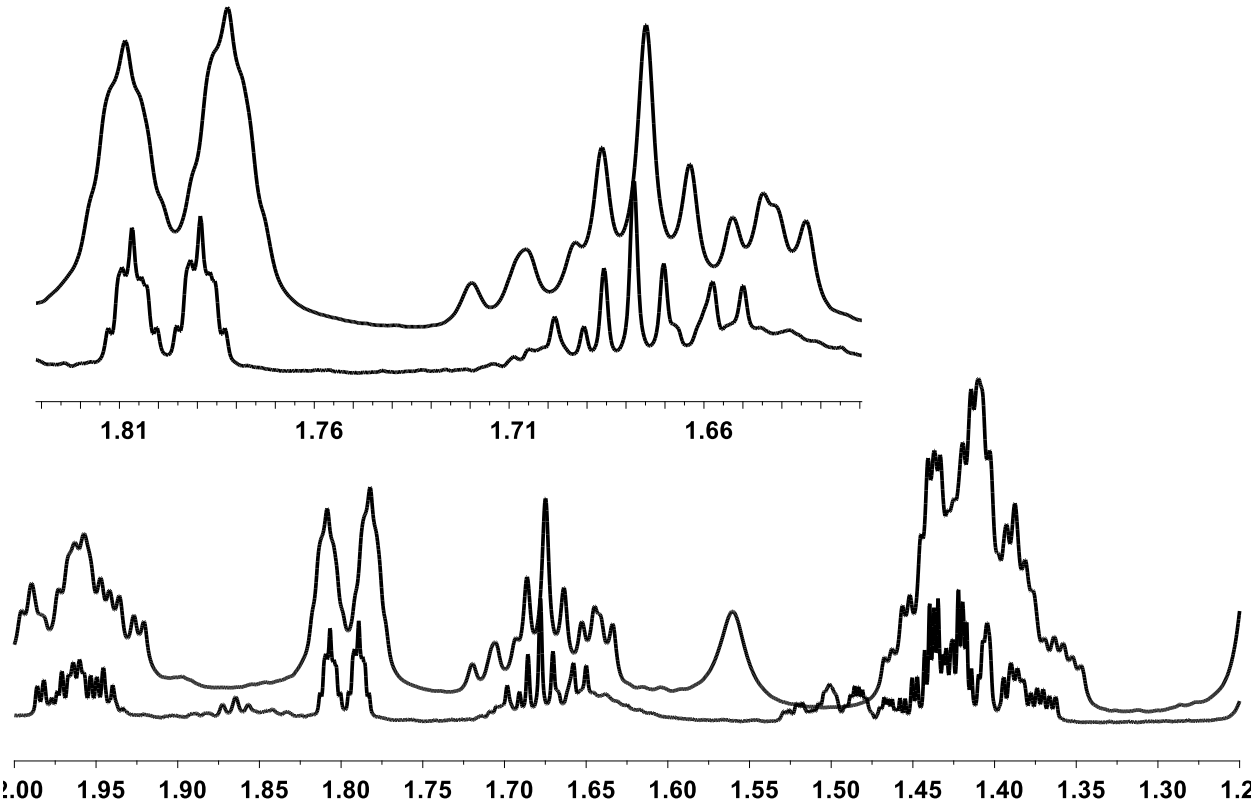

4.6.5.5 GC-MS Trace of Isolated 2C and 2C' Mixture

Included below is a GC-MS trace of purified 2C and 2C', indicating an approximate isomer distribution of 70:30 from compounds with retention times of 2.5 and 2.6 minutes.

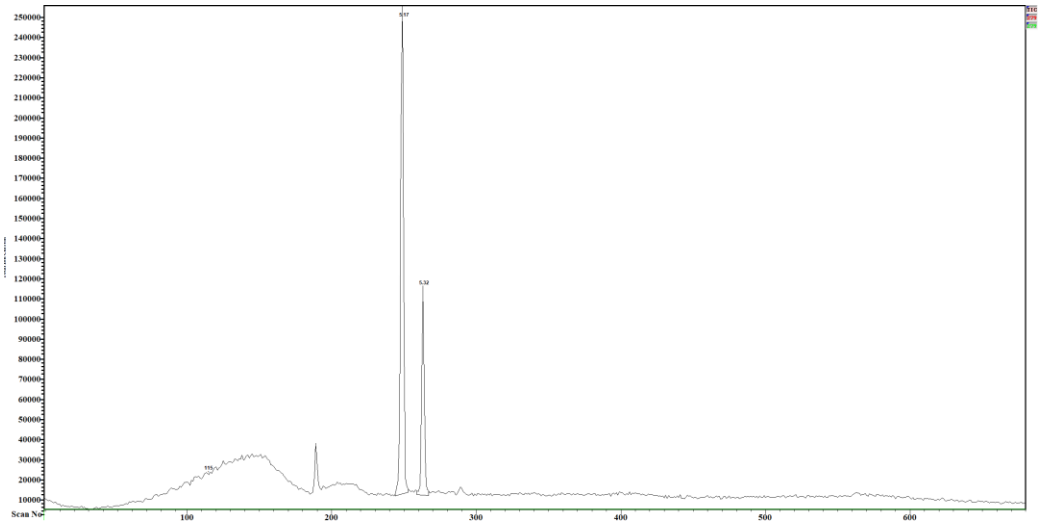

4.6.5.6 GC-MS Trace of Isolated 2F

Included below is a GC-MS trace of purified 2F, indicating an approximate *o*/*m*:*p* isomer distribution of 19:81.

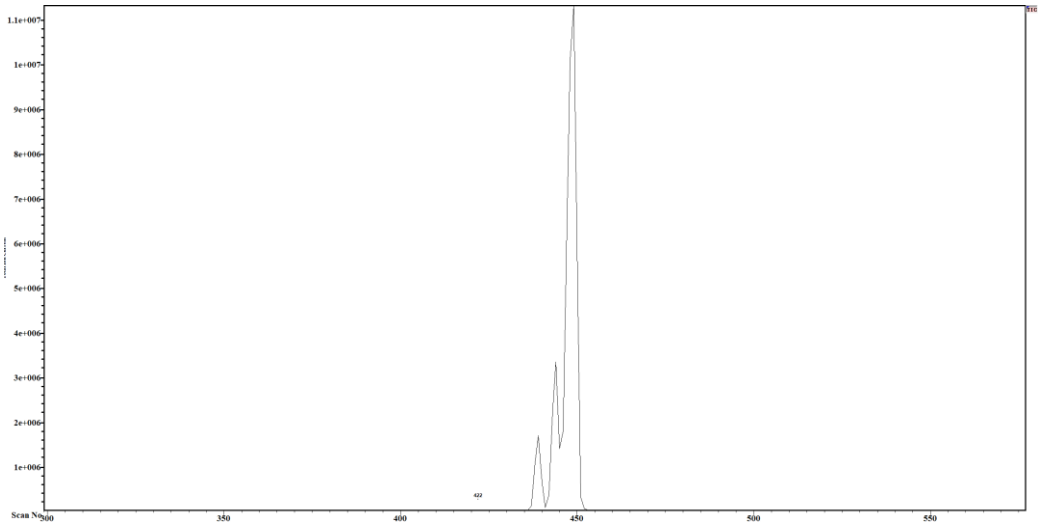

4.6.5.7 Experiments with Perdeuterated Toluene

Experiments with perdeuterated toluene were performed to obtain a more accurate distribution of *ortho*-, *meta*-, and *para*-tolyl selenide isomers. The deutero-tolyl selenide was prepared following analogous reaction conditions used in the synthesis of **2F**, where toluene was replaced with

perdeuterated toluene. From ^{2}H NMR spectroscopy (see below), the CD_3 resonances for each isomer are clearly resolved from 2.50-2.30 ppm. Integrations of those resonances indicate an approximate distribution of: 11:89, *o*/*m*:*p*.

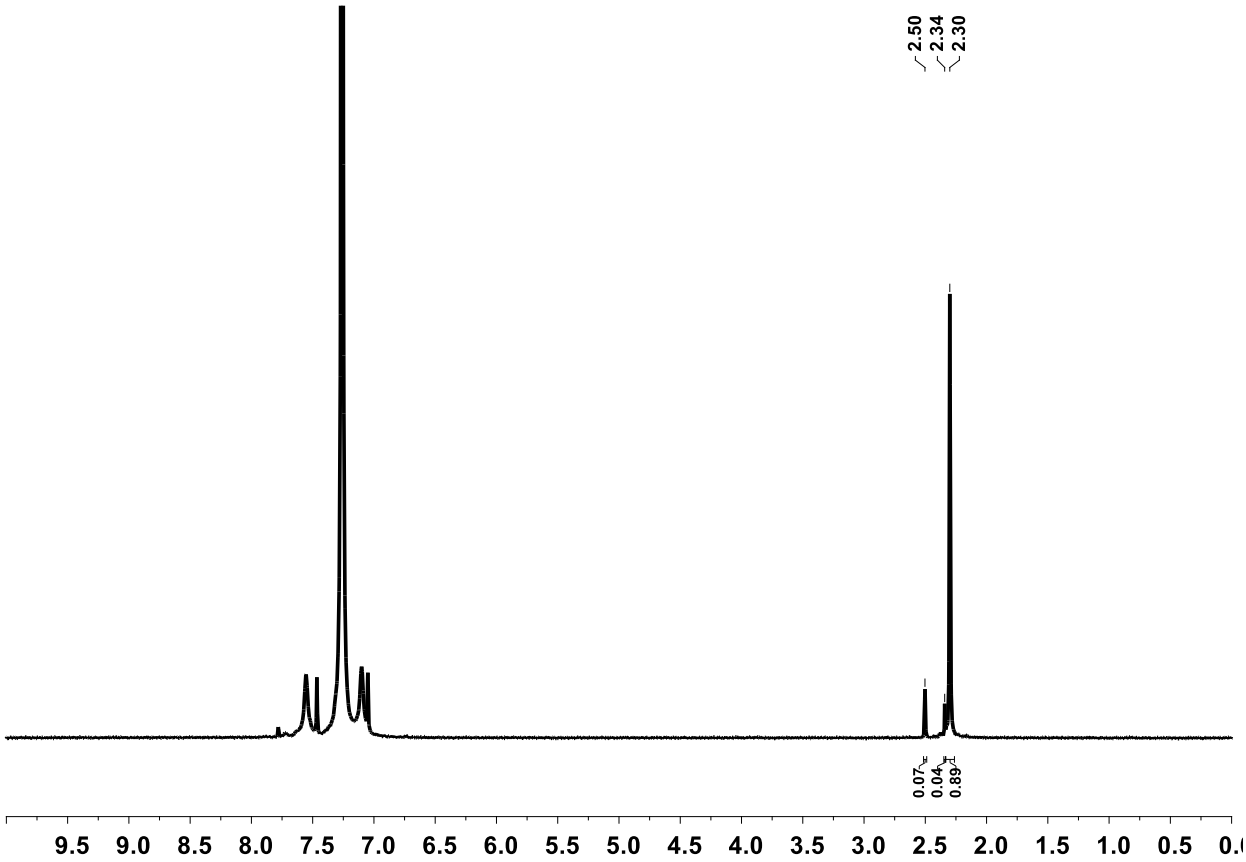

4.6.6 Reactions of Tellurenyl (II) Chloride (3A)

4.6.6.1 Synthesis and Characterization of 3B

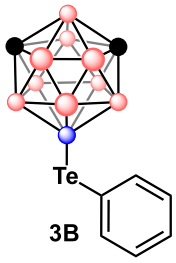

3A (45 mg, 0.15 mmol, 1 eq) was added to an oven dried reaction tube equipped with a stir bar and PTFE cap. The reaction tube was evacuated and backfilled with N_2 three times before adding ~1 mL of anhydrous Et_2O *via* cannula transfer to the tube. Subsequently, a solution of phenylmagnesium bromide (0.15 mL, 3M, 0.45 mmol, 3 eq) was added dropwise to the stirring suspension of **3A** (caution: heat is evolved during

the addition of the Grignard reagent). Once the addition of the Grignard reagent was complete, the reaction was left to stir for 16 h at room temperature. After 16 h, the reaction was quenched by the careful addition of H_2O (5 mL). The quenched reaction mixture was then extracted with Et_2O (2 x 5 mL) and the combined organic layers were dried with Na_2SO_4 before passing the solution through a silica plug and eluting with Et_2O. The solvent was then removed under reduced pressure to yield a white solid.

Yield: 39 mg (75%), white solid

^{1}H NMR (400 MHz, $CDCl_3$): δ 7.82 (d, 2H, $^{1}J_{HH}$ = 6.8 Hz), 7.29 (t, 1H, $^{1}J_{HH}$ = 7.4 Hz), 7.14 (t, 2H, $^{1}J_{HH}$ = 7.6 Hz), 3.6-1.5 (m, 9H, $B_{carborane}$-H), 3.01 (s, 2H, $C_{carborane}$-H)

^{13}C{^{1}H} NMR (100 MHz, $CDCl_3$): δ 140.80, 128.79, 127.46, 108.71, 57.00

^{11}B NMR (128 MHz): δ -5.82 (d, 2B, $^{1}J_{BH}$ = 168 Hz), -8.87 (d, 1B, $^{1}J_{BH}$ = 155 Hz), -12.70 (d, 4B, $^{1}J_{BH}$ = 166 Hz), -15.79 (s, 1B), -16.92 (m, 2B)

^{125}Te NMR (158 MHz): δ 66.9 (q, $^{1}J_{TeB}$ = 159 Hz)

GC-MS *m/z***:** 349.20 (calc. 349.13)

4.6.6.2 Reaction of 3A with Phenylacetylene in Dichloromethane

3A (45 mg, 0.15 mmol, 1 eq) was added to an oven dried reaction tube equipped with a stir bar and PTFE cap before the reaction tube was evacuated and backfilled with N_2 three times. CH_2Cl_2 (1 mL) and phenylacetylene (16.5 µL, 0.15 mmol, 1 eq) were then added to the reaction tube under a positive flow of N_2, and the reaction tube was then sealed. The resulting mixture was then left to stir for 8 h at room temperature. After stirring for 8 h, the CH_2Cl_2 was removed from the vial under high vacuum and redissolved in THF. The resulting solution was then transferred to an NMR tube

for *in situ* ^{11}B NMR spectroscopy to determine conversion to the desired product. The *in situ* ^{11}B NMR is included below. The ^{11}B NMR spectrum reveals that the mixture is largely comprised of starting material and ditelluride (**1B**). Red highlight indicates ^{11}B resonance associated with starting material. Blue highlight indicated ^{11}B resonance associated with **1B**. Green highlight indicates the expected chemical shift for the desired telluride product.

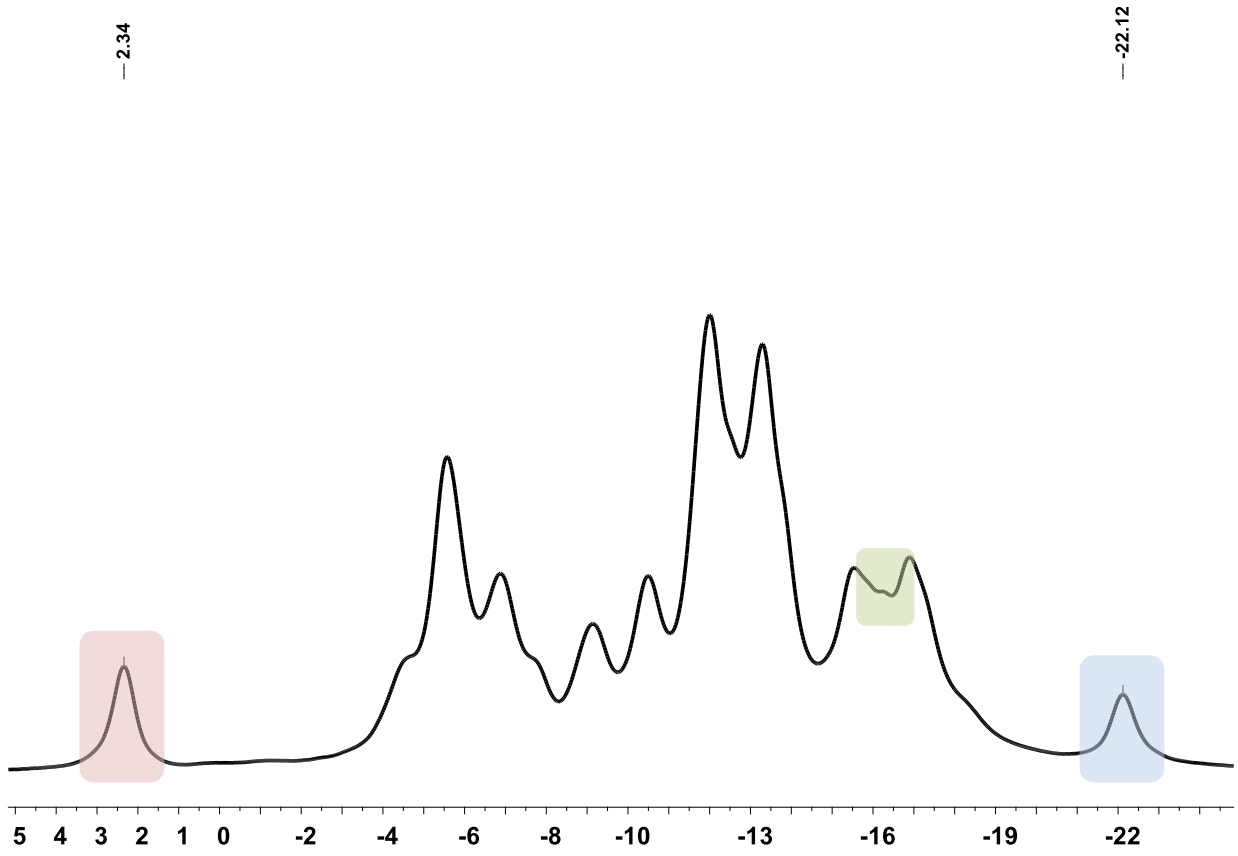

4.6.6.3 Reaction of 3A with Phenylacetylene in Chloroform

3A (57 mg, 0.15 mmol, 1 eq) was added to an oven dried reaction tube equipped with a stir bar and PTFE cap before the reaction tube was evacuated and backfilled with N_2 three times, followed by the addition of $CHCl_3$ (0.75 mL) *via* syringe. Phenylacetylene (33 µL, 0.3 mmol, 2 eq) was then added to the suspension under a positive flow of N_2, and the reaction tube was then sealed. The

resulting mixture was then heated to reflux (65 ˚C) in an oil bath and left to stir for 8 h. After stirring for 8 h, the reaction was allowed to cool to room temperature and the chloroform was removed from the reaction tube under high vacuum and redissolved in THF. The resulting solution was then transferred to an NMR tube for *in situ* ^{11}B NMR spectroscopy to determine conversion to the desired product. The *in situ* ^{11}B NMR is included below. The ^{11}B NMR spectrum reveals that the mixture is largely comprised of starting material and ditelluride (**1B**). Red highlight indicates ^{11}B resonance associated with starting material. Blue highlight indicated ^{11}B resonance associated with **1B**. Green highlight indicates the expected chemical shift for the desired telluride product. The ^{11}B resonance associated with the desired product appears to be slightly more pronounced than when the reaction was performed in CH_2Cl_2, suggesting slightly improved conversion. However, there still remains significant quantities of starting materials and **1B**.

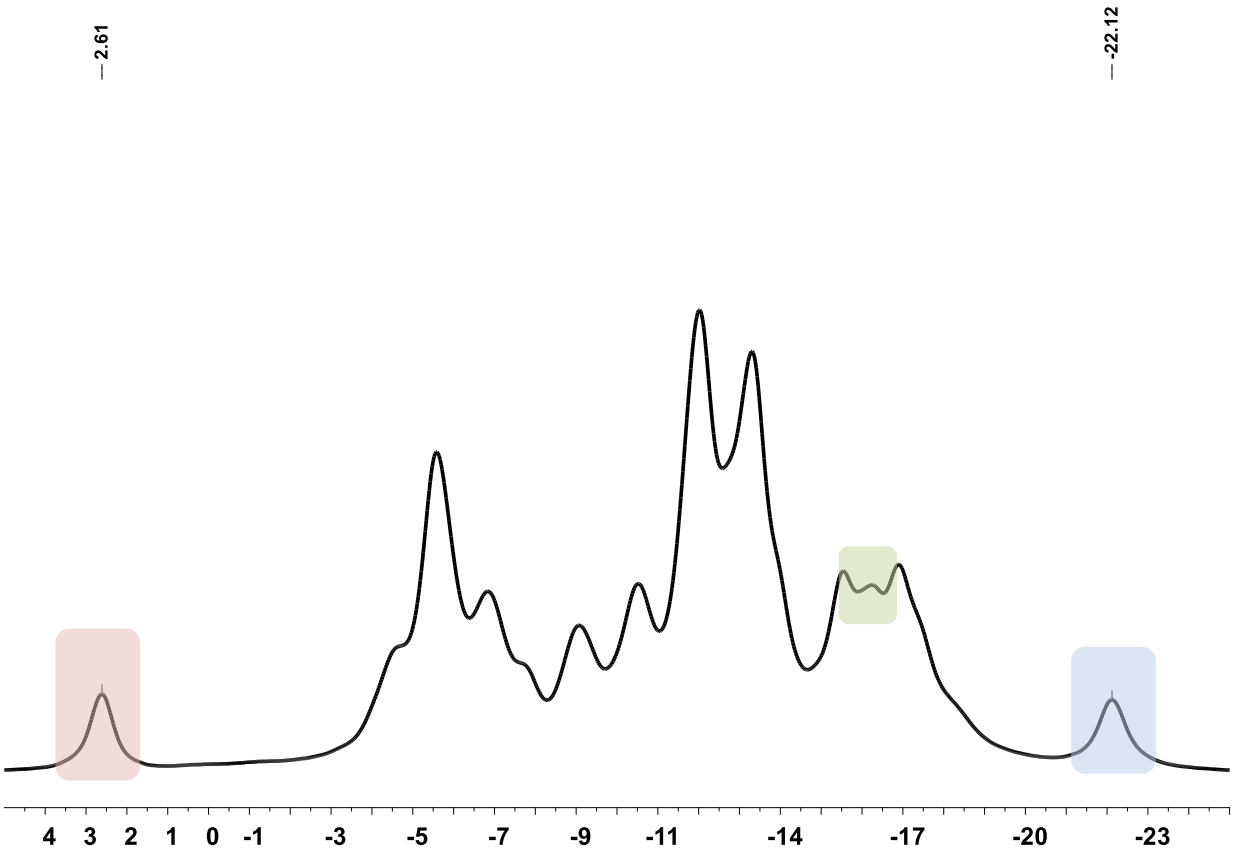

4.6.7 Reactions of Tellurenyl (IV) Chloride (4A)

4.6.7.1 Synthesis and Characterization of 4B and 4B'

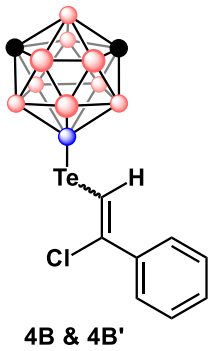

4B & 4B'

4A (57 mg, 0.15 mmol, 1 eq) was added to an oven dried reaction tube equipped with a stir bar and PTFE cap before the reaction tube was evacuated and backfilled with N_2 three times, followed by the addition of $CHCl_3$ (0.75 mL) *via* syringe. Phenylacetylene (33 µL, 0.3 mmol, 2 eq) was then added to the suspension under a positive flow of N_2, and the reaction tube was then sealed. The resulting mixture was then heated to reflux (65 ˚C) in an oil bath and left to stir for 8 h. After stirring for 8 h, the reaction was allowed to cool to room temperature and the reaction mixture was transferred to an NMR tube for *in situ* ^{11}B and ^{125}Te NMR spectroscopy to confirm the formation

of intermediate **4B***. Once the formation of **4B*** was confirmed, the reaction mixture was then transferred back to a reaction tube equipped with a stir bar and 1 mL of an aqueous solution of sodium thiosulfate (0.2 g/mL) was added. The resulting biphasic solution was stirred vigorously for 1 hour and monitored by TLC (10:90 CH_2Cl_2:Hexanes). Once the reaction was determined complete by TLC, the organic layer of the biphasic mixture was collected and the remaining aqueous layer was extracted with CH_2Cl_2 (3 x 3 mL). The crude product was then dry loaded onto silica and volatiles were removed under reduced pressure, before subjecting the crude product to silica gel column chromatography using a hexanes to 20% CH_2Cl_2:Hexanes gradient. The product-containing fractions were collected and volatiles were removed under reduced pressure, affording the product as a yellow-brown oil in 70% isolated yield.

Yield: 43 mg (70%), yellow-brown oil

9-*Te*-*Z*/*E*-(2/2-chloro-2/2-phenylvinyltelluride)-1,7-dicarba-*closo*-dodecaborane (4B/4B')

^{1}H NMR (400 MHz, $CDCl_3$): δ 7.54 (m, 2H), 7.32 (m, 3H), 7.45/7.07 (q, 1H, $^1J_{HB}$ = 2.4/2.7 Hz), 3.6-1.5 (m, 9H, $B_{carborane}$-H), 3.13 (s, 2H, $C_{carborane}$-H)

^{13}C{^{1}H} NMR (100 MHz, $CDCl_3$): δ 139.24, 138.24, 128.89, 128.45, 128.33, 128.23, 128.06, 126.14, 102.30, 97.10, 57.40, 57.27

^{11}B NMR (128 MHz): δ -5.71 (d, 2B, $^1J_{BH}$ = 161 Hz), -8.93 (d, 1B, $^1J_{BH}$ = 153 Hz), -12.42 (d, 4B, $^1J_{BH}$ = 166 Hz), -16.25 (s, 1B), -16.28 (d, 2B, $^1J_{BH}$ = 172 Hz)

^{125}Te NMR (158 MHz): δ -9.8 (q, $^1J_{TeB}$ = 147 Hz), -14.8 (q, $^1J_{TeB}$ = 144 Hz)

GC-MS ***m/z*:** 409.10 (calc. 409.10)

9-*Te*Cl_2-(2-chloro-1-phenylvinyltelluride)-1,7-dicarba-*closo*-dodecaborane (4B*/4B'*)

^{11}B NMR (128 MHz): δ -6.32 (s, 1B), -6.61 (d, 2B), -10.20 (d, 1B, $^1J_{BH}$ = 154 Hz), -13.07 (d, 4B, $^1J_{BH}$ = 163 Hz), -16.82 (d, 2B, $^1J_{BH}$ = 180 Hz)

^{125}Te NMR (158 MHz): δ 566.3 (m), 546.9 (m)

4.6.7.2 Radical Mechanism Inhibition Experiments

4A (38 mg, 0.10 mmol, 1 eq) and dihydroanthracene (18 mg, 0.10 mmol, 1 eq), a known radical inhibitor, were added to an oven dried reaction tube equipped with a stir bar and PTFE cap before the reaction tube was evacuated and backfilled with N_2 three times, followed by the addition of $CHCl_3$ (0.75 mL) *via* syringe. Phenylacetylene (22 µL, 0.2 mmol, 2 eq) was then added to the suspension under a positive flow of N_2, and the reaction tube was then sealed. The resulting mixture was then heated to reflux (65 ˚C) in an oil bath and left to stir for 8 h. After stirring for 8 h, the reaction was allowed to cool to room temperature and the now clear reaction mixture was transferred to an NMR tube for *in situ* ^{125}Te NMR spectroscopy to confirm the formation of desired intermediate and relative intensities for the resonances associated with **4B*** and **4B'***. The *in situ* ^{125}Te NMR provided below shows no significant change in the relative intensity (approx. 1:2) of the two resonances associated with both isomers. The result of this experiment rules out the possibility of a radical-based mechanism in the formation of the minor isomer.

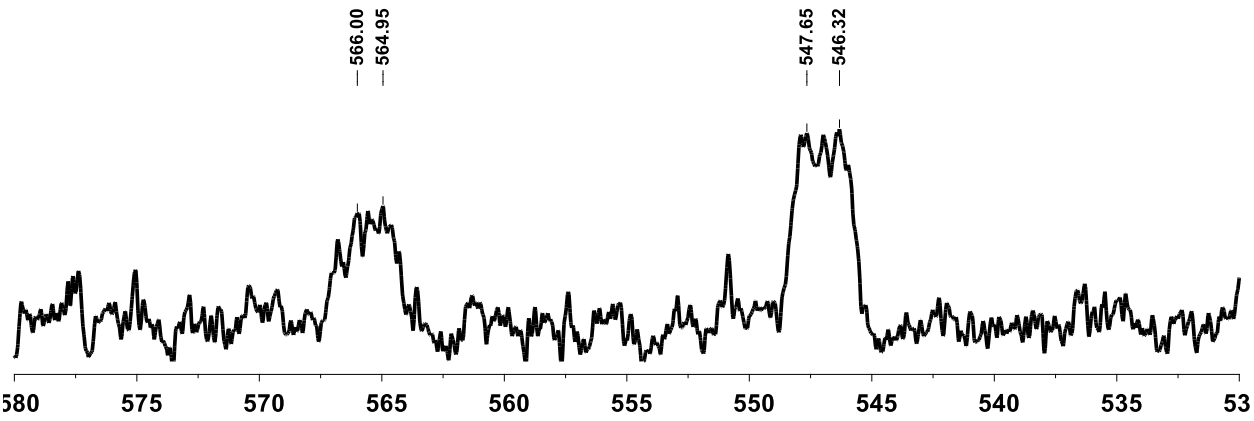

4.6.7.3 Solvent Polarity Experiments

4A (38 mg, 0.10 mmol, 1 eq) was added to an oven dried reaction tube equipped with a stir bar and PTFE cap before the reaction tube was evacuated and backfilled with N_2 three times, followed by the addition of toluene (0.75 mL) *via* syringe. Phenylacetylene (22 µL, 0.2 mmol, 2 eq) was then added to the suspension under a positive flow of N_2, and the reaction tube was then sealed. The resulting mixture was then heated to 65 ˚C in an oil bath and left to stir for 8 h. After stirring for 8 h, the reaction was allowed to cool to room temperature and the now clear reaction mixture was transferred to an NMR tube for *in situ* ^{125}Te NMR spectroscopy to confirm the formation of desired intermediate and relative intensities for the resonances associated with **4B*** and **4B'***. The *in situ* ^{125}Te NMR provided below shows only the formation of the *Z* isomer, with no observable resonance for the *E* isomer. The influence of solvent polarity on isomer distribution agrees with the mechanistic behavior of other organic-based tellurenyl (IV) chlorides.

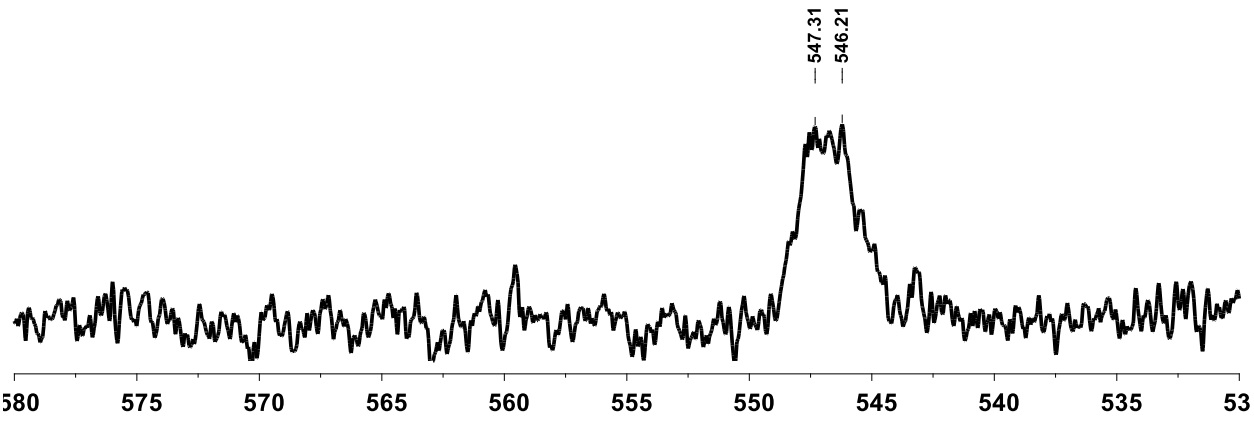

4.6.8 Synthesis and Nucleophilic Reactions of Selenol (5A-B)

4.6.8.1 Synthesis and Characterization of 5A

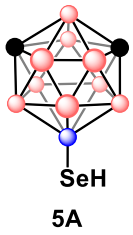

5A

Synthetic procedures adapted from references 4 and 6. **1A** (2.23 g, 5 mmol, 1 eq) was added to a 300 mL round bottomed flask equipped with a stir bar and rubber septum with a bleed needle. A minimal amount of absolute EtOH (30-50 mL) was added to the flask, resulting in a red-orange solution with some solids still suspended (sonication may be required). While stirring the solution of **1A**, an excess of $NaBH_4$ (0.80 g) was carefully added over the course of several minutes. During the course of addition, some heat and gas was generated, with the consumption of **1A** indicated by the reaction mixture turning cloudy and colorless. The reduction was stirred for an additional 15 minutes before the dropwise addition of aqueous HCl (~2M, 10-20 mL) to quench any residual $NaBH_4$ and protonate the selenolate intermediate. Once no more gas was evolved upon the addition of HCl, distilled H_2O (200 mL) was added resulting in a foamy, pale yellow suspension. The product was then extracted from the aqueous solution with CH_2Cl_2 (4 x 30 mL) and the collected organic layers were dried over Na_2SO_4. The dried organic layers were decanted away from the Na_2SO_4 and all volatiles were removed under reduced pressure, leaving the crude product as a pale yellow solid. The crude

product was further purified *via* vacuum sublimation at 90 °C, affording the product as a white, crystalline solid in 58% yield.

Note: for the purpose of synthesizing **5A**, **1A** does not need to be purified *via* silica gel column chromatography first and can be used, as is.

Yield: 1.3 g (58%), white solid

^{1}H NMR (400 MHz, THF-d_8): δ 3.33 (s, 2H, $C_{carborane}$-H), 3.0-1.0 (m, 9H, $B_{carborane}$-H), -2.08 (s, 1H)

^{13}C{^{1}H} NMR (100 MHz, THF-d_8): δ 56.28

^{11}B NMR (128 MHz): δ -5.97 (d, 2B, $^{1}J_{BH}$ = 165 Hz), -7.84 (s, 1B), -8.99 (d, 1B, $^{1}J_{BH}$ = 183 Hz), -12.33 (d, 2B, $^{1}J_{BH}$ = 161 Hz), -13.58 (d, 2B, $^{1}J_{BH}$ = 165 Hz), -17.14 (d, 1B, $^{1}J_{BH}$ = 180 Hz), -19.79 (d, 1B, $^{1}J_{BH}$ = 183 Hz)

^{77}Se NMR (95 MHz): δ -281.3 (m, b)

GC-MS ***m/z*****:** 223.20 (calc. 223.11)

4.6.8.2 Synthesis and Characterization of 5B

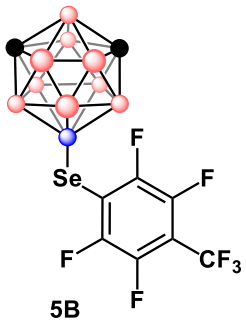

5B

5A (35 mg, 0.15 mmol, 1 eq) and anhydrous Cs_2CO_3 (54 mg, 0.17 mmol, 1.1 eq) were added to an oven dried reaction tube equipped with a stir bar and PTFE cap before the reaction tube was evacuated and backfilled with N_2 three times. Subsequently, anhydrous DMF (1 mL) was added to the reaction tube and the resulting suspension was stirred for 5 minutes before the addition of perfluorotoluene (23.4 µL, 0.15 mmol, 1 eq). The reaction was then left to stir for 16 h at room temperature. After 16 h, distilled H_2O (10 mL) was added to the reaction mixture, and organics

were extracted from the emulsion with Hexanes (3 x 3 mL). The collected organic layers were then passed through a 2 cm silica plug and eluted with hexanes. Volatiles were removed from the filtrate under reduced pressure, affording the product as a white solid in 61% isolated yield.

Yield: 40 mg (61%), white solid

^{1}H NMR (400 MHz, $CDCl_3$): δ 3.5-1.5 (m, 9H, $B_{carborane}$-H), 3.03 (s, 2H, $C_{carborane}$-H)

^{13}C{^{1}H} NMR (100 MHz, $CDCl_3$): δ 55.64

^{19}F NMR (396 MHz): δ -56.31 (t, 3F, $^{1}J_{FF}$ = 21.8 Hz), -123.10 (td, 2F, $^{1}J_{FF}$ = 16.4 Hz, 6.6 Hz), -140.13 (ddd, 2F, $^{1}J_{FF}$ = 22.0 Hz, 15.2 Hz, 9.8 Hz)

^{11}B NMR (128 MHz): δ -5.64 (s, 1B), -6.13 (d, 2B, $^{1}J_{BH}$ = 161 Hz), -9.47 (d, 1B, $^{1}J_{BH}$ = 152 Hz), -13.37 (d, 2B, $^{1}J_{BH}$ = 168 Hz), -17.17 (d, 1B, $^{1}J_{BH}$ = 188 Hz), -19.19 (d, 1B, $^{1}J_{BH}$ = 190 Hz)

^{77}Se NMR (95 MHz): δ -48.2 (m)

GC-MS *m/z***:** 440.20 (calc. 440.09)

4.6.9 Synthesis and Nucleophilic Reactions of Tellurol (6A-C)

4.6.9.1 Synthesis and Characterization of 6A

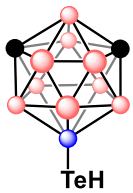

6A

Synthetic procedures adapted from reference 4 and 6. In a darkened fumehood, **1B** (270 mg, 0.5 mmol, 1 eq) was added to a 25 mL Schlenk flask equipped with a stir bar and rubber septum and the flask was subsequently evacuated and back filled with N_2 three times. A minimal amount of absolute EtOH (10 mL) was the added to the flask via syringe, resulting in a deep red solution with some solids still suspended. While stirring the solution of **1B**, an excess of $NaBH_4$ (~150 mg) was carefully added over the course of several

minutes under positive pressure of N_2. During the course of addition, some heat and gas was generated, with the consumption of **1B** indicated by the reaction mixture turning colorless. The reduction was stirred for an additional 15 minutes before the dropwise addition of aqueous HCl (~2M, 10 mL) to quench any residual $NaBH_4$ and protonate the tellurolate intermediate. Once no more gas was evolved upon the addition of HCl, CH_2Cl_2 (3 mL) was added to the Schlenk flask with gentle stirring, resulting in an orange organic layer at the bottom of the flask. The organic layer was then carefully collected from the flask using a glass pipette and deposited in a 50 mL round bottomed flask over a flow of N_2. The remaining aqueous layer was extracted with additional CH_2Cl_2 (2 x 3 mL) and the collected organic layers were dried on a high-vacuum line in the dark, leaving behind an orange powder. The orange powder was then collected in a microsublimator and gradually heated to 50 ^oC in an oil bath while under vacuum. The tellurol was then collected from the cold finger as a white, odorless, crystals in 67% isolated yield and quickly transferred into a glovebox freezer set to -30 ^oC.

Note: for the purpose of synthesizing **6A**, **1B** does need to be purified *via* silica gel column chromatography first.

Yield: 181 mg (67%), white solid

^{1}H NMR (400 MHz, THF-d_8): δ 3.70 (s, 2H, $C_{carborane}$-H), 3.5-1.5 (m, 9H, $B_{carborane}$-H), -7.15 (q, 1H, $^1J_{HB}$ = 5.2 Hz)

^{13}C{^{1}H} NMR (100 MHz, THF-d_8): δ 58.31

^{11}B NMR (128 MHz): δ -5.07 (d, 2B, $^1J_{BH}$ = 168 Hz), -8.00 (d, 1B, $^1J_{BH}$ = 152 Hz), -11.28 (d, 2B, $^1J_{BH}$ = 152 Hz), -12.37 (d, 2B, $^1J_{BH}$ = 155 Hz), -15.98 (d, 1B, $^1J_{BH}$ = 172 Hz), -17.11 (d, 1B, $^1J_{BH}$ = 152 Hz), -20.48 (s, 1B)

^{125}Te NMR (158 MHz): δ -596.5 (q, $^{1}J_{TeB}$ = 126 Hz)

GC-MS *m/z***:** 270.00 (calc. 270.10)

4.6.9.2 Synthesis and Characterization of 6B

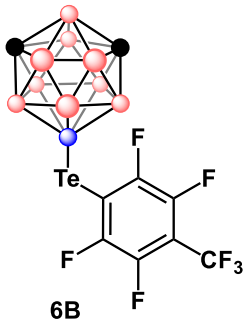

6B

In a dark, N_2-filled glovebox, **6A** (41 mg, 0.15 mmol, 1 eq) and anhydrous Cs_2CO_3 (54 mg, 0.17 mmol, 1.1 eq) were added to 4 mL dram vial equipped with a stir bar and PTFE cap. Subsequently, a solution of degassed, anhydrous DMF (1 mL) and perfluorotoluene (23.4 µL, 0.15 mmol, 1 eq) was quickly added to the vial. The resulting dark red solution was then left to stir for 16 h at room temperature in the dark. After 16 h, the dram vial was removed from the glovebox and the reaction solution was transferred to a separatory funnel containing distilled H_2O (10 mL). Organics were then extracted from the emulsion with Hexanes (3 x 3 mL). The collected organic layers were then passed through a 2 cm silica plug and eluted with hexanes. Volatiles were removed from the filtrate under reduced pressure, affording the product as a white solid in 13% isolated yield.

Yield: 10 mg (13%), white solid

^{1}H NMR (400 MHz, $CDCl_3$): δ 3.8-1.5 (m, 9H, $B_{carborane}$-H), 3.07 (s, 2H, $C_{carborane}$-H)

^{13}C{^{1}H} NMR (100 MHz, $CDCl_3$): δ 57.31

^{19}F NMR (396 MHz): δ -56.37 (t, 3F, $^{1}J_{FF}$ = 21.8 Hz), -111.01 (td, 2F, $^{1}J_{FF}$ = 16.8 Hz, 5.9 Hz), -139.61 (m, 2F)

^{11}B NMR (128 MHz): δ -5.56 (d, 2B, $^{1}J_{BH}$ = 168 Hz), -8.75 (d, 1B, $^{1}J_{BH}$ = 152 Hz), -12.48 (d, 4B, $^{1}J_{BH}$ = 152 Hz), -16.29 (m, 3B)

^{125}Te NMR (158 MHz): δ -84.2 (m)

GC-MS *m/z***:** 489.10 (calc. 489.08)

4.6.9.3 Synthesis and Characterization of 6C

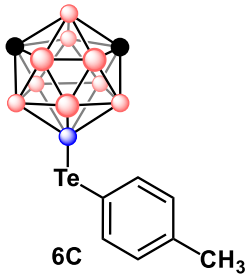

In a dark, N_2-filled glovebox, **6A** (41 mg, 0.15 mmol, 1 eq) and [4-tolyl-PdRuPhos][OTf] (125 mg, 0.15 mmol, 1 eq) were added to 4 mL dram vial equipped with a stir bar and PTFE cap. Subsequently, anhydrous CH_2Cl_2 (2 mL) was added to the vial and the resulting mixture was vigorously stirred for 30 minutes at room temperature. After 30 minutes, the vial was removed from the glovebox and all volatiles were removed under reduced pressure. The crude residue was then subjected to purification *via* a 2 cm plug of silica gel, using 20% CH_2Cl_2:Hexanes as eluent. The product containing fractions were collected and volatiles were removed under reduced pressure, affording the desired product in 56% isolated yield.

Yield: 30 mg (56%), white solid

^{1}H NMR (400 MHz, $CDCl_3$): δ 7.69 (d, 2H, $^{1}J_{HH}$ = 7.9 Hz), 6.96 (d, 2H, $^{1}J_{HH}$ = 7.6 Hz), 3.6-1.6 (m, 9H, $B_{carborane}$-H), 3.00 (s, 2H, $C_{carborane}$-H)

^{13}C{^{1}H} NMR (100 MHz, $CDCl_3$): δ 140.82, 129.78, 56.95, 21.27

^{11}B NMR (128 MHz): δ -5.77 (d, 2B, $^{1}J_{BH}$ = 161 Hz), -8.79 (d, 1B, $^{1}J_{BH}$ = 155 Hz), -12.68 (d, 4B, $^{1}J_{BH}$ = 168 Hz), -16.48 (m, 3B)

^{125}Te NMR (158 MHz): δ 46.5 (q, $^{1}J_{TeB}$ = 161 Hz)

GC-MS *m/z***:** 363.20 (calc. 363.15)

4.6.9.4 *In situ* ^{11}B NMR Spectroscopy of Crude 6B

Representative *in situ* ^{11}B NMR spectrum of crude **6B**. The majority of the reaction mixture (>85%) consists of **1B** as determined by the ^{11}B resonance at -22 ppm.

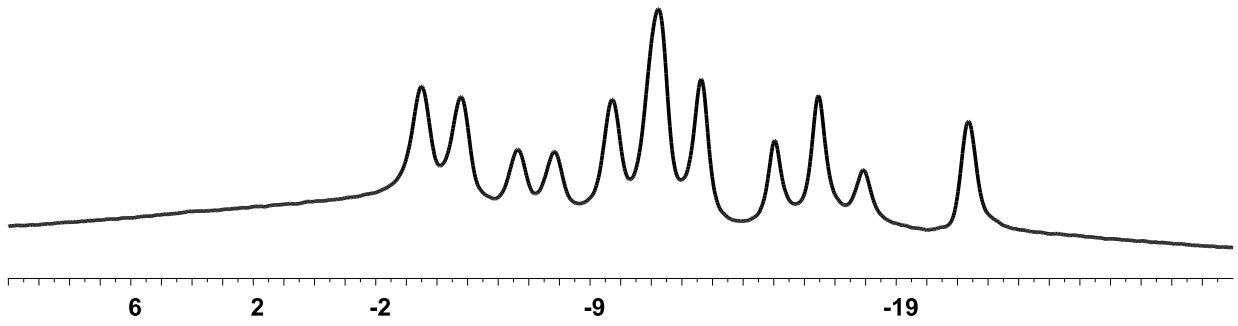

4.6.10 X-Ray Crystallography Details

Table C1. Crystal data and structure refinement for **1A**

CCDC number	2105009	
Empirical formula	$C_4H_{22}B_{20}Se_2$	
Formula weight	444.33	
Temperature	100.0 K	
Wavelength	0.71073 Å	
Crystal system	Orthorhombic	
Space group	*Pbcn*	
Unit cell dimensions	a = 17.3364(5) Å	α= 90°.
	b = 17.1498(7) Å	β= 90°.

	c = 13.1219(5) Å γ = 90°.
Volume	3901.3(2) $Å^3$
Z	8
Density (calculated)	1.513 Mg/m^3
Absorption coefficient	3.775 mm^{-1}
F(000)	1712
Crystal size	0.33 x 0.31 x 0.28 mm^3
Theta range for data collection	2.280 to 28.315°.
Index ranges	-23<=*h*<=23, -22<=*k*<=22, -17<=*l*<=17
Reflections collected	60353
Independent reflections	4828 [*R*(int) = 0.0503]
Completeness to theta = 25.242°	99.6 %
Absorption correction	Semi-empirical from equivalents
Max. and min. transmission	0.688 and 0.488
Refinement method	Full-matrix least-squares on F^2
Data / restraints / parameters	4828 / 0 / 235
Goodness-of-fit on F^2	1.140

Final R indices [$I>2\sigma(I)$]	$R1$ = 0.0446, w$R2$ = 0.0897
R indices (all data)	$R1$ = 0.0536, w$R2$ = 0.0940
Extinction coefficient	n/a
Largest diff. peak and hole	1.037 and -1.930 e.Å^{-3}

Table C2. Crystal data and structure refinement for **1B**

CCDC number	2105007	
Empirical formula	$C_4H_{22}B_{20}Te_2$	
Formula weight	541.61	
Temperature	100.0 K	
Wavelength	0.71073 Å	
Crystal system	Orthorhombic	
Space group	*Pbcn*	
Unit cell dimensions	a = 17.8707(6) Å	α= 90°.
	b = 17.8162(7) Å	β= 90°.
	c = 12.9892(4) Å	γ = 90°.
Volume	4125.6(2) Å^3	
Z	8	
Density (calculated)	1.740 Mg/m^3	

Absorption coefficient	2.807 mm^{-1}
F(000)	2000
Crystal size	0.33 x 0.31 x 0.29 mm^3
Theta range for data collection	1.614 to 25.000°.
Index ranges	-21<=*h*<=21, -21<=*k*<=21, -15<=*l*<=15
Reflections collected	25618
Independent reflections	3644 [*R*(int) = 0.0520, *R*(sigma) = 0.0309]
Completeness to theta = 25.242°	99.9 %
Absorption correction	Semi-empirical from equivalents
Max. and min. transmission	0.7454 and 0.6284
Refinement method	Full-matrix least-squares on F^2
Data / restraints / parameters	3644 / 391 / 235
Goodness-of-fit on F^2	1.464
Final R indices [$I>2\sigma(I)$]	*R*1 = 0.0562, w*R*2 = 0.1461
R indices (all data)	*R*1 = 0.0577, w*R*2 = 0.1472
Extinction coefficient	n/a
Largest diff. peak and hole	1.166 and -1.869 $e.Å^{-3}$

Table C3. Crystal data and structure refinement for **2C**

CCDC number	2105010	
Empirical formula	$C_9H_{21}B_{10}ClSe$	
Formula weight	351.77	
Temperature	100.0 K	
Wavelength	0.71073 Å	
Crystal system	Orthorhombic	
Space group	$P2_12_12_1$	
Unit cell dimensions	a = 9.2033(4) Å	α= 90°.
	b = 10.1545(5) Å	β= 90°.
	c = 17.3382(8) Å	γ = 90°.
Volume	1620.34(13) $Å^3$	
Z	4	
Density (calculated)	1.442 Mg/m^3	
Absorption coefficient	2.461 mm^{-1}	
F(000)	704	
Index ranges	-12<=*h*<=12, -13<=*k*<=13, -22<=*l*<=22	
Max. and min. transmission	0.625 and 0.738	

Goodness-of-fit on F^2	1.74
R indices (all data)	*R*1 = 0.0219, w*R*2 = 0.0522
Extinction coefficient	n/a

Table C4. Crystal data and structure refinement for **2D**

CCDC number	2105008	
Empirical formula	$C_{10}H_{17}B_{10}ClSe$	
Formula weight	359.74	
Temperature	100.0 K	
Wavelength	0.71073 Å	
Crystal system	Monoclinic	
Space group	*P 21/n*	
Unit cell dimensions	a = 7.8512(6) Å	α= 90°.
	b = 10.2780(9) Å	β= 100.930(3)°.
	c = 20.4037(15) Å	γ = 90°.
Volume	1616.6(2) $Å^3$	
Z	4	
Density (calculated)	1.478 Mg/m^3	
Absorption coefficient	2.469 mm^{-1}	

$F(000)$	712
Crystal size	0.33 x 0.29 x 0.11 mm^3
Theta range for data collection	1.981 to 26.411°.
Index ranges	$-9 \leq h \leq 9$, $-12 \leq k \leq 12$, $-25 \leq l \leq 25$
Reflections collected	24508
Independent reflections	3387 [R(int) = 0.0683]
Completeness to theta = 25.242°	99.2 %
Absorption correction	Semi-empirical from equivalents
Max. and min. transmission	0.672 and 0.499
Refinement method	Full-matrix least-squares on F^2
Data / restraints / parameters	3387 / 0 / 200
Goodness-of-fit on F^2	1.123
Final R indices [$I>2\sigma(I)$]	$R1$ = 0.0572, w$R2$ = 0.1832
R indices (all data)	$R1$ = 0.0588, w$R2$ = 0.1875
Twinning	180 deg rotational twin
Largest diff. peak and hole	0.618 and -1.493 e.$Å^{-3}$

4.6.11 NMR, GC-MS, and UV-Vis Data

4.6.11.1 Characterization of 1A

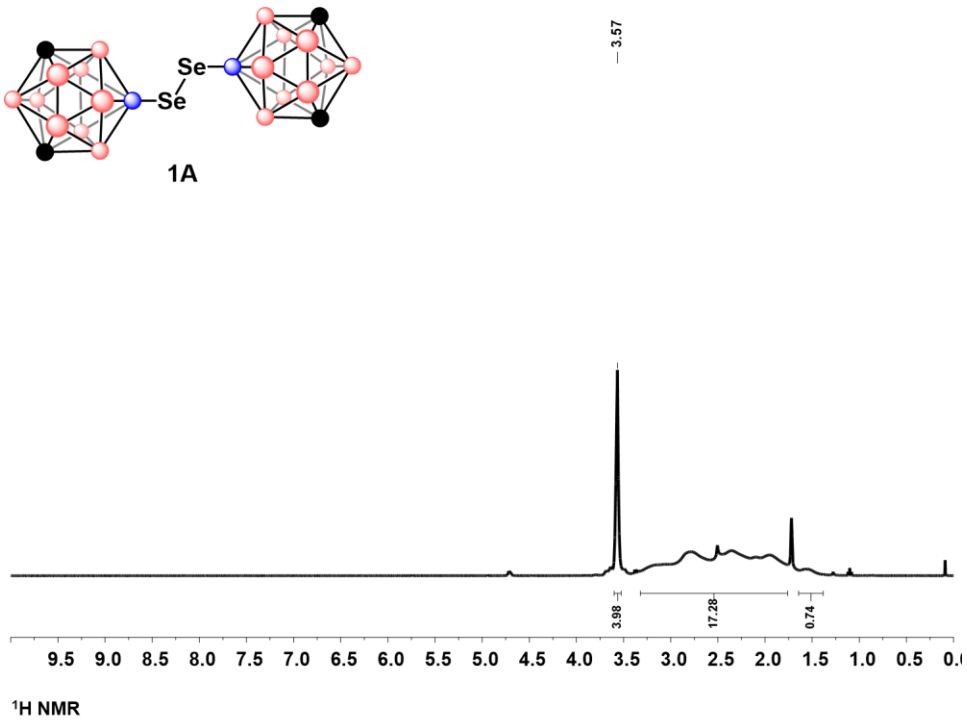

Figure C1.1 ^{1}H NMR of **1A**

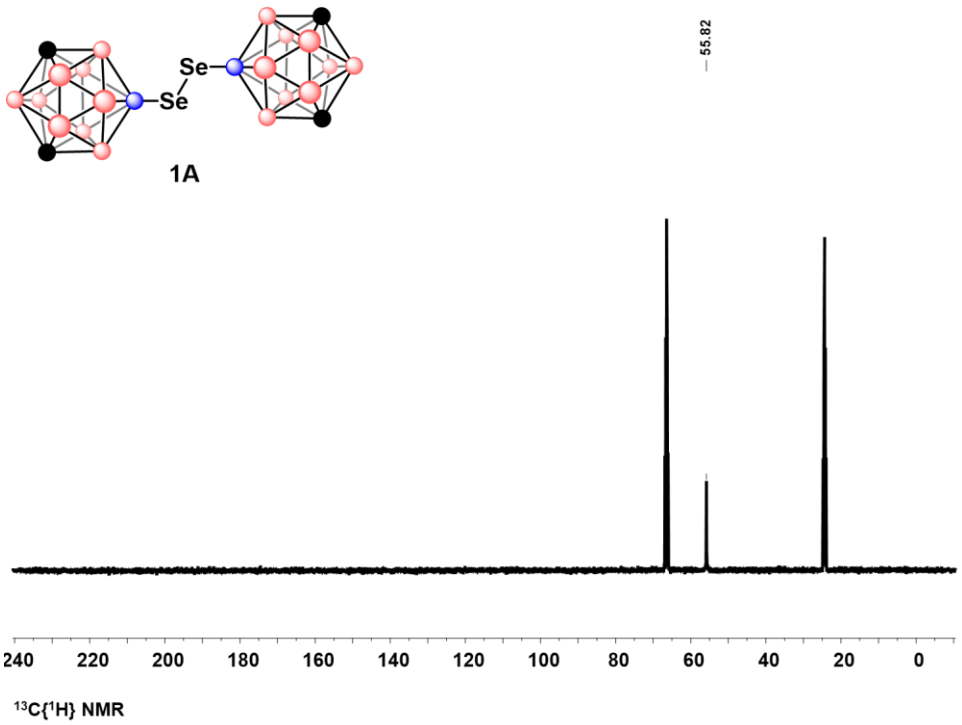

Figure C1.2 $^{13}C\{^{1}H\}$ NMR of **1A**

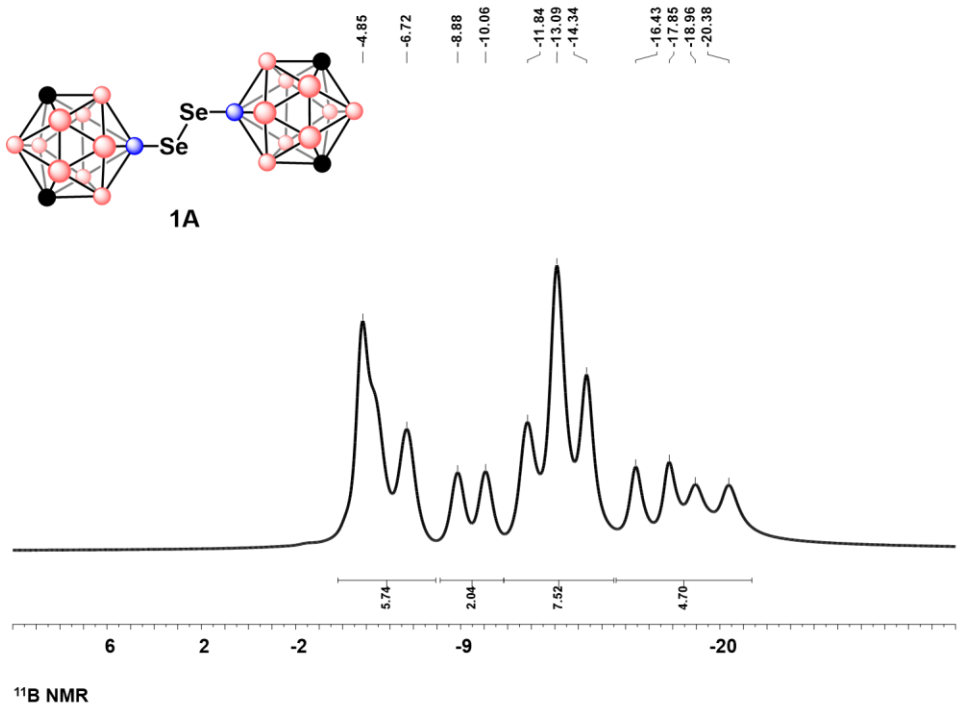

Figure C1.3 ^{11}B NMR of **1A**

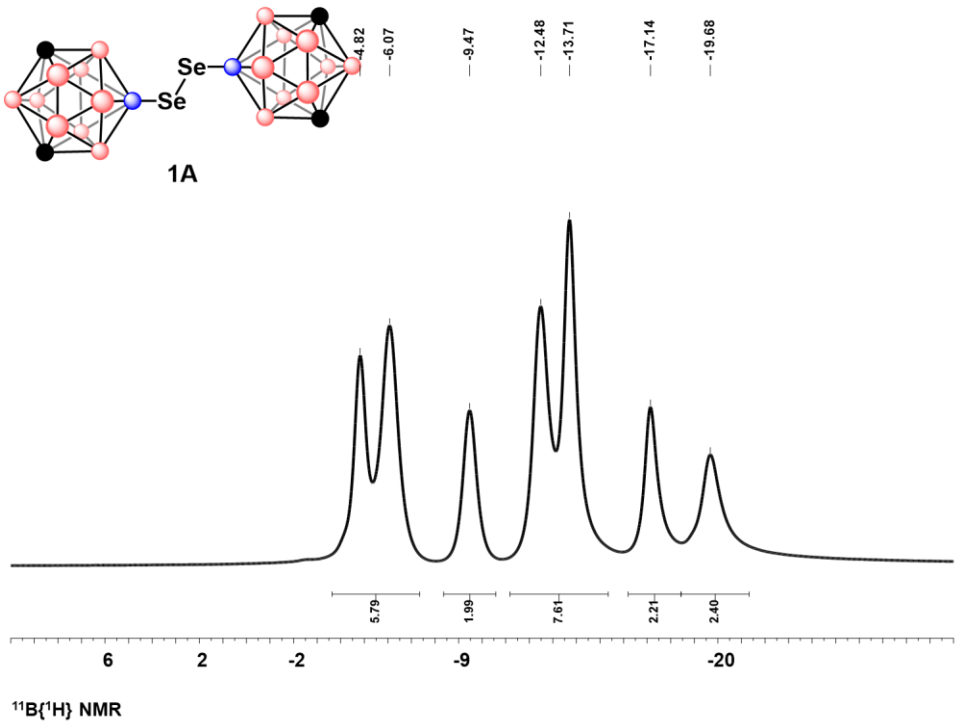

Figure C1.4 $^{11}B\{^{1}H\}$ NMR of **1A**

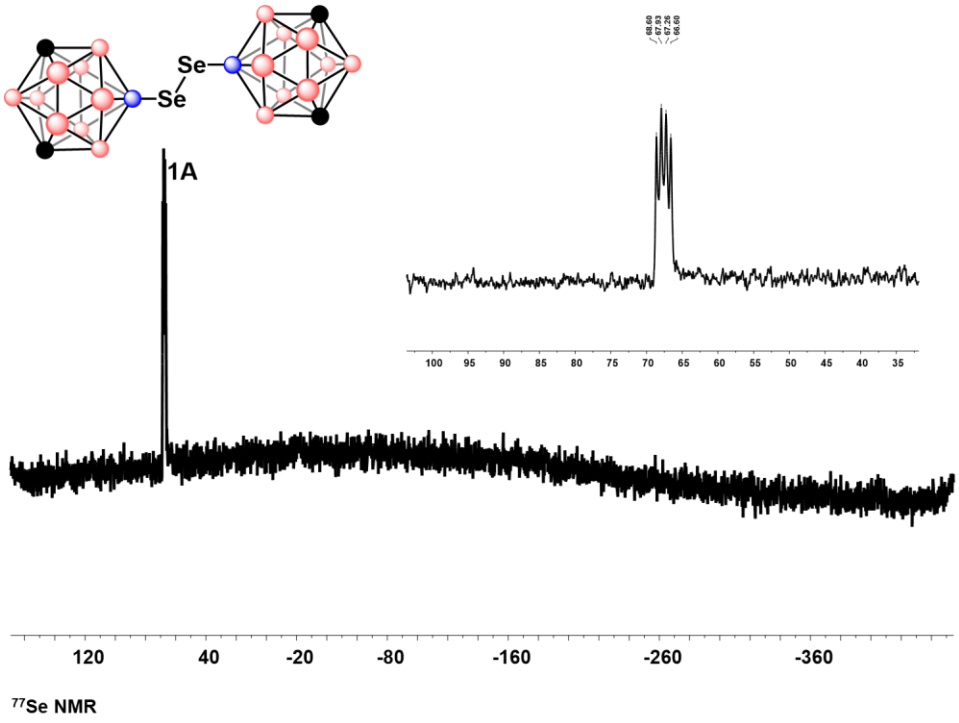

Figure C1.5 ^{77}Se NMR of **1A**

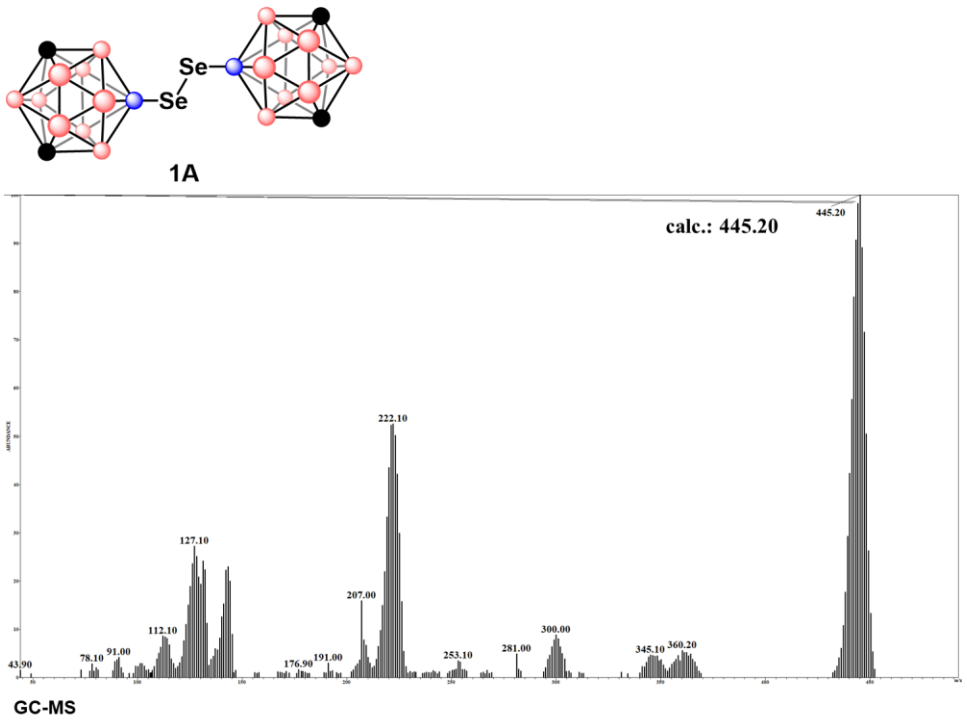

Figure C1.6 GC-MS of **1A**

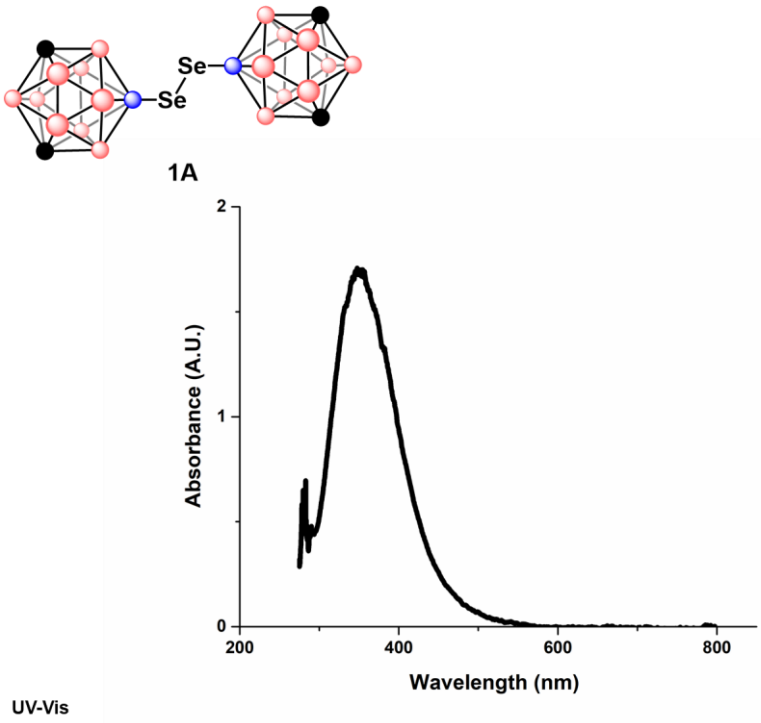

Figure C1.7 UV-Vis of 1A

4.6.11.2 Characterization of 1B

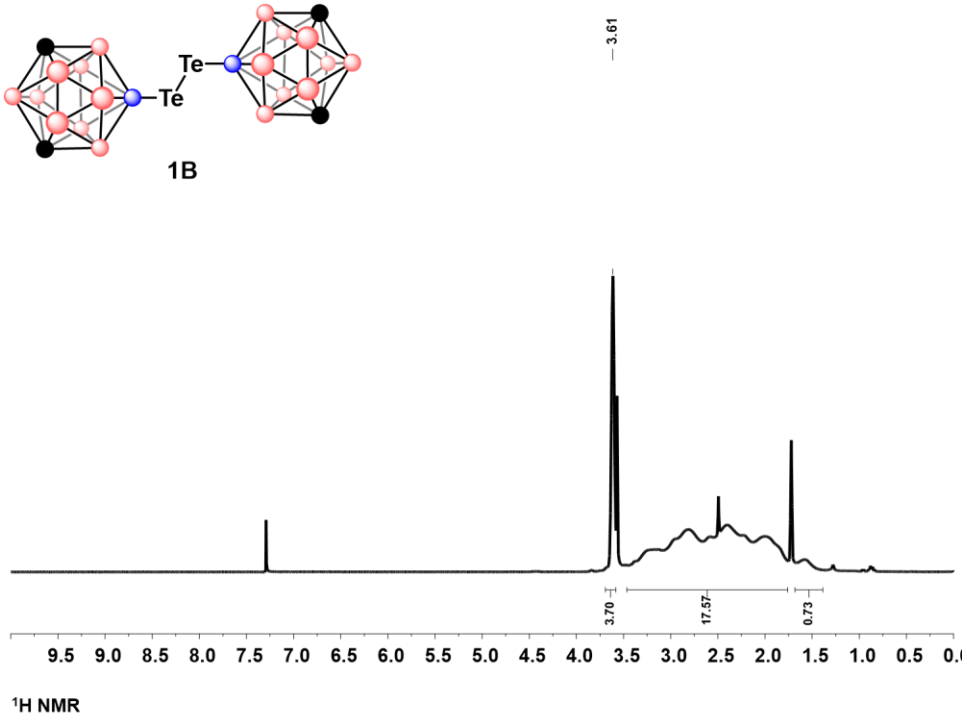

Figure C2.1 ^{1}H NMR of **1B**

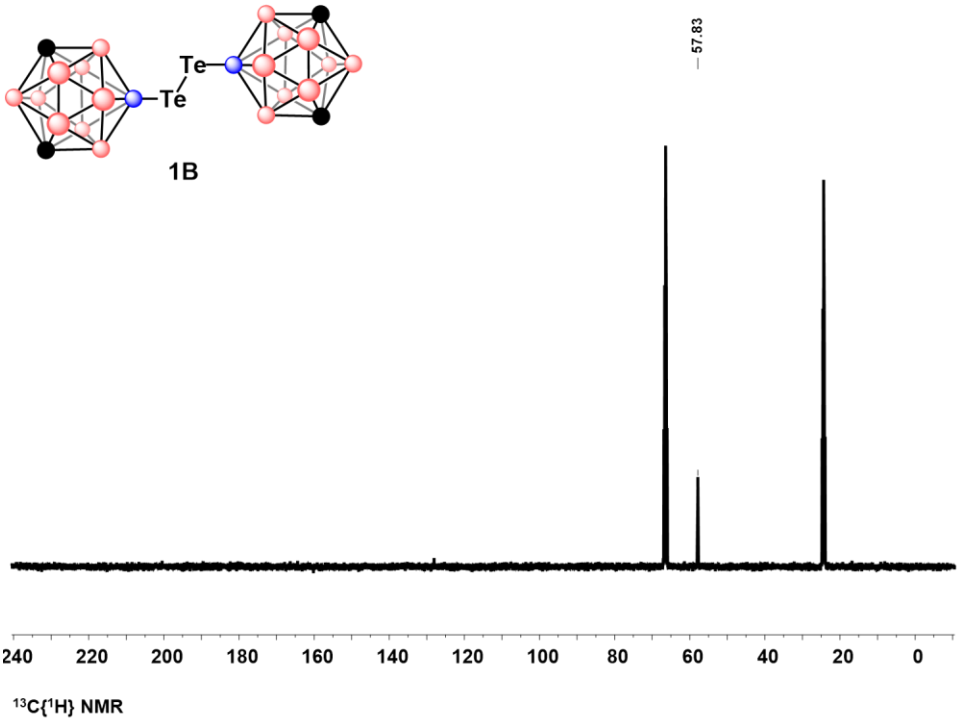

Figure C2.2 $^{13}C\{^{1}H\}$ NMR of **1B**

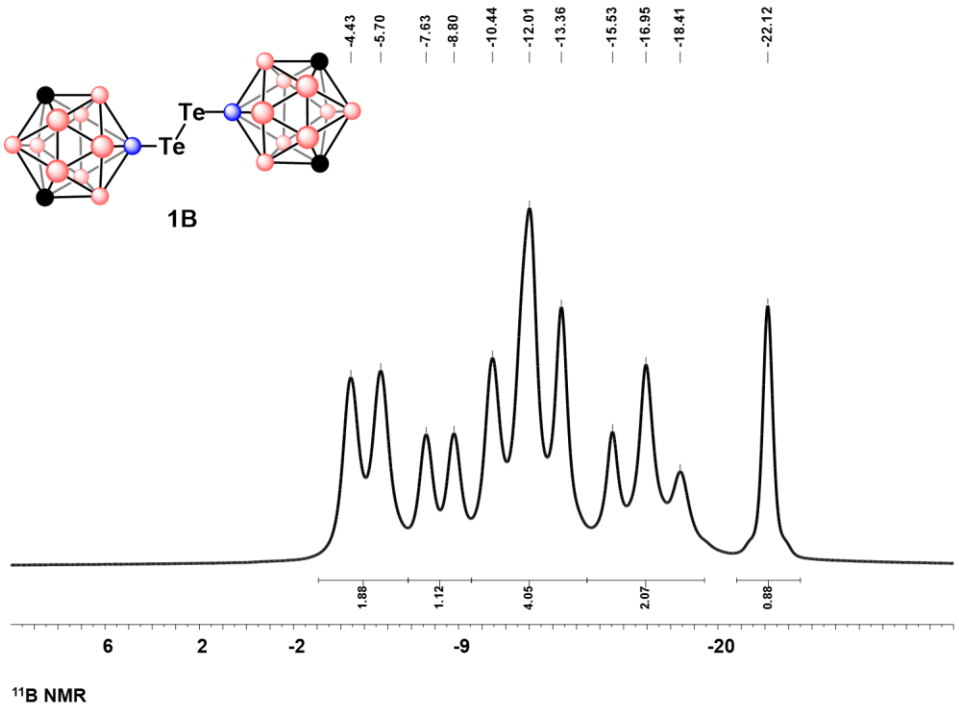

Figure C2.3 ^{11}B NMR of **1B**

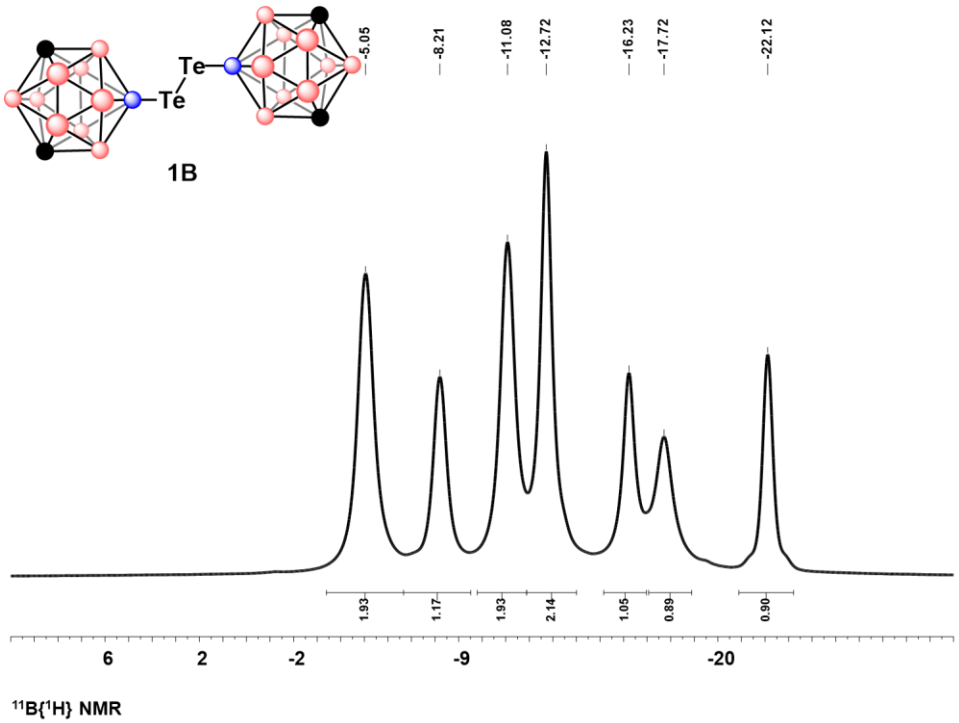

Figure C2.4 $^{11}B\{^{1}H\}$ NMR of **1B**

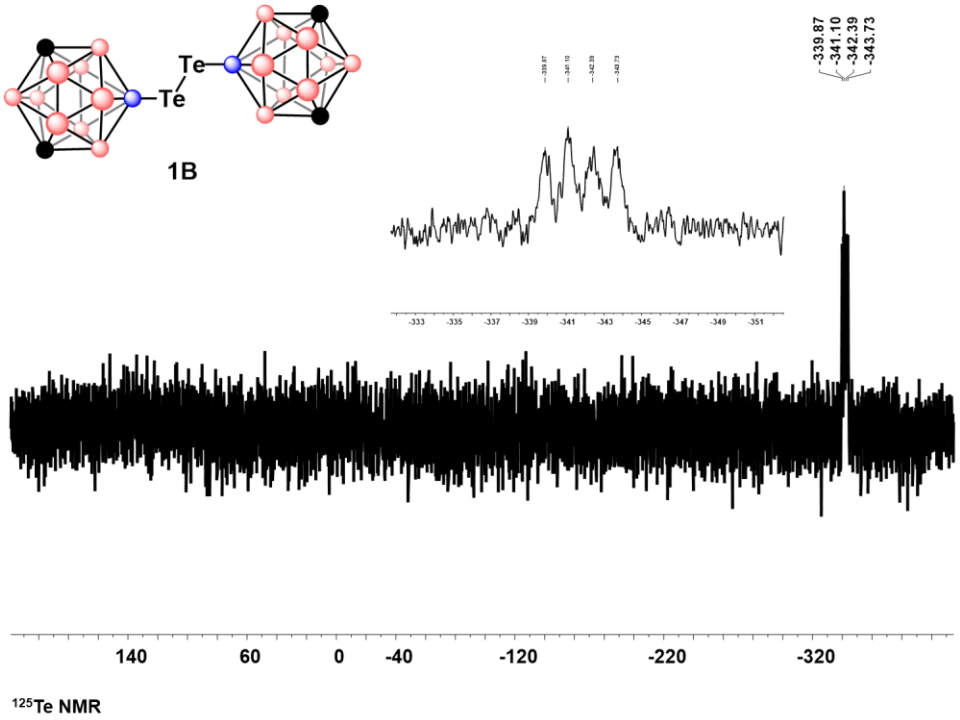

Figure C2.5 ^{125}Te NMR of **1B**

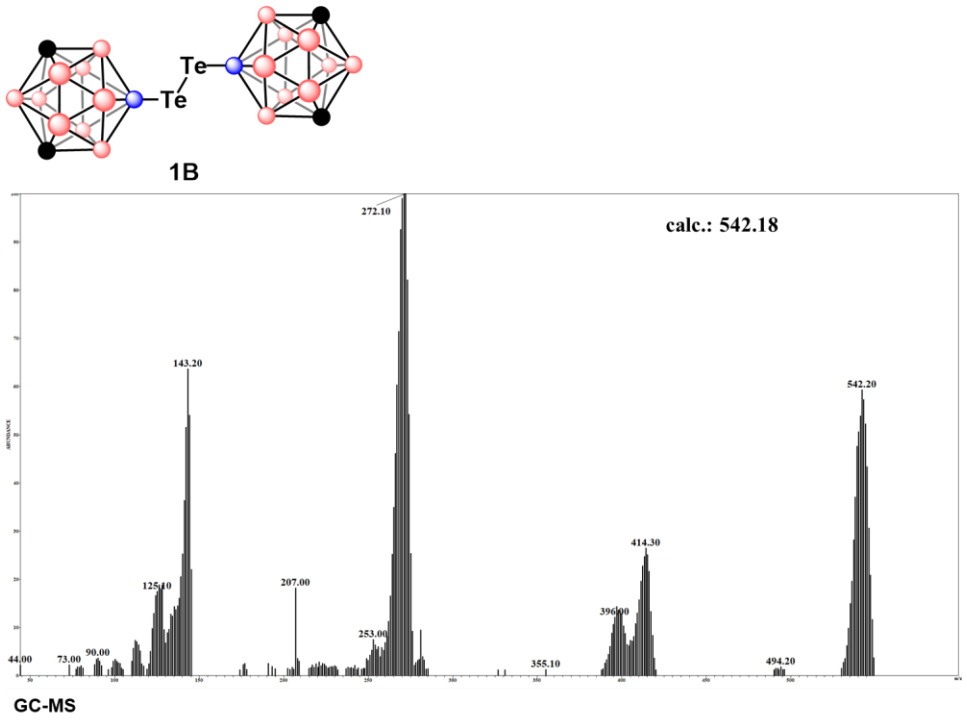

Figure C2.6 GC-MS of **1B**

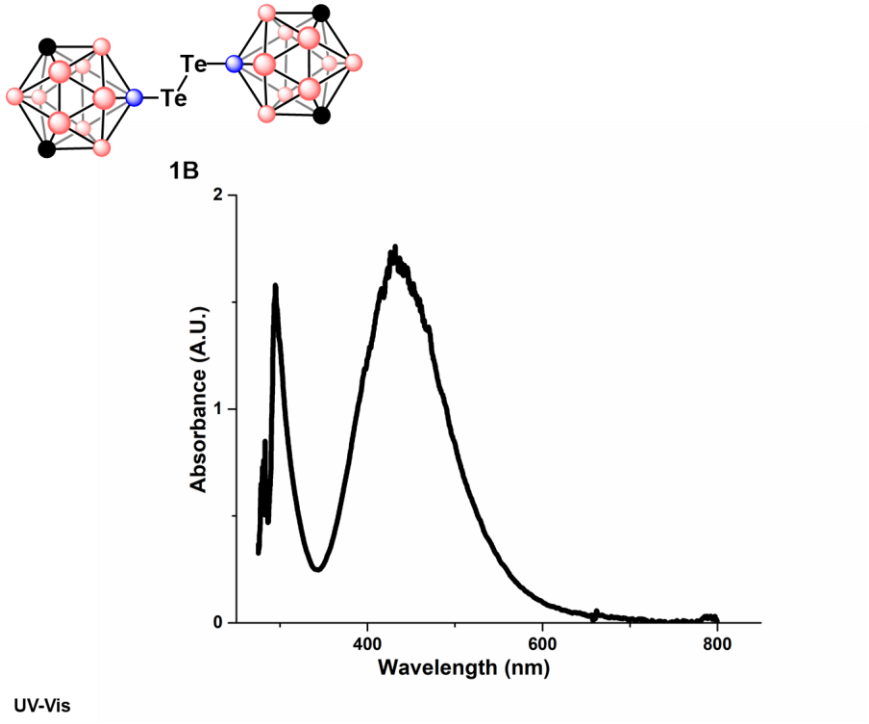

Figure C2.7 UV-Vis of **1B**

4.6.11.3 Characterization of 2A

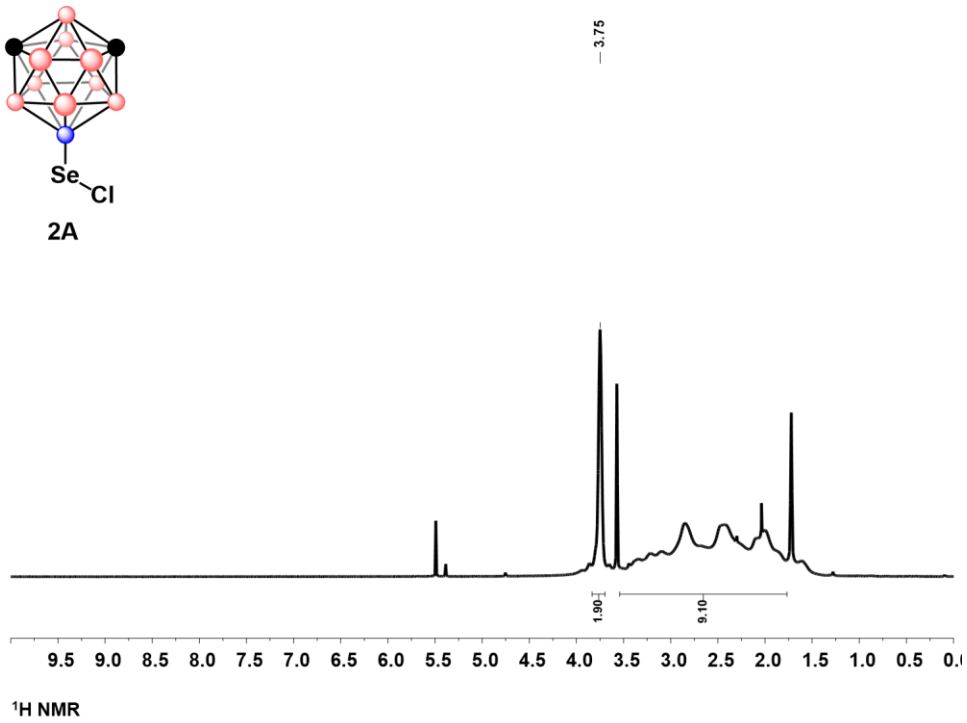

Figure C3.1 ^{1}H NMR of **2A**

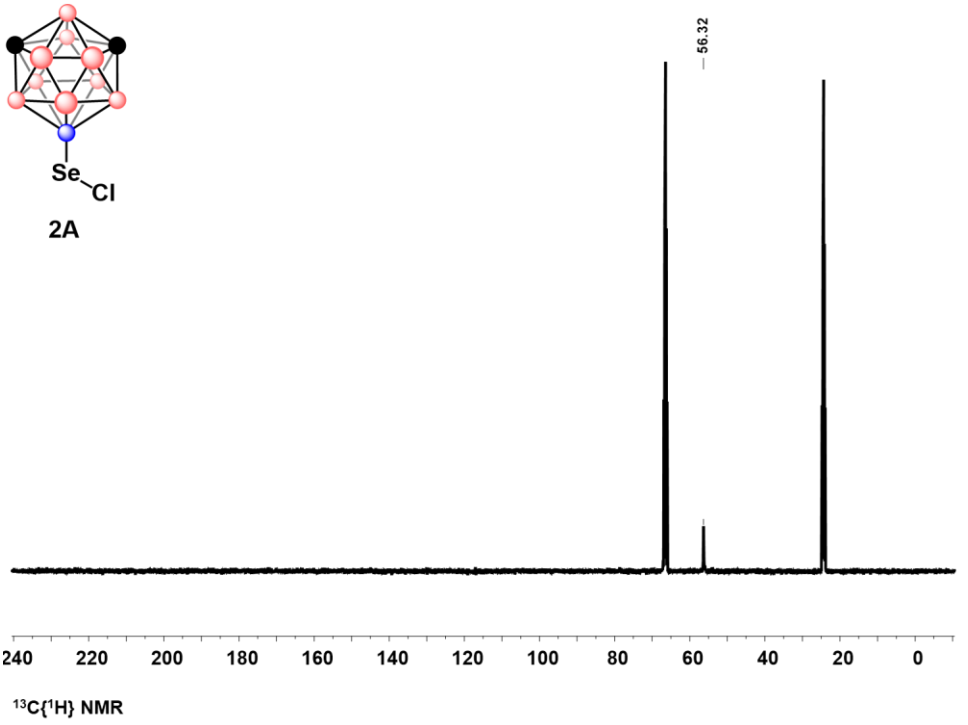

Figure C3.2 ^{13}C{^{1}H} NMR of **2A**

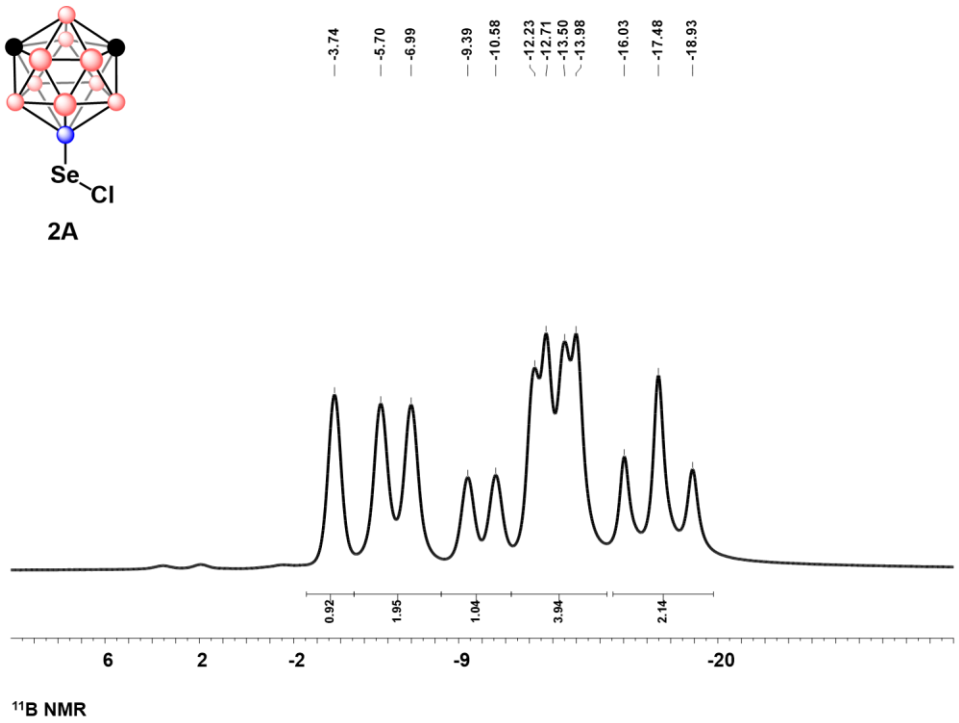

Figure C3.3 ^{11}B NMR of **2A**

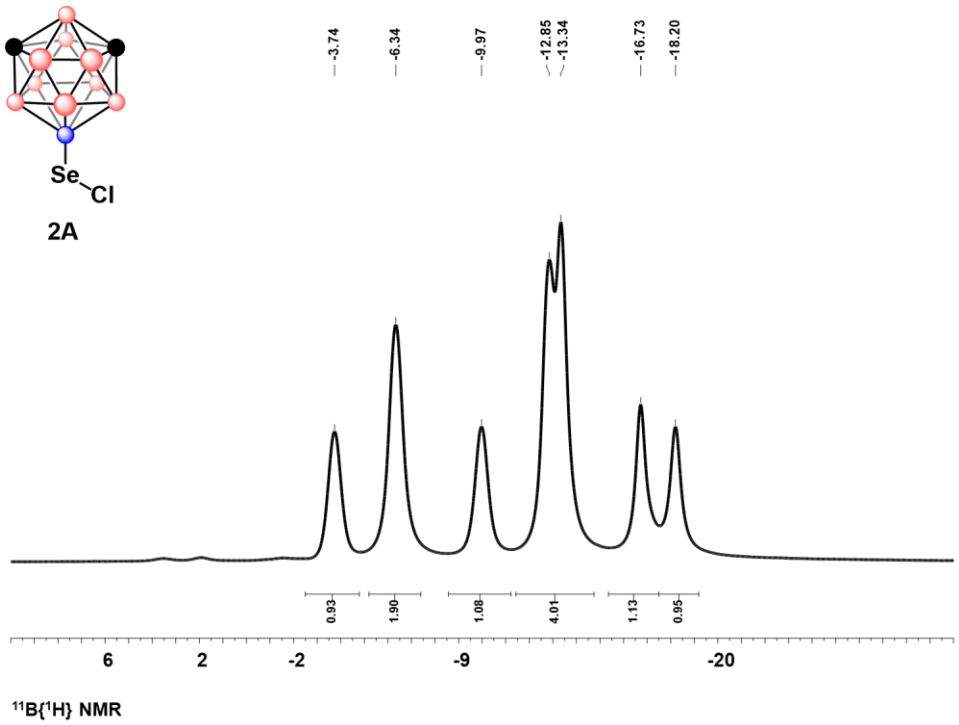

Figure C3.4 ^{11}B{^{1}H} NMR of **2A**

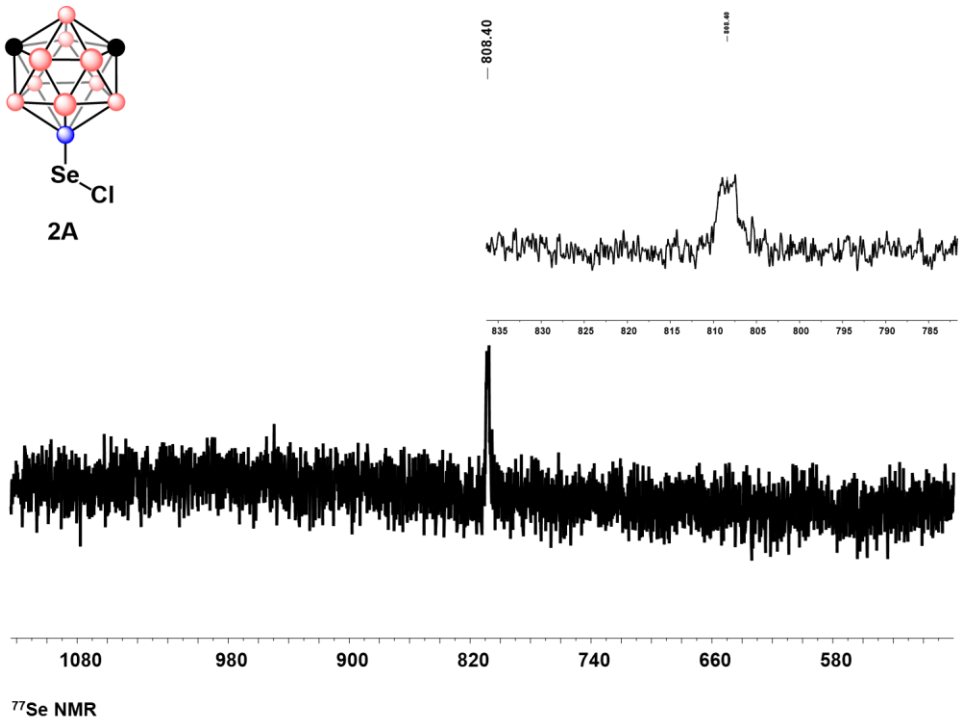

Figure C3.5 ^{77}Se NMR of **2A**

4.6.11.4 Characterization of 3A

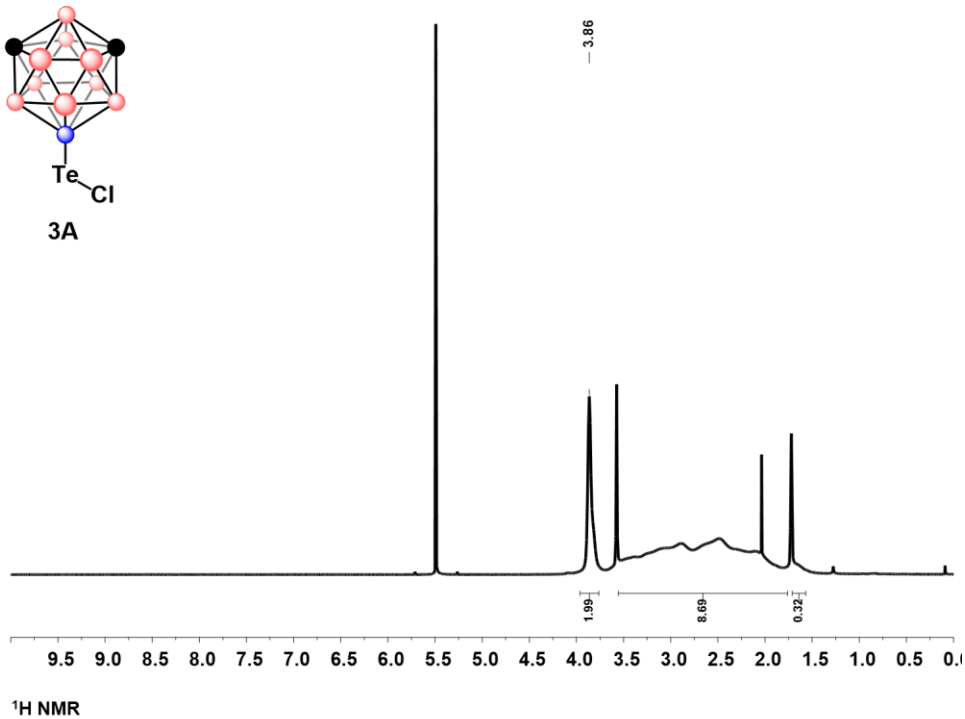

Figure C4.1 ^{1}H NMR of **3A**

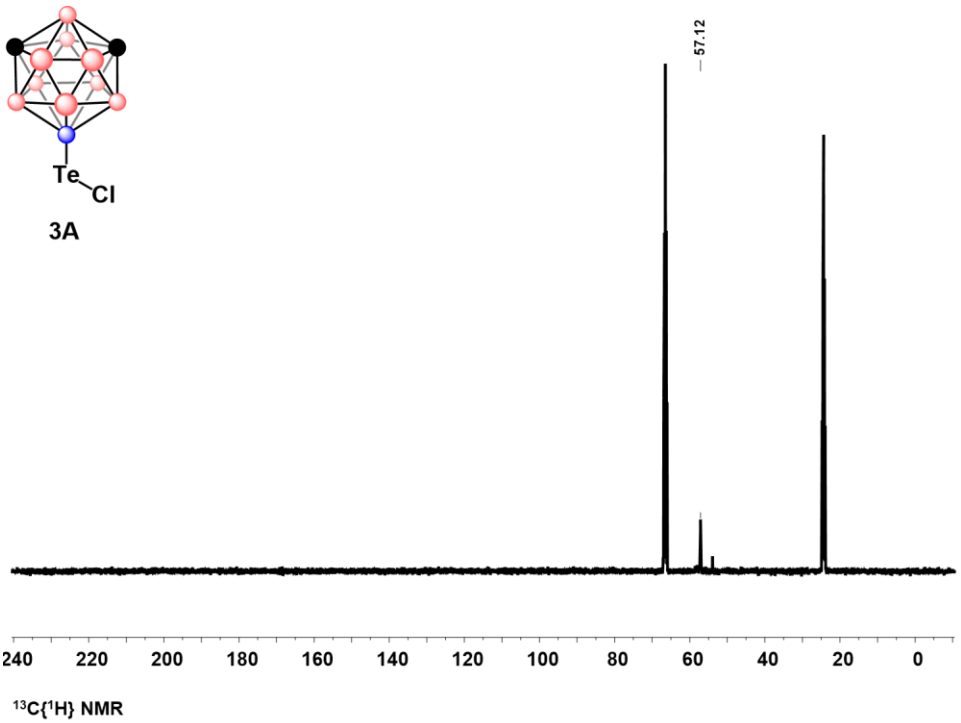

Figure C4.2 ^{13}C{^{1}H} NMR of **3A**

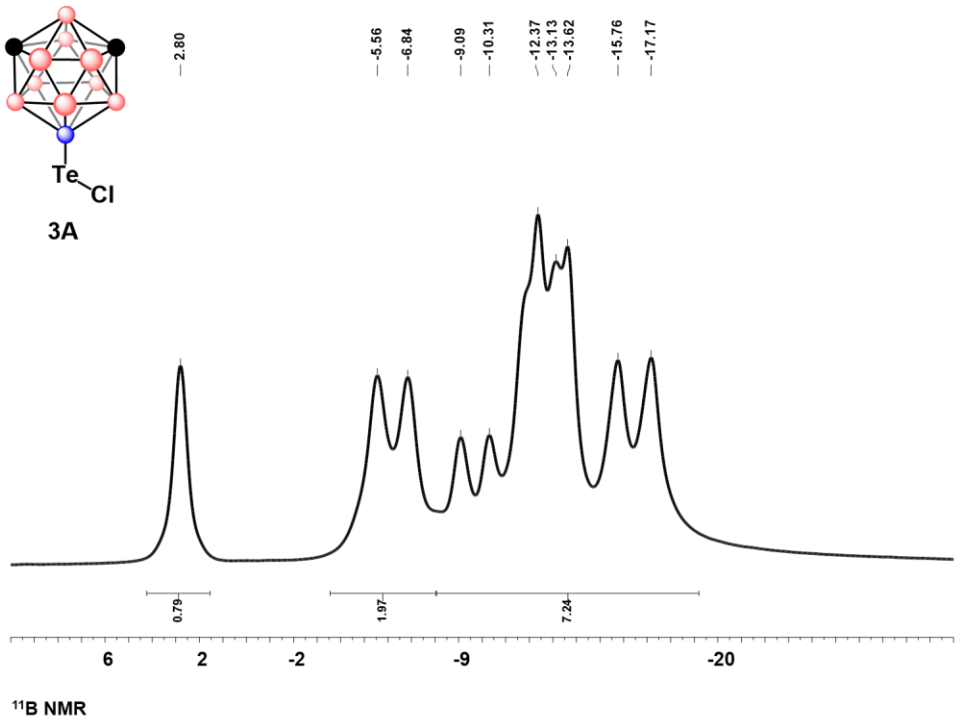

Figure C4.3 ^{11}B NMR of **3A**

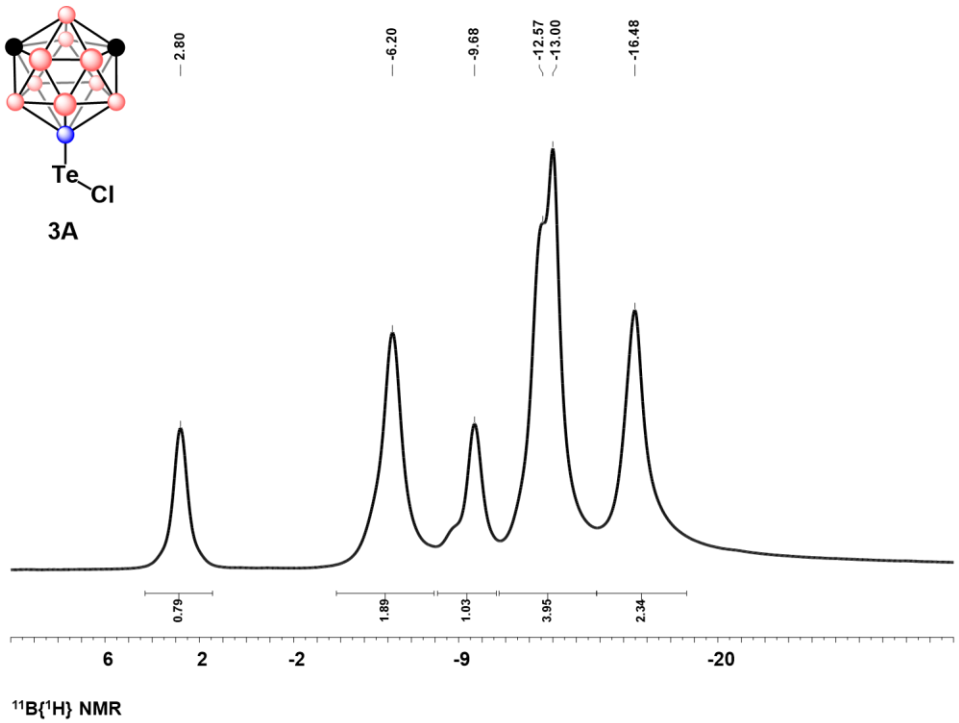

Figure C4.4 ^{11}B{^{1}H} NMR of **3A**

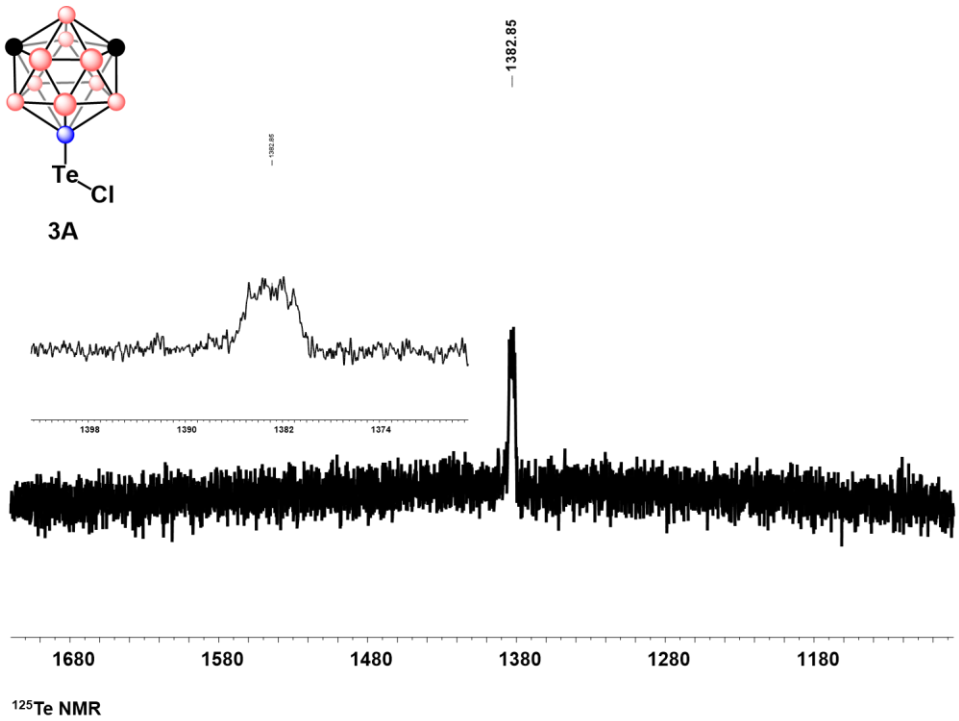

Figure C4.5 ^{125}Te NMR of **3A**

4.6.11.5 Characterization of 4A

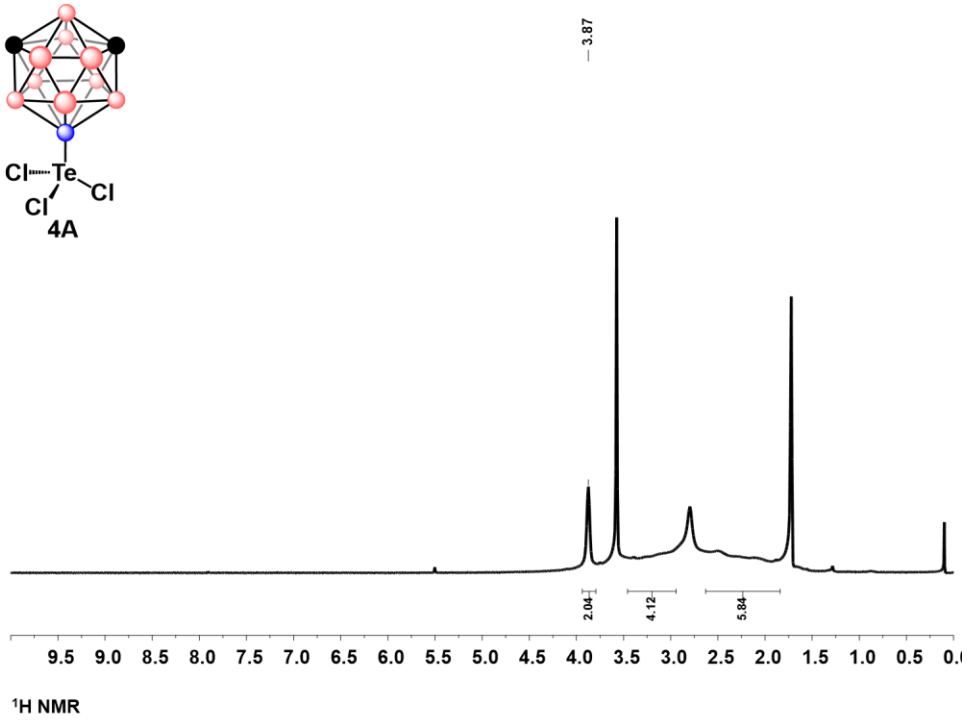

Figure C5.1 ^{1}H NMR of **4A**

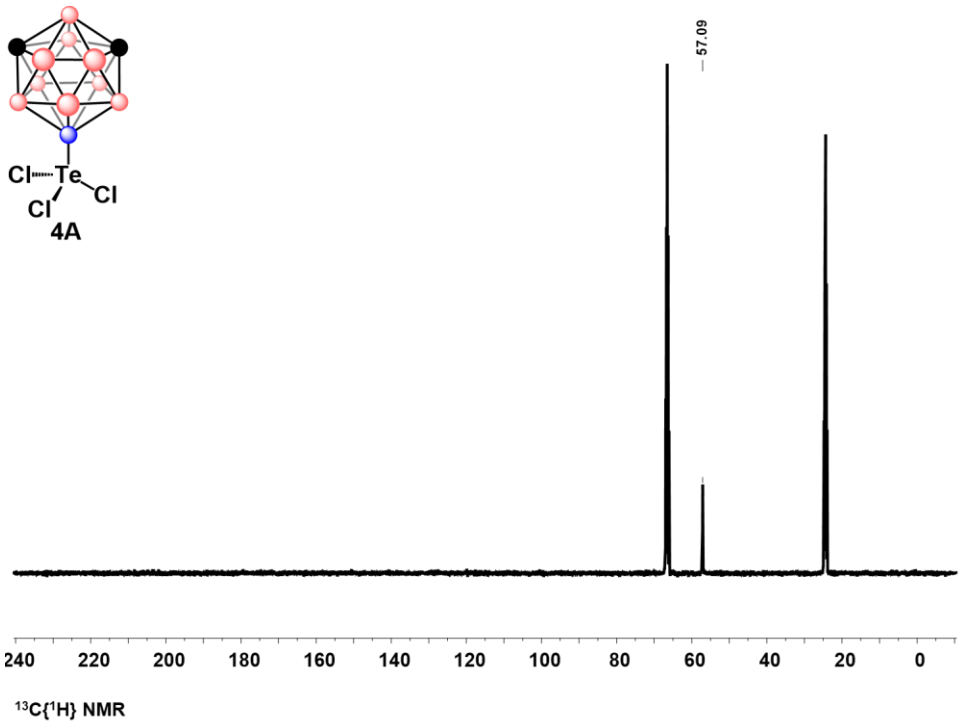

Figure C5.2 $^{13}C\{^{1}H\}$ NMR of **4A**

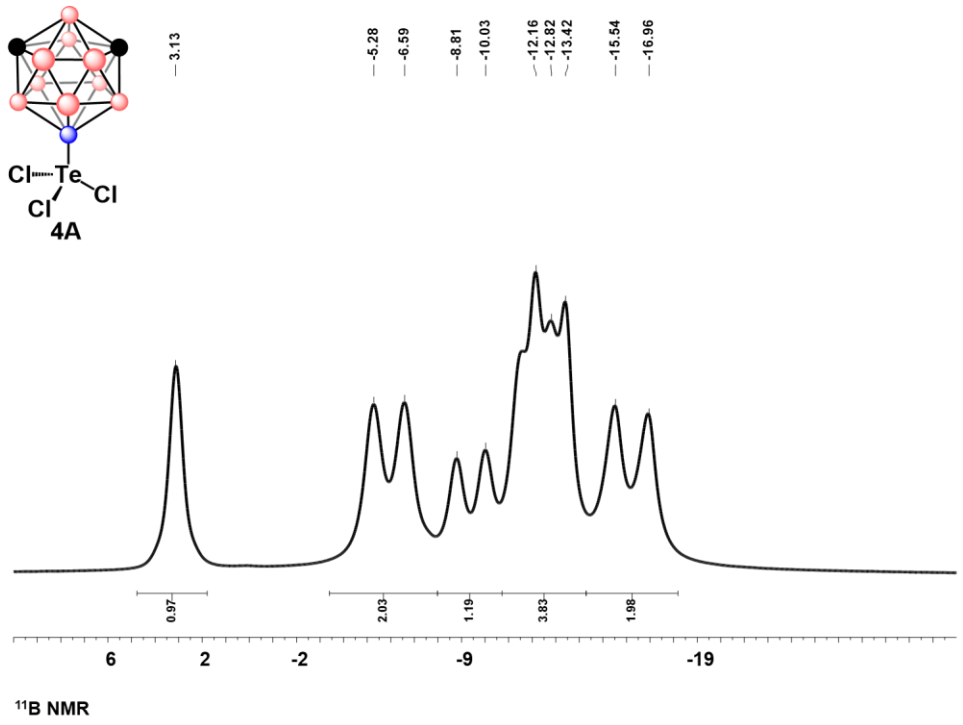

Figure C5.3 ^{11}B NMR of **4A**

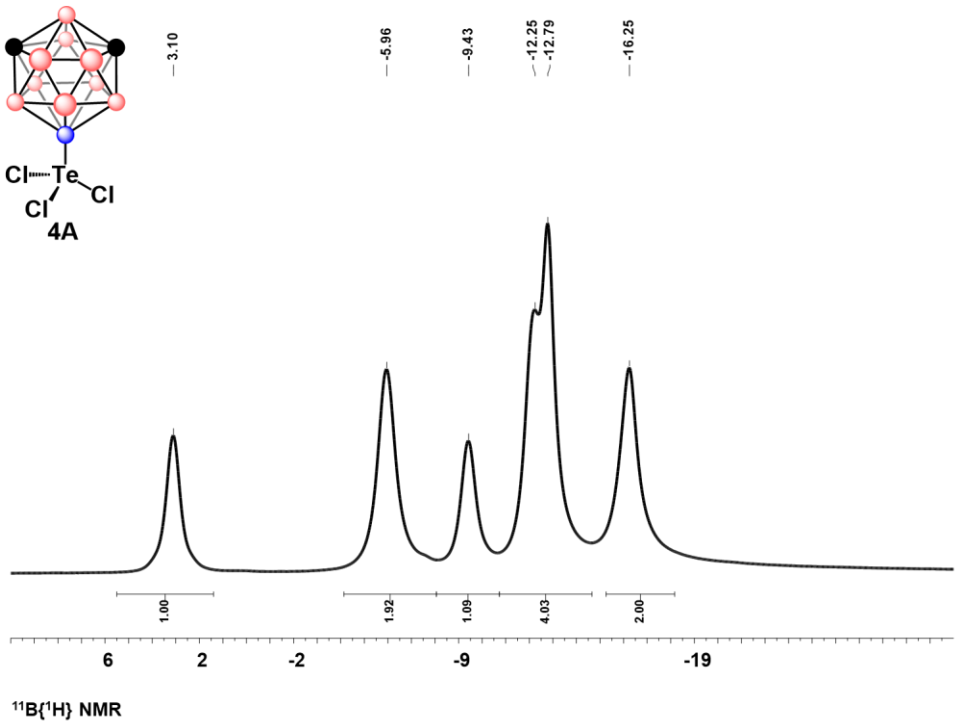

Figure C5.4 $^{11}B\{^{1}H\}$ NMR of **4A**

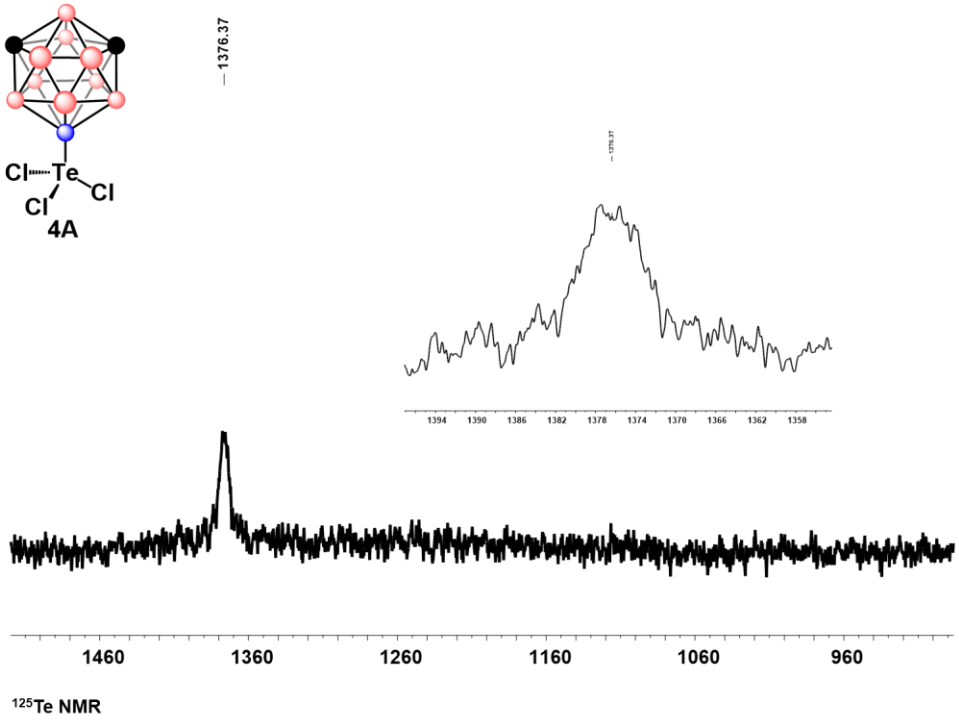

Figure C5.5 ^{125}Te NMR of **4A**

4.6.11.6 Characterization of 2B

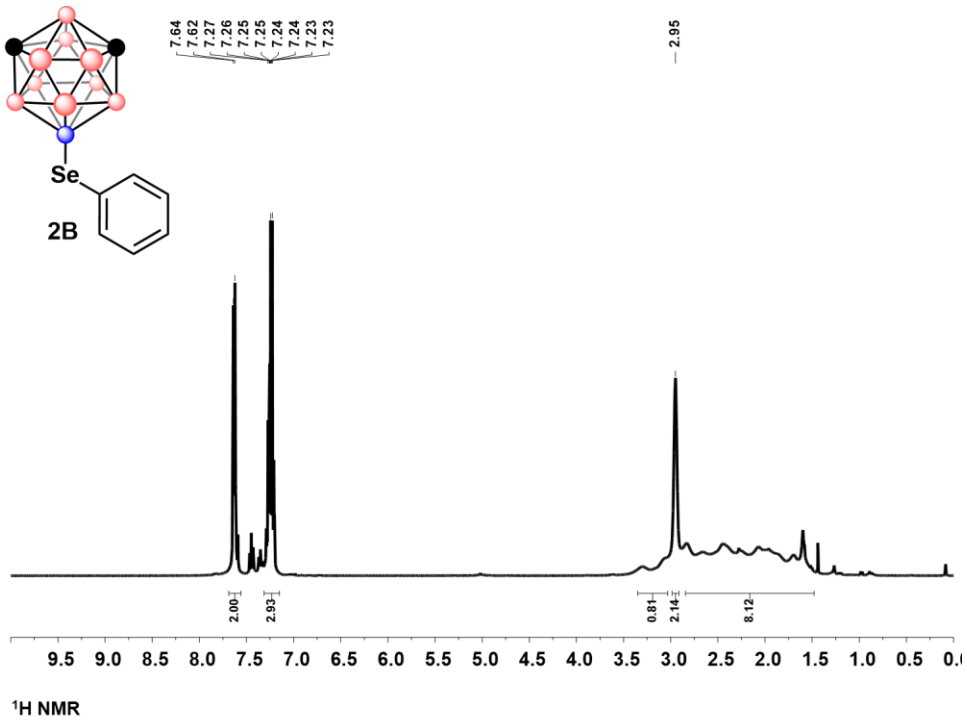

Figure C6.1 ^{1}H NMR of **2B**

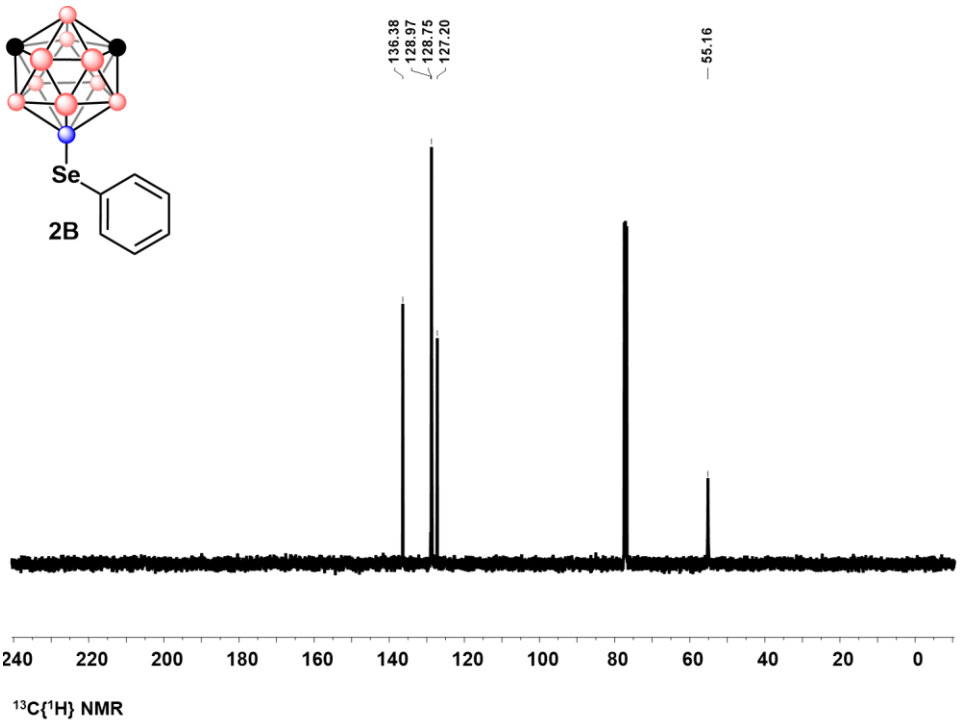

Figure C6.2 $^{13}C\{^{1}H\}$ NMR of **2B**

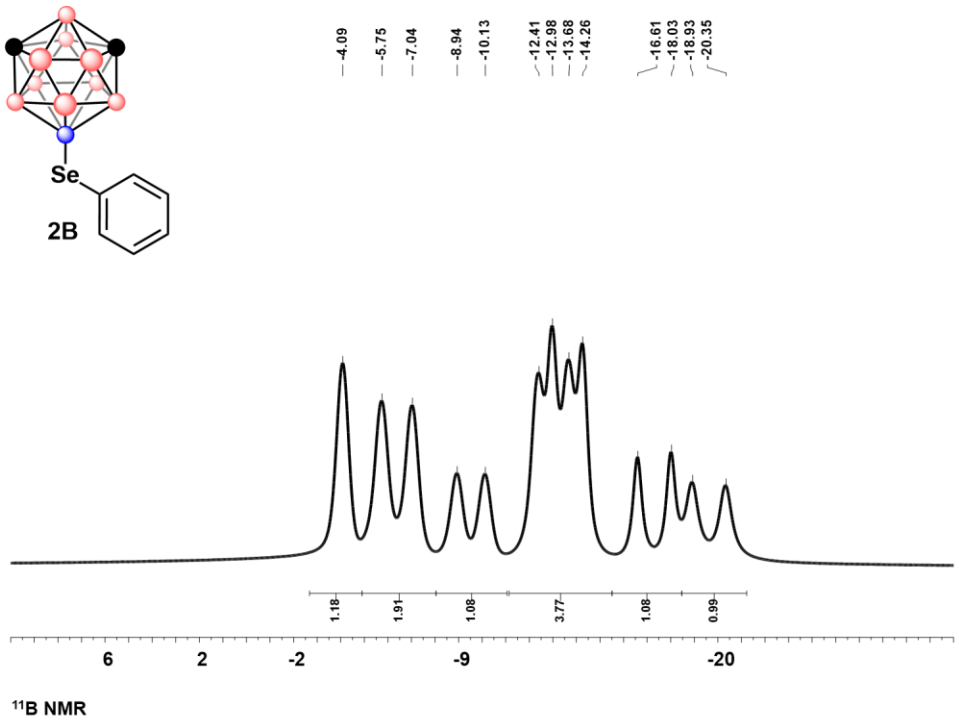

Figure C6.3 ^{11}B NMR of **2B**

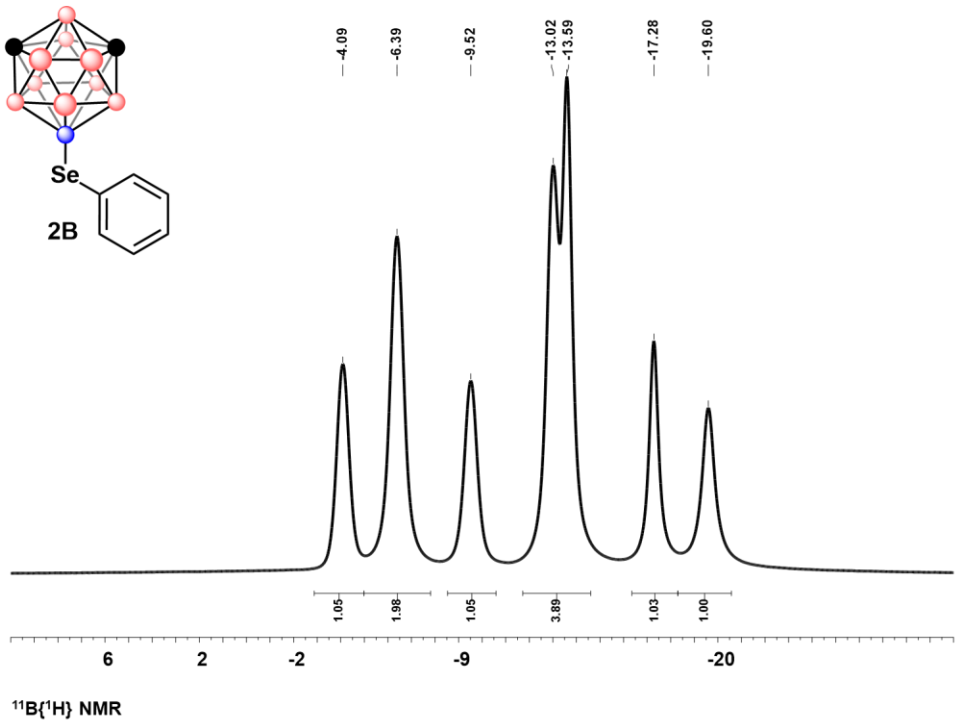

Figure C6.4 $^{11}B\{^{1}H\}$ NMR of **2B**

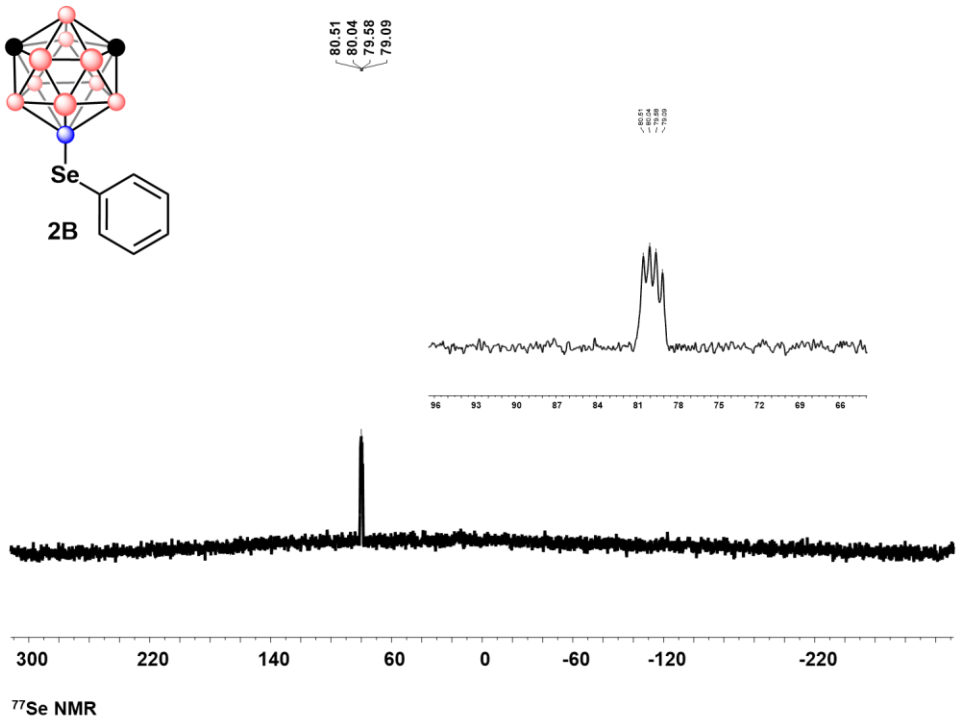

Figure C6.5 ^{77}Se NMR of **2B**

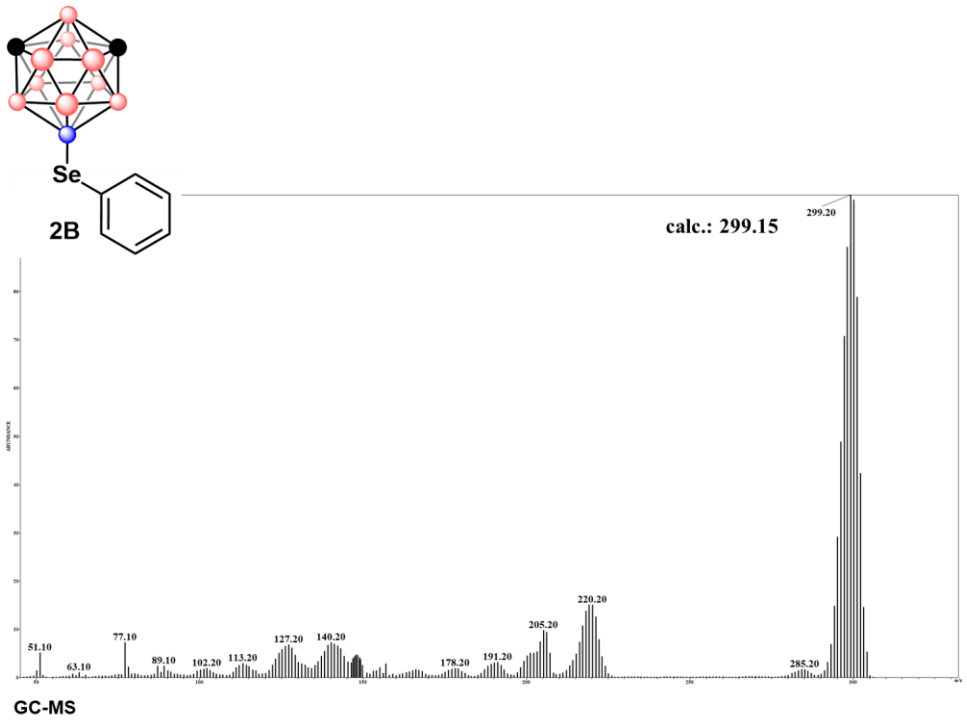

Figure C6.6 GC-MS of **2B**

4.6.11.7 Characterization of 2C

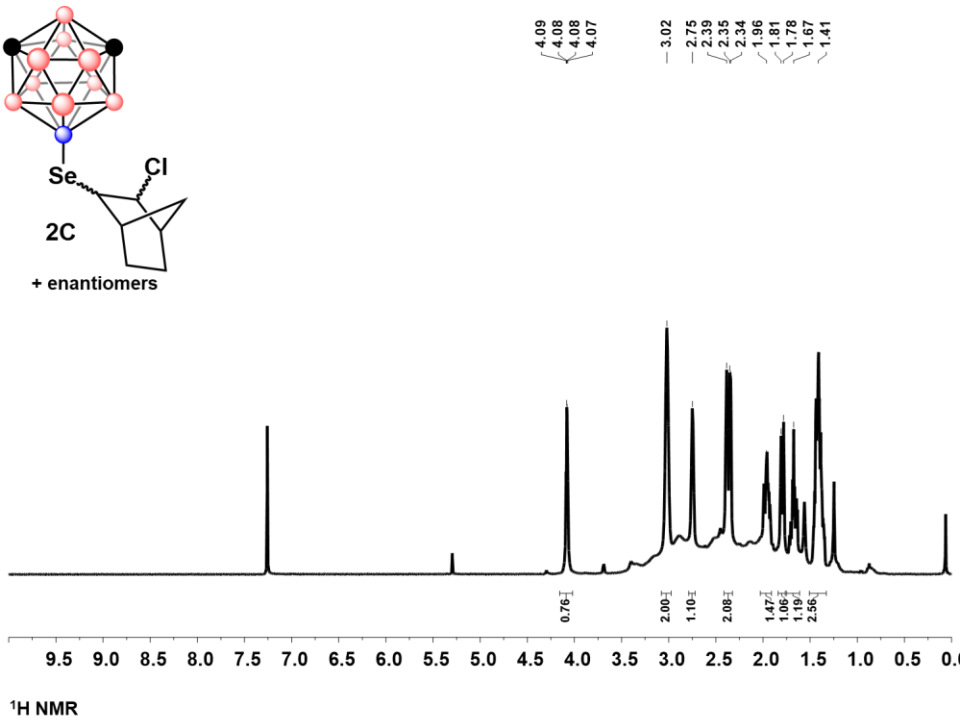

Figure C7.1 ^{1}H NMR of **2C**

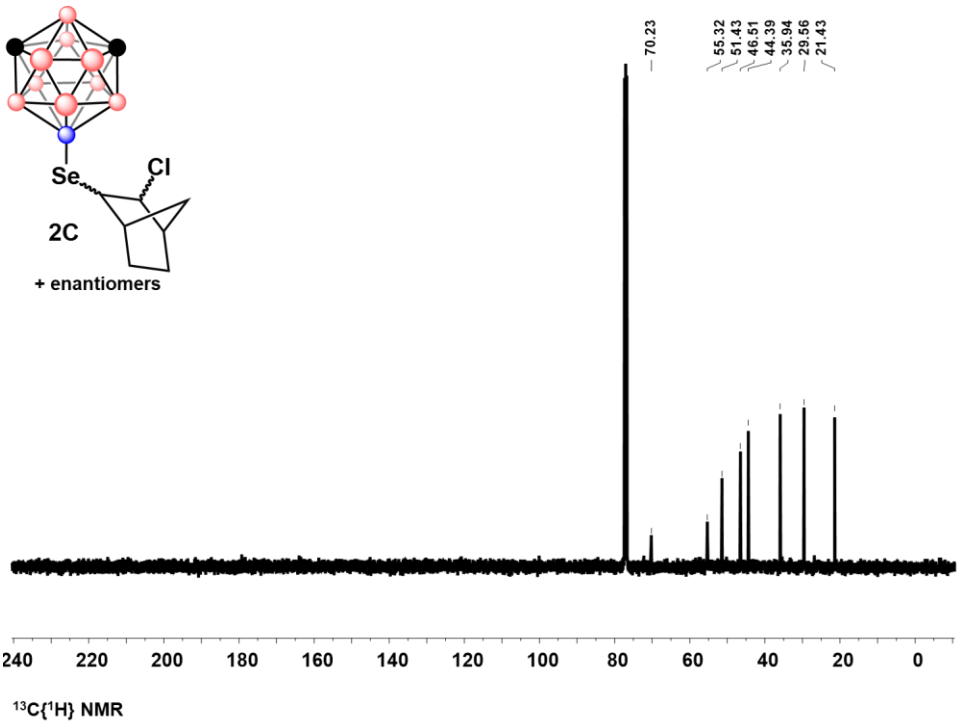

Figure C7.2 $^{13}C\{^{1}H\}$ NMR of **2C**

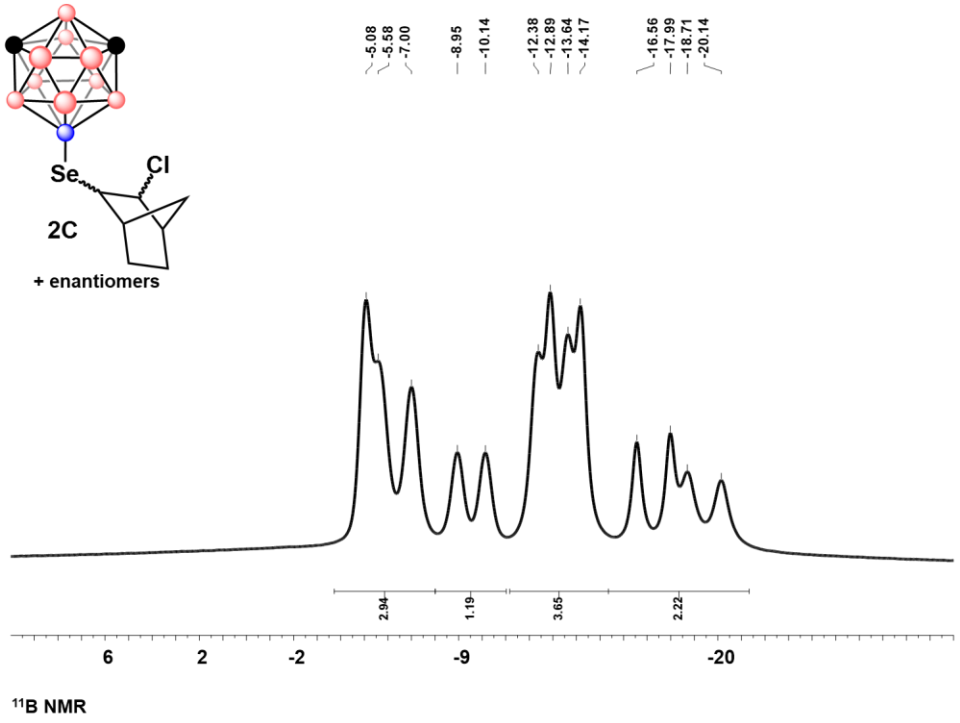

Figure C7.3 ^{11}B NMR of **2C**

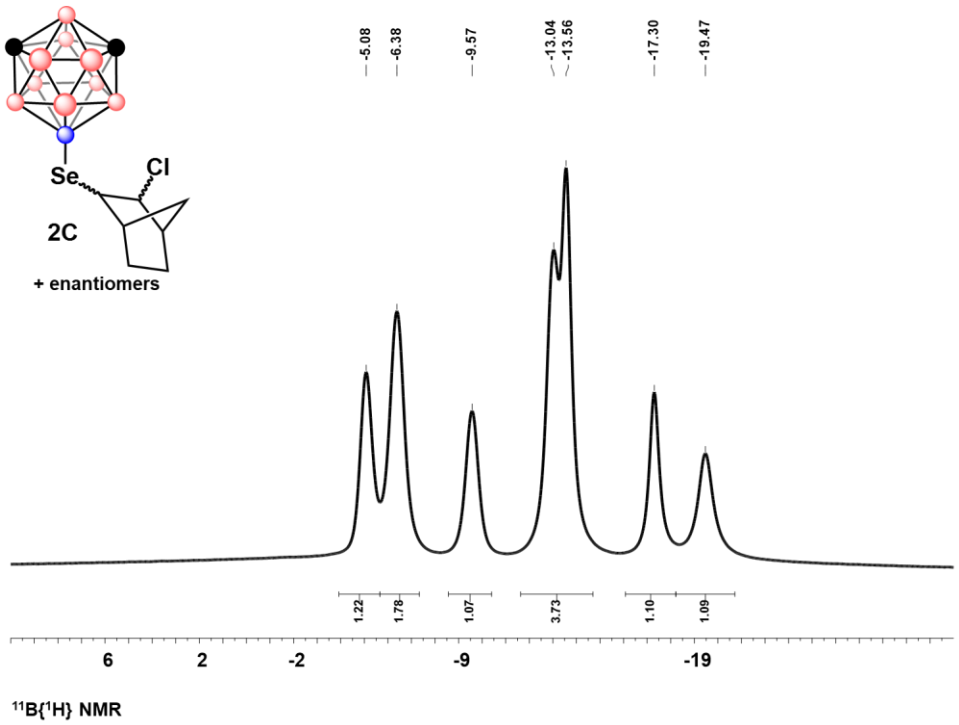

Figure C7.4 $^{11}B\{^{1}H\}$ NMR of **2C**

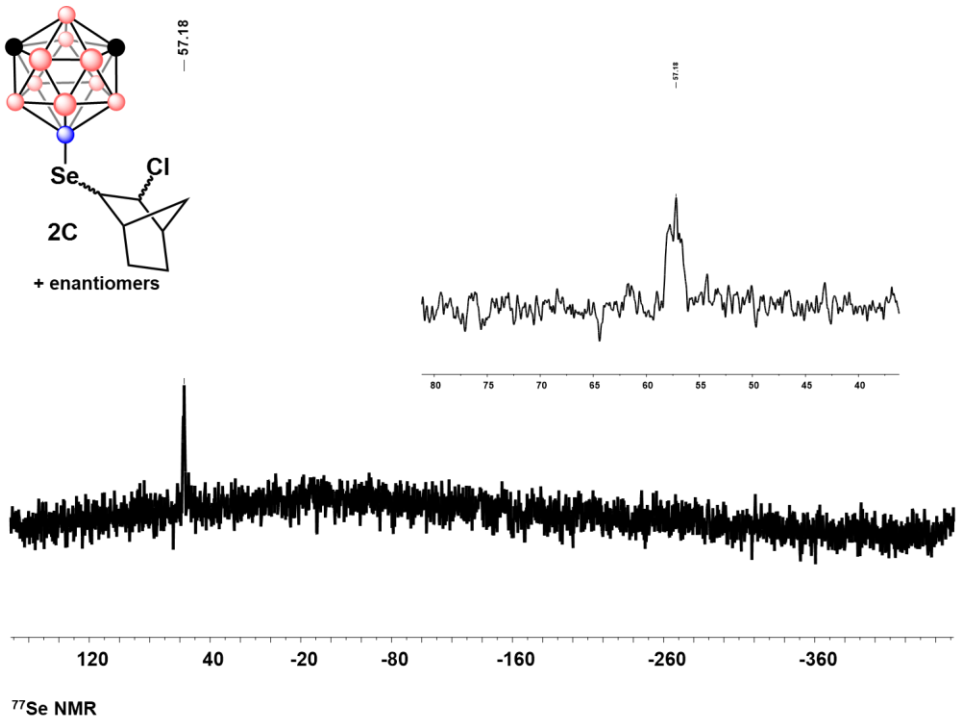

Figure C7.5 ^{77}Se NMR of **2C**

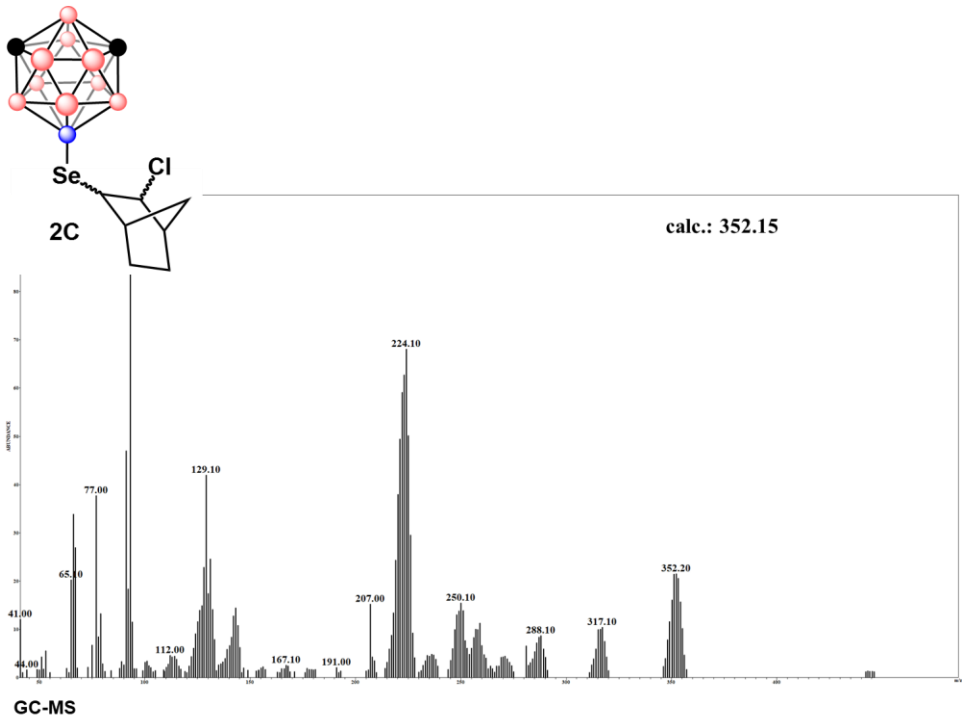

Figure C7.6 GC-MS of **2C**

4.6.11.8 Characterization of 2D

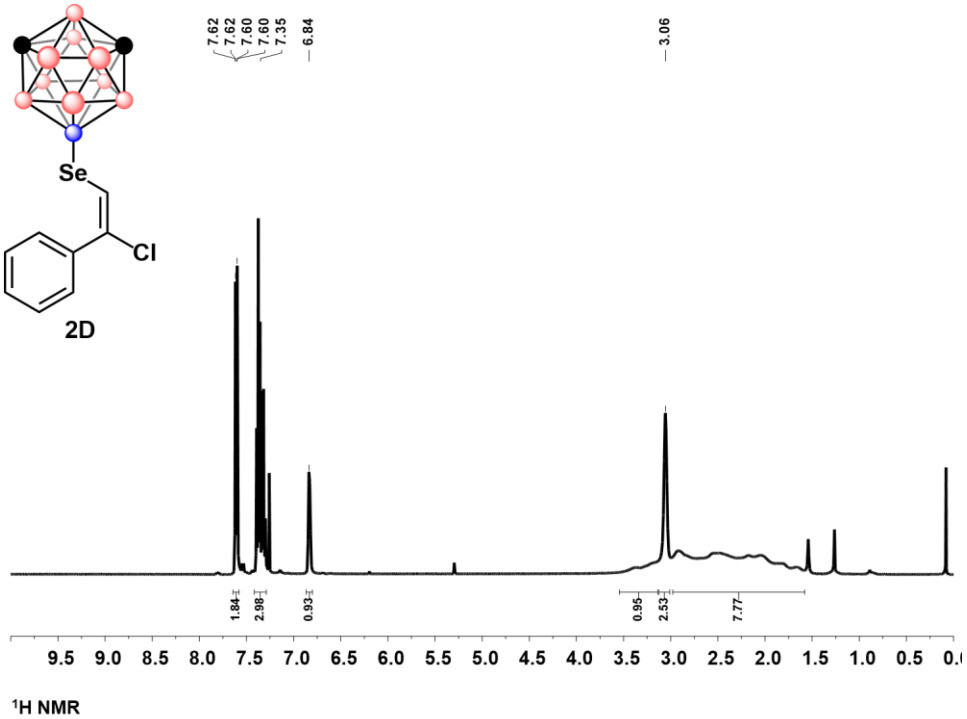

Figure C8.1 ^{1}H NMR of **2D**

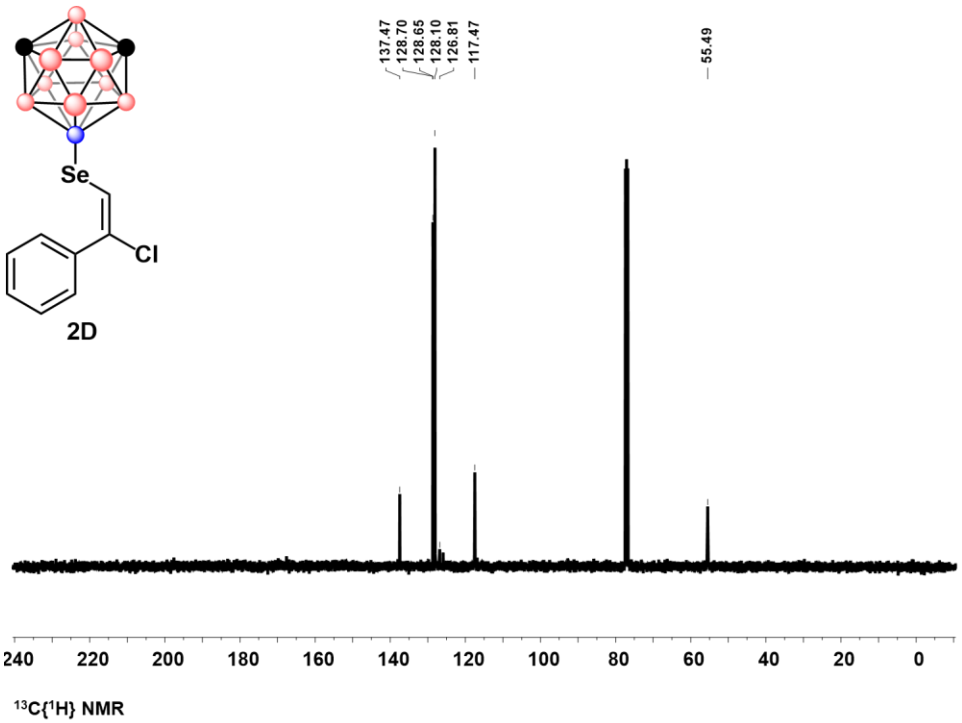

Figure C8.2 ^{13}C{^{1}H} NMR of **2D**

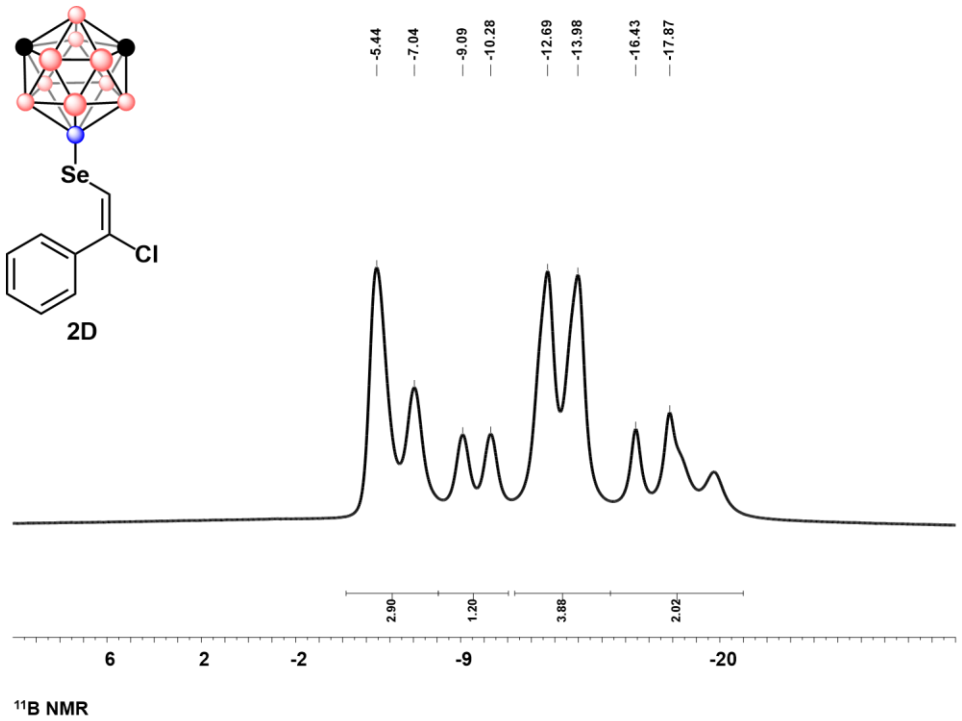

Figure C8.3 ^{11}B NMR of **2D**

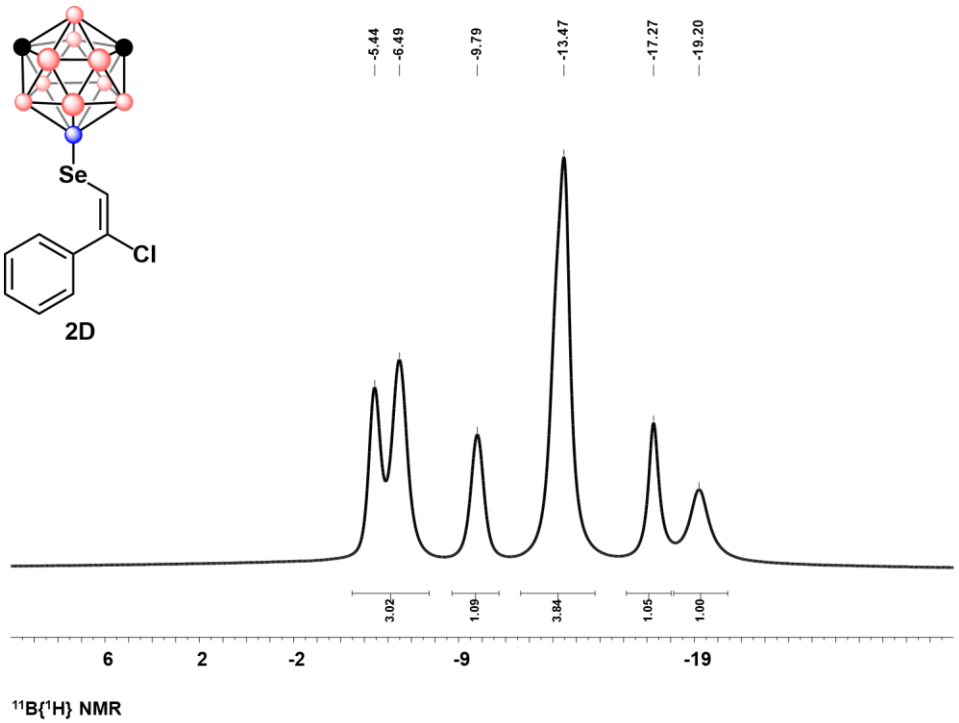

Figure C8.4 ^{11}B{^{1}H} NMR of **2D**

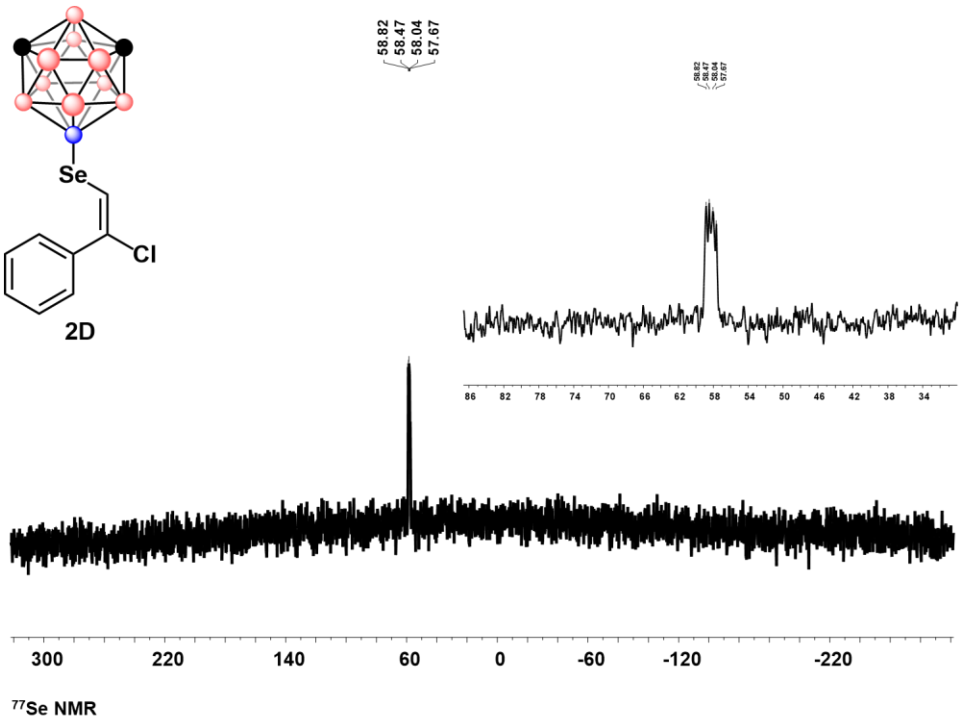

Figure C8.5 ^{77}Se NMR of **2D**

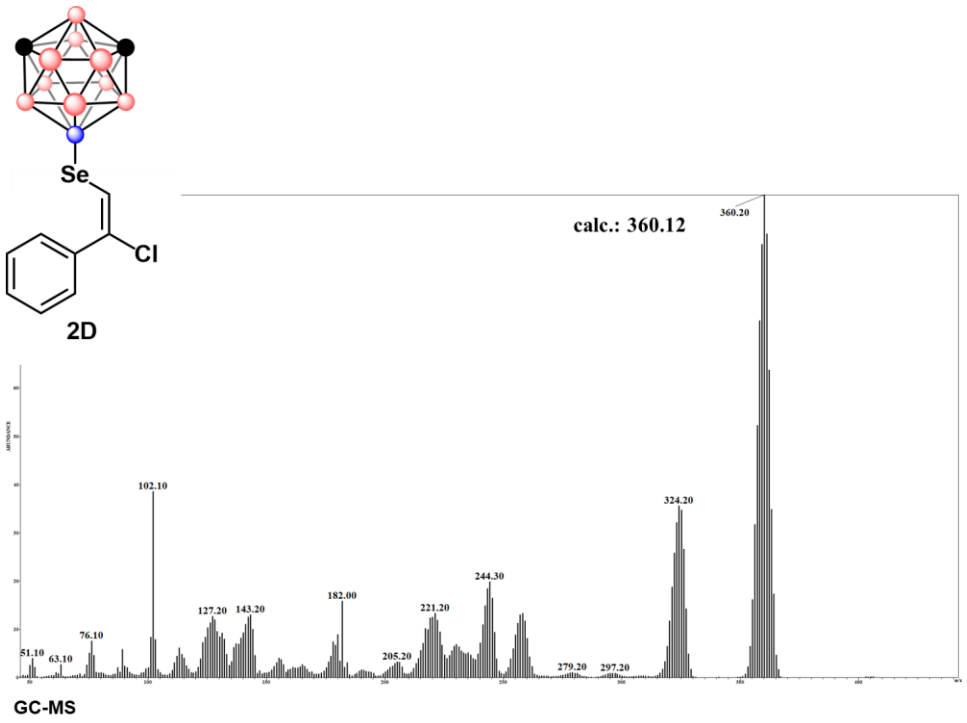

Figure C8.6 GC-MS of **2D**

4.6.11.9 Characterization of 2E

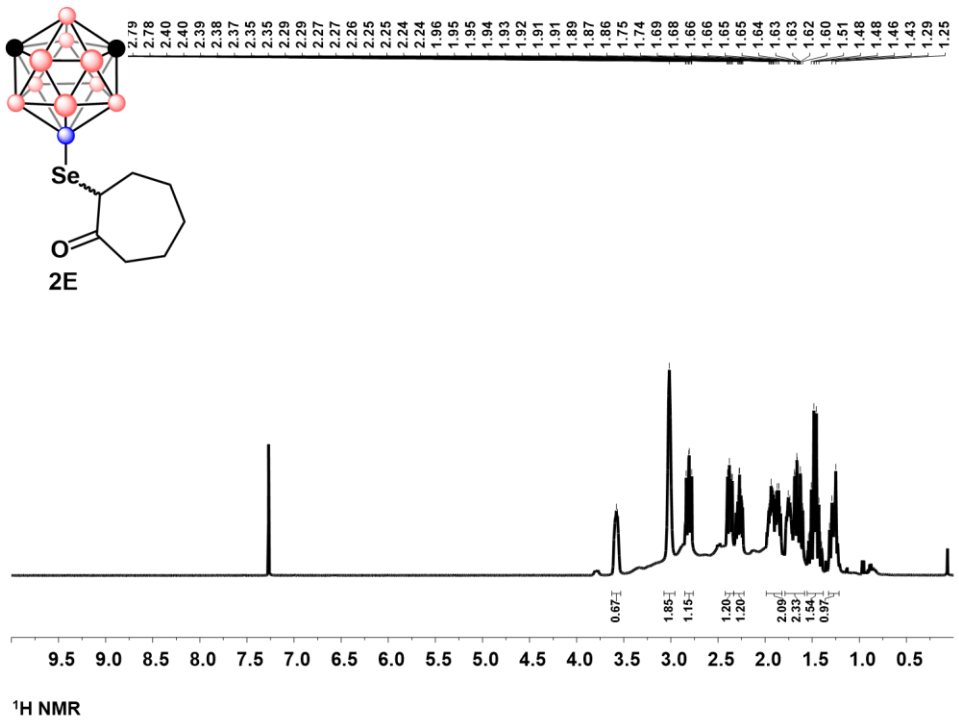

Figure C9.1 ^{1}H NMR of **2E**

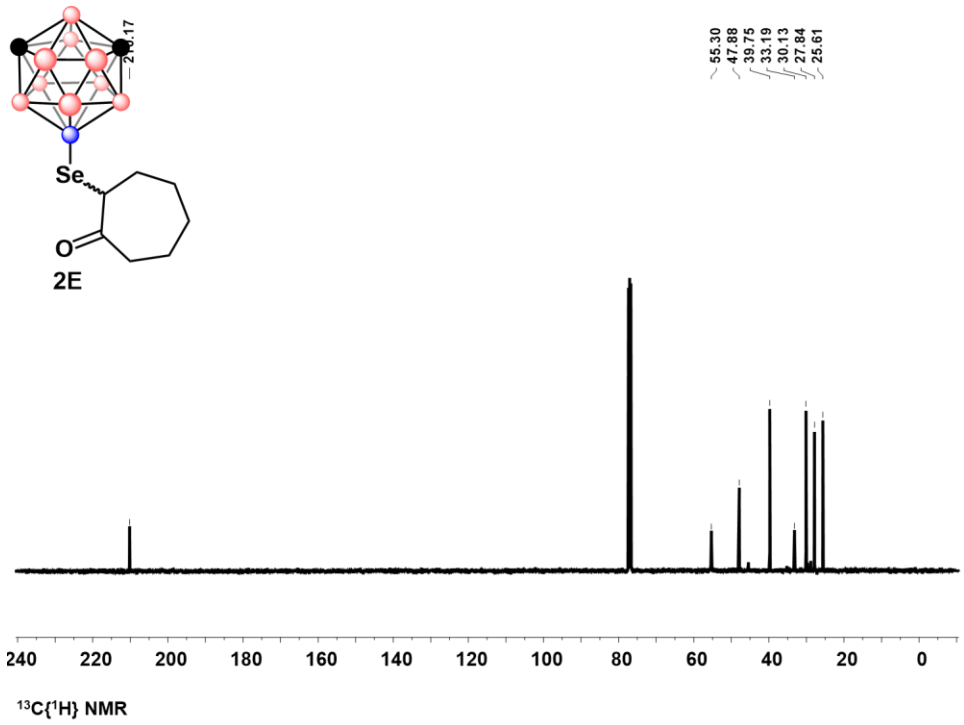

Figure C9.2 ^{13}C{^{1}H} NMR of **2E**

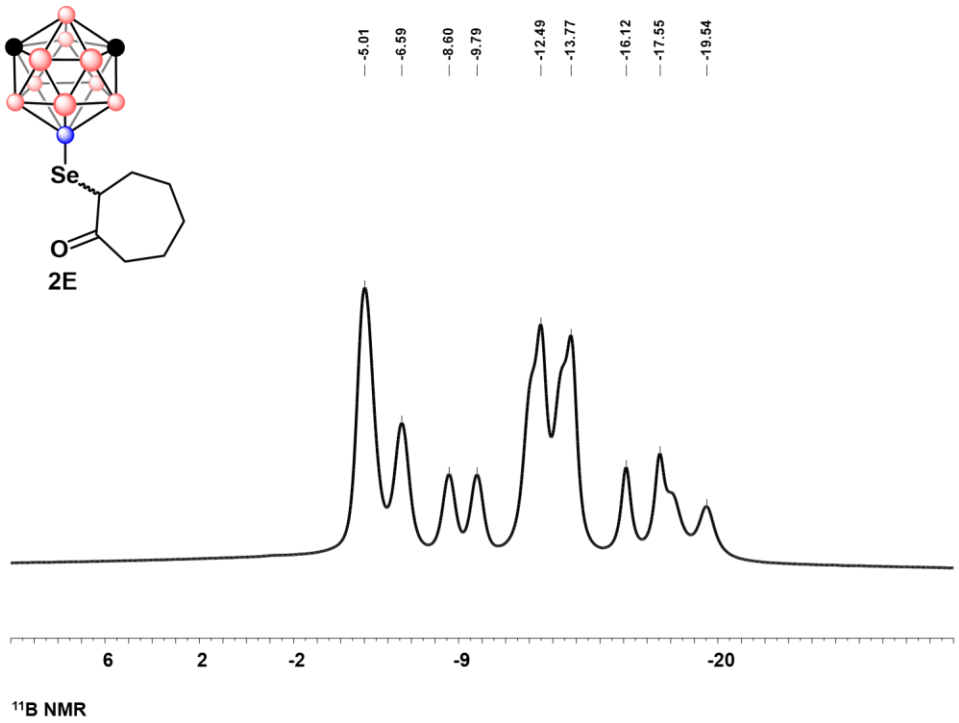

Figure C9.3 ^{11}B NMR of **2E**

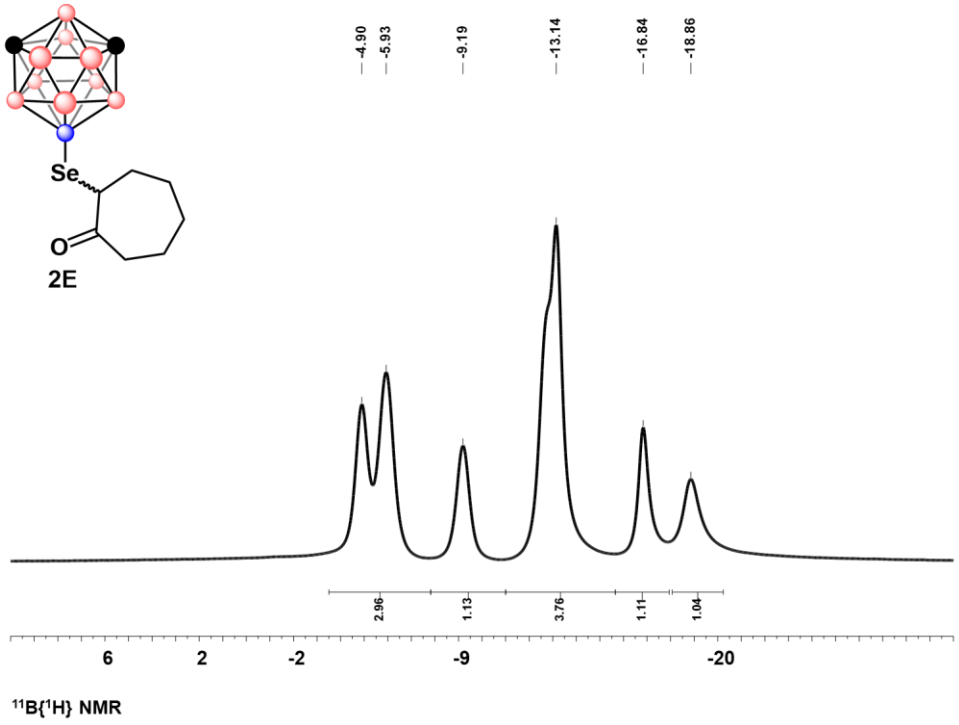

Figure C9.4 ^{11}B{^{1}H} NMR of **2E**

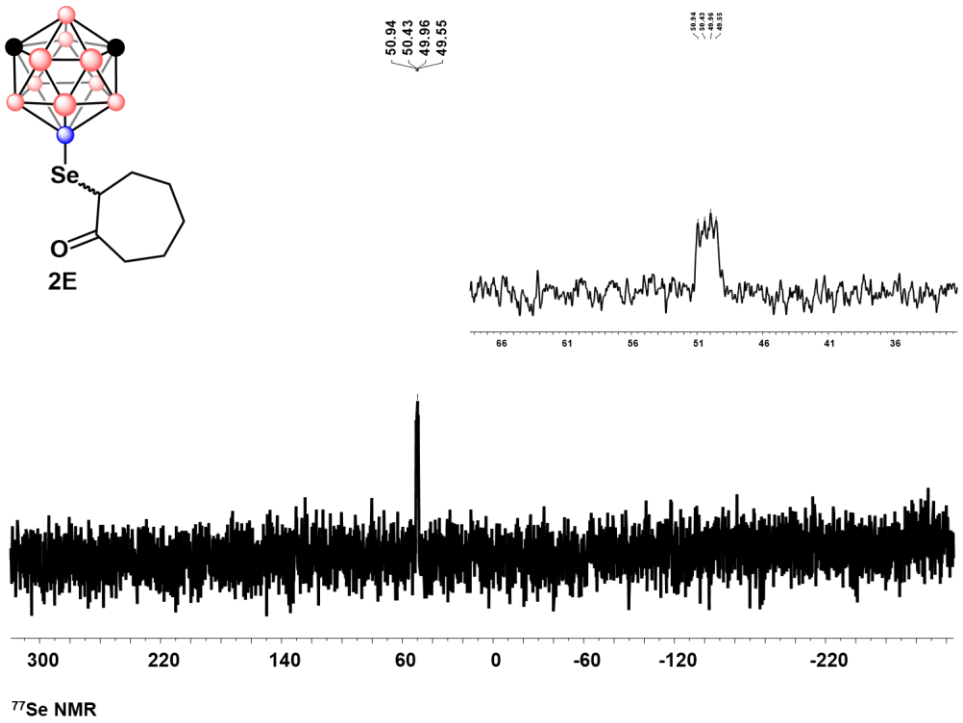

Figure C9.5 ^{77}Se NMR of **2E**

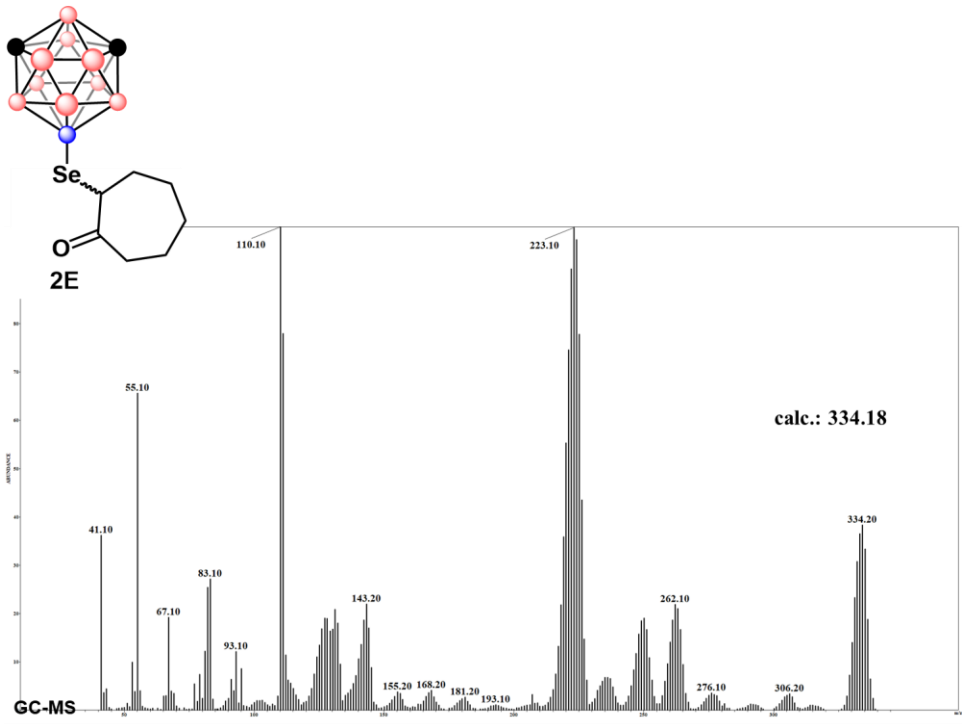

Figure C9.6 GC-MS of **2E**

4.6.11.10 Characterization of 2F

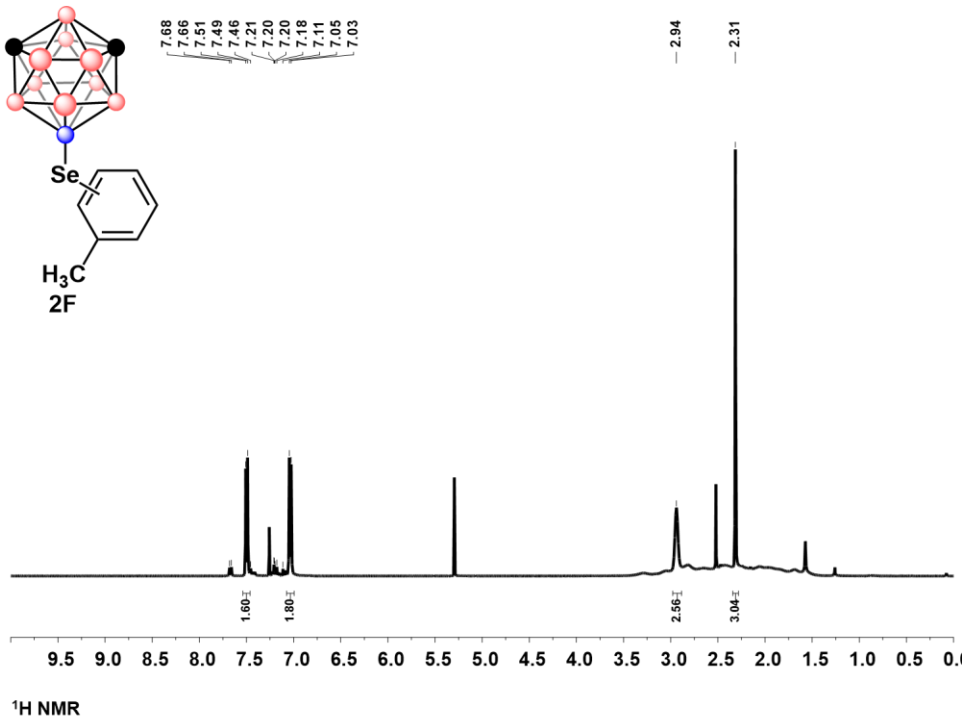

Figure C10.1 ^{1}H NMR of **2F**

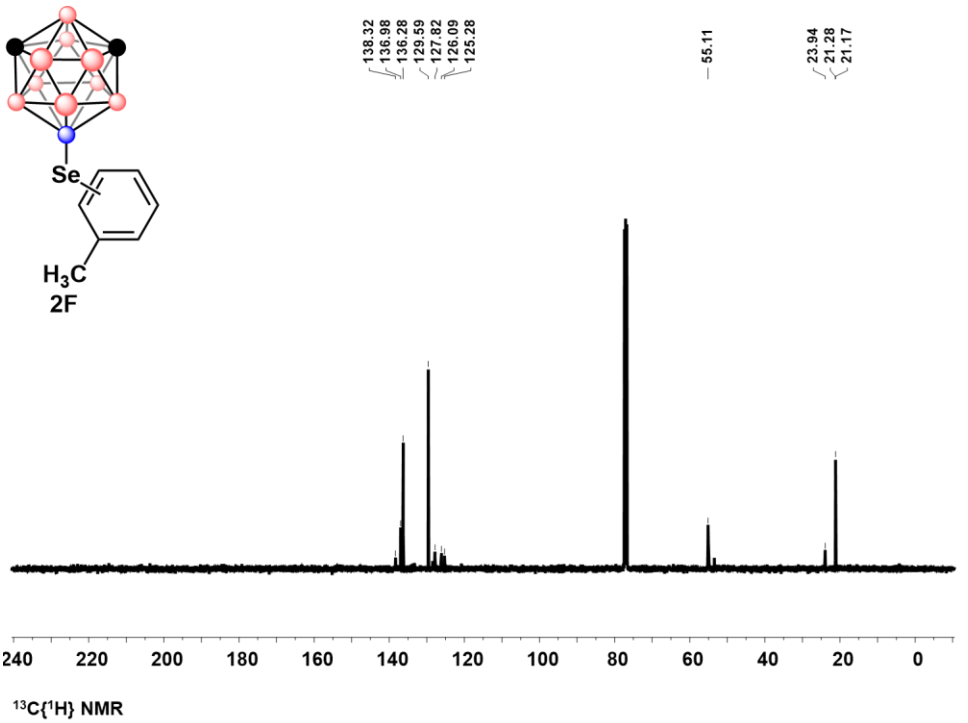

Figure C10.2 $^{13}C\{^{1}H\}$ NMR of **2F**

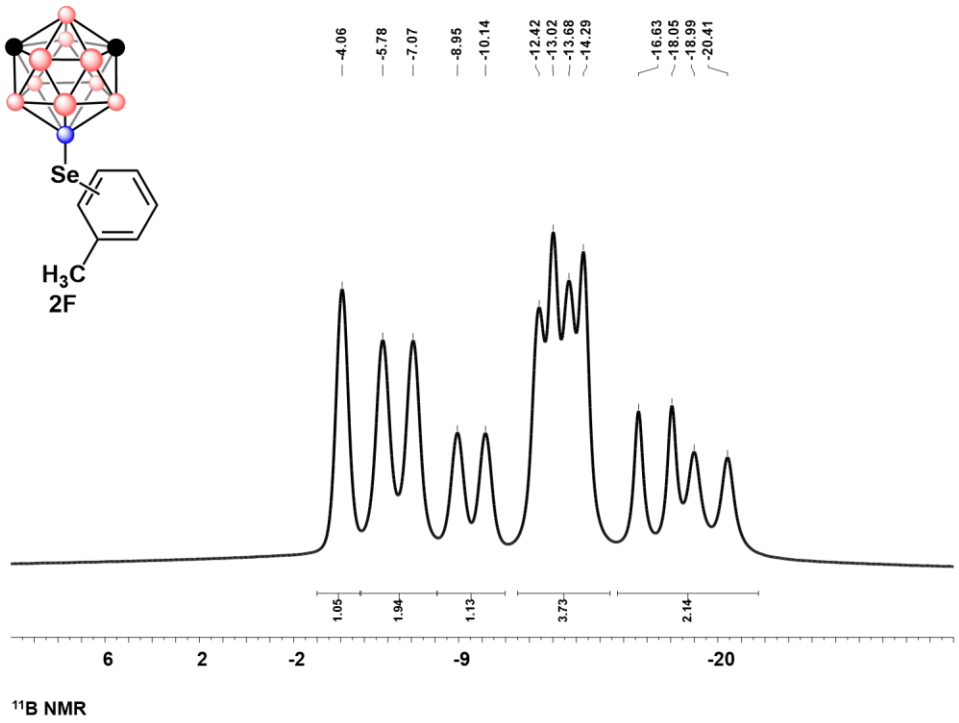

Figure C10.3 ^{11}B NMR of **2F**

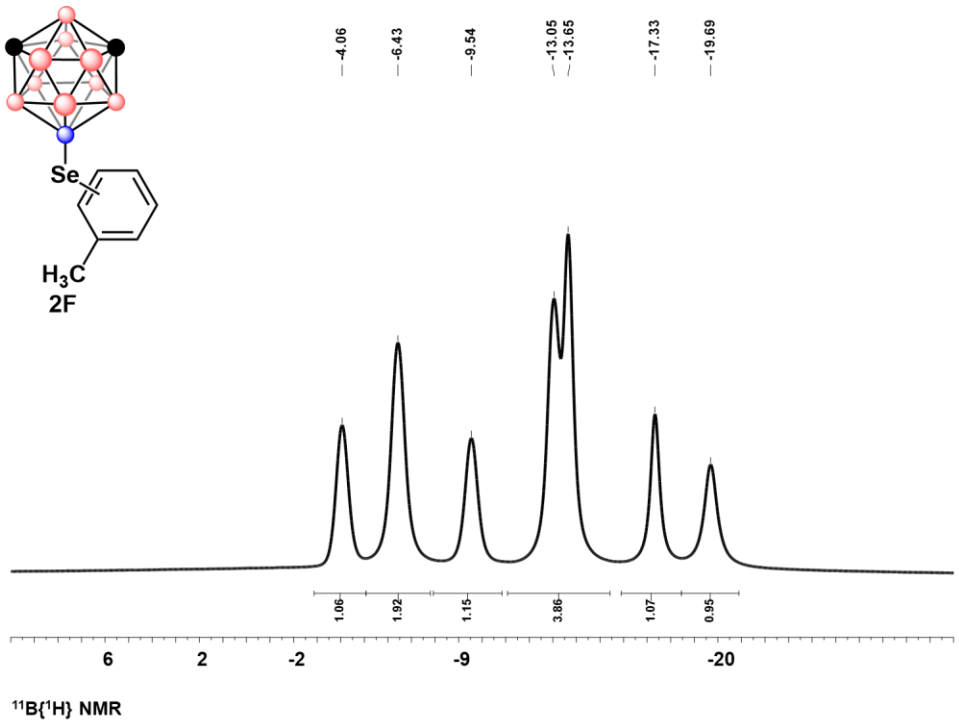

Figure C10.4 $^{11}B\{^{1}H\}$ NMR of **2F**

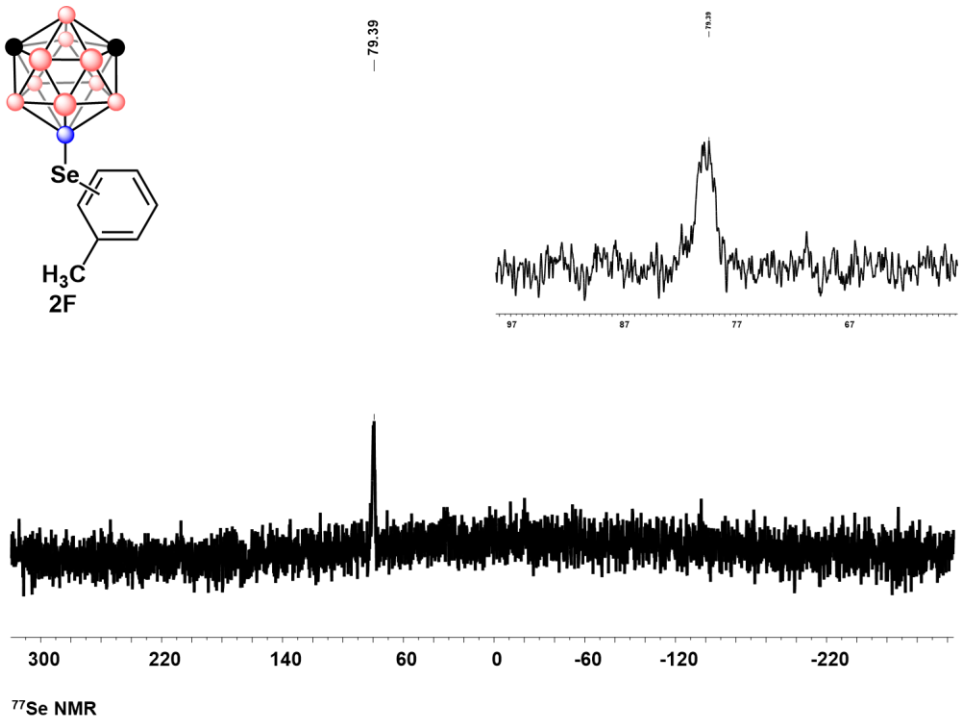

Figure C10.5 ^{77}Se NMR of **2F**

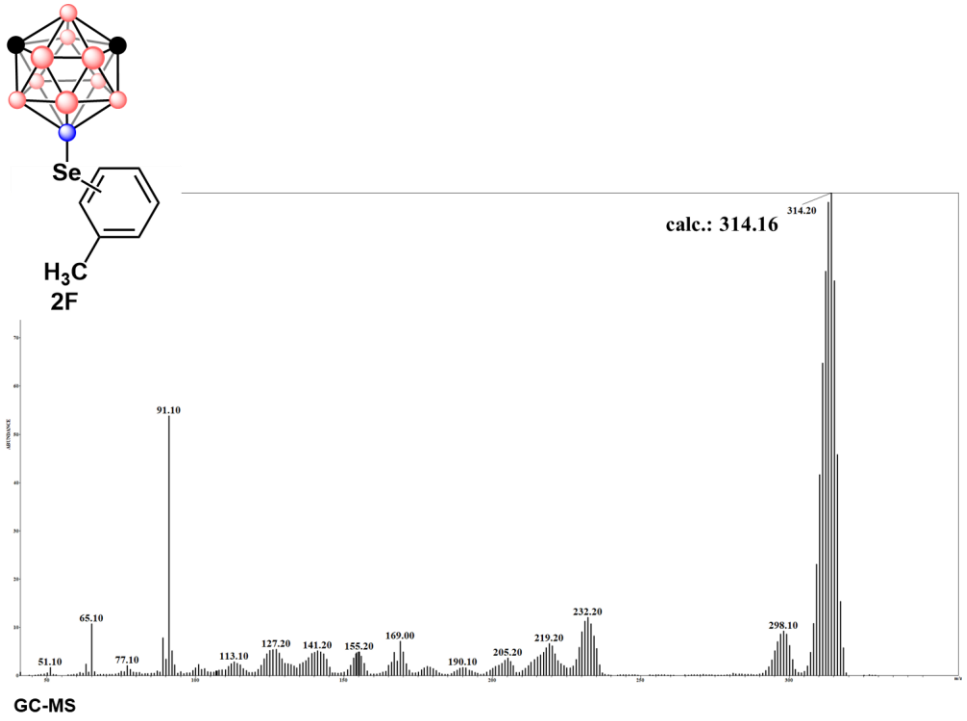

Figure C10.6 GC-MS of **2F**

4.6.11.11 Characterization of 3B

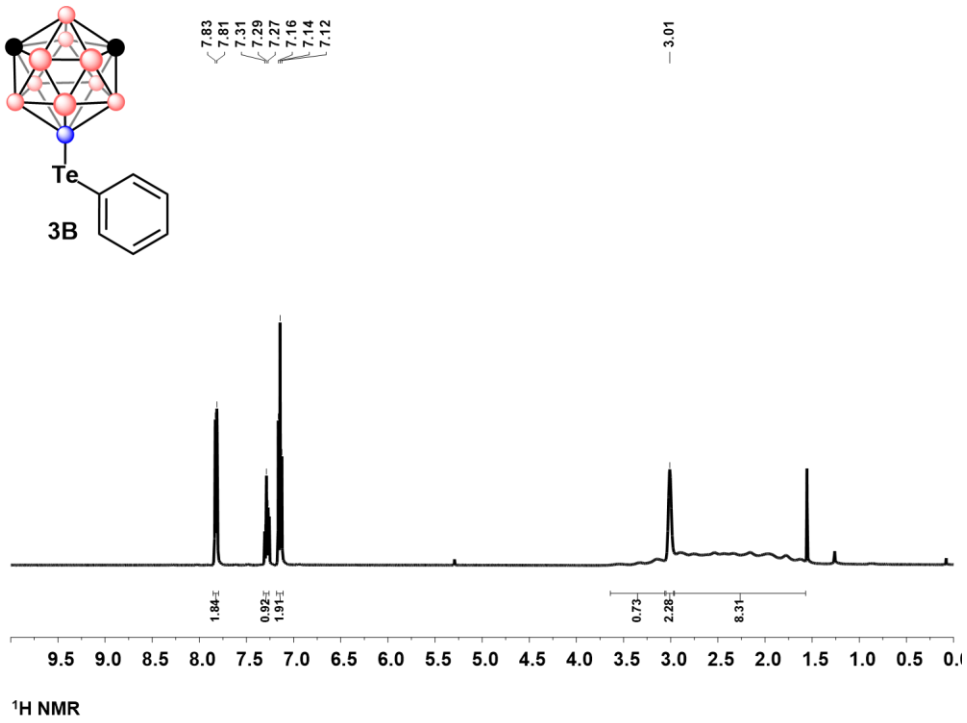

Figure C11.1 ^{1}H NMR of **3B**

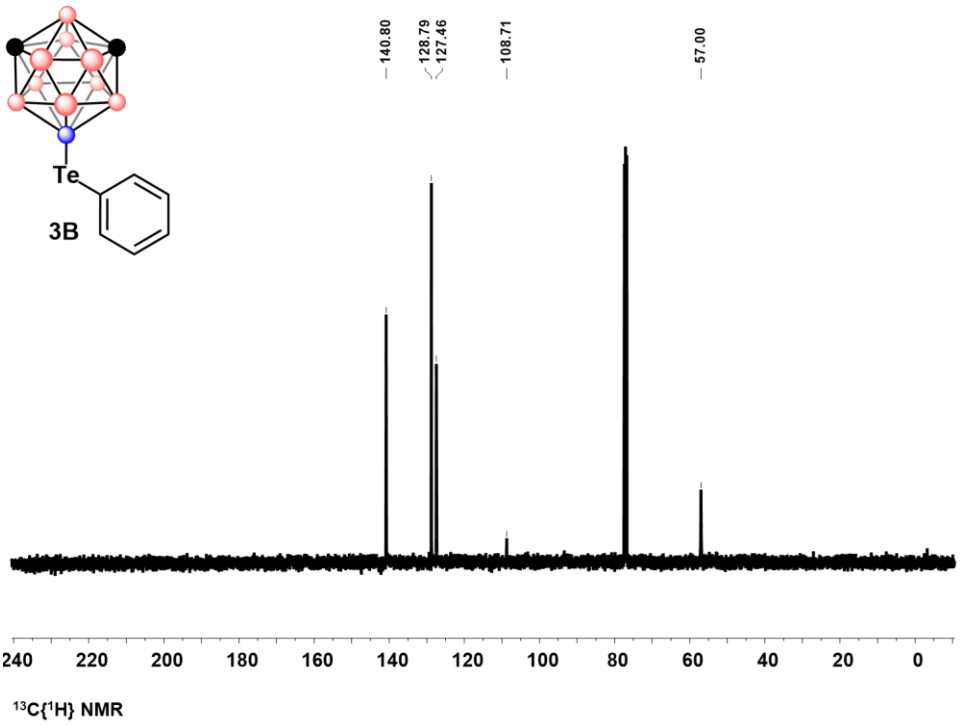

Figure C11.2 $^{13}C\{^{1}H\}$ NMR of **3B**

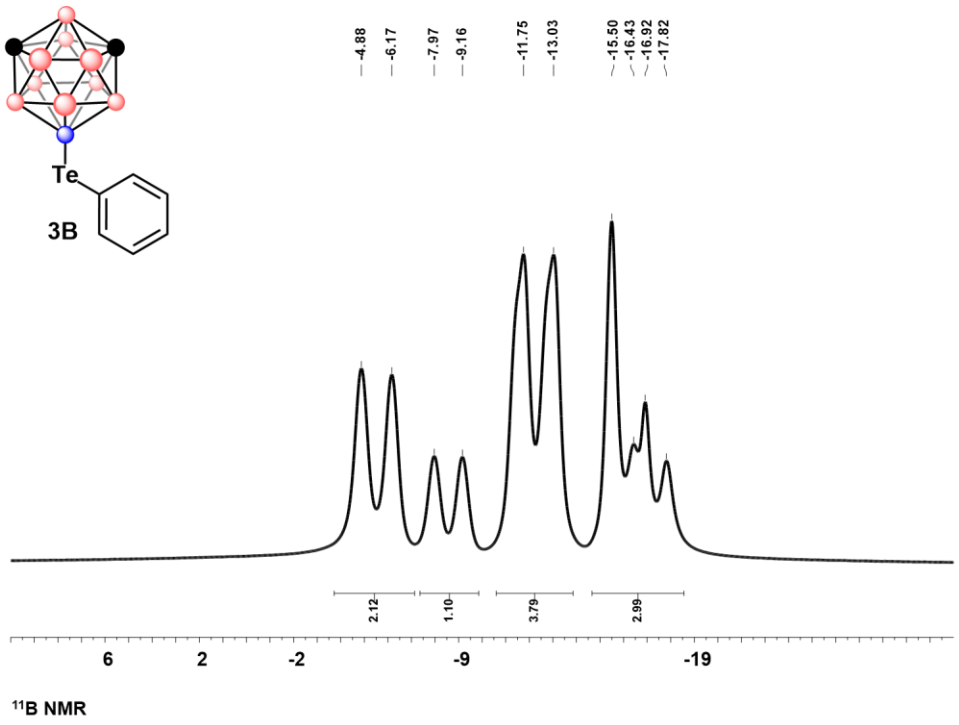

Figure C11.3 ^{11}B NMR of **3B**

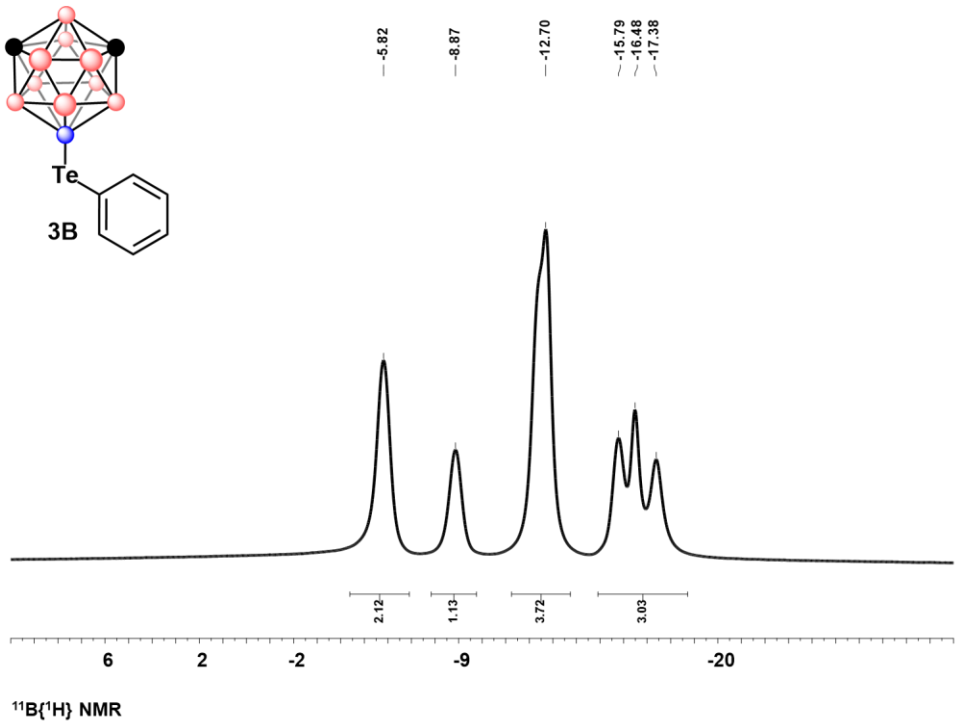

Figure C11.4 $^{11}B\{^{1}H\}$ NMR of **3B**

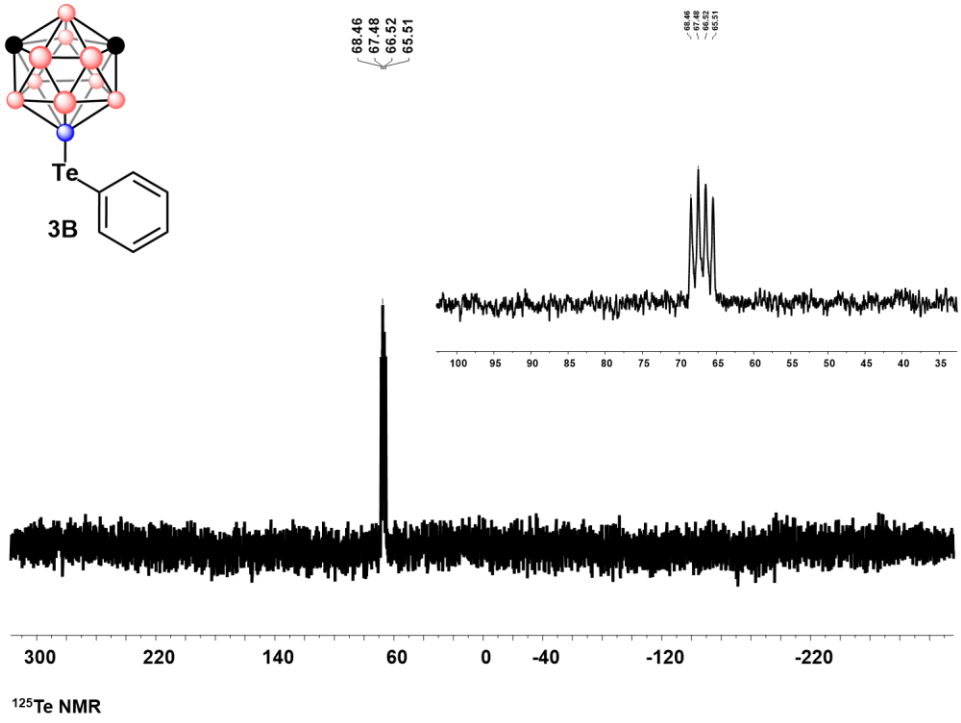

Figure C11.5 ^{125}Te NMR of **3B**

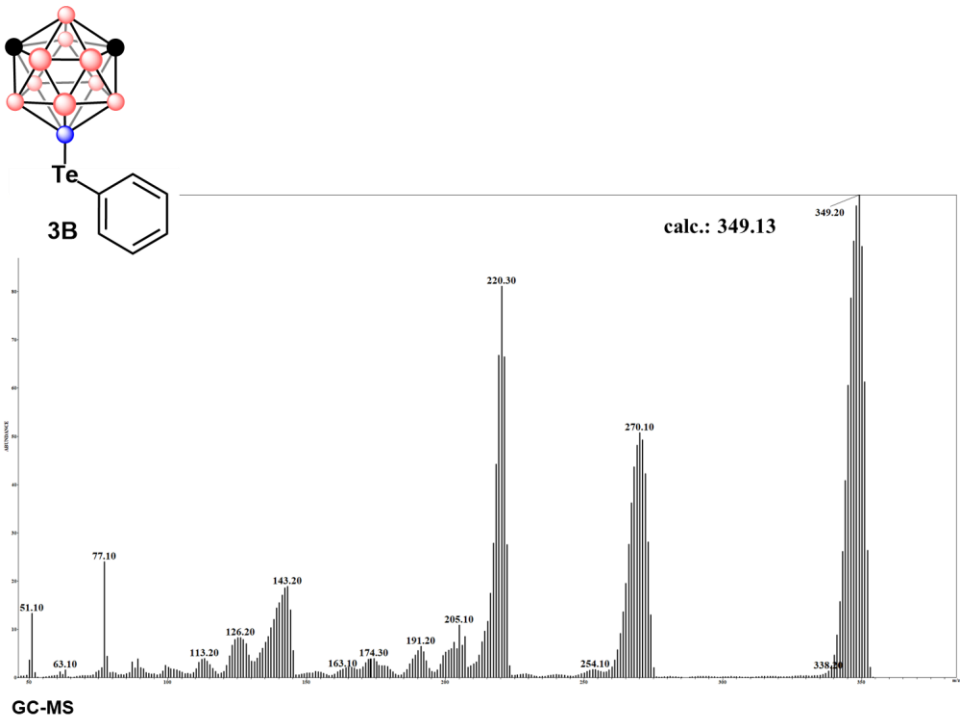

Figure C11.6 GC-MS of **3B**

4.6.11.12 Characterization of 4B and 4B'

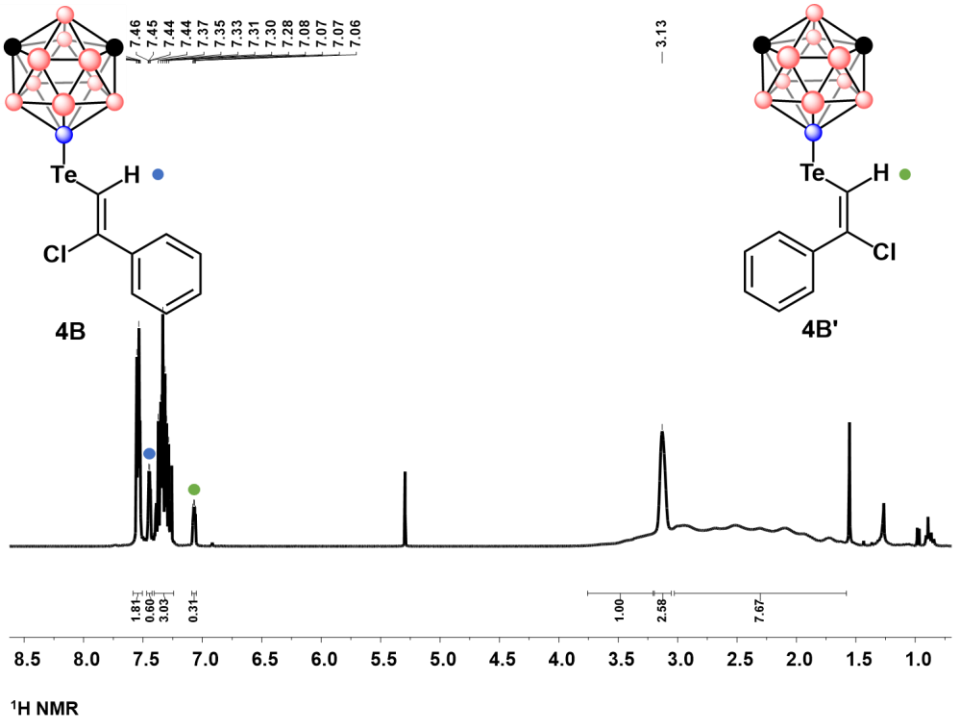

Figure C12.1 ^{1}H NMR of **4B** and **4B'**

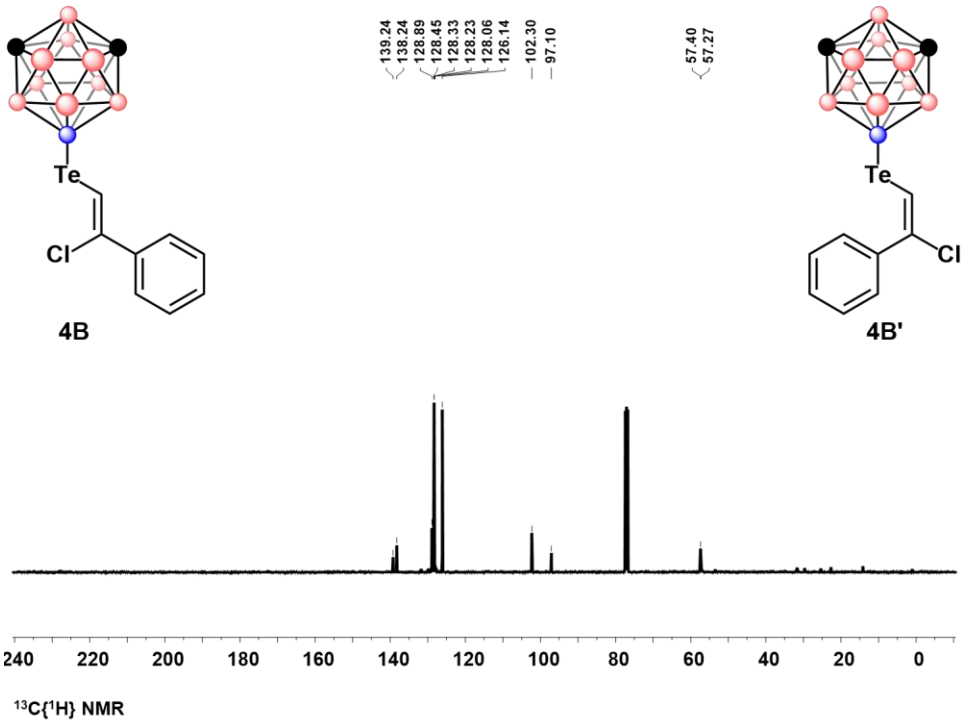

Figure C12.2 ^{13}C{^{1}H} NMR of **4B** and **4B'**

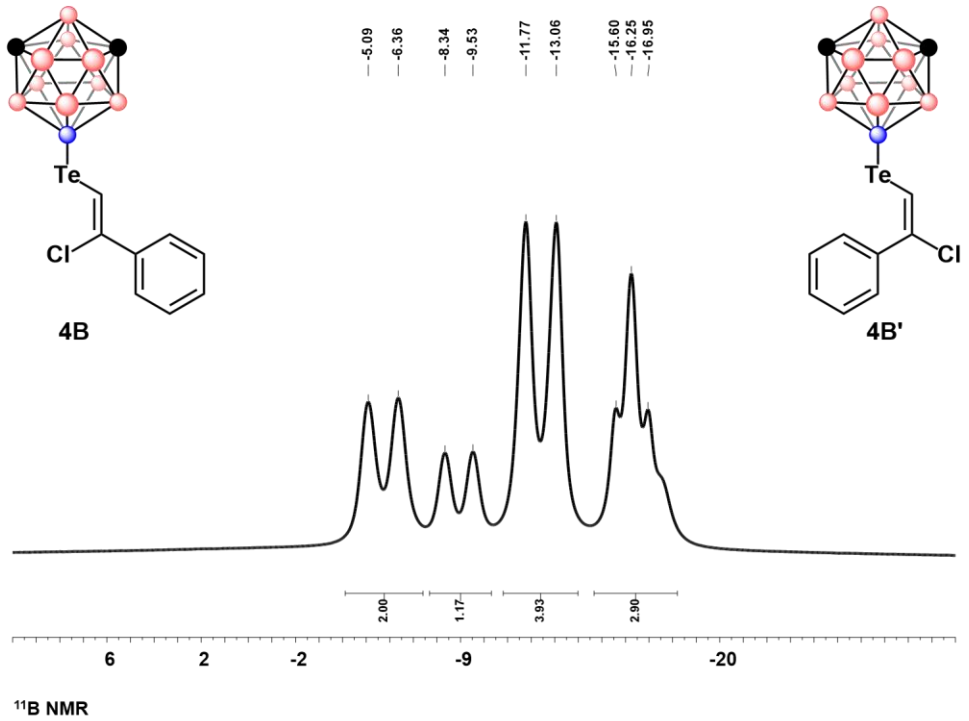

Figure C12.3 ^{11}B NMR of **4B** and **4B'**

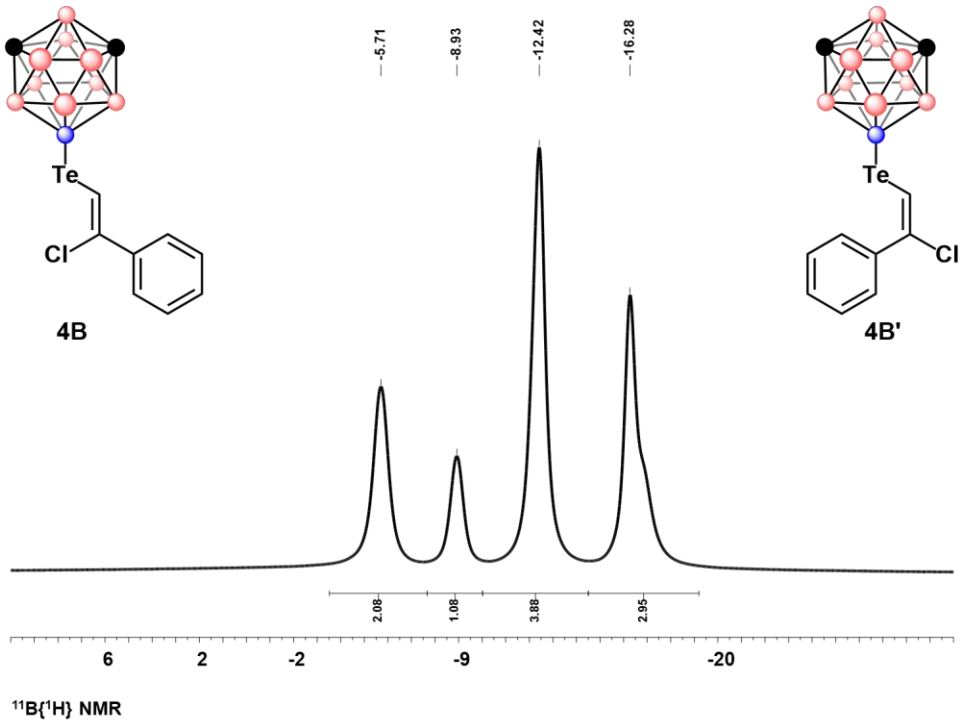

Figure C12.4 ^{11}B{^{1}H} NMR of **4B** and **4B'**

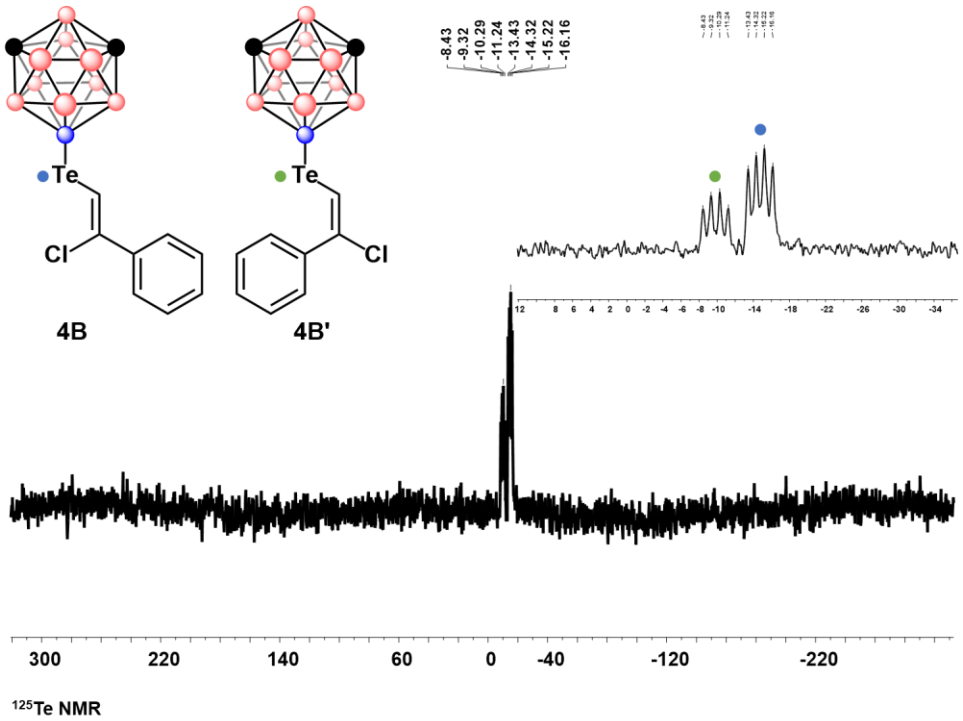

Figure C12.5 ^{125}Te NMR of **4B** and **4B'**

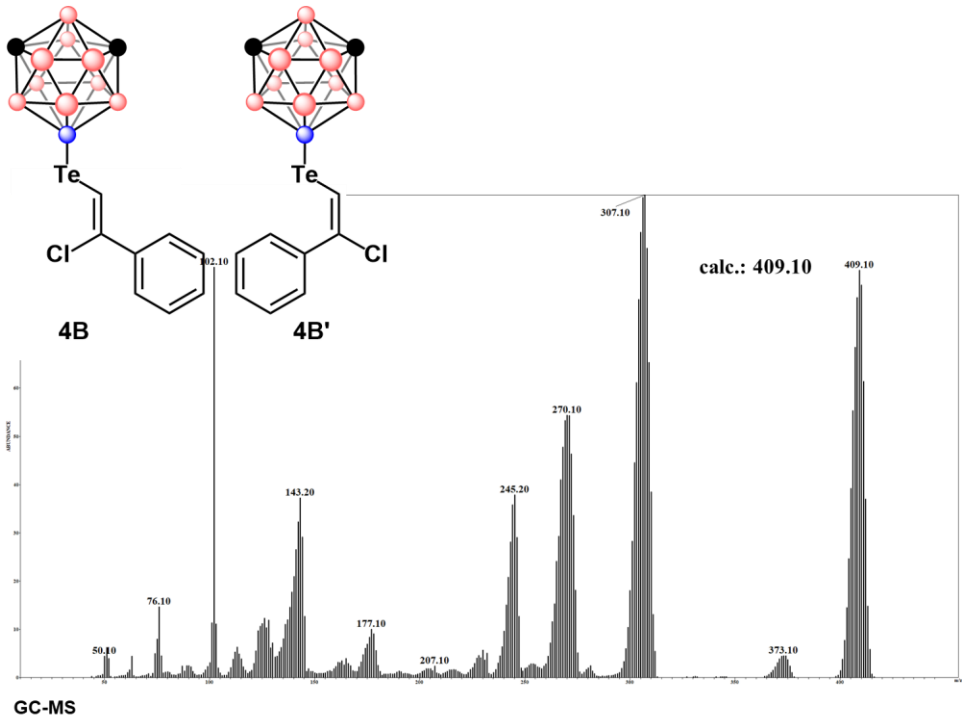

Figure C12.6 GC-MS of **4B** and **4B'**

4.6.11.13 *In Situ* Characterization of 4B* and 4B*'

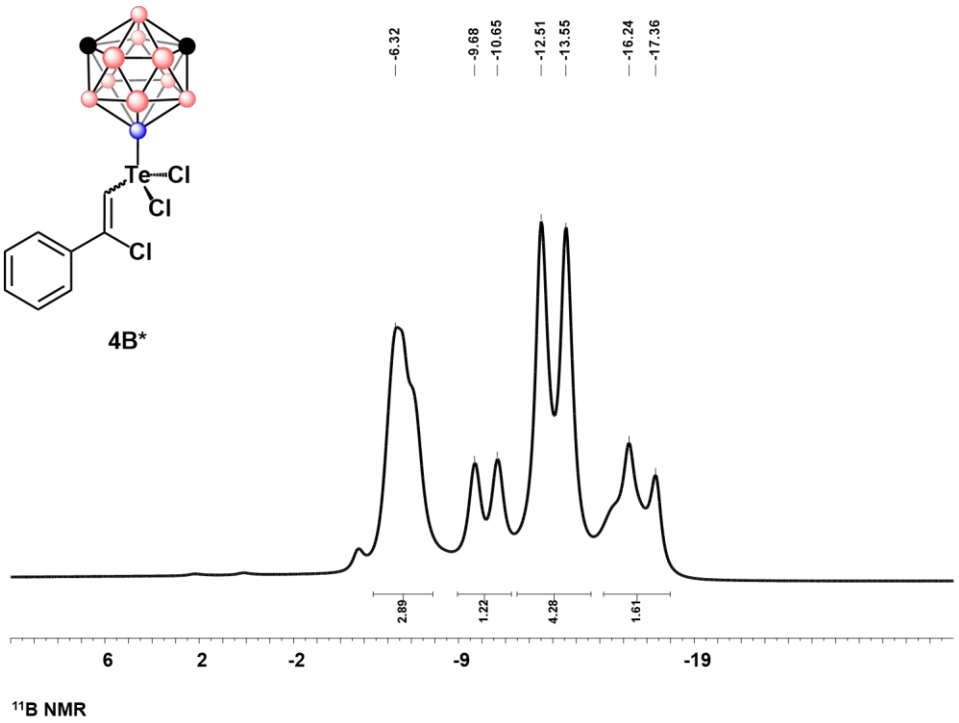

Figure C13.1 *In situ* ^{11}B NMR of **4B*** and **4B*'**

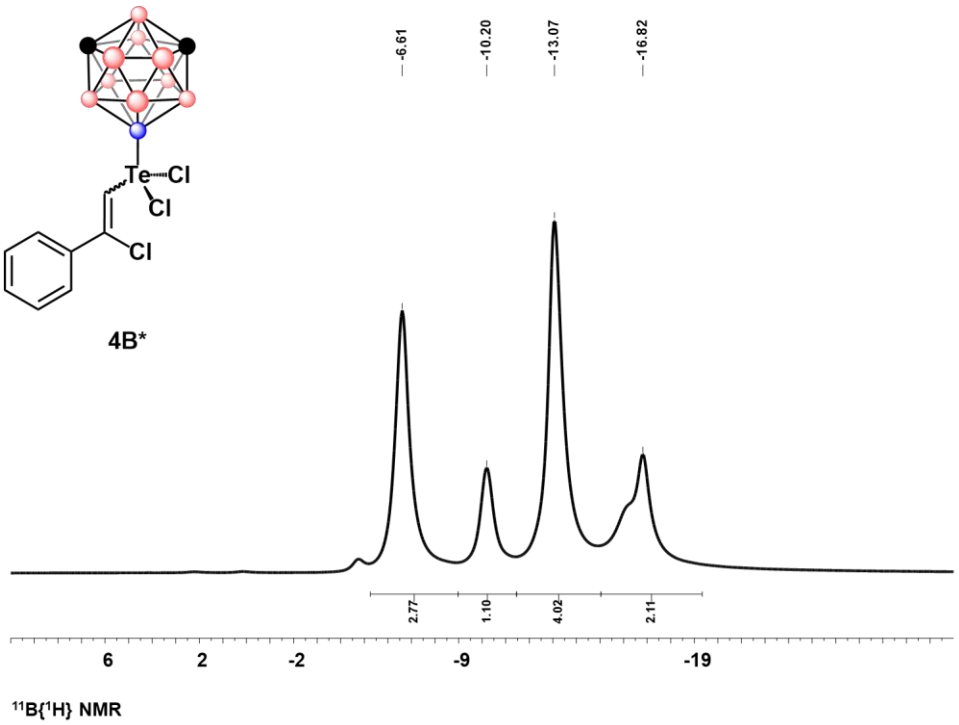

Figure C13.2 *In situ* ^{11}B{^{1}H} NMR of **4B*** and **4B*'**

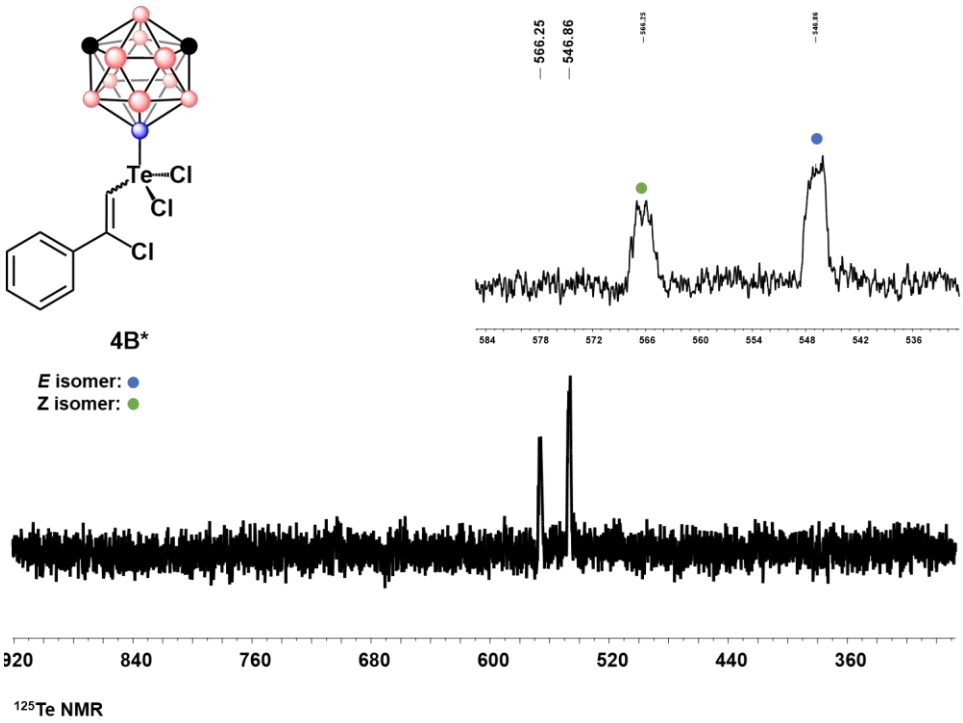

Figure C13.3 *In situ* ^{125}Te NMR of **4B*** and **4B*'**

4.6.11.14 Characterization of 5A

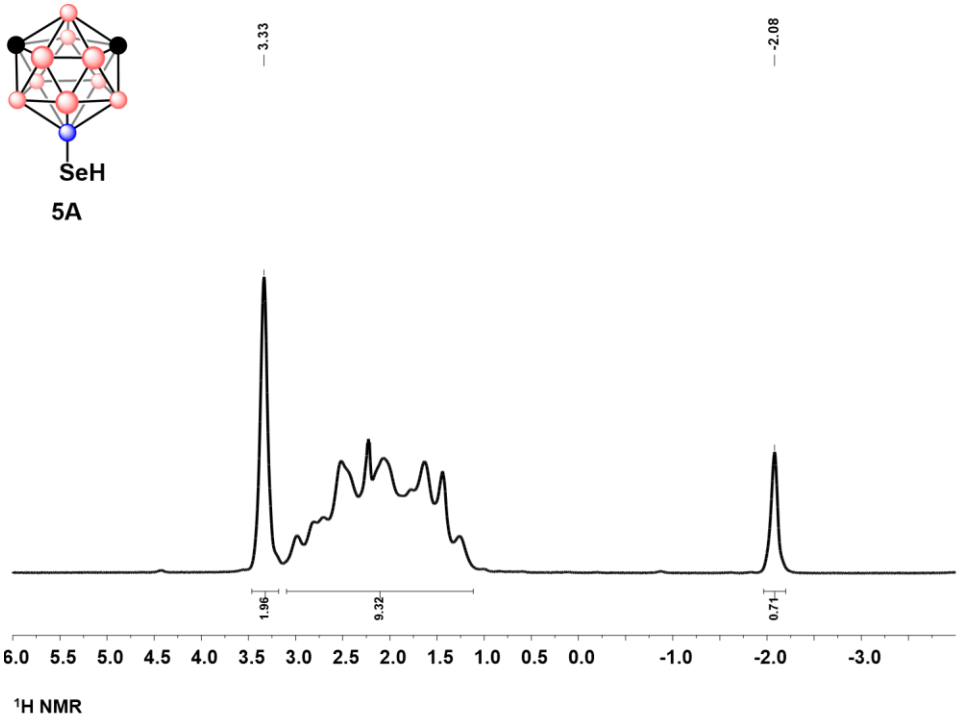

Figure C14.1 ^{1}H NMR of **5A**

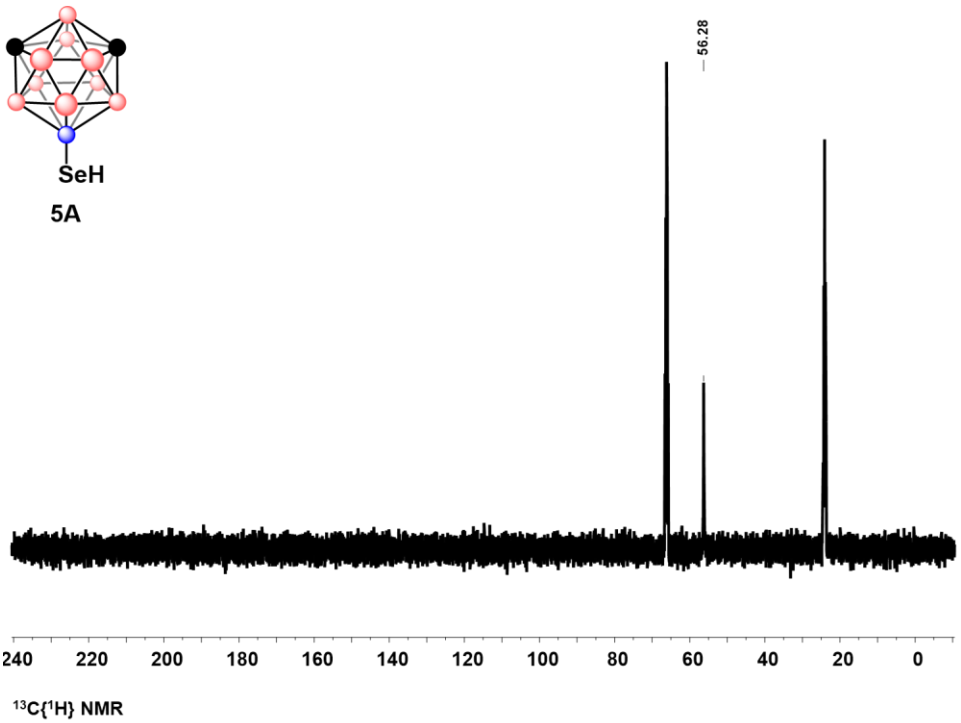

Figure C14.2 ^{13}C{^{1}H} NMR of **5A**

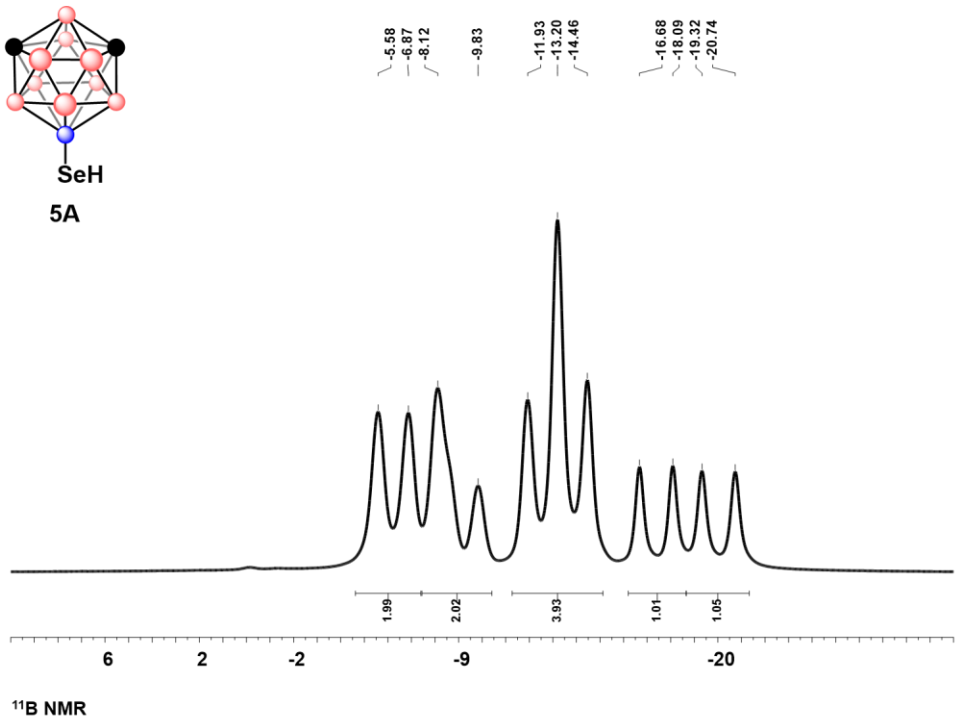

Figure C14.3 ^{11}B NMR of **5A**

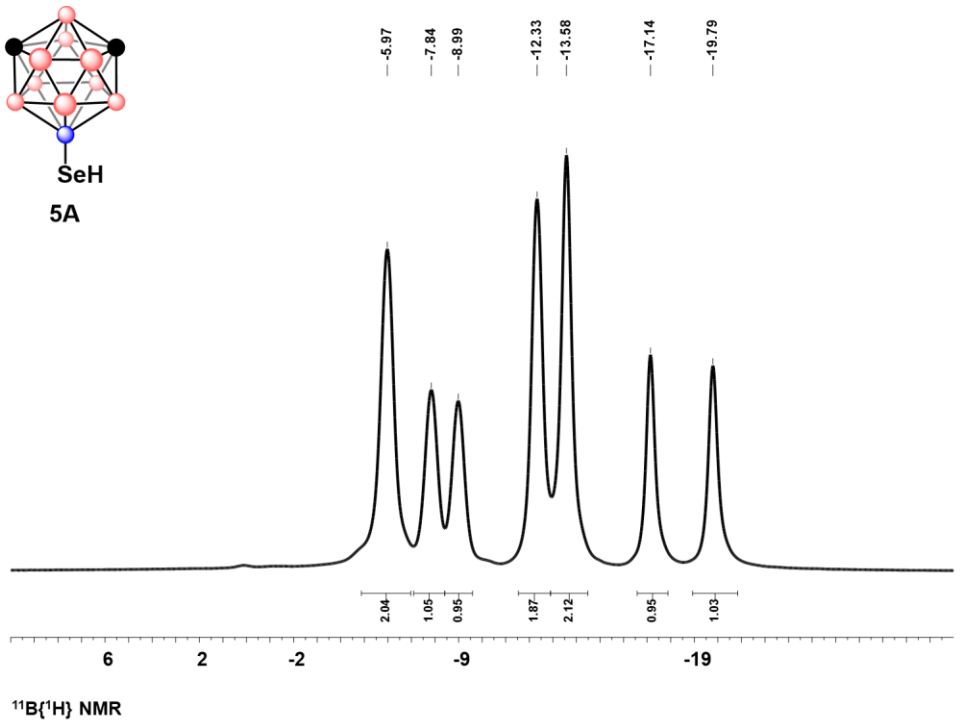

Figure C14.4 ^{11}B{^{1}H} NMR of **5A**

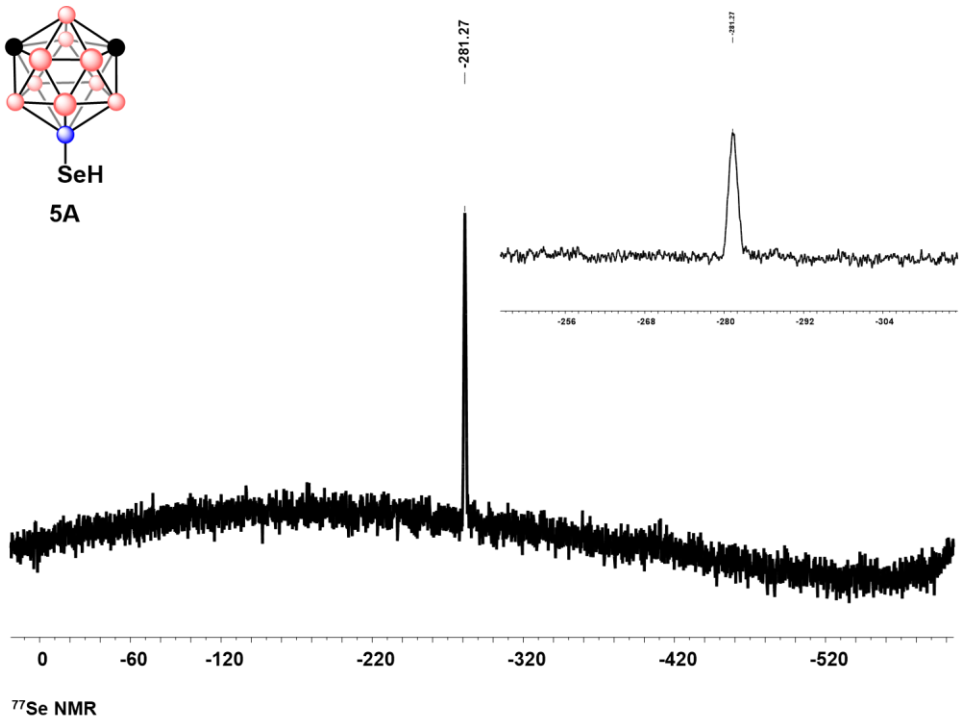

Figure C14.5 ^{77}Se NMR of **5A**

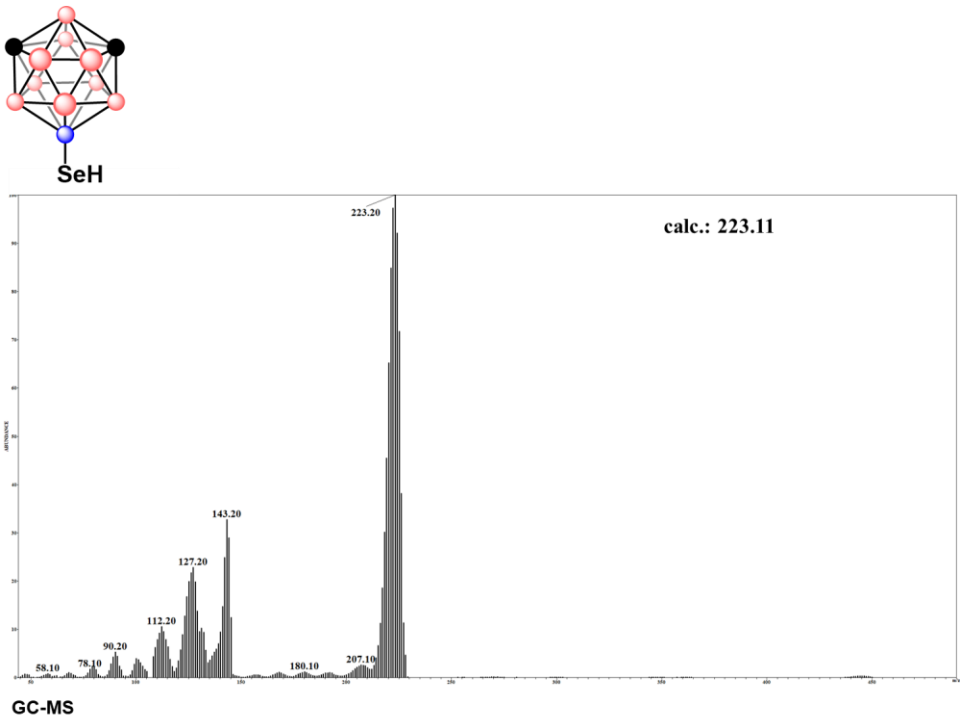

Figure C14.6 GC-MS of **5A**

4.6.11.15 Characterization of 5B

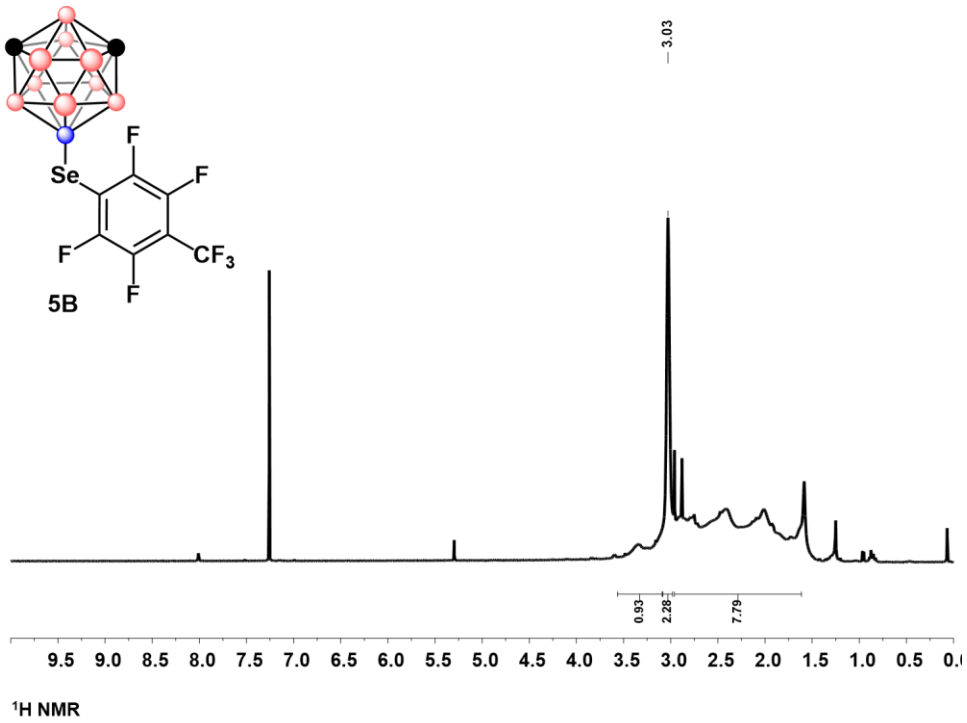

Figure C15.1 ^{1}H NMR of **5B**

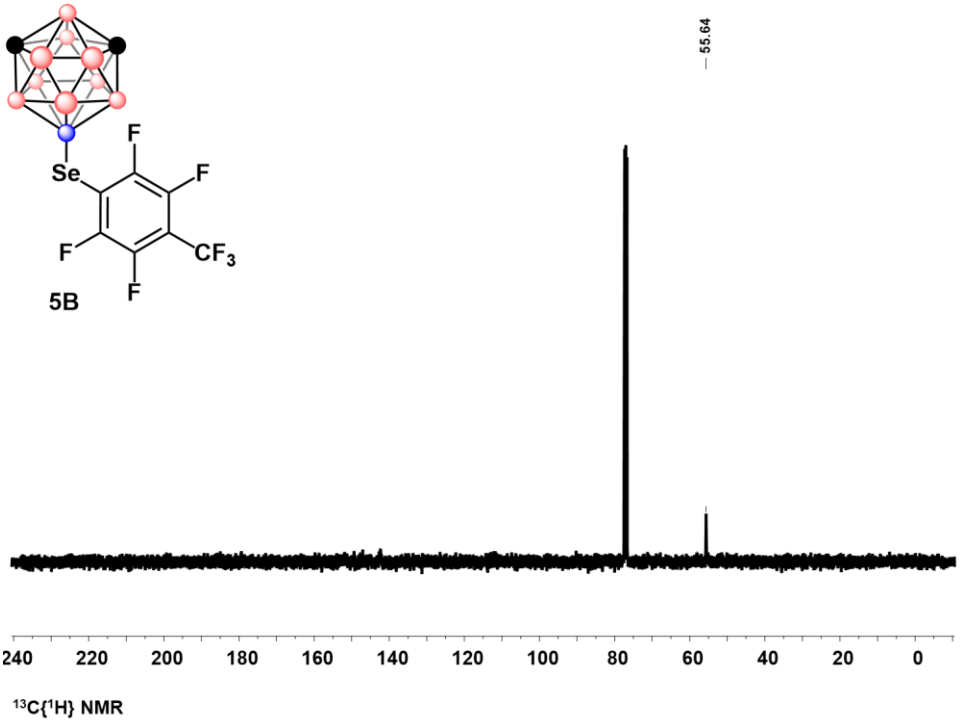

Figure C15.2 ^{13}C{^{1}H} NMR of **5B**

Figure C15.3 ^{19}F NMR of **5B**

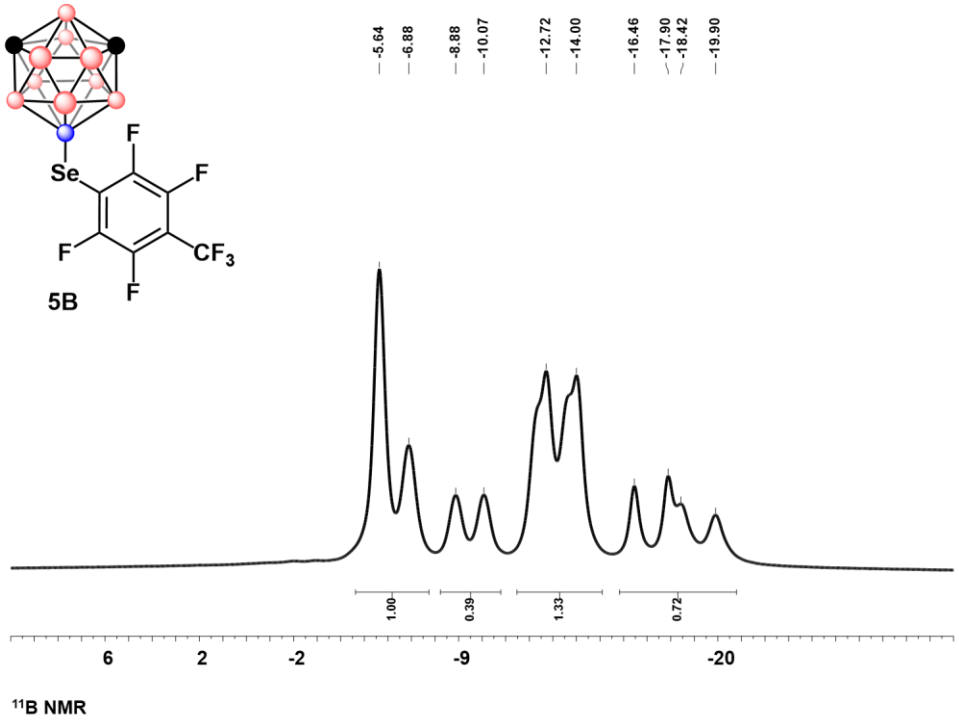

Figure C15.4 ^{11}B NMR of **5B**

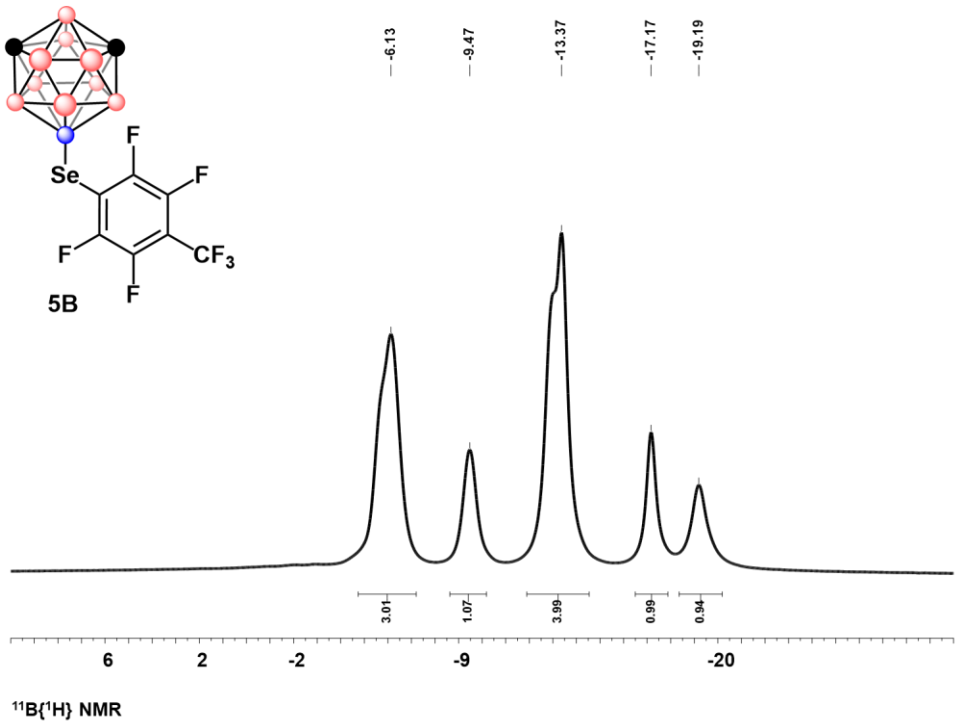

Figure C15.5 $^{11}B\{^{1}H\}$ NMR of **5B**

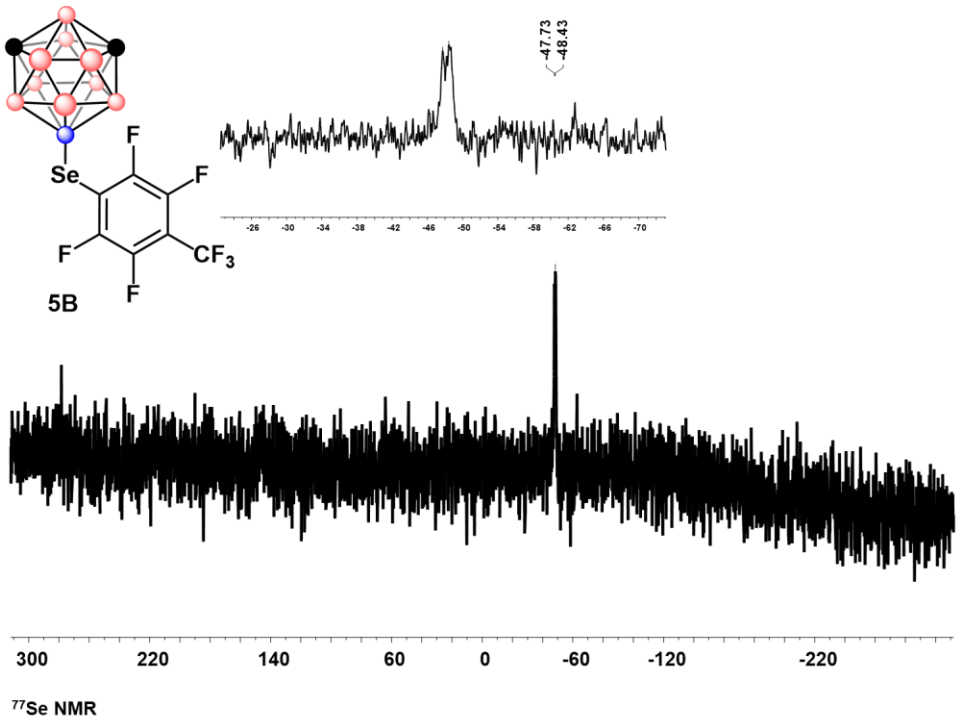

Figure C15.6 ^{77}Se NMR of **5B**

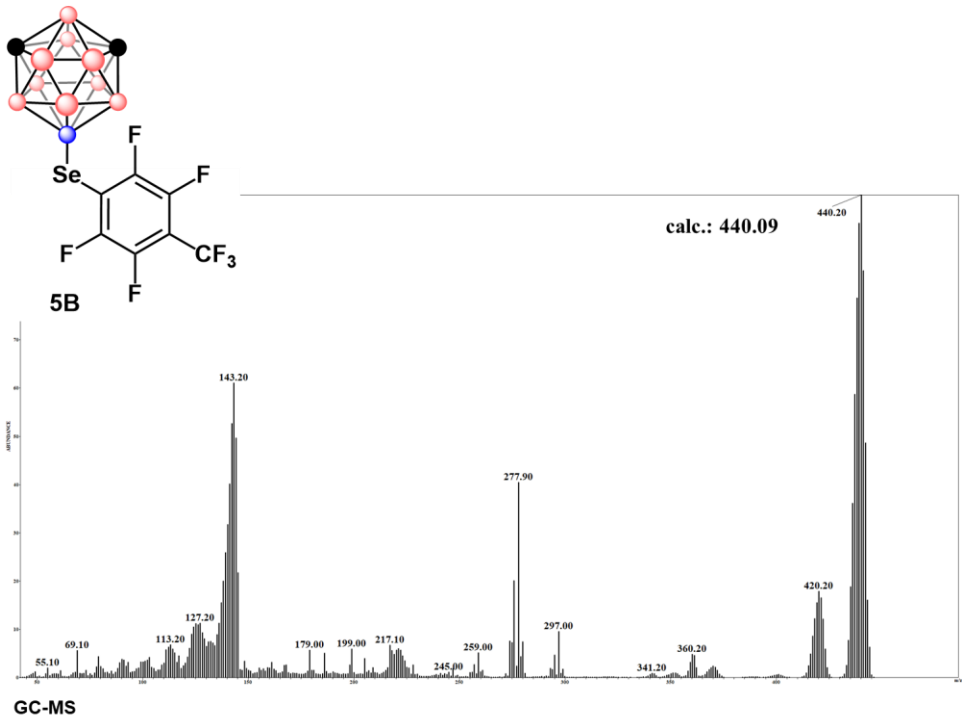

Figure C15.7 GC-MS of **5B**

4.6.11.16 Characterization of 6A

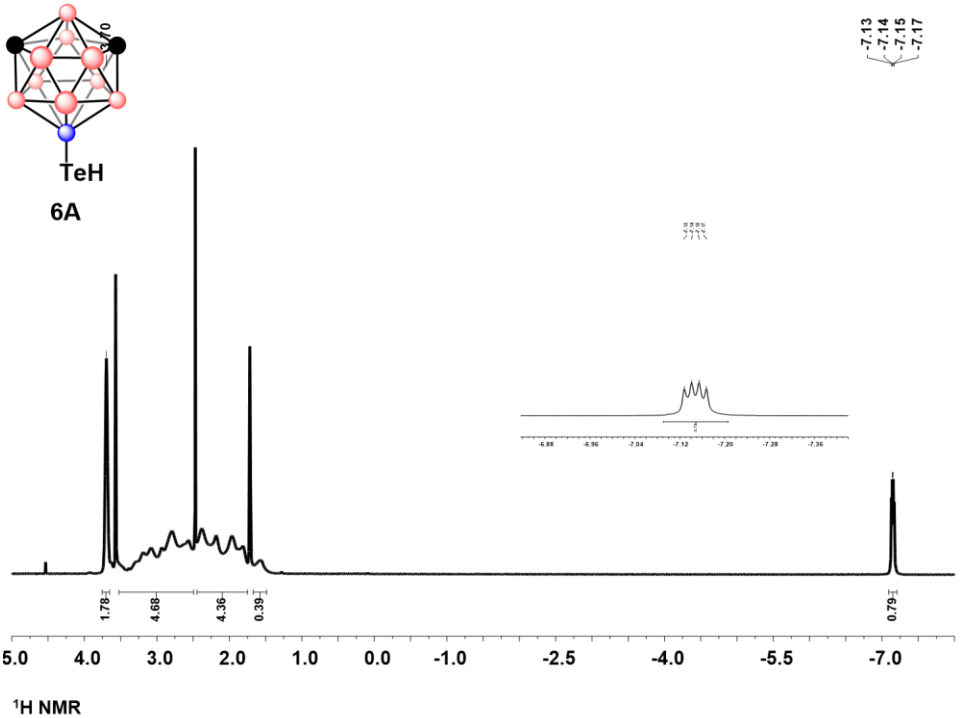

Figure C16.1 ^{1}H NMR of **6A**

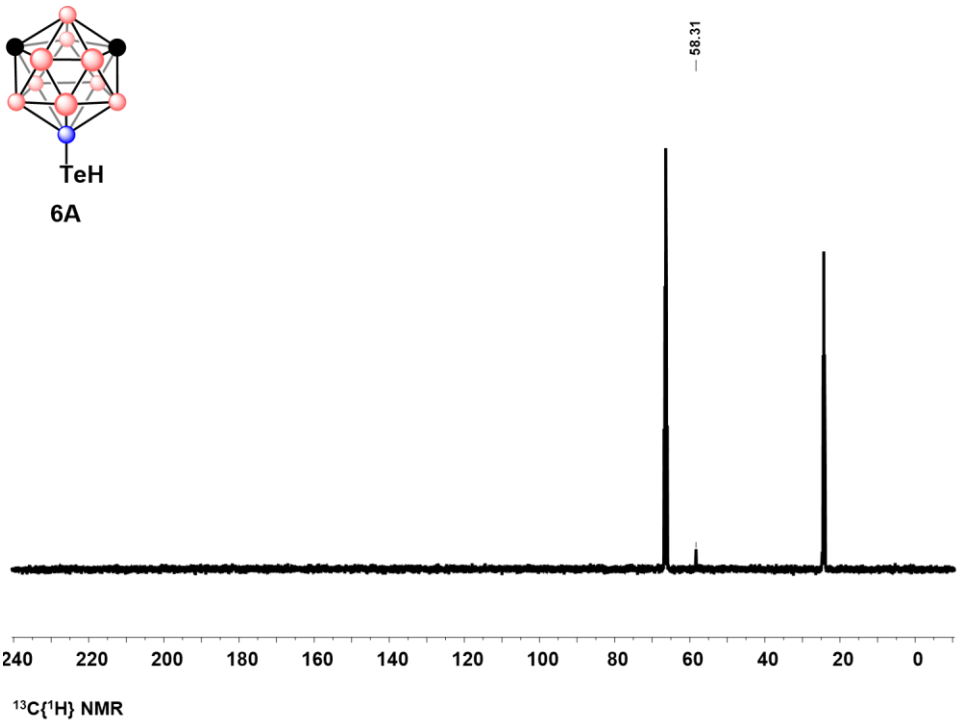

Figure C16.2 ^{13}C{^{1}H} NMR of **6A**

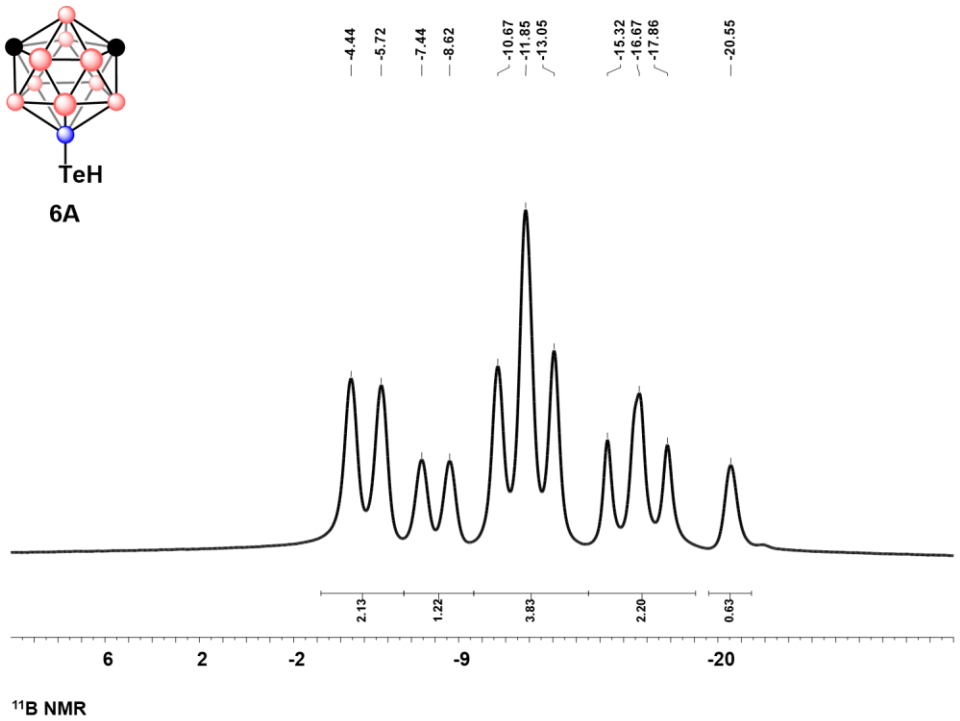

Figure C16.3 ^{11}B NMR of **6A**

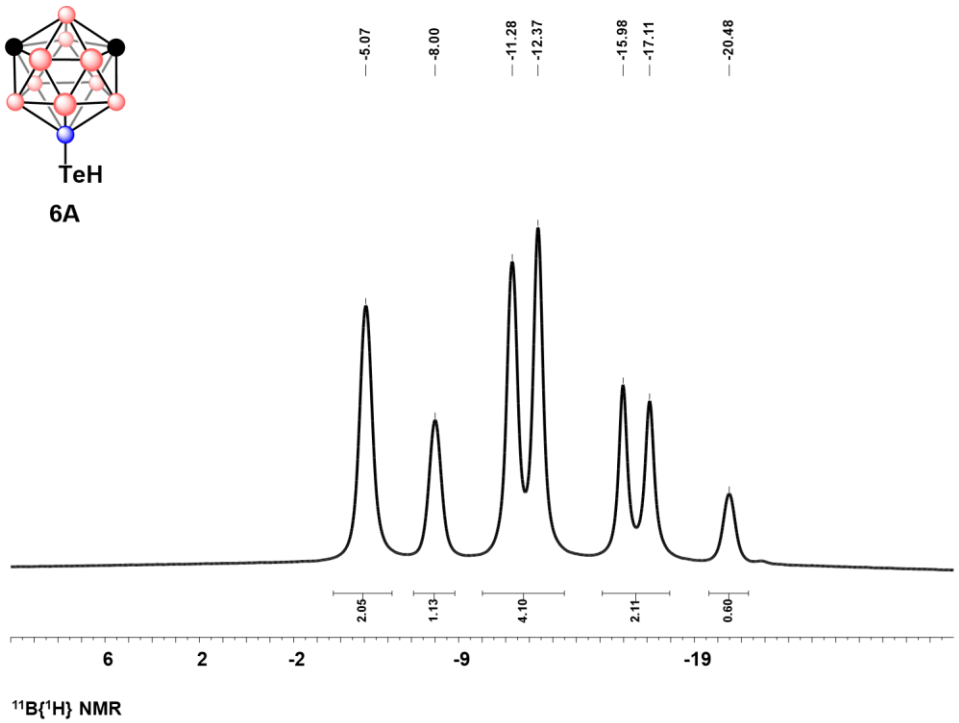

Figure C16.4 ^{11}B{^{1}H} NMR of **6A**

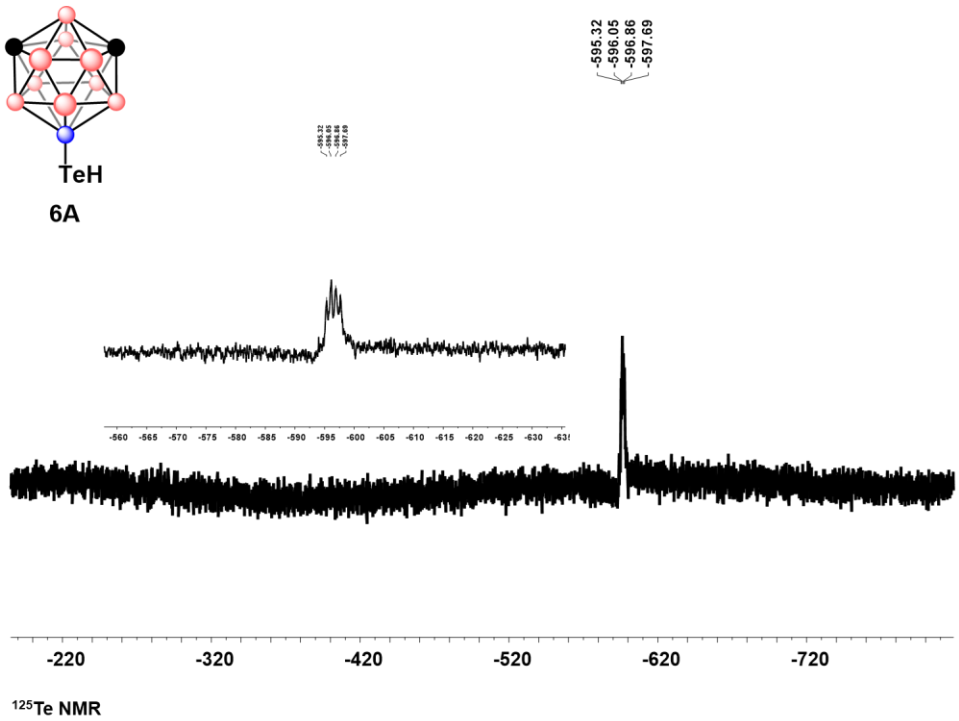

Figure C16.5 ^{125}Te NMR of **6A**

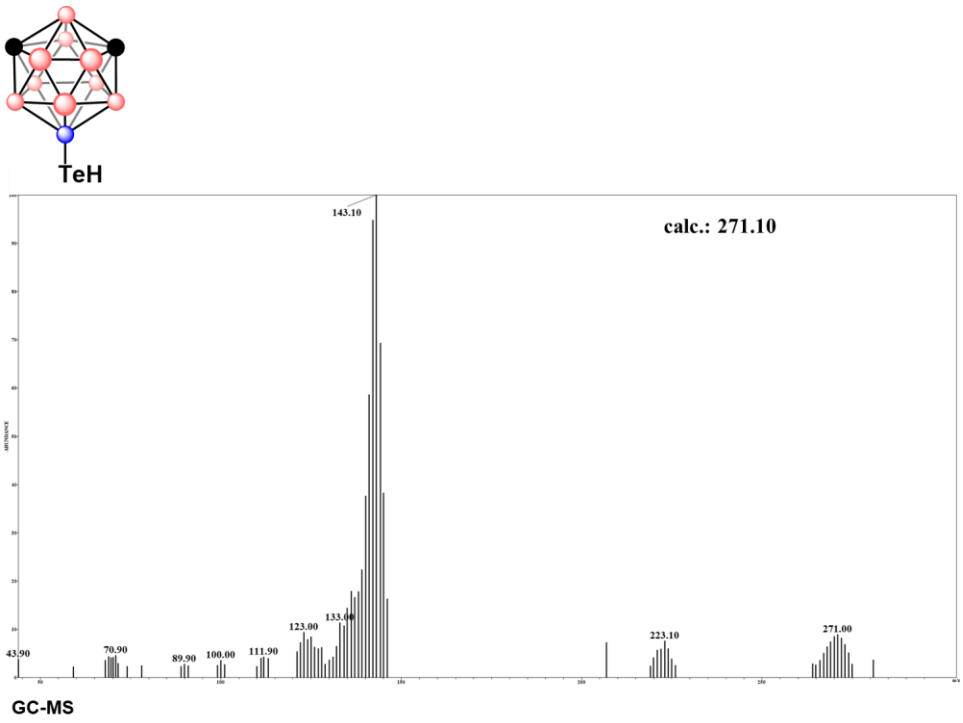

Figure C16.6 GC-MS of **6A**

4.6.11.17 Characterization of 6B

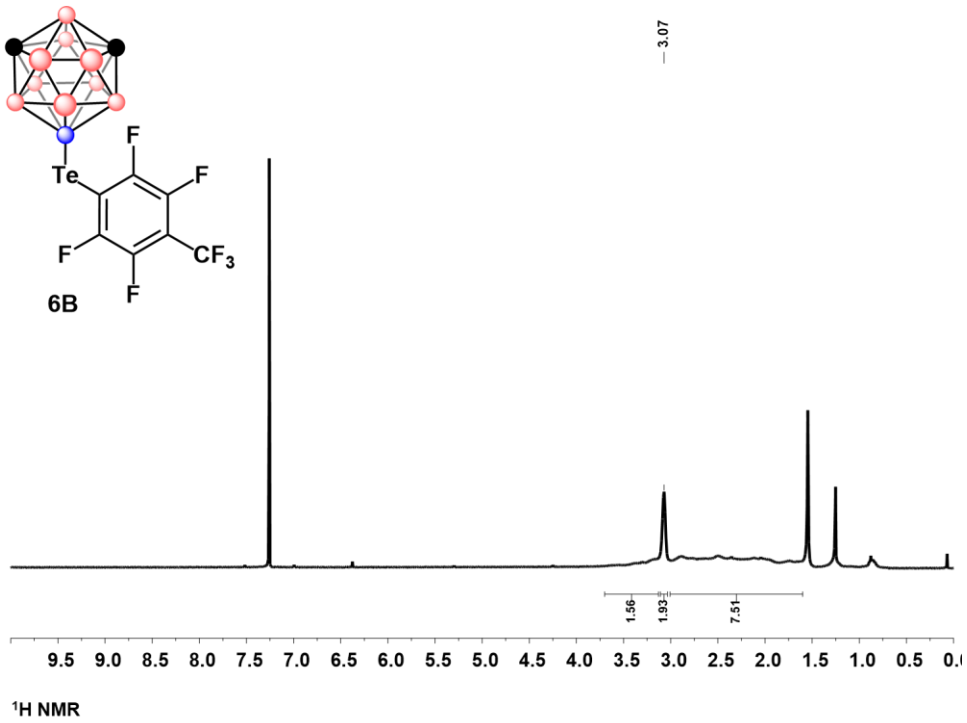

Figure C17.1 ^{1}H NMR of **6B**

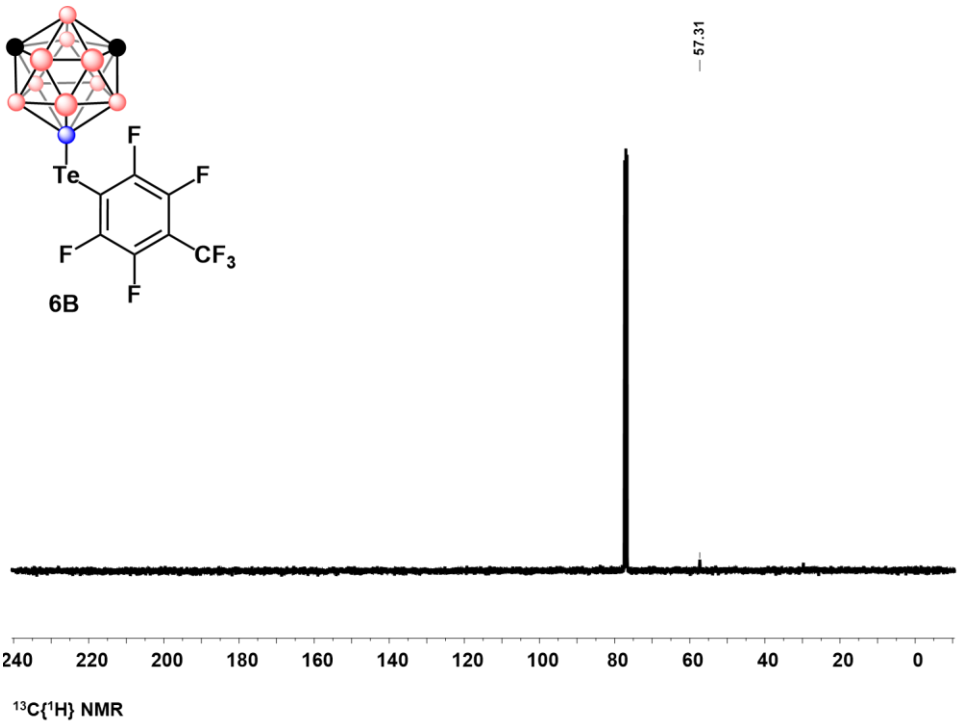

Figure C17.2 ^{13}C{^{1}H} NMR of **6B**

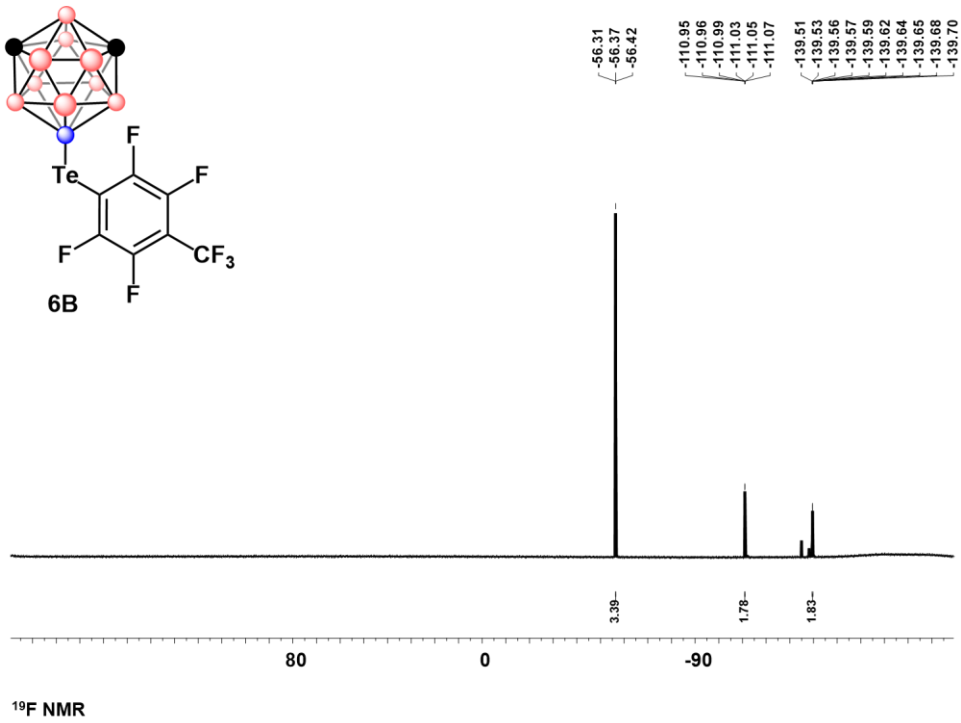

Figure C17.3 ^{19}F NMR of **6B**

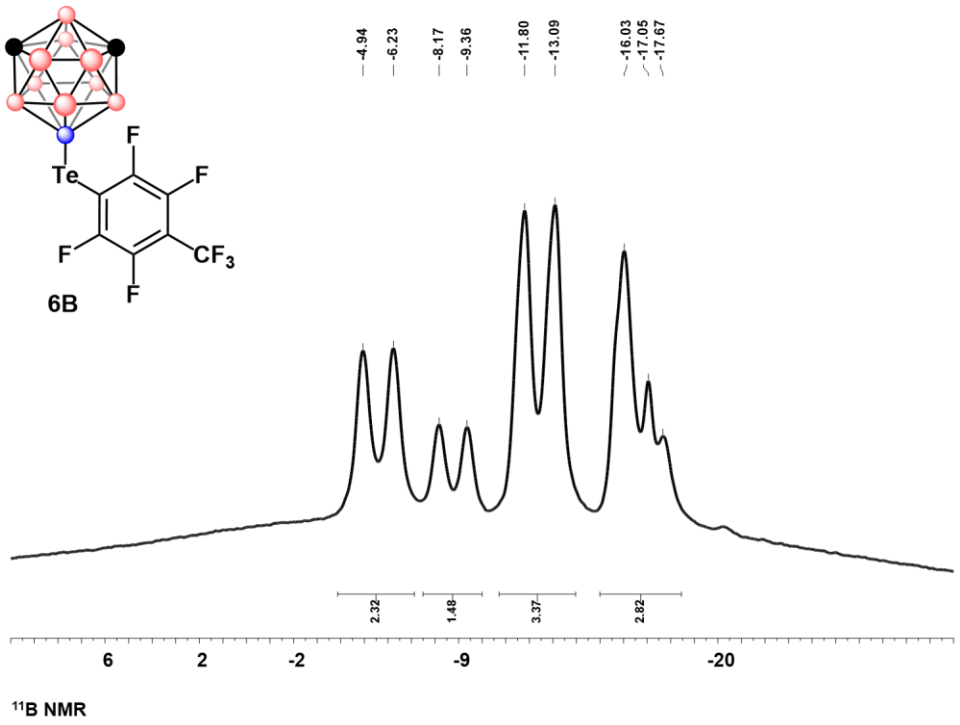

Figure C17.4 ^{11}B NMR of **6B**

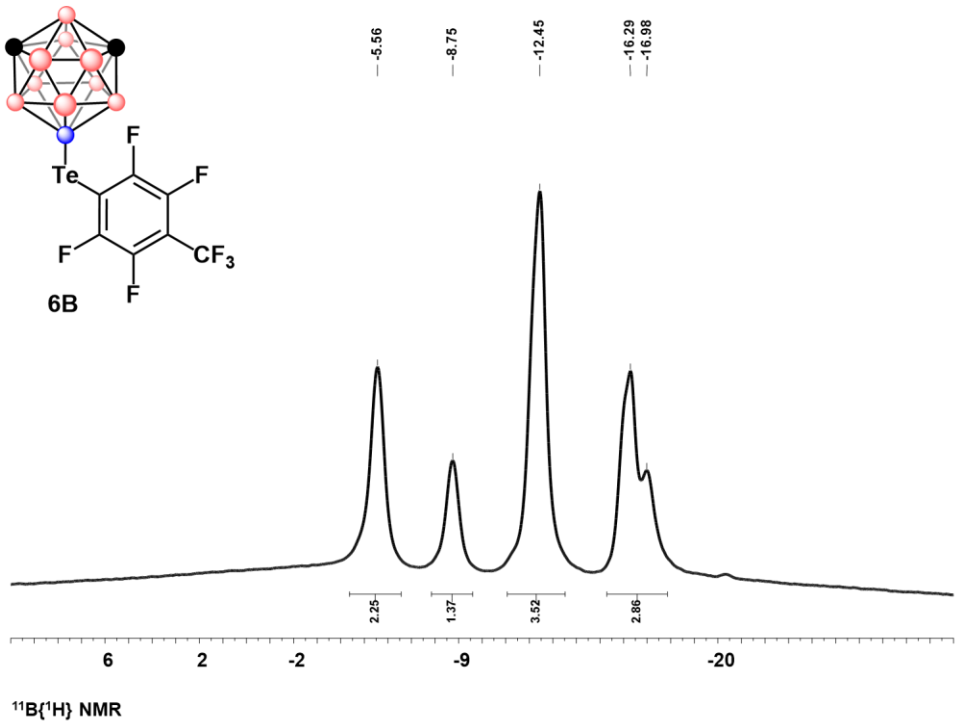

Figure C17.5 $^{11}B\{^{1}H\}$ NMR of **6B**

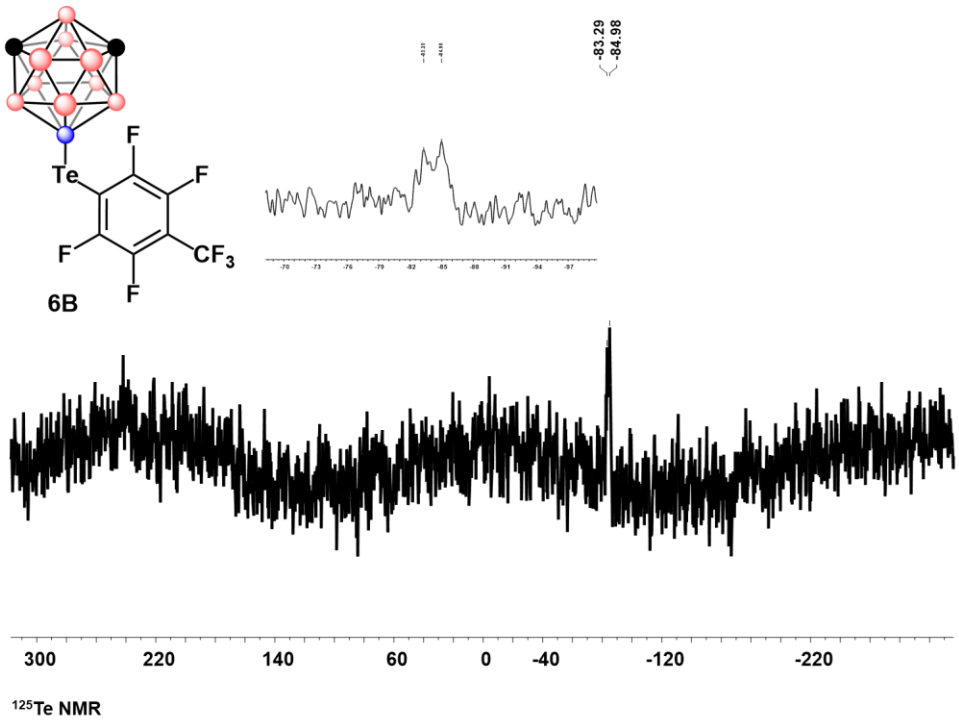

Figure C17.6 ^{125}Te NMR of **6B**

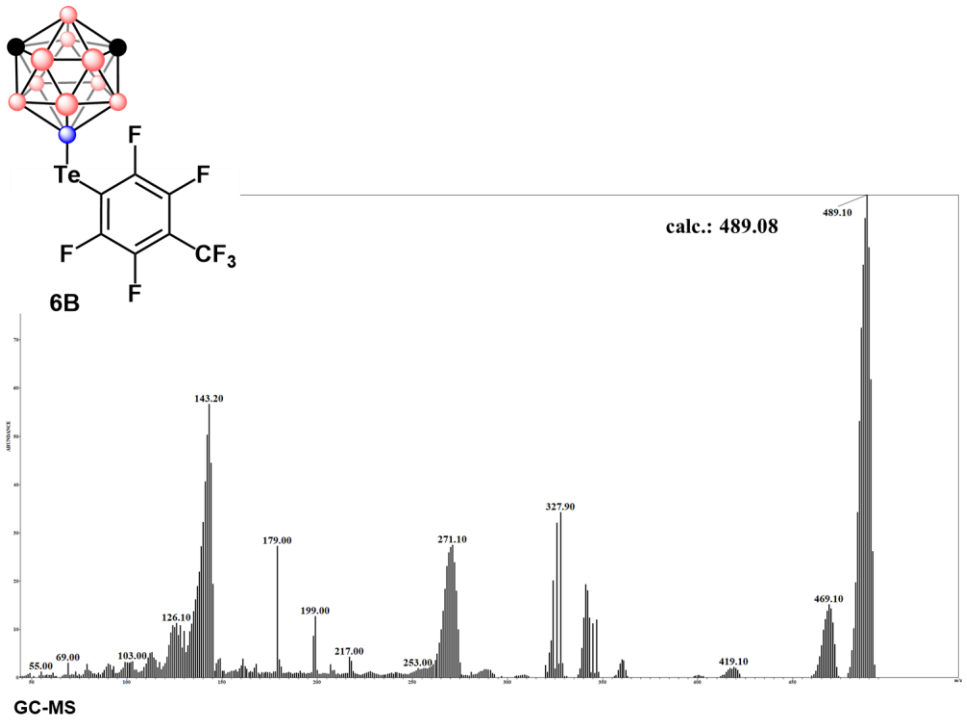

Figure C17.7 GC-MS of **6B**

4.6.11.18 Characterization of 6C

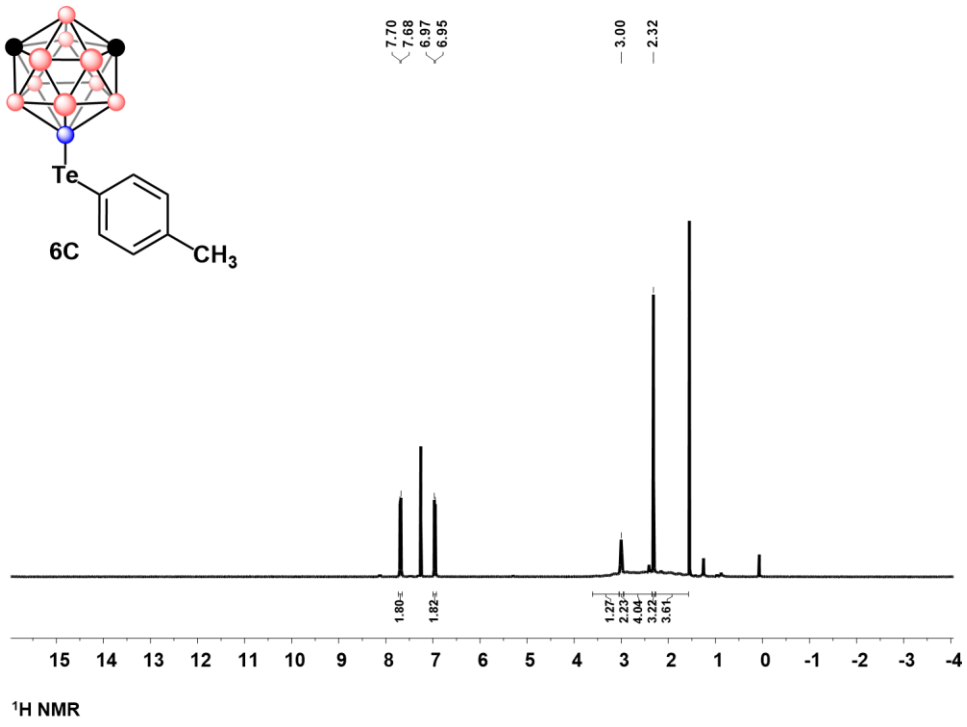

Figure C18.1 ^{1}H NMR of **6C**

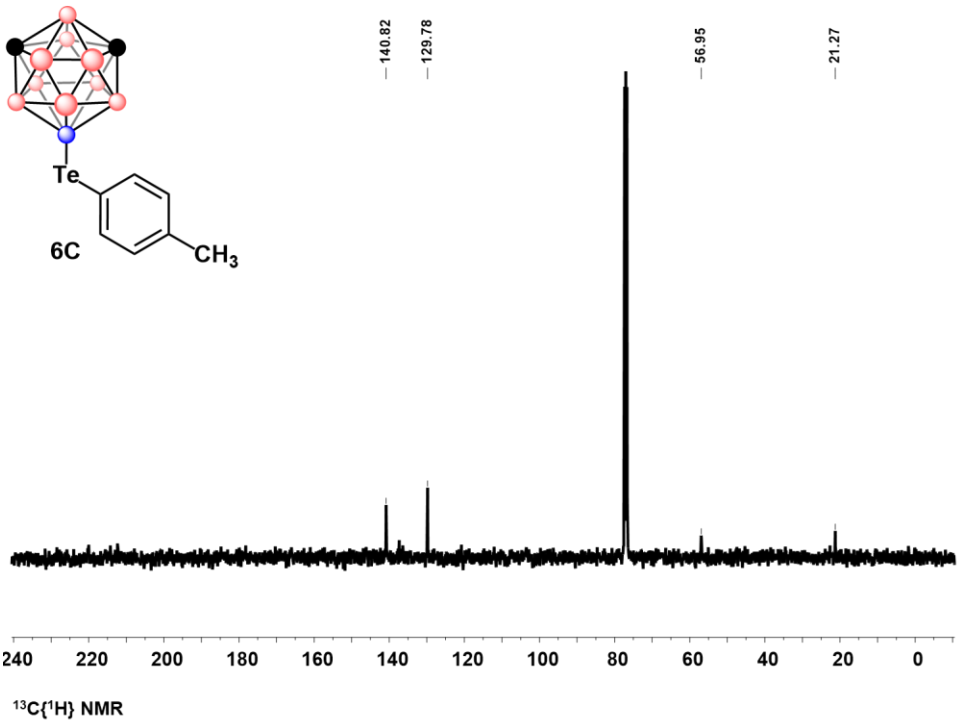

Figure C18.2 ^{13}C{^{1}H} NMR of **6C**

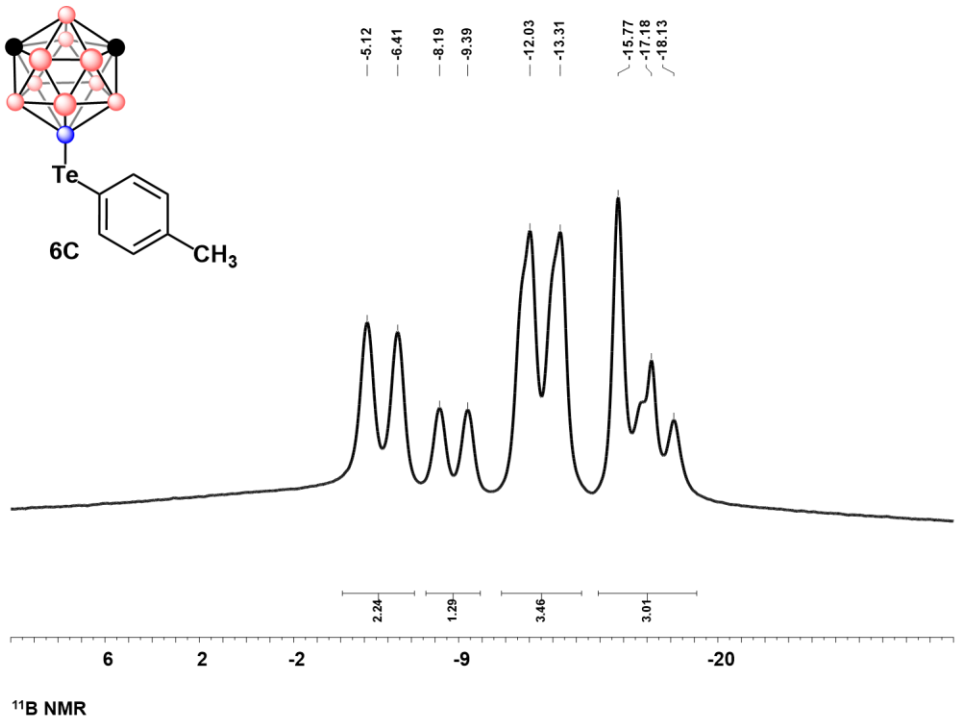

Figure C18.3 ^{11}B NMR of **6C**

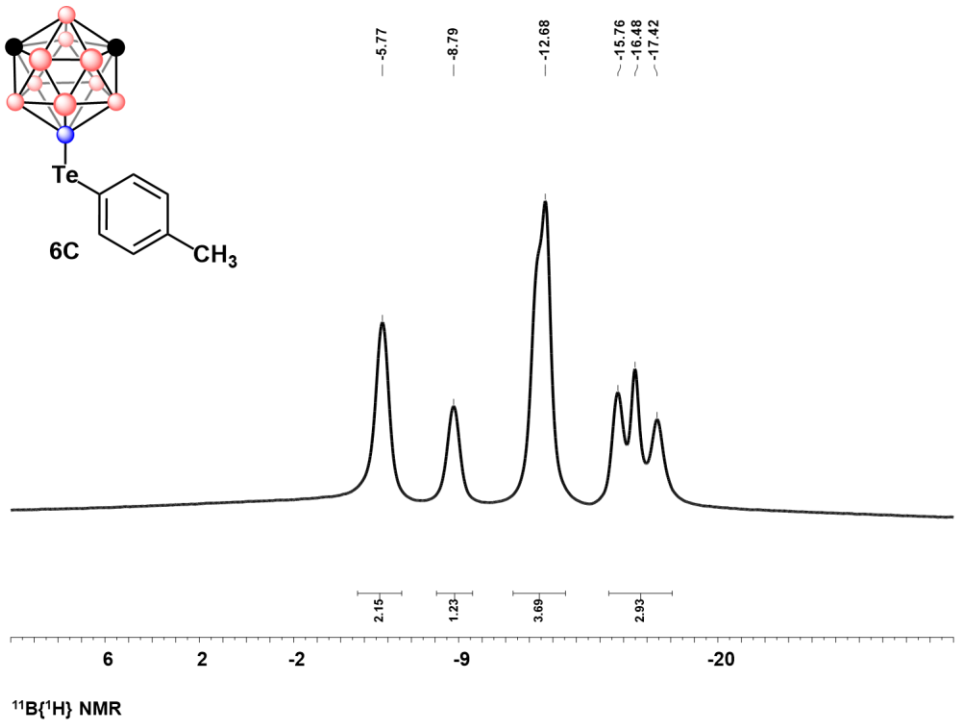

Figure C18.4 ^{11}B{^{1}H} NMR of **6C**

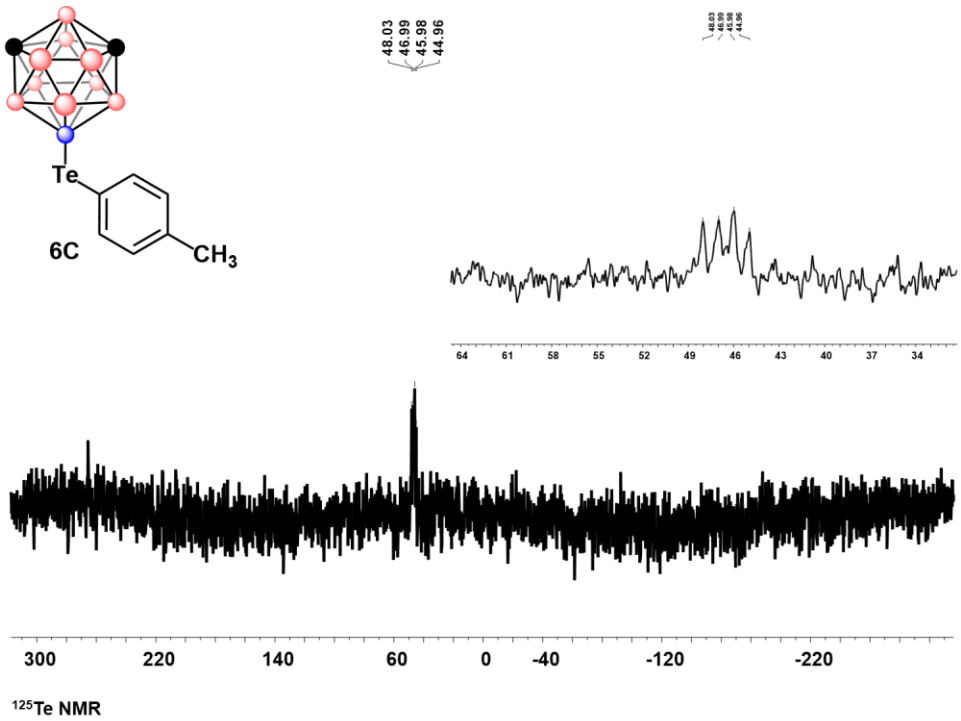

Figure C18.5 ^{125}Te NMR of **6C**

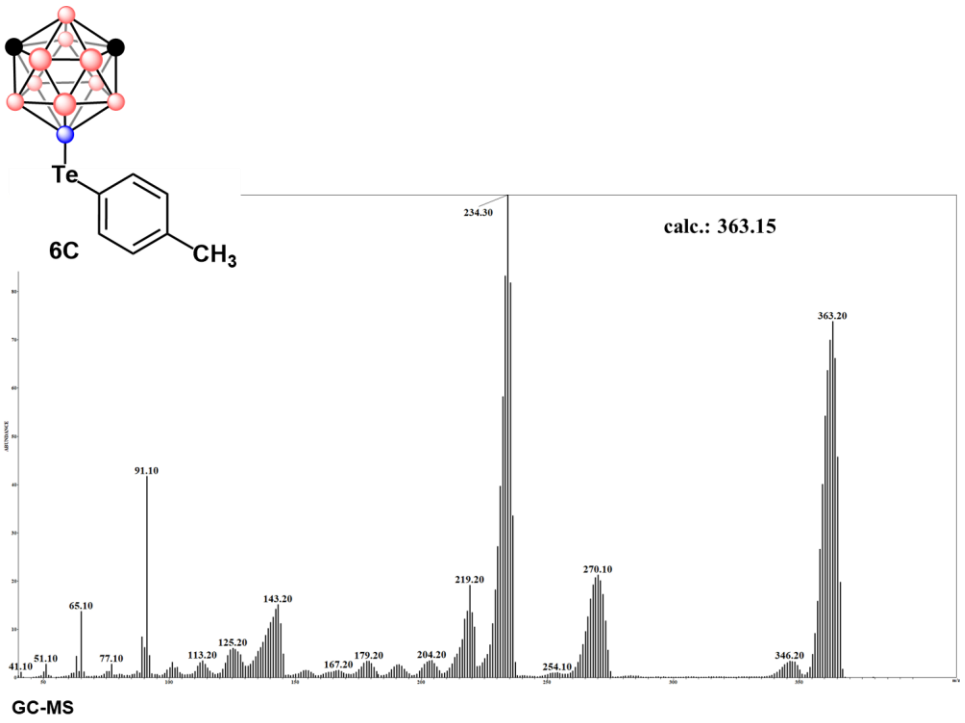

Figure C18.6 GC-MS of **6C**

4.6.12 References for Appendix C

1. Lenher, V.; Kao, C. H. The Preparation of Selenium Monochloride and Monobromide. *J. Am. Chem. Soc.* **1925** 47, 3, 772-774.
2. Petragnani, N.; Mendes, S. R.; Silveria, C. C. Tellurium tetrachloride: an improved method of preparation. *Tet. Lett.* **2008** 49, 15, 2371-2372.
3. Vinogradova, E. V.; Zhang, C.; Spokoyny, A. M.; Pentelute, B. L.; Buchwald, S. L. Organometallic palladium reagents for cysteine bioconjugation. *Nature* **2015**, 526, 687-691.
4. Zakharkin, L. I.; Pisareva, I. V.; Antonovich, V. A. Synthesis of Di(*o*- and *m*-Carboran-9-yl) Diselenides by Electrophilic-Substitution Reactions of *o*- and *m*-Carboranes with Selenium Chlorides Under the Action of $AlCl_3$, and Reactions of These Products.

Zhurnal Obshchei Khimii **1986**, 56, 12, 2721-2728.

5. Zakharkin, L. I.; Pisareva, I. V. Synthesis and Some Conversions of Derivatives of *o*- and *m*-Carborane Containing a B-Te σ Bond. *Izvestiya Akademii Nauk SSSR* **1987**, 4, 877-880.

6. Spokoyny, A. M.; Machan, C. W.; Clingerman, D. J.; Rosen, M. S.; Wiester, M. J.; Kenedy, R. D.; Stern, C. L.; Sarjeant, A. A.; Mirkin, C. A. A coordination chemistry dichotomy for icosahedral carborane-based ligands. *Nat. Chem.* **2011**, 3, 590-596.

CHAPTER 5 – STERICALLY INVARIANT CARBORANE-BASED LIGANDS FOR THE MORPHOLOGICAL AND ELECTRONIC CONTROL OF METAL ORGANIC CHALCOGENOLATE ASSEMBLIES

This chapter is a version of Mills, H. A.; Jones, C. G.; Anderson, K. P.; Ready, A. D.; Djurovich, P. I.; Khan, S. I.; Hohman, J. N.; Nelson, H. M.; Spokoyny, A. M. "Sterically Invariant Carborane-Based Ligands for the Morphological and Electronic Control of Metal Organic Chalcogenolate Assemblies", *to be submitted*

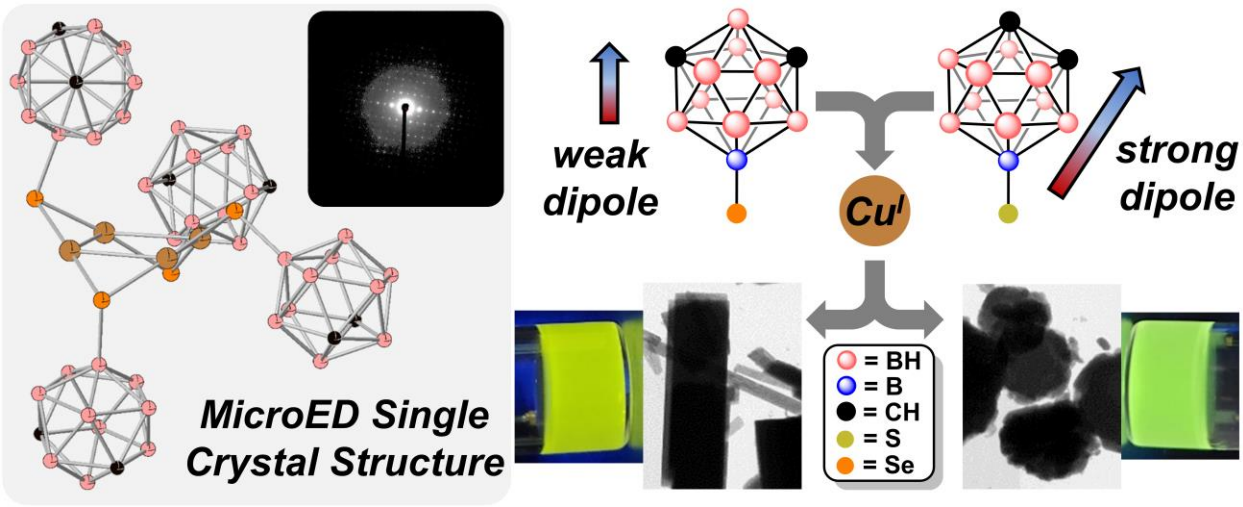

Figure 5.1: Graphical abstract for Chapter 5.

5.1 Abstract

Sterically invariant icosahedral boron cluster-based ligands (-SH, -COOH) have been extensively studied as ligands for self-assembled monolayers on a variety of metal surfaces for the past twenty years. The electronic nonuniformity of neutral clusters (i.e. carboranes) has allowed for unprecedented control of surface properties by modulating the local electronic environment imparted by the ligand when interacting with metal surfaces. While the utility of carborane-based ligands has been established with metal surfaces, their study as potential ligands for the control metal organic chalcogenolate assemblies (MOCHAs) has been limited. Herein, we report the

assessment of carborane-based chalcogenols, containing exopolyhedral B-Se or B-S bonds, as ligands for the formation of photoluminescent copper(I)-based MOCHAs. We show that precise tuning of the carborane dipole by changing the carborane isomer from *meta*- to *ortho*-, allows for exact control over the MOCHA morphology and regulation of the resulting photophysical properties. Furthermore, microcrystal electron diffraction (MicroED) techniques have been demonstrated as a powerful tool for metal chalcogenide structure elucidation. Through the use of MicroED, one of the isolated materials is determined to consist of zero-dimensional $Cu_4(Se\text{-}C_2B_{10}H_{11})_4$ clusters with an unprecedented Cu_4Se_4 geometry.

5.2 Introduction

Transition metal chalcogenides represent a large class of hybrid materials that have been extensively studied in both academic and non-academic research areas due to their promise as materials for a variety of applications, including photoluminescence,[1a-c] electronic devices[1d-f] and electrochemical reactions.[1g-i] Practitioners have often employed dimensional reduction of bulk materials as a facile strategy to tune and diversify material properties.[2] This strategy of dimensional reduction may utilize either a top down[3] or bottom up[4] synthetic approach, resulting in the formation of low-dimensional (zero-, one-, or two-dimensional) materials with a variety of architectures and surface compositions. One established method for the bottom-up dimensional control of metal chalcogenides has made use of the inherent reactivity between organic chalcogenols and metal cation-based precursors. The formed structures, more recently referred to as metal-organic chalcogenolate assemblies (MOCHAs, **Figure 5.2a**), have shown great promise in the preparation of low-dimensional metal-chalcogenide materials.[5] More specifically, some MOCHAs have been synthesized using a biphasic approach from aqueous metal cations (e.g. copper(I)[5a], silver(I)[5d]) layered with chalcogenols (e.g. alkyl thiols, aryl selenols) dissolved in an

organic solvent. At the solvent-solvent interface, the organic chalcogenols react with the metal cations forming intermediary metal complexes, which then nucleate and propagate the growth of small crystallites. Recently, this approach to MOCHA growth has also been extended to methods utilizing metal surfaces and gaseous benzene selenol or diphenyl diselenide reagents, where nucleation and growth of the material occurs at the solid-gas interface.[5f,l] In all cases, while the metal of choice serves as a general framework for MOCHA properties, the overall morphological, physical, and electronic properties are largely dictated by the chalcogenolate-based ligand chosen to template the material formation. It has been further hypothesized, and shown with adamantane and diamantane thiol reagents, that the steric environment of the organic chalcogenols plays an important role in the crystallite propagation, and is a determining factor of the overall material morphology.[5a] Furthermore, the intermolecular forces between adjacent chalcogenolate ligands are also expected to regulate the growth of the crystallites. Critically, with the current ligand scaffolds studied with MOCHAs, it is often impossible to isolate the effect of ligand electronics on MOCHA properties without also altering their steric profile in some way and, thereby inadvertently changing the steric interactions between the chalcogenolate ligands while also varying the electrostatic interaction between ligands.

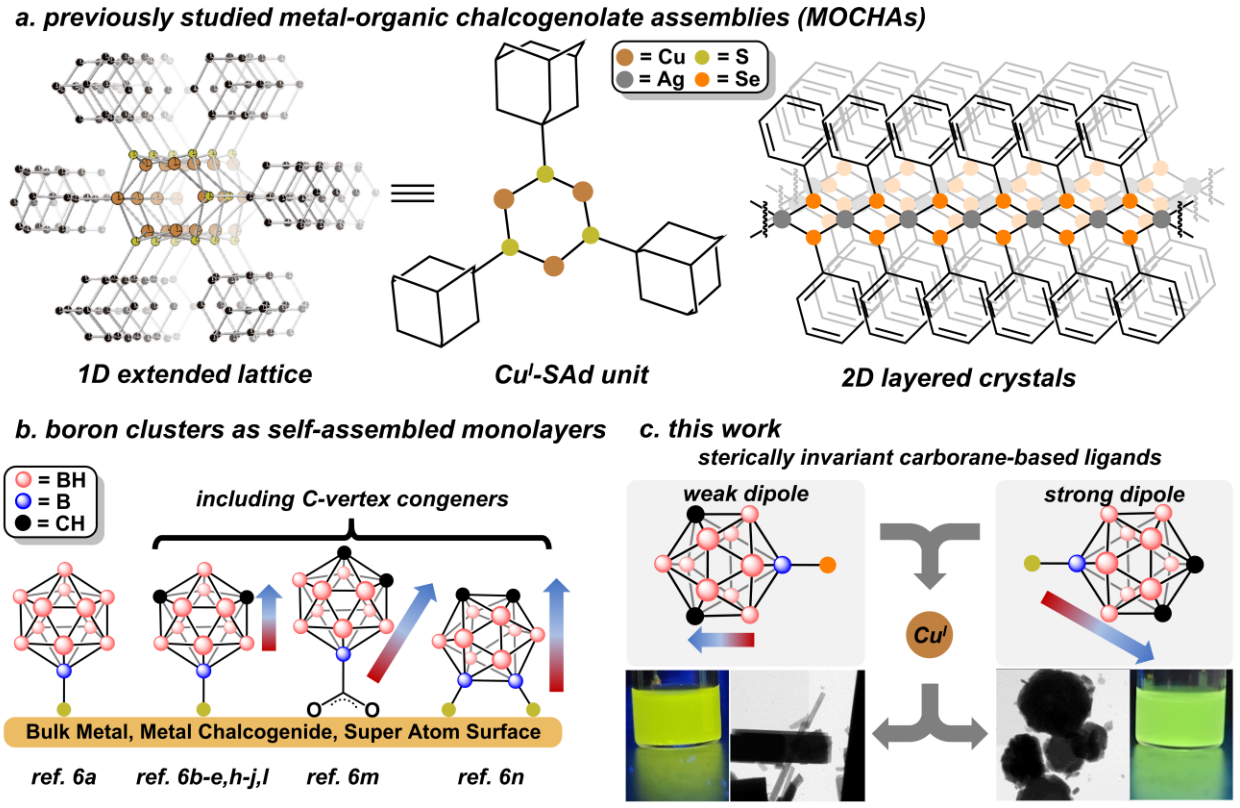

Figure 5.2: **a.** Selected examples of metal-organic chalcogenolate assemblies (MOCHAs) composed of either copper(I) diamondoid thiolates or silver(I) benzene selenolate. **b.** History of functionalized boron clusters (dodecaborates, carboranes) as self-assembled monolayers on bulk metal, metal chalcogenide, or super atom surfaces. The approximate dipoles of carborane-based ligands have been depicted to the right of the respective ligand. **c.** This work, utilizing sterically invariant carborane-based chalcogenolates to modulate morphology and photophysical properties of carborane-containing MOCHAs.

One unique class of chalcogen-containing ligands that have not yet been widely explored in the context of MOCHAs are functionalized boron clusters. This is surprising, considering that boron cluster ligands (thiolates, carboxylic acids) have been extensively studied on bulk surfaces for the past two decades,[6a-q] and more recently with metal chalcogenide nanoparticles[6r-s] as well as

metallic super atoms.[6t-v] The attractiveness of boron clusters in these applications is due in large part to their propensity to form "defect-free" monolayers as a function of both the steric bulk provided by the boron cluster and, in the case of neutral boron clusters (i.e. carboranes), their inherent molecular dipole that enables long-range order (**Figure 5.2b**).[7] Carboranes, with the molecular formula of $C_2B_{10}H_{12}$, exist as three distinct isomers (*ortho*-, *meta*-, *para*-) distinguished by the relative orientation of the two carbon vertices. Importantly, the electronic nonuniformity of *ortho*- and *meta*-carboranes, resulting from the asymmetry introduced by the carbon vertices, has allowed for the precise modulation of metal surface[6] and metal center properties,[8] as determined by the relative positioning of ligating substituents on the sterically invariant boron clusters (**Figure 5.2b**). This electronic nonuniformity is further exemplified by the regioselective chemistry of carboranes that has permitted selective introduction of functional groups to the carbon-based vertices and various boron-based vertices of carboranes.[9]

Despite the potential for carborane-based ligands to tune MOCHA properties, only one recent study has reported the use of 9-*meta*-carboranyl thiolate and cadmium(I) to generate MOCHA-like structures which were preliminarily visualized by scanning electron microscopy with no additional characterization provided. To further develop the understanding of structure-function relationships in the context of MOCHAs, and more specifically, the impact a molecular dipole might have on MOCHA morphology and electronic properties, we report our investigation on the formation of copper(I)-based MOCHA materials with sulfur and selenium-containing electron-rich carborane chalcogenolates. Specifically, we show how sterically invariant carborane-based chalcogenolate ligands can control the morphology and electronic properties of copper(I)-based MOCHAs through differences in the carborane dipole magnitude and orientation between the *ortho*- and *meta*- isomers. The morphology, composition, and stability of all reported materials

have been determined using scanning electron microscopy (SEM), transmission electron microscopy (TEM), powder X-ray diffraction (PXRD), Fourier transform infrared spectroscopy (FTIR), thermogravimetric analysis (TGA), and X-ray photoelectron spectroscopy (XPS). Furthermore, critical structural characterization was obtained by applying emerging microcrystal electron diffraction (MicroED) techniques to determine the unique bonding arrangement between copper(I) and 9-*meta*-carboranyl selenolate for the key MOCHA structure synthesized. All prepared materials exhibit photoluminescence that further exemplify control of MOCHA properties by tuning key photophysical properties, such as quantum yield and emission lifetimes, as a function of both the carborane dipole as well as the chalcogenolate (Se, S) used.

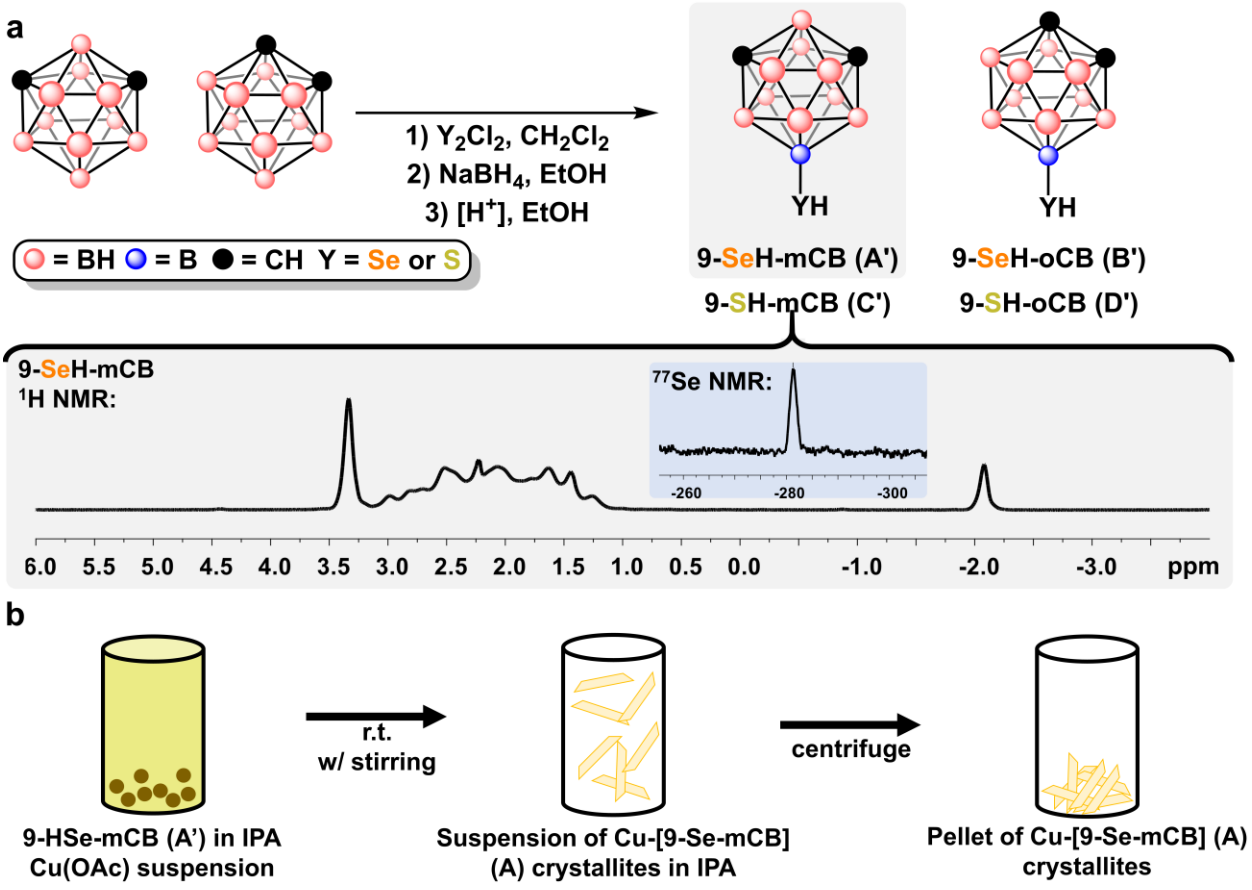

Figure 5.3: **a.** Synthesis of B(9) substituted *meta*- and *ortho*-carborane selenols and thiols following literature procedures. Representative characterization (^{1}H, ^{77}Se NMR) of 9-SeH-mCB in THF-d_6. **b.** General synthesis of carborane chalcogenolate-containing MOCHAs **A**-**D**.

5.3 Results and Discussion

In order to understand whether one can form MOCHAs with sterically encumbering carborane ligands, we first opted to study the reaction between a copper(I) precursor and 9-*meta*-carboranyl selenol (SeH-mCB, **A'**). Copper(I) was chosen due to the previously reported reactivity between copper(I) precursors and sterically encumbered adamantane and diamantane thiol ligands.[5a] Conversely, SeH-mCB was selected as our first ligand of study due to the known stability of exopolyhedral B-Se bonds,[10] the established body of work utilizing *meta*-carborane ligands in self-assembled materials,[6] and lastly, the anticipated reactivity between the selenolate and copper(I). SeH-mCB was synthesized according to literature procedures[10] (**Figure 5.3a**, Appendix D, sec. 5.6.3) and isolated as an air-stable solid that showed little to no oxidation after several months when stored at 5 ºC in laboratory air, in contrast to oxidatively unstable carbon-based selenols. To begin our studies regarding the self-assembly behavior of carborane chalcogenols in the presence of copper(I) salts, SeH-mCB and copper(I) acetate were mixed together as powders in a 4 mL dram vial equipped with stir bar in a nitrogen-filled glovebox. Subsequently, anhydrous *iso*-propanol was added *via* syringe and the reaction mixture was immediately stirred at 700 rpm in the dark (**Figure 5.3b**). This approach takes advantage of gradual etching of the copper(I) acetate particles by the dissolved selenol, decreasing the reaction rate that has previously resulted in non-crystalline MOCHA phases when using benzene selenol.[5d] Within minutes, an off-white precipitate began to form, ultimately resulting in a milky suspension after stirring overnight. To separate the formed precipitate, the suspension was centrifuged and the resulting pellet was

collected and dried *in vacuo* to remove all volatiles, affording Cu-[Se-mCB] (**A**) in 76% yield (Appendix D, sec. 5.6.4).

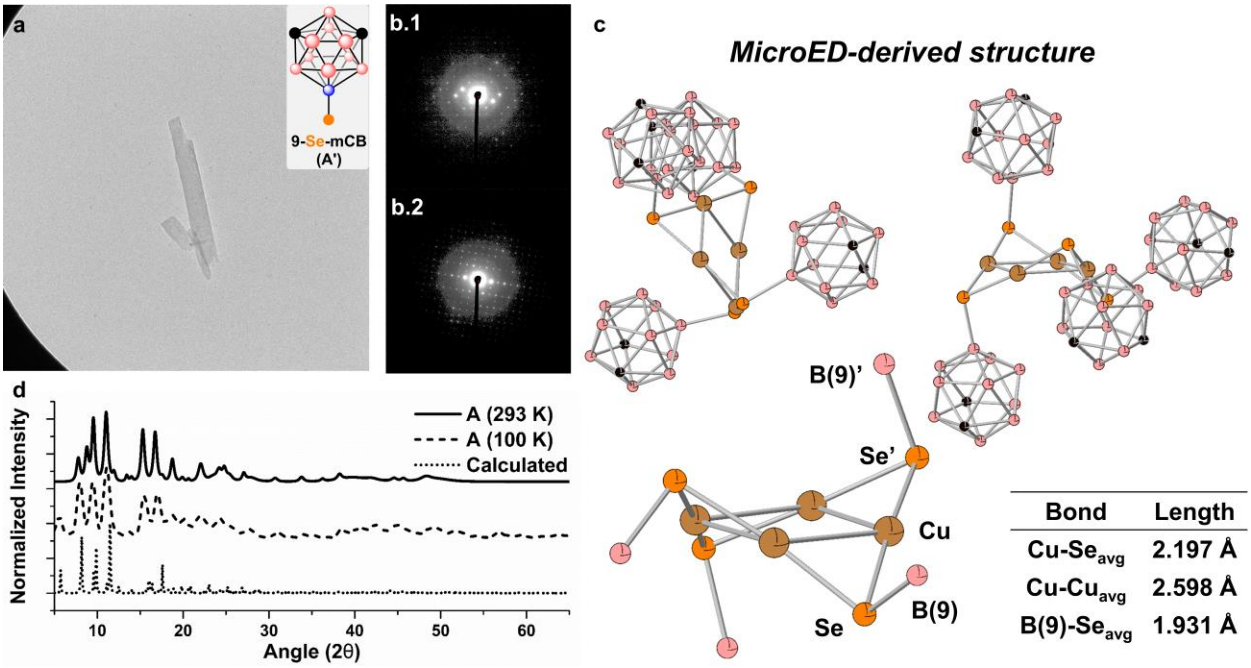

Figure 5.4: **a.** Representative bright field TEM image of **A** crystallite used for MicroED experiments. **b.** Representative frames of MicroED performed of **A** used for refinement. **c.** MicroED-derived structure of **A** revealing a tetrameric Cu-Se core sterically protected by *meta*-carboranyl ligands. Table provides average bond lengths for relevant bonds. The packing of two clusters is also depicted, showing the proximity of the *meta*-carborane cluster to an adjacent selenolate **d.** PXRD pattern of bulk **A** at 293 K and 100 K, as well as the simulated[11] PXRD pattern from MicroED-derived structure. Hydrogens have been omitted for clarity.

When visualizing powders of **A** through electron microscopy (TEM, SEM), the morphology of the crystallites were revealed to be square rods, approximately 5-10 μm in length and 1-2 μm in width (**Figure 5.4a, 5.5a**, Appendix D, sec. 5.6.5.1), somewhat reminiscent of previously imaged MOCHAs composed of Cd-[S-mCB].[6a] The crystallinity of the **A** microcrystals

present on the TEM sample grid was confirmed using selected area electron diffraction (SAED) (**Figure 5.4b**). MicroED techniques were then applied to select crystals located on the TEM grid for structural determination (see Appendix D for full experimental details). In contrast to previously reported materials with copper(I) diamondoid thiolates[5a] or silver(I) benzene selenolates[5d] containing an extended metal-chalcogenolate network ([M-SR/SeR]$_\infty$), **A** crystallites are comprised entirely of isolated tetrameric copper carborane selenolate clusters with a Cu_4Se_4 core surrounded by four *meta*-carboranyl ligands, indicating a zero-dimensional morphology (**Figure 5.4c**). While the C-H vertices of the *meta*-carboranyl ligands cannot be immediately distinguished, the positioning of the exopolyhedral B(9)-Se bond and anticipated dipole-Se interactions between adjacent *meta*-carboranyl selenolates have been used to determine the exact positioning of the carbon-based vertices (**Figure 5.4c**). Notably, the Cu_4Se_4 core in **A** is the first structurally characterized copper(I) selenide tetramer with a planar Cu_4 geometry, the formation of which can likely be correlated to the steric bulk of the carboranyl ligands (Appendix D, sec. 5.6.9). To confirm the validity of the crystal structure obtained *via* MicroED, experimental PXRD data of **A** was compared to the simulated[11] PXRD generated from the single crystal MicroED structure (**Figure 5.4d**). We observed good agreement between the experimental and simulated PXRD patterns despite some minor deviations that could likely be attributed to thermal contraction of the crystallites while performing MicroED. To confirm that this is the case, PXRD experiments were performed while cooling the crystallites to 100 K with liquid nitrogen (**Figure 5.4d**, Appendix D, sec. 5.6.5.2). Importantly, the cryogenic PXRD pattern more closely matches the simulated PXRD pattern, suggesting that the single crystal structure obtained *via* MicroED is characteristic of the bulk material.

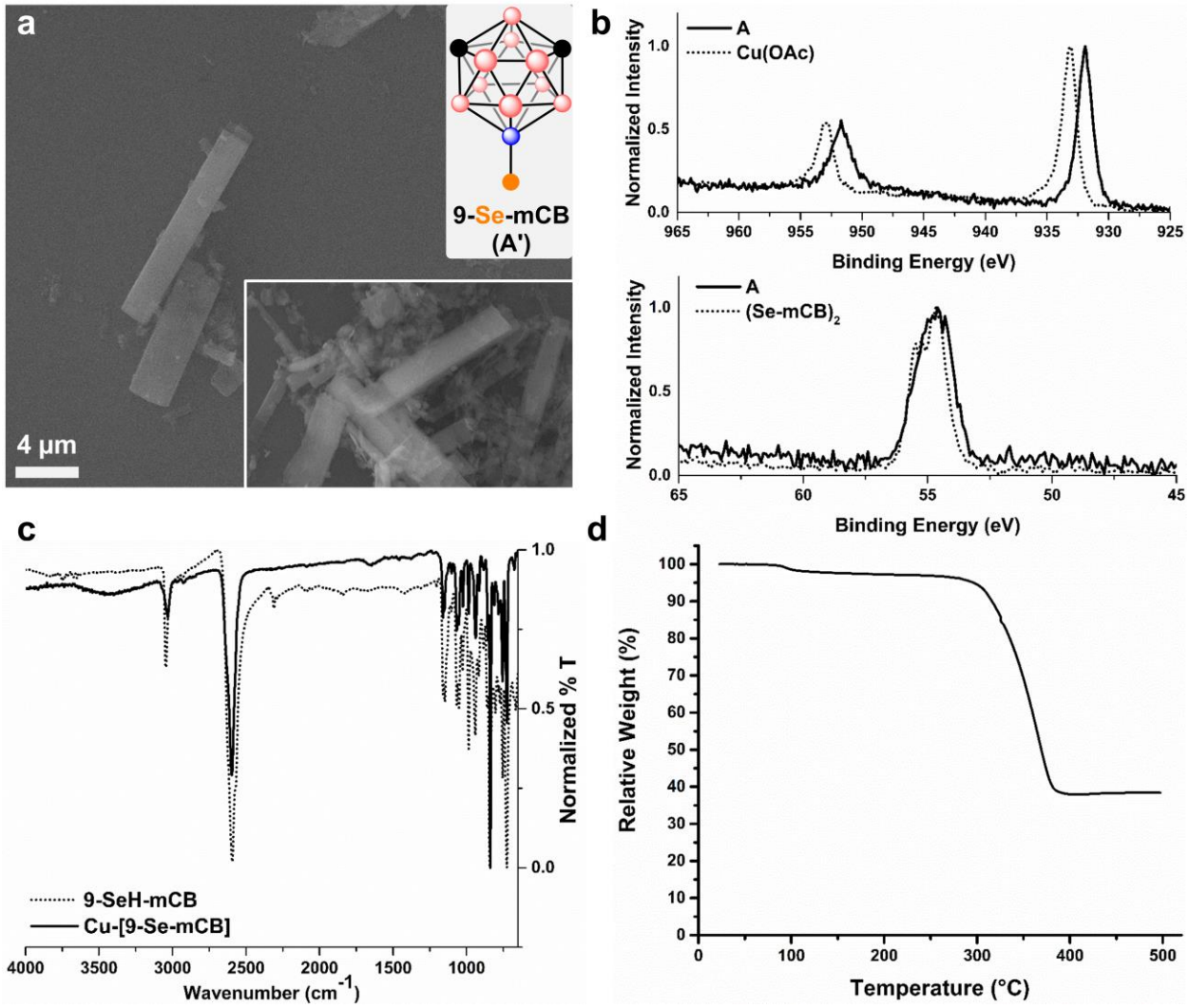

Figure 5.5: **a.** SEM images of **A**. Inset shows a more general overview of crystallite morphology. Scale bar is applied to both SEM images. **b.** XPS measurements of **A**, Cu(OAc), and $(Se\text{-}mCB)_2$. **c.** FTIR of 9-SeH-mCB (red trace) and **A** (black trace). **d.** TGA of **A**.

Based on the crystallographic data, all copper atoms are assigned to be in formal oxidation state of +1. To further corroborate this, XPS measurements of **A** were performed. The XPS measurements of **A** were then compared with those of the copper(I) acetate starting material and $(Se\text{-}mCB)_2$ as an analog of SeH-mCB due to the propensity of carborane chalcogenols to sublime under vacuum (**Figure 5.5b**). The Cu2$p_{1/2}$ and Cu2$p_{3/2}$ peaks of **A**, 952.7 eV and 932.8 eV

respectively, are shifted to a lower binding energy relative to copper(I) acetate and are consistent with the more electron-rich[10] environment experienced by the copper(I) nuclei when interacting with the *meta*-carborane selenolate. There are no satellite peaks present adjacent to the Cu2$p_{1/2}$ peak, which are commonly found in XPS measurements of copper(II) containing materials,[12] indicating that the copper(I) oxidation state is conserved during the course of the reaction. Peak-fitting of the Cu2*p* XPS signals further indicate the presence of a singular copper(I) environment, in agreement with the MicroED-derived structure (Appendix D, sec. 5.6.5.5). Between $(Se\text{-}mCB)_2$ and **A**, there is no significant change in the Se3*d* peak binding energies, and peak-fitting again confirms only one selenium environment (Appendix D, sec. 5.6.5.5). The XPS measurements further allude to the resistance of the copper(I) centers in **A** to oxidation by atmospheric oxygen despite the electron-rich environment imparted by the carborane selenolate,[10] likely a result of the steric protection provided by the *meta*-carboranyl ligands as illustrated by the MicroED-derived single crystal structure.

In addition to XPS measurements, FTIR spectroscopy of **A** was used to confirm the absence of any residual starting materials. Specifically, the FTIR spectrum of **A** revealed a distinct loss of signal associated with the Se-H stretch present in the FTIR spectrum of SeH-mCB at 2400 cm^{-1} (**Figure 5.5c**); though, the remaining cluster structure appears to be intact with only slight deviations in signals present in the fingerprint region (1250-600 cm^{-1}). The presence of intact boron clusters in powder of A is further confirmed by diagnostic B-H resonances (2600 cm^{-1}) in the spectrum. Furthermore, when comparing the FTIR spectrum of **A** with that of the copper(I) acetate starting material, there are no signals present in the formed material that could be correlated to the carbon-oxygen double bond in copper(I) acetate, indicating that the acetate ligand is not present in the resulting hybrid material. Consistent with FTIR, TGA also revealed that there are no substantial

solvent adducts in the **A** crystallites, as indicated by no significant mass loss until 300 ºC, which is most likely associated with the decomposition of the *meta*-carborane selenolate (**Figure 5.5c**) and agrees with the single crystal MicroED structure.

To determine any effects the carborane dipole might impart on the structural behavior of the isolated microcrystals as well as the impact of chalcogenide (Se vs. S), we then studied the reaction of copper(I) acetate with 9-*ortho*-carborane selenol (9-SeH-oCB, **B'**), 9-*meta*-carborane thiol (9-SH-mCB, **C'**), and 9-*ortho*-carborane thiol (9-SH-oCB, **D'**). Notably, the molecular dipole in *ortho*-carborane is significantly larger in magnitude compared to that of *meta*-carborane.[6i,6m,7] Following similar procedures used in the synthesis of **A**, crystalline powders of Cu-[Se-oCB] (**B**), Cu-[S-mCB] (**C**), and Cu-[S-oCB] (**D**) were isolated as white/tan powders in 65%, 84%, and 69% isolated yields respectively (SI sec. 4) and characterized in a similar fashion to **A**. Despite the use of different carborane-based chalcogenols, FTIR, TGA, and XPS data of powders **B**, **C**, and **D** closely resemble the data obtained of **A** (Appendix D, sec. 5.6.6.3-5.6.6.5, 5.6.7.3-5.6.7.5, 5.6.8.3.5), suggesting a molecular similarity. FTIR, for example, revealed that there is no starting carborane chalcogenol or copper(I) acetate present in the isolated powders **B**-**D**, with all materials exhibiting comparable thermal stabilities by TGA. While XPS indicates the copper(I) oxidation state is maintained during the formation of **B**-**D** with similar binding energy for the copper centers measured in **A** (**Figure 5.6a**). Additionally, solution-state ^{1}H and ^{11}B NMR spectroscopic measurement of materials **A**-**D** in dichloromethane further suggested similarities in the molecular structures of the materials and were consistent with FTIR and TGA measurements (Appendix D, sec. 5.6.10).

When comparing the PXRD data (Appendix D, sec. 5.6.6.2, 5.6.7.2, 5.6.8.2) of all four materials, there are clear similarities in the molecular structures of **A**-**D** due to the closely matching diffractions from 5-25 2θ regardless of chalcogen or carborane isomer (**Figure 5.6b**). When comparing the PXRD patterns of materials **A** and **B** (same chalcogen, different carborane isomer) there are some deviations, though they can be explained by the expected differences in molecular packing as a result of differing dipole-dipole interactions within the crystal (**Figure 5.6c**, Appendix D, sec. 5.6.11). In contrast, a closer inspection of PXRD patterns (**Figure 5.6c**) for materials containing the same carborane isomer (*meta*: **A**, **C**; *ortho*: **B**, **D**) reveals nearly identical diffractions with negligible deviations between the data sets (< ±0.5 2θ) that can be explained by the slight changes in d-spacing when the chalcogen is changed from selenium to sulfur (Appendix D, sec. 5.6.11). As expected, this data indicates that the carborane dipole plays a critical role in determining molecular packing of the material while the choice of chalcogen has a minor impact.

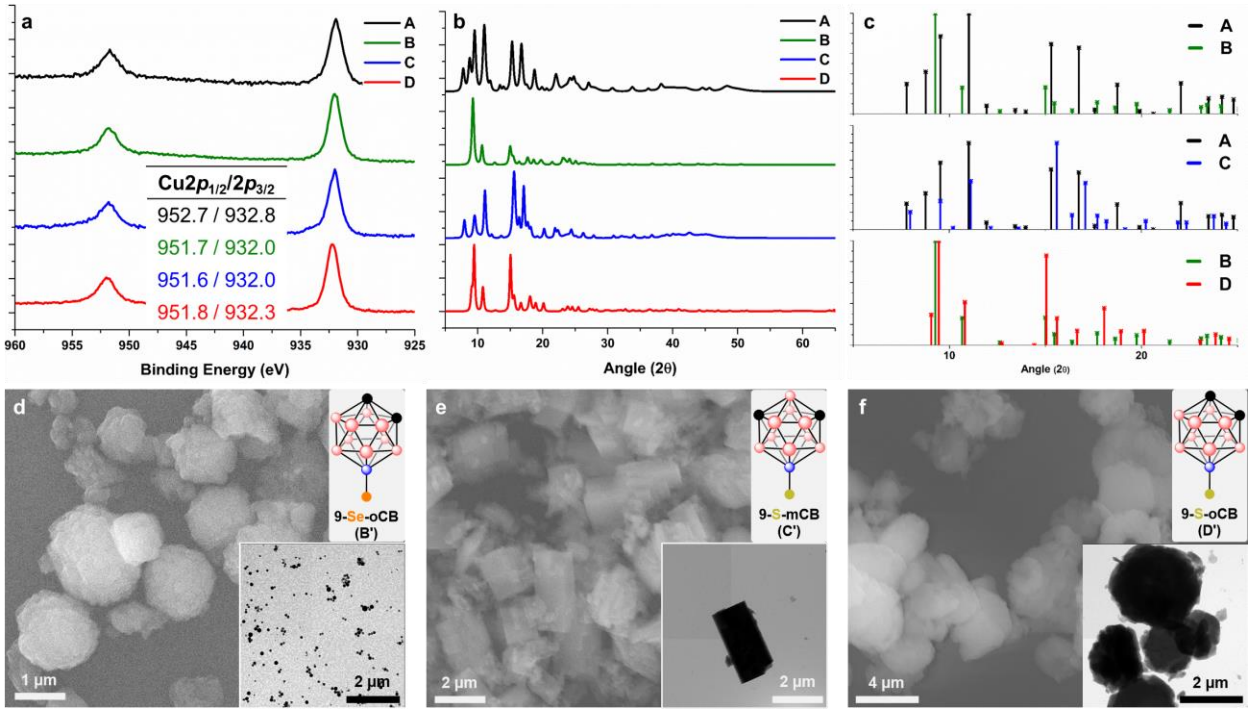

Figure 5.6: **a.** Comparison of Cu2$p_{1/2}$ and Cu2$p_{3/2}$ XPS measurements for materials **A**-**D**. **b.** Stacked PXRD patterns of materials **A**-**D**. **c.** Overlaid peak patterns for materials **A** and **B**, **A** and **C**, **B** and **D**. **d-f.** SEM and TEM (inset) images of **B-D**, respectively.

While FTIR, TGA, XPS, and PXRD suggested a molecular similarity between **A**-**D**, electron microscopy (SEM, TEM, **Figure 5.6d-f**, Appendix D, sec. 5.6.6.1, 5.6.7.1, 5.6.8.1) revealed a distinct difference in crystallite morphology, largely as a function of carborane isomer (i.e. dipole) while also affected by the chalcogen choice (Se, S). **C** crystallites (**Figure 5.6e**) were similar in morphology to **A**, though would be more accurately described as square prisms, being generally thicker (2-3 μm) and significantly shorter (3-5 μm) in length. In contrast, materials **B** and **D**, which contain *ortho*-carborane-based chalcogenolates, favored the formation of spherical particles with two major phases present. In the case of **B**, while some larger particle aggregates (1.10 μm ± 0.31) were present (Figure 5d), TEM revealed that a significant portion of the material consists of nanoscale particles (92 nm ± 25, **Figure 5.6d** inset); in contrast, **D** predominantly favored the formation of larger microscale particles (3.47 μm ± 0.72, **Figure 5.6f**). MicroED measurements of **B** of **C** were attempted, though the crystal morphologies were not easily amenable to electron diffraction. In the case of material **B**, the spherical nature of the particles, ultimately resulted in polycrystalline diffractions, while for material **C**, the thickness of the crystallites inhibited electron diffraction, resulting in both low-intensity diffractions and secondary diffractions.[13] The difference in morphologies (rods vs. spheres) between materials **A**-**D** can primarily be explained by inductive effect of the carborane cluster imparted onto the chalcogenolates, as well as the nature of the carborane dipole present.

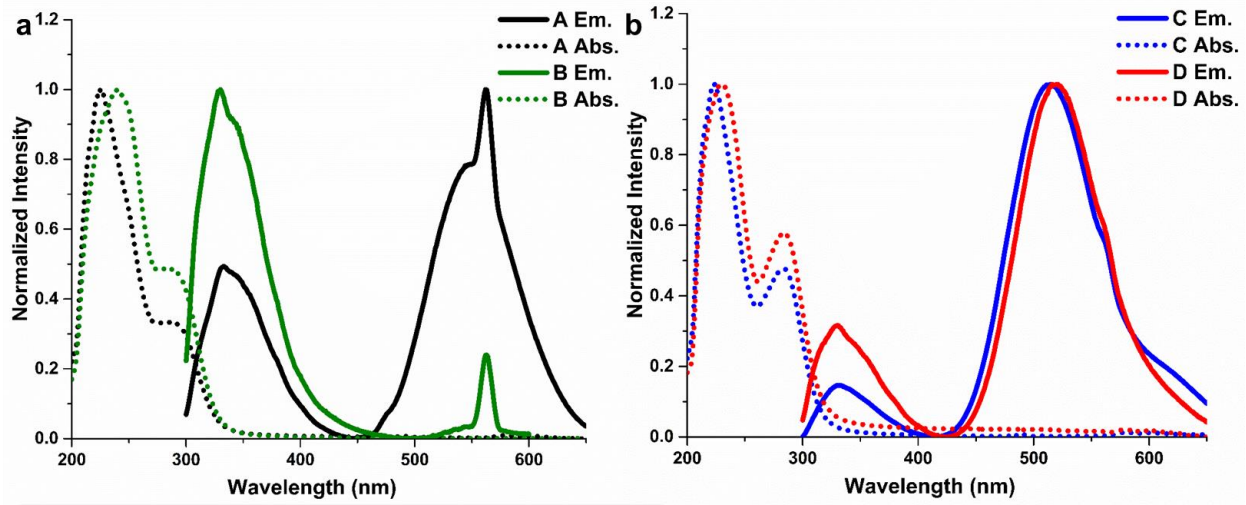

c

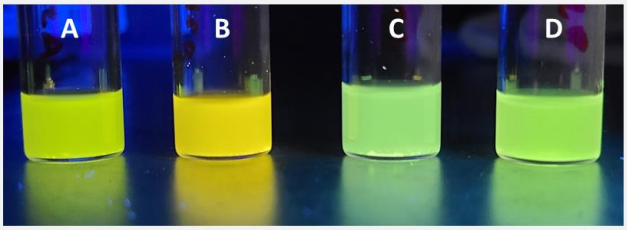

Material	Emission λ_{max}	φ	τ (μs)	k_r (μs^{-1})	k_{nr} (μs^{-1})
A	340, 550	0.20	14	0.0143	0.0571
B	340, 540	0.43	34	0.0126	0.0168
C	335, 515	0.73	46	0.0159	0.00587
D	335, 520	0.93	44	0.0211	0.00159

d

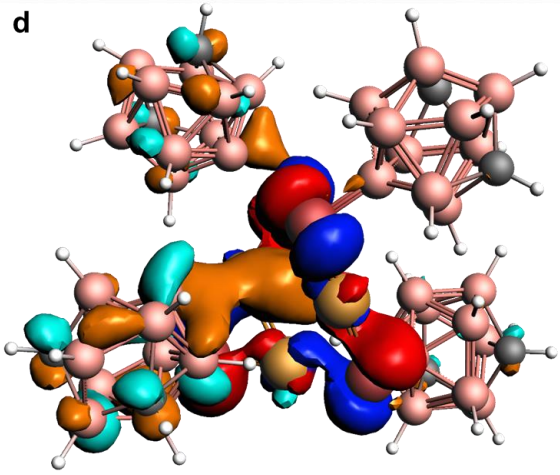

Figure 5.7: **a-b.** Emission (solid trace) and absorption (dotted trace) spectra of materials **A**-**D**. Due to the excitation wavelength used to obtain emission spectra (280 nm) for **A**-**D**, a peak is present at ~560 nm in all spectra that is not part of the emission of materials **A**-**D**. **c.** Images of emissive *iso*-propanol suspensions of **A**-**D** along with their respective emission, quantum yield (ϕ), and lifetime (τ) data. **d.** HOMO (red, blue) and LUMO (orange, teal) of **A**, calculated on the crystallographically derived structure using B3LYP functional DZP basis set. The calculated HOMO-LUMO gap is 4.35 eV, corresponding to 285 nm.

Materials consisting of metal-chalcogenolates, particularly those that are copper-based, often exhibit photoluminescence.[14] Similar properties are therefore expected for materials **A**-**D**.

Differences in the electronic environment experienced by the copper-chalcogenide core are expected to arise as a function of both the carborane isomer (*meta*-, *ortho*-) and chalcogenide (Se, S). Consequently, variations in the photophysical properties of each structure are expected. The normalized UV-Vis absorption spectra for uniform suspensions of **A**-**D** in *iso*-propanol all show two strong absorptions located at 220-240 nm and 280 nm (Figure 6a-b, dotted traces, SI sec. 5-8f). While the wavelengths of absorption do not vary greatly between compounds, differences in relative peak intensity are evident. Using the excitation wavelengths, as indicated by UV-Vis spectroscopy (220 nm and 280 nm), fluorescence measurements were subsequently obtained from the prepared *iso*-propanol suspensions. While the higher energy absorption (220 nm) was the most intense for all materials, no significant emission was associated with this excitation (SI sec. 5-8f). Notably, only the lower energy transition (280 nm) yielded any measurable emission (Figure 6a-b, solid traces). For all four materials, emission was observed at 340 nm and at 450-650 nm, with the latter being significantly broader than the former and distinctly weaker in the case of **B**. Interestingly, when these materials are dissolved in polar aprotic organic solvents, all emissive properties are no longer present (SI sec. 12). To confirm the copper(I) selenide core in **A** was still intact upon dissolution, **A** was precipitated from solution by trituration with pentane and the emission of the as-synthesized crystals was fully regained (SI sec. 12), suggesting that luminescence is contingent upon restricted molecular motion that can be achieved in the solid state. This is further supported by the observation of luminescence in frozen solutions and in polymer matrices embedded with the materials. Notably, while the emission properties can be regained through these methods, they are red-shifted relative to the emission of the as-synthesized crystals (SI sec. 12). Such effects of temperature and aggregation/crystallization on emissive properties are commonly observed phenomena.[15]

To further understand the photophysical properties of these materials quantum yield (ϕ) and lifetime (τ) measurements were performed on **A**-**D** as crystalline powders (see SI for full details). The quantum yields associated with these emissions are 0.20, 0.43, 0.73, and 0.93 for materials **A**-**D**, respectively (Figure 6c). Furthermore, the long lifetimes associated with the emissions (14, 34, 46, and 44 μs for **A**-**D**, respectively), indicate that the luminescence is phosphorescent in nature, which is caused by the presence of the heavier copper, selenium, and sulfur atoms. Materials **A** and **B** exhibited overall weaker emission compared to **C** and **D**, favoring non-radiative relaxation from the excited state (Figure 6c). Furthermore, DFT calculations of **A** indicate that the emission most likely originates from a metal to ligand charge transfer (MLCT) between a copper(I) selenide-centered HOMO and a carborane selenolate-centered LUMO (Figure 6d, SI sec. 5h). While the differences in these photophysical properties are most closely correlated to the chalcogen present in the material (Se: **A**, **B**; S: **C**, **D**), there is a noticeable trend between materials within the same morphology category (rods, spheres) and thus contain the same carborane isomer. Notably, materials containing *ortho*-carborane-based chalcogenolates (**B**, **D**), exhibited higher quantum yields compared to their *meta*-carborane-containing counterparts (**A**, **C**). These results suggest that the tunable inductive effect[7] afforded by the carborane-based ligands using different isomers can be used to fine tune the electronic properties of copper(I) MOCHAs as demonstrated by the precise control over photophysical properties. This is consistent with what has been generally observed with tunable carborane-based ligands.[8b]

5.4 Conclusion

In summary, we have detailed the synthesis and characterization of zero-dimensional carborane chalcogenolate-containing microcrystalline MOCHAs with photoluminescent properties. Importantly, by the use of sterically invariant carborane scaffolds, it has been possible

to change the relative dipole positioning and strength, without also altering the ligand steric environment. Through this tunability, we have shown that the carborane dipole dictates the crystallite morphology, and is able to fine tune photophysical properties, such as quantum yield and emission lifetimes, without affecting the fundamental emission characteristics (Figure 6). Furthermore, MicroED has been used for the first time to structural characterize this class of materials and has provided significant insight into the bonding arrangement between copper(I) and *meta*-carboranyl selenolate. In contrast to other MOCHA materials with an extended metal-chalcogenide core, MicroED has revealed that the synthesized carborane-structured MOCHAs consist of an unprecedented zero-dimensional Cu_4Se_4 that is representative of the smallest building block of bulk CuSe materials. This work establishes the utility of MicroED for material structure elucidation when reaching the limitations of more traditional structural determination methods, such as single crystal X-ray crystallography or powder X-ray diffraction when paired with Rietveld refinement. Furthermore, this work opens a new area of study for carborane-based ligands to the already existing bodies of work utilizing carboranes as tunable ligand scaffolds for rational control of surface, metal center, and molecular properties.[6, 8, 16]

5.5 References for Chapter 5

(1) (a) Rismaningsih, N.; Yamauchi, H.; Kameyama, T.; Yamamoto, T.; Morita, S.; Yukawa, H.; Uematsu, T.; Baba, Y.; Kuwabata, S.; Torimoto, T. Photoluminsecnce properties of quinary Ag-(In,Ga)-(S,Se) quantum dots with a gradiant allow structure for *in vivo* bioimaging. *J. Mater. Chem. C* **2021**, 9, 12791-12801. (b) Toufanian, R.; Chern, M.; Kong, V. H.; Deninis, A. M. Engineering Brightness-Matched Indium Phosphide Quantum Dots. *Chem. Mater.* **2021**, 33, 6, 1964-1975. (c) Naskar, S.; Miethe, J. F.; Sánchez-Paradinas, S.; Schmidt, N.; Kanthasamy, K.; Behrens, P.; Pfnür, H.; Bigall, N. C. Photoluminescent Aerogels from Quantum Wells. *Chem.*

Mater. **2016**, 28, 7, 2089-2099. (d) Liu, Y.; Weiss, N. O.; Duan, X.; Cheng, H.-C.; Huang, Y.; Duan, X. Van der Waals heterostructures and devices. *Nat. Rev. Mater.* **2016**, 1, 16042. (e) Matthews, P. D.; McNaughter, P. D.; Lewis, D. J.; O'Brien, P. Shining a light on transition metal chalcogenides for sustainable photovoltaics. *Chem. Sci.* **2017**, 8, 4177-4187. (f) Maruyama, M.; Nagashio, K.; Okada, S. Influence of Interlayer Stacking on Gate-Induced Carrier Accumulation in Bilayer MoS_2. *ACS Appl. Electron. Mater.* **2020**, 2, 5, 1352-1357. (g) Giufredi, G.; Asset, T.; Liu, Y.; Atanassov, P.; Fonzo, F. D. Transition Metal Chalcogenides as a Versatile and Tunable Platform for Catalytic CO_2 and N_2 Electroreduction. *ACS Mater. Au* **2021**, 1, 1, 6-36. (h) Eng, A. Y. S.; Ambrosi, A.; Sofer, Z.; Šimek, P.; Pumera, M. Electrochemistry of Transition Metal Dichalcogenides: Strong Dependence on the Metal-to-Chalcogen Composition and Exfoliation Method. *ACS Nano* **2014**, 8, 12, 12185-12198. (i) Zhang, D.; Cao, W.; Mao, B.; Liu, Y.; Li, F.; Dong, W.; Jiang, T.; Yong, Y.-C.; Shi, W. Efficient 0D/2D Heterostructured Photoctalysts with Zn-$AgIn_5S_8$ Quantum Dots Embedded in the Ultrathin NiS Nanosheets for Hydrogen Production. *Ind. Eng. Chem. Res.* **2020**, 59, 37.

(2) Tulsky, E. G.; Long, J. R. Dimensional Reduction: A Practical Formalism for Manipulating Solid Structures. *Chem. Mater.* **2001**, 13, 4, 1149-1166.

(3) (a) Coleman, J. N.; Lotya, M.; O'Neill, A.; Bergin, S. D.; King, P. J.; Khan, U.; Young, K.; Gaucher, A.; De, S.; Smith, R. J.; Shvets, I. V.; Arora, S. K.; Stanton, G.; Kim, H.-Y.; Lee, K.; Kim, G. T.; Duesberg, G. S.; Hallam, T.; Boland, J. J.; Wang, J. J.; Donegan, J. F.; Grunlan, J. C.; Moriarty, G.; Shmeliov, A.; Nicholls, R. J.; Perkins, J. M.; Grieveson, E. M.; Theuwissen, K.; McComb, D. W.; Nellist, P. D.; Nicolosi, V. Two-Dimensional Nanosheets Produced by the Liquid Exfoliation of Layered Materials. *Science* **2011**, 331, 568-571. (b) Backes, C.; Szydłowska,

B. M.; Harvey, A.; Yuan, S.; Vega-Mayora, V.; Davies, B. R.; Zhao, P.-L.; Hanlon, D.; Santos, E. J. G.; Katsnelson, M. I.; Blau, W. J.; Gadermaier, C.; Coleman, J. N. Production of Highly Monolayer Enriched Dispersion of Liquid-Exfoliated Nanosheets by Liquid Cascade Centrifugation. *ACS Nano* **2016**, 10, 1, 1589-1601. (c) Bodík, M.; Annušová, A.; Hagara, J.; Mičušík, M.; Omastová, M.; Kotlár, M.; Chlpík, J.; Cirák, J.; Švajdlenková, H.; Anguš, M.; Roldán, A. M.; Veis, P.; Jergal, M.; Majkova, E.; Šiffalovič, P. An elevated concentration of MoS_2 lowers the efficacy of liquid-phase exfoliation and triggers the production of MoO_x nanoparticles. *Phys. Chem. Chem. Phys.* **2019**, 21, 12396-12405.

(4) (a) Manzeli, S.; Ovchinnikov, D.; Pasqeuir, D.; Yazyev, O. V.; Kis, A. 2D transition metal dichalcogenides. *Nat. Rev. Mater.* **2017**, 2, 17033. (b) Jia, C.; Lin, Z.; Huang, Y.; Duan, X. Nanowire Electronics: From Nanoscale to Macroscale. *Chem. Rev.* **2019**, 119, 15, 9074-9135. (c) Enright, M. J.; Dou, F. Y.; Wu, S.; Rabe, E. J.; Monahan, M.; Friedfeld, M. R.; Schlenker, C. W.; Cossairt, B. M. Seeded Growth of Nanoscale Semiconductor Tetrapods: Generality and the Role of Cation Exchange. *Chem. Mater.* **2020**, 32, 11, 4774-4784. (d) Li, T.; Liu, Y.-H.; Porter, S.; Goldberger, J. E. Dimensionally Reduced One-Dimensional Chains of $TiSe_2$. *Chem. Mater.* **2013**, 25, 9, 1477-1479. (d) Chareev, D. A.; Evstingneeva, P.; Phuyal, D.; Man, G. J.; Rensmo, H.; Vasiliev, A. N.; Abdel-Hafiez, M. Growth of Transition Metal-Dichalcogenides by Solvent Evaporation Technique. *Cryst. Growth Des.* **2020**, 20, 10, 6930-6938. (e) Ding, K.; Lu, H.; Zhang, Y.; Snedaker, M. L.; Liu, D.; Maciá-Agulló, J. A.; Stucky, G. D. Microwave Synthesis of Microstructured and Nanostructured Metal Chalcogenides from Elemental Precursors in Phosphonium Ionic Liquids. *J. Am. Chem. Soc.* **2014**, 136, 44, 15465-15468.

(5) (a) Yan, H.; Hohman, J. N.; Li, F. H.; Jia, C.; Solis-Ibarra, D.; Wu, B.; Dahl, J. E. P.; Carlson, R. M. K.; Tkachenko, B. A.; Fokin, A. A.; Schreiner, P. R.; Vailionis, A.; Kim, T. R.; Devereaux, T. P.; Shen, Z.-X.; Melosh, N. A. Hybrid Metal-Organic Chalcogenide Nanowires with Electrically Conductive Inorganic Core through Diamondoid-Directed Assembly. *Nat. Mater.* **2017**, 16, 349-355. (b) Veselska, O.; Podbevšek, D.; Ledoux, G.; Fateeva, A.; Demessence, A. Intrinsic triple-emitting 2D copper thiolate coordination polymer as a ratiometric thermometer working over 400 K range. *Chem. Commun.* 2017, 53, 12225. (c) Veselka, O.; Demessence, A. d^{10} coinage metal organic chalcogenolates: From oligomers to coordination polymers. *Coord. Chem. Rev.* 2018, 355, 240-270. (d) Schriber, E. A.; Popple, D. C.; Yeung, M.; Brady, M. A.; Corlett, S. A.; Hohman, J. N. Mithrene Is a Self-Assembling Robustly Blue Luminescent Metal-Organic Chalcogenolate Assembly for 2D Optoelectronic Applications. *ACS Appl. Nano Mater.* 2018, 1, 7, 3498-3508. (e) Eichhöfer, A.; Lebedkin, S. 1D and 3D Polymeric Manganese(II) Thiolato Complexes: Synthesis, Structure, and Properties of $^{3}_{\infty}[Mn_4(SPh)_8]$ and $^{1}_{\infty}[Mn(SMes)_2]$. *Inorg. Chem.* 2018, 57, 602-608. (f) Trang, B.; Yeung, M.; Popple, D. C.; Schriber, E. A.; Brady, M. A.; Kuykendall, T. R.; Hohman, J. N. Tarnishing Silver Metal into Mithrene. *J. Am. Chem. Soc.* 2018, 140, 42, 13892-13903. (g) Popple, D. C.; Schriber, E. A.; Yeung, M.; Hohman, J. N. Competing Roles of Crystallization and Degradation of a Metal-Organic Chalcogenolate Assembly under Biphasic Solvothermal Conditions. *Langmuir* 2018, 34, 47, 14265-14273. (h) Royappa, A. T.; Tran, C. M.; Papoular, R. J.; Khan, M.; Marbella, L. E.; Millstone, J. E.; Gembicky, M.; Chen, B.; Shepard, W.; Elkaim, E. Copper(I) and gold(I) thiolate precursors to bimetallic nanoparticles. *Polyhedron* 2018, 155, 359-365. (i) Xiao, Q.; Burg, A. J.; Zhou, Y.; Yan, H.; Wang, C.; Ding, Y.; Reed, E.; Miller, R. D.; Dauskardt, R. H. Electrically Conductive Copper Core-Shell Nanowires through Benzenethiol-Directed Assembly. *Nano Lett.* 2018, 18, 4900-4907. (j) Wang, J.; Li, Y.-

L.; Wang, Z.-Y.; Zang, S.-Q. A robust wave-like silver-thiolate chain based metal-organic network: synthesis, structure and luminescence. *CrystEngComm* 2019, 21, 2264. (k) Veselka, O.; Dessal, C.; Melizi, S.; Guillou, N.; Podbevšek, D.; Ledoux, G.; Elkaim, E.; Fateeva, A.; Demessence, A. New Lamellar Silver Thiolate Coordination Polymers with Tunable Photoluminescence Energies by Metal Substitution. *Inorg. Chem.* 2019, 58, 99-105. (l) Yeung, M.; Popple, D. C; Schriber, E. A.; Teat, S. J.; Beavers, C. M.; Demessence, A.; Kuykendall, T. R.; Hohman, J. N. Corrosion of Late- and Post-Transition Metals into Metal-Organic Chalcogenolates and Implications for Nanodevice Architectures. *ACS Appl. Nano Mater.* 2020, 3, 4, 3568-3577. (m) Vaidya, S.; Veselska, O.; Zhadan, A.; Diaz-Lopez, M.; Joly, Y.; Bordet, P.; Guillou, N.; Dujardin, C.; Ledoux, G.; Toche, F.; Chiriac, R.; Fateeva, A.; Horike, S.; Demessence, A. Transparent and luminescent glasses of gold thiolate coordination polymers. *Chem. Sci.* 2020, 11, 6815.

(6) (a) Yeager, L. J.; Saeki, F.; Shelly, K.; Hawthorne, M. F.; Garrell, R. L. A New Class of Self-Assembled Monolayers: *closo*-$B_{12}H_{11}S^{3-}$ on Gold. *J. Am. Chem. Soc.* **1998**, 120, 38, 9961-9962. (b) Baše, T.; Bastl, Z.; Plzák, Z.; Grygar, T.; Plešek, J.; Carr, M. J.; Malina, V.; Šubrt, J.; Boháček, J.; Večerníková, E.; Kříž, O. Carboranethiol-Modifed Gold Surfaces. A Study and Comparison of Modified Cluster and Flat Surfaces. *Langmuir* **2005**, 21, 17, 7776-7785. (c) Baše, T.; Bastl, Z.; Šlouf, M.; Klementová, M.; Šubrt, J.; Vetushka, A.; Ledinský, M.; Fejfar, A.; Macháček, J.; Carr, M. J.; Londesborough, M. G. S. Gold Micrometer Crystals Modifed with Carboranethiol Derivatives. *J. Phys. Chem. C* **2008**, 112, 37, 14446-14455. (d) Hohman, J. N.; Zhang, P.; Morin, E. I.; Han, P.; Kim, M.; Kurland, A. R.; McClanahan, P. D.; Balema, V. P.; Weiss, P. S. Self-Assembly of Carboranethiol Isomer on Au{111}: Intermolecular Interactions Determined by Molecular Dipole Orientations. *ACS Nano* **2009**, 3, 3, 527-536. (e) Baše, T.; Bastl, Z.; Havránek,

V.; Lang, K.; Bould, J.; Londesborough, M. G. S.; Macháček, J.; Plešek, J. Carborane-thiol-silver interactions. A comparative study of the molecular protection of silver surfaces. *Surf. Coat. Tech.* **2010**, 204, 16-17, 2639-2646. (f) Hohman, J. N.; Claridge, S. A.; Kim; M.; Weiss, P. S. Cage molecules for self-assembly. *Mater. Sci. Eng. R Rep.* **2010**, 70, 3-6, 188-208. (g) Lübben, J. F.; Baše, T.; Rupper, P.; Künniger, T.; Macháček, J.; Guimond, S. *J. Colloid Interface Sci.* **2011**, 354, 1, 168-174. (g) Bould, J.; Macháček, J.; Londesborough, M. G. S.; Macías, R.; Kennedy, J. D.; Bastl, Z.; Rupper, P.; Baše, T. Decaborane Thiols as Building Blocks for Self-Assembled Monolayers on Metal Surfaces. *Inorg. Chem.* **2012**, 51, 3, 1685-1694. (h) Baše, T.; Bastl, Z.; Havránek, V.; Macháček, J.; Langecker, J.; Malina, V. Carboranedithiols: Building Blocks for Self-Assembled Monolayers on Copper Surfaces. *Langmuir* **2012**, 28, 34, 12518-12526. (i) Kim, J.; Rim, Y. S.; Liu, Y.; Serino, A. C.; Thomas, J. C.; Chen, H.; Yang, Y.; Weiss, P. S. Interface Control in Organic Electronics Using Mixed Monolayers of Carboranethiol Isomers. *Nano Lett.* **2014**, 14, 2946-2951. (j) Vetushka, A.; Bernard, L.; Guseva, O.; Bastl, Z.; Plocek, J.; Tomandl, I.; Fejfar, A.; Baše, T.; Schmutz, P. Adsorption of oriented carborane dipole on a silver surface. *Phys. Solid State B* **2015**, 253, 3, 591-600. (k) Thomas, J. C.; Boldog, I.; Auluck, H. S.; Bereciartua, P. J.; Dušek, M.; Macháček, J.; Bastl, Z.; Weiss, P. S.; Baše, T. Self-Assembled *p*-Carborane Analogue of *p*-Mercaptobenzoic Acid on Au{111}. *Chem. Mater.* **2015**, 27, 15, 5425-5435. (l) Schwartz, J. J.; Mendoza, A. M.; Wattanatorn, N.; Zhao, Y.; Nguyen, V. T.; Spokoyny, A. M.; Mirkin, C. A.; Baše, T.; Weiss, P. S. Surface Dipole Control of Liquid Crystal Alignment. *J. Am. Chem. Soc.* **2016**, 138, 18, 5957-5967. (m) Serino, A. C.; Anderson, M. E.; Saleh, L. M. A.; Dziedzic, R. M.; Mills, H.; Heindenreich, L. K.; Spokoyny, A. M.; Weiss, P. S. Work Function Control of Germanium through Carborane-Carboxylic Acid Surface Passivation. *ACS Appl. Mater. Interfaces* **2017**, 9, 34592-34596. (n) Thomas, J. C.; Goronzy, D. P.; Serino, A. C.; Auluck,

H. S.; Irving, O. R.; Jimenez-Izal, E.; Deirmenjian, J. M.; Macháček, J.; Sautet, P.; Alexandrova, A. N.; Baše, T.; Weiss, P. S. Acid-Base Control of Valency within Carboranedithiol Self-Assembled Monolayer: Molecules Do the Can-Can. *ACS Nano* **2018**, 12, 3, 2211-2221. (o) Wang, S.; Goronzy, D. P.; Young, T. D.; Wattanatorn, N.; Stewart, L.; Baše, T.; Weiss, P. S. Formation of Highly Ordered Terminal Alkyne Self-Assembled Monolayers on the Au{111} Surface through Substitution of 1-Decaboranethiolate. *J. Phys. Chem. C* **2019**, 123, 2, 1348-1353. (p) Hladík, M.; Vetushka, A.; Fejfar, A.; Vázquez, H. Tuning of the gold work function by carborane films studied using density functional theory. *Phys. Chem. Chem. Phys.* **2019**, 21, 6178-6185. (q) Goronzy, D. P.; Staněk, J.; Avery, E.; Guo, H.; Bastl, Z.; Dušek, M.; Gallup, N. M.; Gün, S.; Kučeráková, M.; Levandowski, B. J.; Macháček, J.; Šícha, V.; Thomas, J. C.; Yavuz, A.; Houk, K. N.; Danişman; Mete, E.; Alexandrova, A. N.; Baše, T.; Weiss, P. S. Influence of Terminal Carboxyl Groups on the Structure and Reactivity of Functionalized *m*-Carboranethiolate Self-Assembled Monolayers. *Chem. Mater.* **2020**, 32, 15, 6800-6809. (r) Li, Y.-L.; Wang, Z.-Y.; Ma, X.-H.; Luo, P.; Du, C.-X.; Zang, S.-Q. Distinct photophysical properties in atom-precise silver and copper nanocluster analogues. *Nanoscale* **2019**, 11, 5151-5157. (s) Saini, A.; Saha, A.; Viñas, C.; Teixidor, F. The key to controlling the morphologies of quantum nanocrystals: spherical carborane ligands. *Chem. Commun.* **2019**, 55, 9817-9820. (t) Wang, Q.-Y.; Wang, J.; Wang, S.; Wang, Z.-Y.; Cao, M.; He, C.-L.; Yang, J.-Q.; Zang, S.-Q.; Mak, T. C. W. *o*-Carborane-Based and Atomically Precise Metal Clusters as Hypergolic Materials. *J. Am. Chem. Soc.* **2020**, 142, 28, 12010-12014. (u) Valušová, E.; Kaňuchová, M.; Baše, T.; Víglaský, V.; Antalík, M. The $Au_{25}(SR)_{18}$ cluster carrying icosahedral dodecaborate and glutathione ligands: A spectroscopic view. *J. Phys. Chem. Solids* **2021**, 150, 109838. (v) Jana, A.; Jash, M.; Poonia, A. K.; Paramasivam, G.; Islam, M. R.; Chakraborty, P.; Antharjanam, S.; Machacek, J.; Ghosh, S.; Adarsh, K. N. V. D.; Base, T.;

Pradeep, T. Light-Activated Intercluster Conversion of an Atomically Precise Silver Nanocluster. *ACS Nano* **2021**, 15, 10, 15781-15793.

(7) For a general overview of carboranes, see: Grimes, R. N. *Carboranes*, 3rd ed; Elsevier: Oxford, 2016.

(8) (a) Eleazer, B. J.; Peryshkov, D. V. Coordination Chemistry of Carborane Cluster: Metal-Boron Bonds in Carborane, Carobranyl, and Carboryne Complexes. *Comments Inorg. Chem.* **2018**, 38, 3, 79-109. (b) Kirlikovali, K. O.; Axtell, J. C.; Anderson, K. P.; Djurovich, P. I.; Rheingold, A. L.; Spokoyny, A. M. Fine-Tuning Electronic Properties of Luminescent Pt(II) Complexes via Vertex-Differentiated Coordination of Sterically Invariant Carborane-Based Ligands. *Organometallics* **2018**, 37, 18, 3122-3131. (c) Eleazer, B. J.; Smith, M. D.; Popov, A. A.; Peryshkov, D. V. Expansion of (BB)>Ru metallacycle with coinage metal cations: formation of B-M-Ru-B (M = Cu, Ag, Au) dimetalacyclodiboryls. *Chem. Sci.* **2018**, 9, 2601-2608. (d) Zhang, J.; Cao, B.; Ding, Y.; Chang, J.; Li, S.; Chen, X. Syntheses and Structure of Group 10 Metal POCOP Pincer Complexes bearing A Mercapto-*o*-carborane Auxiliary Ligand. *ChemistrySelect* **2019**, 4, 4, 1292-1297. (e) Eleazer, B. J.; Smith, M. D.; Peryshkov, D. V. Reaction of a ruthenium B-carboranyl hydride complex and $BH_3(SMe_2)$: Selective formation of a pincer-supported metallaborane $LRu(B_3H_8)$. *Tetrahedron* **2019**, 75, 11, 1471-1474. (f) Zhang, K.; Shen, Y.; Yang, X.; Liu, J.; Jiamg, T.; Finney, N.; Spingler, B.; Duttwyler, S. Atomically Defined Monocarborane Copper(I) Acetylides with Structural and Luminescence Properties Tuned By Ligand Sterics. *Chem. Eur. J.* **2019**, 25, 37, 8754-8759. (g) Mandal, D.; Rosair, G. M. Exploration of Bis(nickelation) of 1,1'-Bis(*o*-carborane). *Crystals* **2021**, 11, 1, 16.

(9) (a) Dziedzic, R. M.; Spokoyny A. M. Metal-Catalyzed Cross-Coupling Chemistry with Polyhedral Boranes. *Chem. Commun.* **2019**, 55, 430-442. (b) Quan, Y.; Tang, C.; Xie, Z. Nucleophilic substitution: a facile strategy for selective B-H functionalization of carboranes. *Dalton Trans.* **2019**, 48, 7494-7498. (c) Quan, Y.; Xie, Z. Controlled functionalization of *o*-carborane *via* transition metal catalyzed B-H activation. *Chem. Soc, Rev,* **2019**, 48, 3660-3673.

(10) (a) Spokoyny A. M.; Machan, C. W.; Clingerman, D. J.; Rosen, M. S.; Wiester, M. J.; Kennedy, R. D.; Stern, C. L.; Sarjeant, A. A.; Mirkin, C. A. A coordination chemistry dichotomy for icosahedral carborane-based ligands. *Nat. Chem,* **2011**, 3, 590-596. (b) Mills, H. A.; Alsarhan, F.; Ong, T.-C.; Gembicky, M.; Rheingold, A. L.; Spokoyny, A. M. Icosahedral Meta-Carboranes Containing Exopolyhedral B-Se and B-Te Bonds. *ChemRxiv* **2021** doi:10.33774/chemrxiv-2021-01xcb

(11) The simulated PXRD pattern of **A** was simulated using Mercury 4.3.0 with the MicroED-derived structure and .cif file.

(12) Biesinger, M. C. Advanced analysis of copper X-ray photoelectron spectra. *Surf. Interface Anal.* **2017**, 49, 13, 1325-1334.

(13) Zou, X.; Hovmóller, S.; Oleynikov, P. *Electron Crystallography: Electron Microscopy and Electron Diffraction*, Oxford Scholarship Online, 2012.

(14) (a) Crespo, O.; Gimeno, M. C.; Lagun, A.; Larraz, C.; Villacampa, M. D. Highly Luminescent Gold(I)-Silver(I) and Gold(I)-Copper(I) Chalcogenide Clusters. *Chem. Eur. J.* **2006** 13, 1, 235-246. (b) Kriegel, I.; Jiang, C.; Rodríguez-Fernández, J.; Schaller, R. D.; Talapin, D. V.; Como, E. D.; Feldmann, J. Tuning the Excitonic and Plasmonic Properties of Copper Chalcogenide

Nanocrystals. *J. Am. Chem. Soc.* **2012**, 134, 3, 1583-1590. (c) Singh, A.; Singh, S.; Levcenko, S.; Unold, T.; Laffir, F.; Ryan, K. M. Compositionally Tunable Photoluminescence Emission in $Cu_2ZnSn(S_{1-x}Se_x)_4$ Nanocrystals. *Angew. Chem. Int. Ed.* **2013**, 52, 35, 9120-9124. (d) Polgar, A. M.; Zhang, A.; Mack, F.; Weigend, F.; Lebedkin, S.; Stillman, M. J.; Dorrigan, J. F. Tuning the Metal/Chalcogen Composition in Copper(I)-Chalcogenide Clusters with Cyclic (Alkyl)(amino)carbene Ligands. *Inorg. Chem.* **2019**, 58, 5, 338-3348.

(15) (a) Mei, J.; Leung, N. L. C.; Kwok, R. T. K.; Lam, J. W. Y.; Tang, B. Z. Aggregation-Induced Emission: Together We Shine, United We Soar! *Chem. Rev.* **2015**, 115, 21, 11718-11940. (b) Chin, P. T. K.; Donegá, C. d. M.; van Bavel, S. S.; Meskers, S. C. J.; Sommerdijk, N. A. J. M.; Janssen, R. A. Highly Luminescent CdTe/CdSe Collodial Heteronanocrystals with Temperature-Dependent Emission Color. *J. Am. Chem. Soc.* **2007**, 129, 48, 14880-14886. (c) Lu, W.; Tarekegne, A. T.; Ou, Y.; Kamiyama, S.; Ou, H. Temperature-dependent photoluminescence properties of porous fluorescent SiC. *Scientific Reports* **2019**, 9, 16333.

(16) (a) Keener, M.; Hunt, C.; Carroll, T. G.; Kampel, V.; Dobrozetsky, R.; Hayton, T. W.; Ménard, G. Redox-switchable carboranes for uranium capture and release. *Nature* **2020**, 577, 652-655. (b) Kim, S.; So, H.; Lee, J. H.; Hwang, H.; Kwon, H.; Park, M. H.; Lee, K. M. Photophysical Properties of Spirobifluorene-Based *o*-Carboranyl Compounds Altered by Structurally Rotating the Carborane Cages. *Molecules* **2019**, 24, 22, 4135. (c) Böhling, L.; Brockhinke, A.; Kahlert, J.; Weber, L.; Harder, R. A.; Yufit, D. S.; Howard, J. A. K.; MacBride, J. A. H.; Fox, M. A. Substituent Effects on the Fluorescence Properties of *ortho*-Carboranes: Unusual Emission Behaviour in *C*-(2'-Pyridyl)-*ortho*-carboranes. *Eur. J. Inorg. Chem.* **2016**, 3, 403-412. (d) Axtell, J. A.; Kirlikovali, K. O.; Djurovich, P. I.; Jung, D.; Nguyen, V. T.; Munekiyo, B.; Royappa, A. T.;

Rheingold, A. L.; Spokoyny, A. M. Blue Phosphorescent Zwitterionic Iridium(III) Complexes Featuring Weakly Coordinating *nido*-Carborane-Base Ligands. *J. Am. Chem. Soc.* **2016**, 138, 48, 15758-15765. (e) Shi, C.; Sun, H.; Jiang, Q.; Zhao, Q.; Wang, J.; Huang, W.; Yan, H. Carborane tuning of photophysical properties of phosphorescent iridium(III) complexes. *Chem. Commun.* **2013**, 49, 4746-4748. (f) Tsang, M. Y.; Viñas, C.; Teixidor, F.; Planas, J. G.; Conde, N.; SanMartin, R.; Herrero, M. T.; Domínguez, E.; Lledós, A.; Vidossich, P.; Choquesillo-Lazarte, D. Synthesis, Structure, and Catalytic Application of *ortho*- and *meta*-Carboranyl Based NBN Pincer-Pd Complexes. *Inorg. Chem.* **2014**, 53, 17, 9284-9295. (g) Spokoyny, A. M.; Lewis, C. D.; Teverovskiy, G.; Buchwald, S. L. Extremely Electron-Rich, Boron-Functionalized, Icosahedral Carborane-Based Phosphinoboranes. *Organometallics* **2012**, 31, 24, 8478-8481.

5.6 Appendix D

5.6.1 General Considerations

Ortho-$C_2B_{10}H_{12}$ (Boron Specialties) was sublimed prior to use. *Meta*-$C_2B_{10}H_{12}$ (Katchem or Alfa Aesar) was used as is. Anhydrous dichloromethane was obtained from a Grubbs column with activated alumina and copper catalyst. Se_2Cl_2 used in the synthesis of **9-HSe-mCB** and **9-HSe-oCB** was prepared according to the procedure found in reference 1 and subsequently stored in a PTFE-capped vial at -15 ^oC. *Iso*-propanol (200 proof) was purchased from Fisher Sci., Certified ACS quality. *Iso*-propanol used in the synthesis of materials **A-D** was dried by refluxing 100 mL of *iso*-propanol over 5g of elemental magnesium chips with vigorous stirring. After refluxing overnight, the anhydrous *iso*-propanol was distilled under an atmosphere of N_2 into a 100 mL Schlenk tube containing activated 3Å molecular sieves. The Schlenk tube was sealed with a Teflon stopper and stored in ambient conditions. Cu(OAc) of 97% purity was purchased from Strem Chemical Inc. and stored in an N_2-filled glovebox at -30 ^oC. All other reagents were purchased from commercial vendors and used as is. All synthesized chalcogenols were stored in an N_2-filled glovebox at -30 ^oC for long term storage. Unless otherwise stated, all reactions were performed under an inert atmosphere of N_2 either in a glovebox or using a Schlenk line, and all manipulations were performed under ambient laboratory air, exposed to ambient light.

5.6.2 Instrumentation

^1H, ^{11}B, and ^{77}Se NMR spectra were recorded on either a Bruker DRX500 or Bruker AVIII HD 400 spectrometers in ambient conditions at room temperature. MestReNova v6.0.2-5475 software was used to process the FID data and visualize the spectra. ^1H and $^{13}C\{^1H\}$ NMR spectra were referenced to residual solvent resonances in deuterated solvents (note: due to high humidity H_2O resonances are often present) and are reported relative to tetramethylsilane ($\delta = 0$ ppm). ^{11}B NMR

spectra were referenced externally to $Et_2O{\cdot}BF_3$ (δ = 0 ppm). ^{77}Se NMR spectra were referenced externally to diphenyldiselenide (δ = 463.15 ppm). Exponential apodization (5-30 Hz) was applied through MestReNova to ^{77}Se spectra in order to enhance the signal to noise ratio.

Elemental analysis of materials **A**-**D** was performed by Atlantic Microlabs.

Transmission electron microscopy (TEM) was carried out using either an FEI T20 iCorr cryo TEM operated at 200 kV or an FEI T12 TEM operated at 120 kV. TEM samples were prepared by adding 5-10 μL of a colloidal suspension of nanoparticles in *iso*-propanol to a copper grid (200 mesh, Formvar/Carbon or Carbon Film only, Ted Pella, Redding, CA).

Samples prepared for TEM were additionally used for microcrystal electron diffraction (MicroED) experiments. The prepared TEM grid was loaded in a Gatan 626 single-tilt cryo holder and cooled with liquid nitrogen. Screening and data collection were performed using a Thermo-Fisher F200C transmission electron microscope operating at 200 kV corresponding to a wavelength of 0.0251 Å. Electron diffraction data were collected using a Thermo-Fischer Ceta-D CMOS 4k × 4k camera. The screening of crystals was done in low-dose mode and diffraction was identified through condensing of the electron beam. After the selection of a crystal on the grid, the crystal was centered, the eucentric height adjusted by tilting the crystal through the desired rotation range, and the selected area aperture and beam stop were inserted (reference 2). Images were collected in a movie format as crystals were continuously rotated in the electron beam (reference 3). Typical data collection was performed using a constant tilt rate of 0.3°/s between the minimum and maximum tilt ranges of -72° to +72°, respectively. During continuous rotation, the camera integrated frames continuously at a rate of 3 seconds per frame. The dose rate was calibrated to <0.03 $e^-/Å^2$ s. Crystals selected for data collection were isolated by a selected area aperture to

reduce the background noise contributions and calibrated to eucentric height to stay in the aperture over the entire tilt range. The electron diffraction data were processed using the XDS suite of programs (reference 4). To achieve a sufficient number of reflections datasets from five different crystals were merged and scaled with XSCALE. The structure was solved *ab initio* using direct methods in SHELXT (reference 5) using ShelXle (reference 6). Structure refinement was performed using electron scattering factors reported by Peng (reference 7). Thermal parameters were refined anisotropically for all non-hydrogen atoms.

Scanning electron microscopy (SEM) was carried out using a ZEISS SUPRAU 40VP Field Emission Scanning Electron Microscope operating at 30 kV. SEM samples were prepared by adding several drops of a colloidal suspension of nanocrystals in *iso*-propanol to a square-cut chip of silicon wafer.

X-ray photoelectron spectroscopy (XPS) measurements were performed on an AXIS Ultra DLD instrument (Kratos Analytical Inc.). Spectra were obtained using a monochromatic AI Kα X-ray source (Filament current: 1.8 A) with a 10 mA emission current and an anode voltage of 15 kV. Survey spectra were conducted with a pass energy of 160 eV, 1 eV step size, and 100 ms dwell time. High-resolution spectra were conducted with a pass energy of 20 eV, 1 eV step size, and 600 ms dwell time. All spectra were measured with automatic charge neutralization and referenced to the adventitious carbon 1s signal at 284.6 eV. XPS data was further processed and peak fitted using CasaXPS Version 2.3.24PR1.0 (reference 8).

Infrared absorption spectra (FTIR) were obtained using a PerkinElmer Spectrum One spectrometer equipped with a universal ATR assembly. Samples were deposited as dry powders.

Thermogravimetric analysis (TGA) was carried out on a PerkinElmer Pyris Diamond TG/DTA under a constant flow of argon gas (200 mL/min). Samples were heated in alumina oxide trays from 25 ^{o}C to 500 ^{o}C at a rate of 20 ^{o}C/min.

Powder X-ray diffraction (PXRD) was conducted using a Panalytical X'Pert Pro X-ray Powder Diffractometer. Samples were deposited as dry powders onto a zero-background sample holder as a level pellet.

UV-Vis absorption measurements were taken using an Ocean Optics Flame Miniature Spectrometer detector and Ocean Optics DH-2000 UV-Vis-NIR source. All samples were suspended in *iso*-propanol and measurements were taken in a 1 cm quartz cuvette.

Fluorescence emission scans were performed using a Horiba Instruments PTI QuantaMaster Series fluorometer equipped with a PMT detector operated under ambient conditions. Dilute suspensions of microcrystals were prepared in *iso*-propanol and measurements were taken in a 1 cm quartz cuvette.

Quantum yield measurements were carried out using a Hamamatsu C9920 system equipped with a xenon lamp, calibrated integrating sphere, and model C10027 photonic multichannel analyzer (PMA). Samples were deposited as dry powders on quartz plates and excited at 290 nm.

Photoluminescence lifetimes were measure by time-correlated single-photon counting using an IBH Fluorocube instrument equipped with an LED excitation source. Samples were deposited as dry powders on quartz plates and were excited at 372 nm and observed at 550 nm.

5.6.3 Synthesis of Chalcogenols

Synthesis of 9-SeH-mCB

Synthetic procedures adapted from reference 9. *Meta*-$C_2B_{10}H_{12}$ (1.44 g, 10 mmol) and $AlCl_3$ (1.33 g, 10 mmol, 1 eq) were added to an oven-dried Schlenk flask equipped with a stir bar and rubber septum and evacuated/backfilled with N_2 three times. Anhydrous CH_2Cl_2 (25 ml), collected from a Grubb's column, was added to the Schlenk flask *via* cannula and the solids were allowed to dissolved. Subsequently, Se_2Cl_2 (0.42 mL, 5 mmol, 0.5 eq) was added dropwise to the stirring suspension *via* syringe, forming a dark red solution that was allowed to stir overnight at room temperature. Upon completion of the reaction, determined by TLC, the reaction was carefully quenched by the addition of distilled H_2O (15 mL), yielding a dark yellow, cloudy suspension. The yellow organic later was separated from the aqueous layer and the aqueous layer was extracted with CH_2Cl_2 (3 x 15 mL). The organic layers were combined and dried with Na_2SO_4, resulting in a clear yellow/orange solution. The solution was then decanted from the Na_2SO_4 and volatiles were removed under reduced pressure to yield the *meta*-carboranyl diselenide. The diselenide was then dissolved in a minimal amount of absolute EtOH (30-50 mL), resulting in a red-orange solution with some solids still suspended (sonication may be required). While stirring the solution of the diselenide, and excess of $NaBH_4$ (0.80 g) was carefully added over the course of several minutes. During the course of the addition, some heat and gas were generated, with the consumption of the diselenide indicated by the reaction mixture turning cloudy and colorless. The reduction was stirred for an additional 15 minutes before the dropwise addition of aqueous HCl (~2M, 10-20 mL) to quench any residual $NaBH_4$ and protonate the selenolate intermediate. Once no more gas was evolved upon addition of HCl, distilled H_2O (200 mL) was added resulting in a foamy, pale yellow suspension. The product was then extracted from the aqueous solution with CH_2Cl_2 (4 x 30 mL) and the collected organic layers were dried over Na_2SO_4. The dried organic layers were decanted away from the Na_2SO_4 and all volatiles were removed under reduced pressure, leaving the crude

product as a pale-yellow solid. The crude product was further purified *via* vacuum sublimation at 90 ^{o}C, affording the product as a white, crystalline solid in 58% yield with a mild odor.

Yield: 1.3 g (58%), white, odorous solid

All characterization matches literature data, and representative ^{1}H and ^{11}B NMR spectra recorded in $CDCl_3$ have been provided below:

^{1}H NMR of 9-SeH-mCB:

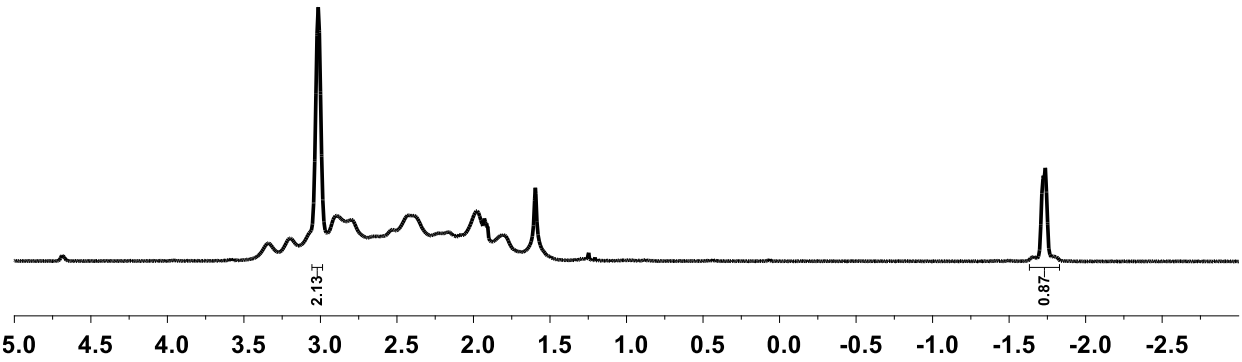

^{11}B NMR of 9-SeH-mCB:

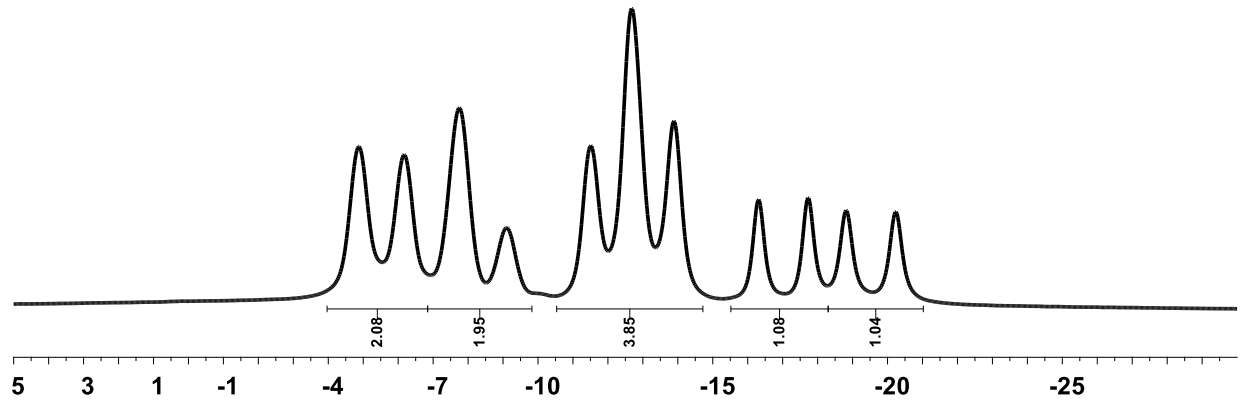

Synthesis of 9-SeH-oCB

9-HSe-oCB was prepared in an analogous manner as 9-HSe-mCB, where *ortho*-$C_2B_{10}H_{12}$ was used instead of *meta*-$C_2B_{10}H_{12}$.

Yield: 720 mg (31%), white, odorous solid

All characterization matches literature data, and representative ^{1}H and ^{11}B NMR spectra recorded in $CDCl_3$ have been provided below:

^{1}H NMR of 9-SeH-oCB:

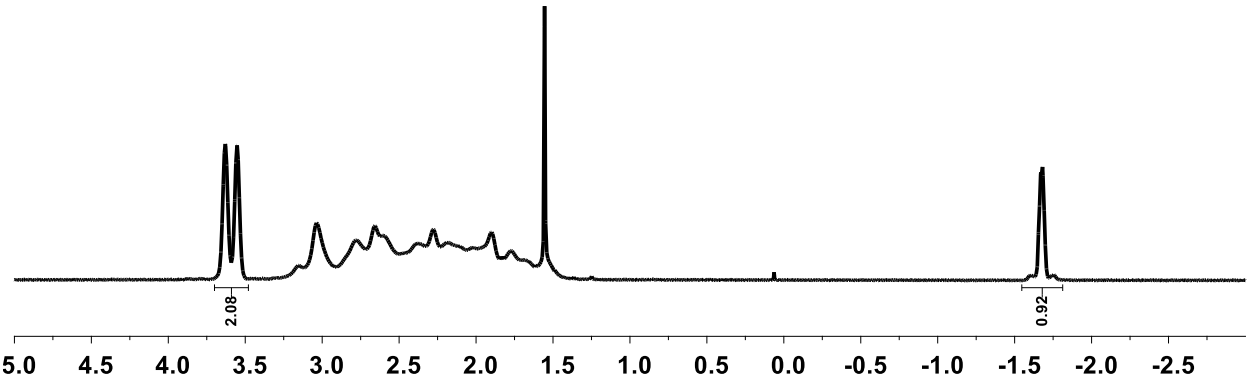

^{11}B NMR of 9-SeH-oCB:

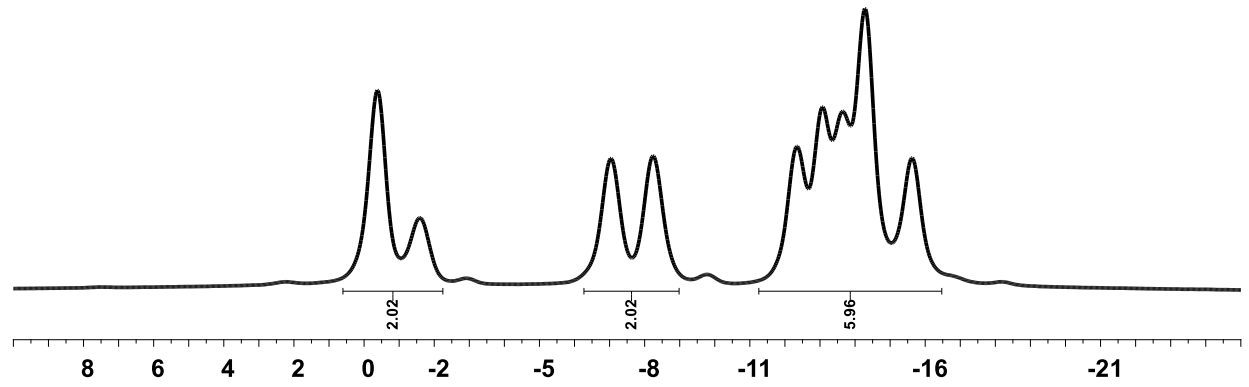

Synthesis of 9-SH-mCB

Synthetic procedures adapted from references 10 and 11. *Meta*-$C_2B_{10}H_{12}$ (1.44 g, 10 mmol) and $AlCl_3$ (1.33 g, 10 mmol, 1 eq) were added to an oven-dried Schlenk flask equipped with a stir bar and rubber septum and evacuated/backfilled with N_2 three times. Anhydrous CH_2Cl_2 (25 ml), collected from a Grubb's column, was added to the Schlenk flask *via* cannula and the solids were allowed to dissolved. Subsequently, S_2Cl_2 (0.42 mL, 5 mmol, 0.5 eq) in 2 mL of anhydrous CH_2Cl_2, was added dropwise to the stirring suspension *via* syringe, forming a red solution that was allowed to stir overnight at room temperature. Upon completion of the reaction, determined by TLC, the reaction was carefully quenched by the addition of distilled H_2O (15 mL), yielding a dark yellow, cloudy suspension. The yellow organic later was separated from the aqueous layer and the aqueous layer was extracted with CH_2Cl_2 (3 x 15 mL). The organic layers were combined and dried with Na_2SO_4, resulting in a clear yellow/orange solution. The solution was then decanted from the Na_2SO_4 and volatiles were removed under reduced pressure to yield the *meta*-carboranyl disulfide. The disulfide was then dissolved in a minimal amount of absolute EtOH (30-50 mL), resulting in a yellow solution (sonication may be required). While stirring the solution of the disulfide, 1-2 chips of NaOH and excess of $NaBH_4$ (0.60 g) was carefully added over the course of several minutes. After completing the addition of NaOH and $NaBH_4$, the flask was capped with a septum and bleed needle before heating to 50 ^oC for 1 hour. After stirring for 1 hour, the reduction was allowed to cool to room temperature before the dropwise addition of aqueous HCl (~2M, 10-20 mL) to quench any residual $NaBH_4$ and protonate the thiolate intermediate. Once no more gas was evolved upon addition of HCl, distilled H_2O (200 mL) was added resulting in a foamy, pale yellow suspension. The product was then extracted from the aqueous solution with CH_2Cl_2 (4 x 30 mL) and the collected organic layers were dried over Na_2SO_4. The dried organic layers were decanted away from the Na_2SO_4 and all volatiles were removed under reduced pressure, leaving

the crude product as a pale-yellow solid. The crude product was further purified *via* vacuum sublimation at 90 ^{o}C, affording the product as a white, crystalline solid in 78% yield with a mild odor.

Yield: 1.4 g (78%), white, odorous solid

All characterization matches literature data, and representative ^{1}H and ^{11}B NMR spectra recorded in $CDCl_3$ have been provided below:

^{1}H NMR of 9-SH-mCB:

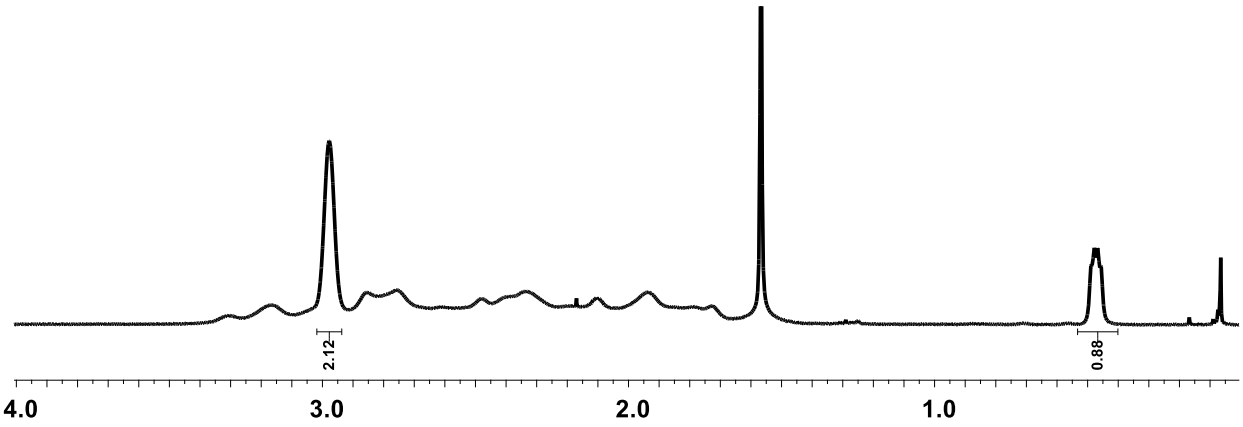

^{11}B NMR of 9-SH-mCB:

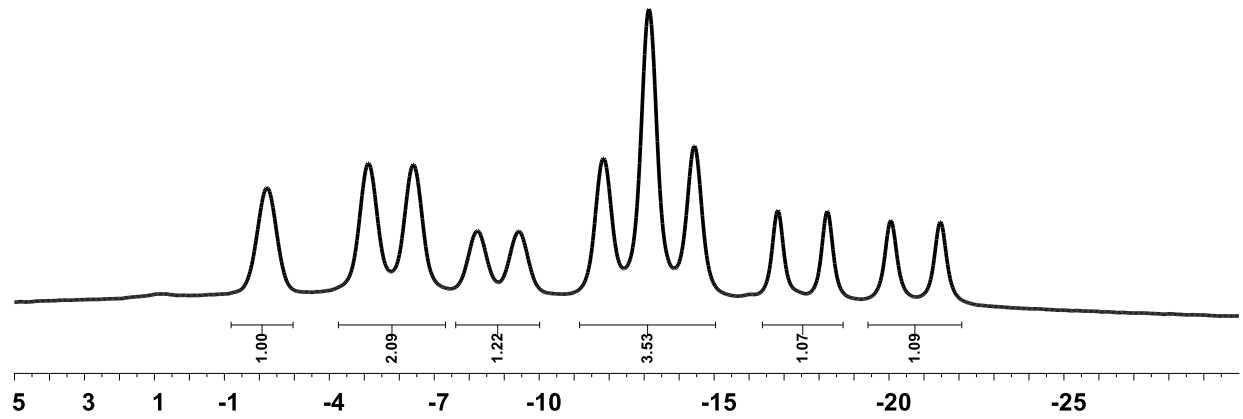

Synthesis of 9-SH-oCB

9-HS-oCB was prepared in an analogous manner as 9-HS-mCB, where *ortho*-$C_2B_{10}H_{12}$ was used instead of *meta*-$C_2B_{10}H_{12}$ and with minor alterations to the reduction procedure. Instead of heating for 1 hour equipped with a bleed needle, the reduction was instead left heating at 50 ^oC overnight under positive nitrogen pressure. All workup procedures were identical.

Yield: 700 mg (40%), white, odorous solid

All characterization matches literature data, and representative ^1H and ^{11}B NMR spectra recorded in $CDCl_3$ have been provided below:

^1H NMR of 9-SH-oCB:

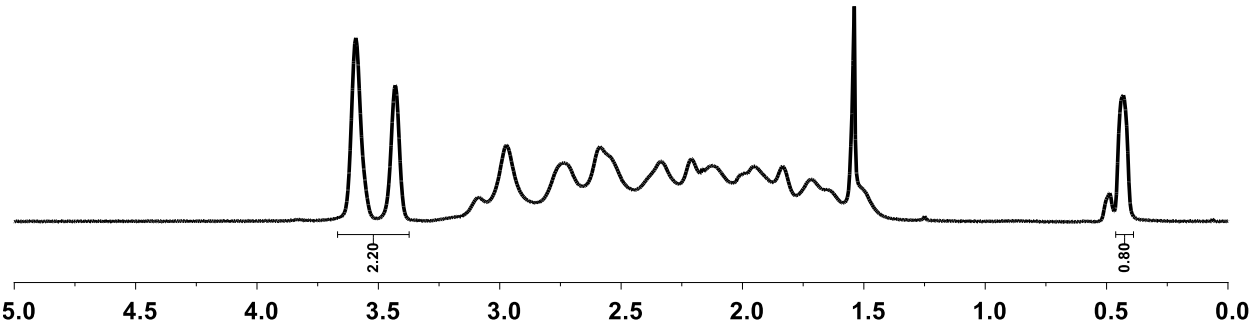

^{11}B NMR of 9-SH-oCB:

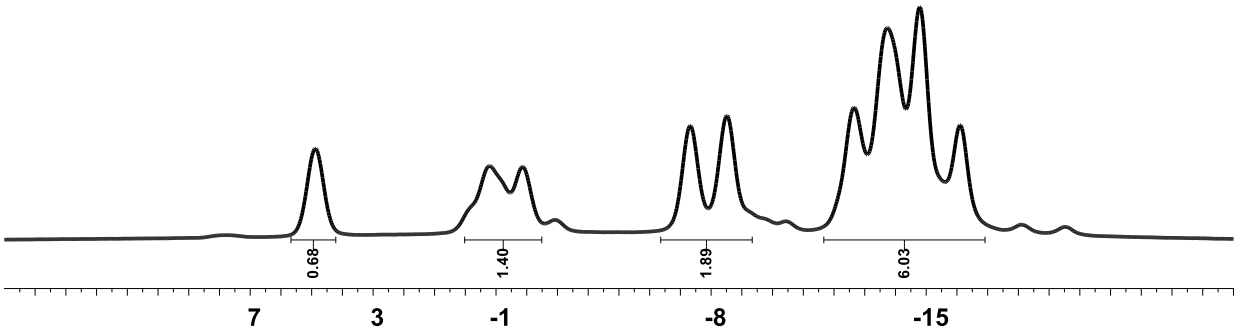

5.6.4 Synthesis of MOCHAs (A-D)

General Procedures

An oven-dried 4 mL dram vial equipped with a stir bar and PTFE septa cap was transferred into a N_2-filled glovebox. In the glovebox, chalcogenol (0.11 mmol; 1.1 eq) and anhydrous copper(I) acetate (12 mg, 0.1 mmol; 1 eq) were subsequently added to the dram vial and sealed with the PTFE cap. The vial was then transferred out of the glove box and anhydrous *iso*-propanol (1 mL, see SI sec. 1 for drying and storage procedures) was quickly added *via* syringe and the resulting suspension was immediately stirred at ~700 rpm. The reaction vial was then covered to limit exposure to light and then left to stir for 24 hours.

After stirring for 24 hours, the reaction appeared as milky white, off-white, or pale-yellow suspension. The suspension mixture was then transferred to a pre-weighed screw-capped tube suitable for centrifugation. Additional *iso*-propanol (non-anhydrous) was added to the reaction vial to maximize transfer of product to the screw-capped tube. The suspension was then centrifuged at 2900xg until all material was pelleted at the bottom of the tube (10 minutes). Once pelleted, the supernatant (*iso*-propanol, excess chalcogenol) was decanted from the tube and additional *iso*-propanol (2 mL, non-anhydrous) was added. The screw-capped tube was then vortexed to resuspend all powder before centrifuging once more, and the supernatant decanted. The above process was repeated once more before drying the pellet on a high-vacuum Schlenk line while in the screw-capped tube to remove all volatiles. After drying, materials **A**-**D** were afforded as free-flowing powders of varying fluffiness.

Yields:

Cu-[9-Se-mCB] (**A**), off-white/pale-yellow powder: 22 mg, 76%

Elemental Analysis: Calculated for $CuSeC_2B_{10}H_{11}$: C, 8.41; H, 3.88; found: C, 8.87; H, 3.78 (average of two duplicate runs)

Cu-[9-Se-oCB] (**B**), off-white/pale-yellow powder: 19 mg, 65%

Elemental Analysis: Calculated for $CuSeC_2B_{10}H_{11}$: C, 8.41; H, 3.88; found: C, 8.66; H, 3.79

Cu-[9-S-mCB] (**C**), off-white/light grey powder: 21 mg, 84%

Elemental Analysis: Calculated for $CuSC_2B_{10}H_{11}$: C, 10.06; H, 4.64; found: C, 10.31; H, 4.63

Cu-[9-S-oCB] (**D**), off-white/light grey powder: 17 mg, 69%

Elemental Analysis: Calculated for $CuSC_2B_{10}H_{11}$: C, 10.06; H, 4.63; found: C, 11.27; H, 4.86 (average of two duplicate runs). In the case of **D**, the experimental analysis deviates more significantly from the calculated values than the other three samples. However, when calculated with an impurity of *iso*-propanol (~10%), the calculated percent composition (C, 11.28; H, 4.86) matches the experimental data nearly exactly. These results suggest that the deviation between experimental and theoretical percent composition can be attributed to a small amount of *iso*-propanol impurity.

5.6.5 Supplementary Characterization and Data of A

5.6.5.1 Additional Electron Microscopy Images

Scanning Electron Microscopy

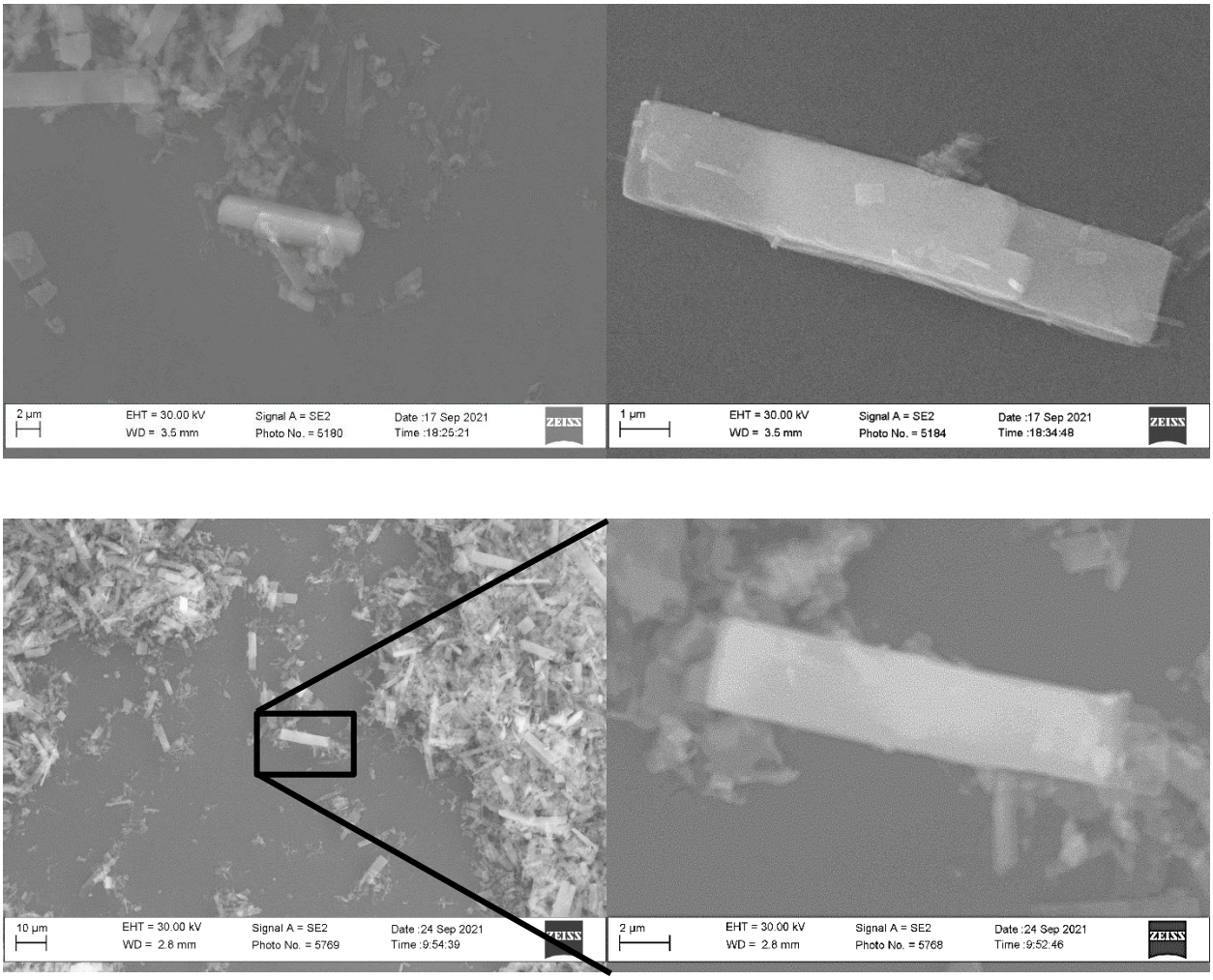

SEM images reveal a consist crystallite morphology throughout the bulk material. Crystallites are typically between 5-10 µm in length and 1-2 µm in width. While there are some crystallites that exceed these dimensions, they maintain a consistent morphology of square rods.

Transmission Electron Microscopy

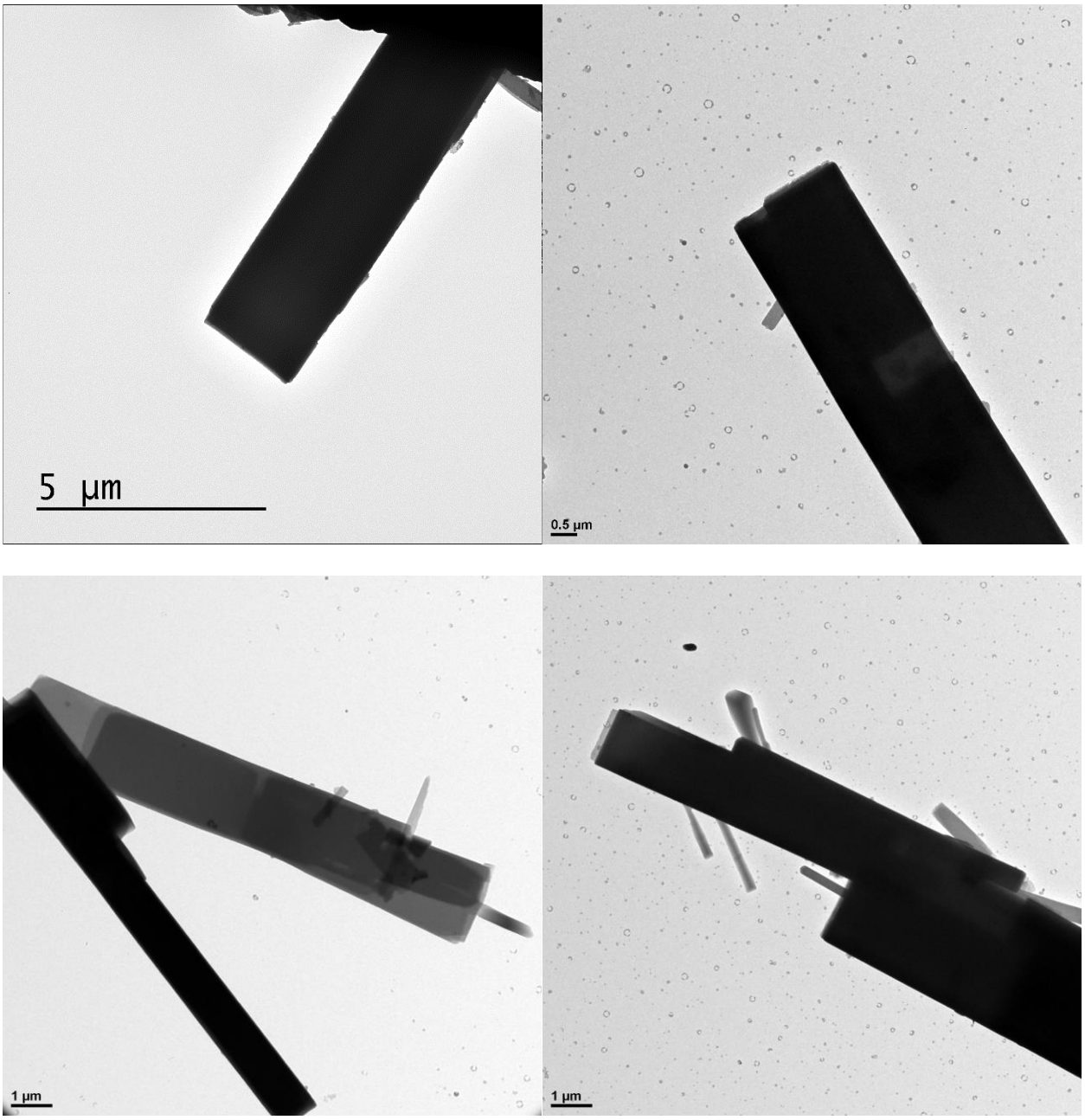

TEM images reveal the presence of rod-like microcrystals generally 5-10 µm in length and 1-2 µm in width. There is also evidence of smaller rods as shown in the bottom right TEM image.

5.6.5.2 Powder X-ray Diffraction Pattern

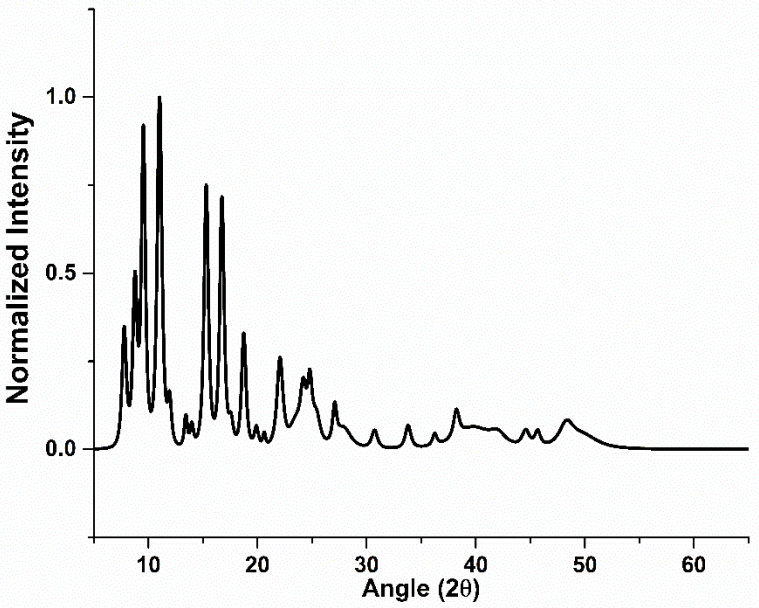

PXRD pattern of **A**. Sample was diffracted from 5.000^{o} to 65.000^{o} with a step size of 0.016^{o}. See included spreadsheet for peak list and corresponding intensities.

Cryo PXRD of A to Determine Effect of Thermal Contraction on PXRD Pattern

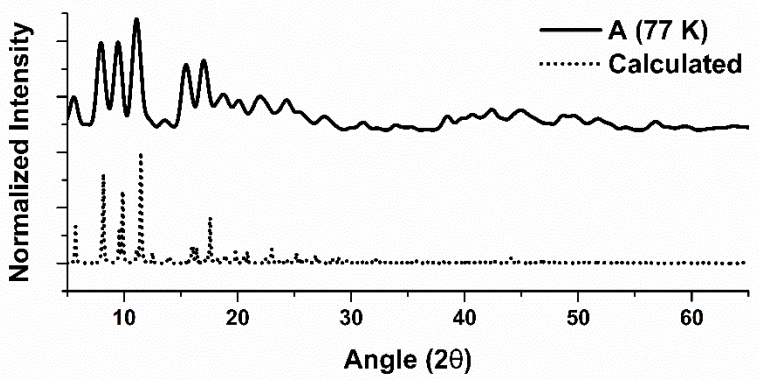

When comparing the ambient temperature PXRD pattern of **A** with the calculated PXRD pattern determined from the MicroED structure, some deviations between the diffraction peaks was evident. To confirm that these differences were a result of thermal contraction/expansion from the two pieces of data obtained at separate temperatures, Cryo PXRD (depicted above) experiments

were performed. The powder diffraction data were measured at 100K(2) on a Bruker Smart Apex2 CCD-based X-ray diffractometer system equipped with a micro-focus Cu-Kα radiation (λ = 1.54 Å). A total of 5 frames were collected to cover the entire 2-theta range. The frames were integrated with the Bruker Pilot software package (Apex v2014) to obtain the raw data file to plot and analyze the data. Importantly, the diffractions peaks matched the calculated PXRD almost exactly, suggesting that the previously observed deviations are likely attributed to thermal contraction/expansion of the crystallites.

5.6.5.3 Infrared Spectroscopy

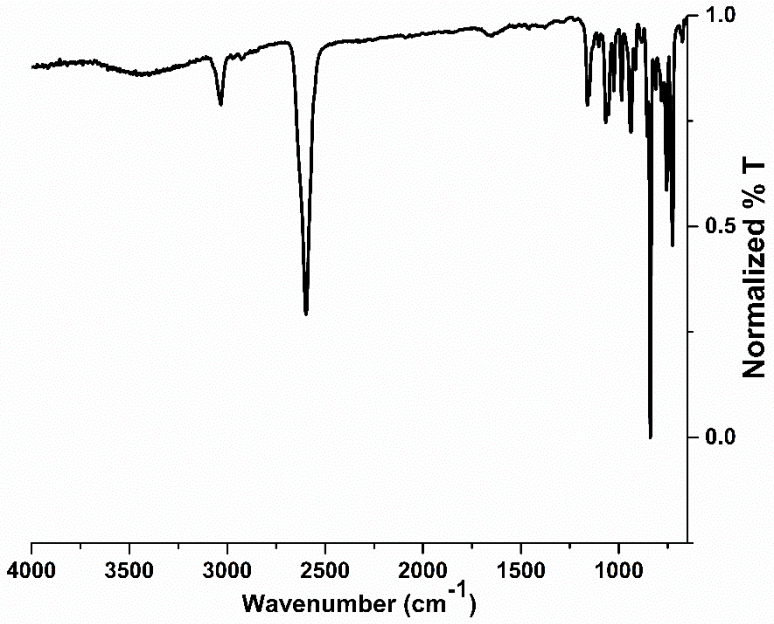

FTIR spectrum of **A** reveals no signals that could be correlated to residual starting material (CuOAC (C=O: ~1500 cm^{-1}), HSe-mCB (H-Se: ~2250 cm^{-1}), *iso*-propanol (H-C: ~3000 cm^{-1}; H-O: ~3500 cm^{-1})). Two diagnostic resonances attributed to the carborane cluster (H-$C_{carborane}$: 3000 cm^{-1}; H-$B_{carborane}$: 2700 cm^{-1}) are present and are expected to be symmetric as a function of the *meta*-carboranyl-selenolate symmetry.

5.6.5.4 Thermogravimetric Analysis

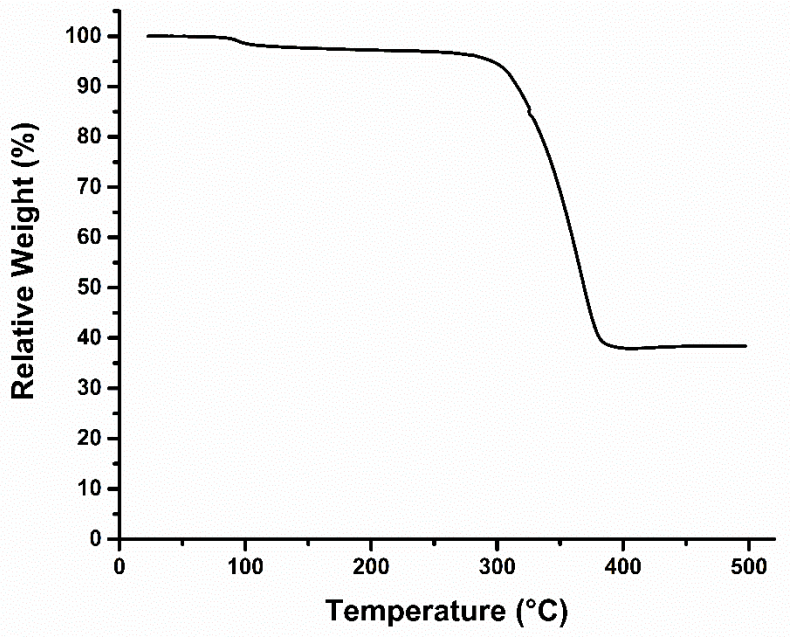

TGA of **A** indicates the material is thermally stable until 300 ^{o}C, after which, the material decomposes until reaching 40% relative weight at 375 ^{o}C. There is no evident desolvation step that would indicate the presence of solvent adducts within the material, which would be expected near 100 ^{o}C.

5.6.5.5 X-ray Photoelectron Spectroscopy

Cu 2*p* Region of A

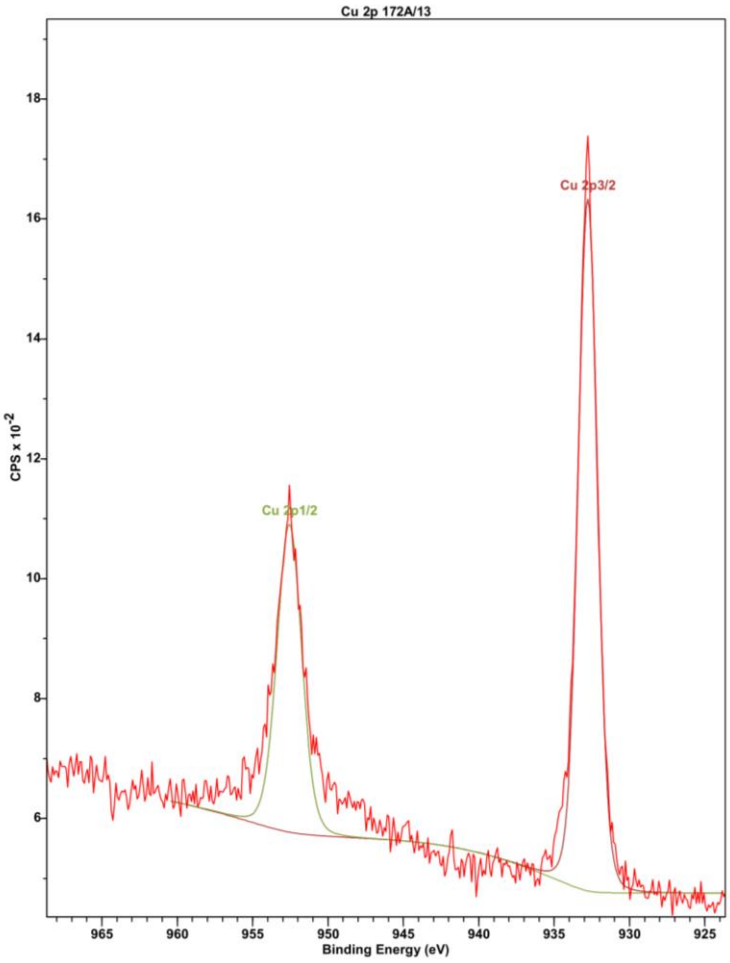

XPS data of **A** was processed and peak-fitted using CasaXPS. Peak fitting indicates the presence of only a single copper(I) environment, and is in agreement with all other structural characterization.

Se 3*d* Region of A

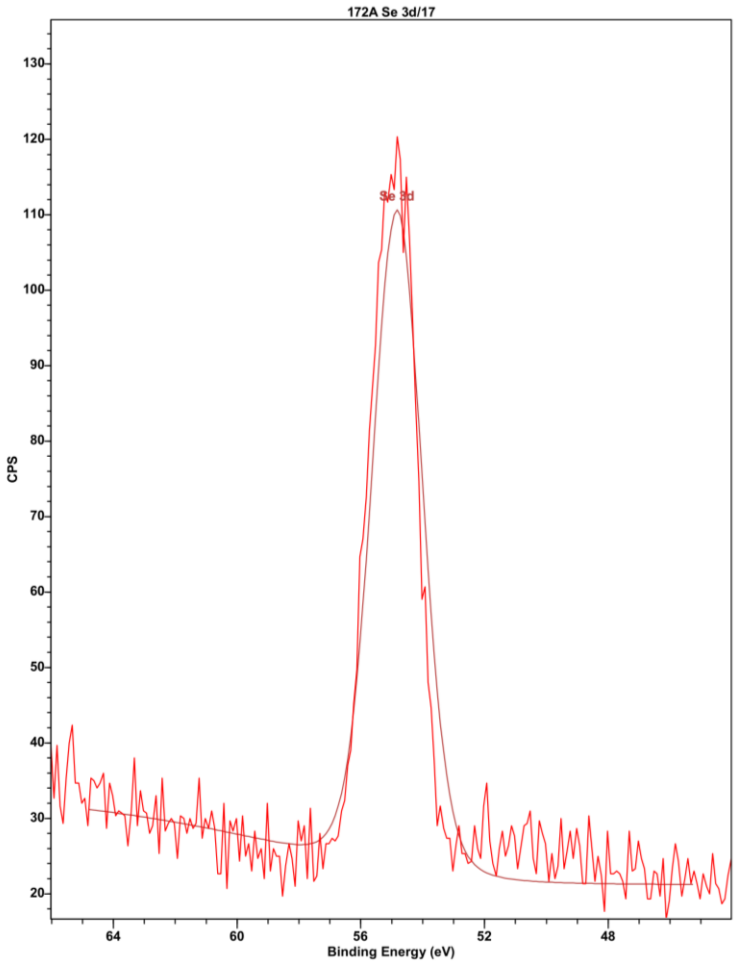

XPS data of **A** was processed and peak-fitted using CasaXPS. Peak fitting indicates the presence of only a single selenolate environment, and is in agreement with all other structural characterization.

5.6.5.6 Photophysical Measurements

Absorption and Emission Measurements

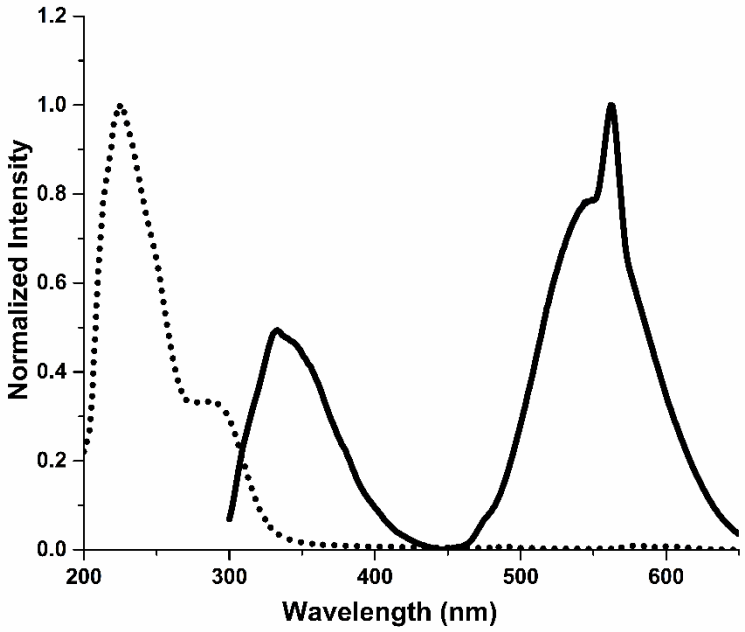

Absorption (dotted trace) and emission (solid trace) of **A** have been normalized and plotted on the same set of axes. Both measurements were performed on suspension of **A** in *iso*-propanol. Emission spectrum was obtained by exciting the suspension with 280 nm light, and the emission was monitored between 300-650 nm. The sharp peak at 560 nm is an artifact of the excitation wavelength (280 nm), and is not a result of emission from **A**.

Comparison of Emission Intensity at Different Excitation Wavelengths

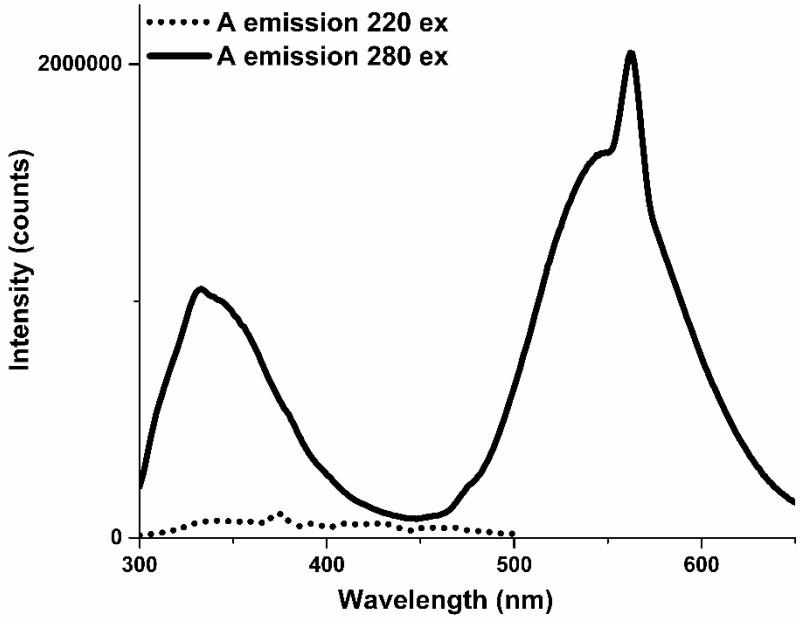

Emission traces when exciting a suspension of **A** in *iso*-propanol at 220 nm (dotted trace) and 280 nm (solid trace). Negligible emission can be correlated to excitation at 220 nm.

Lifetime Measurements

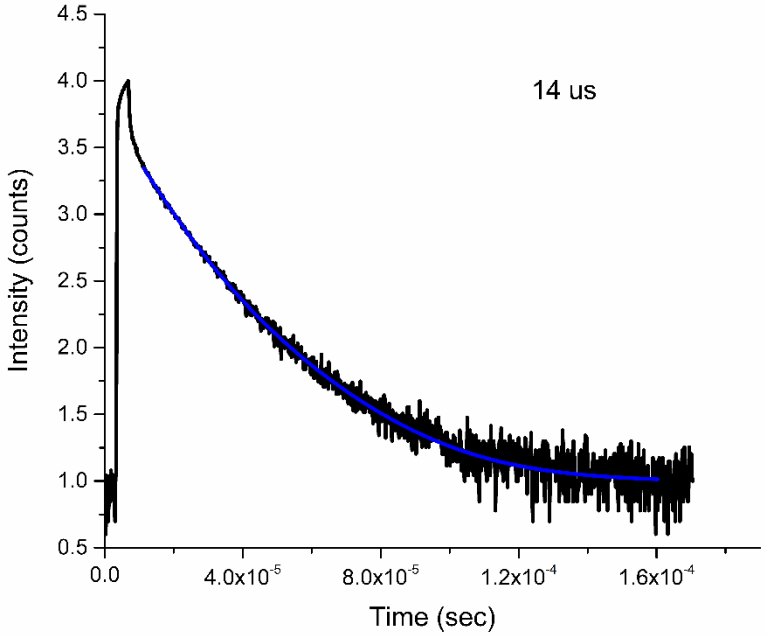

Lifetime plot of **A**, indicating a lifetime emission of 14 µs.

5.6.5.7 DFT Calculations

DFT calculations of **A** were performed using B3LYP functional with DZP basis set. The single crystal derived by MicroED was used for calculations of the molecular orbitals of **A**.

Atomic Coordinates:

B	-4.46822700	9.01069500	18.61489900	B	-2.37503300	10.92236900	19.24403100
B	2.67677300	9.14329000	13.97659400	B	2.56511100	6.28385000	14.42993900
C	1.40147700	1.08382000	19.78681100	C	3.07051400	1.15300000	17.59410200
B	3.75695800	9.43154000	25.08508800	B	2.31381200	10.80130400	22.96947800
Se	3.12285800	8.50222200	18.31883700	B	2.13885600	9.27012000	22.08437600
Se	-0.69886300	6.62975000	19.00656400	B	-1.65209500	9.60449000	18.27874500
Cu	1.19179600	7.61441200	18.77218200	Se	4.07544500	4.64428400	20.12296500
B	3.06332300	8.08253000	16.55480100	Cu	3.46166800	6.50637900	19.21627500
B	3.48353900	6.50292000	15.95034100	B	3.01124800	3.25261300	19.35813800
B	3.19123100	2.90440700	17.67120100	B	1.81745700	7.10248000	15.83623400
C	-3.28887600	10.13487000	17.97343100	B	3.96986500	1.87939000	18.91712900
C	1.64189100	7.74816000	14.21714500	B	1.25105000	9.51916800	23.61402900
B	2.92167000	0.45428200	19.18851900	B	-2.94758200	8.42843000	17.89324800
C	2.34608400	10.39198900	24.66875000	Se	1.18177600	6.34495900	23.00648500
B	-2.96256200	10.22480400	20.77985200	Cu	2.56444700	5.49404500	21.51383900
B	3.10836100	7.55215000	13.27036300	B	2.09148000	8.04217500	23.30563100
B	1.49566000	0.58803000	18.09987400	B	1.87898600	8.86657000	15.55559200
B	3.86260000	10.76556100	23.87308400	B	2.89547700	1.82174000	20.33267500
B	-4.11272500	10.56263300	19.45990900	Cu	0.29477800	6.57210000	21.01423500
B	1.66406300	2.12152000	17.17159700	B	-1.86125400	8.17131100	19.22244300
B	3.73986800	10.02994700	22.24474300	B	3.58421200	9.33930000	15.49391200

B	1.45583300	2.82485000	19.96259800	H	3.75676724	3.76550436	17.06947936
B	3.57325900	7.90266200	24.18456600	H	1.26563348	2.22851144	16.05513101
B	-2.59289500	8.47339700	20.76134900	H	-4.94569154	11.34103548	19.81427006
B	4.58868500	7.89805000	15.74679800	H	-3.90091593	6.59685371	19.52087693
B	1.64885800	3.48321300	18.31883700	H	-5.39629337	8.84360624	17.88005707
B	3.56649000	8.26239800	22.42978100	H	-3.41012589	8.10153648	16.85806986
B	-1.44958400	9.63446800	20.04894900	H	-2.08084574	7.84781518	21.64067151
C	4.23724700	6.82576000	14.39293100	H	-0.38277667	9.82436143	20.53899804
B	2.14388000	8.67056000	24.91546900	H	-2.99342150	10.84923110	21.79282831
B	-3.52080000	7.72164100	19.42598600	H	-0.74201764	9.80177943	17.53641460
C	-4.19295700	9.05450900	20.34192700	H	-1.86410918	11.99125588	19.39687578
B	4.34832100	8.54373000	14.09995300	H	3.80896452	5.43441895	16.37450674
B	0.60838600	2.06617600	18.58405900	H	1.94917826	5.30598957	14.12810262
C	4.56008700	9.19517500	23.54926600	H	3.40587408	7.35456458	12.13103978
H	4.98652400	6.18008000	14.04444200	H	5.30797584	9.05590660	13.57226127
H	0.70864300	7.71357000	13.73912800	H	2.11920473	10.00854801	13.36473020
H	0.82702400	0.50732000	20.45603500	H	3.94015672	10.40617644	15.88537625
H	3.59027200	0.63415000	16.84161100	H	1.23402597	9.67514048	16.14998230
H	5.60412300	9.08564000	23.51225800	H	0.92888442	6.57742719	16.42525283
H	1.95299500	11.06880000	25.37498200	H	5.64474423	7.94354013	16.29567166
H	-4.99397600	8.87810000	21.00189900	H	3.98832985	6.85339983	24.56834531
H	-3.50563200	10.66525000	17.08832900	H	4.50354687	11.78241792	23.95253690
H	1.21329880	4.55124948	18.03426446	H	1.97357490	11.93316070	22.77050855
H	0.97645698	3.64404127	20.68729267	H	1.58025130	8.17737769	25.84094306
H	-0.57788637	2.13620653	18.50576360	H	4.31110459	9.49062940	26.13875402
H	3.32730396	1.70452228	21.43648619	H	0.05096366	9.66278452	23.54141361
H	5.11632103	1.96134113	19.24200738	H	4.01843285	7.48395087	21.65332006
H	3.38467358	-0.59713361	19.50125489	H	4.28522433	10.33224774	21.24294425
H	1.08300532	-0.28661754	17.39941833	H	2.26418057	9.67616380	20.98354805

5.6.6 Supplementary Characterization and Data of B

5.6.6.1 Additional Electron Microscope Images

Scanning Electron Microscopy

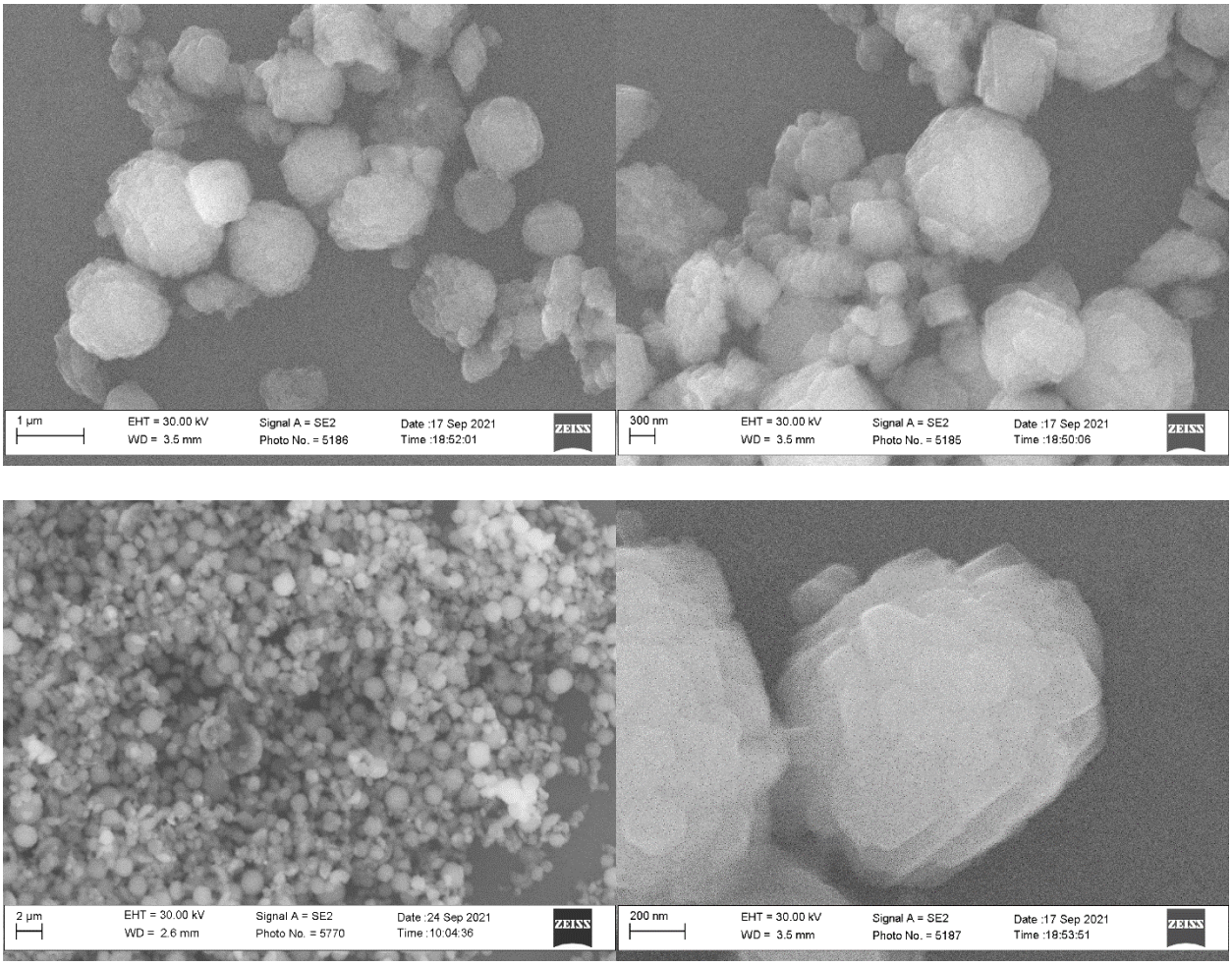

SEM images reveal a microscale particle phase present in bulk **B**. The upper two images were used to determine the average microscale particle size to be 1.10 µm ± 0.31 in diameter. While spherical in nature, in higher magnification images (bottom right), the particles appear to be comprised of platelets stacked on top of one another.

Transmission Electron Microscopy

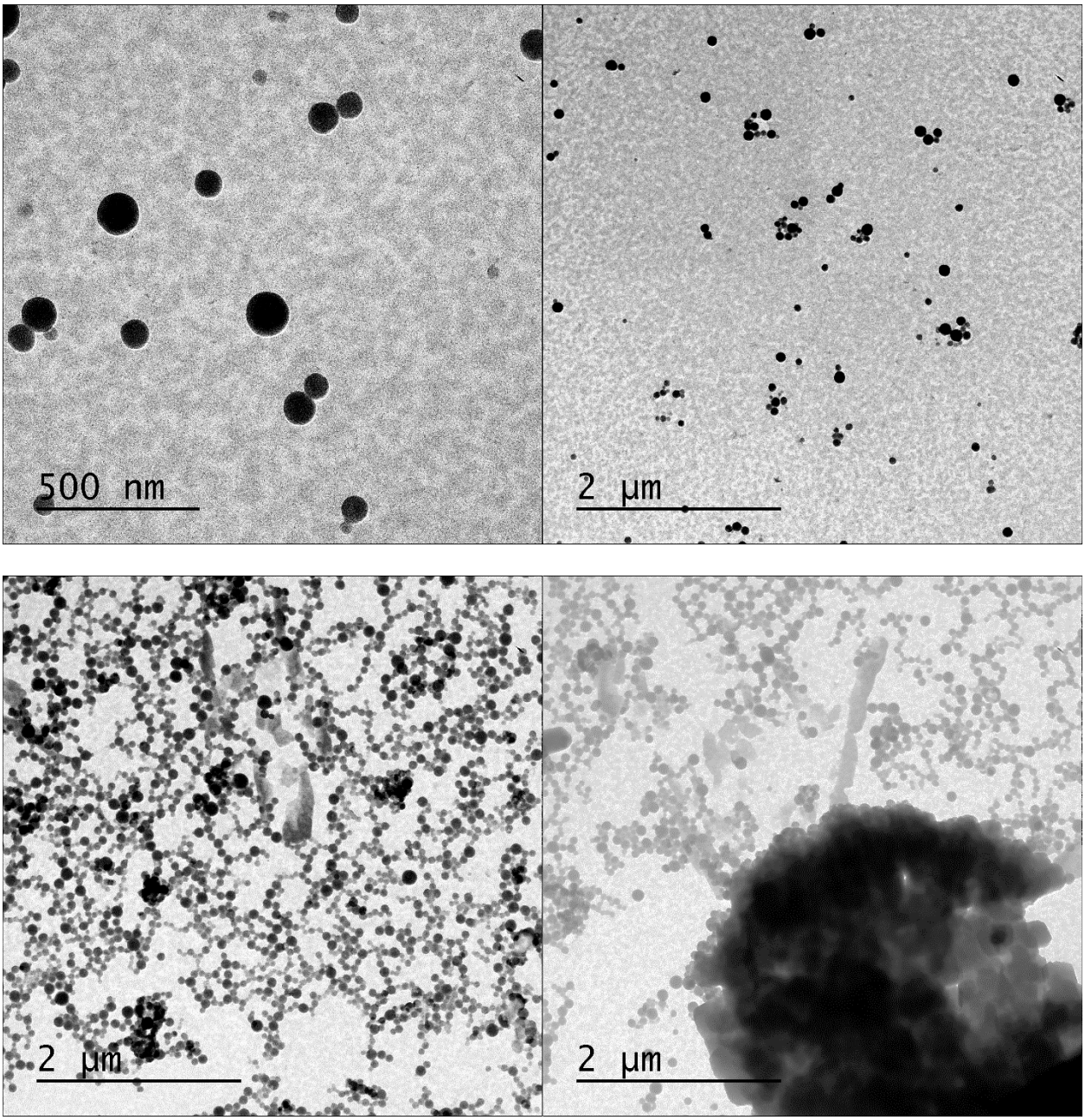

TEM images reveal the presence of spherical nanoparticles comingled with the larger aggregates observed by SEM (bottom right). The upper two images were used to determine the average nanoparticle size to be 92 nm ± 25 nm in diameter.

5.6.6.2 Powder X-ray Diffraction Pattern

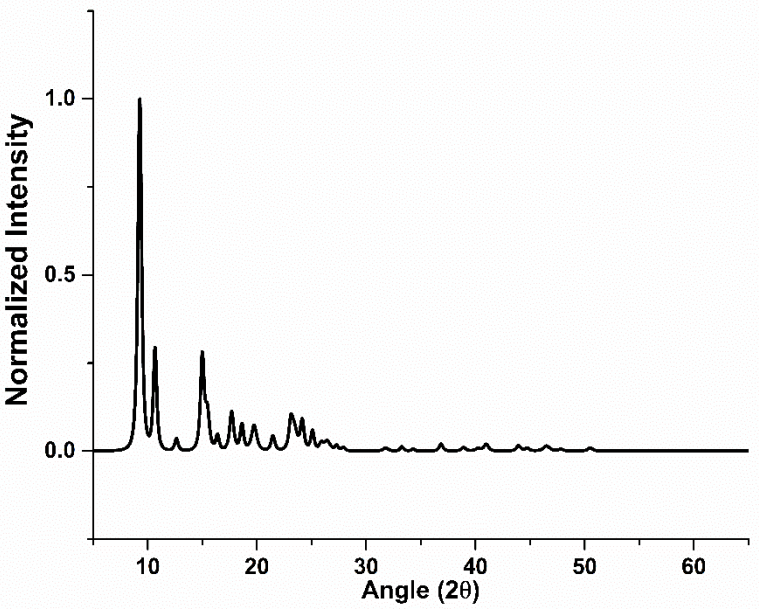

PXRD pattern of **B**. Sample was diffracted from 5.000° to 65.000° with a step size of 0.016°. See included spreadsheet for peak list and corresponding intensities.

5.6.6.3 Infrared Spectroscopy

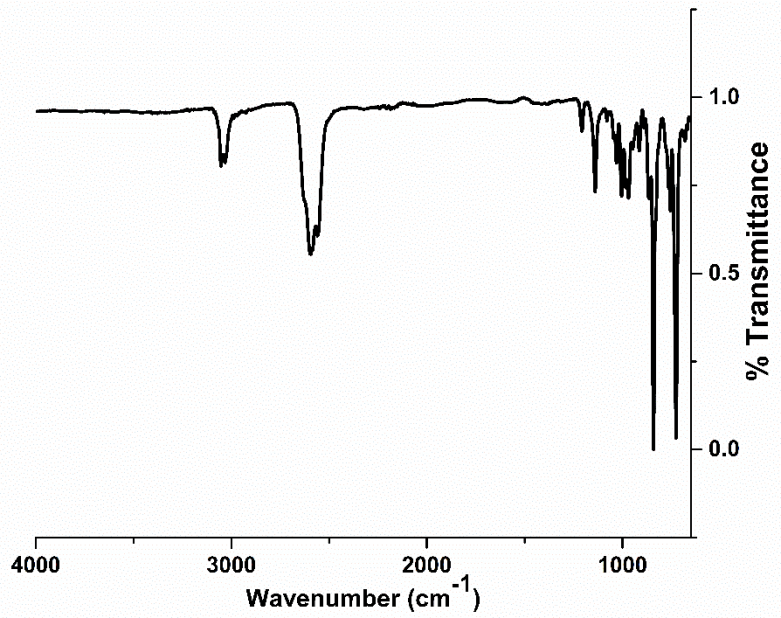

FTIR spectrum of **B** reveals no signals that could be correlated to residual starting material (CuOAC (C=O: ~1500 cm^{-1}), HSe-oCB (H-Se: ~2250 cm^{-1}), *iso*-propanol (H-C: ~3000 cm^{-1}; H-

O: ~3500 cm^{-1})). Two diagnostic resonances attributed to the carborane cluster (H-$C_{carborane}$: 3000 cm^{-1}; H-$B_{carborane}$: 2500 cm^{-1}) are present and are expected to be slightly asymmetric as a function of the *ortho*-carboranyl-selenolate asymmetry.

5.6.6.4 Thermogravimetric Analysis

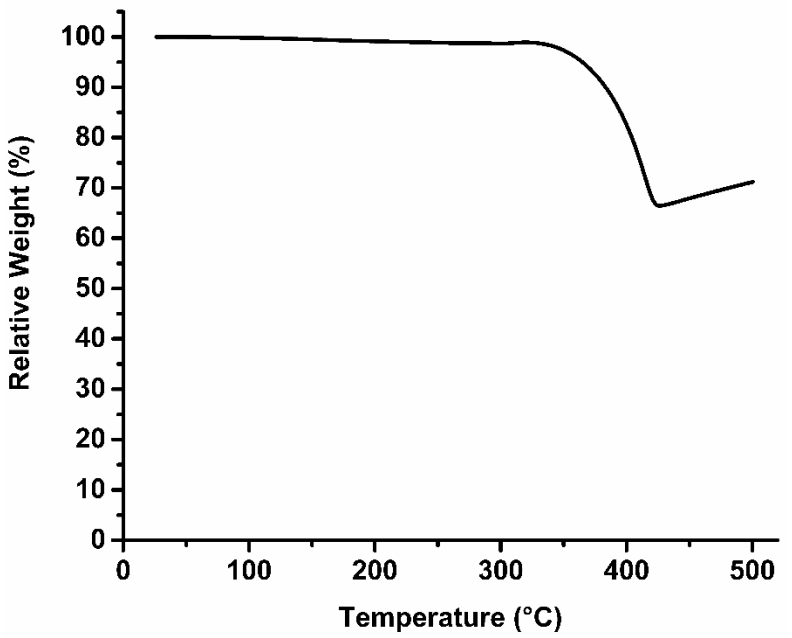

TGA of **B** indicates the material is thermally stable until 350 ^{o}C, after which, the material decomposes until reaching 65% relative weight at 400 ^{o}C. There is no evident desolvation step that would indicate the presence of solvent adducts within the material, which would be expected near 100 ^{o}C.

5.6.6.5 X-ray Photoelectron Spectroscopy

Cu 2*p* Region of B

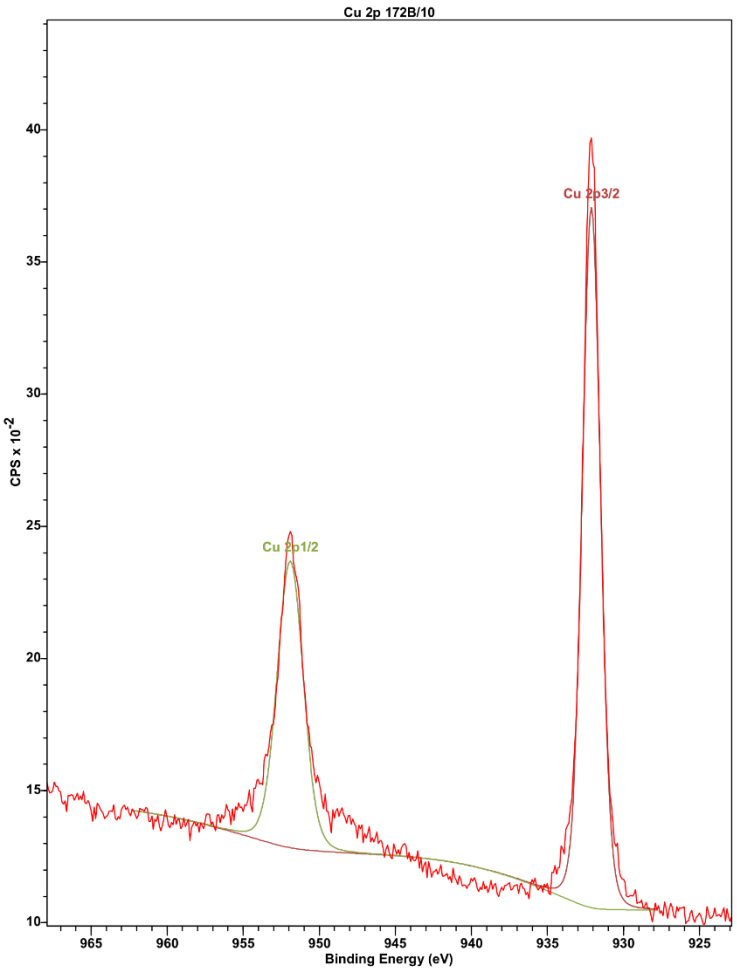

4

XPS data of **B** was processed and peak-fitted using CasaXPS. Peak fitting indicates the presence of only a single copper(I) environment, and is in agreement with all other structural characterization.

Se 3*d* Region of B

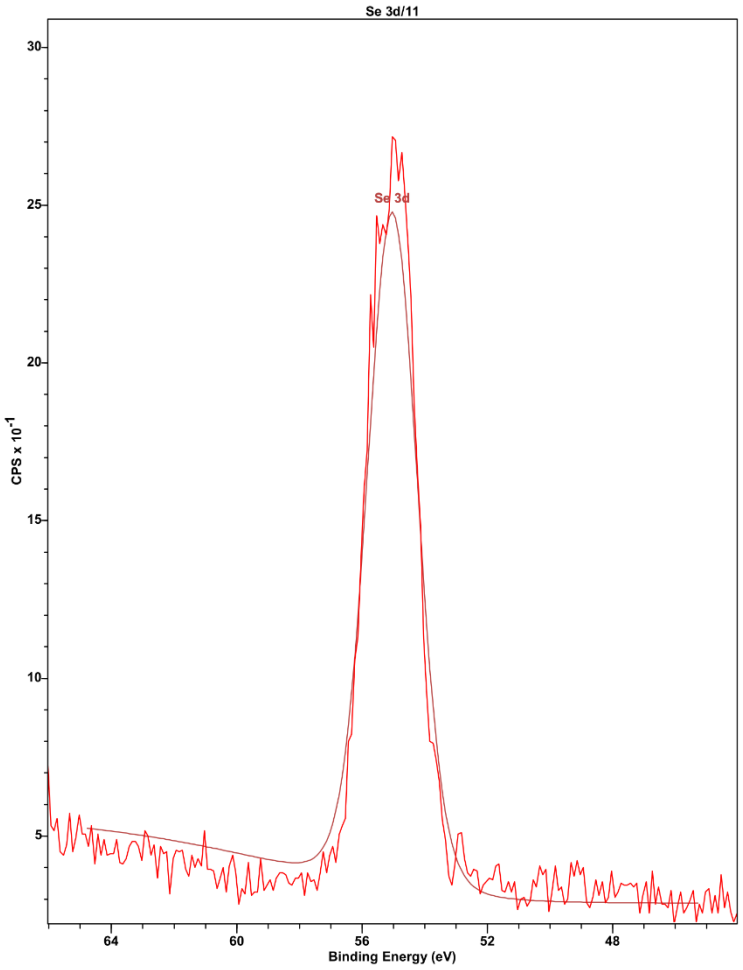

XPS data of **B** was processed and peak-fitted using CasaXPS. Peak fitting indicates the presence of only a single selenolate environment, and is in agreement with all other structural characterization.

5.6.6.6 Photophysical Measurements

Absorption and Emission Measurements

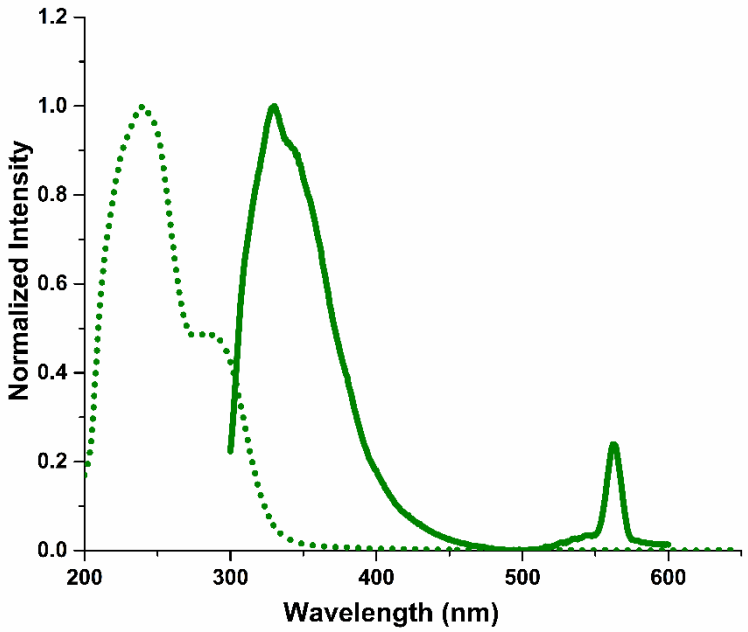

Absorption (dotted trace) and emission (solid trace) of **B** have been normalized and plotted on the same set of axes. Both measurements were performed on suspension of **B** in *iso*-propanol. Emission spectrum was obtained by exciting the suspension with 280 nm light, and the emission was monitored between 300-600 nm. The sharp peak at 560 nm is an artifact of the excitation wavelength (280 nm), and is not a result of emission from **B**.

Comparison of Emission Intensity at Different Excitation Wavelengths

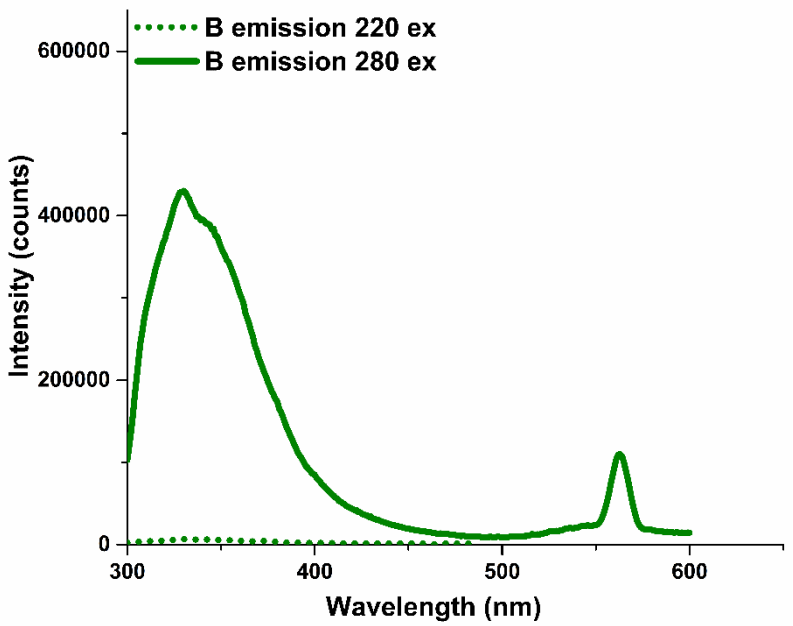

Emission traces when exciting a suspension of **B** in *iso*-propanol at 220 nm (dotted trace) and 280 nm (solid trace). Negligible emission can be correlated to excitation at 220 nm.

Lifetime Measurements

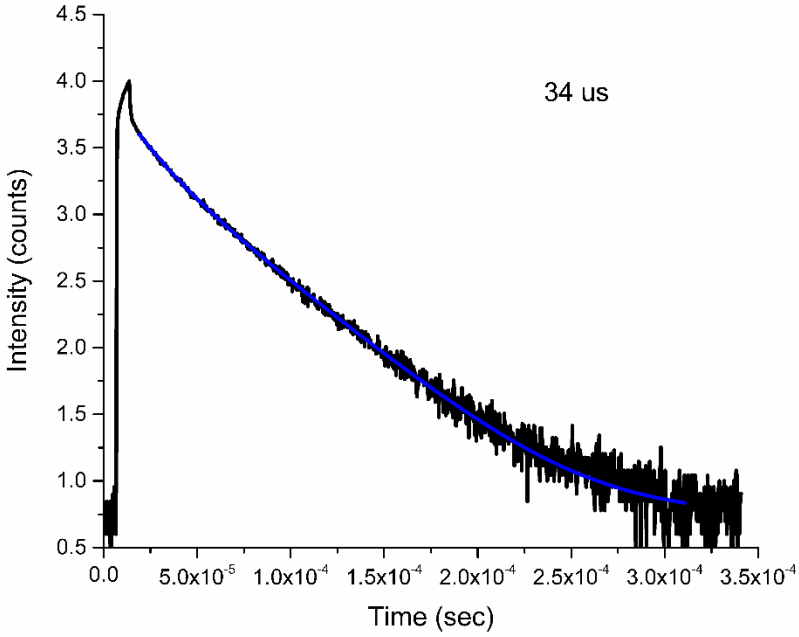

Lifetime plot of **B**, indicating a lifetime emission of 34 µs.

5.6.7 Supplementary Characterization and Data of C

5.6.7.1 Additional Electron Microscopy Images

Scanning Electron Microscopy

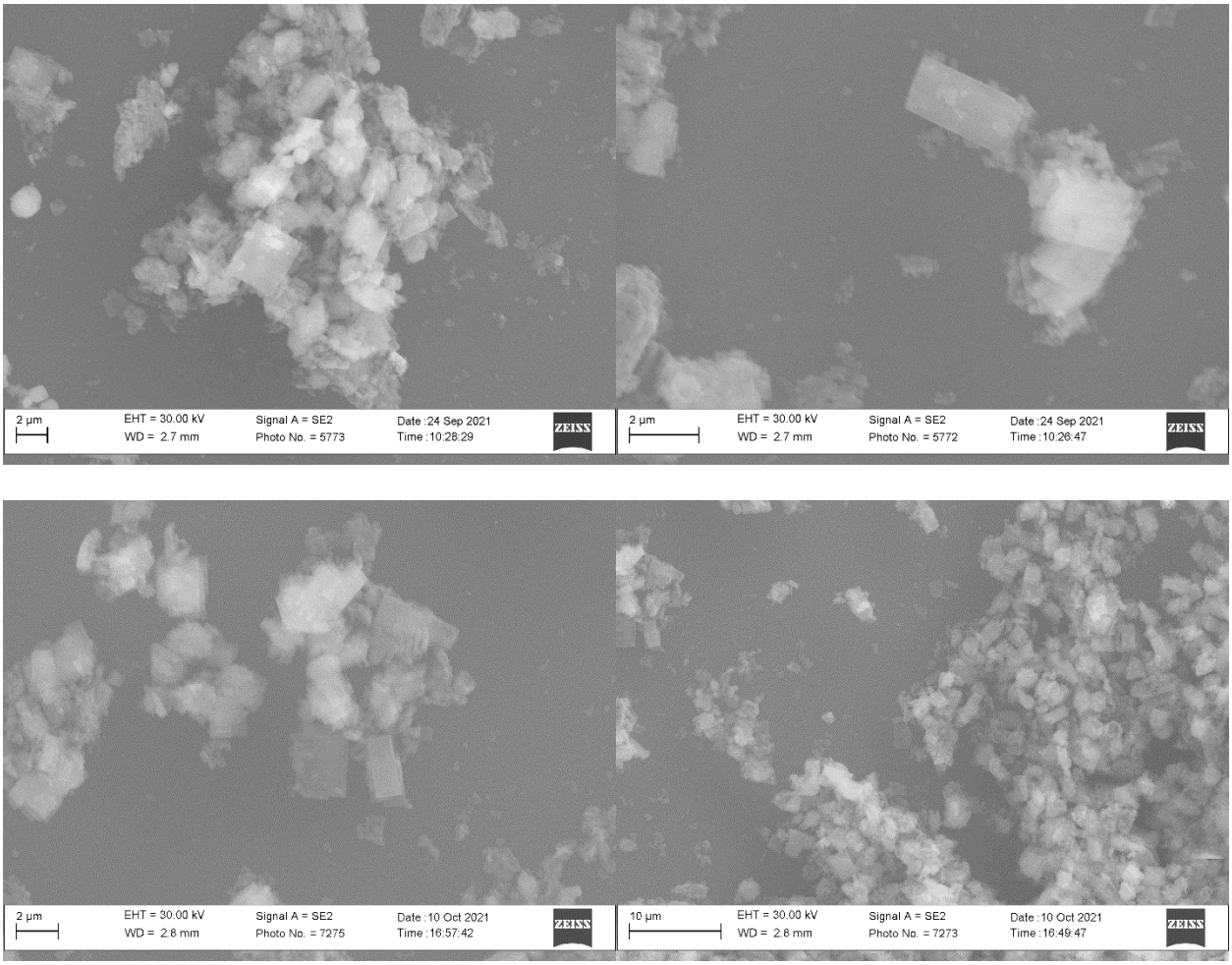

SEM images reveal a consistent crystallite morphology throughout the bulk material. Crystallites are typically between 3-5 µm in length and 2-3 µm in width. While there are some crystallites that exceed these dimensions, they maintain a consistent morphology of square prisms.

Transmission Electron Microscopy

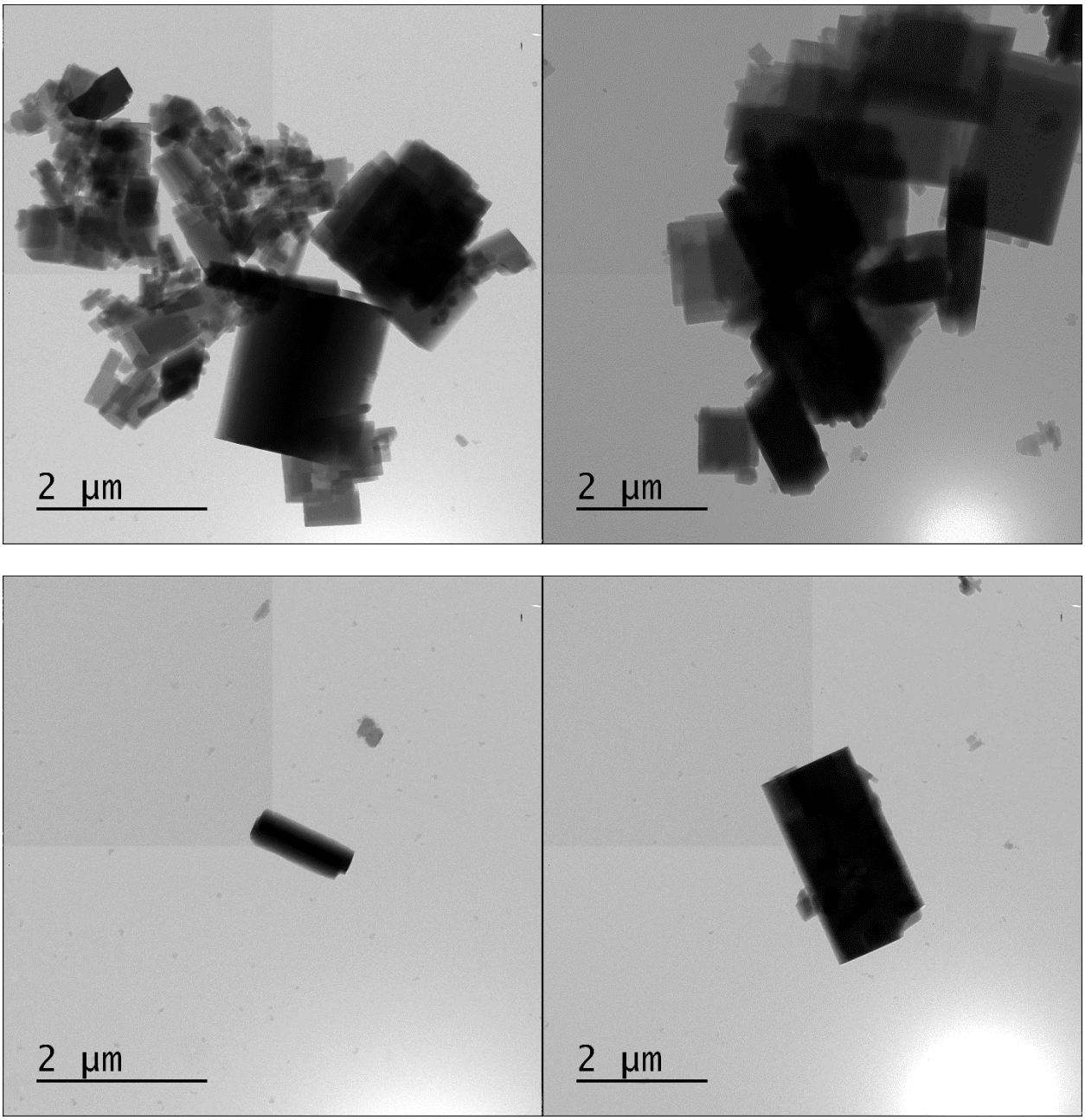

TEM images reveal the presence of cubic crystallites, in agreement with morphology observed by SEM.

5.6.7.2 Powder X-ray Diffraction

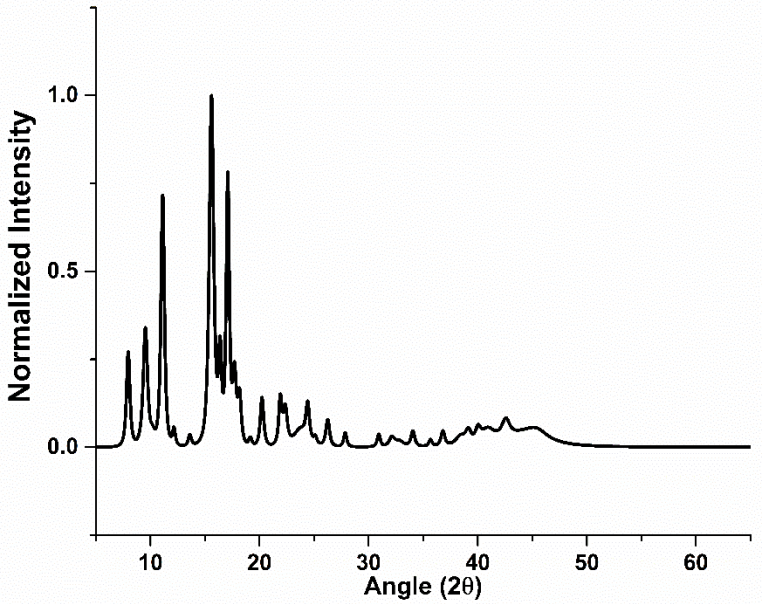

PXRD pattern of **C**. Sample was diffracted from 5.000° to 65.000° with a step size of 0.016°. See included spreadsheet for peak list and corresponding intensities.

5.6.7.3 Infrared Spectroscopy

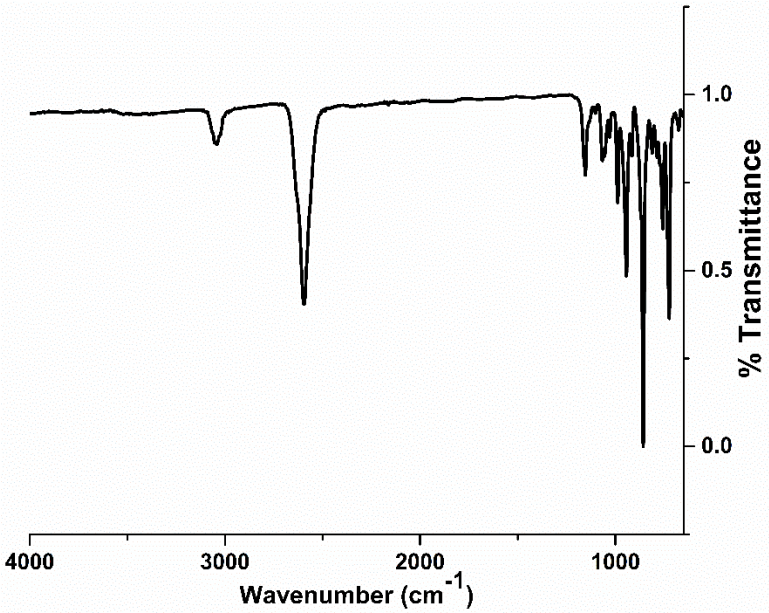

FTIR spectrum of **C** reveals no signals that could be correlated to residual starting material (CuOAC (C=O: ~1500 cm^{-1}), HS-mCB (H-S: ~2500 cm^{-1}), *iso*-propanol (H-C: ~3000 cm^{-1}; H-O:

~3500 cm^{-1})). Two diagnostic resonances attributed to the carborane cluster (H-$C_{carborane}$: 3000 cm^{-1}; H-$B_{carborane}$: 2600 cm^{-1}) are present and are expected to be symmetric as a function of the *meta*-carboranyl-thiolate symmetry.

5.6.7.4 Thermogravimetric Analysis

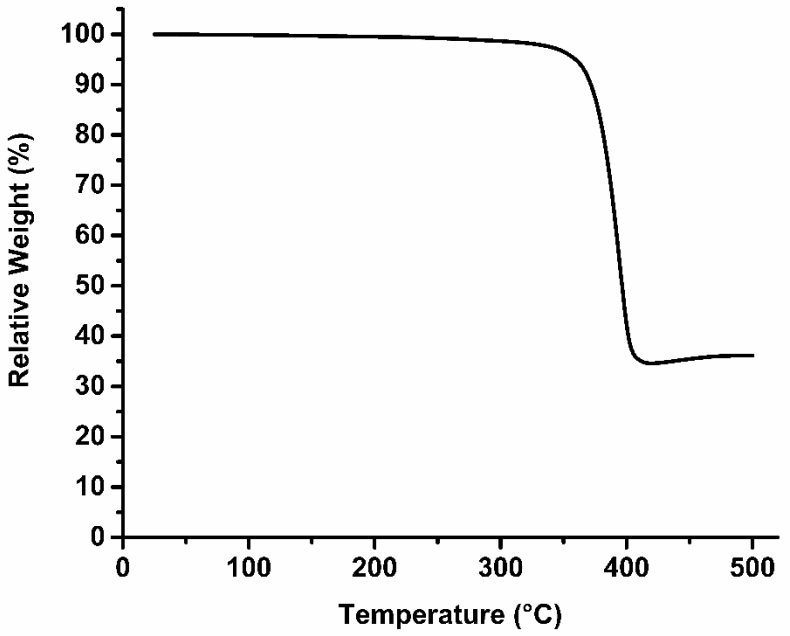

TGA of **C** indicates the material is thermally stable until 350 ^{o}C, after which, the material decomposes until reaching 40% relative weight at 400 ^{o}C. There is no evident desolvation step that would indicate the presence of solvent adducts within the material, which would be expected near 100 ^{o}C.

5.6.7.5 X-ray Photoelectron Spectroscopy

Cu 2*p* Region of C

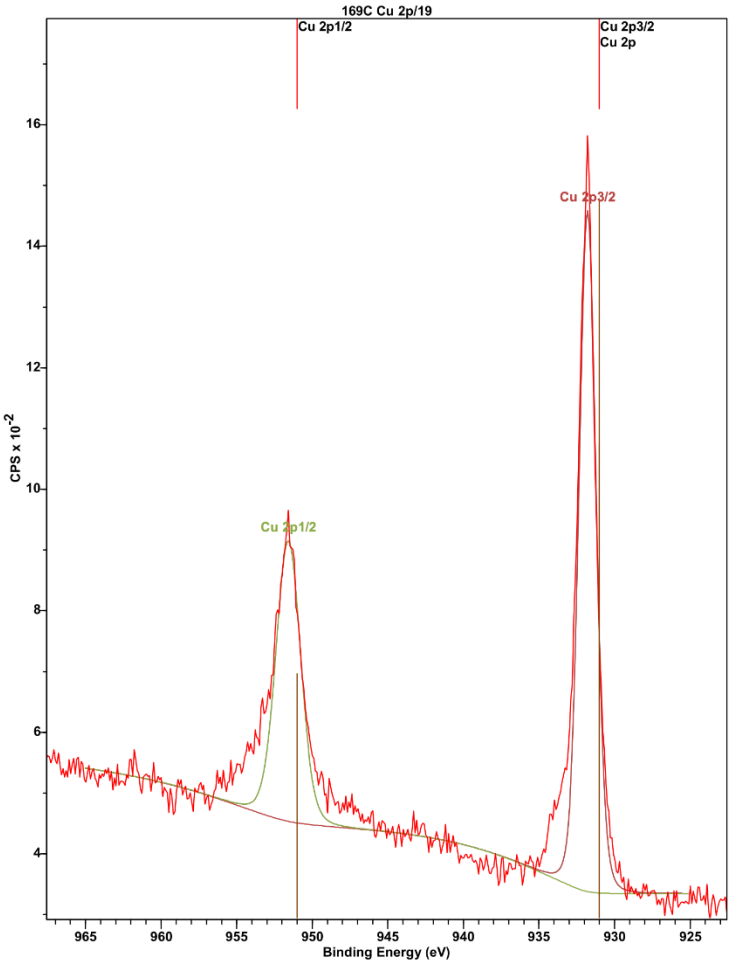

XPS data of **C** was processed and peak-fitted using CasaXPS. Peak fitting indicates the presence of only a single copper(I) environment, and is in agreement with all other structural characterization.

S 2*p* Region of C

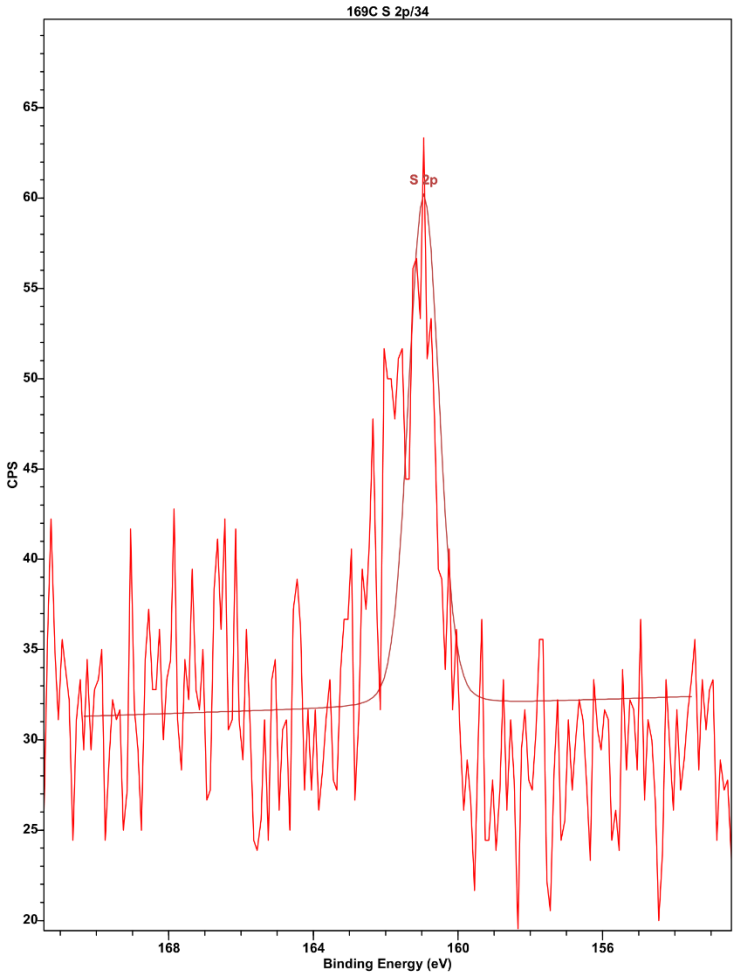

XPS data of **C** was processed and peak-fitted using CasaXPS. Peak fitting indicates the presence of only a single thiolate environment, and is in agreement with all other structural characterization.

Note: The XPS instrument used to obtain measurements currently has decreased sensitivity in the S 2*p* region, resulting in lower signal to noise ration.

5.6.7.6 Photophysical Measurements

Absorption and Emission Measurements

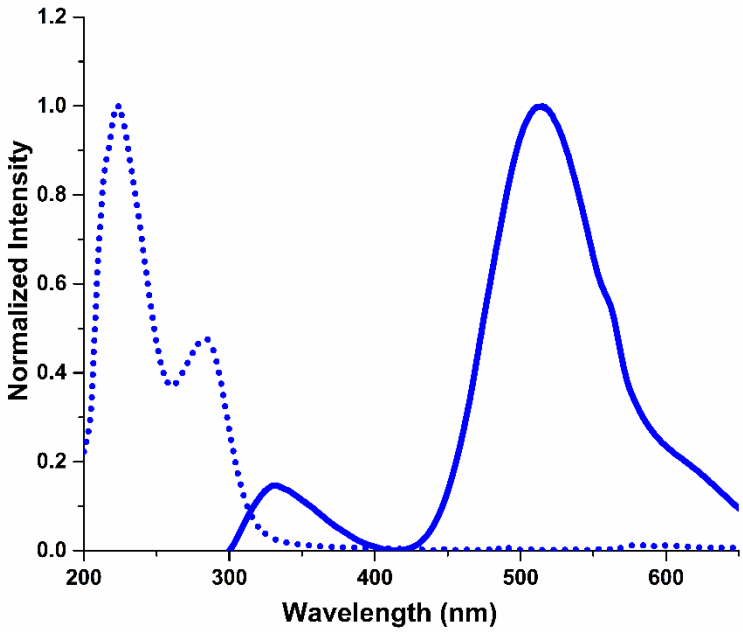

Absorption (dotted trace) and emission (solid trace) of **C** have been normalized and plotted on the same set of axes. Both measurements were performed on suspension of **C** in *iso*-propanol. Emission spectrum was obtained by exciting the suspension with 280 nm light, and the emission was monitored between 300-650 nm. Although not as evident as in materials **A** and **B**, the artifact from the excitation wavelength (280 nm) is present as a slight shoulder at 560 nm.

Comparison of Emission Intensity at Different Excitation Wavelengths

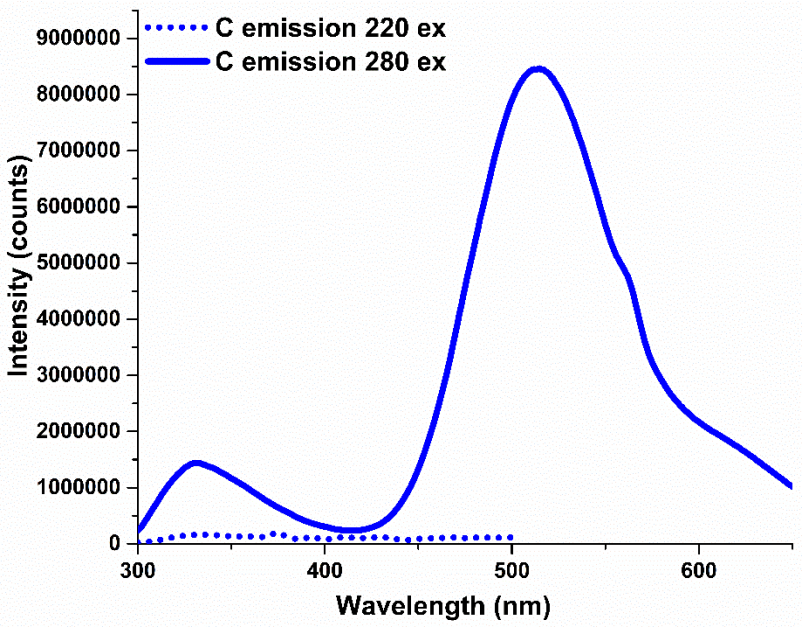

Emission traces when exciting a suspension of **C** in *iso*-propanol at 220 nm (dotted trace) and 280 nm (solid trace). Negligible emission can be correlated to excitation at 220 nm.

Lifetime Measurements

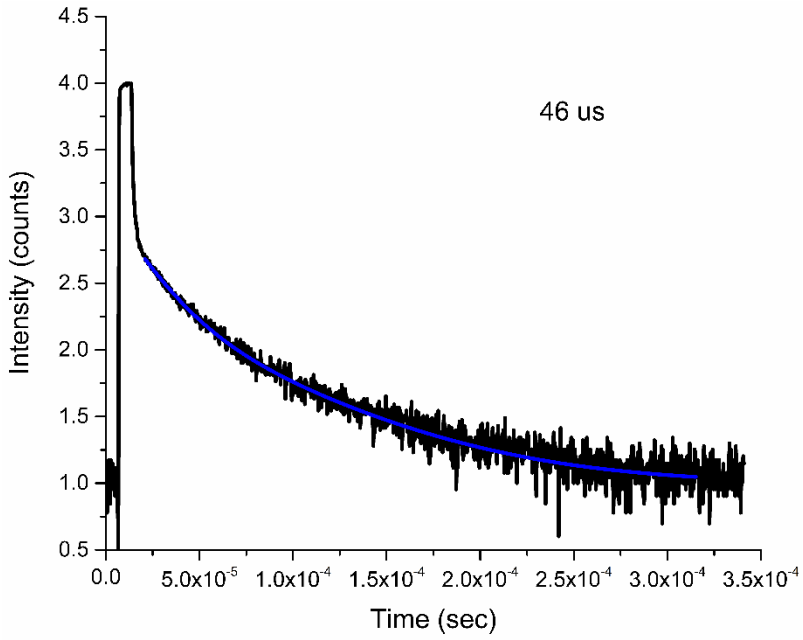

Lifetime plot of **C**, indicating a lifetime emission of 46 µs.

5.6.8 Supplementary Characterization and Data of D

5.6.8.1 Additional Electron Microscopy Images

Scanning Electron Microscopy

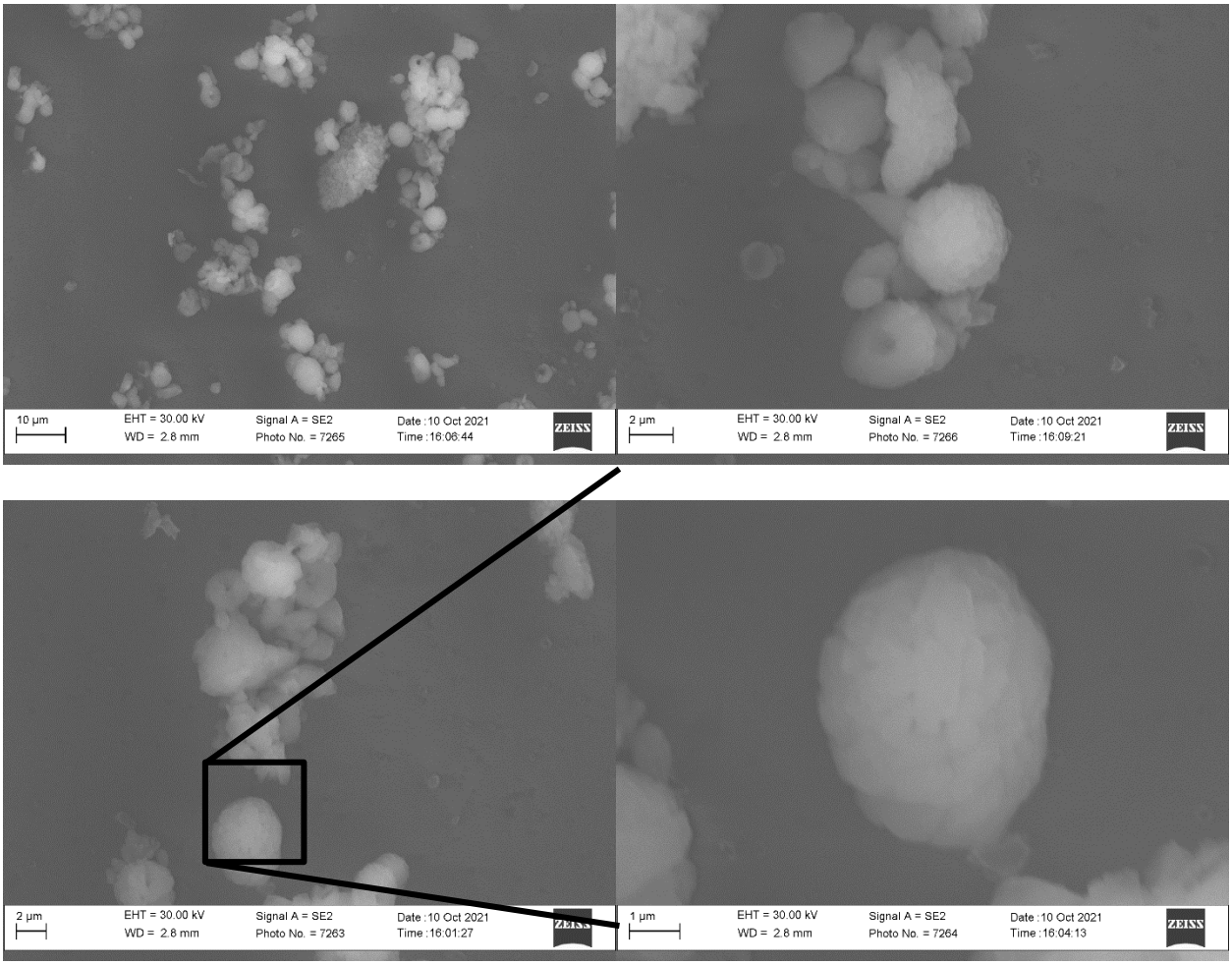

SEM images reveal a microscale particle phase present in bulk **D** with an average particle size diameter of 3.47 µm ± 0.72. While spherical in nature, in higher magnification images (bottom right), the particles appear to be comprised of platelets stacked on top of one another. There is also some evidence of "donut-like" morphologies as seen in the top right SEM image.

Transmission Electron Microscopy

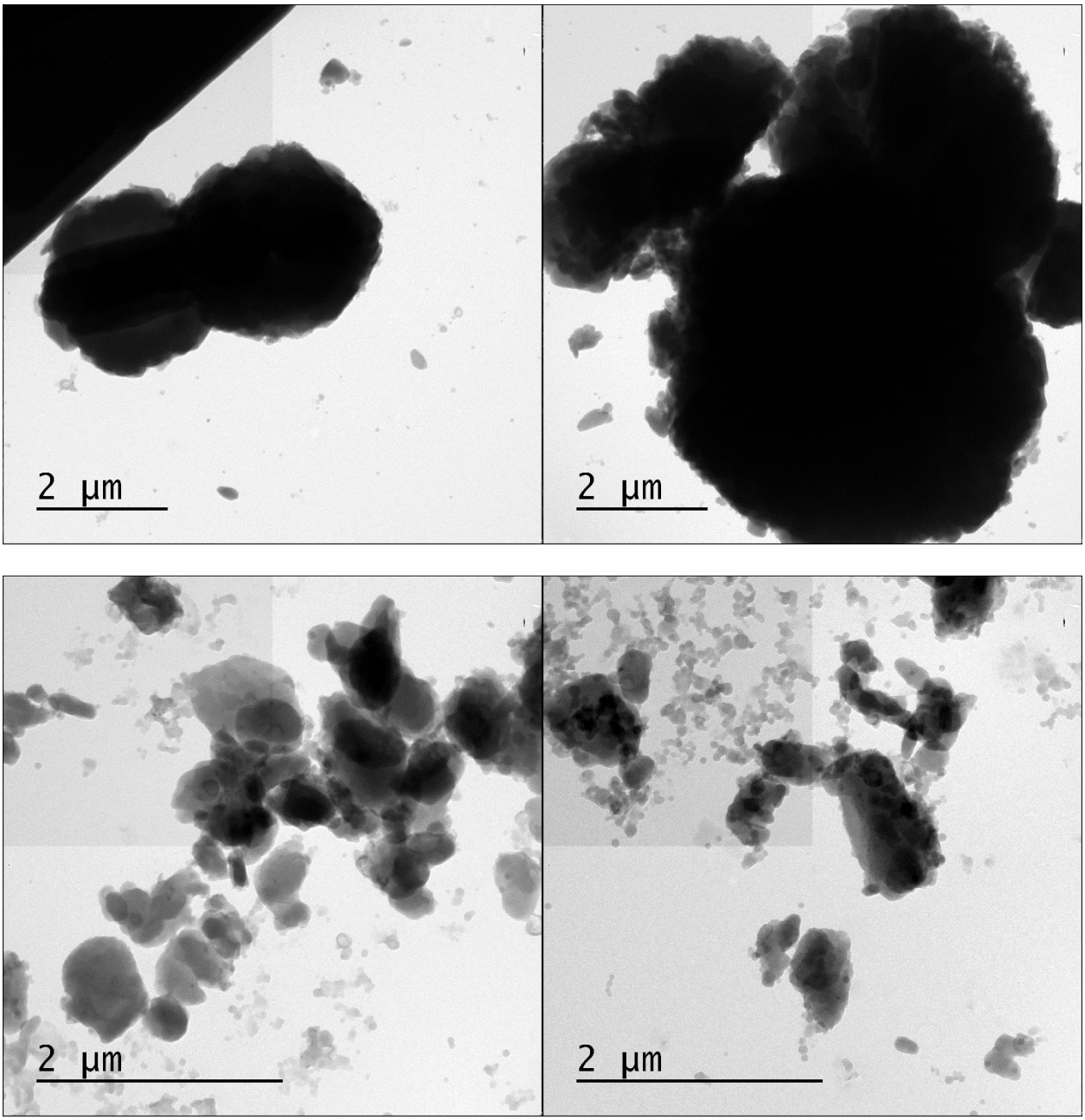

TEM images of **D** reveal the presence of spherical nanoparticles comingled with the larger aggregates observed by SEM, though significantly less prominent than in **B**.

5.6.8.2 Powder X-ray Diffraction Pattern

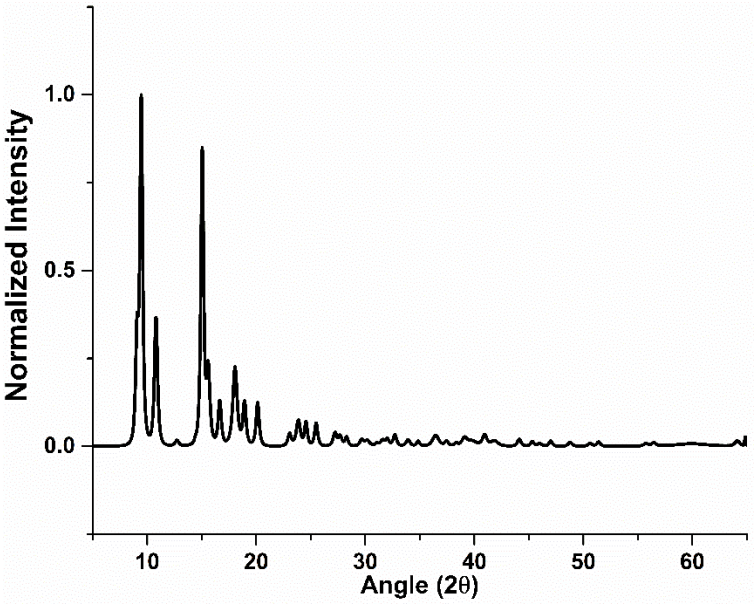

PXRD pattern of **D**. Sample was diffracted from 5.000^{o} to 65.000^{o} with a step size of 0.016^{o}. See included spreadsheet for peak list and corresponding intensities.

5.6.8.3 Infrared Spectroscopy

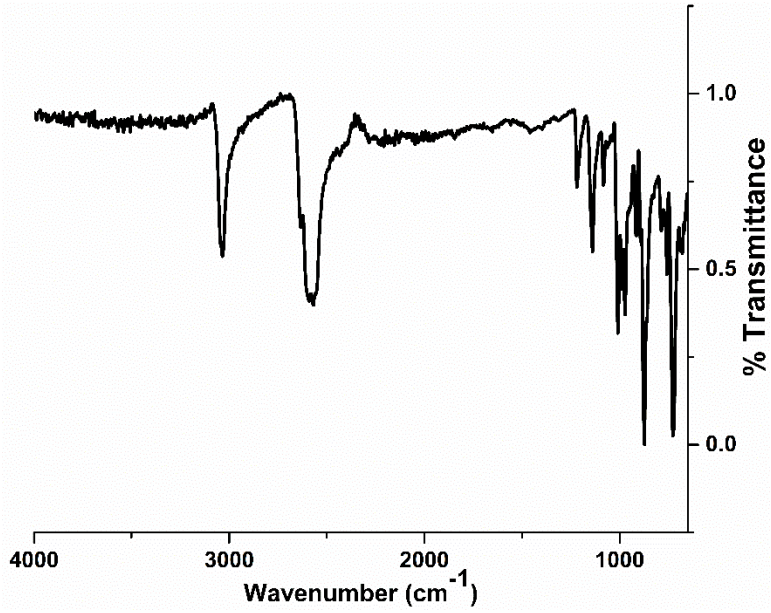

FTIR spectrum of **D** reveals no signals that could be correlated to residual starting material (CuOAC (C=O: ~1500 cm^{-1}), HS-oCB (H-Se: ~2500 cm^{-1}), *iso*-propanol (H-C: ~3000 cm^{-1}; H-O:

~3500 cm^{-1})). Two diagnostic resonances attributed to the carborane cluster (H-$C_{carborane}$: 3000 cm^{-1}; H-$B_{carborane}$: 2500 cm^{-1}) are present and are expected to be slightly asymmetric as a function of the *ortho*-carboranyl-selenolate asymmetry.

5.6.8.4 Thermogravimetric Analysis

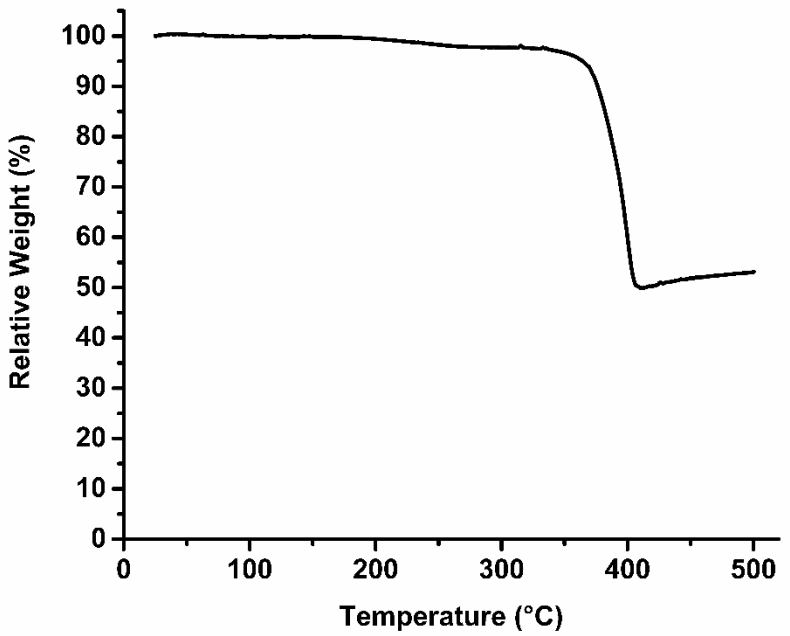

TGA of **D** indicates the material is thermally stable until 375 ^{o}C, after which, the material decomposes until reaching 50% relative weight at 400 ^{o}C. There is no evident desolvation step that would indicate the presence of solvent adducts within the material, which would be expected near 100 ^{o}C.

5.6.8.5 X-ray Photoelectron Microscopy

Cu 2*p* Region of D

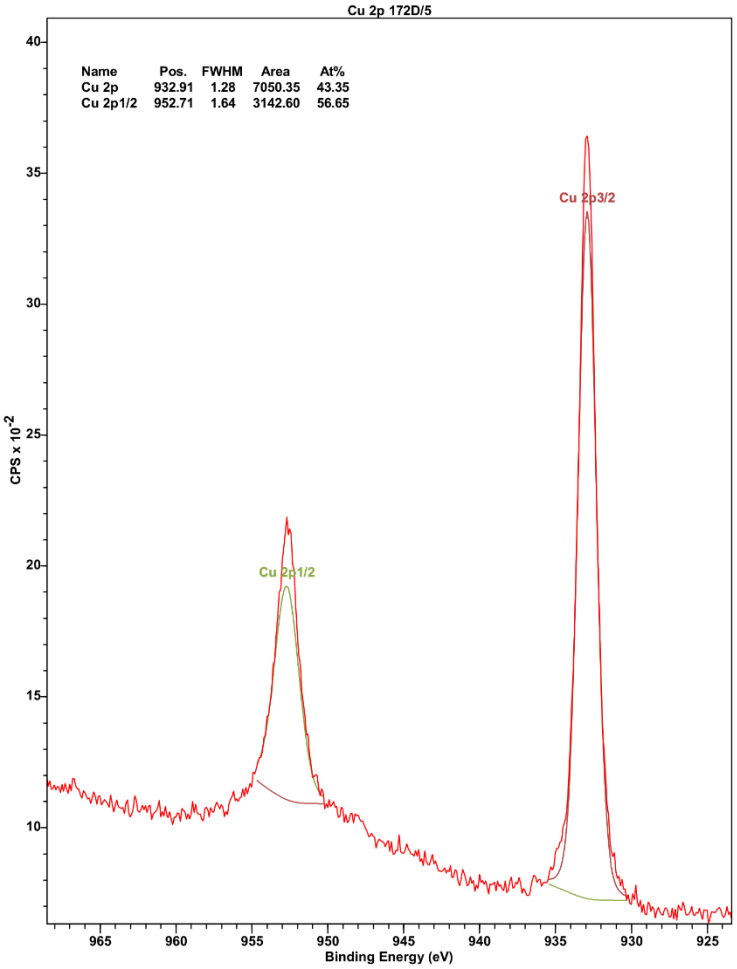

XPS data of **D** was processed and peak-fitted using CasaXPS. Peak fitting indicates the presence of only a single copper(I) environment, and is in agreement with all other structural characterization.

S 2*p* Region of D

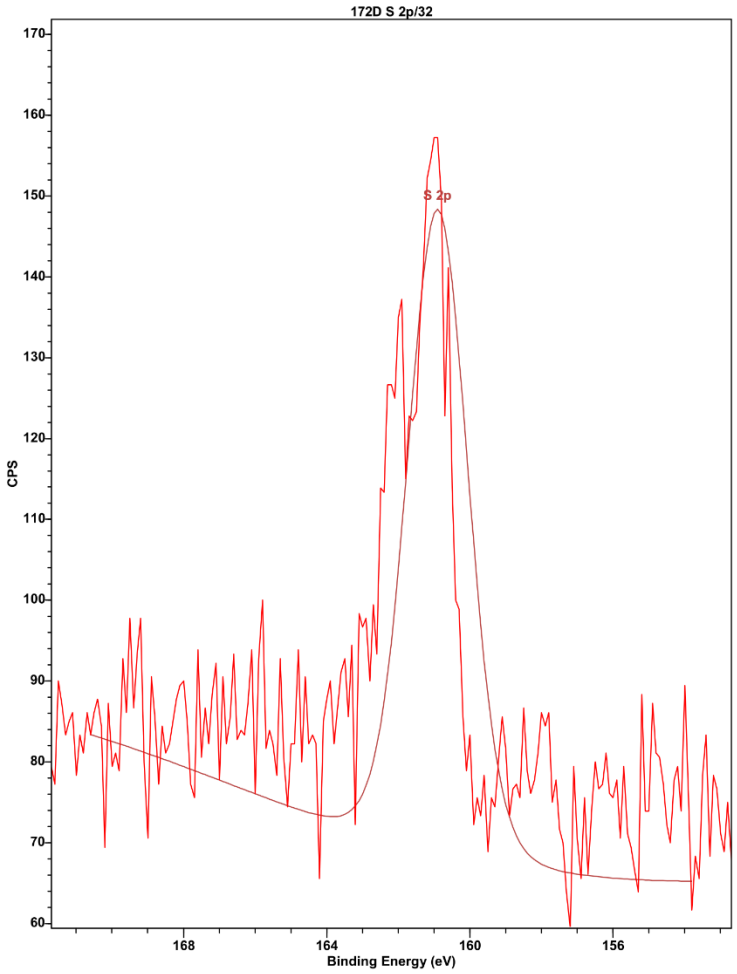

XPS data of **D** was processed and peak-fitted using CasaXPS. Peak fitting indicates the presence of only a single thiolate environment, and is in agreement with all other structural characterization.

Note: The XPS instrument used to obtain measurements currently has decreased sensitivity in the S 2*p* region, resulting in lower signal to noise ration.

5.6.8.6 Photophysical Measurements

Absorption and Emission Measurements

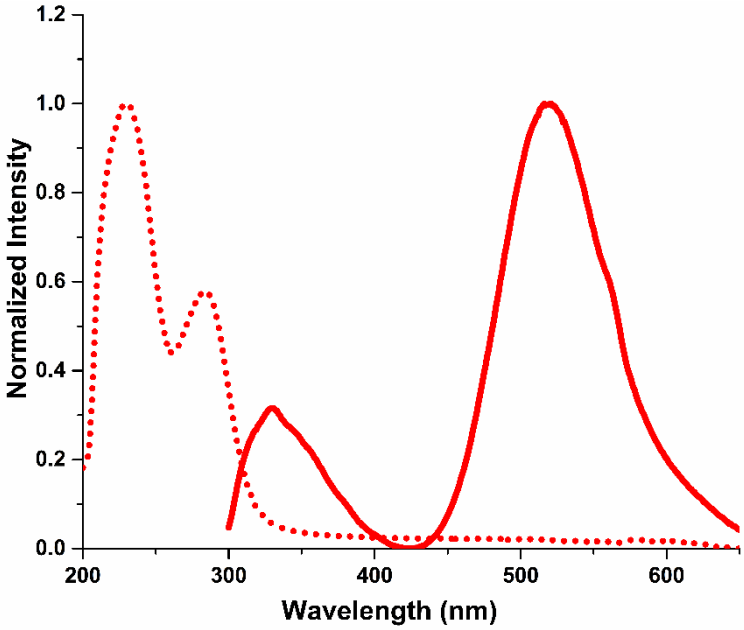

Absorption (dotted trace) and emission (solid trace) of **D** have been normalized and plotted on the same set of axes. Both measurements were performed on suspension of **D** in *iso*-propanol. Emission spectrum was obtained by exciting the suspension with 280 nm light, and the emission was monitored between 300-650 nm. Although not as evident as in materials **A** and **B**, the artifact from the excitation wavelength (280 nm) is present as a slight shoulder at 560 nm.

Comparison of Emission Intensity at Different Excitation Wavelengths

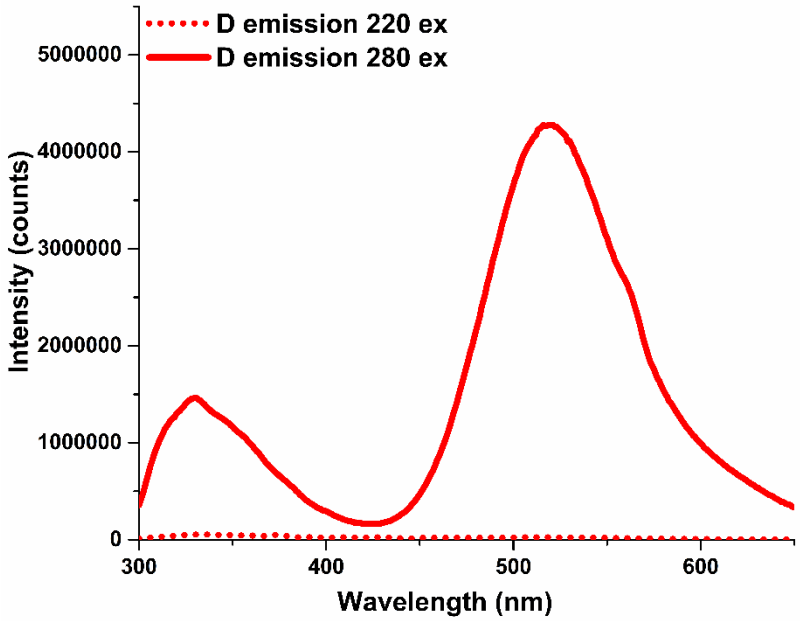

Emission traces when exciting a suspension of **D** in *iso*-propanol at 220 nm (dotted trace) and 280 nm (solid trace). Negligible emission can be correlated to excitation at 220 nm.

Lifetime Measurements

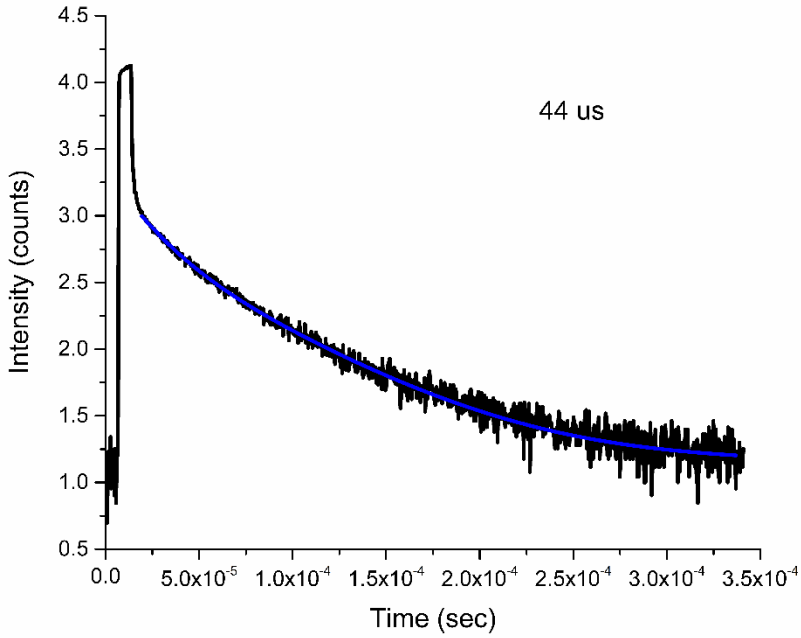

Lifetime plot of **D**, indicating a lifetime emission of 44 µs.

5.6.9 Further Analysis of Literature Copper Selenide Clusters

To further understand the Cu-Se bonding arrangement, a search of the CCDC was performed, targeting the isolated Cu_4Se_4 observed by MicroED. Using ConQuest 2.0.4, a build query was developed using the below search parameters:

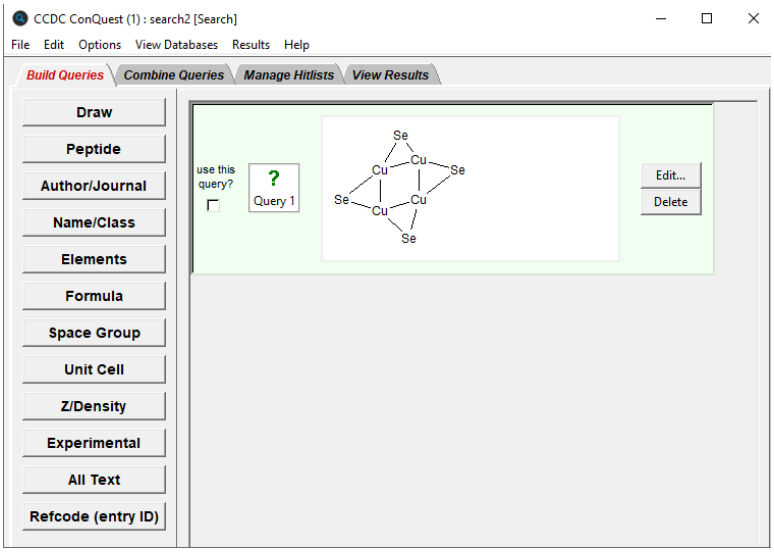

Searching for this bonding arrangement yielded 39 results of crystallographically characterized Cu_4Se_4 bonding units, see below for tabulated RefCodes for each entry.

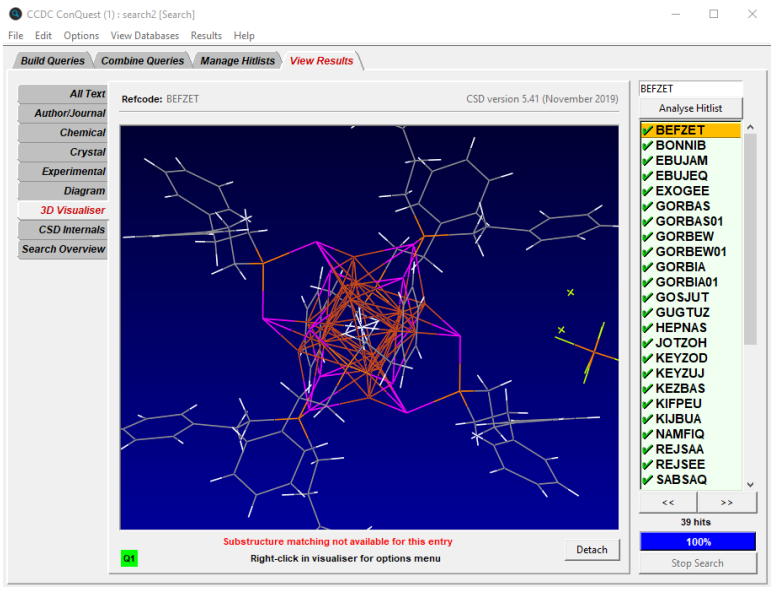

BEFZET	BONNIB	EBUJAM	EBUJEQ	EXOGEE	GORBAS	GORBAS01	GORBEW
GORBEW01	GORBIA	GORBIA01	GOSJUT	GUGTUZ	HEPNAS	JOTZOH	KEYZOD
KEYZUJ	KEZBAS	KIFPEU	KIJBUA	NAMFIQ	REJSAA	REJSEE	SABSAQ
TAMYEL	TUNBIP	VEYROH	VEYRUN	WESQIV	WESQOB	WIXDUF	XAHMAU
XAHMAU01	XAHMEY	XAHMEY01	XAJGIZ	XUBKUA	XUBLAH	YUKBEL	

Surprisingly, over half (21) of the entries consist of larger copper-selenide clusters with complex Cu-Cu and Cu-Se bonding arrangements. Meanwhile, some smaller, molecular, clusters have been crystallographically characterized and contain more analogous Cu_4Se_4 bonding arrangements to that found in **A**. A few selected examples have been rendered below accompanied by their RefCode (atoms comprising the ligands, other than the carbon atom bound to the selenolate have been hidden for clarity).

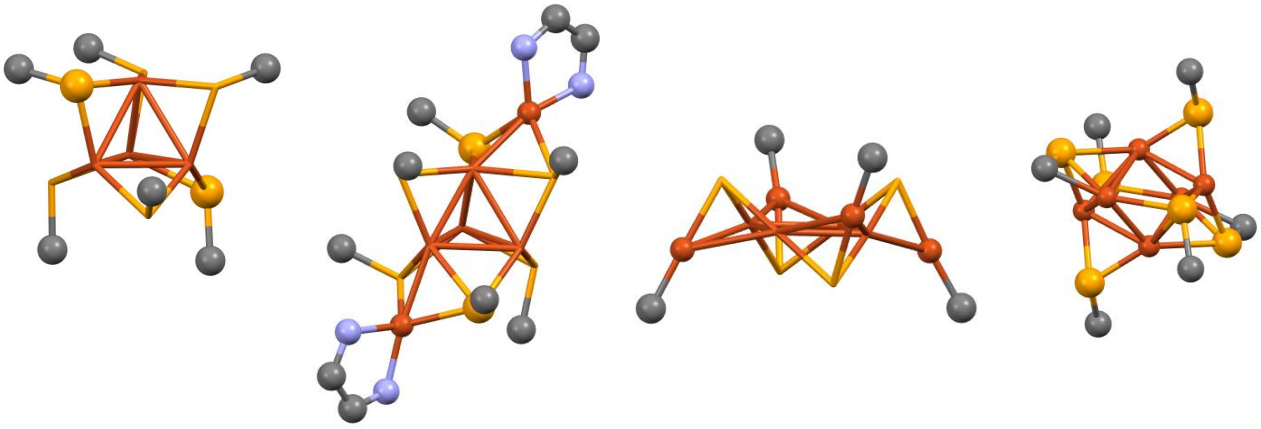

RefCodes (left to right): BONNIB, GUGTUZ, WIXDUF, YUKBEL

Of the smaller clusters, the vast majority contain tetrahedral copper tetramers (see BONNIB, GUGTUZ, YUKBEL) with only one example (WIXDUF, reference 12) somewhat resembling the observed Cu_4Se_4 in material **A** with some notable differences. Unlike in **A**, there are no ligands attached to the selenolate and the cluster is instead structured by N-heterocyclic carbenes bound

to the peripheral copper atoms (see below). Furthermore, the cluster in WIXDUF is substantial larger with an overall molecular formula of Cu_8Se_4.

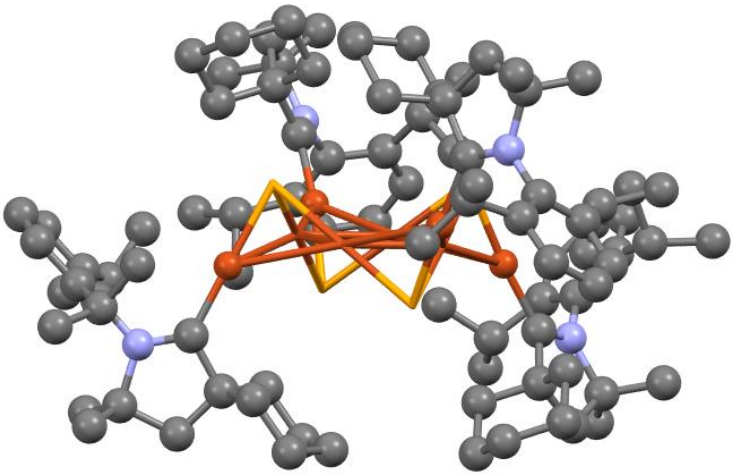

5.6.10 ^{1}H and ^{11}B NMR Experiments of Dissolved Materials A-D

As a further assessment of both purity from starting materials (chalcogenols, *iso*-propanol) in addition to understanding potential intermolecular forces between the copper chalcogenides clusters. Approximately 10 mg of each material was added to an NMR tube and dissolved in 0.4 mL of CD_2Cl_2. Unexpectedly, the materials appear to be only partially soluble in dichloromethane, particularly those containing *ortho*-carborane (see right, samples are **A**, **B**, **C**, **D** from left to right).

In contrast to the purity of the materials suggested by TGA, ^{1}H NMR of **A**-**D** suggested the presence of up to 20% *iso*-propanol. This apparent impurity is likely inflated from the real purity due to the poor solubility of materials **B** and **D**, and should be more closely associated with the lack of solvent adducts observed by TGA. In all ^{1}H NMRs (see below), no chalcogenol resonance is observed and agrees with the experimental FTIR spectra.

^{1}H NMR of A:

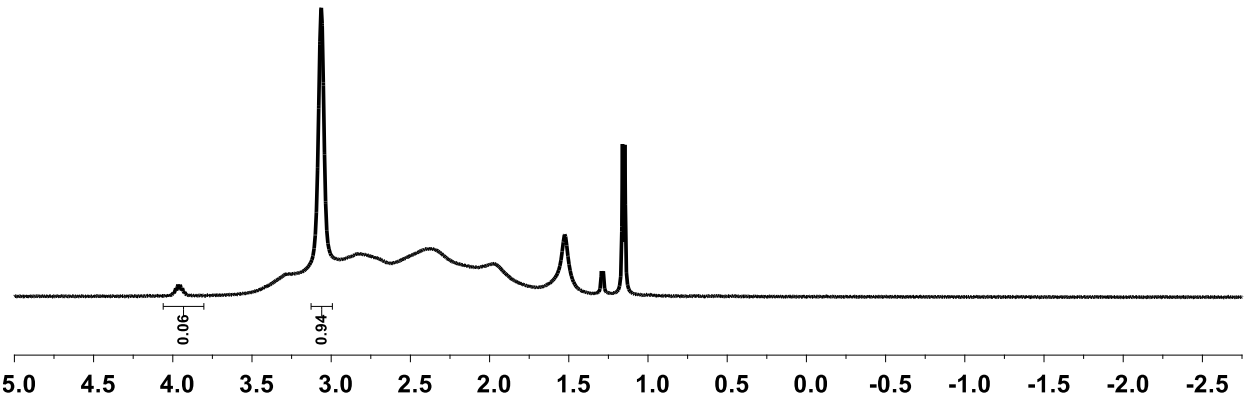

^{1}H NMR of B:

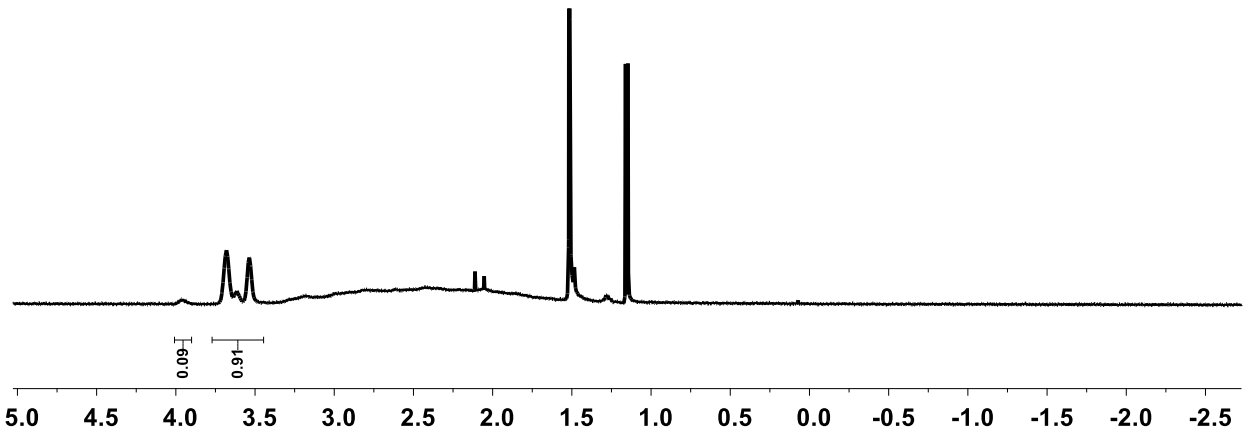

^{1}H NMR of C:

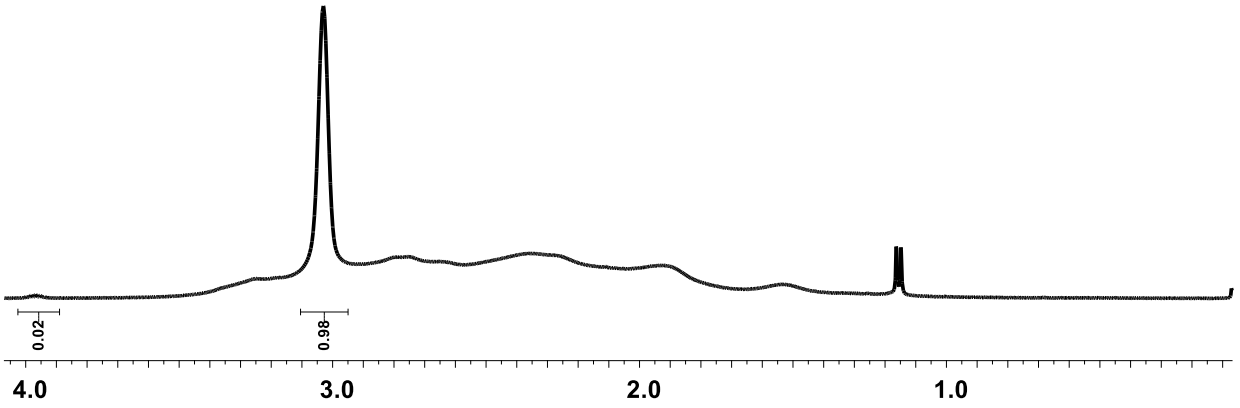

^{1}H NMR of D:

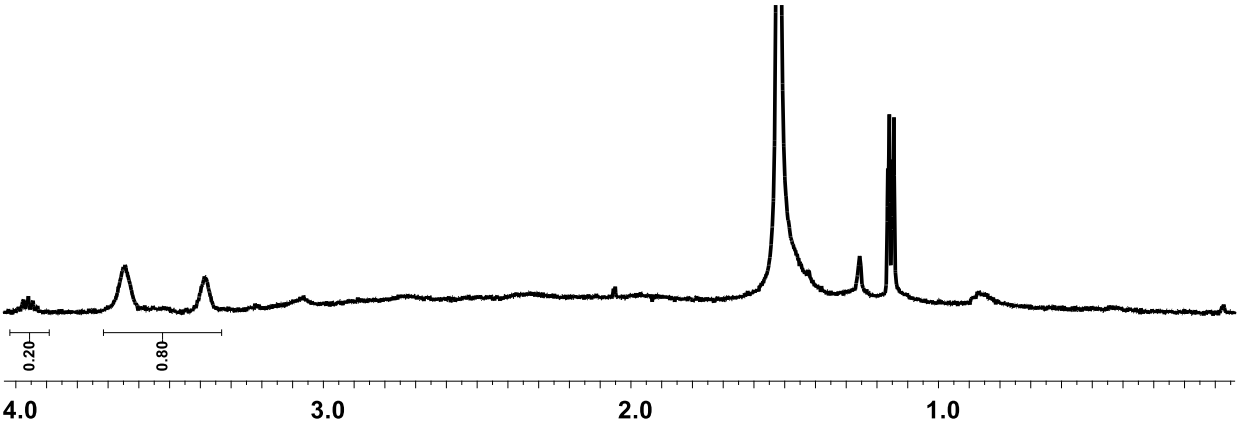

^{11}B NMR spectroscopy of materials **A**-**D** further corroborated the observations made by FTIR spectroscopy (see below). The NMR spectra indicate that the boron cluster cage is fully intact with no decomposition of the cluster observed. As expected, there are slight shifts in the ^{11}B NMR resonances attributed to the boron nucleus bound to the exopolyhedral chalcogen-based substituent (Se, S). More noticeably, however, is the significant broadening of the ^{11}B NMR resonance assigned to the B(3) boron vertex in a position distal to the exopolyhedral boron-chaclogen bond. While this is difficult to see in materials **B** and **D** due to overlapping resonances in the upfield

region, it is quite prominent in materials **A** and **C**. This broadening is likely attributed to the rotation of the carborane cage relative to the exopolyhedral B-Se or B-S bond while the copper cluster is dissolved in solution.

^{11}B NMR of A:

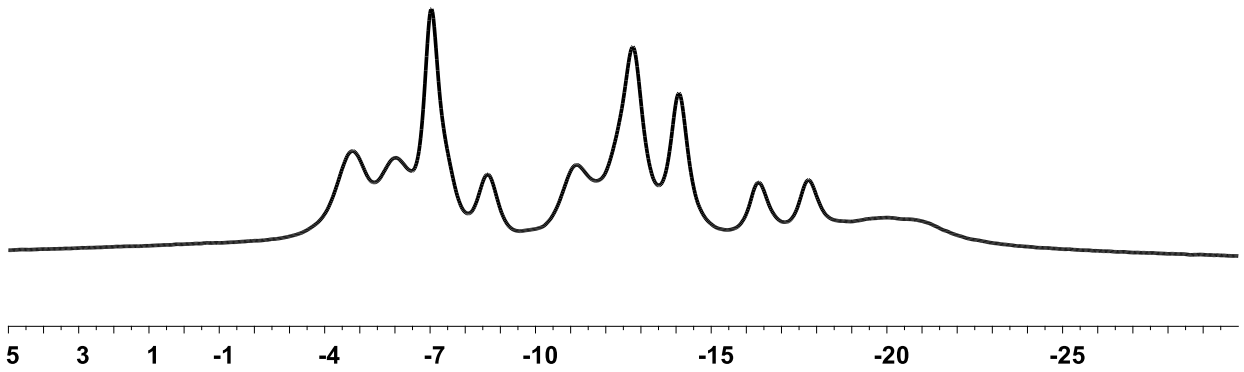

^{11}B NMR of B:

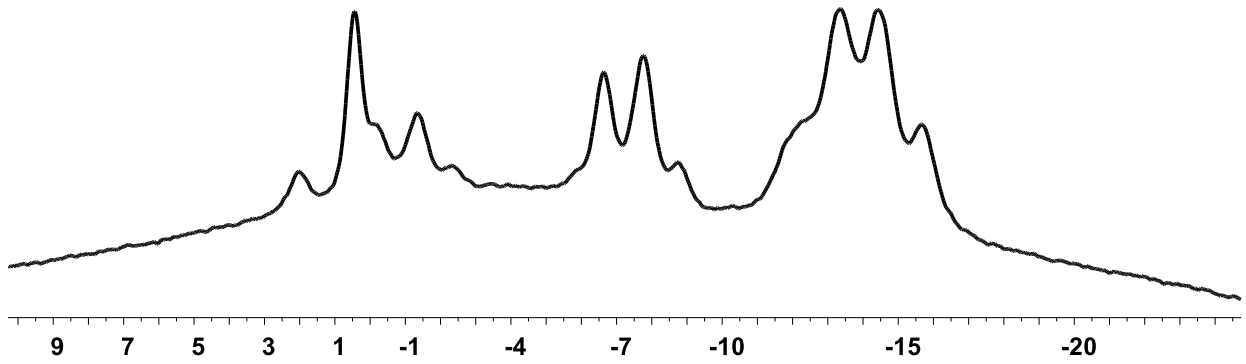

^{11}B NMR of C:

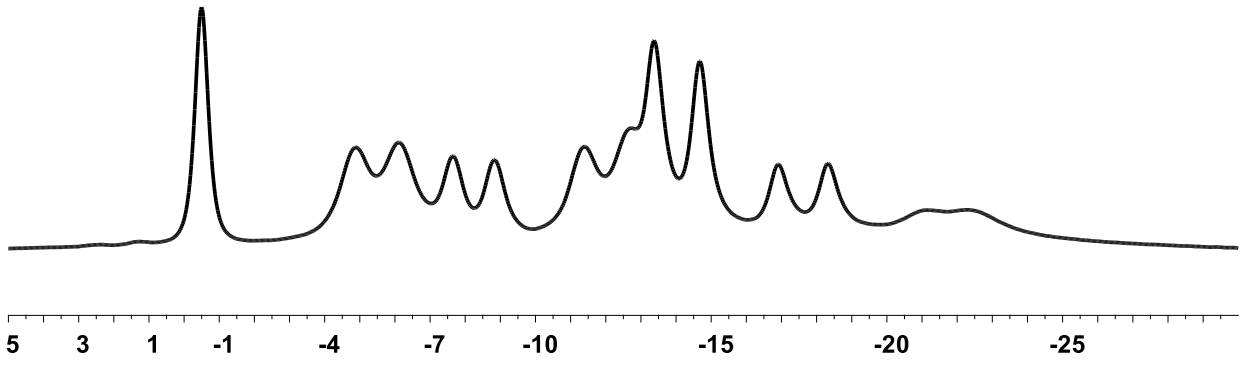

^{11}B NMR of D:

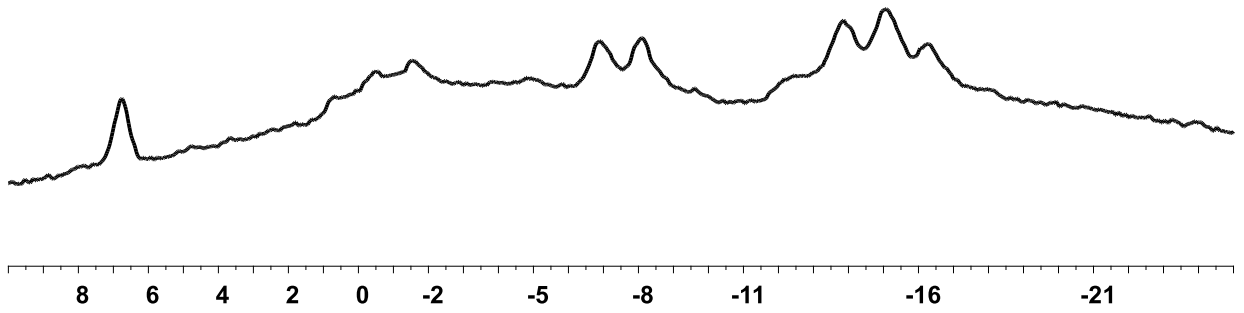

5.6.11 Study and Comparison of Literautre PXRD Patterns with Varying Carborane Isomers and Chalcogens

To validate the observed differences in the PXRD patterns of materials **A** and **B**, **B** and **C**, and **C** and **D**, the comparison of simulated PXRD patterns of molecular carborane-based compounds with different carborane isomer and chalcogens was performed (references 9 and 13).

Comparison of Simulated PXRD for 9-TEMPO-*Ortho*-Carborane and 9-TEMPO-*Meta*-Carborane

Similar to the observed differences in the PXRD peaks between materials **A** and **B**, or **C** and **D**, minor deviations are expected as a result of different molecular packing in the solid state as a result of the carborane dipole. Below you will find the simulated PXRD peak patterns of 9-TEMPO-*ortho*-carborane (green) and 9-TEMPO-*meta*-carborane (black). Despite the molecular similarity between the two TEMPO adducts, the two PXRD patterns show differences on a similar magnitude as seen when comparing the PXRD patterns of materials containing separate carborane isomers.

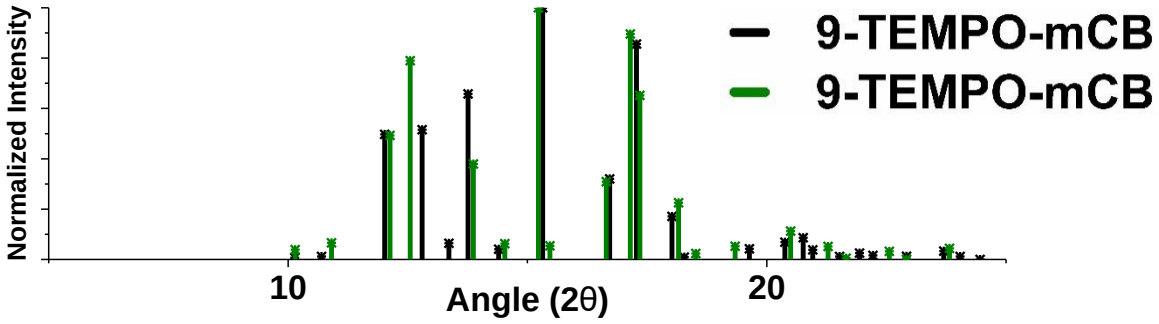

Comparison of Simulated PXRD for *Meta*-Carborane Diselenide and Ditelluride

Similar to the observed differences in the PXRD peaks between materials **A** and **C**, or **B** and **D**, minor deviations are expected as a result of the presence of differently sized chalcogens present in the material. Below you will find the simulated PXRD peak patterns of *meta*-carborane diselenide (black) and *meta*-carborane ditelluride (green). As expected, by increasing the size of the chalcogen present in the crystal, a general shift to lower 2theta values is observed. This trend is also evident when comparing the PXRD patterns of material **A** and **C**, or **B** and **D**

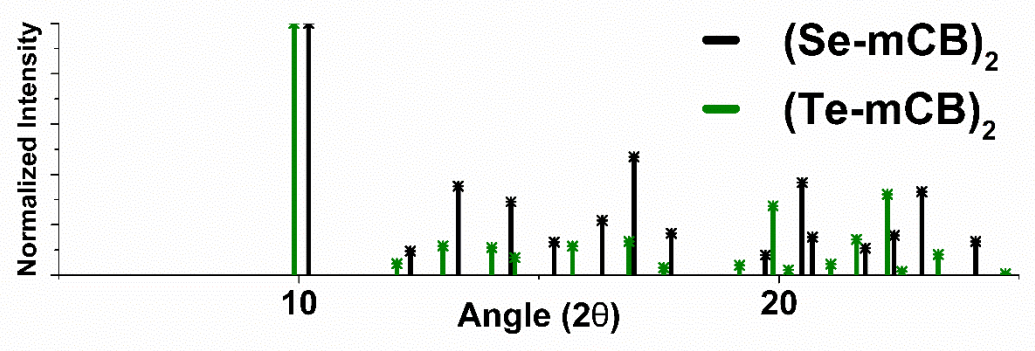

5.6.12 Qualitative Assessment of Emission Properties in Various Solvents and Media

To further understand the emission properties and mechanism at play in materials **A**-**D** the emission of materials **A** and **B** were qualitatively assessed in several solvents and media.

Emission of Soluble Solutions of A and B in Organic Solvents

Surprisingly, all materials are partially soluble in several polar, aprotic organic solvents, and all emissive properties are no longer present after dissolution at room temperature (see below). Unexpectedly, the solubility of **B** in dichloromethane is significantly lower than that of **A**. This is likely a result of the stronger intermolecular forces present in the *ortho*-carborane-containing material hindering dissolution. Upon freezing the solutions of **A** and **B** to 77 K in liquid nitrogen, emission of the copper chalcogenide clusters in all cases return, albeit significantly red-shifted relative to the room temperature emission from the microcrystals as obtained from the reaction mixture (see below). This suggests that emission from the copper chalcogenide clusters occurs only when molecular movements are decreased either through decreasing the temperature of the molecule, as is the case in the below organic solutions, or by enforcing the clusters into a crystalline lattice, where motion would be limited by intermolecular interactions between adjacent clusters.

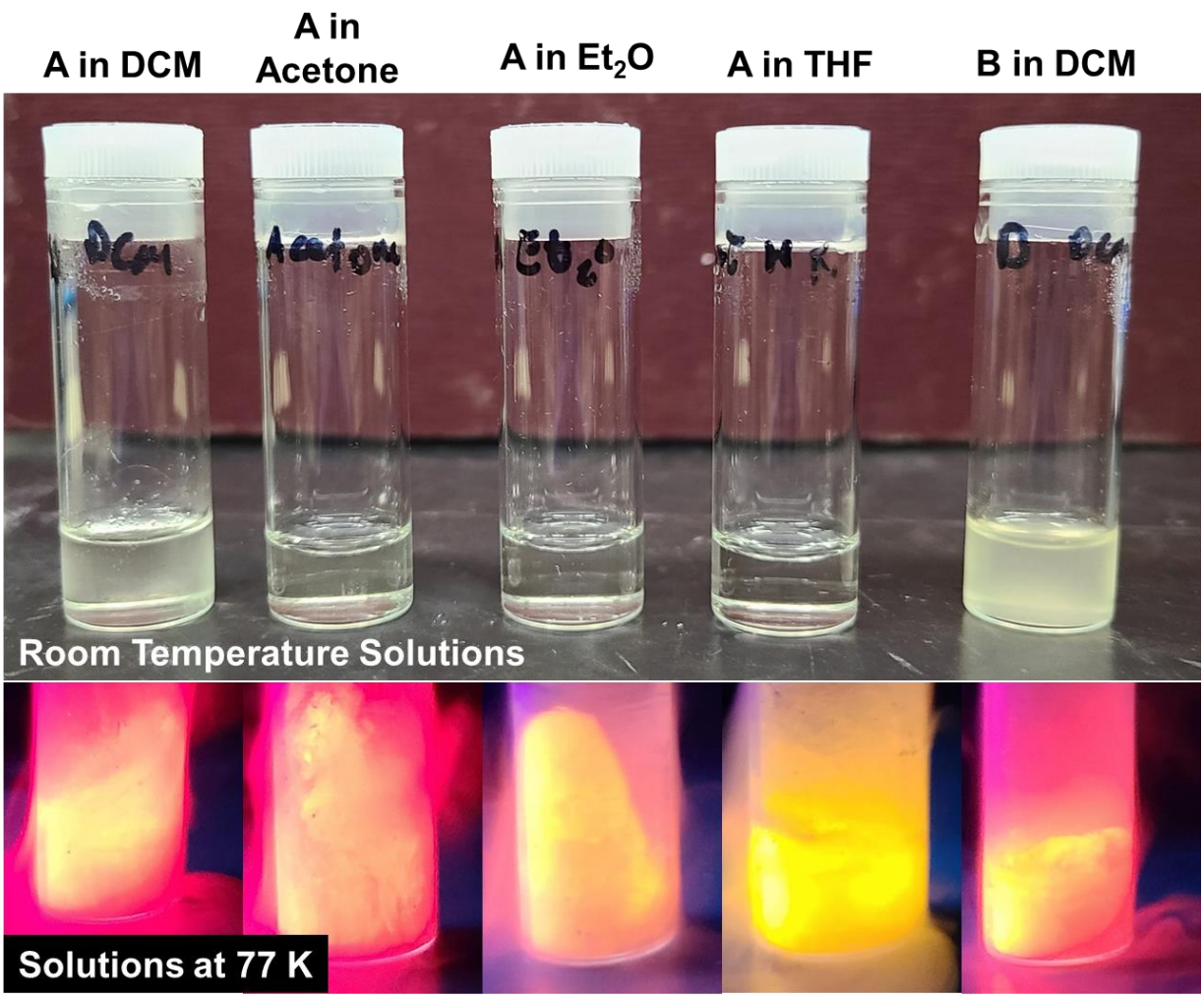

To confirm that the copper selenide clusters were still intact for material **A**, the dichloromethane solution was triturated with pentane, and the acetone solution was layered with *iso*-propanol. In both cases, **A** precipitated, and the initial green emission of the as synthesized microcrystals returned (see below).

Triturated by pentane
from DCM (298 K)

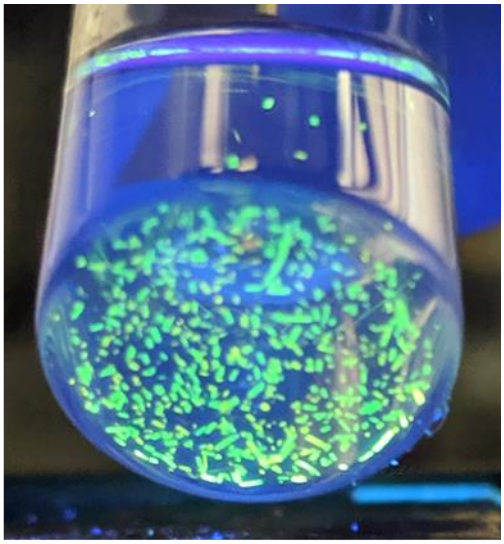

Dissolved in acetone,
layered by IPA (298 K)

Emission of A in Polymer Films

In addition to restricting molecular movement in the excited state by either freezing or crystallizing the copper selenide clusters, movement can also by restricted by a polymer matrix. In this situation, molecular movement would theoretically be limited by intermolecular interactions between the polymer matrix and copper selenide cluster, conceptually similar to crystallization. Solutions of PMMA (top) and polystyrene (bottom) were prepared in dichloromethane before the addition of several milligrams of **A**. Once fully dissolved, the solution were cast onto quartz plates. Surprisingly, the as cast films exhibited similar luminescence to the frozen solutions though were still red-shifted relative to the pristine crystals (see below). This suggest that molecular movement is in fact somewhat limited while in the polymer matrix, but still less of that when in a crystalline matrix.

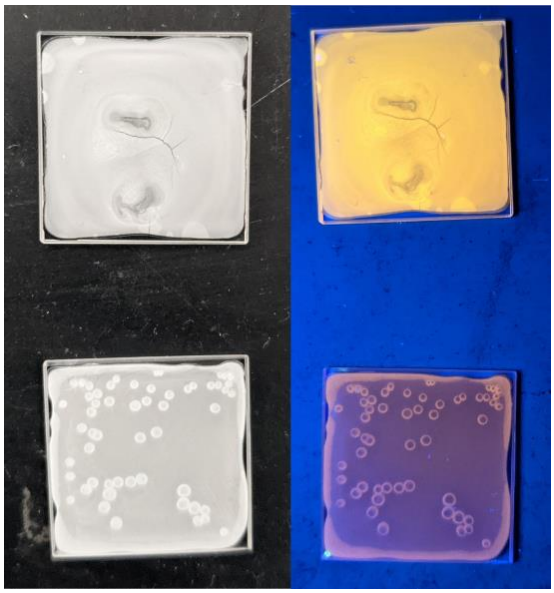

5.6.13 References for Appendix D

1. Lenher *et al. J. Am. Chem. Soc.* **1925** 47, 3, 772-774.
2. Hattne *et al. Acta Crystallogr. A Found. Adv.* **2015**, *71*, 353-360.
3. Nannenga *et al. Nat. Methods* **2014**, *11*, 927-930.
4. Kabsch *Acta Crystallogr. D Biol. Crystallogr.* **2010**, *66*, 125-132.
5. Sheldrick *et al. Acta Crystallogr. A Found. Adv.* **2015**, *71*, 3-8.
6. Hubschle *et al. J. Appl. Crystallogr.* **2011**, *44*, 1281-1284.
7. Peng *Micron* **1999**, *30*, 625-648.
8. Fairley *et al. Applied Surface Science Advances* **2021** doi.org/10.1016/j.apsadv.2021.100112
9. Mills *et al. ChemRxiv* **2021** doi.org/10.33774/chemrxiv-2021-01xcb
10. Plešek *et al. Coll. Czech. Chem. Commun.* **1981**, 46, 687-692.
11. Zakharkin *et al. Phosphorus and Sulfur* **1984**, 20, 357-370.
12. Polgar *et al. Inorg. Chem.* **2019**, 58, 5, 3338-3348.
13. Mils *et al. J. Am. Chem. Soc.* **2020**, 142, 4586-4591.